Université de Liège

UNIVERSITY OF LIEGE
Faculty of Science
Department of Astrophysics,
Geophysics and Oceanography

Detection and characterization of transiting hot Jupiters

A dissertation presented by

Laetitia DELREZ

on September 30, 2016

in fulfillment of the requirements for the degree of

Doctor of Philosophy in Science

Specialization in Space Sciences

Thesis Supervisor:

Dr Michaël Gillon (University of Liege)

Jury Members:

Prof. Denis Grodent, President (University of Liege)
Dr Emmanuël Jehin, Secretary (University of Liege)
Dr Michaël Gillon, Supervisor (University of Liege)
Prof. Coel Hellier (University of Keele)
Prof. Pierre Magain (University of Liege)
Prof. Didier Queloz (University of Cambridge)

Abstract

More than twenty years after the discovery of the first hot Jupiter, the formation, evolution, and atmospheric properties of these extreme short-period gas giants remain poorly understood. This thesis focuses on improving our understanding of these enigmatic worlds through a twofold approach: *(1)* the detection and first characterization of new transiting hot Jupiters, and *(2)* the atmospheric characterization of known transiting gas giants using both transmission and emission spectroscopy.

First, I have been actively involved in the WASP transit survey, taking charge of the photometric follow-up of planetary candidates and confirmed planets with the 0.6m TRAPPIST robotic telescope. This follow-up resulted in the identification of false positives among the planetary candidates and in an improved characterization of many confirmed planets. I contributed in this way to the discovery of about eighty hot Jupiters, among which WASP-68 b, WASP-73 b, WASP-88 b, and WASP-121 b, whose discoveries are reported here.

The hot Jupiters WASP-68 b, WASP-73 b, and WASP-88 b are all three in 4–5 days orbits around evolved late-F/early-G stars, yet they have very different bulk properties. With a mass of $\sim$0.95 $M_{\rm Jup}$ and a radius of $\sim$1.24 $R_{\rm Jup}$, WASP-68 b is a typical hot Jupiter in a $\sim$5.08 days orbit around a G0-type star. WASP-73 b is a dense $\sim$1.88 $M_{\rm Jup}$, $\sim$1.16 $R_{\rm Jup}$ planet, which might be enriched in heavy elements and orbits its F9-type host star every $\sim$4.09 days. With a mass of $\sim$0.56 $M_{\rm Jup}$ and a radius of $\sim$1.70 $R_{\rm Jup}$, WASP-88 b is on the contrary one of the less dense planets known to date, orbiting a F6-type star with a period of $\sim$4.95 days. These three planets illustrate well the great diversity of the hot Jupiter population.

WASP-121 b has a mass of $\sim$1.18 $M_{\rm Jup}$, a super-inflated radius of $\sim$1.86 $R_{\rm Jup}$ and orbits an active F6V star with a very short $\sim$1.27 days period. Its orbital semi-major axis is only $\sim$15% larger than its Roche limit, meaning that the planet might be close to tidal disruption. A measurement of the Rossiter-McLaughlin effect with the CORALIE spectrograph suggests that its orbital axis is significantly misaligned with the spin axis of the host star, which could favor a migration pathway involving few-body dynamical interactions. WASP-121 b is also a prime target for atmospheric characterization, through both transmission and emission spectroscopy. Using TRAPPIST, I detected the planet's occultation in the z'-band (0.9μm) at better than 4-σ, providing a first constraint on its dayside emission spectrum.

In the context of the second approach mentioned above, I studied the transmission spectra of two low-density sub-Jupiters, WASP-49 b and WASP-80 b, between 740 and 1020nm with the FORS2 instrument at the VLT. The transmission spectrum of WASP-49 b does not show any obvious absorption features and is best fitted by atmospheric models containing a cloud deck at a pressure level of 1 mbar or less that efficiently obscures the atmospheric spectral signatures. The transmission spectrum of WASP-80 b shows a slope of increasing effective planetary radius from longer towards shorter wavelengths, detected at a 3.6-σ significance level. This slope is marginally inconsistent with Rayleigh scattering (at the 2.2-σ level) and is not likely to be caused by unocculted star spots or an unresolved stellar object. Except for this slope, the transmission spectrum does not show any obvious additional features.

Finally, I report the results of an intensive ground-based photometric campaign aiming at probing both the transmission and emission spectra of the ultra-short-period hot Jupiter WASP-103 b. The planet's broad-band optical transmission spectrum is found to be better

explained by atmosphere models containing either high-altitude hazes or gaseous TiO. The measurements of the planet's dayside thermal emission in the z' (0.9μm) and $K_{\rm S}$ (2.1μm) bands can be equally well explained by two models: a model with a thermal inversion, low TiO abundance, and high CO abundance, or a model without a thermal inversion and with the opposite composition, i.e. modest CO abundance but a non-negligible TiO abundance. Both models require a TiO abundance of at least $0.1\times$ that predicted for thermochemical equilibrium with solar elemental abundances. More data are needed to confirm these results, distinguish between the two scenarios, and better constrain the atmospheric properties of this extreme hot Jupiter.

Acknowledgements

Many people deserve to be thanked for helping me through this PhD. In the first place, I would like to warmly thank my supervisor, Michaël Gillon. Michaël, thank you for your guidance and support during these four years and for opening up many great opportunities for me. You gave me the opportunity to work in a very stimulating environment with much independence and freedom. I have learned a lot and I am sure this experience will be useful in the future.

A special thanks goes to Pierre Magain. Pierre, thank you for your moral support during these last months, as well as for your great advices and careful reading of the manuscript.

I would like to thank the members of my thesis jury Denis Grodent, Emmanuël Jehin, Coel Hellier, and Didier Queloz for taking the time to read this dissertation. In particular, thank you Didier for welcoming me at Cambridge for the next step of my scientific journey. I am looking forward to this new adventure!

Next, I would like to thank the WASP consortium. It has been a privilege to contribute to this amazingly successful project. Thank you also to Monika Lendl and Amaury Triaud for enthusiastic collaborations and insightful discussions.

Then, I would like to thank all my colleagues here at the Institute. Without you, the day-to-day life would not have been as fun as it was. A special thanks goes to Cyrielle: it has been a great pleasure to share an office with you during these four years. Your support and friendship helped me a lot! Thank you Gaël, for the chats during coffee breaks and for your continuous encouragements. Thank you Sandrine and Angela, for your precious technical support and your availability. Thank you Valérie, Artem, Catarina, Judith, Clémentine, Audrey, Sébastien, Françoise, and Lorraine for the great chats and for your encouragements.

Finally, I would like to thank the most important people in my life: my family and friends. Words have only limited power to express my gratitude to my boyfriend, Julien. Thank you for your unconditional support and for putting up with my emotional ups and downs during these last months. You have always believed in me and managed to instill confidence in me when I needed it. A special thanks to my parents, who allowed me to pursue my dreams and continuously supported me during my studies and the four years of my PhD. None of this would have been possible without you. I also would like to thank my Grandma, Anne-France, Luc, Clarisse, and my lovely godson Lilian. Finally, a big thanks goes to Marimay, Quentin (and my mini-miss Noélia), and Valérie for being the best friends I could have wished for.

Last, thanks to anyone, colleagues, family, or friends, who contributed in some ways to the fulfillment of this work.

Contents

Chapter 1

Introduction

Where do we come from? What is our place in the Universe? Is our Solar System unique? Are there any other worlds with life out there or are we alone? These questions have fascinated mankind since time immemorial. As early as around 400 B.C., the Greek philosopher Metrodorus of Chios was writing: "*A single ear of corn in a large field is as strange as a single world in infinite space.*" About one century later, Epicurus was asserting in his *Letter to Herodotus*: "*There are infinite worlds both like and unlike this world of ours.* [...] *We must believe that in all worlds there are living creatures and plants and other things we see in this world.*" This theory of a *plurality of worlds* has however been overshadowed for more than 1500 years by the geocentric model of Aristotle (ca. 350 B.C.), further developed by Ptolemy in the 2^{nd} century (ca. 130 A.D.), in which the Earth was placed at the center of the Universe and was therefore unique, with all the other celestial bodies revolving around it.

The Copernican Revolution took place in the 16^{th} and 17^{th} centuries. It started in 1543 with the publication by Nicolaus Copernicus of a heliocentric theory, in which the Earth was one of several planets revolving around the Sun and was thus deprived of its unique and privileged status. This theory, though controversial at the time, marked the beginning of a new way of thinking about the design of the Universe. In 1584, the Italian philosopher Giordano Bruno was asserting in his book *De L'infinito Universo E Mondi*: "*There are countless suns and countless earths all rotating around their suns in exactly the same way as the seven planets of our system.* [...] *The countless worlds in the Universe are no worse and no less inhabited than our Earth.*" The heliocentric theory was observationally supported in the early 17^{th} century by Galileo Galilei, who built a powerful (at the time) astronomical telescope and used it to notably discover the four largest moons of Jupiter and to show that Venus had a full set of phases, an observation that could only be explained if Venus was orbiting around the Sun and not the Earth. He also found that the Milky Way was composed of a multitude of stars. Contemporaneously with these remarkable discoveries, Johannes Kepler established his three laws of planetary motion, describing the motions of the planets along elliptical orbits around the Sun. In 1687, Sir Isaac Newton published his famous book *Philosophiæ Naturalis Principia Mathematica*, in which he presented his theory of universal gravitation and his three laws of motion. He demonstrated that the physical laws governing the motions of celestial bodies were the same laws that governed motion on the Earth's surface, and suggested also the possibility of planets orbiting other stars: "*And if the fixed stars are the centers of similar systems, they will all be constructed according to a similar design and subject to the dominion of One.*" Of course, given the limited observational tools available at that time, the existence of planets around stars other than the Sun remained purely speculative.

The first published claim for the detection of an extrasolar planet came in 1855, when Capt. W. S. Jacob (Madras observatory) reported anomalies in astrometric observations of the binary star 70 Ophiuchi that he interpreted as "*evidence in favor of the existence of a*

planetary body in connexion with this system" (Jacob 1855). This detection later turned out to be spurious (Moulton 1899, Heintz 1988) and marked the beginning of a ∼140-year period of exoplanet discovery false alarms. The most famous example is probably the claim by the Dutch astronomer Piet van de Kamp in the 1960s for the astrometric detection of two Jupiter-mass planets around Barnard's star (van de Kamp 1963, van de Kamp 1969), a red dwarf with a large proper motion, located about six light-years from Earth. Although several follow-up studies were unable to confirm the discovery (e.g. Gatewood and Eichhorn 1973) and there was strong evidence that the detected "signal" was in fact related to adjustments and modifications of the telescope's optical system (Hershey 1973), Van de Kamp never acknowledged any error and died in 1995 still convinced of his findings.

The first two *bona fide* extrasolar planets were announced by the radio astronomers Aleksander Wolszczan and Dale Frail in 1992. Those planets of a few Earth masses were found orbiting the millisecond pulsar PSR1257+12 (Wolszczan and Frail 1992), located about 2300 light-years from Earth in the constellation Virgo. They were detected through anomalies in the timing of the radio pulses received from the rapidly rotating neutron star that they orbit and are thought to have likely formed from the remnants of the supernova that produced this neutron star in the first place (second-generation planets, e.g. Wang, Chakrabarty, and Kaplan 2006). Because of the extreme environment of these planets, their discovery was received with only limited enthusiasm.

Three years later, the Swiss astronomers Michel Mayor and Didier Queloz announced a groundbreaking discovery: they had found a giant planet orbiting 51 Pegasi, a Sun-like star located about 50 light-years from Earth in the constellation Pegasus (Mayor and Queloz 1995). This planet was detected using the radial velocity (RV) technique, which consists in measuring the Doppler shifts of the star's spectral lines caused by its back and forth movement around the center of mass of the star-planet system. The observed change in the RV of the star depending on both the mass of the planet and the inclination of its orbital plane relative to the plane of the sky, a parameter that cannot be determined from the RV signal alone, the RV method only yields the minimum mass of the planetary companion (assuming the stellar mass is known). The planet found by Mayor and Queloz (1995), named 51 Peg b, has a minimum mass of 0.5 Jupiter mass and completes its orbit every 4.2 days, at a distance of 0.05 AU from its star (about one eighth of the Sun-Mercury distance). It was the prototype of a new class of planets: the *hot Jupiters*, planets with masses comparable to or larger than Jupiter's mass (noted hereafter $M_{\rm Jup}$), but less than the deuterium-burning mass limit (∼13 $M_{\rm Jup}$), that orbit their host star within 0.1 AU. The existence of this population challenged the existing theories of planet formation and evolution, gas giants not being expected to exist in orbits so close to their star, and led to the introduction of the planetary migration concept. It should be noted, however, that the possible existence of such planets had been suggested as early as 1952 by the Russian-American astronomer Otto Struve, who wrote (Struve 1952): "*We know that stellar companions can exist at very small distances. It is not unreasonable that a planet might exist at a distance of 1/50 astronomical unit, or about 3,000,000 km.* [...] *If the mass of this planet were equal to that of Jupiter, it would cause the observed radial velocity of the parent star to oscillate with a range of ±0.2 km/sec.*" Otto Struve also described how such a planet could be detected by measuring the small drop in the parent star's apparent brightness that would occur if the planet passes (or transits) in front of it, as seen from an Earth-based observer: "*There would, of course, also be eclipses. Assuming that the mean density of the planet is five times that of the star (which may be optimistic for such a*

large planet) the projected eclipsed area is about 1/50th of that of the star, and the loss of light in stellar magnitudes is about 0.02." The first exoplanetary transit was detected by Charbonneau et al. (2000, see also Henry et al. 2000) on HD 209458, a Sun-like star which was known from RV measurements to host a hot Jupiter in a 3.5 days orbit (Mazeh et al. 2000). Transit observations provide a measurement of the orbital inclination and radius of the planet (assuming the stellar radius is known) and, when combined with RV data, allow to derive the planet's true mass. For the first time, it was thus possible to measure the radius and mass of an exoplanet, and constrain its internal composition. The planet orbiting HD 209458 was found to have a mass of 0.7 $M_{\rm Jup}$ and a radius some 40% larger than that of Jupiter (noted hereafter $R_{\rm Jup}$), which confirmed its short-period gas giant nature.

Since these pioneering discoveries, more than three thousand exoplanets have been found and over four thousand candidates are awaiting confirmation[1]. Figure 1.1 presents the exoplanets known to date in a mass vs semi-major axis diagram. They show an astounding diversity in their physical and orbital properties, demonstrating that the characteristics of our Solar System are only one particular outcome in a continuum of possibilities.

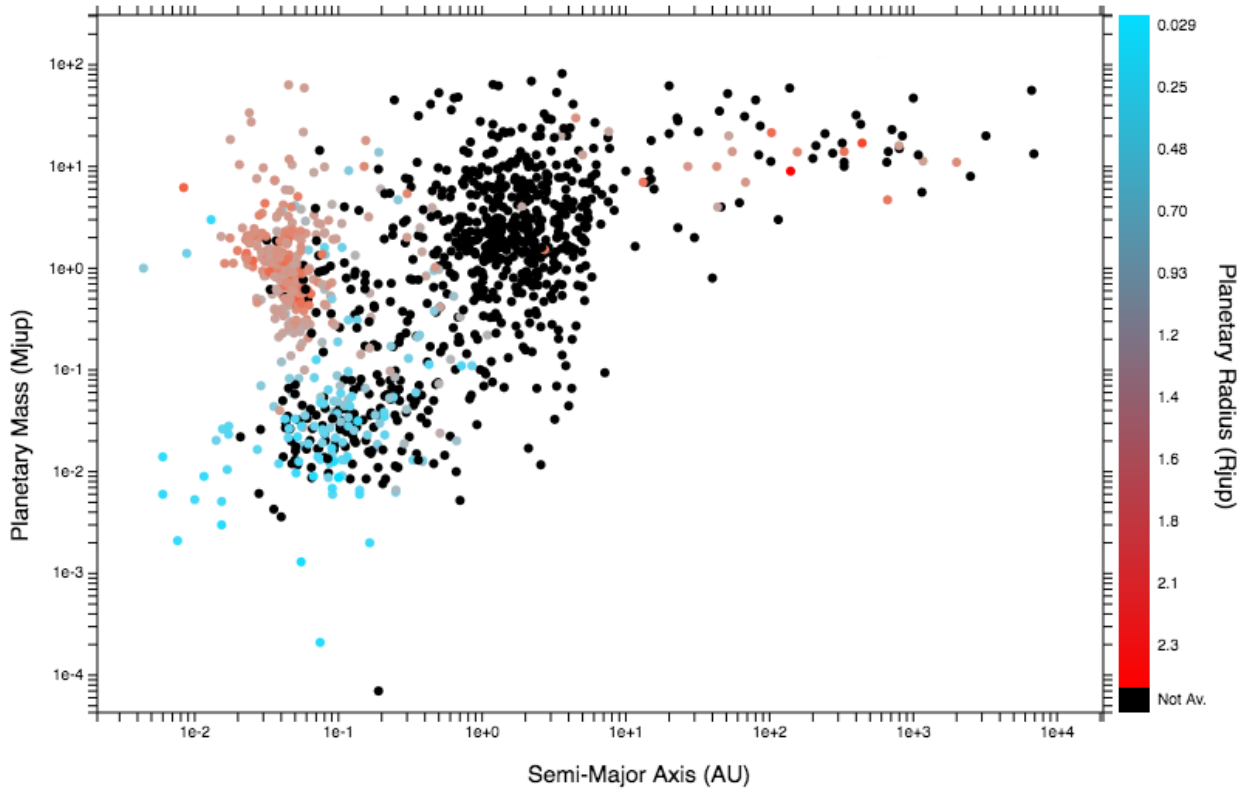

FIGURE 1.1: Known exoplanets as of June 2016 in a mass vs semi-major axis diagram (only planets with estimates of both these parameters are shown). Transiting planets are colored on a scale from blue to red based on their radius. Other planets, which were mostly detected using the RV technique, are plotted in black. Source: `exoplanet.eu`.

To understand how planetary systems form and evolve, and place our Solar System in context, it is necessary to both enlarge our sample by searching for more exoplanets, and characterize these worlds (newly found or previously known) by deriving their structural, orbital, and atmospheric properties as accurately as possible. This thesis focuses on the

[1]Source: NASA Exoplanet Archive (`http://exoplanetarchive.ipac.caltech.edu/`, June 2016).

detection and characterization of transiting hot Jupiters, those extreme and enigmatic gas giants whose formation, evolution, and atmospheric properties are still not fully understood, more than twenty years after the discovery of 51 Peg b. In this introductory chapter, I will first cover the general aspects of transiting exoplanets: the fundamental equations, how transiting planets can be characterized, and how they are found. I will then give a brief overview of the hot Jupiter population and describe where we stand in understanding their origin and physical properties. Finally, I will give the outline of the rest of the thesis.

1.1 Transiting exoplanets

1.1.1 The basics

Geometry of a planetary orbit and transit geometric probability

Kepler's first law of planetary motion states that the orbit of a planet around its star is an ellipse with the star at one focus. In a polar coordinate system centered on the star, the planet's position is given by (Equation 20 of Murray and Correia 2010):

$$r = \frac{a\,(1-e^2)}{1+e\cos f} \tag{1.1}$$

where r is the distance between the planet and the star, a is the orbital semi-major axis, e is the orbital eccentricity, and f is the true anomaly (i.e. the angle between the direction of the periastron and the planet's position as seen from the star, see Fig. 1.2). Consider a Cartesian coordinate system (X, Y, Z) centered on the star, with the $+Z$-axis pointing towards an observer and the sky in the $X-Y$ plane (i.e. the $X-Y$ plane is perpendicular to the line of sight). The line of nodes is defined as the line formed by the intersection of the orbital plane with the plane of the sky. The ascending node is the point where the orbit crosses the plane of the sky, with the planet moving in the $+Z$ direction. The orientation of the line of nodes being usually unknown, we can without loss of generality choose to align the X-axis with it, with the ascending node placed on the $-X$-axis (i.e. the longitude of the ascending node $\Omega = 180°$ in Fig. 1.2). In the (X, Y, Z) coordinate system, the planet's position is expressed as (Equations 2-4 of Winn 2010):

$$X = -r\cos(\omega+f) \tag{1.2}$$
$$Y = -r\sin(\omega+f)\cos i \tag{1.3}$$
$$Z = r\sin(\omega+f)\sin i \tag{1.4}$$

where ω is the argument of periastron (i.e. the angle between the ascending node and the periastron, as seen from the star), and i is the orbital inclination (i.e. the angle between the orbital plane and the plane of the sky). The sky-projected distance $r_{\rm sky}$ between the center of the stellar disc and the center of the planetary disc is then given by:

$$r_{\rm sky} \equiv \sqrt{X^2+Y^2} = r\sqrt{1-\sin^2(\omega+f)\sin^2 i} \tag{1.5}$$
$$= \frac{a\,(1-e^2)}{1+e\cos f}\sqrt{1-\sin^2(\omega+f)\sin^2 i} \tag{1.6}$$

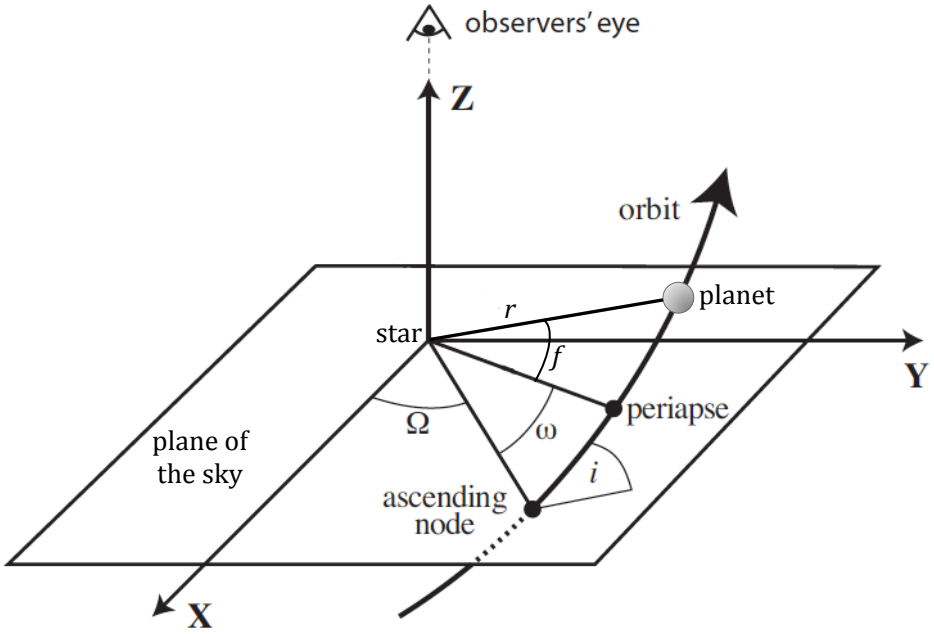

FIGURE 1.2: Geometry of a planetary orbit. The coordinate system as well as the various angles discussed in Section 1.1.1 are shown. Figure adapted from Murray and Correia (2010).

$r_{\rm sky}$ is minimal when X=0, i.e. when the planet is at inferior (X=0, Z>0) or superior (X=0, Z<0) conjunction. If the orbital plane of the planet is oriented so that transits occur, we can consider that these transits are approximately[2] centered around inferior conjunction, for which $f = \pi/2 - \omega$. The transit impact parameter b (see Fig. 1.3), defined as the $r_{\rm sky}$ distance at mid-transit normalized by the stellar radius $R_\star$, can thus be expressed as:

$$b = \frac{a\cos i}{R_\star}\left(\frac{1-e^2}{1+e\sin\omega}\right) \tag{1.7}$$

From the observer's point of view, transits of a planet of radius $R_{\rm p}$ occur if the condition

$$|b| < 1 + \frac{R_{\rm p}}{R_\star} \tag{1.8}$$

is satisfied (cf. Fig. 1.3). If $1 - R_{\rm p}/R_\star < |b| < 1 + R_{\rm p}/R_\star$, the transits are grazing, i.e. only a part of the planetary disc passes in front of the stellar disc. Full (non-grazing) transits occur if $|b| \leq 1 - R_{\rm p}/R_\star$. Using Equation 1.7, we can rewrite the inequality 1.8 as:

$$|\cos i| < \left(\frac{R_\star + R_{\rm p}}{a}\right)\left(\frac{1+e\sin\omega}{1-e^2}\right) \tag{1.9}$$

Since $|\cos i|$ may take any random value between 0 and 1 for a randomly-placed observer, the geometric probability $p_{\rm tra}$ of transits (grazing or full) occurring is given by:

$$p_{\rm tra} = \frac{\int_0^{\left(\frac{R_\star+R_{\rm p}}{a}\right)\left(\frac{1+e\sin\omega}{1-e^2}\right)} \mathrm{d}(\cos i)}{\int_0^1 \mathrm{d}(\cos i)} = \left(\frac{R_\star + R_{\rm p}}{a}\right)\left(\frac{1+e\sin\omega}{1-e^2}\right) \tag{1.10}$$

[2]This approximation is not valid for planets in very eccentric orbits.

In the case of a circular orbit ($e = 0$) and assuming $R_\mathrm{p} \ll R_\star$, this probability can be expressed simply as:

$$p_\mathrm{tra} = \frac{R_\star + R_\mathrm{p}}{a} \approx \frac{R_\star}{a} \tag{1.11}$$

The transit method thus favors the detection of planets in close orbits around their stars. For example, a typical hot Jupiter ($a = 0.05$ AU) orbiting a Sun-like star has a relatively high transit probability of ∼10%. The probability of transits of our Earth being visible to a randomly-placed hypothetical extraterrestrial observer is only ∼0.5%. This probability is even lower for Jupiter, which orbits at about 5.2 AU from the Sun: ∼0.1%.

Period and duration of a transit

The time interval between successive transits is given by the planet's orbital period P, which is related to the orbital semi-major axis a via Kepler's third law of planetary motion:

$$\frac{P^2}{a^3} = \frac{4\pi^2}{G(M_\star + M_\mathrm{p})} \tag{1.12}$$

where G is the universal gravitational constant, $M_\star$ is the stellar mass, and M_p is the planetary mass.

A non-grazing transit is characterized by four contact points, illustrated in Fig. 1.3. First contact occurs when the leading edge of the planetary disc just "touches" the edge of the stellar disc, as seen by the observer. The transit begins at this point. Second and third contacts are respectively the first and last instants when the entire disc of the planet is in front of the stellar disc. These points mark the end of the transit ingress and the beginning of the transit egress, respectively. Fourth contact is when the trailing edge of the planetary disc just "touches" the edge of the stellar disc, marking the end of the transit. The second and third contact points do not occur in the case of a grazing transit. The total transit duration (or width) W, defined as the time interval between first and fourth contacts, is related to the orbital period P by the expression (combination of Equations 14 and 16 of Winn 2010):

$$W = \frac{P}{\pi} \arcsin \left[\frac{R_\star}{a} \frac{\sqrt{\left(1 + \frac{R_\mathrm{p}}{R_\star}\right)^2 - b^2}}{\sin i} \right] \frac{\sqrt{1-e^2}}{1 + e \sin \omega} \tag{1.13}$$

Similarly, the time interval T_F between second and third contacts, during which the planetary disc is fully superimposed on the stellar disc, can be expressed as (combination of Equations 15 and 16 of Winn 2010):

$$T_\mathrm{F} = \frac{P}{\pi} \arcsin \left[\frac{R_\star}{a} \frac{\sqrt{\left(1 - \frac{R_\mathrm{p}}{R_\star}\right)^2 - b^2}}{\sin i} \right] \frac{\sqrt{1-e^2}}{1 + e \sin \omega} \tag{1.14}$$

Details about the derivation of these last two equations can be found e.g. in Winn (2010) and references therein. They are actually obtained using Kepler's second law of planetary

motion, which states that the line joining the planet and the star sweeps out equal areas in equal times. Given a set of orbital parameters, this law can be used to compute the time between any two points on the elliptical orbit. The dependence of W and $T_{\rm F}$ on the impact parameter b (or the orbital inclination i), the other parameters being fixed, is illustrated in Fig. 1.3.

Close-in planets have typical transit durations of a few hours, so that their transits can be easily observed in their entirety from the ground. In contrast, transits of our Earth observed by an hypothetical extraterrestrial observer would last ∼13hrs, while transits of Jupiter would be ∼30hr-long.

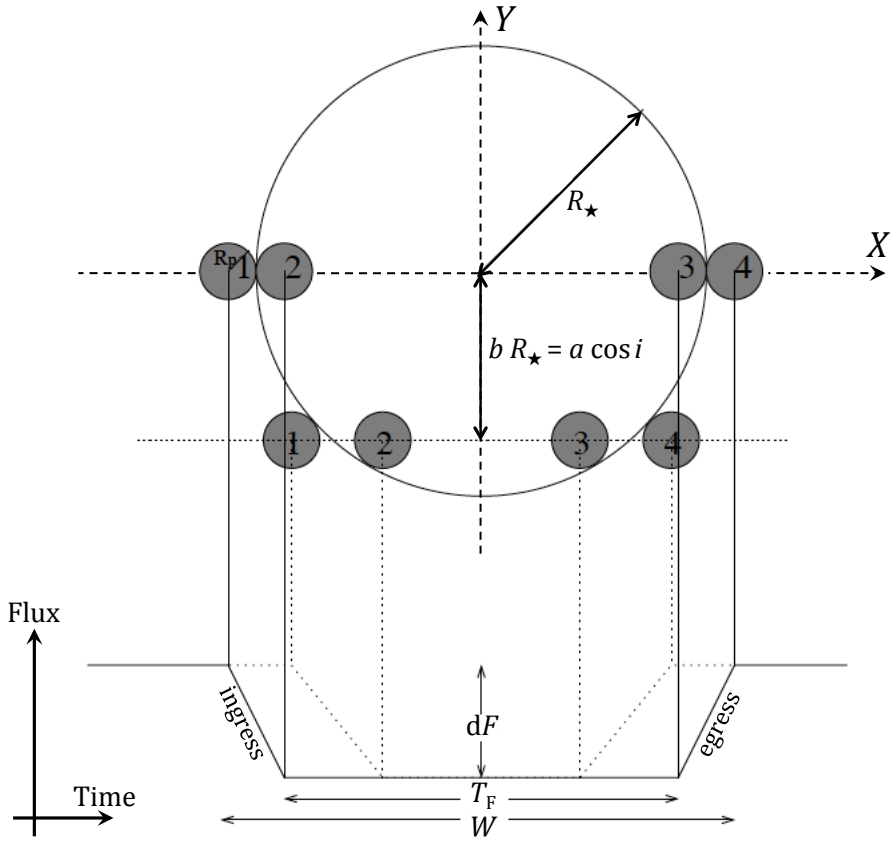

FIGURE 1.3: Illustration of a transit, showing the four contact points (for a planet moving from left to right) and various parameters that are discussed in Section 1.1.1. Two schematic transit light curves are shown at the bottom corresponding to different impact parameters b (or orbital inclinations i). The solid light curve is for a "central" transit ($i = 90°$, $b = 0$), while the dotted light curve is for a transit with a significant impact parameter. The effect of stellar limb-darkening is neglected here. The coordinate system discussed in Section 1.1.1 is also shown. Figure adapted from Seager and Mallén-Ornelas (2003).

Drop in flux during a transit

The transit depth $\mathrm{d}F$ (see Fig. 1.3) is defined as the amplitude of the relative decrease in the combined flux F of the planet and star, due to the planet blocking a fraction of the starlight

during transit:

$$\mathrm{d}F \equiv \frac{F_{\text{no transit}} - F_{\text{transit}}}{F_{\text{no transit}}} \tag{1.15}$$

where $F_{\text{no transit}}$ is the combined flux outside transit and F_{transit} is the combined flux when the entire disc of the planet is in front of the stellar disc. Assuming that the stellar and planetary discs have uniform brightnesses, we have:

$$F_{\text{no transit}} = F_{\star,\mathrm{s}}\pi R_\star^2 + F_{\mathrm{p,s}}\pi R_\mathrm{p}^2 \tag{1.16}$$

$$F_{\text{transit}} = F_{\star,\mathrm{s}}(\pi R_\star^2 - \pi R_\mathrm{p}^2) + F_{\mathrm{p,s}}\pi R_\mathrm{p}^2 \tag{1.17}$$

$$\mathrm{d}F = \frac{F_{\star,\mathrm{s}}\pi R_\mathrm{p}^2}{F_{\star,\mathrm{s}}\pi R_\star^2 + F_{\mathrm{p,s}}\pi R_\mathrm{p}^2} \tag{1.18}$$

where $F_{\star,\mathrm{s}}$ and $F_{\mathrm{p,s}}$ are the surface brightnesses of the star and planet, respectively. During transit (and just before/after), the flux from the planetary disc stems mostly from the planet's nightside and can usually be considered negligible compared to the flux from the stellar disc: $F_{\mathrm{p,s}}\pi R_\mathrm{p}^2 \ll F_{\star,\mathrm{s}}\pi R_\star^2$. We thus have:

$$\mathrm{d}F = \left(\frac{R_\mathrm{p}}{R_\star}\right)^2 \tag{1.19}$$

The transit depth thus provides a direct measurement of the planet's radius relative to the radius of the star. For Jupiter-sized and Earth-sized planets transiting across a Sun-like star, the transit depth is ∼1% and ∼0.01%, respectively.

In practice, the stellar disc does not have a uniform brightness and appears brighter at its center than at its limb (see e.g. Fig. 1.4, left). This phenomenon, known as limb-darkening, can be explained by radiative transfer in the stellar atmosphere and simple geometrical considerations. In brief, most of the light with frequency ν emerging from the star and reaching a distant observer originates, to a first approximation, from layers in the stellar atmosphere with an optical depth[3] $\tau_\nu = 1$ (Eddington-Barbier approximation). Due to the system's geometry, light emerging from the center of the stellar disc and directed towards the observer is traveling radially outwards through the stellar atmosphere (see Fig. 1.4, right). Conversely, light emerging from elsewhere on the stellar disc in the direction towards the observer is traveling through the stellar atmosphere at an angle θ to the radially outwards direction. This means that the optical depth of an atmospheric layer located at a given physical depth below the stellar surface increases towards the limb of the stellar disc. In other words, an optical depth $\tau_\nu = 1$ corresponds to progressively outer and thus (usually) cooler and less emissive layers of the stellar atmosphere from the center towards the limb of the stellar disc, which results in an apparent dimming of the stellar limb.

This limb-darkening is wavelength-dependent. Indeed, the difference in brightness between the center and the limb of the stellar disc at a given wavelength λ can be approximated as the difference in the radiation emitted at this wavelength by two black bodies of different temperatures. The derivative of the Planck function with respect to temperature

[3] At a given frequency ν, the optical depth $\tau_\nu(x)$ of a layer of the stellar atmosphere located at a position x along the line of sight from an observer at infinity is the integral along this line of sight of the opacity $\kappa_\nu(s)$ multiplied by the density $\rho(s)$, with s indicating the position along the line: $\tau_\nu(x) = \int_x^\infty \kappa_\nu(s)\rho(s)\mathrm{d}s$. $\tau_\nu = 0$ at the stellar surface and increases along the line of sight inward into the star.

being roughly proportional to λ^{-4}, limb-darkening is more pronounced at shorter wavelengths.

There are several parametrizations for stellar limb-darkening, a frequently used one being quadratic limb-darkening, which describes the intensity profile $I_{\star,\lambda}$ of the stellar disc at a wavelength λ as:

$$\frac{I_{\star,\lambda}(\mu)}{I_{\star,\lambda}(1)} = 1 - u_{1,\lambda}(1-\mu) - u_{2,\lambda}(1-\mu)^2 \tag{1.20}$$

where $\mu \equiv \cos\theta = \sqrt{1-X^2-Y^2}$, $I_{\star,\lambda}(1)$ is the intensity at the center of the stellar disc ($\theta = 0°$), and ($u_{1,\lambda}$, $u_{2,\lambda}$) are the two quadratic limb-darkening coefficients. Theoretical values of these coefficients can be computed from stellar atmosphere models (see e.g. Claret and Bloemen 2011).

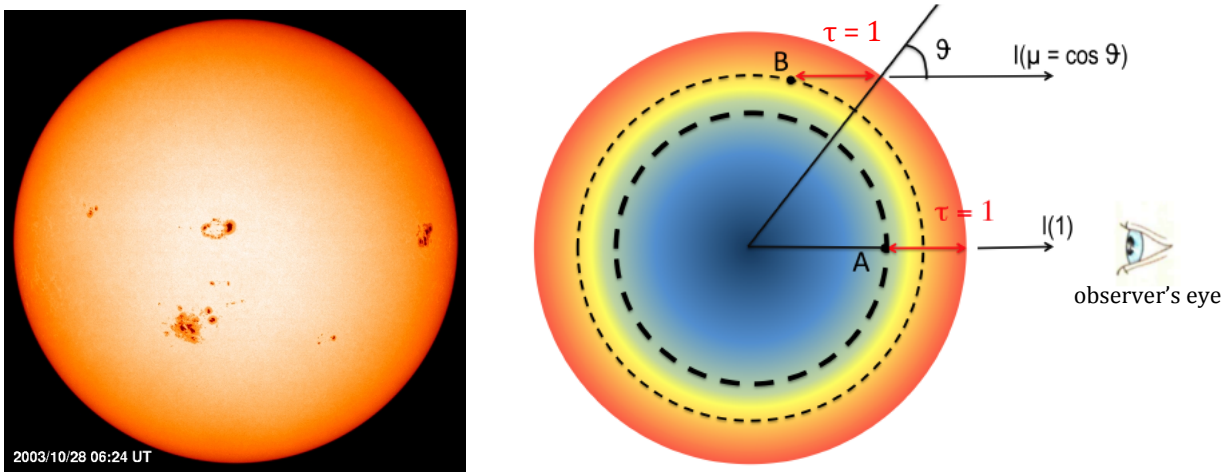

FIGURE 1.4: *Left:* An optical image of the Sun showing the limb-darkening effect, taken from the SOHO gallery: http://sohowww.nascom.nasa.gov/gallery/images/mdi20031028.html. *Right:* Cross-section through a star, with the hotter regions colored in blue and the cooler ones in red. The observer is on the right, at infinity. Points A and B both have an optical depth of unity but are located in atmospheric layers of different temperatures. Figure adapted from Lanotte (2015).

Due to stellar limb-darkening, a transit light curve is not completely flat-bottomed (as the schematic light curves shown in Fig. 1.3) but rather shows a rounded U-shape (see Fig. 1.5), since the planet masks stellar regions of varying brightness during the transit. The flux drop is larger than $(R_\mathrm{p}/R_\star)^2$ near the center of the transit, when the planetary disc covers bright regions of the stellar disc. Conversely, it is lower than $(R_\mathrm{p}/R_\star)^2$ when the planetary disc is near the limb of the stellar disc and masks dimmer regions. Due to the wavelength-dependence of stellar limb-darkening, this effect is increasingly pronounced for transits observed at shorter wavelengths (see Fig. 1.5).

Precise calculation of the drop in flux at any given time during a transit (at a wavelength λ) requires integrating the intensity $I_{\star,\lambda}(\mu)$ over the area of the stellar disc that is occulted by the planet at this time. The most widely used analytical model of transit light curve is that of Mandel and Agol (2002). This model takes as inputs the sky-projected distance between the centers of the stellar and planetary discs (Equation 1.6) normalized by the stellar radius

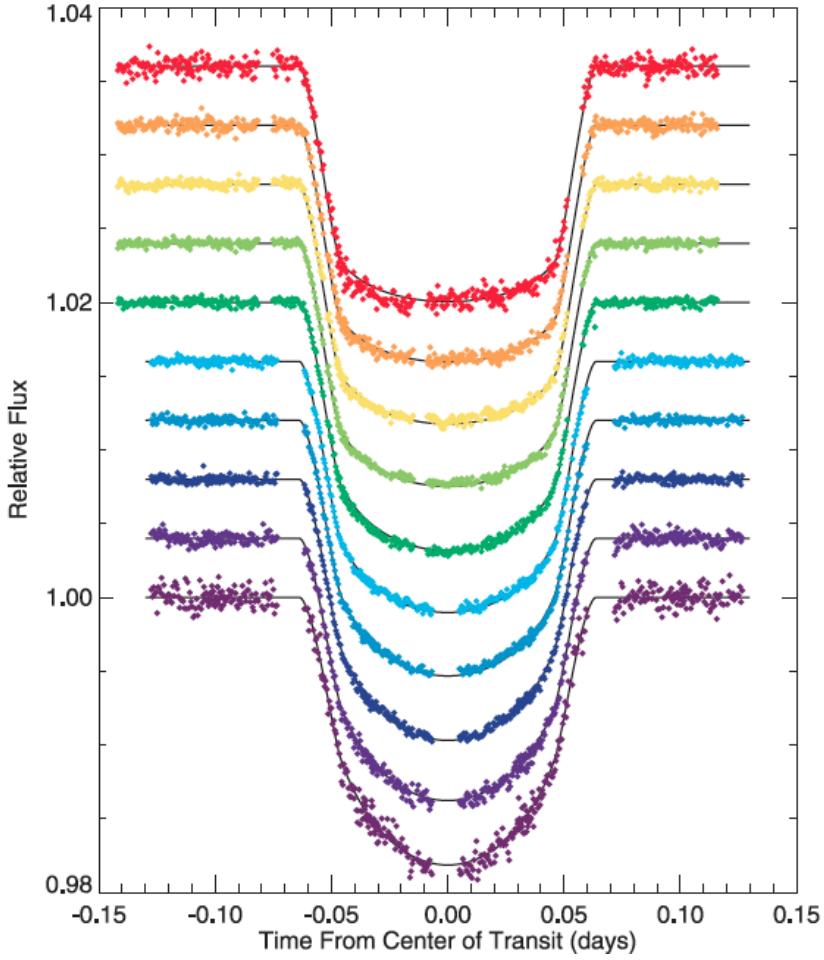

FIGURE 1.5: Multi-color transit light curves of the hot Jupiter HD 209458 b obtained using the STIS spectrograph on the *Hubble Space Telescope*. The different passbands of the light curves span the wavelength range from 290nm (bottom) to 1030nm (top). The light curves are shifted along the y-axis for clarity. The shorter the wavelength, the stronger the stellar limb-darkening effect. Figure 3 of Knutson et al. (2007).

($r_{\rm sky}/R_\star$), the planet-to-star radius ratio ($R_{\rm p}/R_\star$), and the limb-darkening coefficients ($u_{1,\lambda}$ and $u_{2,\lambda}$ if a quadratic limb-darkening is assumed), and provides the corresponding flux deficit assuming a spherical limb-darkened star and an opaque, dark, and spherical planet.

Besides limb-darkening, stellar active regions (dark spots or bright plages) also affect the brightness of the stellar disc. Depending on their size and flux ratio with the quiet photosphere, anomalies can be observed in the transit light curve when the planet masks them. Generally speaking, a planetary transit thus provides a way of mapping the stellar surface along the transit chord (see e.g. Silva-Valio and Lanza 2011).

1.1.2 Characterization of transiting exoplanets

In this section, I will describe the main methods by which transiting planets can be characterized. The major results that were obtained with these methods regarding the hot Jupiter population during the last fifteen years will be briefly presented in Section 1.2.

System physical parameters

Several physical parameters of a planetary system can be directly derived from light curves of its transits. The full data analysis procedure used in this thesis to derive the transit and physical parameters of the studied planetary systems will be described in detail in Chapter 2 (Section 2). Here, I only present some simplified expressions for the case of a circular orbit ($e = 0$) and assuming $R_\star \ll a$, with the aim of giving a sense of how transit light curves can constrain system parameters.

Transit light curves offer the four observables $\mathrm{d}F$, W, T_F, and P (if at least two transits are observed). In the limiting case described above, the planet-to-star radius ratio $R_\mathrm{p}/R_\star$, the transit impact parameter b, and the scale parameter $a/R_\star$ can be directly derived from these observables:

$$\frac{R_\mathrm{p}}{R_\star} = \sqrt{\mathrm{d}F} \tag{1.21}$$

$$b = \sqrt{\frac{(1-\sqrt{\mathrm{d}F})^2 - \left(\frac{T_\mathrm{F}}{W}\right)^2 (1+\sqrt{\mathrm{d}F})^2}{1-\left(\frac{T_\mathrm{F}}{W}\right)^2}} \tag{1.22}$$

$$\frac{a}{R_\star} = \frac{2\,P}{\pi} \frac{\mathrm{d}F^{1/4}}{\sqrt{W^2 - T_\mathrm{F}^2}} \tag{1.23}$$

The expression 1.21 follows directly from Equation 1.19, while expressions 1.22 and 1.23 (Equations 17 and 18 of Seager and Mallén-Ornelas 2003) are obtained by inverting Equations 1.13 and 1.14. Since $b = (a/R_\star)\cos i$ for a circular orbit (Equation 1.7 with $e = 0$), the orbital inclination i can be directly deduced from b and $a/R_\star$. Under the reasonable assumption that $M_\mathrm{p} \ll M_\star$, the mean stellar density $\rho_\star \equiv M_\star/(\frac{4}{3}\pi R_\star^3)$ can also be derived from $a/R_\star$ via Kepler's third law (Seager and Mallén-Ornelas 2003):

$$a^3 = \frac{P^2 G}{4\pi^2}(M_\star + M_\mathrm{p}) \approx \frac{P^2 G M_\star}{4\pi^2} \tag{1.24}$$

$$\Leftrightarrow \frac{a^3}{R_\star^3} \approx \left(\frac{P^2 G M_\star}{4\pi^2}\right)\frac{1}{R_\star^3} \tag{1.25}$$

$$\Leftrightarrow \rho_\star \approx \frac{3\pi}{P^2 G}\left(\frac{a}{R_\star}\right)^3 \tag{1.26}$$

Transit light curves thus give access to a number of system parameters. However, they do not provide absolute values for R_p and a, but relative quantities with respect to the stellar radius $R_\star$, and reveal nothing about the planetary mass M_p. Radial velocity measurements of the star as well as some external information about its properties are needed to evaluate these key parameters of the planet.

The radial velocity V_r of the star orbiting around the barycenter of the star-planet system is expressed as (see e.g. Murray and Correia 2010):

$$V_\mathrm{r} = V_\gamma + K\left[\cos(\omega + f) + e\cos\omega\right] \tag{1.27}$$

where V_γ is the systemic velocity (the radial velocity of the system's barycenter) and K is the RV semi-amplitude, given by:

$$K = \frac{M_\mathrm{p} \sin i}{(M_\mathrm{p} + M_\star)^{2/3} \sqrt{1-e^2}} \left(\frac{2\pi G}{P}\right)^{1/3} \tag{1.28}$$

Assuming $M_\mathrm{p} \ll M_\star$, RV observations thus constrain the quantity:

$$\frac{M_\mathrm{p} \sin i}{M_\star^{2/3}} = K\sqrt{1-e^2} \left(\frac{P}{2\pi G}\right)^{1/3} \tag{1.29}$$

where K, e, and P are measured from the RV signal. Alone, RV observations thus provide the minimum planetary mass $M_\mathrm{p} \sin i$ with respect to $M_\star$. In the case of a transiting planet, i is obtained from the transit light curves (see above) and the $M_\mathrm{p} \sin i$ degeneracy can be broken. While transits provide the planet-to-star radius ratio $R_\mathrm{p}/R_\star$, radial velocities thus yield the mass ratio $M_\mathrm{p}/M_\star^{2/3}$.

To determine the absolute radius R_p and mass M_p of the planet, it is necessary to supplement the transit and RV data with some additional information about the star, obtained e.g. from a spectroscopic analysis, stellar evolution models, empirical laws calibrated on eclipsing binaries, interferometry, or asteroseismology. A typical approach is to use the stellar density $\rho_\star$ derived from the transit light curves, together with the stellar effective temperature T_eff and metallicity [Fe/H] obtained from a spectroscopic analysis, as inputs of stellar evolution models or empirical laws in order to constrain $M_\star$. The stellar radius $R_\star$ is derived from $M_\star$ and $\rho_\star$, and the parameters a, R_p, and M_p then follow. At this point, other parameters of interest that can immediately be obtained are the planet's surface gravity $g_\mathrm{p} \equiv GM_\mathrm{p}/R_\mathrm{p}^2$ and mean density $\rho_\mathrm{p} \equiv M_\mathrm{p}/(\frac{4}{3}\pi R_\mathrm{p}^3)$, from which inferences regarding its internal composition may be drawn (see e.g. Fortney, Marley, and Barnes 2007).

The Rossiter-McLaughlin effect

The transit of a planet in front of a rotating star produces variations of the line profiles in the stellar spectrum. Unless the spin axis of the star points exactly towards the observer, light from one half of the stellar disc is blueshifted because this part of the disc is rotating towards the observer, while light from the other, receding, half is redshifted. Outside of transits, the spin of the star simply results in a broadening of the lines of the stellar spectrum, with no overall Doppler shift[4], the starlight being integrated over the entire unresolved disc. During transits, the planet blocks some of the starlight, either blueshifted or redshifted depending on the planet's location in front of the stellar disc. This causes a distortion of the line profile and an anomaly in the measured radial velocity (see Fig. 1.6). When the planet covers part of the blueshifted (resp. redshifted) hemisphere, the disc-integrated starlight appears slightly redshifted (resp. blueshifted), and the measured radial velocity is higher (resp. lower) than the value expected from the star's orbital motion.

Depending on the orientation of the stellar rotation axis, the speed of this rotation, and the path the planet takes across the stellar disc, the anomaly observed in the RV signal has a different shape and amplitude. Modeling of this effect thus provides the projected rotation

[4] Apart from the Doppler shift caused by the star's orbital motion around the barycenter of the star-planet system.

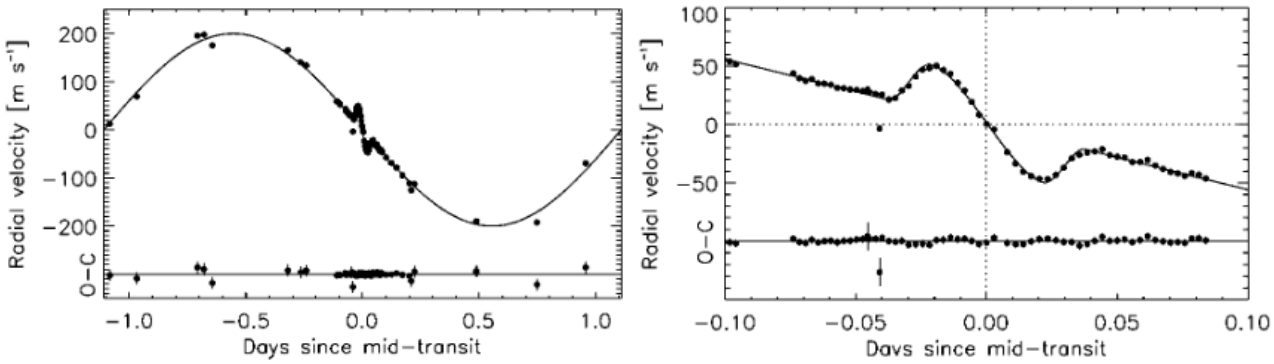

FIGURE 1.6: *Left:* Radial velocities obtained for HD 189733, a star with a transiting hot Jupiter, folded on the planet's orbital period. During transit, the RVs depart from the expected orbital signal. *Right:* Zoom on this anomaly. Figure from Winn et al. (2006).

velocity $v_\star \sin i_\star$ of the star (where the stellar inclination $i_\star$ is the angle between the stellar spin axis and the line of sight) and the sky-projected obliquity β, i.e. the sky-projected angle between the spin axis of the star and the orbital axis of the planet. β is of prime importance in constraining the dynamical history of the planet, notably its migration pathway (e.g. Fabrycky and Winn 2009, Morton and Johnson 2011).

Figure 1.7 shows the dependence of the RV anomaly on β. If the planet's orbital axis is aligned with the stellar spin axis ($\beta = 0°$), the perturbation to the orbital RV is antisymmetric about the time of mid-transit (left panel). Conversely, if the orbit is strongly misaligned and the planet blocks only red-shifted light from the receding half of the stellar disc during transits (right panel), then only an anomalous decrease is seen in the measured RV. The maximum amplitude of the signal, observed if the orbit is aligned ($\beta = 0°$) or anti-aligned ($\beta = 180°$), is approximately:

$$\Delta V_\mathrm{r} \approx \left(\frac{R_\mathrm{p}}{R_\star}\right)^2 \sqrt{1-b^2}\ v_\star \sin i_\star \tag{1.30}$$

For Jupiter-sized and Earth-sized planets transiting across a Sun-like star ($v_\star \sin i_\star \sim 2\mathrm{km/s}$), this maximum amplitude is ∼20m/s and ∼0.2m/s (assuming $b = 0$), respectively.

The RV anomaly is known as the Rossiter-McLaughlin (RM) effect, after the two astronomers who achieved in 1924 the first definitive measurements of this effect for eclipsing binary stars, where it is also seen (Rossiter 1924, McLaughlin 1924). The first successful measurement of the RM effect of a transiting exoplanet was for HD 209458 b by Queloz et al. (2000). Since then, it has been detected for many planetary systems (see e.g. Triaud et al. 2010, Albrecht et al. 2012). I will elaborate a bit on this in Section 1.2.1.

Transmission spectroscopy

So far, we have assumed that the transit depth and thus the inferred planetary radius are wavelength-independent. This is not accurate for a planet possessing an atmosphere. During a transit, some of the starlight is filtered through the planet's atmosphere at the day-night terminator region, where it is more or less absorbed and scattered by the atmospheric constituents depending on the wavelength considered. This translates into a wavelength-dependent transit depth $\mathrm{d}F_\lambda$ and effective planetary radius $R_{\mathrm{p},\lambda} = R_\star\sqrt{\mathrm{d}F_\lambda}$. Measuring

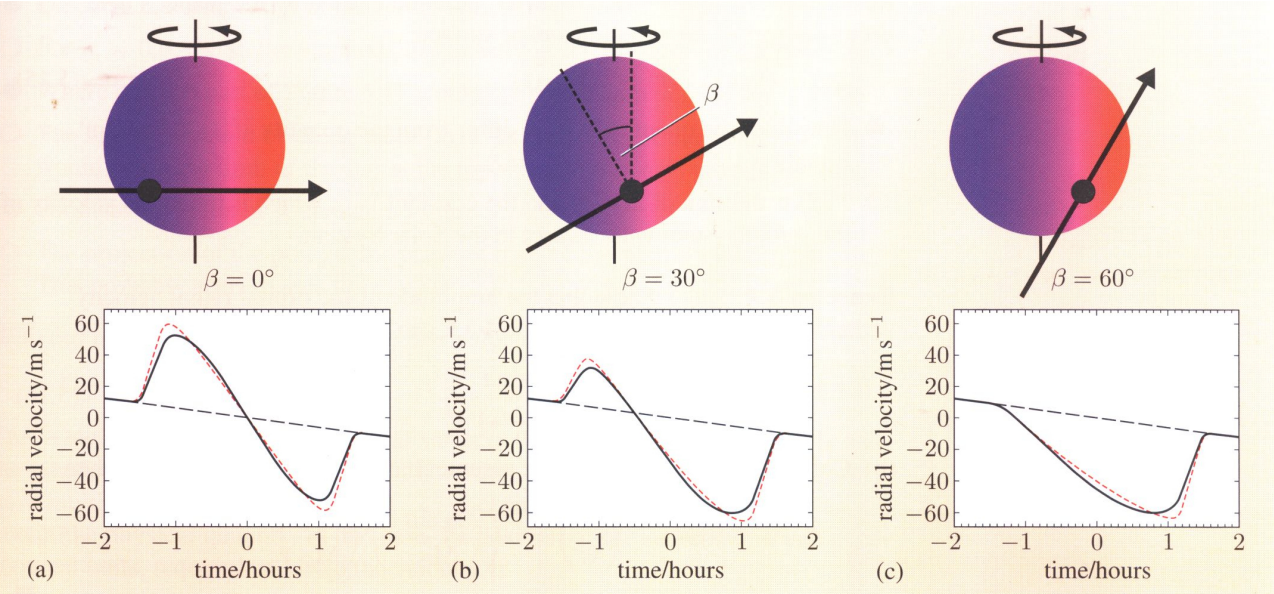

FIGURE 1.7: Simulated Rossiter-McLaughlin effects for three different trajectories of a transiting planet in front of a star whose spin axis is in the plane of the sky. The sky-projected spin-orbit angle β is indicated in each case. The black solid lines are computed accounting for stellar limb-darkening, while the red dashed lines are for the case of no limb-darkening. The black dashed lines show the expected orbital signal. Figure adapted from Gaudi and Winn (2007).

this quantity as a function of wavelength yields the planet's transmission spectrum, from which insights may be gained about some properties of the planetary atmosphere, most notably its chemical composition, as will be shown below.

To interpret the variation of $R_{\mathrm{p},\lambda}$ with wavelength, one must compute the radiative transfer along a grazing trajectory through the planet's atmosphere using a detailed atmosphere model (see e.g. Madhusudhan and Seager 2009, Fortney et al. 2010). Here, I present some first-order equations derived by Lecavelier Des Etangs et al. (2008) for an ideal-gas atmosphere in hydrostatic equilibrium, with the aim of giving a sense of the atmospheric properties that can be constrained from a planet's transmission spectrum. Following Lecavelier Des Etangs et al. (2008), the optical depth τ_λ in a line of sight grazing the planetary limb at an altitude z in the planet's atmosphere is given by:

$$\tau_\lambda(z) \approx \sigma_{\mathrm{abs},\lambda}\, n_{\mathrm{abs}}(z)\, \sqrt{2\pi R_{\mathrm{p}} H} \tag{1.31}$$

where $n_{\mathrm{abs}}(z)$ is the volume density at the altitude z of the dominant absorbing species with a cross-section $\sigma_{\mathrm{abs},\lambda}$, R_{p} is the radius within which the planet is optically thick at all wavelengths, and H is the atmospheric scale height. H is expressed as:

$$H = \frac{k_{\mathrm{B}} T}{\mu_{\mathrm{m}} g_{\mathrm{p}}} \tag{1.32}$$

where k_{B} is the Boltzmann's constant, T is the atmospheric temperature (assumed constant here), μ_{m} is the mean molecular mass, and g_{p} is the surface gravity. H is a useful parameter to quantify the extent of the planetary atmosphere. It is the altitude range over which the

atmospheric pressure P and thus the (total) volume density $n = P/k_{\rm B}T$ decrease by a factor of e:

$$P(z) = P_0 \exp\left(\frac{-z}{H}\right) \quad (1.33)$$

$$n(z) = n_0 \exp\left(\frac{-z}{H}\right) \quad (1.34)$$

where P_0 and $n_0 = P_0/k_{\rm B}T$ are the pressure and volume density at $z = 0$, respectively. Equation 1.31 was simply obtained using the definition of optical depth (see Section 1.1.1, footnote 3), the Equation 1.34, and basic geometry. $n_{\rm abs}$ being related to n by the abundance $\xi_{\rm abs}$ of the main absorbing species ($n_{\rm abs} = \xi_{\rm abs} n$), we have, using Equation 1.34:

$$n_{\rm abs}(z) = \xi_{\rm abs}\, n_0 \exp\left(\frac{-z}{H}\right) \quad (1.35)$$

and Equation 1.31 can be rewritten as:

$$\tau_\lambda(z) \approx \sigma_{{\rm abs},\lambda}\, \xi_{\rm abs}\, n_0 \exp\left(\frac{-z}{H}\right) \sqrt{2\pi R_{\rm p} H} \quad (1.36)$$

For a given wavelength, $R_{{\rm p},\lambda}$ is determined by the altitude $z_{{\rm eff},\lambda}$ in the planet's atmosphere at which light passing through the atmosphere at grazing incidence encounters an optical depth $\tau_\lambda(z) = \tau_{\rm eff}$, with $\tau_{\rm eff}$ of order unity. In other words, $R_{{\rm p},\lambda} = R_{\rm p} + z_{{\rm eff},\lambda}$, with $z_{{\rm eff},\lambda} = z(\tau_\lambda = \tau_{\rm eff})$. Using Equation 1.36 with $\tau_\lambda(z) = \tau_{\rm eff}$ and solving for z, we have:

$$z_{{\rm eff},\lambda} = H \ln\left(\frac{\xi_{\rm abs} P_0 \sigma_{{\rm abs},\lambda}}{\tau_{\rm eff}} \sqrt{\frac{2\pi R_{\rm p}}{k_{\rm B} T \mu_{\rm m} g_{\rm p}}}\right) \quad (1.37)$$

From an exoplanet's transmission spectrum, knowledge can thus be gained about the extent of its atmosphere (through H), its chemical composition along the day-night terminator (through $\sigma_{\rm abs}$ and $\xi_{\rm abs}$), and the local P-T profile (embedded in H and $\sigma_{\rm abs}$). At the wavelength of a strong atomic or molecular transition of a main absorbing species, $R_{{\rm p},\lambda}$ can grow by a few ($\sim$5) atmospheric scale heights (at moderate spectral resolution). The transit depth variation ${\rm d}dF_\lambda$ corresponding to an increase in $R_{{\rm p},\lambda}$ of $1H$ is expressed as:

$${\rm d}dF_\lambda \equiv \frac{(R_{\rm p} + H)^2}{R_\star^2} - \frac{R_{\rm p}^2}{R_\star^2} = \frac{2R_{\rm p}H + H^2}{R_\star^2} \approx 2\,{\rm d}F\,\frac{H}{R_{\rm p}} \quad (1.38)$$

assuming $H \ll R_{\rm p}$. This means that the most favorable targets for transmission spectroscopy are planets showing deep transits and having a large atmospheric scale height, i.e. hot planets with a low atmospheric mean molecular mass and/or a low surface gravity. Equation 1.38 gives a transit depth variation $\sim$100ppm for a typical hot Jupiter (${\rm d}F\sim1\%$, $T\sim$1300K, $\mu_{\rm m}\sim$2.3 atomic mass units, $g_{\rm p}\sim25{\rm m/s^2}$) around a Sun-like star and only $\sim$1ppm for an Earth-twin (${\rm d}F\sim0.01\%$, $T\sim$273K, $\mu_{\rm m}\sim$28 atomic mass units, $g_{\rm p}\sim10{\rm m/s^2}$).

Figure 1.8 shows model transmission spectra of a hot Jupiter having a radius of 1.25 $R_{\rm Jup}$, a surface gravity of $10{\rm m/s^2}$, and a clear isothermal atmosphere, for five different atmospheric temperatures (Fortney et al. 2010). The most prominent absorption signatures in

the optical are: absorption bands of TiO and VO for very hot atmospheres (T=2000–2500K); at lower temperatures, a slope due to Rayleigh scattering by H_2 molecules, and absorption features due to Na and K doublets (T=1000–1500K) or CH_4 absorption bands (T=500K). At wavelengths redwards of 900nm, the transmission spectrum is dominated by absorption bands of H_2O, and CO (T=1500–2500K) or CH_4 (T=500–1000K).

An exoplanet's transmission spectrum is also sensitive to the presence of high-altitude condensates (clouds or hazes) in its atmosphere. Depending on their composition, density, and altitude, these condensates can weaken or even completely mute the spectral features from molecular and atomic absorbers. Instead, they produce a flat transmission spectrum (high-altitude opaque cloud deck) or a spectrum showing their scattering signature (Rayleigh scattering for condensates that are small compared to wavelength or Mie scattering for bigger particles).

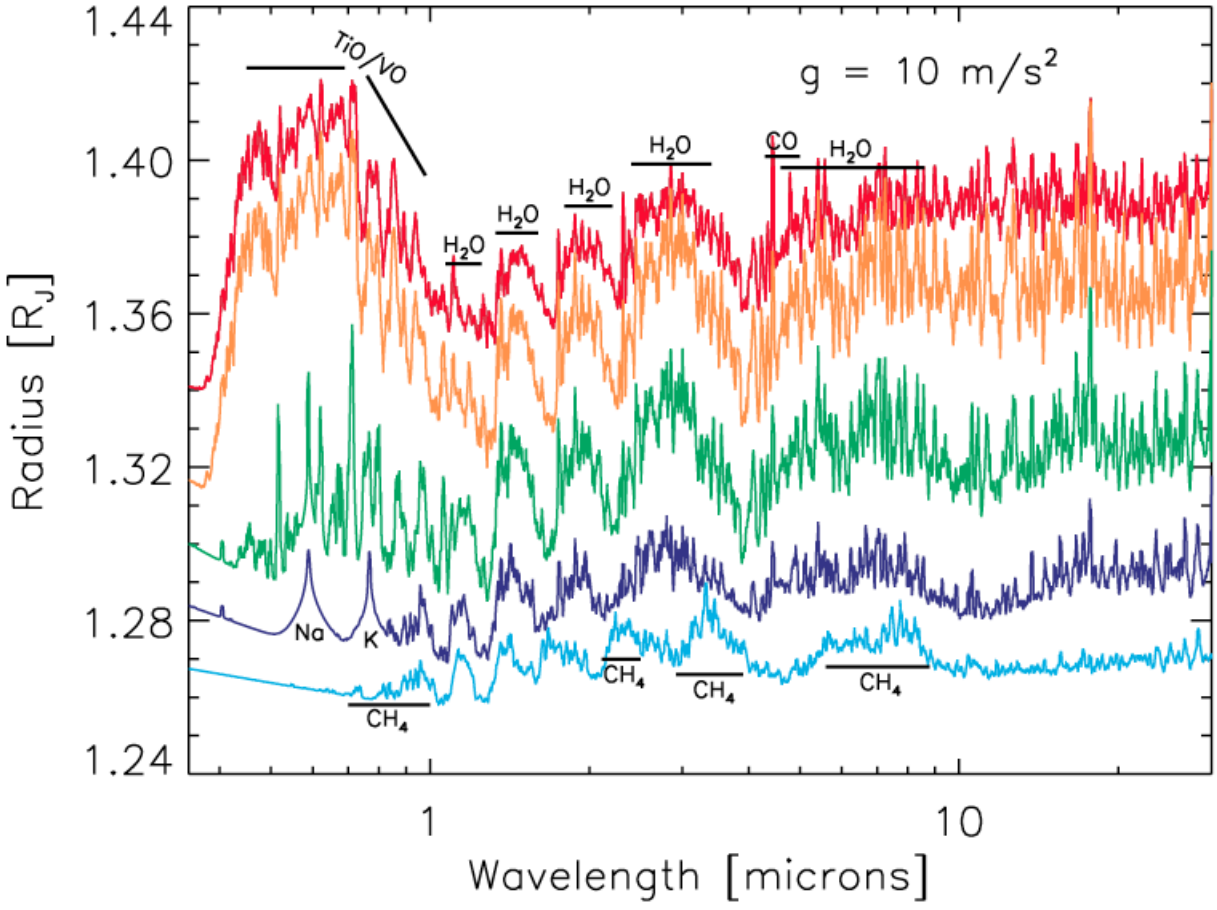

FIGURE 1.8: Model transmission spectra of a hot Jupiter having a radius of 1.25 $R_{\rm Jup}$, a surface gravity of 10m/s^2, and a clear isothermal atmosphere, for five different atmospheric temperatures (from top to bottom, T=2500, 2000, 1500, 1000, and 500K). Prominent absorption features, corresponding to an increase in the apparent planetary radius, are labeled. Figure from Fortney et al. (2010).

Occultation spectroscopy

The passage of the planet behind its host star, about half an orbit after transit at superior conjunction ($f = -\pi/2 - \omega$), is termed either an occultation or a secondary eclipse. The geometric probability $p_{\rm occ}$ of occultations occurring for a given planetary system and a randomly-placed observer can be obtained in a similar way as the transit probability $p_{\rm tra}$ (see Section 1.1.1, Equation 1.10) and is expressed as:

$$p_{\rm occ} = \left(\frac{R_\star + R_{\rm p}}{a}\right)\left(\frac{1 - e\sin\omega}{1 - e^2}\right) \tag{1.39}$$

A transiting planet in a circular orbit systematically also shows occultations, but a planet in an eccentric orbit can produce transits and no occultations, or vice versa.

The occultation depth $\mathrm{d}F_{\rm occ}$ is defined as the amplitude of the relative decrease in the combined flux F of the planet and star, due to the planet being hidden by the star during occultation:

$$\mathrm{d}F_{\rm occ} \equiv \frac{F_{\rm no\ occ} - F_{\rm occ}}{F_{\rm no\ occ}} \tag{1.40}$$

where $F_{\rm no\ occ}$ is the combined flux just before/after occultation and $F_{\rm occ}$ is the flux when the entire disc of the planet is behind the stellar disc. Assuming that the stellar and planetary discs have uniform surface brightnesses $F_{\star,\rm s}$ and $F_{\rm p,s}$, respectively, we have:

$$F_{\rm no\ occ} = F_{\star,\rm s}\pi R_\star^2 + F_{\rm p,s}\pi R_{\rm p}^2 \tag{1.41}$$

$$F_{\rm occ} = F_{\star,\rm s}\pi R_\star^2 \tag{1.42}$$

$$\mathrm{d}F_{\rm occ} = \frac{F_{\rm p,s}\pi R_{\rm p}^2}{F_{\star,\rm s}\pi R_\star^2 + F_{\rm p,s}\pi R_{\rm p}^2} \approx \left(\frac{R_{\rm p}}{R_\star}\right)^2 \frac{F_{\rm p,s}}{F_{\star,\rm s}} \tag{1.43}$$

where we assumed $F_{\rm p,s}\pi R_{\rm p}^2 \ll F_{\star,\rm s}\pi R_\star^2$. Near occultation, the flux from the planet stems mostly from the planet's dayside. If $R_{\rm p}^2/R_\star^2$ is known from transits, occultation observations thus provide a measurement of the surface brightness of the planet's dayside relative to the surface brightness of the star. These two quantities being wavelength-dependent, the same applies to the occultation depth.

The planetary radiation consists of two components: the planet's thermal emission and reflected starlight. The planet being colder than the star, the thermal emission component peaks at longer wavelengths (in the IR) than the reflected light component (in the optical for a solar-type star), as illustrated in Fig. 1.9 for some of the Solar System planets and a representative hot Jupiter.

Assuming an observing wavelength that is long enough for thermal emission to largely dominate over reflected starlight (i.e. the reflected component can be neglected) and supposing that both the star and the planet's dayside emit as black bodies, the occultation depth is given by:

$$\mathrm{d}F_{{\rm occ},\lambda} = \left(\frac{R_{\rm p}}{R_\star}\right)^2 \frac{B_\lambda(T_{\rm p,day})}{B_\lambda(T_{\rm eff})} \tag{1.44}$$

where $B_\lambda(T)$ denotes the Planck function at temperature T, $T_{\rm p,day}$ is the temperature of

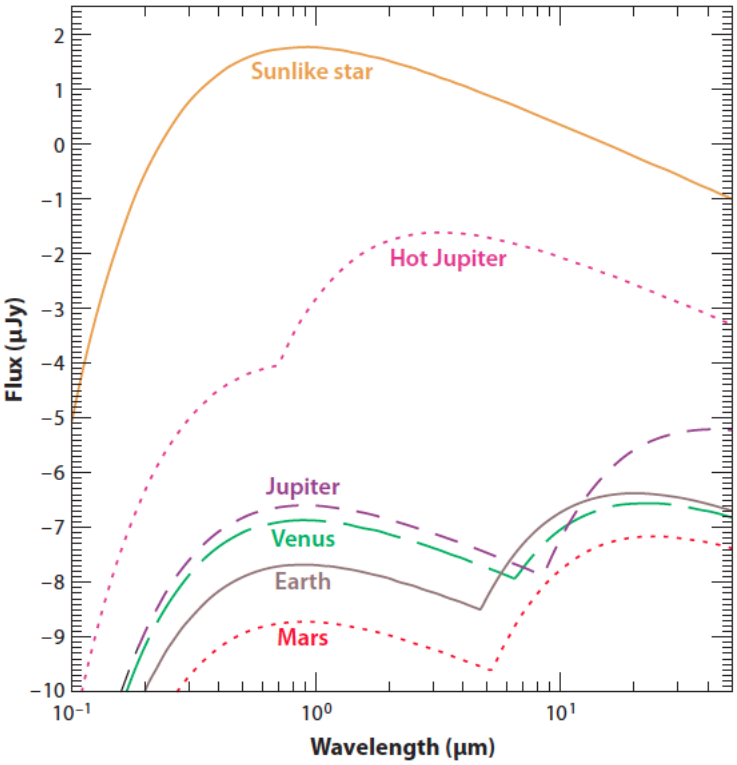

FIGURE 1.9: Approximate spectra (black body fluxes) of the Sun, Jupiter, Mars, Earth, Venus, and an hypothetical hot Jupiter as seen from 10pc. The planets have two peaks in their spectra. The shortest-wavelength peak (in the optical) is due to starlight reflected by the planet. This component thus peaks at the same wavelength as the star. The longest-wevelength peak (in the IR) is from the thermal emission of the planet itself. This component peaks at the wavelength corresponding to the planet's effective temperature, given by Wien's law. Figure from Seager and Deming (2010).

the planet's dayside, and $T_{\rm eff}$ is the stellar effective temperature. An estimation of $T_{\rm p,day}$ is given by the equilibrium temperature of the planet's dayside, $T_{\rm eq,day}$, defined as its effective temperature assuming that the planet has no internal luminosity and is in equilibrium with the radiative energy from the host star. By equating the energy that the planet's dayside receives from the host star and absorbs with the energy that it reradiates, $T_{\rm eq,day}$ can be expressed as (see e.g. Seager 2010):

$$T_{\rm eq,day} = T_{\rm eff}\left(\frac{R_\star}{a}\right)^{1/2}[f(1-A_{\rm B})]^{1/4} \tag{1.45}$$

where $A_{\rm B}$ is the planetary Bond albedo[5] and f is a redistribution factor representing the efficiency of heat transport from the dayside to the nightside of the planet. This factor ranges from $1/4$ to $2/3$, where $f = 1/4$ indicates efficient heat redistribution and isotropic reradiation over the whole planet[6] and $f = 2/3$ corresponds to instantaneous reradiation of the incident energy by the dayside with no heat redistribution. A hot Jupiter typically has $T_{\rm eq,day}$ between 1000 and 3000K (for very hot planets), meaning that its emission peaks in the near-IR (via Wien's law). The contrast between the star and the hot Jupiter is thus decreased in the (near-)IR (see Fig. 1.9), which translates into favorable occultation depths of order $\sim$0.1% at these wavelengths (assuming a solar-type host star). The most favorable planets for thermal emission measurements via occultation observations in the (near-)IR are very hot and large planets in very-short-period orbits around their stars.

Of course, a planet is not a black body and its spectral energy distribution (SED) may depart significantly from a Planck function. We thus define the brightness temperature

[5]The Bond albedo $A_{\rm B}$ is the fraction of stellar incident energy that is scattered back into space ($0 \leq A_{\rm B} \leq 1$).

[6]In this case, the entire planet is characterized by a single equilibrium temperature, $T_{\rm eq}$, with $T_{\rm eq} = T_{\rm eq,day} = T_{\rm eq,night}$ (where $T_{\rm eq,night}$ is the equilibrium temperature of the planet's nightside).

$T_{\mathrm{br},\lambda}$ of the planet's dayside as the temperature of a black body for which the flux emitted at the wavelength λ would match the planetary flux measured from $\mathrm{d}F_{\mathrm{occ},\lambda}$. $T_{\mathrm{br},\lambda}$ is a wavelength-dependent observable temperature that is derived from the measured occultation depth $\mathrm{d}F_{\mathrm{occ},\lambda}$, as opposed to $T_{\mathrm{eq,day}}$ which is a theoretical quantity and does not refer to any flux measurement of the planet. Comparing both quantities may allow to place constraints on the Bond albedo, or more specifically on the spherical albedo $A_{\mathrm{S},\lambda}$ (defined as the Bond albedo but at a specific wavelength[7]), and on the day-night heat redistribution efficiency of the planet (Equation 1.45).

By observing occultations at different wavelengths in the (near-)IR, one can probe the emission spectrum of the planet's dayside, the stellar SED being estimated from stellar atmosphere models. Deviations of the planetary SED from a perfect black body (in other words, variations in $T_{\mathrm{br},\lambda}$ with wavelength) can then be used to gain insights on the properties of the planet's dayside atmosphere, most notably its thermal structure and chemical composition, as will be shown below. Depending on the planet's energy redistribution efficiency, the properties of the dayside atmosphere can vary significantly from those of the atmosphere near the day-night terminator, probed with transmission spectroscopy. Transmission and emission spectroscopy thus provide complementary insights into a transiting planet's atmosphere.

Model emission spectra, just like model transmission spectra, rely on calculations of radiative transfer across the planetary atmosphere using a detailed atmosphere model (see e.g. Madhusudhan and Seager 2009; Burrows, Budaj, and Hubeny 2008). Of course, in the emissive case, the light path through the planet atmosphere is not grazing but radial, and the initial intensity stems from the thermal emission of the planet itself and not from incident starlight. Here, I only provide a conceptual description of a planet's emission spectrum with the aim of giving a sense of how it can be used to constrain the dayside atmospheric properties. In brief, most of the light with wavelength λ emerging from the planet's atmosphere originates, to a first approximation, from layers in the atmosphere with an optical depth $\tau_\lambda = \tau_{\mathrm{em}}$, with τ_{em} of order unity (Eddington-Barbier approximation). The condition $\tau_\lambda = \tau_{\mathrm{em}}$ occurs at different altitudes in the planetary atmosphere depending on the wavelength considered. At the wavelength λ_1 of a strong molecular band of a main atmospheric constituent, $\tau_{\lambda_1} = \tau_{\mathrm{em}}$ is reached[8] at an altitude z_1 in the planetary atmosphere that is higher than the altitude z_2 at which $\tau_{\lambda_2} = \tau_{\mathrm{em}}$ occurs, assuming a wavelength λ_2 outside any strong molecular band. Different wavelengths thus probe different atmospheric layers, expected to have different temperatures. If the atmospheric temperature T_1 at the altitude z_1 is lower than the atmospheric temperature T_2 at the altitude z_2, i.e. the temperature decreases with altitude, the brightness temperature $T_{\mathrm{br},\lambda_1}$ measured at λ_1 is lower than the brightness temperature $T_{\mathrm{br},\lambda_2}$ measured at λ_2, and the molecular band is seen in absorption in the dayside emission spectrum. Conversely, if $T_1 > T_2$, i.e. there is a thermal inversion (as in the Earth's stratosphere), then $T_{\mathrm{br},\lambda_1} > T_{\mathrm{br},\lambda_2}$ and the molecular band is seen in emission in the dayside emission spectrum. This is illustrated in Fig. 1.10, which shows models of dayside thermal emission from a typical hot Jupiter atmosphere with and without a thermal inversion. The emission spectrum thus provides constraints not only on the chemical composition of the dayside atmosphere but also on its vertical temperature structure, whose gradient manifests itself in the amplitude of the molecular features.

[7] $A_{\mathrm{B}} = \int_0^\infty A_{\mathrm{S},\lambda}\mathrm{d}\lambda$.

[8] $\tau_\lambda = 0$ at the top of the planet's atmosphere and increases inwards.

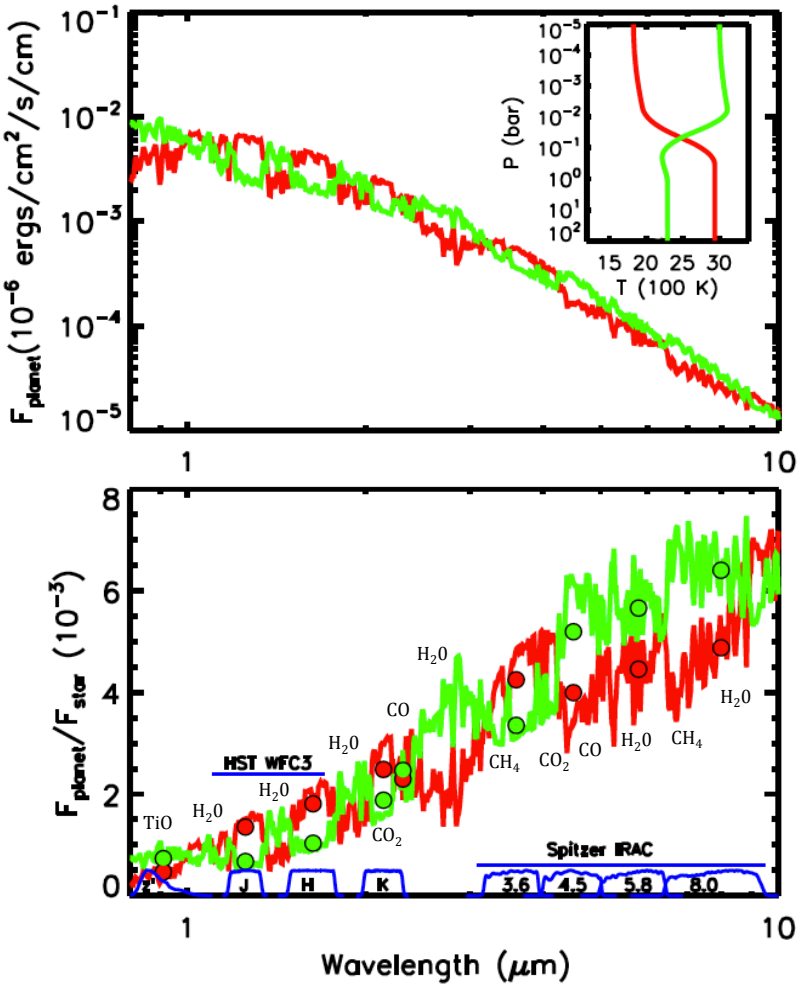

FIGURE 1.10: Models of dayside thermal emission from a typical hot Jupiter atmosphere. *Top:* Emergent dayside spectra for two models with (green) and without (red) a thermal inversion in the atmosphere (the corresponding $P-T$ profiles are shown in the inset). The model without (resp. with) a temperature inversion shows molecular bands in absorption (resp. emission). *Bottom:* The corresponding model spectra of the planet-to-star flux ratio. The filled circles show the models binned in the various photometric passbands shown at the bottom (blue). Figure adapted from Madhusudhan et al. (2014).

By observing occultations at shorter wavelengths, in the optical, one can probe the reflectance spectrum of the planet's dayside. The occultation depth due to reflected starlight alone is given by (Winn 2010):

$$\mathrm{d}F_{\mathrm{occ},\lambda} \quad = \quad A_{\mathrm{g},\lambda}\left(\frac{R_{\mathrm{p}}}{a}\right) \tag{1.46}$$

where $A_{\mathrm{g},\lambda}$ is the geometric albedo, defined as the ratio of the flux reflected by the planet when viewed at zero phase angle[9] to the flux that would be reflected by a flat, isotropically diffusing surface (Lambert surface) with the same cross-sectional area as the planet. For a hot Jupiter, the signal amplitude is of order ∼100ppm. From $A_{\mathrm{g},\lambda}$, insights may be gained on the existence of reflective clouds in the planet's dayside atmosphere and on their composition.

A word about phase curves

By observing a planetary system during a complete planet's orbit, one can monitor the change in the combined flux of the planet and star as a function of the planetary phase, referred to as the planet's phase curve. Again, depending on the wavelength of observation, the modulation of either the thermal emission component (IR) or the reflected starlight

[9]The phase angle is the star-planet-observer angle.

component (optical) throughout the planet's orbit is tracked. Phase curves provide a wealth of information about planetary atmospheric dynamics and energetics but have not been studied in this thesis and are thus only briefly described here.

Short-period planets like hot Jupiters experience strong tidal interactions with their host star and are expected to be tidally locked[10], with permanent day- and night- sides (see e.g. Guillot et al. 1996). In this case, different planetary hemispheres are visible to the observer along a planet's orbit and a longitudinal brightness map of the planet can be generated from its phase curve (Cowan and Agol 2008), thereby constraining the atmospheric conditions across the planet's surface. IR phase curves allow to estimate the atmospheric temperature as a function of longitude. An example of a hot Jupiter's IR phase curve is shown in Fig. 1.11. The phase curve amplitude determines the day-night temperature contrast, while the locations of flux maxima and minima indicate the locations of the hottest and coldest regions in the planet's atmosphere. In the absence of heat transport in the atmosphere, these regions are expected to be located at the substellar and anti-stellar points[11], respectively, resulting in the flux maximum being centered on the occultation and the flux minimum being centered on the transit. An offset from this configuration, such as the one shown in Fig. 1.11, is indicative of atmospheric circulation processes that shift the locations of these hottest and coldest regions eastward of their original locations and transport heat around the planet. Key insights on the atmospheric circulation patterns may thus be gained from the phase curve morphology. By observing phase curves at multiple wavelengths in the IR, one can obtain a longitudinal map of the emission spectrum. Since different wavelengths probe different depths in the planetary atmosphere, one can then study variations in the atmospheric circulation patterns as a function of altitude in the atmosphere. Optical phase curves, on their side, provide information on variations in the properties of clouds as a function of longitude.

1.1.3 Detection of transiting exoplanets

As discussed in Section 1.1.1, a typical hot Jupiter orbiting a Sun-like star has a transit geometric probability $p_{\rm tra}$ ∼10%. The occurrence rate of hot Jupiters around solar-type stars is known from RV surveys to be ∼1% (e.g. Mayor et al. 2011, Wright et al. 2012). The detection of a hot Jupiter transiting a solar-type star thus requires the photometric monitoring, over a few weeks, of at least one thousand such stars, with a precision and cadence that are high enough to detect ∼1% flux drops of a few hours. This is achievable from the ground. The detection of a transiting Earth analog around a Sun-like star is far more challenging and only possible from space: its transit probability is considerably lower ($p_{\rm tra}$∼0.5%) and the detection of its transits requires a much higher precision ($\mathrm{d}F$∼0.01%) and a longer time coverage (P=1yr, W∼13hrs). In any case, the photometric monitoring of several thousand stars simultaneously in very wide field-of-views is required. A number of wide-field transit surveys were undertaken during the last ∼15 years, so that more than two thousands transiting exoplanets have been confirmed to date, representing about 80% of the total number of known exoplanets[12].

[10] i.e., the planet rotates synchronously with its orbital period ($P_{\rm rot} = P_{\rm orb}$), similarly to the Moon around the Earth.

[11] The substellar point is the point on the planet's surface that directly faces the star and receives the highest level of incident flux, while the opposing anti-stellar point receives no starlight at all.

[12] Source: NASA Exoplanet Archive (http://exoplanetarchive.ipac.caltech.edu/, July 2016).

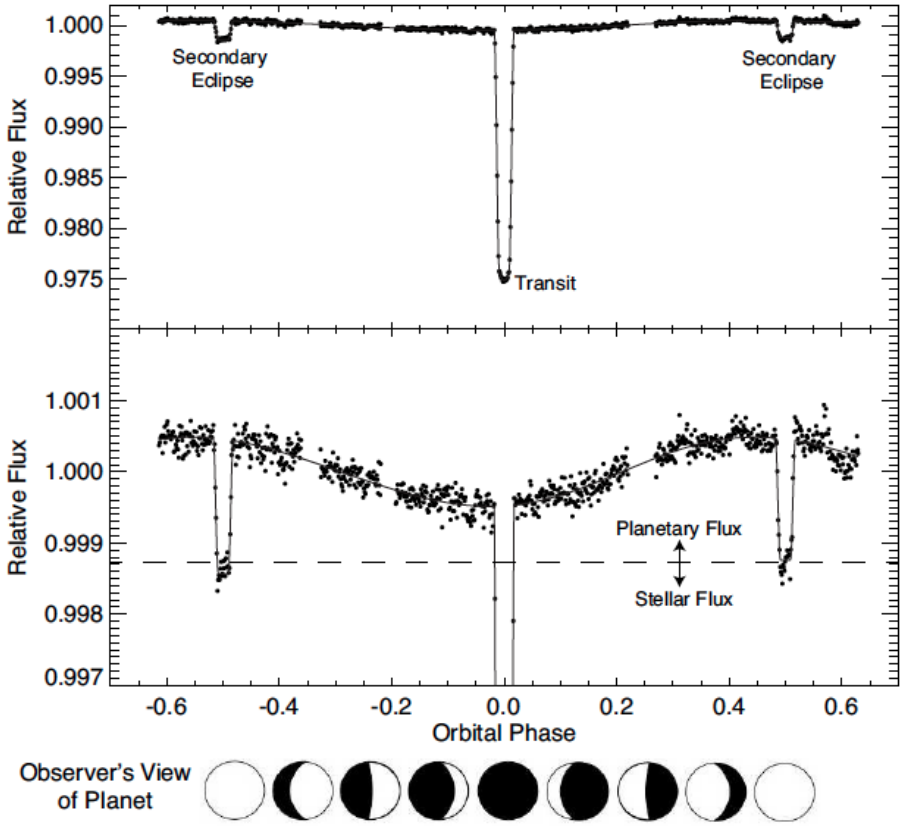

FIGURE 1.11: Thermal phase curve of the hot Jupiter HD 189733 b measured in the *Spitzer* 4.5μm IRAC band (Knutson et al. 2012). The lower panel shows the same data as the upper panel, but with an expanded y-axis for a better view of the change in flux as a function of orbital phase. The horizontal dashed line indicates the measured flux level during occultation, when only the star is visible. The flux from the planet at any given time is thus given by the difference between the total measured flux and the dashed line. One can note a phase offset: the flux maximum occurs before the center of the occultation and the flux minimum occurs before the center of the transit. Figure from Madhusudhan et al. (2014).

From the ground, several teams have engaged into transit searches using automated small aperture (∼10cm) telescopes, capable of monitoring thousands of stars simultaneously in very wide field of views. The main wide-field ground-based transit surveys have been (in order of increasing number of reported planet detections): TrES (Trans-Atlantic Exoplanet Survey, Alonso et al. 2004, not operating anymore), XO (McCullough et al. 2005, not operating anymore), QES (Qatar Exoplanet Survey, Alsubai et al. 2013), KELT (Kilodegree Extremely Little Telescope, Pepper et al. 2007), HATSouth (Bakos et al. 2013), HATNet (Hungarian Automated Telescope Network, Bakos et al. 2004), and WASP (Wide Angle Search for Planets, Pollacco et al. 2006, Hellier et al. 2011). Together, these surveys reported the detections of about 250 transiting giant planets with orbital periods less than ∼15 days orbiting stars with $8<V<15$. WASP has been the most productive of these surveys to date, with about 130 planets published[13]. All these projects need follow-up observations of their planetary candidates in order to reject astrophysical or instrumental false positives and confirm their planetary nature. Since they monitor very wide fields at low angular resolution,

[13] https://wasp-planets.net/

blended eclipsing binaries, that can mimic the signal of a planetary transit, are for example very common in their data. During my PhD, I have been involved in the photometric follow-up of WASP candidates, using the TRAPPIST robotic telescope (TRAnsiting Planets and PlanetesImals Small Telescope, Jehin et al. 2011b and Gillon et al. 2011a). I will thus provide a detailed description of the WASP instrumentation, observing strategy, candidate selection procedures, false positives rejection, and planet confirmation process in Chapter 3. Building on the experience of WASP, the Next Generation Transit Survey (NGTS, Wheatley et al. 2013) has been operating from ESO Paranal Observatory (Chile) since early 2016. This project employs an array of twelve fully-robotized 20cm telescopes to search for planets of Neptune-size and smaller around bright (V<13) K and early-M stars. These planets will be prime targets for detailed characterization studies.

The *CoRoT* mission (COnvection ROtation and planetary Transits, Auvergne et al. 2009) was the first spaceborne transit survey. The satellite was launched in December 2006 into a polar orbit at 900km altitude and operated for about 6 years until a fatal computer failure in November 2012 put an end to the mission. The telescope had a diameter of 27cm and provided a field of view of $2.7^\circ \times 3.05^\circ$. It observed 3 to 4 different fields per year for an average duration of 78 days each, with the aim of studying stellar properties via asteroseismology and finding planetary transits. All fields were located close to the two intersections of the galactic plane with the ecliptic. A total of 28 planets have been published to date from the *CoRoT* mission, among which CoRoT-7 b, the first known transiting super-Earth ($R_\mathrm{p} \sim 1.7 R_\oplus$ and $M_\mathrm{p} \sim 5 M_\oplus$, see Léger et al. 2009 and Queloz et al. 2009). More than 100 candidates are still under investigation.

The *Kepler* mission (Borucki et al. 2010) has been by far the most prolific transit survey to date, with ∼2300 planets confirmed and over 4000 candidates awaiting confirmation. *Kepler* consists of a Schmidt telescope with an effective aperture of 0.95m, whose focal plane is made out of 42 CCDs of 2200×1024 pixels giving a field of view of 115 deg^2 (∼0.28% of the sky) at a plate scale of 4″/pixel. The satellite was launched in March 2009 into an Earth-trailing heliocentric orbit. The primary mission was to observe a single field, in the Cygnus constellation, for 3.5 years with the main objective of detecting Earth-sized planets in the habitable zone[14] of Sun-like stars. Shortly after the mission was extended, in May 2013, the spacecraft suffered a failure of its third remaining reaction wheel (out of four in total), leaving the telescope unable to point precisely at its original field and ending its primary mission. A new mode of operation, the K2 mission (Howell et al. 2014), has been ongoing since then. In this mode, the telescope observes target fields (each for ∼75 days) along the ecliptic, which allows to minimize the rate of drift caused by unbalanced solar radiation pressure on the spacecraft and thus achieve a reasonably stable pointing. Besides the outstanding number of transiting exoplanets it has found, *Kepler* has brought many key contributions to the field of exoplanetology, among which:

- the discovery of transiting circumbinary planets (e.g. Kepler-16(AB) b, Doyle et al. 2011; Kepler-34(AB) b and Kepler-35(AB) b, Welsh et al. 2012);
- the detection of several closely-packed systems of multiple transiting low-mass planets (e.g. the Kepler-11 system, Lissauer et al. 2011);

[14]The habitable zone (HZ) is the region around a star in which a rocky planet may maintain liquid water on its surface (e.g. Kopparapu et al. 2013).

- the discovery of several transiting planets with $R_{\rm p}$<2$R_{\oplus}$ in the habitable zone of their stars (e.g. Kepler-62 e and f, Borucki et al. 2013; Kepler-186 f, Quintana et al. 2014; Kepler-1229 b, Morton et al. 2016);
- the detection of transiting planets smaller than the Earth (e.g. Kepler-37 b, Barclay et al. 2013);
- the discovery of disintegrating rocky planets in ultra-short-period orbits (e.g. KIC 12557548 b, Rappaport et al. 2012; K2-22 b, Sanchis-Ojeda et al. 2015);
- the thorough characterization of several transiting hot Jupiters via ultra-high-precision optical phase curves (see e.g. the map of clouds on Kepler-7 b by Demory et al. 2013);
- estimates of planet occurrence rates as a function of planetary size, orbital period, and stellar effective temperature (e.g. Borucki et al. 2011, Howard et al. 2012, Fressin et al. 2013, Dressing and Charbonneau 2013).

Two wide-field spaceborne transit surveys are planned for the next decade: TESS (Transiting Exoplanet Survey Satellite, Ricker et al. 2014) and PLATO 2.0 (PLAnetary Transits and Oscillations of stars, Rauer et al. 2014). TESS is a NASA satellite scheduled for launch in December 2017. It will explore the nearly entire sky for planets of Neptune-size and smaller transiting bright (I∼4−13) and nearby stars with spectral types F5 to M5. These planets will be prime targets for detailed characterization studies. The two-year mission will tile the sky with 26 observation sectors, remaining ∼27 days on each $24^{\circ}\times96^{\circ}$ sector. The sectors overlap at ecliptic poles, so that the mission will be sensitive to smaller and longer period planets in these fields. PLATO 2.0 is an ESA mission scheduled for launch in 2024. With its 34 small aperture telescopes that will provide a 2232 deg^2 field of view, it will conduct two long pointed (2-3 years) campaigns, covering in total ∼50% of the sky in about 6 years. For bright (V∼4−11) stars, it should be able to detect and characterize planets down to Earth-size out to the habitable zone.

Another way to find planetary transits, besides conducting wide-field photometric surveillance as the surveys mentioned above, consists in searching for the transits of planets previously found from RV surveys, by monitoring the brightness of their host star throughout the inferior conjunction (estimated from the parameters of the spectroscopic orbit). This was the path to the observation of the first exoplanetary transit by Charbonneau et al. (2000, see also Henry et al. 2000) on HD 209458. Transiting planets found in this way are often extremely valuable since they transit very bright stars and can thus be intensively studied. A few examples are: the hot Jupiter HD 189733 b (Bouchy et al. 2005), the hot Neptune GJ436 b (Butler et al. 2004, Gillon et al. 2007), the super-Earths 55 Cnc e (McArthur et al. 2004, Winn et al. 2011, Demory et al. 2011) and HD 219134 b (Motalebi et al. 2015). In this perspective, one of the key goals of the ESA CHEOPS mission (CHaracterising ExOPlanets Satellite, Broeg et al. 2013), a 32cm telescope scheduled for launch in 2017, will be to search for planetary transits by performing ultra-high precision photometry on bright stars already known from RV surveys to host low-mass planets.

Finally, some transit surveys also perform individual observations of specific target stars that would present a high scientific interest, should they be found to host transiting planets. An example is the MEarth ground-based transit survey (Charbonneau et al. 2008, Irwin et al. 2015), which aims to find super-Earths in the habitable zones of nearby (<33pc)

M-dwarfs smaller than $0.35 R_{\odot}$. Beginning in September 2016, the SPECULOOS ground-based transit survey (Search for habitable Planets EClipsing ULtra-cOOl Stars, Gillon et al. 2013b) will search for planets of Earth-size and below transiting the ∼500 nearest southern ultra-cool dwarfs (stellar-like objects with effective temperatures of 2700K and below). These objects having radii close to Jupiter's, the transit signal of Earth-sized planets is greatly enhanced, allowing their detection from the ground. I will discuss the nearby ultra-cool dwarfs opportunity and the potential of SPECULOOS in Chapter 6.

1.2 Hot Jupiters

Over the past decade, RV surveys and data from the *Kepler* mission have revealed the existence of an extremely rich population of low-mass planets in tight orbits, these planets being frequently members of multi-planetary systems (e.g. Mayor et al. 2011, Fressin et al. 2013). Mayor et al. (2011), for example, reported that about 50% of solar-type stars host one or several planets with masses lower than $30 M_{\oplus}$ (super-Earths and Neptune-mass planets) in orbits with periods shorter than 100 days. Conversely, Jupiter analogs are relatively uncommon, occurring around less than 10% of solar-type stars: Wittenmyer et al. (2016) derived a frequency of $6.2^{+2.8}_{-1.6}$% for giant planets in orbits with semi-major axes between 3 and 7 AU around solar-type stars. Hot Jupiters are even less common, their occurrence rate around solar-type stars being of order ∼1% (e.g. Marcy et al. 2005, Mayor et al. 2011, Wright et al. 2012). Nevertheless, in the past years these rare planets have proved to be extremely rewarding targets, from both a theoretical and observational point of view. In this section, I give an overview of the knowledge and results gathered so far about the hot Jupiter population.

1.2.1 Formation, migration, and tidal evolution

Formation

Ever since the historical detection of 51 Peg b (Mayor and Queloz 1995), the existence of hot Jupiters has challenged the theories of planetary formation and evolution, as such massive planets are not expected to form so close to their star. The most widely accepted mechanism for the formation of gas giant planets is the **core accretion model** (see Safronov 1972, Pollack et al. 1996, and the review by D'Angelo, Durisen, and Lissauer 2010). This model describes a multi-step formation process, which starts in the outer part of the protoplanetary disc, most likely beyond the snow line, where disc temperatures allow for the formation of micron-sized ice and solid dust grains by condensation. These grains coagulate into larger particles of centimeter-size and settle in the disc midplane, where they aggregate to form kilometer-sized rock-ice bodies, the planetesimals. The planetesimals grow larger by collisional accretion, the most massive ones becoming planetary embryos. These embryos accrete the nearby planetesimals, at a fast rate that increases as their mass increases (runaway growth). The depletion of small bodies and their increasingly eccentric orbits in the vicinity of the biggest planetary embryos decrease the probability of accretion, so that

largest bodies are then the slowest to evolve (oligarchic growth). The planetary embryos finally deplete their neighborhood (feeding zone[15]). On much longer timescales, they collide with each other to eventually form the cores of the giant planets. Once a planetary core is massive enough for the escape velocity from its surface to be higher than the thermal speed of the surrounding disk's gas, it starts accreting gas. The gas accretion rate is then regulated by thermal pressure effects within the gaseous envelope. At first, the envelope is optically thin, so that the thermal energy released by impacting bodies and by contraction can be effectively radiated away. The envelope cools, contracts, and additional gas can be accreted. As the envelope grows, its optical thickness increases, and it thus becomes both hotter and denser than the local disk's gas. The thermal pressure in the envelope opposes gravitational contraction, resulting in a phase of quasi-static contraction with slow accretion rates. The protoplanet's total mass finally reaches a critical value ($\sim 32 M_\oplus$ with a core of $\sim 16 M_\oplus$, D'Angelo, Durisen, and Lissauer 2010) beyond which this pseudo-hydrostatic equilibrium can no longer be maintained. The envelope collapses and the protoplanet enters a runaway gas accretion phase, where it accretes all the gas along its orbit, at an ever-increasing rate. Once its mass exceeds a few tenths of Jupiter's mass, tidal interactions with the disc cause a gap to open around the orbit. The planet continues to grow, this time at an ever-decreasing rate, until there is no more gas available within its gravitational reach, finally forming a giant planet.

An alternative model that is occasionally discussed is the **disc instability model** (Boss 1997), in which giant planets are formed by gravitational collapse of the external (and thus coldest) parts of massive gaseous discs. However, this model does not seem to predict the strong positive correlation that is observed between stellar metallicity and the frequency of giant planets (e.g. Udry and Santos 2007). Conversely, this trend is well reproduced by the core accretion scenario (e.g. Mordasini et al. 2009), as the stellar metallicity reflects the density of solids in the protoplanetary disc, and more solids mean more available material to build up the massive cores from which giant planets form. Still, some massive giant planets detected at very large distance from their host star (such as HR 8799 b, c, and d, Marois et al. 2008) may have formed by disc instability (Boss 2011).

Migration

It is clear that hot Jupiters have not formed at their current location, but rather at larger orbital separations from their host star, most likely beyond the snow line, where disc temperatures are low enough that ices can condense, enhancing the abundance of solid materials available to build up the massive planetary cores. Also, due to the radiation pressure from the central protostar, only in the outer parts of the disc is the gas content high enough for the planets' gaseous envelopes to form. This means that hot Jupiters migrated inward from the region where they formed to their current hot location. There are two broad classes of models to explain this migration: (1) disc migration and (2) few-body gravitational dynamics followed by tidal dissipation.

Disc migration refers to the migration of a growing protoplanet through gravitational interactions with the gaseous disc from which it forms (see e.g. Lin, Bodenheimer, and

[15] The feeding zone of an embryo is the region within which it is able to deflect the trajectories of the passing smaller bodies toward itself. This region has a radial extent of several Hill radii (the Hill radius is the radius of the sphere around the embryo in which its gravity dominates over the gravity of the central protostar).

Richardson 1996, Ward 1997, and the review by Lubow and Ida 2010). There are two distinct regimes of disc migration, depending on whether or not the protoplanet can strongly disturb the density structure of the disc in its vicinity.

- **Type I migration**. This regime occurs for a relatively small-mass protoplanet that is still well-embedded in the disc, i.e. not massive enough to open and sustain a gap. In this regime, the density structure of the disc is only significantly affected by the presence of the planet at the inner and outer Lindblad resonance sites[16], where the planet excites spiral density waves. These density perturbations act back on the planet, so that the planet typically experiences a net negative torque, causing it to migrate inward with a speed proportional to its mass.

- **Type II migration**. This regime occurs when the planet is massive enough (a few tenths of Jupiter's mass) to open a gap in the disc about its orbit. The planet is then "locked" in the gap and follows the viscous evolution of the disc, thus migrating toward the star along with the accretion inflow of the gas. Once the mass of the planet (which is still accreting gas) becomes comparable to that of the local disc's mass, the migration slows down and eventually stops (e.g. Mordasini, Alibert, and Benz 2009).

The second class of models describe the migration of gas giants to small orbital separations through **dynamical interactions with one or several other bodies followed by tidal dissipation**.

- **Planet-planet scattering.** Dynamical interactions between two or more giant planets can gradually increase their orbital eccentricities and inclinations (through angular momentum exchanges) and lead to close encounters between planets. These strong dynamical events may place one of the planets into a highly eccentric orbit with a small periastron distance. At periastron passage, the planet experiences strong tidal interactions with the star and loses orbital energy through tidal dissipation, heating up in the process. The orbital semi-major axis decreases and the orbit circularizes, finally forming a hot Jupiter (Rasio and Ford 1996, Weidenschilling and Marzari 1996). As a result of these dynamical events, the other planets may be scattered outward into distant eccentric orbits or ejected from the systems.

- **Kozai cycles.** This process occurs when a planet orbits a star with a stellar companion (binary star system) or another massive planet in an outer orbit that is very inclined to that of the first planet (mutual inclination $> 39.2°$). In this case, the mutual inclination between both orbital planes and the orbital eccentricity of the inner planet undergo cyclic coupled variations (through conservation of angular momentum), known as Kozai cycles (Kozai 1962). This can result in the inner planet being at some point in a highly eccentric orbit with a small periastron distance, so that it experiences strong tidal interactions with the star at periastron passage. Again, tidal dissipation circularizes and shrinks the planet's orbit, forming a hot Jupiter (Wu and Murray 2003, Fabrycky and Tremaine 2007).

While disc migration naturally predicts orbits whose axes are well-aligned with the stellar spin axes (unless the disc itself is misaligned, see e.g. Bate, Lodato, and Pringle 2010, Lai,

[16]Lindblad resonances occur at distances r from the star satisfying the condition $\Omega(r) - \Omega_\mathrm{p} \approx \pm\Omega(r)/m$, where m is a positive integer, Ω_p is the orbital frequency of the planet, and $\Omega(r)$ is the orbital frequency of the gas at the distance r. The sign on the right-hand side indicates outer $(-)$ and inner $(+)$ resonances.

Foucart, and Lin 2011), migration involving few-body dynamical interactions can produce a broad range of orbital obliquities.

Tidal evolution

Whatever their migration mechanism, hot Jupiters experience strong tidal interactions with their host star once they are in a sufficiently close orbit. Tidal dissipation inside both the planet and star should then lead in most cases to (e.g. Matsumura, Peale, and Rasio 2010):

- the synchronization of the planet's rotation period with its orbital period (tidal locking) through tidal dissipation inside the planet;
- the circularization of the planetary orbit, mainly through tidal dissipation inside the planet;
- the realignment of the planet's orbital axis with the stellar spin axis (orbital obliquity damping) through tidal dissipation inside the star;
- the planet's orbital decay (decrease in the orbital semi-major axis), mainly through tidal dissipation inside the star, until the planet reaches its Roche limit where it is tidally disrupted.

The timescales of these processes depend on the tidal dissipation efficiencies of both bodies, parameters that are poorly constrained. Tidal locking should be reached very quickly ($\sim$1 Myr, Rasio and Ford 1996). The circularization of the orbit is then expected to be achieved before its realignment, which occurs on a shorter or similar timescale to orbital decay (e.g. Lai 2012).

Constraints from measurements of the Rossiter-McLaughlin effect

The sky-projected orbital obliquities of many transiting hot Jupiters have been measured via the Rossiter-McLaughlin effect (see Section 1.1.2), revealing a wide range of orbital configurations: well-aligned orbits (e.g. HD 189733 b, Winn et al. 2006, Triaud et al. 2009; WASP-31 b, Brown et al. 2012), substantial misalignments (e.g. XO-3 b, Winn et al. 2009, Hirano et al. 2011; WASP-117 b, Lendl et al. 2014), and even retrograde orbits (e.g. WASP-8 b, Queloz et al. 2010; WASP-17 b, Anderson et al. 2010b, Triaud et al. 2010, Bayliss et al. 2010). Misaligned systems, including retrograde configurations, arise naturally in scenarios that involve few-body dynamical interactions (e.g. Nagasawa, Ida, and Bessho 2008), while they are hardly explained by disc migration, unless the disc itself is originally misaligned. Some authors proposed that protoplanetary discs could be misaligned as a result of the chaotic accretion environment within the stellar cluster (Bate, Lodato, and Pringle 2010) or magnetic interactions between the protostar and the inner disc (Lai, Foucart, and Lin 2011), so that misaligned systems could still be understood in the context of disc migration. However, Watson et al. (2011), estimating the stellar rotation axes of a sample of stars which host spatially-resolved debris discs, found no evidence of misaligned discs.

Some trends were also found that suggest that many of the observed low obliquities are the results of star-planet tidal interactions having realigned previously misaligned systems. Winn et al. (2010) pointed out that misaligned systems are preferentially found around hot stars ($T_{\rm eff}$>6250K, see Fig. 1.12 left), which they interpreted as evidence for these stars being less efficient than cooler stars at realigning with their planetary orbits, having lower

tidal dissipation efficiencies due to their thin or quasi-nonexistent convective envelopes. This trend was independently confirmed by Schlaufman (2010). Triaud (2011) reported a tentative correlation between the degree of misalignment of the systems and their ages (see Fig. 1.12 right), as expected if they were initially misaligned and tidally realigned over time. Based on a larger sample, Albrecht et al. (2012) confirmed both the correlations with stellar effective temperature and age and showed that systems for which the expected tidal timescale is short are globally well-aligned, while systems for which this timescale is long present a wide range of obliquities.

The observed obliquity distribution thus seems to indicate that migration involving dynamical events is quite common and that disc migration alone cannot explain all systems. However, this does not preclude the possibility that disc migration has operated in systems that were later shaped by few-body dynamics and star-planet tidal interactions.

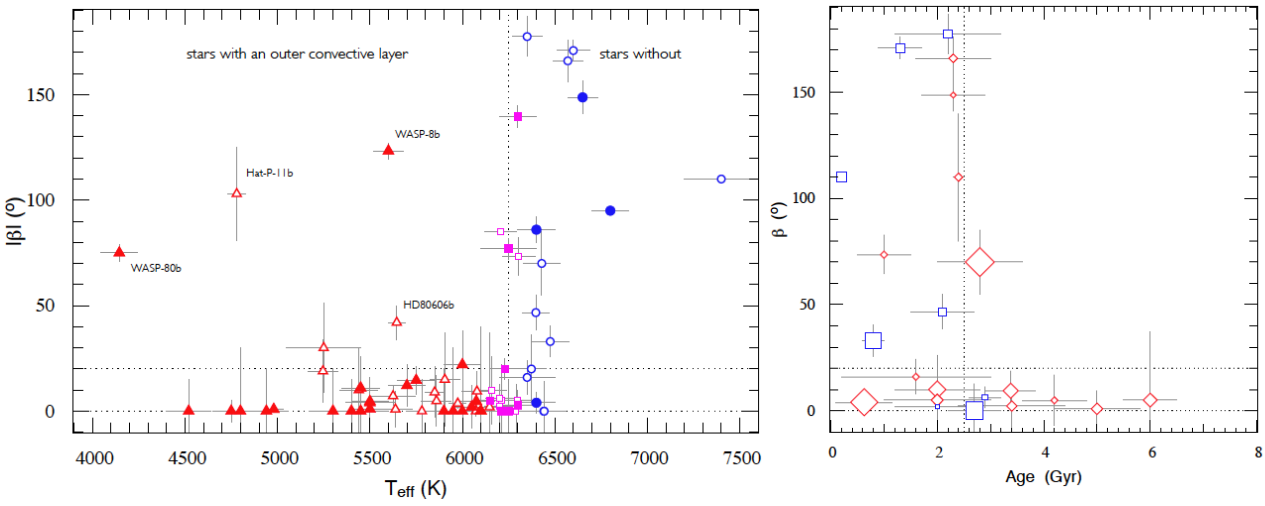

FIGURE 1.12: *Left:* Dependence of the sky-projected obliquity (β) on the effective temperature of the host star ($T_{\rm eff}$). Symbols are shaped and color-coded as a function of $T_{\rm eff}$. Figure from Triaud et al. (2014), updated from Winn et al. (2010). *Right:* Sky-projected obliquity as a function of age for stars with $M_\star$>1.2$M_\odot$. Size of the symbols scales with planetary mass, while their shape and color are function of the stellar mass. Figure from Triaud et al. (2014), updated from Triaud (2011).

1.2.2 Mass-radius relationship

Hot Jupiters receive intense irradiation from their host stars ($\sim10^8-10^{10}$ erg s^{-1}cm^{-2}) and are also subject to strong tides. Studying their density response to such extreme conditions provides a unique opportunity to extend our knowledge on planetary structure, composition, and physics. Comparisons between mass-radius measurements of transiting hot Jupiters and structural evolution models of irradiated giant planets (e.g. Fortney, Marley, and Barnes 2007) have revealed that some hot Jupiters must be strongly enriched in heavy elements: e.g. WASP-84 b (Anderson et al. 2014, planet's heavy element mass $M_{\rm z}\sim54M_\oplus$), WASP-59 b ($M_{\rm z}\sim128M_\oplus$, Hébrard et al. 2013), or HAT-P-20 b (Bakos et al. 2011), a $\sim7.2M_{\rm Jup}$ planet for which models give an extreme $M_{\rm z}\sim660M_\oplus\sim2M_{\rm Jup}$ (all the $M_{\rm z}$ values are from Thorngren, Fortney, and Lopez 2015). In such cases, all heavy elements are not likely to be located solely in the planetary cores, which suggests large amounts of heavy elements within the H/He envelopes. Miller and Fortney (2011) reported correlations between the

planetary heavy element mass M_z and both the stellar metallicity [Fe/H] (clear correlation) and the total planetary mass M_p (tentative correlation), which is consistent with the core accretion model of giant planet formation. Based on a roughly three times larger sample, Thorngren, Fortney, and Lopez (2015) confirmed a clear correlation between M_z and M_p, but found a weaker correlation between M_z and [Fe/H] than reported by Miller and Fortney (2011). Their results suggest that planets rich in heavy elements are preferentially (but not exclusively) found around stars with a high metallicity, while there is no clear pattern for planets with lower heavy-element contents.

In parallel, many transiting hot Jupiters have been found to have inflated radii, i.e. larger radii than predicted by structural evolution models for pure H/He objects (lowest-density models). This is illustrated in Fig. 1.13. Some planets with super-inflated radii are, for example, WASP-17 b ($M_p \sim 0.49 M_{Jup}$, $R_p \sim 2 R_{Jup}$, Anderson et al. 2010b, Anderson et al. 2011a), WASP-76 b ($M_p \sim 0.92 M_{Jup}$, $R_p \sim 1.83\ R_{Jup}$, West et al. 2016), and HATS-26 b ($M_p \sim 0.65 M_{Jup}$, $R_p \sim 1.75 R_{Jup}$, Espinoza et al. 2016). The origin of this "radius anomaly" has been the subject of intense debate over the past years. Many inflation mechanisms have been proposed (see e.g. the reviews by Fortney and Nettelmann 2010 and Baraffe et al. 2014), including:

- **Atmospheric circulation.** Strong winds driven by a large day-night temperature contrast could produce a downward kinetic energy flux that would deposit $\sim$1% of the absorbed stellar incident energy in the planet's interior, slowing down its contraction (Showman and Guillot 2002).

- **Enhanced atmospheric opacities.** A super-solar metallicity in the planetary atmosphere, absorbing clouds, or an underestimation of opacities in model atmospheres could result in enhanced atmospheric opacities that would retain internal heat and slow down the contraction of the planet (Burrows et al. 2007).

- **Layered convection.** The break-up of convection into several layers, due to the presence of a compositional gradient, could reduce the heat transport efficiency in the planet's interior and slow down its contraction (Chabrier and Baraffe 2007).

- **Tidal dissipation.** Provided the planet has an eccentric ($e \neq 0$) orbit or a non-synchronous rotation ($P_{rot} \neq P_{orb}$), tidal dissipation within the planet produces a heating which can slow down its contraction (Bodenheimer, Lin, and Mardling 2001). This effect acts only on a limited timescale (it drops to zero once the orbit is circularized and the rotation is synchronized), but past tidal heating could still contribute to the currently observed inflated planetary radius. Thermal tides could also help extending the timescale of tidal heating, by pushing the planet away from a synchronous rotation state (Arras and Socrates 2010). In brief, the thermal inertia of the atmosphere is generally not negligible, so that the maximum temperature tends to lag the maximum irradiation (occurring at the substellar point). The thermal bulge, resulting from the hot and cold parts of the atmosphere having different densities, is thus misaligned with the star-planet line. While the gravitational tide torque acts to synchronize the planet's rotation, the thermal tide torque acts against it, as illustrated in Fig. 1.14.

- **Ohmic dissipation.** Hot Jupiters having high atmospheric temperatures ($T \gtrsim 1000$K), alkali metals present in their atmosphere (predominantly Na and K) are expected to be thermally ionized (at least partially). These charged particules are advected with

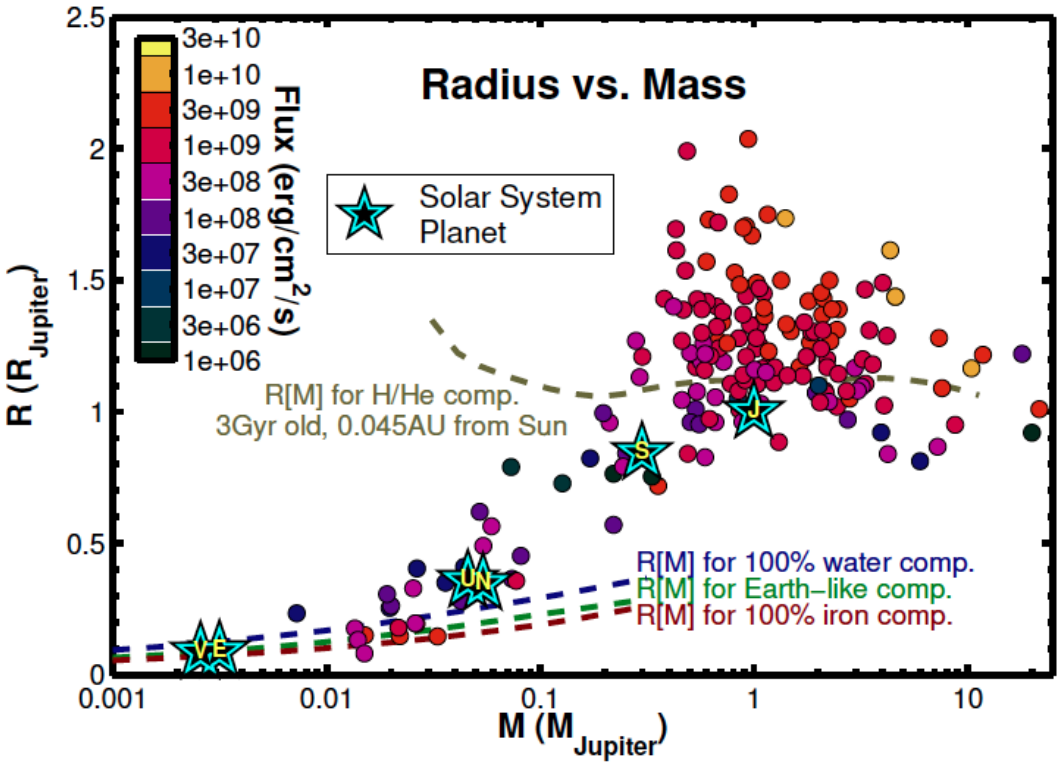

FIGURE 1.13: Radius vs mass diagram for a sample of well-characterized transiting exoplanets and the planets of our Solar System. Transiting exoplanets are represented by filled circles that are color-coded based on the incident stellar flux. Radius-vs-mass relationships for various internal chemical compositions are shown for comparison. Many hot Jupiters have larger radii than predicted by the pure H/He model (top right side of the diagram). The planets with the largest radii tend to be close to Jupiter's mass and highly irradiated. Figure from Spiegel, Fortney, and Sotin (2014).

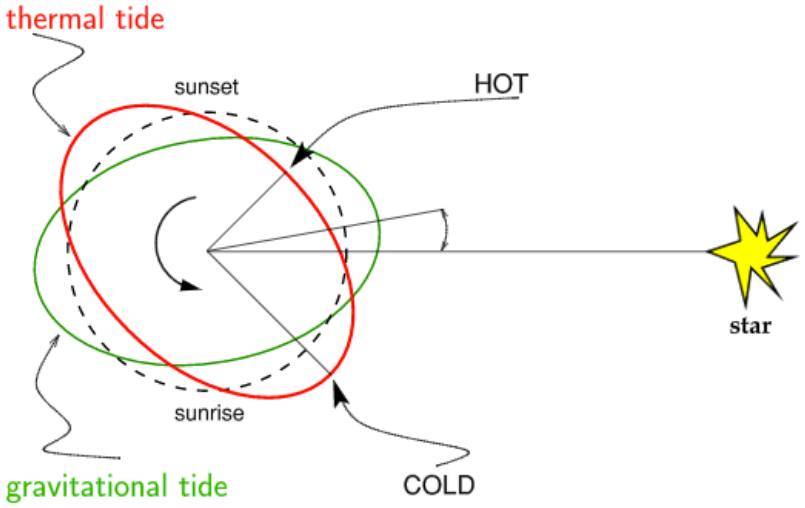

FIGURE 1.14: Geometry of the thermal and gravitational bulges for a planet rotating counterclockwise, and with $P_{\rm rot}$<$P_{\rm orb}$. In this configuration, the gravitational tide torque tends to slow down the planet's rotation, while the thermal tide torque acts to spin it up. Figure adapted from Arras and Socrates (2010).

the strong atmospheric winds and thus produce a magnetic field, distinct from the planetary magnetic field. This in turn generates an induced current that flows inwards and deposits energy by ohmic dissipation in the planet's interior, thus slowing down its contraction (Batygin and Stevenson 2010).

To date, no universal mechanism seems to fully account for the observed radius anomalies (e.g. Baraffe et al. 2014). Some important physics might be missing in the evolution models of irradiated giant planets. The observed inflated radii could also result from the combination of various processes. Several works showed that hot Jupiters' radii correlate well with their incident irradiations (e.g. Demory and Seager 2011; Enoch, Collier Cameron, and Horne 2012; Weiss et al. 2013), so that this parameter must be an important factor in the inflating process. However, mechanisms that are not expected to depend directly on the incident stellar flux (for example, layered convection) might still have a part to play in shaping the planetary internal structures.

1.2.3 Atmospheres

Much of the knowledge gained so far about the atmospheric properties of transiting hot Jupiters has relied on the opportunity offered by their eclipsing configuration to study their transmission and dayside emission spectra (see Section 1.1.2). Here, I provide a brief overview of the main global results that have been obtained using these two techniques. For comprehensive reviews, the interested reader may refer to e.g. Madhusudhan et al. (2014), Bailey (2014), or Crossfield (2015).

In transmission, some planets have sufficiently clear atmospheres to allow detections of atomic and molecular species, in particular Na (e.g. HAT-P-1 b, Nikolov et al. 2014; WASP-17 b, Zhou and Bayliss 2012), K (e.g. XO-2 b, Sing et al. 2011a; WASP-31 b, Sing et al. 2015), and H_2O (e.g. WASP-19 b, Huitson et al. 2013; XO-1 b Deming et al. 2013), while others appear to harbor high-altitude clouds or hazes that completely hide the spectral features of the atmospheric components (e.g. WASP-12 b, Sing et al. 2013; WASP-29 b, Gibson et al. 2013). Even when detected, atmospheric spectral signatures are often less pronounced than predicted by theoretical models of clear atmospheres with solar abundances (e.g. Deming et al. 2013), suggesting either sub-solar atmospheric abundances or that an extra opacity source is still present, at some level, in otherwise predominantly cloud-free atmospheres. This second picture is supported by evidences for high-altitude atmospheric hazes reported for several hot Jupiters (e.g. HD 189733 b, Pont et al. 2013; WASP-6 b, Nikolov et al. 2015; WASP-31 b, Sing et al. 2015), based on their Rayleigh or Mie scattering signature in the planets' transmission spectra. Recently, Sing et al. (2016) reported results from a comparative study of the transmission spectra of ten hot Jupiters between 0.3 and 5μm (combination of HST/STIS, HST/ACS, HST/WFC3, and *Spitzer*/IRAC data). These transmission spectra, shown in Fig. 1.15, exhibit a variety of scattering slopes and absorption feature strengths. Sing et al. (2016) identified the difference between the effective planetary radius measured in the blue-optical (0.3$-$0.57μm) and mid-infrared (3$-$5μm) as an effective metric for distinguishing clear atmospheres from hazy/cloudy ones. They found this index to be correlated with the strength of the water absorption feature between 1.34 and 1.49μm, strong water absorption being seen in clear atmospheres, while atmospheres dominated by clouds/hazes show weaker features. These results support a global picture where high-altitude condensates (e.g. silicates such as $MgSiO_3$ and Mg_2SiO_4), rather than sub-solar

abundances, are the cause of weaker spectral signatures. Clouds and hazes appear to be quite common in hot Jupiters' atmospheres, these planets showing a continuum from clear to cloudy atmospheres in their transmission spectra.

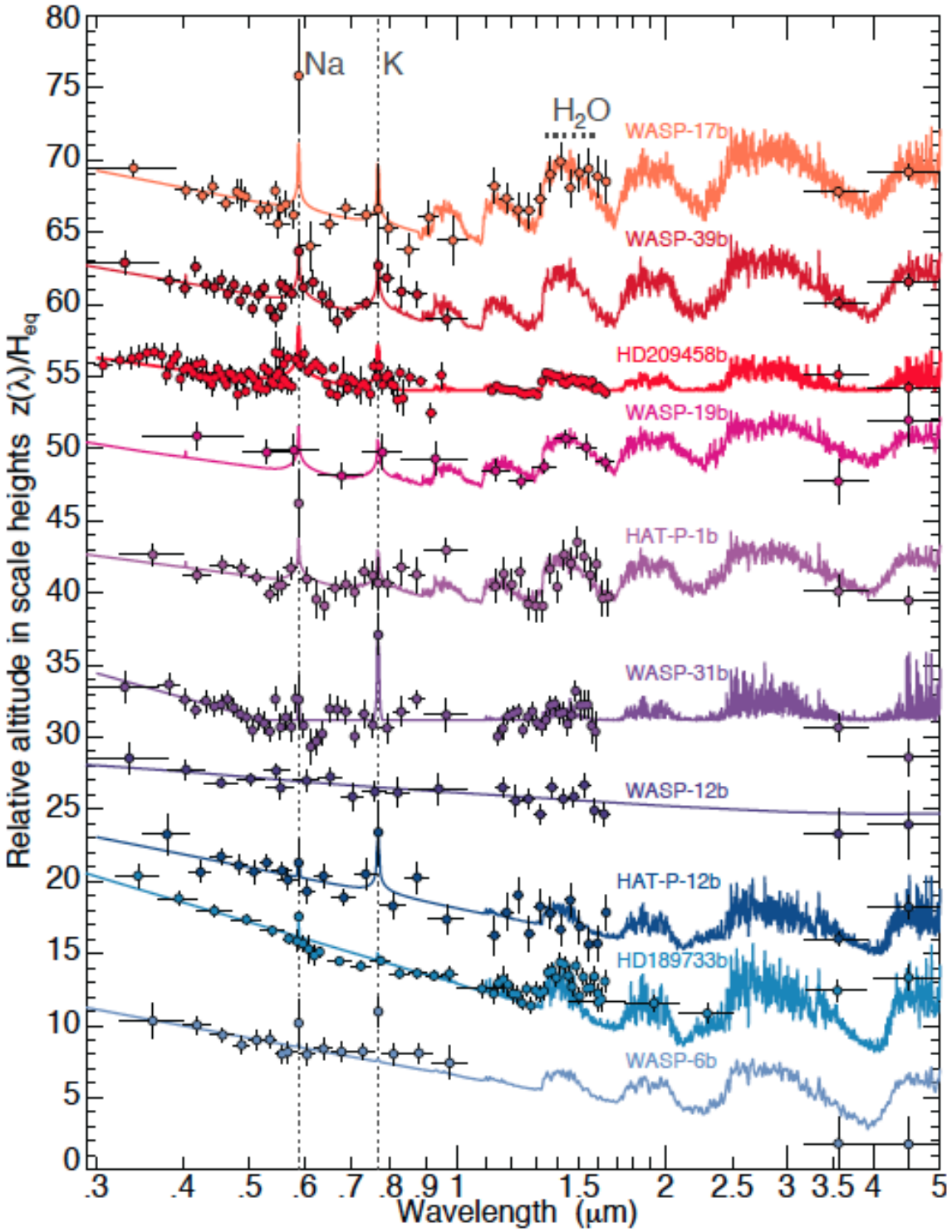

FIGURE 1.15: Comparative set of hot Jupiters' transmission spectra between 0.3 and 5μm. The various measurements are shown as the colored circles with error bars. Solid colored lines show fitted atmospheric models with prominent spectral features indicated. The spectra are ordered vertically from predominantly clear atmospheres (top) to increasingly hazy/cloudy atmospheres (bottom). Figure from Sing et al. (2016).

On the emission side, the data gathered so far have not shown strong evidence for the existence of thermal inversions in hot Jupiters' dayside atmospheres. Most emission spectra are well-fitted by isothermal atmosphere models[17] (see e.g. Hansen, Schwartz, and Cowan 2014) and a few seem to indicate atmospheric temperatures decreasing with altitude (e.g. HD 189733 b, Crouzet et al. 2014; WASP-43 b, Kreidberg et al. 2014). To date, the only planet showing clear evidence for a temperature inversion in its dayside emission spectrum is WASP-33 b (Haynes et al. 2015). This lack of detected thermal inversions came as quite a surprise. Indeed, temperature inversions were an early prediction from atmospheric models of highly irradiated giant planets (e.g. Hubeny, Burrows, and Sudarsky 2003, Fortney et al. 2008), that suggested two classes of hot Jupiters based on their degree of irradiation. The hotter class was predicted to display thermal inversions in their atmospheres due to strong absorption of incident UV/visible irradiation at high altitude by high-temperature absorbers, such as gaseous TiO and VO (commonly found in low-mass stars and brown dwarfs), while cooler atmospheres were expected to be devoid of thermal inversions due to the condensation of these absorbing compounds. Thermal inversions have been previously claimed for several hot Jupiters based on *Spitzer* observations (e.g. HD 209458 b, Knutson et al. 2008; XO-1 b, Machalek et al. 2008; TrES-4 b, Knutson et al. 2009), but recently these detections were seriously called into question (e.g. Hansen, Schwartz, and Cowan 2014, Diamond-Lowe et al. 2014, Schwarz et al. 2015). Even before these recent enlightening results were published, several hot Jupiters belonging to the hotter class of Fortney et al. (2008), did not show sign of the predicted temperature inversions (for example the highly irradiated hot Jupiter WASP-19 b, see Fig. 1.16, Bean et al. 2013). It has been suggested that TiO and VO may not remain suspended in the upper atmospheres of hot Jupiters due to cold-trapping, that would occur either deeper in the dayside atmosphere or on the cooler nightside, and would cause their condensation and downward drag by gravitational settling (e.g. Spiegel, Silverio, and Burrows 2009). Inversion-causing compounds may also be photodissociated by high chromospheric emission from the host star, so that the formation of inversions may be correlated with stellar activity (e.g. Knutson, Howard, and Isaacson 2010). Another important factor is of course the atmospheric chemistry. For example, the atmospheric carbon-to-oxygen (C/O) ratio can control the abundance of TiO/VO, with a C/O$\geq$1 causing substantial depletion of TiO, most available oxygen being taken up by CO molecules in this case thus leaving no oxygen for gaseous TiO (Madhusudhan 2012). Another interesting possibility is that the black-body-like (isothermal) emission spectra observed for many hot Jupiters result in fact from the presence of a high-altitude cloud deck in their dayside atmosphere (e.g. Sing et al. 2013). The atmosphere could be optically thin at all wavelengths above the cloud deck and become optically thick at the level of the cloud deck, so that the emitting surface (cf. Section 1.1.2) would be the same at all wavelengths, with the same temperature (that of the cloud deck). This would result in an emission spectrum that is consistent with an isothermal atmosphere, even if the atmosphere is in fact not isothermal. Such cloud decks in the planets' dayside atmospheres could thus prevent some thermal inversions from being detected, just like clouds at the planets' day-night terminator regions weaken or suppress atmospheric absorption features in transmission spectra (see above). Nevertheless, hottest planets are still the best candidates to look for thermal inversions. Indeed, as mentioned above, the only planet showing clear evidence for a temperature inversion to date is WASP-33 b (Haynes et al. 2015), a rare specimen of hot Jupiter

[17] i.e. the emission spectrum does not show any significant spectral feature (neither in emission nor in absorption) and is well-fitted by a simple black body model of a given temperature.

that orbits an A-type δ-Scuti star once every $\sim$1.22 days (Collier Cameron et al. 2010) and is the most highly irradiated hot Jupiter currently known ($\sim 1.2\times10^{10}$ erg $\mathrm{s^{-1}cm^{-2}}$, $\sim$8430 times the irradiation of Earth).

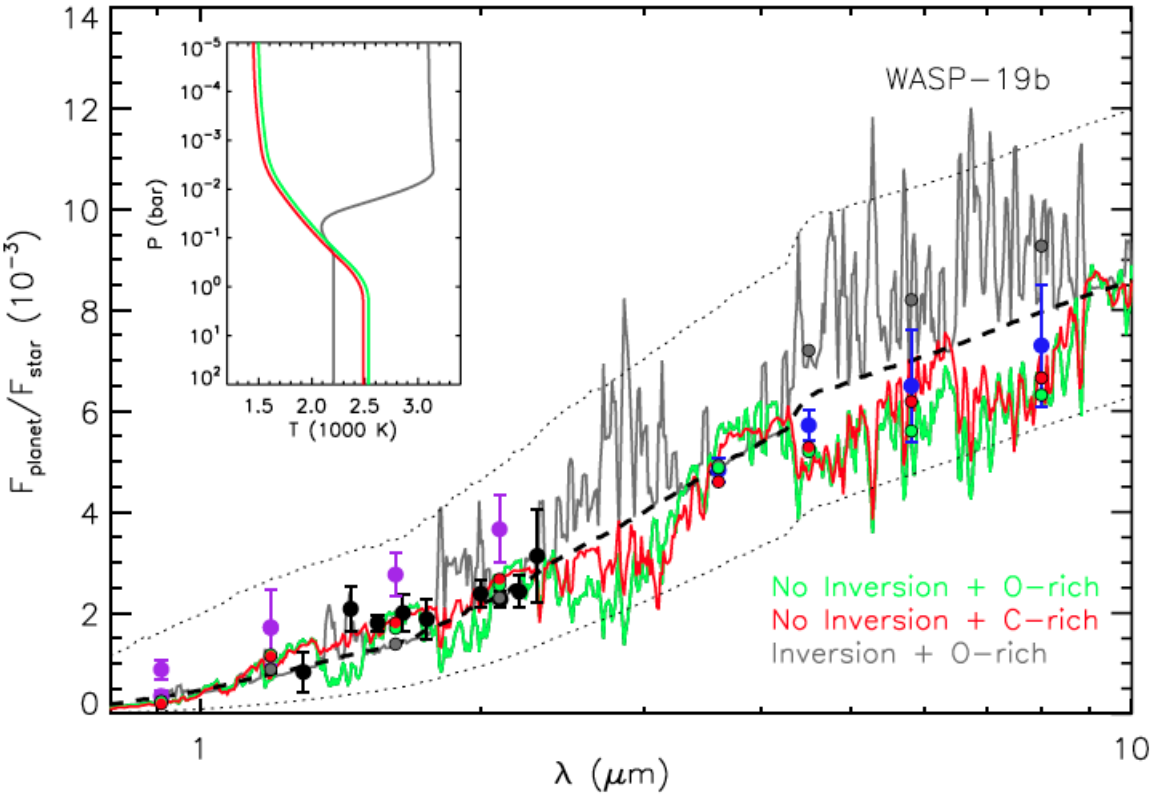

FIGURE 1.16: The dayside thermal emission spectrum of WASP-19 b in terms of the planet-to-star flux ratio, as presented by Bean et al. (2013). The Magellan II/MMIRS measurements from Bean et al. (2013) are shown as the black circles. Measurements from Anderson et al. (2010), Gibson et al. (2010), Burton et al. (2012), Anderson et al. (2013), and Lendl et al. (2013) are also shown as the blue (*Spitzer*/IRAC) and purple (ground-based: VLT/HAWK-I, NTT/ULTRACAM, Euler/EulerCam, and TRAPPIST) circles. The green and red lines represent models with atmospheric temperatures decreasing with altitude, assuming respectively a roughly solar (C/O=0.5) and a carbon-rich (C/O=1.0) composition. The gray line shows a model with a thermal inversion and solar composition. The green, red, and gray points show the respective values of the models integrated over the passbands of the photometric data points. The inset shows the corresponding temperature-pressure profiles for the models. The dashed line is a model assuming that the planet's dayside radiates as a black body with a temperature T of 2250K. The dotted lines are black body models with T=1800K (lower line) and T=2900K (upper line). The data suggest that the planet does not have a thermal inversion, despite receiving high irradiation from its host star ($\sim 4\times10^{9}$ erg $\mathrm{s^{-1}cm^{-2}}$).

As mentioned in Section 1.1.2, a planet's dayside emission spectrum also contains information about its Bond albedo and day-night heat redistribution efficiency. Hot Jupiters have been found to have generally low Bond albedos ($\lesssim$0.35) but show a wide variety of heat redistribution efficiencies, following a trend in which hottest planets are usually less efficient at redistributing the incident stellar energy than colder planets (Cowan and Agol 2011). This picture is also supported by the *Spitzer* thermal phase curve data that have been gathered for a dozen hot Jupiters so far and provided direct measurements of

their day-night temperature contrasts (e.g. Schwartz and Cowan 2015). The explanation commonly given for this trend is that for hotter planets the radiative time-scale is shorter than the advective time-scale, causing these planets to reradiate the incident stellar energy rather than advecting it through winds. Both timescales are in fact expected to be shorter for hotter planets, but the temperature-dependence of the radiative timescale is stronger, leading to reduced heat redistribution efficiencies for hotter planets (e.g. Cowan and Agol 2011, Perez-Becker and Showman 2013).

1.3 Thesis outline

Section 1.2 shows that many open questions remain about hot Jupiters. For example, what mechanism is actually responsible for their migration? How do their internal structure and atmosphere adapt to their extreme environment? What mechanism is responsible for the inflated radii measured for many hot Jupiters? What process governs the formation of clouds in hot Jupiters' atmospheres? During my PhD, I have focused on improving our knowledge of these curious worlds through a twofold approach: (1) the detection and first characterization of new transiting hot Jupiters by taking part in the follow-up of the WASP transit survey with the TRAPPIST telescope, and (2) the atmospheric characterization of known transiting hot Jupiters through both transmission and emission spectroscopy.

In Chapter 2, I describe the data analysis method that has been used in the various studies presented in this thesis. In Chapter 3, I present the TRAPPIST and WASP projects, as well as the overall planet discovery process and my contribution to it. As part of my collaboration with WASP, I led the analysis and publication of four planetary systems: WASP-68, WASP-73, WASP-88, and WASP-121. These discoveries are also described in detail in this chapter. Chapter 4 presents studies of the transmission spectra of two low-density hot Jupiters, WASP-49 b and WASP-80 b, in the optical with the FORS2 instrument at the VLT. In Chapter 5, I present the results of an intense ground-based photometric campaign aiming at probing both the emission and transmission spectra of the ultra-short-period hot Jupiter WASP-103 b. Finally, I summarize my work and discuss plans for future research in Chapter 6.

Chapter 2

Method: combined Bayesian analysis

The best strategy for constraining the parameters of a planetary system is to use all available data (e.g. photometry, RVs) and information (e.g. parameters of the star obtained from an independent spectroscopic analysis or stellar evolution models) as inputs of a single combined analysis. This allows to obtain the strongest constraints on the system parameters and identify the most consistent global solution or, alternatively, reveal a consistency problem. In this thesis, I made use of the most recent version of the adaptive Markov Chain Monte Carlo (MCMC) code described in Gillon et al. (2012, and references therein) to perform the combined data analyses for all the systems that I have studied. To summarize, MCMC is a Bayesian inference method that derives the posterior probability distribution functions (PDFs) of the global model parameters, basing on stochastic simulations. In this section, I describe the main aspects of this MCMC code. For more details about the MCMC technique, the interested reader may refer to e.g. Gelman et al. (2003), Tegmark et al. (2004), Gregory (2005), Ford (2005), or Ford (2006).

2.1 Data

Before describing the MCMC method, I briefly introduce here the different types of data that have been used in the studies presented in this thesis. The data, instruments, and reduction procedures will be described in detail in the corresponding chapters. Here, I just introduce some basic concepts and terminology that will be used in the following sections.

- **Eclipse photometry** refers to observations that produce transit or occultation light curves in a single wavelength band. These data are obtained using an imaging device, e.g. a CCD camera (optical) or an IR detector. The field-of-view of this imager is usually relatively large, so that the fluxes of the target star and several reference stars can be monitored simultaneously. The eclipse light curves are then created via differential photometry: the flux of the target star is divided by the sum of the fluxes of a set of reference stars having similar brightness and color as the target. This allows to correct the eclipse light curves for atmospheric effects (and to a lesser extent, for some instrumental effects).

- **Transmission spectrophotometry** consists in producing simultaneous multi-wavelength transit light curves from low- to mid- resolution spectra. In practice, the target field is observed during a transit using a multi-object spectrograph. The spectra of the target and reference stars are binned into wavelength intervals and differential transit light curves are constructed from the resulting fluxes for each wavelength bin. In this way, simultaneous multi-wavelength observations of transits can be obtained,

which is a great advantage when studying the transmission spectrum of an exoplanet as it allows the suppression of possible effects due to stellar variability.

- **Radial velocities** are measured by cross-correlating high-resolution stellar spectra with an appropriate spectral template and fitting a gaussian to the resulting cross-correlation function (CCF), the mean of this gaussian giving the radial velocity. The CCF is representative of the average profile of the spectral lines and can also be used e.g. to detect signatures of stellar activity (Queloz et al. 2001).

2.2 A Markov Chain Monte Carlo

As mentioned above, MCMC is a Bayesian inference method. It is thus based on Bayes' theorem (Bayes and Price 1763), formulated here as (e.g. Gregory 2005):

$$P(\theta|D, I, M_1) = \frac{P(D|\theta, I, M_1)P(\theta|I, M_1)}{\int P(D|\theta, I, M_1)P(\theta|I, M_1)\, d\theta} \tag{2.1}$$

where

- θ is a set of values for the model parameters;
- D denotes the data;
- I is the prior information;
- M_1 is the model 1 parametrized by the model parameter vector θ;
- $P(\theta|D, I, M_1)$ is the posterior probability of the θ values for the parameters of the model M_1 (the quantity of interest);
- $P(D|\theta, I, M_1)$ is the likelihood, i.e. the probability of D if θ, I, and M_1 are true;
- $P(\theta|I, M_1)$ is the prior probability of the θ values for the parameters of the model M_1;
- the lower integral is the marginal likelihood $P(D|I, M_1)$. The ratio $P(D|I, M_1)/P(D|I, M_2)$ for two different models M_1 and M_2 is the Bayes factor, i.e. the ratio of their probabilities on the basis of observed data D. The Bayes factor provides a way of comparing two models (Bayesian model comparison). When a model is selected, the lower integral is simply a normalization factor.

I will describe below how this theorem is used in the MCMC code.

A Markov chain is a succession of states where the probability distribution of the next state depends only on the current one and not on the sequence of states that preceded it. Here, each of the states is a set of parameters, referred to as the "jump parameters", from which a model is derived and compared to the data. The Monte Carlo aspect of a MCMC refers to the randomness in the generation of each subsequent state. The set of jump parameters and models used in the code will be described in the next section. Here, I explain the basic principle of the method.

In the MCMC code used here, the chains are constructed using the Metropolis-Hastings algorithm (Metropolis et al. 1953, Hastings 1970). The transition (or jump) from one set of parameters to the next is implemented as:

$$\theta_{i?,j} = \theta_{i-1,j} + f\sigma_{\theta_j} N(0,1) \tag{2.2}$$

where θ is the set of jump parameters, the index j denotes each of the jump parameters, and the index i refers to the step increment. The current state is "$i-1$", from which a new state "$i?$" is proposed and will be either accepted or rejected following a procedure that is described below. The quantity $f\sigma_{\theta_j} N(0,1)$ is the step size, which is specific to each jump parameter. σ_{θ_j} is a standard deviation attached to each jump parameter θ_j, $N(0,1)$ is a random number drawn from a normal distribution with zero mean and unit variance, and f is a scaling factor ensuring that a certain percentage of the steps are accepted (I will come back to this below). A model (μ) is generated from the proposed set of parameters $\theta_{i?}$ and is compared to the data (ν) using the usual χ^2 statistic:

$$\chi^2_{i?} = \sum_{k=1}^{k_{\rm tot}} \frac{(\nu_k - \mu_k)^2}{\sigma^2_{\nu_k}} \tag{2.3}$$

where ν_k is the k-th data point with a measurement error σ_{ν_k}, μ_k is the value predicted by the model for this point, and $k_{\rm tot}$ is the total number of data points. The merit function M used in deciding whether the proposed step should be accepted or not (see below) is based on this χ^2. M also accounts for *a priori* knowledge we may have of some of the system parameters (from e.g. previous observations, physical models, etc) by including "Bayesian penalties". It is calculated as follows:

$$M^2_{i?} = \chi^2_{i?} + \sum_j \frac{(\theta'_{i?,j} - \theta'_{{\rm exp},j})^2}{\sigma^2_{\theta'_{{\rm exp},j}}} \tag{2.4}$$

where we expect the parameter θ'_j to lie within a normal distribution with mean $\theta'_{{\rm exp},j}$ and standard deviation $\sigma_{\theta'_{{\rm exp},j}}$ (normal prior PDF). The parameters on which the priors are imposed are noted here θ' and not θ as previously, as they can be either jump parameters or other system parameters deduced from them (see Section 2.4). The likelihood ratio r of the two states "$i?$" and "$i-1$" is given by $r = e^{-(M^2_{i?} - M^2_{i-1})/2}$. The decision as to whether accept or not the new state "$i?$" is made as follows:

1. $r \geq 1$ (i.e. $M^2_{i?} \leq M^2_{i-1}$): the step is accepted, i is incremented, $\theta_i = \theta_{i?}$;
2. $r < 1$ (i.e. $M^2_{i?} > M^2_{i-1}$): a random number u is drawn from a uniform distribution between 0 and 1;
   - $r \geq u$: the step is accepted, i is incremented, $\theta_i = \theta_{i?}$;
   - $r < u$: the step is rejected, i is still incremented but $\theta_i = \theta_{i-1}$, i.e. the set of parameters is left unchanged, it is just copied into the new state.

A new set of parameters is then proposed. θ_i is the new θ_{i-1} and the process is repeated iteratively. As demonstrated by e.g. Gregory (2005), the chain generated by this algorithm converges to a stationary distribution corresponding to the joint posterior PDF of the set of

jump parameters, from which the marginalized posterior PDFs of the individual parameters can be directly deduced. Looking back at Bayes' theorem (Equation 2.1), the χ^2 reflects $P(D|\theta, I, M_1)$, the Bayesian penalties account for $P(\theta|I, M_1)$, and the MCMC converges to $P(\theta|D, I, M_1)$.

Although the algorithm will always converge regardless of the step sizes of the jump parameters, some tricks are used in the code to speed up the convergence. If the step sizes are too small, even if $r < 1$, the condition $r \geq u$ is easily obtained and the steps are accepted most of the time. The chain behaves like a random walk and a lot of steps are needed to get close to the most likely solution, so that the convergence is very slow. Alternatively, if the step sizes are too large, then $r < u$ is obtained most of the time and a large fraction of the steps are rejected. The chain remains at the same state for a number of steps before a step is accepted and the convergence is again very slow. To avoid such issues, on every S-th step (S=statistical length, a value of 100 is often used), the acceptance rate $A = N_{\text{acc}}/S$ is evaluated (N_{acc} = number of accepted steps during the last S steps) and the step sizes of the jump parameters are rescaled via the factor f from Equation 2.2, so as to reach an optimal acceptance rate of ∼25%, which has been shown theoretically to maximize the efficiency of the algorithm (e.g. Roberts, Gelman, and Gilks 1997). Every S-th step, f is thus adjusted as follows: $f_{\text{new}} = (A/0.25) \times f_{\text{old}}$, the initial value of f being 1. If A is lower (resp. higher) than 0.25, the step sizes are thus decreased (resp. increased), in agreement with the above considerations.

In practice, the initial values $\theta_{0,j}$ of the jump parameters as well as the standard deviations σ_{θ_j} attached to each of them (which are kept fixed during the chain) are either guessed from the data, known from previous observations, or estimated by running a preliminary MCMC. It may be possible that some of the σ_{θ_j} are overestimated, while others are on the contrary underestimated. In this case, rescaling the step sizes of all parameters by a common factor f may not be efficient. For this reason, during a first phase of the chain referred to as its "burn-in" phase (usually the first ∼20%), a Gibbs sampler is used, that alters only one parameter of the jump parameter set at each step (instead of the whole set). This allows to monitor the acceptance rates for steps involving each parameter separately (acceptance criteria are the same as described above) and compute an individual step scaling factor f_j for each jump parameter θ_j. Once the burn-in phase is complete, the whole set of jump parameters is varied at each step and the step sizes of all jump parameters are rescaled by the same factor f on every S-th step.

This process ensures that the chain converges quickly to the region of the most likely solution, which is then efficiently explored, i.e. the MCMC samples the posterior PDFs of the jump parameters. While most other techniques focus on minimizing the merit function, here the second criterion of the Metropolis-Hastings algorithm allows a step with a higher merit function than the previous one to still be accepted, with a probability proportional to its likelihood. This enables the chain to efficiently explore the parameter space, while avoiding getting stuck in a local minimum of the merit function.

In practice, several chains are launched to test whether they converge to similar posterior PDFs. This convergence is checked using the statistical test of Gelman and Rubin (1992), which compares the variance of each jump parameter within each chain with the variance of the parameter across multiple chains (after having discarded the burn-in phases of the chains), large differences between the two being indicative of non-convergence.

The final joint posterior PDF is obtained by merging the chains together, after having discarded their burn-in phases. The values of all jump parameters and derived system

parameters having been stored at each step throughout the algorithm, their marginalized posterior PDFs can be directly derived. The values and errors generally adopted for the parameters are the medians[1] and 1σ limits of these PDFs, respectively.

2.3 Models and jump parameters

The MCMC code assumes as model for the (spectro)photometric time-series the eclipse model of Mandel and Agol (2002) multiplied by a baseline model aiming at accounting for photometric variations not related to the eclipses but rather to external astrophysical, instrumental, or environmental effects. This photometric baseline model will be described below. A quadratic law[2] is assumed for the stellar limb-darkening (Equation 1.20). As mentioned in Section 1.1.1, the model of Mandel and Agol (2002) takes as inputs the sky-projected distance between the centers of the stellar and planetary discs normalized by the stellar radius ($r_{\rm sky}/R_\star$), the planet-to-star radius ratio ($R_{\rm p}/R_\star$), and the quadratic limb-darkening coefficients u_1 and u_2. On their side, the RVs are modeled using a classical Keplerian model (Equation 1.27) added to a baseline model accounting for the systemic velocity and for stellar and instrumental variability. Again, the RV baseline model will be described below. The Keplerian model takes as inputs the true anomaly f, the RV orbital semi-amplitude K, the orbital eccentricity e, and the argument of periastron ω. For RVs obtained during a transit, the Rossiter-McLaughlin (RM) effect is modeled following Giménez (2006), taking as inputs the same parameters needed to model a photometric transit[3] ($r_{\rm sky}/R_\star$, $R_{\rm p}/R_\star$, u_1, u_2), as well as the sum of the scaled radii $rs = R_{\rm p}/a + R_\star/a$ (where a is the orbital semi-major axis), the projected stellar rotation velocity $v_\star \sin i_\star$, and the sky-projected obliquity β.

To ensure efficiency of the algorithm, the jump parameters should be chosen with minimum correlation between them and as often as possible as direct observables. Thus, they do not necessarily correspond to input parameters of the models. In this MCMC code, the main jump parameters are:

- the transit depth $\mathrm{d}F = (R_{\rm p}/R_\star)^2$ (if a single value of the transit depth is desired);
- the transit impact parameter in the case of a circular orbit $b' = a\cos i/R_\star$ (where i is the orbital inclination);
- the transit width (duration) W;
- the time of inferior conjunction (mid-transit) T_0;
- the orbital period P;
- the two parameters $\sqrt{e}\cos\omega$ and $\sqrt{e}\sin\omega$ (following Triaud et al. 2011);
- the stellar effective temperature $T_{\rm eff}$ and metallicity [Fe/H];
- the linear combinations ($c_{1,j}$, $c_{2,j}$) of the quadratic limb-darkening coefficients ($u_{1,j}$, $u_{2,j}$) in each wavelength band j (following Holman et al. 2006): $c_{1,j} = 2u_{1,j} + u_{2,j}$ and $c_{2,j} = u_{1,j} - 2u_{2,j}$;

[1] The median is preferred over the mode as it is more representative of the PDF.
[2] A four-parameter limb-darkening law is also implemented in the code, but it was not used in this thesis.
[3] That makes sense since the RM effect is nothing else than a spectroscopic transit.

- if RV data are available, the parameter $K_2 = K\sqrt{1-e^2}\,P^{1/3}$, where K is the RV orbital semi-amplitude;
- if RM data are available, the parameters $\sqrt{v_\star \sin i_\star}\cos\beta$ and $\sqrt{v_\star \sin i_\star}\sin\beta$ (following Triaud et al. 2011);
- if occultation light curves are available, the occultation depths $\mathrm{d}F_{\mathrm{occ},j}$ in each wavelength band j;
- if a transmission spectrum is fitted, the transit depth differences $\mathrm{dd}F_j = \mathrm{d}F_j - \mathrm{d}F$ in each wavelength band j, $\mathrm{d}F$ being then the transit depth in one of the wavelength band.

At each MCMC step, a new set of values is proposed for these jump parameters, following Equation 2.2. Normal prior PDFs are generally assumed for T_{eff}, [Fe/H], $u_{1,j}$, and $u_{2,j}$. For T_{eff} and [Fe/H], the normal priors are usually based on the results obtained from an independent spectroscopic analysis, with expectations and standard deviations corresponding to the measurements and errors, respectively. As for the normal priors imposed on $u_{1,j}$ and $u_{2,j}$, their expectations and standard deviations correspond respectively to the theoretical values and 1σ errors interpolated in Claret and Bloemen's tables (2011) at the beginning of the analysis, basing on T_{eff}, [Fe/H], and $\log g_\star$ (parameters that are generally known from an independent spectroscopic analysis). Uniform (non-informative) priors are usually assumed for the other parameters.

I will now describe how the models are generated from the jump parameters. The modeling of the eclipse light curves requires to compute $r_{\mathrm{sky}}/R_\star$ at each time t_k of observation (i.e. for each photometric measurement). Using Equation 1.6, this quantity, noted here $r_{\mathrm{sky},t_k}/R_\star$, is expressed as:

$$\frac{r_{\mathrm{sky},t_k}}{R_\star} = \frac{a}{R_\star}\frac{(1-e^2)}{1+e\cos f_{t_k}}\sqrt{1-\sin^2(\omega+f_{t_k})\sin^2 i} \tag{2.5}$$

The true anomaly f_{t_k} must thus be computed at each time t_k. To this end, the time of periastron passage T_{peri} is first evaluated from ω, e, P, and T_0, using the following equations:

$$f_{T_0} = \frac{\pi}{2} - \omega \tag{2.6}$$

$$E_{T_0} = 2\tan^{-1}\left(\sqrt{\frac{1-e}{1+e}}\tan\left(\frac{f_{T_0}}{2}\right)\right) \tag{2.7}$$

$$M_{T_0} = E_{T_0} - e\sin E_{T_0} \tag{2.8}$$

$$T_{\mathrm{peri}} = T_0 - \left(M_{T_0}\frac{P}{2\pi}\right) \tag{2.9}$$

where E is the eccentric anomaly, M is the mean anomaly, and the subscript "T_0" refers to the values of these orbital parameters at the time of inferior conjunction. Equation 2.8 is known as Kepler's equation (see e.g. Murray and Correia 2010). The true anomaly f_{t_k} at each time t_k of observation is then computed by using the three previous equations, this time from bottom to top, replacing T_0 by t_k. M_{t_k} is first obtained using:

$$M_{t_k} = \frac{2\pi}{P}(t_k - T_{\mathrm{peri}}) \tag{2.10}$$

E_{t_k} is then obtained by numerically solving Kepler's equation. f_{t_k} is finally given by:

$$f_{t_k} = 2\tan^{-1}\left(\sqrt{\frac{1+e}{1-e}}\tan\left(\frac{E_{t_k}}{2}\right)\right) \quad (2.11)$$

The computation of $r_{\mathrm{sky},t_k}/R_\star$ (Equation 2.5) also requires the scale parameter $a/R_\star$, which can be derived directly from the transit duration equation (Equation 1.13):

$$\frac{a}{R_\star} = \sqrt{\frac{\left(1+\frac{R_\mathrm{p}}{R_\star}\right)^2 - \left(b'\frac{1-e^2}{1+e\sin\omega}\right)^2}{\sin^2\left[\frac{W\pi}{P}\frac{1+e\sin\omega}{\sqrt{1-e^2}}\right]} + b'^2} \quad (2.12)$$

All parameters on the right-hand side of this equation are either jump parameters or can be directly derived from them: $R_\mathrm{p}/R_\star = \sqrt{\mathrm{d}F}$, e and ω are obtained from $\sqrt{e}\cos\omega$ and $\sqrt{e}\sin\omega$. The last parameter needed to compute $r_{\mathrm{sky},t_k}/R_\star$ via Equation 2.5 is i, which can be derived from b' and $a/R_\star$. Besides $r_{\mathrm{sky},t_k}/R_\star$ and $R_\mathrm{p}/R_\star$, the eclipse model also needs u_1 and u_2 which are directly obtained from c_1 and c_2. The modeling of the RV data requires to compute the true anomaly f_{t_k} at each time t_k of RV observation, which is done in the same way as described above. Besides e and ω, the RV model also needs K, which can be derived from K_2, e, and P. The modeling of the RM effect requires as additional parameters $v_\star \sin i_\star$ and β that are directly given by the jump parameters $\sqrt{v_\star \sin i_\star}\cos\beta$ and $\sqrt{v_\star \sin i_\star}\sin\beta$, as well as rs, which can be obtained from $R_\mathrm{p}/R_\star$ and $a/R_\star$. This is how the photometric eclipse, Keplerian RV, and RM models are generated from the jump parameters at each step of the MCMC.

An interesting feature of the MCMC code is that it can model the photometric and RV planetary signals simultaneously with complex trends (noise) that can affect the photometric and RV time series. This is done via the baseline models introduced above. The photometric baseline model is different for each light curve. It can be made up of a first- to fourth-order polynomial with respect to, e.g., time, airmass, PSF FWHM, sky background, stellar position on the detector, or any combination of these parameters. For transit light curves that were obtained simultaneously and show similar noise structures, e.g. spectrophotometric light curves, it is also possible to construct a common noise model (CNM) that can then be used as baseline parameter. This CNM is created at each MCMC step by generating a model transit light curve based on the current jump parameter state and on an estimate of the overall transit depth $\mathrm{d}F_\mathrm{group}$, and then co-adding the residuals. $\mathrm{d}F_\mathrm{group}$, the overall transit depth of the group of light curves for which the CNM is constructed, is a jump parameter for which a pre-defined normal prior distribution is assumed. For each time t_k of the light curves, the CNM is calculated as:

$$CNM_k = \sum_{l=1}^{n_\mathrm{lc}}\left(\frac{\nu_{k,l}}{\mu_{k,l}}\frac{1}{w_{k,l}}\right) \quad (2.13)$$

where n_lc is the total number of light curves the CNM is calculated for, $\nu_{k,l}$ is the k-th data point of the l-th light curve with a measurement error $\sigma_{k,l}$, and $\mu_{k,l}$ is the model value for

this point. Weights $w_{k,l}$ are attributed based on the measurement errors:

$$w_{k,l} = \sigma_{k,l}^2 \sum_{l'=1}^{n_{\rm lc}} \frac{1}{\sigma_{k,l'}^2} \tag{2.14}$$

The CNM is then used as baseline parameter for the light curves considered, i.e. a first- or second-order polynomial with respect to the CNM is included in the baseline model of these light curves. For the RVs, the minimal baseline model is a scalar representing the systemic velocity. It can be combined with a first- to fourth-order polynomial with respect to time, CCF FWHM, bisector span[4], contrast[5], or any combination of these parameters. The RV baseline model is different for each RV data set. For each photometric and RV time series, the selection of the optimal baseline model, i.e. the model minimizing the level of noise in the residuals with a minimum number of parameters, is made by running preliminary MCMCs and identifying the baseline model that minimizes the Bayesian Information Criterion (BIC, Schwarz 1978):

$$BIC = Q^2 + n_{\rm par} \ln k_{\rm tot} \tag{2.15}$$

where Q is the smallest merit function found in the MCMCs, $n_{\rm par}$ is the number of free parameters of the model, and $k_{\rm tot}$ is the number of data points. From the BIC derived for two models, the quantity $\mathrm{e}^{-\Delta BIC/2}$ is actually an estimate of their marginal likelihood ratio (Bayes factor, Equation 2.1). The baseline model coefficients are not jump parameters. They are determined at each step of the MCMC by linear least-squares minimization, using a singular value decomposition method (Press et al. 1992).

2.4 Deduced system parameters

At each MCMC step, a value for the stellar mean density $\rho_\star$ is derived from $a/R_\star$ using Equation 1.26. A value for the stellar mass $M_\star$ is then obtained using one of the two following methods (defined at the beginning of the analysis):

- The $\rho_\star$ value and the current values for $T_{\rm eff}$ and [Fe/H] (jump parameters under the control of normal priors, see above) are used to determine a value for $M_\star$ through an empirical law $M_\star(\rho_\star, T_{\rm eff}, [\mathrm{Fe/H}])$ (Enoch et al. 2010, Gillon et al. 2011b) that is calibrated using the set of well-constrained detached eclipsing binary (EB) systems presented by Southworth (2011). In order to propagate correctly the error on the empirical law, the parameters of the EBs are normally perturbed within their observational error bars and the coefficients of the law are redetermined at each MCMC step. The inability of the empirical law to perfectly reproduce the distribution of the stellar masses is also taken into account by determining at each MCMC step the quadratic difference between the RMS of the residuals of the modeling of the EB masses by the empirical law and the mean mass error for the EB sample. At each MCMC step, a value for $M_\star$ is drawn from a normal distribution having as expectation and standard

[4]The bisector span of the CCF is defined as the difference between the bisector slopes at the top and bottom of the profile (Queloz et al. 2001).

[5]The contrast is the height of the CCF.

deviation the mass originally determined by the empirical law and the quadratic difference mentioned above, respectively.

- A normal prior PDF is assumed for $M_\star$, based e.g. on stellar evolution modeling or previous results. In this case, a value for $M_\star$ is drawn from this normal prior PDF at each MCMC step. To still use the information on $\rho_\star$ provided by the transit light curves, the analysis can for example be performed in two steps. A first analysis is done in order to determine precisely $\rho_\star$, which is then used as input of a stellar evolution modeling, together with $T_{\rm eff}$ and [Fe/H]. The value and error obtained for $M_\star$ from this stellar evolution modeling are then used to define the normal prior PDF assumed for $M_\star$ in a second analysis.

The stellar radius $R_\star$ is then derived from $\rho_\star$ and $M_\star$. The other physical parameters of the system (e.g. $M_{\rm p}$, $R_{\rm p}$, a) are deduced from the jump parameters, $M_\star$, and $R_\star$.

2.5 Error adaptation

Although the photometric errors are usually computed considering scintillation, sky, dark, readout and photon noises, they are known to be often moderately underestimated. Not taking this into account can result in underestimated error bars for the system parameters. In practice, a preliminary MCMC analysis is thus performed (once the baseline models have been selected) to determine the correction factors CF to be applied to the error bars of each photometric time series. For each light curve, CF is the product of two contributions, β_w and β_r. On one side, β_w represents the under- or overestimation of the white noise of each measurement. It is computed as the ratio between the standard deviation of the residuals and the mean photometric error. On the other side, β_r allows to account for possible correlated noise present in the light curve. This scaling factor is determined by following a procedure similar to the one described by Winn et al. (2008). It is obtained by comparing the standard deviations of the binned and unbinned residuals for different binning intervals ranging from 5 to 120min, i.e. the typical time scales of an eclipse light curve (e.g. the duration of ingress or egress). For each binning, β_r is calculated as:

$$\beta_r = \frac{\sigma_N}{\sigma_1}\sqrt{\frac{N(M-1)}{M}} \tag{2.16}$$

where N is the mean number of points in each bin, M is the number of bins, and σ_1 and σ_N are respectively the standard deviation of the unbinned and binned residuals. The largest value obtained with the different binnings is kept as β_r. The correction factors $CF = \beta_w \times \beta_r$ obtained in this way for each light curve are then used as inputs of the subsequent MCMC analysis, in which the photometric errors of each light curve will thus be multiplied by the corresponding CF.

Similarly, the need to rescale the RV error bars can also be assessed from this preliminary MCMC analysis. A “jitter" noise (e.g. Wright 2005) is computed for each RV data set as the value that should be added quadratically to the RV errors to equal their mean value to the standard deviation of the residuals. These jitters are then used as inputs of the subsequent MCMC analysis, in which they are thus added quadratically to the RV errors of the corresponding RV data sets.

Chapter 3

Photometric follow-up of WASP candidates and planets with TRAPPIST

Shortly after the beginning of my PhD, I took charge of the photometric follow-up of WASP planetary candidates and confirmed planets with the TRAPPIST robotic telescope. I really enjoyed this daily work with TRAPPIST. It gave me an invaluable experience in conducting an observing program, from the scheduling and preparation of the observations to the data analysis, and taught me how to manage the instrumental and technical aspects of a robotic observatory. It has also been a real privilege to be part of an active international collaboration like WASP. In this chapter, I describe the TRAPPIST and WASP projects, as well as the overall planet discovery process and my contribution to it.

3.1 TRAPPIST

3.1.1 Project and science case

TRAPPIST[1] (TRAnsiting Planets and PlanetesImals Small Telescope, Jehin et al. 2011b and Gillon et al. 2011a) is a 0.6m robotic telescope that has been in operation at the ESO La Silla Observatory (Chile) since 2010. The project is led by the Origins in Cosmology and Astrophysics (OrCA) group at the Department of Astrophysics, Geophysics and Oceanography (AGO) of the University of Liège (Belgium), in close collaboration with the Geneva Observatory (Switzerland). It is funded by the Belgian Fund for Scientific Research (F.R.S.-FNRS), with the participation of the Swiss National Science Fundation (SNF). TRAPPIST is fully dedicated to the study of planetary systems via two complementary approaches: the detection and characterization of transiting exoplanets, and the study of comets and other small bodies in the Solar System.

TRAPPIST's exoplanet program, which accounts for ∼75% of its total observational time, consists of three main parts:

- The photometric follow-up of planetary candidates from transit surveys (mostly WASP, but also CoRoT and K2). For a given candidate, these follow-up observations aim at checking the reality of the transit signal, identify the star it originates from (in the case of crowded fields), and reject possible false positive scenarios (see Section 3.2.4). Once the planetary nature of a candidate is confirmed (by parallel RV measurements), several high-precision transit light curves are gathered in order to precisely determine the system parameters. This program led to the co-detection of 105 exoplanets (77

[1] http://www.orca.ulg.ac.be/TRAPPIST/Trappist_main/Home.html

published, 28 still unpublished) from December 2010 to April 2016 (more detailed results are given in Section 3.4).

- The photometric monitoring of the eclipses (transits and/or occultations) of some interesting known transiting systems, the main goals being (1) to refine their physical and orbital parameters, (2) to assess to presence of additional bodies in the systems through Transit Timing Variations (TTV) studies, and (3) for the most highly irradiated planets, to measure or put an upper limit on their very-near-IR ($\sim$0.9μm) dayside emission in order to constrain their atmospheric properties. Planetary systems that were extensively followed up with TRAPPIST are, e.g., WASP-43 (Gillon et al. 2012), WASP-19 (Lendl et al. 2013), and WASP-103 (Chapter 5, Delrez et al. in prep). TRAPPIST follow-up transit light curves were also used in studies of a number of other transiting systems, for example, GJ1214 (Fraine et al. 2013), WASP-57 (Southworth et al. 2015b), and K2-19 (Narita et al. 2015).

- The photometric monitoring of $\sim$60 among the brightest ($J\leq$12) southern ultra-cool dwarfs (stellar-like objects with effective temperatures of 2700K and below), with the aims of exploring them for transiting planets and assessing their variability. This program, named UCDTS (Ultra-Cool Dwarfs Transit Survey, Gillon et al. 2013c), is the prototype of the ground-based transit survey SPECULOOS[2] (Search for habitable Planets EClipsing ULtra-cOOl Stars, Gillon et al. 2013b), that will search for planets of Earth-size and below transiting the $\sim$500 nearest southern ($J\leq$14, DEC$\leq$+10°) ultra-cool dwarfs from September 2016 onwards (see Chapter 6). The UCDTS survey notably revealed a fast-evolving weather for the coolest component of the nearby binary brown dwarf Luhman 16 (Gillon et al. 2013a), and, more recently, also led to the outstanding discovery of three temperate Earth-size planets transiting an M8-type dwarf star only 12 parsecs away, TRAPPIST-1 (Gillon et al. 2016).

The comet and small bodies program of TRAPPIST accounts for $\sim$25% of its total observational time and consists in:

- The narrow-band photometric and imaging monitoring of bright comets (V<12), with the aims of following the evolution of their gas (e.g., OH, NH, CN, C_3, C_2) and dust production rates, as well as the evolution of their morphology and coma composition, along their orbit. More than 30 bright comets have been observed in the frame of this program, e.g., 103P/Hartley2 (Jehin et al. 2011a), C/2012 F6 (Lemmon) (Opitom et al. 2015a), and C/2013 R1 (Lovejoy) (Opitom et al. 2015b).

- The broad-band photometric and astrometric monitoring of faint comets (12<V<20), in order to measure their dust production rate and send regular reports on their magnitudes and positions to the IAU Minor Planet Center.

- High-cadence photometric observations of stellar occultations by trans-Neptunian objects and Centaurs, that can provide valuable information (if at least one other chord is observed from a different site) on their diameters, shapes, geometric albedos, and possible atmospheres and rings. TRAPPIST was notably involved in the finding that the dwarf planet Eris has a Pluto-like radius[3] (Sicardy et al. 2011), in the

[2] http://www.orca.ulg.ac.be/SPECULOOS/Speculoos_main/Home.html

[3] That was a surprise, since the supposed larger size of Eris was one of the factors that led to the reclassification of Pluto from planet to dwarf planet in 2006.

first size measurement of the dwarf planet Makemake (Ortiz et al. 2012), and in the discovery of a ring system around the Centaur (10199) Chariklo (Braga-Ribas et al. 2014).

- Photometric observations of asteroids, that are used to constrain their rotation and shape (see e.g. Pravec et al. 2014).

The TRAPPIST project is currently extended to the northern hemisphere, thanks to the installation of a twin telescope at the Oukaimeden Observatory (Morocco), whose first light was in June 2016.

3.1.2 Equipment

The telescope is a 0.6m f/8 Ritchey-Chrétien, with an open design of carbon fiber and aluminum components (see Fig. 3.1) resulting in a light weight of only 65 kg. It is manoeuvred with a compact German equatorial mount using direct drive torque motors, which allows very fast slewing (up to 50°/sec), accurate pointing (pointing accuracy better than 1′ with a pointing model) and tracking (tracking accuracy without autoguider better than 2″/10min), without periodic errors.

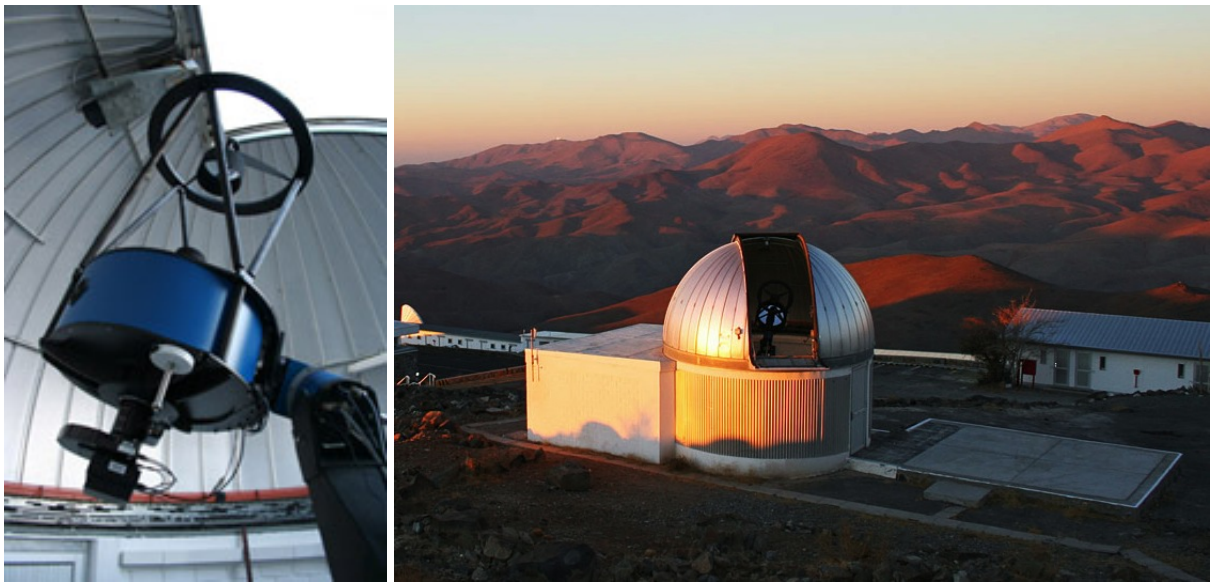

FIGURE 3.1: The TRAPPIST telescope at ESO La Silla Observatory (Chile).

The instrument is a thermoelectrically-cooled CCD camera with a thinned back-illuminated chip of 2048×2048 pixels, each 15μm in size. The field of view on sky is 22′×22′, yielding a pixel scale of 0.64″/pixel. During exoplanet observations, the positions of the stars on the chip are retained on the same few pixels, thanks to a "software guiding" system that derives an instant astrometric solution on the images and sends real-time pointing corrections to the mount when needed. The detector provides a good sensitivity from 300nm to ∼950nm, the quantum efficiency (QE) peaking at 97% near 740nm (see top of Fig. 3.2). The gain is 1.26 e^-/ADU. The camera is usually operated at -35°C with a dark current of ∼0.1 e^-/s/pixel. There are three readout modes available: a slow mode (readout time=6s, readout noise=9.5 e^-/pixel), a fast mode (readout time=4s, readout noise=13.5 e^-/pixel), and a very fast mode (readout time=2s, readout noise=13.5 e^-/pixel). Exoplanet observations

are usually performed using the fast readout mode, as the very fast mode proved to be less stable.

The camera is combined with a double filter wheel containing seven broad-band filters (Johnson-Cousins B, V, Rc, Ic, Sloan z', and special exoplanet filters "$I + z$" and "blue-blocking"), as well as eleven narrow-band cometary filters (OH, NH, CN, CO+, C3, and C2 gaseous species; UC, BC, GC, and RC solar continuum windows; and a NaI D filter), which were designed by NASA for the Hale-Bopp campaign (Farnham, Schleicher, and A'Hearn 2000). The transmission curves of the broad-band filters used for exoplanet photometry are shown in Fig. 3.2 (bottom).

The observatory is fully robotic and can be controlled from anywhere where there is access to the internet, through a Virtual Private Network (VPN) connection between La Silla and the University of Liège. Observing plans, consisting of very simple text files, are submitted every day to the ACP Observatory Control Software (Denny 2011) installed on the control computer, which is placed close to the telescope. ACP works in combination with the control programs of the individual subsystems and handles all aspects of the observatory: control of the 5m-diameter automated dome, pointing, filter wheel's management, image acquisition, focusing, astrometry and software guiding, etc. A weather station, also connected to ACP, is installed on the roof, which allows to close the dome automatically in case of bad conditions. Finally, the observatory is also equipped with an uninterruptable power supply (UPS), and several webcams and microphones placed inside and outside the building.

3.1.3 Data reduction

I will now briefly describe the standard reduction procedure used to extract high-precision light curves from TRAPPIST exoplanet data. Hundreds of images (of ∼8.7 MB each) are gathered for each exoplanet observing run, usually consisting in several hours of continuous observations. The data reduction is thus performed on-site, on dedicated computers installed in TRAPPIST's control room at La Silla, and only some reduction products are transferred to Liège for more interactive final steps. All TRAPPIST exoplanet data are reduced using `TRAPPHOT`, a `PyRAF`[4] package developed by my supervisor, Michaël Gillon. The main steps of the reduction pipeline are the following:

- **Creation of a master bias image.** A number of bias images, preferentially obtained on the same night as the science frames, are combined by averaging to create a master bias image. Outlier pixels are rejected by using a sigma clipping algorithm.
- **Creation of a master dark image.** A set of dark frames obtained with several exposure times, preferentially on the same night as the science frames, are scaled by their mean and then combined by averaging to produce a master dark image. Outlier pixels are rejected by using a sigma clipping algorithm.
- **Creation of a master flat image.** Twilight flats acquired in the same filter and readout mode as the science frames, with various exposure times, are scaled by their mode

[4] `PyRAF` is a command language for running `IRAF` tasks that is based on the `Python` scripting language. `IRAF` is distributed by the National Optical Astronomy Observatory, which is operated by the Association of Universities for Research in Astronomy, Inc., under cooperative agreement with the National Science Foundation.

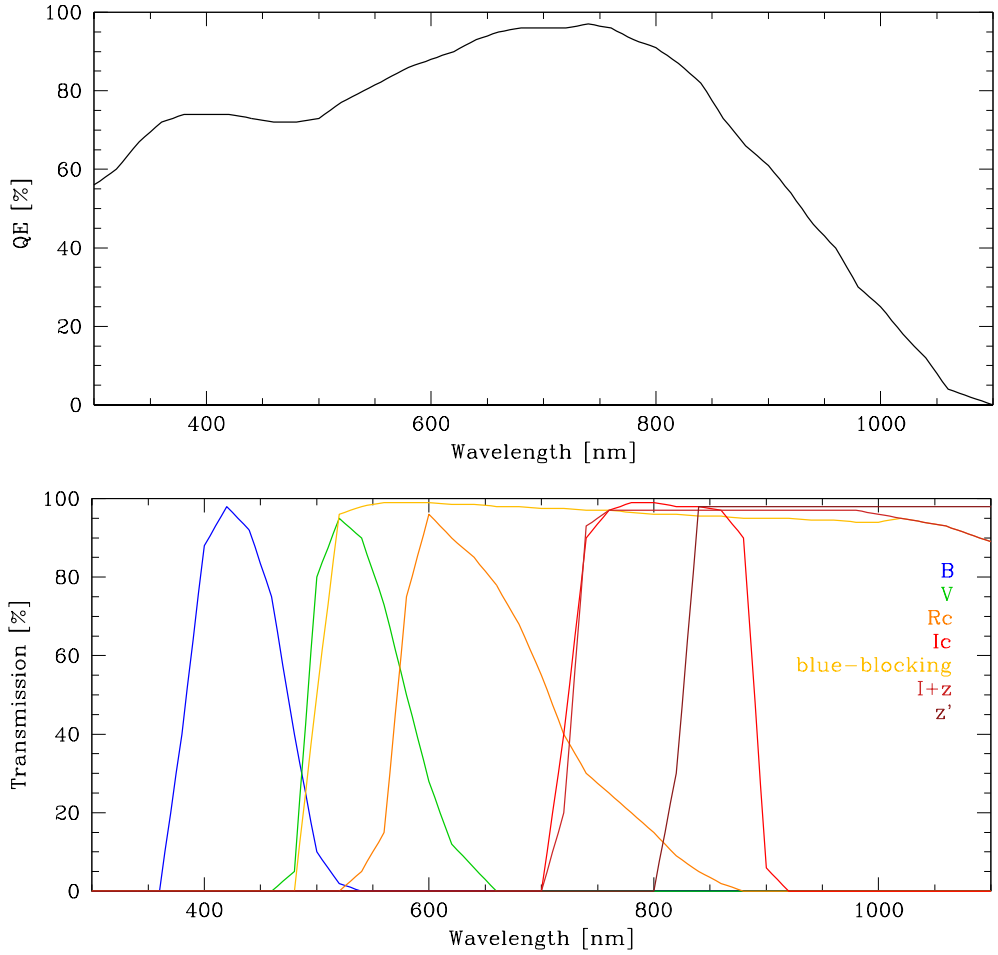

FIGURE 3.2: *Top:* QE curve of TRAPPIST's CCD chip. *Bottom:* Transmission curves of the TRAPPIST's broad-band filters used for exoplanet photometry.

and then combined by averaging to create a master flat image. Outlier pixels are rejected by using a sigma clipping algorithm. The twilight flats are ideally obtained on the same night as the science images. When not possible, the most recent set of adequate flats is used.

- **Calibration of the science images.** The master bias is subtracted from the master dark. The master bias and the bias-corrected master dark are subtracted from the master flat, which is then normalized. The science frames are calibrated using these corrected master images (bias and dark subtraction, flat division).

- **Alignment and stacking of the science images.** Stars are first detected in the individual science frames using the `daofind` task of the `IRAF/DAOPHOT` aperture photometry package (Stetson 1987). The images (or, in the case of crowded fields, only a defined portion of the images to speed up the process) are searched for local density maxima, with a peak value higher than a certain sigma threshold above the local background and with an estimated FWHM value. The (x, y) coordinates of the detected objects are computed as the x and y positions of the best-fitting 1D Gaussian functions in x and y, respectively. As mentioned in Section 3.1.2, TRAPPIST is equipped

with a "software guiding" system that computes an instant astrometric solution on the images and sends real-time pointing corrections to the mount in order to retain the stars on the same few pixels during the observations. However, there are still some small coordinate shifts between the images. The above (x, y) coordinates are used to calculate, for each image, the mean x and y shifts from the first image of the scientific sequence. The images are then aligned based on these mean x and y shift values, and combined by averaging to produce a stacked image. Outlier pixels are rejected by using a sigma clipping algorithm.

- **Aperture photometry on the aligned science images.** Stars are first detected in the stacked image following the same detection procedure as described in the previous step. The (x, y) coordinates of the detected objects serve as initial coordinates for the stars whose fluxes will be subsequently extracted from each individual aligned science image, using the aperture photometry task `phot` of `IRAF/DAOPHOT`. For each image, the coordinates of each star are refined by fitting 1D Gaussian functions in x and y on a region of a few pixels centered on the star's initial coordinates. The stellar fluxes are then extracted for eight different fixed apertures (multiples of the mean FWHM of the PSF over all images of the scientific sequence) centered on these refined coordinates. The flux F_i of each star i (in ADUs) is calculated as $F_i = S_i - n_{pix}\, sky_i$, where S_i is the sum of the counts from all pixels that fall within the star's photometric aperture, n_{pix} is the area of the aperture in square pixels, and sky_i is the local sky value per pixel (in ADUs/pixel). This sky value is computed for each star as the mode of the pixel distribution in the sky annulus, with outliers rejected using a sigma clipping algorithm.

Three reduction products are finally transferred to Liège: the stacked image, a coordinate file containing the (x, y) coordinates of the stars in the stacked image (for visualization), and a photometry file containing the fluxes of the stars (in ADUs) in all images. A careful selection of both the best photometric aperture and combination of reference stars is then performed interactively to obtain the most precise differential light curve for the target. This process consists of several steps:

- **Creation of a preliminary differential light curve.** Some comparison stars having a brightness and color similar to the target are first selected manually. One of the eight photometric apertures is chosen (usually the medium-size one) and a preliminary differential light curve is created by dividing the target's flux (F_T) by the sum of the fluxes of the reference stars ($F_C = \sum_{i=0}^{n_C} F_{C_i}$, where n_C is the number of comparison stars), and by normalizing the resulting target's differential flux. The photometric errors σ are calculated as the quadratic sum of the noise contributions from the target and comparison stars:

$$\sigma = \sqrt{\frac{N_T}{(G\,F_T)^2} + \frac{N_C}{(G\,F_C)^2}} \tag{3.1}$$

where G is the gain (1.26 e^-/ADU) and

$$N_T = G\,F_T + (G\,F_T\,\sigma_{sci})^2 + n_{pix}\,(G\ <sky>\ + RON^2) \tag{3.2}$$

$$N_C = G\,F_C + (G\,F_C\,\sigma_{sci})^2 + n_C\,n_{pix}\,(G\ <sky>\ + RON^2) \tag{3.3}$$

In the above equations, the first term accounts for the Poisson noise, $< sky >$ is the average sky value per pixel (in ADUs/pixel), RON is the readout noise (13.5 e^-/pixel), and σ_{sci} is the scintillation noise given by (Young 1967, Gilliland et al. 1993):

$$\sigma_{sci} = 0.09\, D^{-2/3} X^{1.75} e^{-h/8000} \frac{1}{\sqrt{2\, t_{exp}}} \tag{3.4}$$

where D is the telescope diameter (60 cm), X is the airmass, h is the altitude of the observatory (2350 m), and t_{exp} is the exposure time (in seconds).

- **Selection of the best photometric aperture.** Still using the same sample of comparison stars as in the previous step, the various photometric apertures are tested and the one yielding the most precise light curve is kept. This choice is based on the evaluation of several "quality" parameters: the mean photometric error, the standard deviations of different parts of the light curve (defined manually, e.g., the ingress, bottom, egress, and out-of-eclipse parts), and a red noise estimation (see Section 2.5).

- **Selection of the best combination of reference stars.** Once the optimal photometric aperture is chosen, the best ensemble of comparison stars is determined via an iterative process. Up to 100 000 possible combinations of comparison stars are tested. These stars must meet some criteria to be eligible, such as showing a flux contrast with the target below a certain value and being located relatively close to it in the sky. The best combination is determined as the one that minimizes a merit function, which is based on the above "quality" parameters.

A final light curve file is produced, containing for each image the time of mid-exposure, the normalized differential flux, the photometric error, as well as several parameters that can be used to model the photometric baseline in a MCMC analysis (e.g., the airmass, PSF FWHM, background, target's position on the chip, etc). Plots showing the evolution of these parameters are also created, in order to check the system performance during the observations. Fig. 3.3 shows an example of a TRAPPIST transit data set.

Note. TRAPPIST is equipped with a German equatorial mount, thus the telescope has to perform a 180° rotation when the observed target crosses the meridian (meridian flip), resulting in different positions of the stellar images on the detector before and after the flip. For this reason, the images corresponding to either side of the meridian are usually reduced separately, resulting in two light curves, that are then concatenated into a single file. A meridian flip can cause a jump in the differential photometry (due to the changing positions of the stars on the chip), which is taken into account in a MCMC analysis by introducing an offset in the baseline model of the light curve at the time of the flip.

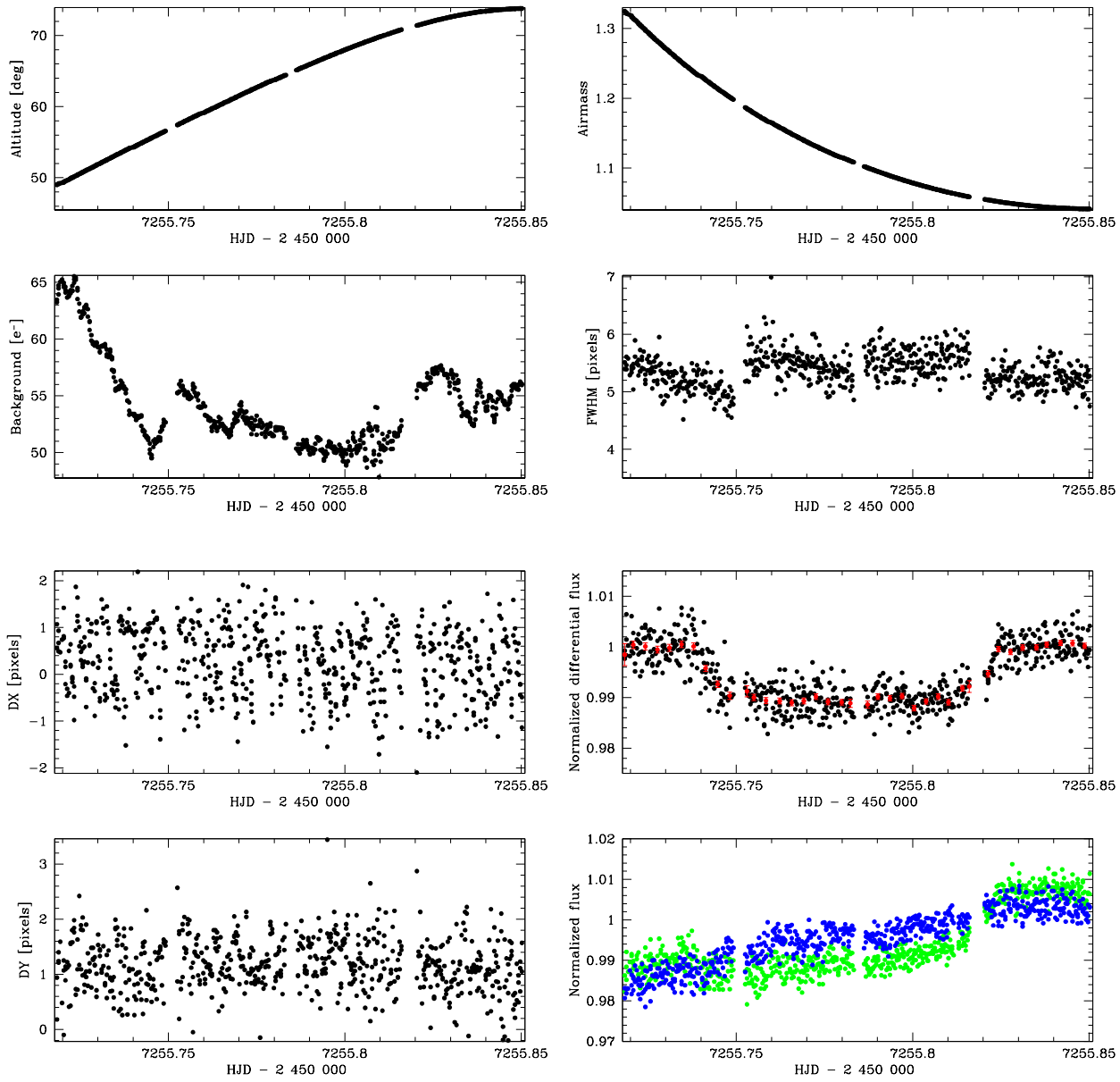

FIGURE 3.3: An example of a TRAPPIST transit data set: a transit of WASP-18 b (Hellier et al. 2009) observed on 21st August 2015 in the Sloan-z' filter and with the telescope slightly defocused. The plots show (from top to bottom and from left to right): the altitude, sky background, x and y coordinate shifts, airmass, PSF FWHM, the normalized differential light curve (black points=unbinned, red points=binned in 5min bins), and the normalized fluxes for the target (green) and for the ensemble of reference stars (blue). The regularly spaced gaps in the data are due to autofocus, that are performed every ∼45min. The RMS of the light curve is ∼690 ppm (5min bins).

3.2 The WASP survey

The WASP[5] project (Wide Angle Search for Planets, Pollacco et al. 2006, Hellier et al. 2011) has been the most successful ground-based transit survey to date. It has discovered more than 160 planets[6] (about 130 are public and a few tens are awaiting publication), mostly hot Jupiters but also some Saturn- (e.g. WASP-29 b, Hellier et al. 2010) and Neptune-mass (e.g. WASP-166 b, not yet published) objects, as well as two brown dwarfs (WASP-30 b and WASP-128 b, Anderson et al. 2011b and Triaud et al. in prep.). Ongoing WASP discoveries are important for the field of exoplanetology, as these systems tend to be particularly prone to follow-up studies, owing to their bright host stars ($9<V<13$), short orbits, and favorable planet-to-star area ratios. Therefore, they will be prime targets for thorough characterizations with future facilities, like CHEOPS and JWST.

WASP is a consortium of several institutions: Cambridge University, the Instituto de Astrofisica de Canarias (IAC), the Isaac Newton Group of telescopes (ING), Keele University, Leicester University, the Open University, Queen's University Belfast, St Andrews University, and Warwick University. The project is currently funded and operated by Warwick University and Keele University.

3.2.1 Instrumentation and observing strategy

The WASP facilities consist of two robotic observatories, SuperWASP-North and WASP-South, located respectively at the Observatorio del Roque de los Muchachos at La Palma (Canary Islands, Spain) and at the site of the South African Astronomical Observatory (SAAO) near Sutherland (South Africa). Each installation comprises eight wide-field cameras mounted on a single equatorial fork mount (see Fig. 3.4, left), which is housed within a reinforced fibreglass enclosure equipped with a slide-away roof (see Fig. 3.4, right). Each camera consisted initially of a 200mm f/1.8 telephoto lens (0.11m aperture) paired with a thinned back-illuminated CCD of 2048×2048 13.5μm-size pixels, yielding a field of view of 7.8°×7.8° at a plate scale of 13.7″/pixel. However, WASP-South is now operating with wider angle 85mm f/1.2 lenses (Smith and WASP Consortium 2014), with the aim of finding planets transiting even brighter stars ($V\sim7$). This new set-up gives a wider field of view of 18°×18°, at plate scale of 31.6″/pixel.

The observing strategy has been designed to maximize the number of stars sampled, while avoiding overcrowded fields near the galactic plane, as they would result in large amounts of blends in the low-angular-resolution WASP images. Each observatory typically observes around a dozen fields per night, in a repetitive sequence of seven or eight fields, that are separated by one hour right ascension along a strip of constant declination. The average time interval between visits to each field is ∼6-10 minutes. Two 30s exposures are taken at each visit through a broad-band filter that gives a 400-700 nm bandpass.

SuperWASP-North has been operating since 2004, while WASP-South started in 2006. As of May 2016, more than 545 $\times$ 10^9 data points of more than 31 $\times$ 10^6 individual stars had been gathered by WASP, this over 2676 individual nights[7].

[5] http://www.superwasp.org
[6] https://wasp-planets.net
[7] Those numbers were kindly provided by Pierre Maxted and estimated on 9 May 2016.

FIGURE 3.4: The WASP-South observatory at the Sutherland site of the SAAO (South Africa). Photographs taken from the WASP website: http://www.superwasp.org.

3.2.2 Data reduction

The raw images, which can amount to 40 GB of data per observatory and per night, are transferred to the UK where they are processed and stored in the WASP archive at Warwick (formerly at Leicester). The reduction pipeline is described in detail in Pollacco et al. (2006). After a standard pre-processing (bias, dark, flat-field, and shutter[8] corrections), a precise astrometric solution is computed for each image by matching the detected stars with the Tycho-2 (Høg et al. 2000) and USNO-B1.0 (Monet et al. 2003) catalogs. Aperture photometry is then performed on all stars (typically brighter than R=15 in the USNO system), using three different aperture sizes of 2.5, 3.5, and 4.5 pixels, respectively. Each object is assigned a blending index, derived from the ratios of the fluxes in the various apertures, which is intended to help spot blended stars and extended, non-stellar objects. The extracted fluxes are finally corrected for primary and secondary extinction, for the instrumental color response, and for the system zero-point, before being archived. At the end of this reduction procedure, a photometric precision of $\sim$0.4% is achieved for stars with $V\sim$9.5, degrading to $\sim$1% for stars with V$\sim$12.5.

3.2.3 Candidate selection

The full details of the transit searching and candidate selection procedures are given in Collier Cameron et al. (2006) and Collier Cameron et al. (2007). The low-level systematic effects left in the data after reduction (due, e.g., to imperfect extinction correction, temperature-dependent focus, etc.) are first identified and removed using the SYSREM algorithm of Tamuz, Mazeh, and Zucker (2005) and the Trend-Filtering Algorithm (TFA) of Kovács, Bakos, and Noyes (2005). An initial search for transit signals is then performed using a modified Box-fitting Least Squares (BLS) algorithm (Kovács, Zucker, and Mazeh 2002), with a coarse search grid of frequencies and transit epochs. The expected transit width (i.e. the box width) at each orbital period is estimated via Kepler's third law, assuming a stellar

[8]Correction for the slightly uneven illumination pattern caused by the finite speed of the camera iris shutter.

mass of 0.9 $M_\odot$ (a rough estimate is enough here). The transit parameters (period, epoch, depth, and width) of each of the five strongest peaks of the BLS periodogram are refined using the analytically differentiable transit profile model of Protopapas, Jimenez, and Alcock 2005 (instead of a pure box function) and a Newton-Raphson approach. Several tests, designed to help filter out a first batch of astrophysical false positives, are conducted: 2MASS magnitudes (Skrutskie et al. 2006) and USNO-B1.0 proper motions of potential candidates are used to place them in a $J-H$ vs J-band Reduced Proper Motion[9] (RPM$_J$) diagram and spot likely giants[10] (see e.g. Gould and Morgan 2003), the ellipsoidal variability in the out-of-transit light curve of each candidate is estimated in order to eliminate probable stellar binaries (see e.g. Drake 2003), etc.

The system parameters of the surviving candidates are determined through an MCMC analysis of their light curves, where the best BLS solution is taken as the MCMC starting point. The MCMC algorithm is described in detail in Collier Cameron et al. (2007). Normal priors are imposed on $M_\star$ and $R_\star$ based on the values expected for these parameters from the 2MASS $J-H$ color of the candidate, assuming that it is on the main-sequence. These priors allow to quantify the departure of the best-fit stellar parameters from their expected main-sequence values which, when significant, is indicative of a probable astrophysical false positive[11]. The probability that the companion's radius is compatible with a planetary object (i.e. is lower than a specified value) is also determined.

Candidates that passed all the tests are subjected to an individual visual inspection, to check the reality of the transits and reject spurious signals, and the most promising ones are finally selected for follow-up observations. That is where I come in!

3.2.4 From a candidate to a confirmed planet

Several astrophysical objects or instrumental effects (further discussed below) can mimic the signal of a planet in the WASP photometry. High-precision spectroscopic and photometric follow-up observations are thus required to confirm the planetary nature of a candidate and, when it turns out to be a planet, precisely determine the system parameters. The main facilities used for the WASP-South follow-up, in which I have been strongly involved during my PhD, are: the CORALIE high-precision fibre-fed echelle spectrograph (see e.g. Queloz et al. 2000b) mounted on the 1.2m *Euler*-Swiss telescope at La Silla, the EulerCam CCD imager (Lendl et al. 2012) also installed on *Euler*, and, of course, TRAPPIST (see Section 3.1). This follow-up is coordinated via the WASP/*Hunter* website, where each candidate has its own dedicated page, an example of which is shown in Fig. 3.5. This page contains various data, graphs, and information, that are useful to assess the candidate's potential and plan follow-up observations. The WASP photometry is available, divided by field/camera/season[12] (links at the top right of the page) or combined. For each photometric data set, the BLS periodogram is shown, as well as the light curve, folded on the

[9] RPM$_J = J + 5\log_{10}\mu$, where μ is the proper motion in arcsec yr^{-1}.

[10] Giant stars are considered as likely false positives, since dips of $\sim$1% (the typical depth sought by WASP) in their brightness cannot be caused by a planetary-size object. Giant stars are more distant than dwarfs of the same magnitude, and thus exhibit smaller proper motions. In a $J-H$ vs RPM$_J$ diagram, giants have lower RPM$_J$ values than dwarfs of the same $J-H$ color.

[11] In the case of a grazing eclipsing binary or an eclipsing binary blended with another star, the measured transit width will be inconsistent with the main-sequence stellar radius expected from the $J-H$ color. The best-fit $M_\star$ and $R_\star$ parameters will be inconsistent with their expected main-sequence values.

[12] A candidate can fall in several overlapping WASP fields.

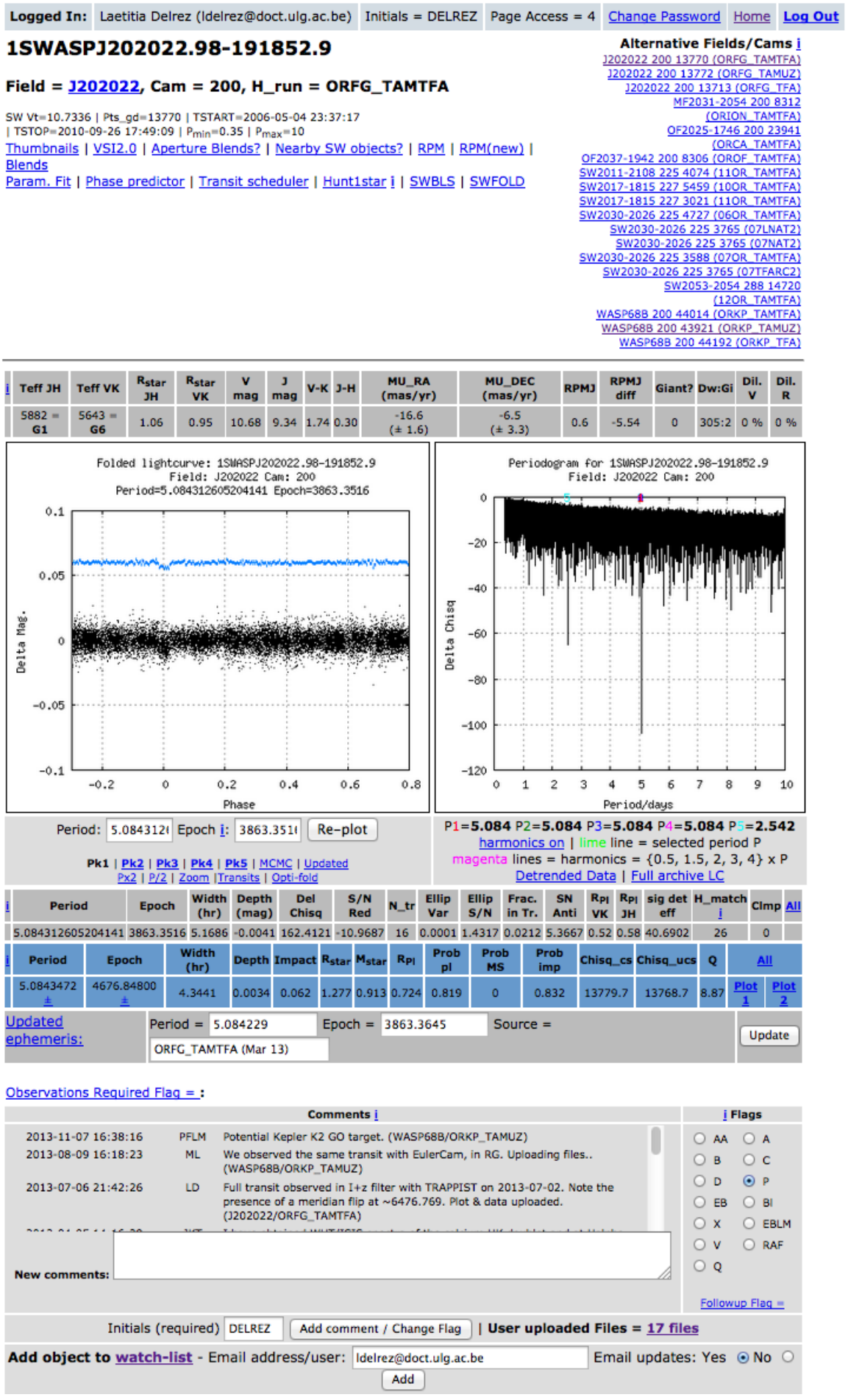

FIGURE 3.5: An example of a WASP candidate page on the WASP/*Hunter* website. In this case, the candidate was confirmed as a planet (WASP-68 b, Delrez et al. 2014).

period of each of the five strongest peaks of the periodogram (links *Pk1-5*). The system parameters derived from the MCMC analysis are presented, together with several metrics used in the candidate selection process. The possible contamination from nearby stars can also be assessed thanks to a finding chart on which the three apertures used to extract the photometry are displayed (accessible via the link *Nearby SW objects?*). Finally, one can post comments, upload data, update the candidate's ephemeris or flag (at the bottom of the page), thus allowing good communication between the members of the collaboration and efficient organization of the follow-up efforts.

I will now briefly describe the kinds of false positives that are most commonly found among WASP candidates (see Fig. 3.6), and how they can be identified and rejected thanks to follow-up observations, in particular with TRAPPIST. I will also show some typical examples of how I have used TRAPPIST to contribute to this effort during my PhD. For a more comprehensive description of the various false positive scenarios that can mimic planetary transits in ground-based surveys, please refer to e.g. Brown (2003).

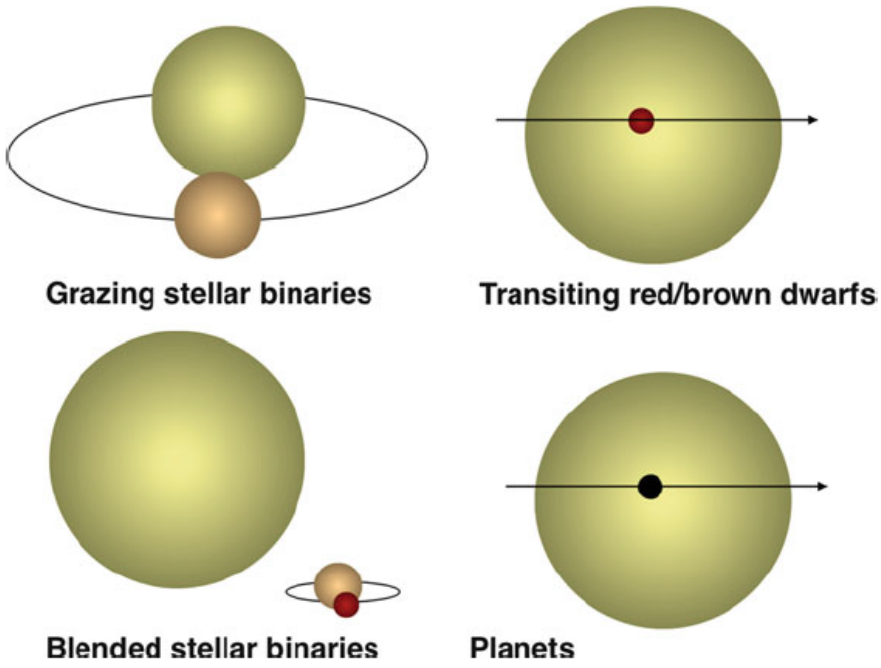

FIGURE 3.6: Four types of astrophysical situations producing transits or transit-like signals. The blended stellar binary may be either a background object or physically linked to the brighter star, thus forming a hierarchical triple system. Figure from Collier Cameron (2016).

Grazing eclipsing binaries

Eclipsing binaries, when they are composed of two stars of roughly equal mass, usually produce deep eclipses (up to several tens of percents deep) that can be easily distinguished from the shallow brightness dips caused by planetary transits. However, it may happen that eclipsing binaries have orbital inclinations with respect to our line of sight such that they exhibit grazing eclipses, whose depths are then comparable to those expected for transiting planets. Follow-up eclipse photometry at high precision with TRAPPIST may allow

to identify such systems, as they produce very typical V-shaped[13] eclipses that can be distinguished from the flat-bottomed[14] U-shaped transits of a planet. These V-shaped eclipses are also usually too deep to be caused by grazing planetary transits[15]. A definitive identification of these objects may be provided by CORALIE spectra, as such systems are often double-lined spectroscopic binaries (SB2s) and show large RV variations.

A typical example of such a false positive scenario is shown in Fig. 3.7. The candidate 1SWASPJ 102008.80-473317.9 (2MASS10200881-4733177, V=11.6) showed periodic brightness dips in the WASP photometry, with a period of ∼5.83 days and a depth of ∼1.1% (see Fig. 3.7, left). This depth was compatible with planetary transits, since the candidate was thought to be a late-F star, based on its colors. On 7 June 2013, a partial "transit" window was observed with TRAPPIST in the $I + z$ filter. As can be seen on Fig. 3.7 (right/top), the eclipse is V-shaped and has a depth of ∼2%, which is probably too deep for grazing planetary transits around a late-F star. Indeed, a quick MCMC analysis of the light curve led to b'∼0.98 $R_\star$, $\rho_\star$∼0.91 $\rho_\odot$, $R_\star$∼1.14 $R_\odot$, and R_p∼2.4 R_Jup, assuming $M_\star$=1.32 $M_\odot$ (main-sequence value expected from the star's colors), P=5.827029 d (most likely period returned by the BLS periodogram), and e=0 (circular orbit). The high impact parameter, close to 1, and large size of the eclipsing body are suggestive of a grazing eclipsing binary, the largest planets found to date having radii of ∼2 R_Jup (e.g. WASP-17 b, Anderson et al. 2011a). A CORALIE spectrum of the candidate, obtained by Amaury Triaud, confirmed this suggestion, by showing two distinct peaks, indicative of a SB2, in its cross-correlation function (see Fig. 3.7, right/bottom).

High mass ratio eclipsing binaries

Eclipsing binaries that are composed of two objects with very different masses, e.g. a M-dwarf or a brown dwarf around an A, F, or G-type star, or a dwarf star around a giant star, produce shallow flat-bottomed eclipses closely similar to planetary transits. Such systems are easy to resolve with CORALIE spectroscopic observations, as they show large RV variations that are incompatible with planetary-mass companions.

A nice example of a high mass ratio binary is WASP-128 (Triaud et al. in prep.), an interesting system, although not a planetary one, that deserves to have its detection reported. The object is not yet public, so I will not give its coordinates here. The primary star, an early-G dwarf, showed periodic brightness dips in the WASP photometry, with a period of ∼2.2 days and a depth of ∼0.5% (see Fig. 3.8, left). A total of four transits were observed with TRAPPIST in the blue-blocking filter between February 2014 and May 2015. The combined transit light curve is shown in Fig. 3.8 (right/top). The transit is flat-bottomed and ∼0.7% deep, which is fully compatible with a transiting planet around this star. However, CORALIE RV measurements obtained by Amaury Triaud revealed a ∼2.2 days periodic variation in phase with the photometry, but with a large semi-amplitude of ∼5.3 km/s (see Fig. 3.8, right/bottom), identifying the transiting body as a ∼39 M_Jup brown dwarf. This is thus not a planet, but still a very interesting object, as this is one of only a few known transiting brown dwarfs, which are key objects to constrain models of brown dwarf formation and evolution.

[13]This V-shape relates to the fact that the area of the stellar disk occulted is constantly changing.

[14]Neglecting here the effect of stellar limb-darkening.

[15]Grazing planetary transits also produce V-shaped light curves. However, the depth of such grazing transits is lower than for "normal" transits (for a given planetary size).

Blended eclipsing binaries

A bright star (usually the candidate) blended with a fainter deeply eclipsing stellar binary results in diluted eclipses, that can have a depth comparable to that expected for a planetary transit. The blended stellar binary may be either a background object or physically linked to the brighter star, thus forming a hierarchical triple system. Blends are very common in the WASP photometry, due to the low angular resolution of the images (plate scale of 13.7″/31.6″ per pixel with the 200mm/85mm lenses) and inherently large photometric apertures used (minimal aperture = 34.25″).

Follow-up eclipse photometry at higher spatial resolution (0.64″/pixel) with TRAPPIST allows to efficiently identify blended eclipsing binaries, provided that the angular separation between the binary and the third star is larger than a few arc seconds. A typical example of such a situation is presented in Fig. 3.9. In the WASP photometry, the candidate 1SWASPJ113725.66-261925.6 (2MASS11372567-2619256, V=11.4) showed periodic brightness dips of ∼0.4% with a period of ∼1.33 days. Its color indices suggest a late-F/early-G spectral type, so these eclipses were compatible with the transits of a planetary object. However, as can be seen on Fig. 3.9 (left), two nearby fainter stars fall within the apertures used to extract the WASP photometry. On 11 December 2013, a "transit" window was observed with TRAPPIST in the $I+z$ filter and with the telescope kept in focus. The stars were clearly resolved in the higher resolution TRAPPIST images and the resulting photometry revealed a ∼20%-deep V-shaped eclipse on the closest faint star (see Fig. 3.9, right). This is an eclipsing binary, whose eclipses were diluted to shallow planet-like dips in the WASP photometry centered on the brighter candidate.

Less straightforward is the identification of blended eclipsing binaries with a so small angular separation between the components that they cannot be resolved with TRAPPIST or EulerCam, as is often the case for hierarchical triple systems. Most of these objects can be resolved with CORALIE spectroscopic observations, thanks to the presence of several components in the spectra (double or triple-lined spectroscopic systems, SB2s or SB3s) or the detection of large RV variations. However, it may happen that the parameters of the components are such that the system produces both photometric signals similar to planetary transits and planet-like RV variations, due to the blend of several sets of lines in the spectra. In such a case, the measured RV variations originate in fact from changes in the shape of the asymmetric[16] cross-correlation function (CCF, Section 2.1), caused by relative shifts of the blended spectral lines. The existence of a correlation between the RVs and the CCF bisector spans[17] allows to identify such a scenario (see e.g. Santos et al. 2002). Additional evidence may be provided by multi-color eclipse photometry, as these systems are likely to show wavelength-dependent eclipse depths, due to the different colors of the blended stars.

False alarms

False alarms are objects showing some patterns in their WASP light curve that are wrongly interpreted as transit-like events by the transit-search algorithm, whereas no genuine transits or eclipses are in fact present. The photometric patterns may be due to observational

[16]The cross-correlation function is representative of the average profile of the spectral lines (Queloz et al. 2001). In this case, the spectral lines are blended and thus distorted.

[17]The bisector span of the CCF is defined as the difference between the bisector slopes at the top and bottom of the profile (Queloz et al. 2001). This is a measurement of the shape of the line profile.

artifacts, instrumental effects or intrinsic stellar variability. These objects show no signs of eclipses or RV variations in photometric and spectroscopic follow-up observations. They may also be identified by further visual inspection of the WASP photometry or with new WASP data (e.g. another campaign on the same field) that are not affected by the same artifacts, and in which the initial signal is thus not detected anymore.

... and when we find a planet?

All the above false positive scenarios need to be fully discarded in order for a candidate to be validated as a new transiting planet. Once the planetary nature of a candidate has been confirmed, additional CORALIE RVs and high-precision TRAPPIST and EulerCam transit light curves are gathered, to precisely determine the system parameters. A spectroscopic analysis is first performed to establish the stellar parameters (effective temperature, surface gravity, metallicity, etc.). The physical and orbital parameters of the system are then obtained from a combined analysis of the photometric and RV data. Detailed descriptions of this process in the cases of the WASP-68, -73, -88, and -121 planetary systems (Delrez et al. 2014, Delrez et al. 2016) are given in Sections 3.2.6 and 3.2.7.

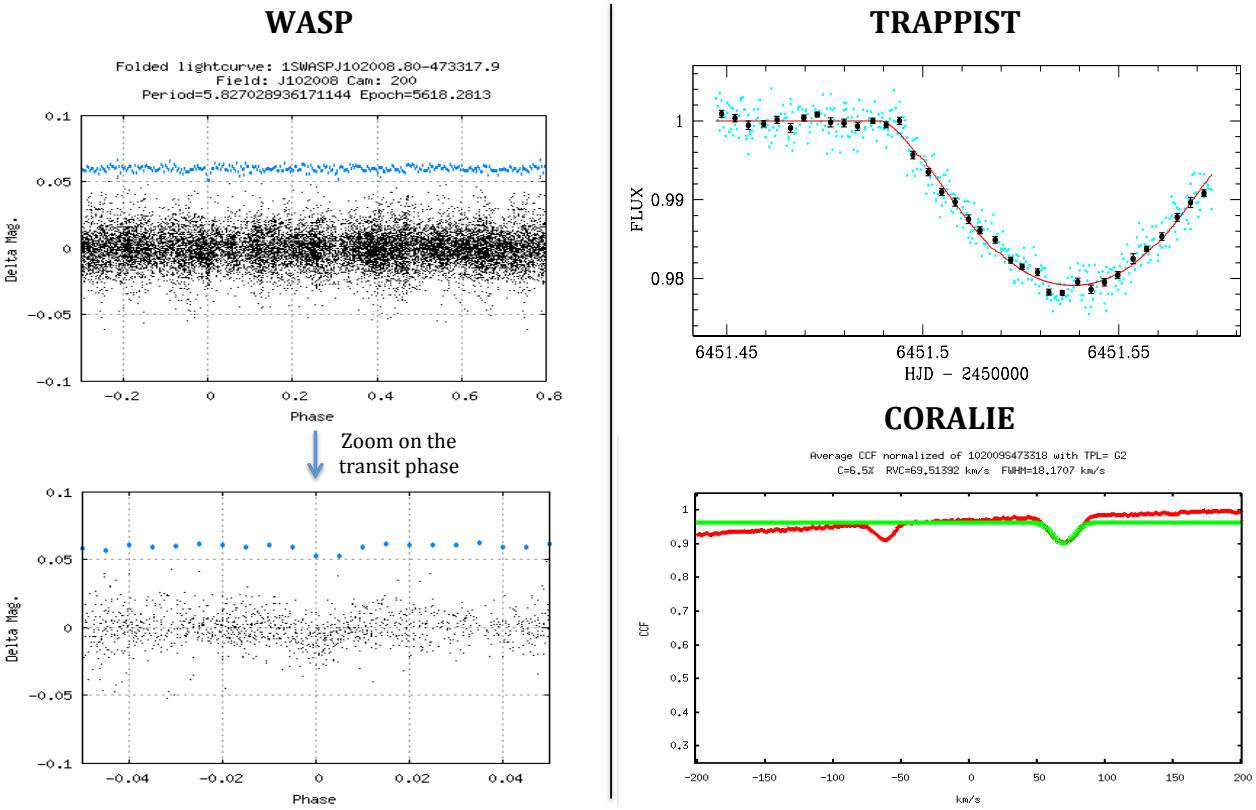

FIGURE 3.7: An example of a WASP candidate that turned out to be a grazing eclipsing binary, as revealed by TRAPPIST and CORALIE follow-up observations. *Left/top:* The WASP light curve, folded on the most likely period of the candidate. *Left/bottom:* A zoom on the transit phase. *Right/top:* A high-precision follow-up eclipse light curve obtained with TRAPPIST in the $I + z$ filter (cyan points=unbinned, black points=binned in 5min bins), together with the best-fit eclipse model (red line). The eclipse is V-shaped and ∼2% deep, which strongly suggests a grazing eclipsing binary. *Right/bottom:* The cross-correlation function of a CORALIE spectrum of the candidate with a G2 mask is shown in red. Two well-resolved peaks, indicative of a SB2, are clearly visible. A Gaussian fit to the main peak is shown in green. This last result was provided by Amaury Triaud.

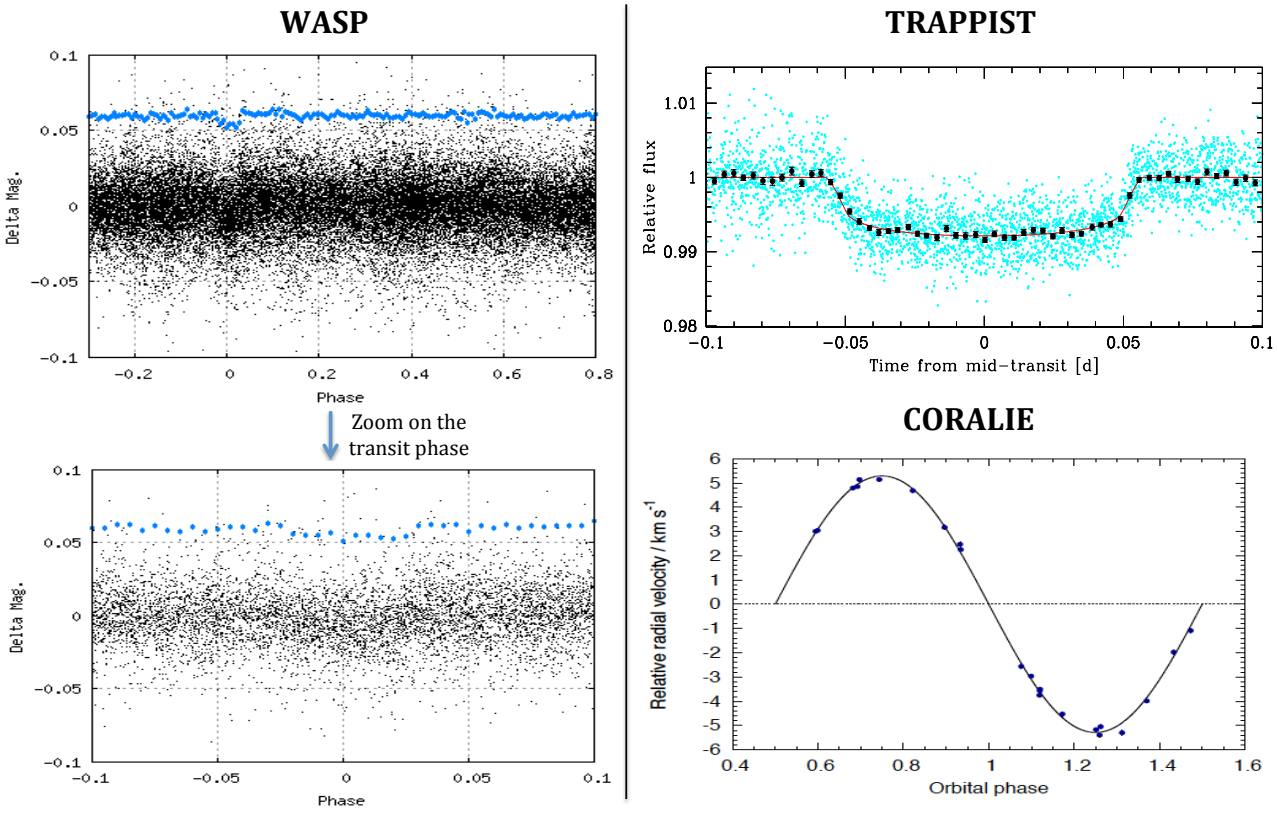

FIGURE 3.8: An example of a WASP candidate that turned out to be a high mass ratio eclipsing binary, but of a very interesting kind: the WASP-128 system. *Left/top:* The WASP light curve, folded on the most likely period of the candidate. *Left/bottom:* A zoom on the transit phase. *Right/top:* Combined follow-up transit photometry obtained with TRAPPIST in the blue-blocking filter (cyan points=unbinned, black points=binned in 5min bins), together with the best-fit transit model (red line). The transit is shallow and flat-bottomed, as expected for a transiting planet. *Right/bottom:* CORALIE RV measurements (blue points) obtained by Amaury Triaud, together with the best-fit Keplerian model (black line). The large RV variation reveals that the transiting body is not a planet, but a $\sim$39 $M_{\rm Jup}$ brown dwarf.

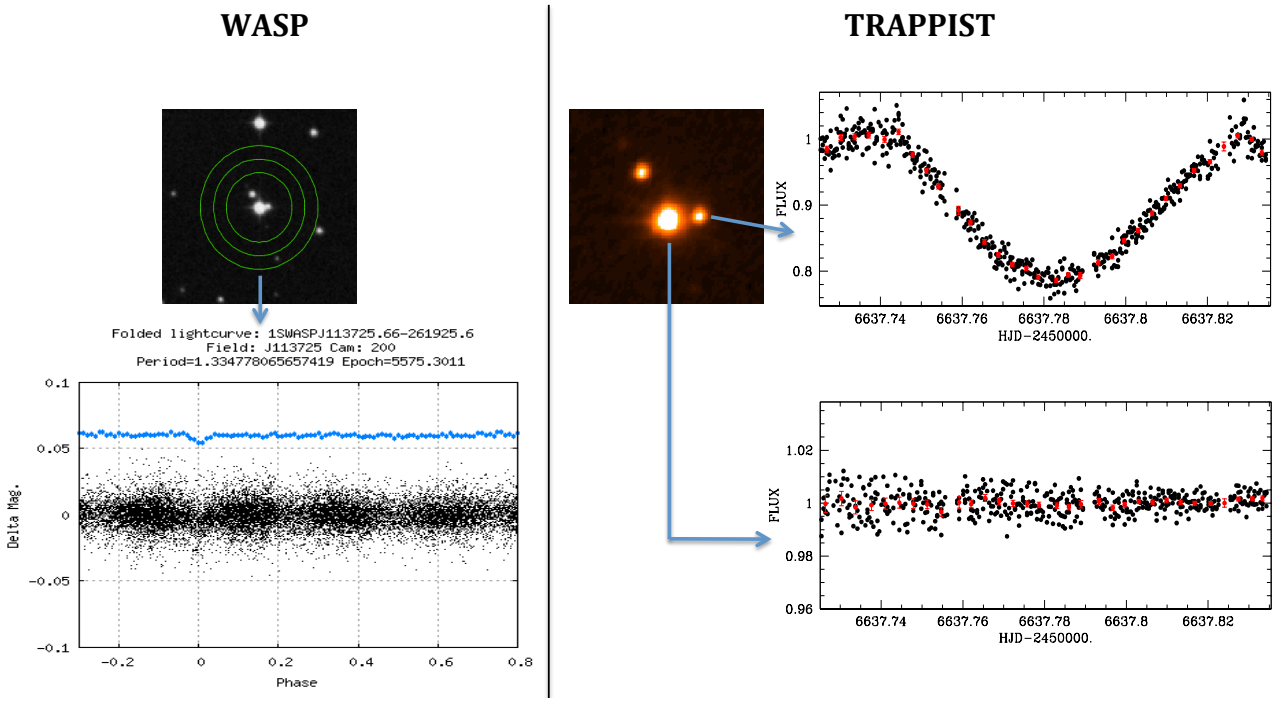

FIGURE 3.9: An example of a WASP candidate that turned out to be a blended eclipsing binary, as revealed by TRAPPIST observations. *Left:* Digitized Sky Survey image showing the bright candidate (in the centre) and two nearby fainter stars, as well as the three apertures used to extract the WASP photometry. The WASP images have actually a much poorer angular resolution than this Sky Survey image (shown here for the purpose of illustration, http://archive.eso.org/dss/dss), resulting in the candidate being blended with the two nearby stars. The WASP light curve, folded on the most likely period of the candidate, is also presented. *Right:* TRAPPIST high-precision follow-up light curves (black points=unbinned, red points=binned in 5min bins). The stars are clearly resolved in the TRAPPIST images. The candidate shows a flat light curve, while a 20%-deep eclipse is caught on the closest faint star, identifying the candidate as a blended eclipsing binary.

3.2.5 WASP planets co-detected with TRAPPIST

Having been in charge of the WASP-South photometric follow-up with TRAPPIST for most of my PhD, I contributed to many planet discoveries. Details of these findings can be found in the resulting publications[18] (see Appendix A), whose first pages are presented in Appendix B to give an idea of the high success of the WASP collaboration. Some special planets that I would like to highlight briefly are:

- WASP-94A b: A planet with a mass of ∼0.45 $M_{\rm Jup}$ and a radius of ∼1.72 $R_{\rm Jup}$, in a ∼3.95 days orbit around a bright (V=10.1) F8V star in a wide F8+F9 binary system (Neveu-VanMalle et al. 2014). What makes this system truly special is that a second non-transiting hot Jupiter, WASP-94B b, was detected by CORALIE RVs around the binary companion, WASP-94B. Hot Jupiters being rare, the discovery of two of these planets in the same star system could provide some interesting insights into their formation process.

- WASP-103 b: This extreme hot Jupiter has a mass of ∼1.5 $M_{\rm Jup}$, an inflated radius of ∼1.6 $R_{\rm Jup}$, and is in an ultra-short-period orbit (P∼22.2 hrs) around a relatively bright (V = 12.1) F8V star (Gillon et al. 2014). It is one of the most highly irradiated (∼9×10^9 erg $\rm s^{-1}cm^{-2}$) planets known to date and a prime target for atmospheric characterization studies, especially via emission spectroscopy (see Chapter 5). Its orbital semi-major axis is also only ∼1.16 times larger than its Roche limit, meaning that the planet might be close to tidal disruption.

- WASP-127A b: A highly inflated sub-Saturn-mass planet (∼0.18 $M_{\rm Jup}$, ∼1.34 $R_{\rm Jup}$) in a ∼4.2 days orbit around a bright (V=10.2) G2V star in a wide G2+G6 binary system (Lam et al., submitted to A&A). Having a very low density (∼0.075 $\rho_{\rm Jup}$) and a moderately high equilibrium temperature (∼1492K assuming a null Bond albedo and an efficient day-night heat redistribution), it should possess a large extended atmosphere, making it an excellent target for atmospheric studies via transmission spectroscopy. The binary companion, WASP-127B (V=11), is also an ideal comparison star for such studies.

- WASP-130 b: This planet orbits its G6V host star (V=11.1) every ∼11.55 days, the longest orbital period yet found by WASP, and is thus a "warm Jupiter" (Hellier et al. 2016). It has a radius of ∼0.89 $R_{\rm Jup}$ for a mass of ∼1.23 $M_{\rm Jup}$, in line with the trend noted by e.g. Demory and Seager (2011) that modestly irradiated ($\lesssim2\times10^8$ erg $\rm s^{-1}cm^{-2}$) Jupiters do not have inflated radii, in contrast to many hotter giant planets.

- WASP-166 b: This planet has a mass of only ∼0.07 $M_{\rm Jup}$ (∼1.3 Neptune masses) but a radius of ∼0.8 $R_{\rm Jup}$, and is in a ∼5.4 days orbit around a bright (V=9.4) F8V star (not yet published). It is the lowest-mass planet yet discovered by WASP and one of the most optimal targets for transmission spectroscopy known to date.

I also had the great opportunity to lead the analysis and publication of four planetary systems: WASP-68, -73, -88 (Delrez et al. 2014), and WASP-121 (Delrez et al. 2016). Their discovery is described in detail in the next two sections.

[18] About thirty confirmed planets have not yet been published.

3.2.6 WASP-68 b, WASP-73 b, and WASP-88 b

All three planets are hot Jupiters in ∼4–5 days orbits around evolved late-F/early-G stars, yet they have very different bulk properties. With a mass of 0.95±0.03 $M_{\rm Jup}$ and a radius of $1.24^{+0.10}_{-0.06}$ $R_{\rm Jup}$, WASP-68 b is a typical hot Jupiter that orbits a G0-type star every ∼5.08 days. WASP-73 b is a dense $1.88^{+0.07}_{-0.06}$ $M_{\rm Jup}$, $1.16^{+0.12}_{-0.08}$ $R_{\rm Jup}$ planet in a ∼4.09 days orbit around a F9 star. Its high mean density ($1.20^{+0.26}_{-0.30}$ $\rho_{\rm Jup}$), despite its high irradiation (∼2.3×10^9 erg $\rm s^{-1}cm^{-2}$), suggests that the planet might be enriched in heavy elements. With a mass of 0.56±0.08 $M_{\rm Jup}$ and a radius of $1.70^{+0.13}_{-0.07}$ $R_{\rm Jup}$, WASP-88 b is, on the contrary, a super-bloated hot Jupiter orbiting a F6-type star with a period of ∼4.95 days. Its extremely low mean density of 0.11±0.03 $\rho_{\rm Jup}$ makes it one of the less dense planets known to date.

The three host stars are significantly evolved (especially WASP-73) and thus have large radii (1.7–2.1 $R_\odot$), which translates into long (5–6 hrs) and shallow (0.3–0.7 %) transits for the planets. Such transits being harder to spot, the detection of these three planets demonstrates well the high efficiency of the WASP survey. The discovery paper (Delrez et al. 2014), published in A&A in 2014, is presented below.

A&A 563, A143 (2014)
DOI: 10.1051/0004-6361/201323204

Astronomy & Astrophysics

Transiting planets from WASP-South, Euler, and TRAPPIST

WASP-68 b, WASP-73 b, and WASP-88 b, three hot Jupiters transiting evolved solar-type stars⋆,⋆⋆

L. Delrez[1], V. Van Grootel[1,⋆⋆⋆], D. R. Anderson[2], A. Collier-Cameron[3], A. P. Doyle[2], A. Fumel[1], M. Gillon[1], C. Hellier[2], E. Jehin[1], M. Lendl[4], M. Neveu-VanMalle[4,6], P. F. L. Maxted[2], F. Pepe[4], D. Pollacco[5], D. Queloz[6,4], D. Ségransan[4], B. Smalley[2], A. M. S. Smith[7,2], J. Southworth[2], A. H. M. J. Triaud[8,4,⋆⋆⋆⋆], S. Udry[4], and R. G. West[5]

[1] Institut d'Astrophysique et Géophysique, Université de Liège, allée du 6 Août 17, 4000 Liège, Belgium
e-mail: ldelrez@ulg.ac.be
[2] Astrophysics Group, Keele University, Staffordshire, ST5 5BG, UK
[3] SUPA, School of Physics and Astronomy, University of St. Andrews, North Haugh, Fife, KY16 9SS, UK
[4] Observatoire de Genève, Université de Genève, 51 Chemin des Maillettes, 1290 Sauverny, Switzerland
[5] Department of Physics, University of Warwick, Coventry CV4 7AL, UK
[6] Cavendish Laboratory, Department of Physics, University of Cambridge, JJ Thomson Avenue, Cambridge, CB3 0HE, UK
[7] N. Copernicus Astronomical Centre, Polish Academy of Sciences, Bartycka 18, 00-716 Warsaw, Poland
[8] Department of Physics and Kavli Institute for Astrophysics & Space Research, Massachusetts Institute of Technology, Cambridge MA 02139, USA

Received 6 December 2013 / Accepted 18 January 2014

ABSTRACT

Using the WASP transit survey, we report the discovery of three new hot Jupiters, WASP-68 b, WASP-73 b and WASP-88 b. The planet WASP-68 b has a mass of 0.95 ± 0.03 $M_{\rm Jup}$, a radius of $1.24^{+0.10}_{-0.06}$ $R_{\rm Jup}$, and orbits a V = 10.7 G0-type star (1.24 ± 0.03 $M_\odot$, $1.69^{+0.11}_{-0.06}$ $R_\odot$, $T_{\rm eff}$ = 5911 ± 60 K) with a period of 5.084298 ± 0.000015 days. Its size is typical of hot Jupiters with similar masses. The planet WASP-73 b is significantly more massive ($1.88^{+0.07}_{-0.06}$ $M_{\rm Jup}$) and slightly larger ($1.16^{+0.12}_{-0.08}$ $R_{\rm Jup}$) than Jupiter. It orbits a V = 10.5 F9-type star ($1.34^{+0.05}_{-0.04}$ $M_\odot$, $2.07^{+0.19}_{-0.08}$ $R_\odot$, $T_{\rm eff}$ = 6036 ± 120 K) every 4.08722 ± 0.00022 days. Despite its high irradiation (~2.3 × 10^9 erg s^{-1} cm^{-2}), WASP-73 b has a high mean density ($1.20^{+0.26}_{-0.30}$ $\rho_{\rm Jup}$) that suggests an enrichment of the planet in heavy elements. The planet WASP-88 b is a 0.56 ± 0.08 $M_{\rm Jup}$ hot Jupiter orbiting a V = 11.4 F6-type star (1.45 ± 0.05 $M_\odot$, $2.08^{+0.12}_{-0.06}$ $R_\odot$, $T_{\rm eff}$ = 6431 ± 130 K) with a period of 4.954000 ± 0.000019 days. With a radius of $1.70^{+0.13}_{-0.07}$ $R_{\rm Jup}$, it joins the handful of planets with super-inflated radii. The ranges of ages we determine through stellar evolution modeling are 4.5–7.0 Gyr for WASP-68, 2.8-5.7 Gyr for WASP-73 and 1.8–4.3 Gyr for WASP-88. The star WASP-73 appears to be significantly evolved, close to or already in the subgiant phase. The stars WASP-68 and WASP-88 are less evolved, although in an advanced stage of core H-burning.

Key words. planetary systems – techniques: photometric – techniques: radial velocities – techniques: spectroscopic

1. Introduction

Since the discovery of the first extrasolar planet around a solar-type star by Mayor & Queloz (1995), more than 1000 planets have been detected outside our solar system[1]. Among this large harvest, the sub-sample of planets that transit the disc of their host star is extremely valuable. Indeed, transiting exoplanets allow parameters such as mass, radius, and density to be accurately determined (e.g. Charbonneau et al. 2000), and their atmospheric properties to be studied during their transits and occultations (e.g. Seager & Deming 2010). At the time of writing, over 400 transiting planets have been discovered[1]; a significant fraction of them are Jovian-type planets orbiting within 0.1 AU of their host star. Most of these so-called "hot Jupiters" were detected by ground-based transit surveys, among which the Wide Angle Search for Planets (WASP) survey (Pollacco et al. 2006) has been the most successful with now more than 100 planets discovered (Hellier et al. 2013). Ongoing WASP discoveries are important for the field of exoplanetology, as these systems tend to be particularly prone to thorough characterizations, owing to their bright host stars (9 < V < 13), short orbits, and favorable planet-to-star area ratios. Therefore, they will be prime targets for thorough characterizations with future facilities, such as CHaracterising ExOPlanets Satellite (CHEOPS, Broeg et al. 2013) and *James Webb* Space Telescope (JWST, Gardner et al. 2006).

In this paper, we report the discovery of three additional transiting planets by the WASP survey. The planet WASP-68 b is a 0.95 $M_{\rm Jup}$ hot Jupiter in a 5 days orbit around a G0-type star; WASP-73 b is a dense 1.88 $M_{\rm Jup}$ planet that

⋆ Tables 1–3 are available in electronic form at http://www.aanda.org
⋆⋆ The photometric time-series used in this work are only available at the CDS via anonymous ftp to cdsarc.u-strasbg.fr (130.79.128.5) or via http://cdsarc.u-strasbg.fr/viz-bin/qcat?J/A+A/563/A143
⋆⋆⋆ Chargée de recherches, Fonds de la Recherche Scientifique, FNRS, rue d'Egmont 5, 1000 Bruxelles, Belgium.
⋆⋆⋆⋆ Fellow of the Swiss National Science Foundation.
[1] http://exoplanet.eu/

A&A 563, A143 (2014)

orbits an F9-type star every 4.1 days, while WASP-88 b is a super-bloated 0.56 $M_{\rm Jup}$ planet in a 4.9 days orbit around an F6-type star. All three host stars appear to be significantly evolved. Consequently, they have relatively large radii ($R_\star$ = 1.7–2.1 $R_\odot$), translating into long (5–6 h) and low-amplitude transits for the three planets: ∼0.6% for WASP-68 b, ∼0.3% for WASP-73 b (the shallowest transits yet for a WASP planet), and ∼0.7% for WASP-88 b. Their detection demonstrates, therefore, the excellent photometric potential of the WASP survey.

Section 2 presents the WASP discovery photometry, as well as the follow-up photometric and spectroscopic observations that we used to confirm and characterize the three systems. In Sect. 3, we describe the spectroscopic determination of the stellar atmospheric properties and the derivation of the systems' parameters through combined analyses of our photometric and spectroscopic data. Finally, we discuss and summarize our results in Sect. 4.

2. Observations

2.1. WASP transit detection photometry

The WASP transit survey is operated from two sites with one for each hemisphere: the Observatorio del Roque de los Muchachos in the Canary Islands in the North and the Sutherland Station of the South African Astronomical Observatory (SAAO) in the South. Each facility consists of eight Canon 200 mm f/1.8 focal lenses coupled to e2v 2048 × 2048 pixels CCDs, which yields a field of view of 450 deg^2 for each site with a corresponding pixel scale of 13.7″/pixel. Further details of the instruments, survey, and data reduction procedures can be found in Pollacco et al. (2006), while details of the candidate selection process can be found in Collier Cameron et al. (2006, 2007). The three targets presented here, WASP-68 (1SWASPJ202022.98-191852.9 = 2MASS20202298-1918528, V = 10.7, K = 8.9), WASP-73 (1SWASPJ211947.91-580856.0 = 2MASS21194790-5808559, V = 10.5, K = 9.0), and WASP-88 (1SWASPJ203802.70-482743.2 = 2MASS20380268-4827434, V = 11.4, K = 10.3), were observed exclusively from the southern WASP site. In total, 20 804 data points were obtained for WASP-68 between May 2006 and October 2011, 50 588 measurements were gathered for WASP-73 between June 2008 and November 2011, while 39 906 data points were obtained for WASP-88 between June 2008 and October 2011. For each target, the WASP data were processed and searched for transit signals, as described in Collier Cameron et al. (2006), leading to the detection of periodic dimmings in the light curves of WASP-68, –73 and –88 with periods of 5.084 d, 4.087 d and 4.954 d, respectively. For the three objects, Fig. 1 presents the WASP photometry folded on the deduced transit ephemeris.

The method described in Maxted et al. (2011) was used to search for rotational modulation in the photometry of each object. The analysis was performed over the frequency interval 0–1.5 cycles/day at 8192 evenly spaced frequencies. No periodic signal was found above the mmag amplitude.

2.2. Spectroscopy and radial velocities

Spectroscopic measurements of each star were obtained using the CORALIE spectrograph mounted on the 1.2 m Euler-Swiss telescope at the La Silla site (Chile). A total of 43 spectra were gathered for WASP-68 between May 2011 and August 2013; 20 spectra were obtained for WASP-73 from October 2011 to September 2013, while 23 spectra were gathered for WASP-88 between September 2011 and October 2013. For all spectroscopic observations, radial velocities (RVs) were computed using the weighted cross-correlation technique described in Pepe et al. (2002). These RVs are presented in Tables 1–3. For each star, RV variations were detected with periods similar to those found in the WASP photometry and with semi-amplitudes consistent with planetary-mass companions (see Figs. 2, 4, and 6, upper panels).

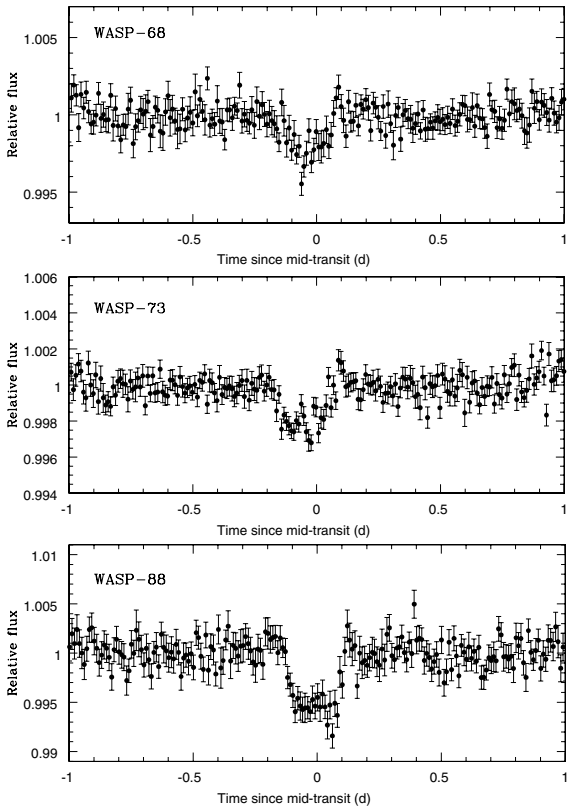

Fig. 1. WASP photometry for WASP-68 (*top*), WASP-73 (*middle*), and WASP-88 (*bottom*) folded on the best-fitting transit ephemeris from the transit search algorithm presented in Collier Cameron et al. (2006), and binned per 0.01 d intervals.

To discard any false-positive scenarios that could create RV variations that mimic planetary signatures, we checked the CORALIE cross-correlation functions (CCF) bisector spans, according to the technique described by Queloz et al. (2001). Indeed, false positives, such as blended eclipsing binaries or starspots, would also induce spectral-line distortions, resulting in correlated variations of RVs and bisector spans. This effect was, for example, observed for the HD 41004 system (Santos et al. 2002), which consists of a K-dwarf blended with an M-dwarf companion (separation of ∼0.5″) that is orbited itself by a short-period brown dwarf. For this extreme system, the RVs showed a clear signal at the period of the brown dwarf orbit (1.3 d) and with an amplitude ∼50 m s^{-1} that could have been interpreted as the signal of a sub-Saturn mass planet orbiting the K-dwarf. However, the 0.67 ± 0.03 slope of the RV-bisector relation clearly revealed that the observed signal did not originate from the K-dwarf and shed light on the blended nature of the system.

For our three systems, the bisector spans revealed to be stable; their standard deviation are close to their average error

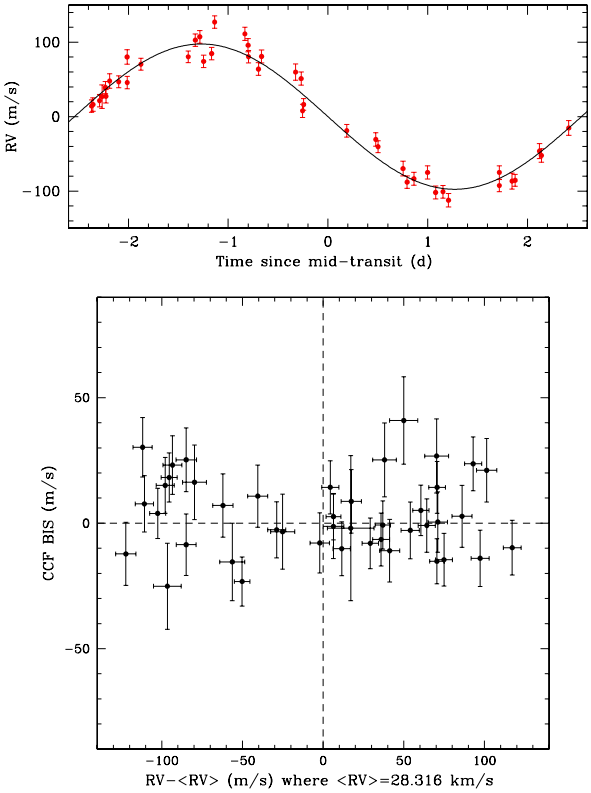

Fig. 2. *Top*: CORALIE RVs for WASP-68 phase-folded on the best-fit orbital period with the best-fit Keplerian model over-imposed in red. *Bottom*: correlation diagram CCF bisector span vs. RV.

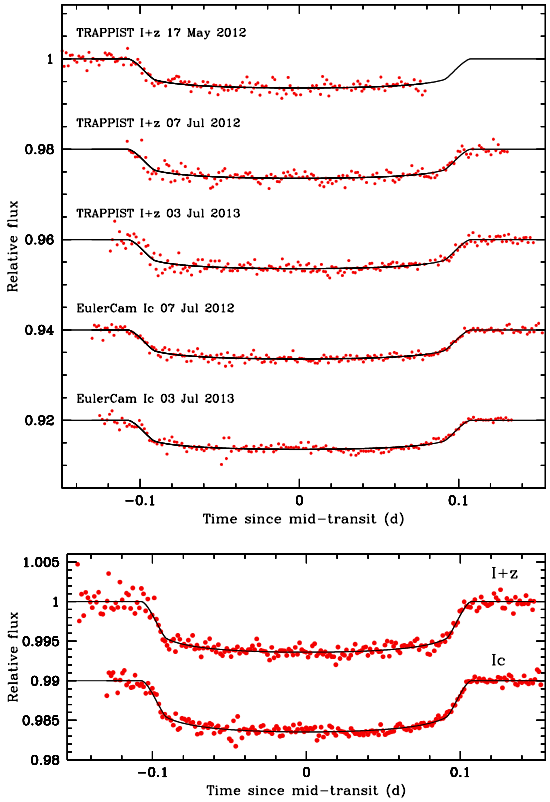

Fig. 3. *Top*: individual follow-up transit light curves for WASP-68 b. *Bottom*: combined follow-up photometry for WASP-68 b. The observations are shown as red points (bin width =2min) and are period-folded on the best-fit transit ephemeris. Each light curve has been divided by the respective photometric baseline model (see Sect. 3.2). For each filter, the superimposed, solid black line is our best-fit transit model. The light curves are shifted along the *y*-axis for clarity.

(15 vs. 12 m s^{-1} for WASP-68, 27 vs. 18 m s^{-1} for WASP-73 and 48 vs. 45 m s^{-1} for WASP-88). No correlation between the RVs and the bisector spans was found (see Figs. 2, 4, and 6, lower panels); the slopes deduced from linear regressions were -0.01 ± 0.03 (WASP-68), 0.04 ± 0.05 (WASP-73), and 0.10 ± 0.21 (WASP-88). These values and errors support our conclusion that the periodic dimming and RV variation of each system are caused by a transiting planet. This conclusion is also strengthened by the consistency of the solutions derived from the global analysis of our spectroscopic and photometric data (see Sect. 3.2).

2.3. Follow-up photometry

To refine the systems' parameters, high-quality transit observations were obtained using the 0.6 m TRAPPIST robotic telescope (TRAnsiting Planets and PlanetesImals Small Telescope) and the EulerCam CCD camera that is mounted on the 1.2 m Euler-Swiss telescope, which are both located at ESO La Silla Observatory. These follow-up light curves are summarized in Table 4 and presented in Figs. 3, 5, and 7.

2.3.1. TRAPPIST observations

TRAPPIST is a 60 cm robotic telescope dedicated to the detection and characterization of transiting exoplanets and to the photometric monitoring of bright comets and other small bodies. It is equipped with a thermoelectrically-cooled 2K × 2K CCD, which has a pixel scale of 0.65″ that translates into a 22′ × 22′ field of view. For details of TRAPPIST, see Gillon et al. (2011b) and Jehin et al. (2011). The TRAPPIST photometry was obtained using a readout mode of 2 × 2 MHz with 1 × 1 binning, which results in a readout + overhead time of 6.1 s and a readout noise of 13.5 e^-. A slight defocus was applied to the telescope to improve the duty cycle, spread the light over more pixels, and, thereby, improve the sampling of the PSF. Three transits of WASP-68 b and two transits of WASP-88 b were observed through a special "$I + z$" filter that has a transmittance >90% from 750 nm to beyond 1100 nm[2]. For WASP-73b, two transits were observed in a Sloan z' filter ($\lambda_{\rm eff} = 915.9 \pm 0.5$ nm). During the runs, the positions of the stars on the chip were maintained to within a few pixels thanks to a "software guiding" system that regularly derives an astrometric solution for the most recently acquired image and sends pointing corrections to the mount if needed. After a standard pre-reduction (bias, dark, and flatfield correction), the stellar fluxes were extracted from the images using the IRAF/DAOPHOT[3] aperture photometry software (Stetson 1987). For each light curve, we tested several sets

[2] http://www.astrodon.com/products/filters/near-infrared/

[3] IRAF is distributed by the National Optical Astronomy Observatory, which is operated by the Association of Universities for Research in Astronomy, Inc., under cooperative agreement with the National Science Foundation.

A&A 563, A143 (2014)

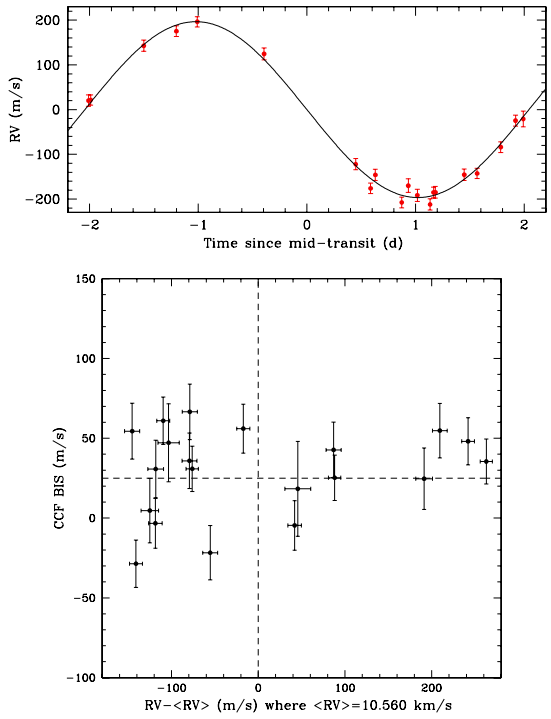

Fig. 4. *Top*: CORALIE RVs for WASP-73 phase-folded on the best-fit orbital period with the best-fit Keplerian model over-imposed in red. *Bottom*: correlation diagram CCF bisector span vs. RV.

of reduction parameters and kept the one giving the most precise photometry for the stars of similar brightness as the target. After a careful selection of reference stars, the transit light curves were finally obtained using differential photometry.

2.3.2. EulerCam observations

EulerCam is an E2V 4K × 4K back-illuminated, deep-depletion CCD detector installed at the Cassegrain focus of the 1.2 m Euler-Swiss telescope. The field of view of EulerCam is 15.7′ × 15.7′, producing a pixel scale of 0.23″. To keep the stars on the same locations on the detector during the observations, EulerCam employs an "Absolute Tracking" system that is very similar to the one of TRAPPIST, which matches the point sources in each image with a catalog, and if needed, adjusts the telescope pointing between exposures to compensate for drifts. Two transits of WASP-73 b and three transits of WASP-88 b were observed with EulerCam through Gunn-r' filter ($\lambda_{\rm eff}$ = 620.4 ± 0.5 nm), while two transits of WASP-68 b were observed in an I_c filter ($\lambda_{\rm eff}$ = 806 ± 0.5 nm). A slight defocus was applied to the telescope to optimize the observation efficiency and to minimize pixel-to-pixel effects. The reduction procedure used to extract the transit light curves was similar to that performed on TRAPPIST data. Further details of the EulerCam instrument and data reduction procedures can be found in Lendl et al. (2012).

3. Analysis

3.1. Spectroscopic analysis: Stellar atmospheric properties

For each star, the individual CORALIE spectra were co-added to produce a single spectrum with a typical S/N of around 100:1.

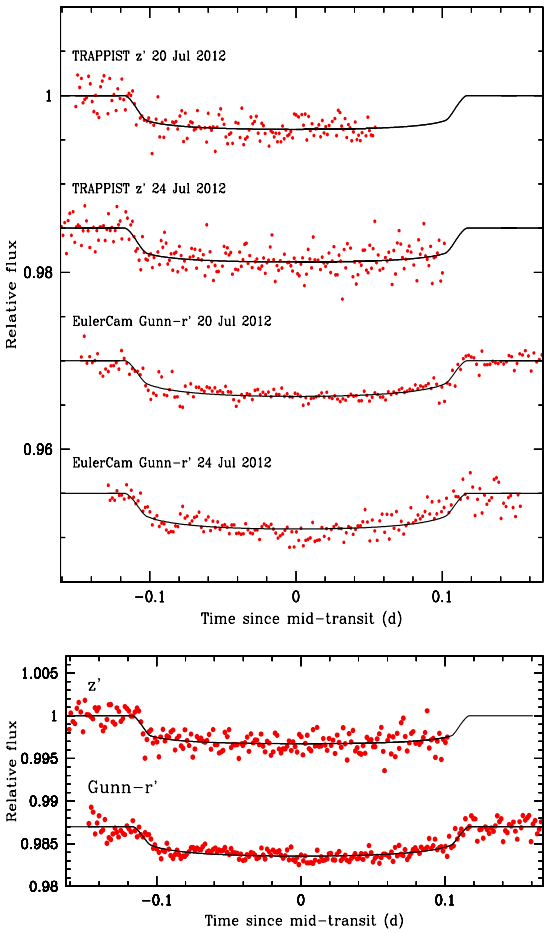

Fig. 5. *Top*: individual follow-up transit light curves for WASP-73 b. *Bottom*: combined follow-up photometry for WASP-73 b. The observations are shown as red points (bin width =2 min) and are period-folded on the best-fit transit ephemeris. Each light curve has been divided by the respective photometric baseline model (see Sect. 3.2). For each filter, the superimposed, solid black line is our best-fit transit model. The light curves are shifted along the y-axis for clarity.

The stellar atmospheric parameters were then derived using the methods given in Doyle et al. (2013). These parameters are listed in Tables 6–8 for WASP-68, WASP-73, and WASP-88, respectively. The excitation balance of the Fe lines was used to determine the effective temperature $T_{\rm eff}$. The surface gravity log $g_\star$ was determined from the ionisation balance of Fe and Fe . The Ca line at 6439 Å and the Na D lines were also used as $log\, g_\star$ diagnostics. The elemental abundances were determined from equivalent width measurements of several unblended lines. Iron abundances are relative to the solar values obtained by Asplund et al. (2009). Values for microturbulence ($\xi_{\rm t}$) were determined from Fe using the method of Magain (1984). The quoted error estimates include that given by the uncertainties in $T_{\rm eff}$ and log $g_\star$, as well as the scatter due to measurement and atomic data uncertainties. The projected stellar rotation velocity v sin $i_\star$ was determined by fitting the profiles of several unblended Fe lines. An instrumental FWHM of 0.11 ± 0.01 Å was determined for the three stars from the telluric lines around 6300 Å. Macroturbulence ($v_{\rm mac}$) values were obtained from the calibration of Bruntt et al. (2010). Spectral

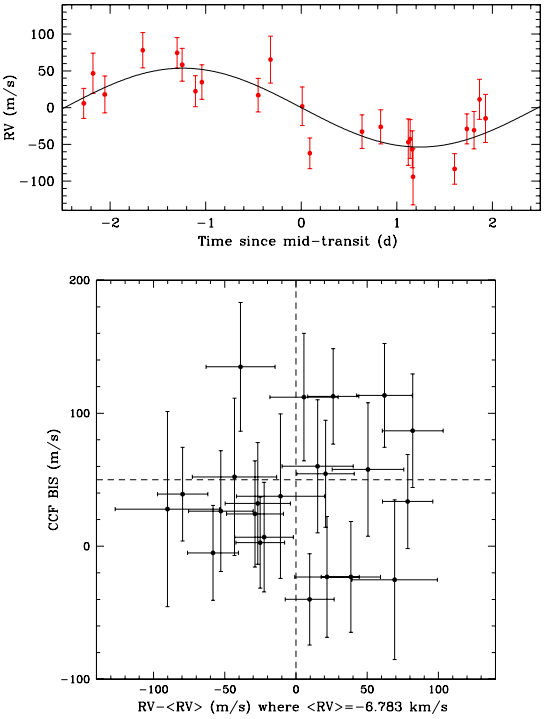

Fig. 6. *Top*: CORALIE RVs for WASP-88 phase-folded on the best-fit orbital period with the best-fit Keplerian model over-imposed in red. *Bottom*: correlation diagram CCF bisector span vs. RV.

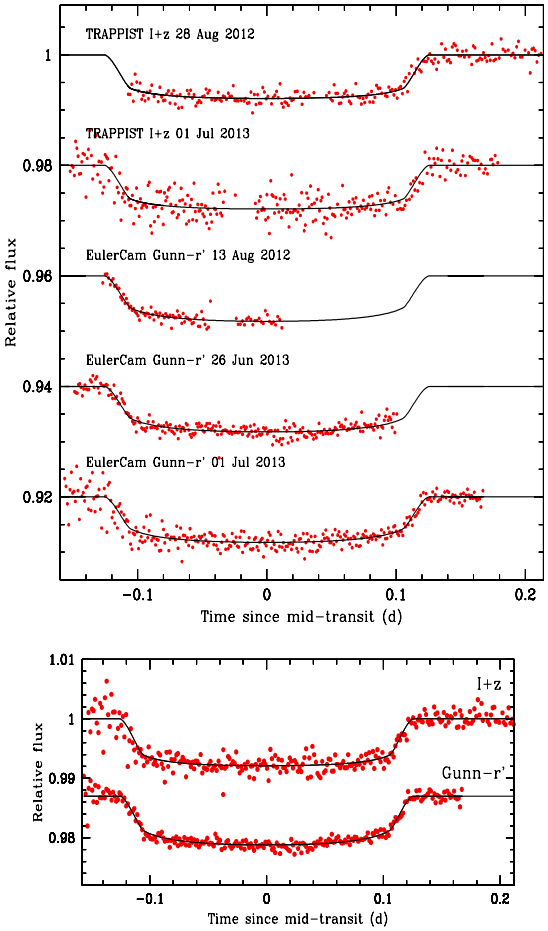

Fig. 7. *Top*: individual follow-up transit light curves for WASP-88 b. *Bottom*: combined follow-up photometry for WASP-88 b. The observations are shown as red points (bin width =2min) and are period-folded on the best-fit transit ephemeris. Each light curve has been divided by the respective photometric baseline model (see Sect. 3.2). For each filter, the superimposed, solid black line is our best-fit transit model. The light curves are shifted along the *y*-axis for clarity.

types were estimated from $T_{\rm eff}$ using the table in Gray (2008). Finally, we also used the Torres et al. (2010) calibration to obtain first stellar mass estimates: $1.24 \pm 0.10\ M_\odot$ for WASP-68, $1.40 \pm 0.12\ M_\odot$ for WASP-73, and $1.38 \pm 0.12\ M_\odot$ for WASP-88.

3.2. Global analysis

To determine the parameters of each system, we performed a combined analysis of the follow-up photometry and the RV data, using for this purpose the adaptive Markov chain Monte-Carlo (MCMC) code described in Gillon et al. (2012) and references therein. The algorithm simultaneously models the data, using for the photometry, the transit model by Mandel & Agol (2002) multiplied by a different baseline model for each light curve, and a classical Keplerian model for the RVs (e.g. Murray & Correia 2010).

The photometric baseline models aim to represent astrophysical, instrumental, or environmental effects, which are able to produce photometric variations and can, therefore, affect the transit light curves. They are made up of different first to fourth-order polynomials with respect to time or other variables, such as airmass, PSF full-width at half maximum, background, or stellar position on the detector. To find the optimal baseline function for each light curve, i.e. the model minimizing the number of parameters and the level of noise in the best-fit residuals, the Bayes factor, as estimated from the Bayesian Information Criterion (Schwarz 1978), was used. The best photometric model functions are listed in Table 4. For six TRAPPIST light curves (see Table 4), a normalization offset was also part of the baseline model to represent the effect of the meridian flip; that is, the 180° rotation that the German equatorial mount telescope has to undergo when the meridian is reached. This movement results in different positions of the stellar images on the detector before and after the flip, and the normalization offset allows to take into account a possible consecutive jump in the differential photometry at the time of the flip.

Concerning the RVs, a model with a trend was tested for each system. Such a trend would be indicative of the presence of an additional massive body in the system. A model with a slope was slightly favored in the case of WASP-68 with a Bayes factor ~90. We thus adopted this model for this system but the Bayes factor value is not high enough to be decisive (Jeffreys 1961) and more RVs are needed to confirm this possible trend.

The basic jump parameters in our MCMC analyses, i.e. the parameters that are randomly perturbed at each step of the MCMC, were: the planet/star area ratio $(R_{\rm p}/R_\star)^2$; the transit impact parameter in the case of a circular orbit $b' = a \cos i_{\rm p}/R_\star$ where a is the orbital semi-major axis and $i_{\rm p}$ is the orbital inclination; the transit width (from 1st to 4th contact) W; the time of mid-transit T_0; the orbital period P; the parameter $K_2 = K\sqrt{1-e^2}\ P^{1/3}$ where K is the RV orbital semi-amplitude and e is the orbital eccentricity; and the two

A&A 563, A143 (2014)

Table 4. Summary of follow-up photometry obtained for WASP-68, WASP-73, and WASP-88.

Target	Night	Telescope	Filter	N_p	T_{exp} (s)	Baseline function	σ (%)	σ_{120s} (%)	β_w	β_r	CF
WASP-68	2012 May 16–17	TRAPPIST	$I+z$	1139	8	$p(a^1+f^1+xy^1)+o$	0.28	0.10	1.03	1.22	1.26
WASP-68	2012 Jul. 06–07	TRAPPIST	$I+z$	1181	8	$p(a^2+b^1+xy^2)+o$	0.30	0.11	1.21	1.27	1.54
WASP-68	2013 Jul. 02–03	TRAPPIST	$I+z$	1357	8	$p(t^2+b^1+xy^1)+o$	0.25	0.10	0.88	1.57	1.39
WASP-68	2012 Jul. 06–07	EulerCam	I_c	412	40	$p(t^2+f^2+b^1)$	0.10	0.07	1.40	1.00	1.40
WASP-68	2013 Jul. 02–03	EulerCam	I_c	333	50	$p(a^1+f^1+xy^1)$	0.10	0.08	1.36	2.15	2.93
WASP-73	2012 Jul. 19–20	TRAPPIST	z'	476	25	$p(t^2)$	0.22	0.12	1.13	1.08	1.22
WASP-73	2012 Jul. 23–24	TRAPPIST	z'	640	25	$p(a^1+f^1)+o$	0.25	0.14	1.47	1.11	1.63
WASP-73	2012 Jul. 19–20	EulerCam	Gunn-r'	346	60	$p(t^2+f^2+xy^1)$	0.10	0.07	1.48	1.54	2.27
WASP-73	2012 Jul. 23–24	EulerCam	Gunn-r'	352	50	$p(a^1+xy^1)$	0.13	0.10	1.61	2.55	4.11
WASP-88	2012 Aug. 27–28	TRAPPIST	$I+z$	867	20	$p(a^1)+o$	0.23	0.11	1.10	1.19	1.31
WASP-88	2013 Jun. 30–Jul. 01	TRAPPIST	$I+z$	837	20	$p(t^2)+o$	0.37	0.21	1.59	1.14	1.82
WASP-88	2012 Aug. 12–13	EulerCam	Gunn-r'	95	80	$p(a^1+xy^2)$	0.08	0.08	1.25	1.00	1.25
WASP-88	2013 Jun. 25–26	EulerCam	Gunn-r'	246	70	$p(a^1+f^1)$	0.09	0.09	1.31	2.33	3.05
WASP-88	2013 Jun. 30-Jul. 01	EulerCam	Gunn-r'	317	70	$p(t^2+b^1)$	0.17	0.17	2.45	1.08	2.65

Notes. For each light curve, this table shows the date of acquisition, the used instrument and filter, the number of data points, the exposure time, the selected baseline function, the standard deviation of the best-fit residuals (unbinned and binned per intervals of 2 min), and the deduced values for β_w, β_r and $CF = \beta_w \times \beta_r$. For the baseline function, $p(\epsilon^N)$ denotes, respectively, a N-order polynomial function of time ($\epsilon = t$), airmass ($\epsilon = a$), PSF full-width at half maximum ($\epsilon = f$), background ($\epsilon = b$), and x and y positions ($\epsilon = xy$). The symbol o denotes an offset fixed at the time of the meridian flip.

parameters $\sqrt{e}\cos\omega$ and $\sqrt{e}\sin\omega$, where ω is the argument of the periastron. The reasons to use $\sqrt{e}\cos\omega$ and $\sqrt{e}\sin\omega$ as jump parameters instead of the more traditional $e\cos\omega$ and $e\sin\omega$ are detailed in Triaud et al. (2011). For all these jump parameters, we assumed a uniform prior distribution. The photometric baseline model parameters were not actual jump parameters; they were determined by a least-square minimization at each step of the MCMC.

The effect of stellar limb-darkening on our transit light curves was accounted for using a quadratic limb-darkening law, where the quadratic coefficients u_1 and u_2 were allowed to float in our MCMC analysis. However, we did not use these coefficients themselves as jump parameters but their combinations, $c_1 = 2\times u_1 + u_2$ and $c_2 = u_1 - 2\times u_2$, to minimize the correlation of the obtained uncertainties as introduced by Holman et al. (2006). To obtain a limb-darkening solution consistent with theory, we used normal prior distributions for u_1 and u_2 based on theoretical values and 1σ errors interpolated in the tables by Claret & Bloemen (2011). For the non-standard $I+z$ filter, the modes of the normal prior distributions for u_1 and u_2 were taken as the averages of the values interpolated in the tables for the standard filters I_c and z', while the errors were computed as the quadratic sums of the errors for these two filters. For the three systems, the prior distributions used for u_1 and u_2 are presented in Table 5.

For each system, a preliminary analysis was performed to determine the correction factors (CF) for our photometric errors, as described in Gillon et al. (2012). For each light curve, CF is the product of two contributions, β_w and β_r. On one side, β_w represents the under- or overestimation of the white noise of each measurement. It is computed as the ratio between the standard deviation of the residuals and the mean photometric error. On the other side, β_r allows us to take into account the correlated noise present in the light curve (i.e., the inability of our model to perfectly fit the data). It is calculated from the standard deviations of the binned and unbinned residuals for different binning intervals ranging from 5 to 120 min with the largest value being kept as β_r. The standard deviation of the best-fit residuals (unbinned and binned per intervals of 2 min) and the deduced values for β_w, β_r and $CF = \beta_w \times \beta_r$ for each light curve are presented in Table 4. For each RV time-series, a "jitter" noise was determined and added quadratically to the errors to equal their mean value to the standard deviation of the best-fit residuals. These RV jitters take into account the instrumental and astrophysical effects (such as stellar activity) that are not included in the initial error estimation. The derived jitter values were 6.6 m s^{-1} for WASP-68, 9.2 m s^{-1} for WASP-73 and 10.9 m s^{-1} for WASP-88.

Table 5. Expectations and standard deviations of the normal distributions used as prior distributions for the quadratic limb-darkening (LD) coefficients u_1 and u_2 in our MCMC analyses.

LD coefficient	WASP-68	WASP-73	WASP-88
$u_{1,I+z}$	0.256 ± 0.021	–	0.187 ± 0.016
$u_{2,I+z}$	0.283 ± 0.003	–	0.303 ± 0.005
u_{1,I_c}	0.275 ± 0.010	–	–
u_{2,I_c}	0.286 ± 0.005	–	–
$u_{1,z'}$	–	0.213 ± 0.015	–
$u_{2,z'}$	–	0.291 ± 0.005	–
$u_{1,\mathrm{Gunn}-r'}$	–	0.349 ± 0.020	0.293 ± 0.012
$u_{2,\mathrm{Gunn}-r'}$	–	0.301 ± 0.008	0.319 ± 0.005

Our final analyses consisted each of five Markov chains of 10^5 steps, whose convergence was checked using the statistical test of Gelman & Rubin (1992). At each step of the Markov chains, the stellar density $\rho_\star$ was derived from the Kepler's third law and the jump parameters $(R_p/R_\star)^2$, b', W, P, $\sqrt{e}\cos\omega$ and $\sqrt{e}\sin\omega$ (see e.g. Seager & Mallén-Ornelas 2003 and Winn 2010). The resulting stellar density and values for $T_{\rm eff}$ and [Fe/H] drawn from the normal distributions deduced from our spectroscopic analysis (see Sect. 3.1) were used to determine a value for the stellar mass $M_\star$ through an empirical law $M_\star(\rho_\star, T_{\rm eff}, [\mathrm{Fe/H}])$ (Enoch et al. 2010, Gillon et al. 2011a) that is calibrated using the set of well-constrained

detached binary systems presented by Southworth (2011). For WASP-68, this set was reduced to the 116 stars with a mass between 0.7 and 1.7 $M_\odot$, while the 119 stars with a mass between 0.9 and 1.9 $M_\odot$ were used for WASP-73 and WASP-88. The goal of these selections was to benefit from our preliminary estimation of the stellar masses (see Sect. 3.1) to improve the determination of the values of the systems' parameters. To correctly propagate the error on the empirical law, the parameters of the selected subset of calibration stars were normally perturbed within their observational error bars and the coefficients of the law were redetermined at each MCMC step. The other physical parameters were then deduced from the jump parameters and stellar mass.

For each system, two analyses were performed: one assuming a circular orbit ($e = 0$) and one with a free eccentricity. For the three systems, the resulting Bayes factors (~1100 for WASP-68, ~1800 for WASP-73, and ~1800 for WASP-88) favored the circular solutions. We thus adopt the corresponding results as our nominal solutions but we present the derived parameters for both models in Table 6 (WASP-68), Table 7 (WASP-73), and Table 8 (WASP-88) for the sake of completeness. The best-fit transit models for the circular solutions are shown in Figs. 3, 5, and 7.

3.3. Stellar evolution modeling

After the completion of the MCMC analyses, we performed a stellar evolution modeling based on the CLES code (Scuflaire et al. 2008) for the three systems with the aim to assess the reliability of the deduced stellar masses and to estimate the age of the systems. We used as inputs the stellar densities deduced from the MCMC analyses, and the effective temperatures and metallicities as derived from spectroscopy (see Tables 6–8). We considered here that [Fe/H] represents the global metallicity with respect to the Sun, defined as $[\log(Z/X)_* - \log(Z/X)_\odot]$, where X and Z are the fractional mass of hydrogen and elements heavier than helium respectively. We used the most recent solar mixture of Asplund et al. (2009), which gives for the current Sun $(Z/X)_\odot = 0.0181$. The parameter of the mixing-length theory (MLT) of convection was kept fixed to the solar calibration ($\alpha_{\rm MLT} = 1.8$), and microscopic diffusion (gravitational settling) of elements was included.

The resulting stellar masses are $1.27 \pm 0.11\ M_\odot$ (WASP-68), $1.40 \pm 0.16\ M_\odot$ (WASP-73), and $1.41 \pm 0.14\ M_\odot$ (WASP-88). These 1σ uncertainties were obtained by considering the respective 1σ range for the effective temperatures, metallicities, and stellar densities but also by varying the internal stellar physics. We indeed computed, since the helium atmospheric abundance cannot be directly measured from spectroscopy, evolutionary tracks with two initial helium abundances: the solar value ($Y_\odot = 0.2485$) and a value labelled $Y_{\rm G}$ that increases with Z (as expected if the local medium follows the general trend observed for the chemical evolution of galaxies; Izotov & Thuan 2010). We also investigated the effects of the possible convective core overshooting by varying $\alpha_{\rm ov}$ between 0 and 0.3. Within the same hypotheses, the resulting stellar ages range 4.5–7.0 Gyr (WASP-68), 2.8–5.7 Gyr (WASP-73), and 1.8–4.3 Gyr (WASP-88). Three evolutionary tracks, respectively, for the central value for the stellar mass and metallicity of WASP-68, WASP-73, and WASP-88, are shown in Fig. 8. These evolutionary tracks span from the beginning (zero-age) of the main sequence to the beginning of the subgiant phase (core H-burning exhaustion). WASP-73 appears to be the most evolved star, close to or already in the subgiant phase. The

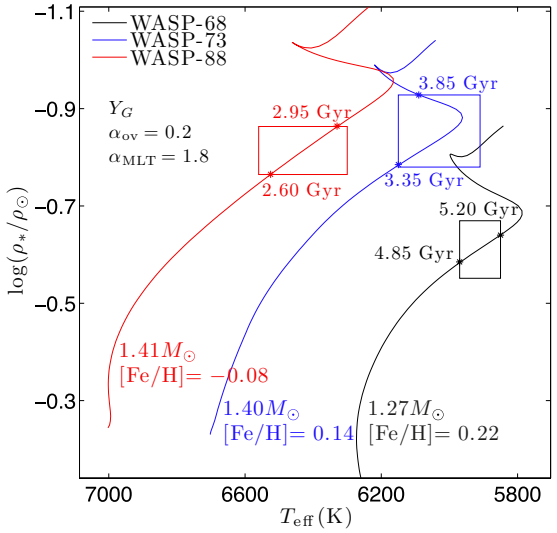

Fig. 8. Evolutionary tracks in a $T_{\rm eff} - \log(\rho_*/\rho_\odot)$ HR diagram for WASP-68 (black), WASP-73 (blue), and WASP-88 (red), for their respective central masses and metallicities. These evolutionary tracks span from the zero-age main sequence to the beginning of the subgiant phase. The ages of the stars when they cross their respective 1σ box $T_{\rm eff} - \log(\rho_*/\rho_\odot)$ are also indicated.

stars WASP-68 and WASP-88 are less evolved, although in an advanced stage of core H-burning. The subgiant phase is also a possibility, although very unlikely.

The masses derived for WASP-68 and WASP-88 are in excellent agreement with the MCMC results obtained through an empirical law $M_\star(\rho_\star, T_{\rm eff}, [{\rm Fe/H}])$ that is calibrated using a set of well-constrained detached eclipsing binary (EB) systems (see Sect. 3.2). The agreement is also good for WASP-73, which is close to core H-burning exhaustion or already in the subgiant phase, despite that the EB sample contains only a small fraction of significantly evolved objects. This shows that the EB empirical law used in the MCMC analyses is valid for the three stars considered here.

For even more evolved stars, the EB empirical law would reach its limit of applicability and could lead to inaccurate results. In such a case, a more reliable alternative would be to implement the stellar evolutionary models in the MCMC analysis, by assuming realistic prior probability distributions on the different stellar physics parameters (overshooting, diffusion, initial composition, etc.) and computing at each step M_* from ρ_*, $T_{\rm eff}$, and [Fe/H]. This is a long-term goal we are pursuing (e.g., Triaud et al. 2011). Obtaining an accurate stellar mass from evolution modeling primarily needs accurate spectroscopic estimates for the effective temperature but also, very importantly, for the metallicity (compare the tracks of two very close stellar masses, 1.40 $M_\odot$ and 1.41 $M_\odot$, but with quite different metallicities in Fig. 8).

4. Discussion and summary

We presented three newly discovered transiting hot Jupiters from the WASP survey, WASP-68 b, WASP-73 b, and WASP-88 b. We derived the parameters of each system from a joint analysis of the CORALIE spectroscopy and the high-precision photometry from TRAPPIST and EulerCam.

A&A 563, A143 (2014)

Table 6. System parameters for WASP-68.

General information		
RA (J2000)	20 20 22.98	
Dec (J2000)	–19 18 52.9	
V	10.7	
K	8.9	
Stellar parameters from spectroscopic analysis		
$T_{\rm eff}$ (K)	5910 ± 60	
log $g_\star$ [cgs]	4.17 ± 0.11	
[Fe/H]	0.22 ± 0.08	
$\xi_{\rm t}$ (km s^{-1})	1.4 ± 0.1	
$v_{\rm mac}$ (km s^{-1})	2.6 ± 0.3	
$v \sin i_\star$ (km s^{-1})	2.3 ± 0.8	
Sp. type	G0	
Parameters from MCMC analyses		
Jump parameters	$e \geq 0$	$e = 0$ (adopted)
Planet/star area ratio $(R_{\rm p}/R_\star)^2$ [%]	0.57 ± 0.03	$0.57^{+0.03}_{-0.02}$
$b' = a \cos i_{\rm p}/R_\star$ [$R_\star$]	$0.27^{+0.16}_{-0.18}$	$0.26^{+0.15}_{-0.18}$
Transit width W [d]	$0.214^{+0.003}_{-0.002}$	$0.214^{+0.003}_{-0.002}$
T_0 [HJD$_{\rm TDB}$]	$2456064.86355^{+0.00064}_{-0.00062}$	$2456064.86356^{+0.00060}_{-0.00061}$
Orbital period P [d]	5.084299 ± 0.000015	5.084298 ± 0.000015
RV K_2 [m s^{-1} d$^{1/3}$]	168.2 ± 3.3	$168.3^{+3.2}_{-3.3}$
RV slope [m s^{-1} y^{-1}]	14 ± 2	14 ± 2
$\sqrt{e} \cos \omega$	$0.091^{+0.041}_{-0.058}$	0 (fixed)
$\sqrt{e} \sin \omega$	$-0.037^{+0.100}_{-0.091}$	0 (fixed)
$c_{1,I+z}$	0.79 ± 0.04	$0.79^{+0.05}_{-0.04}$
$c_{2,I+z}$	–0.31 ± 0.02	–0.31 ± 0.03
c_{1,I_c}	0.84 ± 0.03	0.84 ± 0.02
c_{2,I_c}	–0.29 ± 0.02	–0.29 ± 0.02
Effective temperature $T_{\rm eff}$ [K][a]	5911 ± 60	5911^{+59}_{-60}
Metallicity [Fe/H] [dex][a]	0.22 ± 0.08	0.22 ± 0.08
Deduced stellar parameters		
Mean density $\rho_\star$ [$\rho_\odot$]	$0.26^{+0.03}_{-0.05}$	$0.26^{+0.03}_{-0.05}$
Surface gravity log $g_\star$ [cgs]	$4.09^{+0.13}_{-0.08}$	$4.09^{+0.13}_{-0.08}$
Mass $M_\star$ [$M_\odot$]	1.23 ± 0.03	1.24 ± 0.03
Radius $R_\star$ [$R_\odot$]	$1.69^{+0.13}_{-0.07}$	$1.69^{+0.11}_{-0.06}$
Luminosity $L_\star$ [$L_\odot$]	$3.1^{+0.5}_{-0.3}$	$3.2^{+0.4}_{-0.3}$
$u_{1,I+z}$	0.25 ± 0.02	$0.26^{+0.03}_{-0.02}$
$u_{2,I+z}$	0.28 ± 0.01	0.28 ± 0.01
u_{1,I_c}	0.28 ± 0.01	0.28 ± 0.01
u_{2,I_c}	0.28 ± 0.01	0.28 ± 0.01
Deduced planet parameters		
RV K [m s^{-1}]	97.9 ± 1.9	97.9 ± 1.9
Planet/star radius ratio $R_{\rm p}/R_\star$	0.075 ± 0.002	0.075 ± 0.002
$b_{\rm tr}$ [$R_\star$]	$0.27^{+0.16}_{-0.18}$	$0.26^{+0.15}_{-0.18}$
$b_{\rm oc}$ [$R_\star$]	$0.27^{+0.16}_{-0.18}$	$0.26^{+0.15}_{-0.18}$
$T_{\rm oc}$ [HJD$_{\rm TDB}$]	2456067.444 ± 0.029	2456067.406 ± 0.001
Scaled semi-major axis $a/R_\star$	$7.91^{+0.29}_{-0.50}$	$7.90^{+0.25}_{-0.46}$
Orbital semi-major axis a [AU]	$0.06204^{+0.00049}_{-0.00042}$	$0.06206^{+0.00045}_{-0.00040}$
Orbital inclination $i_{\rm p}$ [deg]	$88.1^{+1.3}_{-1.4}$	88.1 ± 1.3
Orbital eccentricity e	$0.017^{+0.012}_{-0.010}$, < 0.063 (95 %)	0 (fixed)
Argument of periastron ω [deg]	338^{+63}_{-42}	–
Mean density $\rho_{\rm p}$ [$\rho_{\rm Jup}$]	$0.50^{+0.08}_{-0.11}$	$0.50^{+0.07}_{-0.10}$
Surface gravity log $g_{\rm p}$ [cgs]	$3.19^{+0.04}_{-0.07}$	$3.19^{+0.04}_{-0.06}$
Mass $M_{\rm p}$ [$M_{\rm Jup}$]	0.95 ± 0.03	0.95 ± 0.03
Radius $R_{\rm p}$ [$R_{\rm Jup}$]	$1.27^{+0.11}_{-0.06}$	$1.24^{+0.10}_{-0.06}$
Roche limit $a_{\rm R}$ [AU][b]	$0.01413^{+0.00130}_{-0.00075}$	$0.01415^{+0.00120}_{-0.00065}$
$a/a_{\rm R}$	$4.39^{+0.23}_{-0.35}$	$4.38^{+0.19}_{-0.32}$
Equilibrium temperature $T_{\rm eq}$ [K][c]	1488^{+49}_{-32}	1490^{+44}_{-29}
Irradiation [erg s^{-1}cm^{-2}]	$1.1^{+0.3}_{-0.2}\ 10^9$	$1.1^{+0.3}_{-0.2}\ 10^9$

Notes. The values given for the parameters derived from our MCMC analyses are medians and 1σ limits of the marginalized posterior probability distributions. [(a)] Using as priors the values derived from the spectroscopic analysis. [(b)] Using $a_{\rm R} = 2.46\ R_{\rm p}(M_\star/M_{\rm p})^{1/3}$ (Chandrasekhar 1987). [(c)] Assuming a null Bond albedo and an efficient heat distribution between both hemispheres.

Table 7. System parameters for WASP-73.

General information		
RA (J2000)	21 19 47.91	
Dec (J2000)	–58 08 56.0	
V	10.5	
K	9.0	
Stellar parameters from spectroscopic analysis		
$T_{\rm eff}$ (K)	6030 ± 120	
log $g_\star$	3.92 ± 0.08	
[Fe/H]	0.14 ± 0.14	
$\xi_{\rm t}$ (km s^{-1})	1.1 ± 0.2	
$v_{\rm mac}$ (km s^{-1})	3.3 ± 0.3	
$v \sin i_\star$ (km s^{-1})	6.1 ± 0.6	
Sp. type	F9	
Parameters from MCMC analyses		
Jump parameters	$e \geq 0$	$e = 0$ (adopted)
Planet/star area ratio $(R_{\rm p}/R_\star)^2$ [%]	0.33 ± 0.03	0.33 ± 0.03
$b' = a \cos i_{\rm p}/R_\star$ [$R_\star$]	$0.26^{+0.20}_{-0.17}$	$0.26^{+0.20}_{-0.18}$
Transit width W [d]	0.233 ± 0.003	0.233 ± 0.003
T_0 [HJD$_{\rm TDB}$]	2456128.7063 ± 0.0011	2456128.7063 ± 0.0011
Orbital period P [d]	4.08721 ± 0.00022	4.08722 ± 0.00022
RV K_2 [m s^{-1} d$^{1/3}$]	313.5 ± 6.9	313.9 ± 6.6
$\sqrt{e} \cos \omega$	$-0.021^{+0.065}_{-0.061}$	0 (fixed)
$\sqrt{e} \sin \omega$	$0.039^{+0.100}_{-0.110}$	0 (fixed)
$c_{1,z'}$	0.71 ± 0.03	$0.71^{+0.04}_{-0.03}$
$c_{2,z'}$	–0.37 ± 0.02	–0.37 ± 0.02
$c_{1,{\rm Gunn}-r'}$	$1.01^{+0.04}_{-0.05}$	$1.01^{+0.04}_{-0.05}$
$c_{2,{\rm Gunn}-r'}$	–0.25 ± 0.03	–0.25 ± 0.03
Effective temperature $T_{\rm eff}$ [K]^a	6030 ± 120	6036 ± 120
Metallicity [Fe/H] [dex]^a	0.14 ± 0.14	0.14 ± 0.14
Deduced stellar parameters		
Mean density $\rho_\star$ [$\rho_\odot$]	$0.15^{+0.02}_{-0.03}$	$0.15^{+0.02}_{-0.04}$
Surface gravity log $g_\star$ [cgs]	$3.92^{+0.04}_{-0.06}$	$3.93^{+0.04}_{-0.06}$
Mass $M_\star$ [$M_\odot$]	$1.34^{+0.05}_{-0.04}$	$1.34^{+0.05}_{-0.04}$
Radius $R_\star$ [$R_\odot$]	$2.09^{+0.18}_{-0.09}$	$2.07^{+0.19}_{-0.08}$
Luminosity $L_\star$ [$L_\odot$]	$5.2^{+1.0}_{-0.7}$	$5.2^{+1.0}_{-0.6}$
$u_{1,z'}$	0.21 ± 0.02	0.21 ± 0.02
$u_{2,z'}$	0.29 ± 0.01	0.29 ± 0.01
$u_{1,{\rm Gunn}-r'}$	0.35 ± 0.03	0.35 ± 0.03
$u_{2,{\rm Gunn}-r'}$	0.30 ± 0.01	0.30 ± 0.01
Deduced planet parameters		
RV K [m s^{-1}]	196.1 ± 4.3	196.3 ± 4.1
Planet/star radius ratio $R_{\rm p}/R_\star$	0.057 ± 0.003	0.057 ± 0.003
$b_{\rm tr}$ [$R_\star$]	$0.25^{+0.20}_{-0.17}$	$0.26^{+0.20}_{-0.18}$
$b_{\rm oc}$ [$R_\star$]	$0.26^{+0.20}_{-0.17}$	$0.26^{+0.20}_{-0.18}$
$T_{\rm oc}$ [HJD$_{\rm TDB}$]	$2456130.746^{+0.013}_{-0.021}$	2456130.750 ± 0.002
Scaled semi-major axis $a/R_\star$	$5.68^{+0.21}_{-0.42}$	$5.73^{+0.18}_{-0.45}$
Orbital semi-major axis a [AU]	$0.05514^{+0.00061}_{-0.00054}$	$0.05512^{+0.00060}_{-0.00053}$
Orbital inclination $i_{\rm p}$ [deg]	$87.4^{+1.8}_{-2.4}$	$87.4^{+1.8}_{-2.4}$
Orbital eccentricity e	$0.011^{+0.015}_{-0.008}$, < 0.074 (95 %)	0 (fixed)
Argument of periastron ω [deg]	108^{+110}_{-68}	–
Mean density $\rho_{\rm p}$ [$\rho_{\rm Jup}$]	$1.19^{+0.25}_{-0.29}$	$1.20^{+0.26}_{-0.30}$
Surface gravity log $g_{\rm p}$ [cgs]	$3.54^{+0.06}_{-0.08}$	$3.54^{+0.06}_{-0.08}$
Mass $M_{\rm p}$ [$M_{\rm Jup}$]	1.88 ± 0.06	$1.88^{+0.07}_{-0.06}$
Radius $R_{\rm p}$ [$R_{\rm Jup}$]	$1.16^{+0.12}_{-0.08}$	$1.16^{+0.12}_{-0.08}$
Roche limit $a_{\rm R}$ [AU]^b	$0.01090^{+0.00120}_{-0.00072}$	$0.01089^{+0.00120}_{-0.00072}$
$a/a_{\rm R}$	$5.05^{+0.34}_{-0.45}$	$5.07^{+0.34}_{-0.46}$
Equilibrium temperature $T_{\rm eq}$ [K]^c	1795^{+73}_{-52}	1790^{+75}_{-51}
Irradiation [erg s^{-1}cm^{-2}]	$2.4^{+0.7}_{-0.4}\ 10^9$	$2.3^{+0.8}_{-0.4}\ 10^9$

Notes. The values given for the parameters derived from our MCMC analyses are medians and 1σ limits of the marginalized posterior probability distributions. [(a)] Using as priors the values derived from the spectroscopic analysis. [(b)] Using $a_{\rm R} = 2.46\ R_{\rm p}(M_\star/M_{\rm p})^{1/3}$ (Chandrasekhar 1987). [(c)] Assuming a null Bond albedo and an efficient heat distribution between both hemispheres.

A&A 563, A143 (2014)

Table 8. System parameters for WASP-88.

General information		
RA (J2000)	20 38 02.70	
Dec (J2000)	–48 27 43.2	
V	11.4	
K	10.3	
Stellar parameters from spectroscopic analysis		
$T_{\rm eff}$ (K)	6430 ± 130	
log $g_\star$	4.03 ± 0.09	
[Fe/H]	–0.08 ± 0.12	
$\xi_{\rm t}$ (km s^{-1})	1.4 ± 0.1	
$v_{\rm mac}$ (km s^{-1})	4.7 ± 0.3	
$v \sin i_\star$ (km s^{-1})	8.4 ± 0.8	
Sp. type	F6	
Parameters from MCMC analyses		
Jump parameters	$e \geq 0$	$e = 0$ (adopted)
Planet/star area ratio $(R_{\rm p}/R_\star)^2$ [%]	$0.71^{+0.04}_{-0.03}$	0.70 ± 0.03
$b' = a \cos i_{\rm p}/R_\star$ [$R_\star$]	$0.24^{+0.15}_{-0.16}$	0.23 ± 0.15
Transit width W [d]	$0.252^{+0.003}_{-0.002}$	$0.252^{+0.003}_{-0.002}$
T_0 [HJD$_{\rm TDB}$]	$2456474.73145^{+0.00084}_{-0.00089}$	$2456474.73154^{+0.00085}_{-0.00086}$
Orbital period P [d]	4.954000 ± 0.000019	4.954000 ± 0.000019
RV K_2 [m s^{-1} d$^{1/3}$]	90.3 ± 11.0	89.4 ± 11.0
$\sqrt{e} \cos \omega$	$-0.147^{+0.190}_{-0.140}$	0 (fixed)
$\sqrt{e} \sin \omega$	$-0.010^{+0.260}_{-0.250}$	0 (fixed)
$c_{1,I+z}$	0.67 ± 0.04	0.67 ± 0.04
$c_{2,I+z}$	–0.42 ± 0.02	–0.42 ± 0.02
$c_{1,{\rm Gunn}-r'}$	0.90 ± 0.03	0.90 ± 0.03
$c_{2,{\rm Gunn}-r'}$	–0.35 ± 0.02	–0.35 ± 0.02
Effective temperature $T_{\rm eff}$ [K][a]	6431 ± 130	6431 ± 130
Metallicity [Fe/H] [dex][a]	–0.08 ± 0.12	–0.08 ± 0.12
Deduced stellar parameters		
Mean density $\rho_\star$ [$\rho_\odot$]	$0.16^{+0.05}_{-0.04}$	$0.16^{+0.02}_{-0.03}$
Surface gravity log $g_\star$ [cgs]	$3.95^{+0.07}_{-0.09}$	$3.96^{+0.02}_{-0.05}$
Mass $M_\star$ [$M_\odot$]	1.45 ± 0.06	1.45 ± 0.05
Radius $R_\star$ [$R_\odot$]	$2.10^{+0.24}_{-0.18}$	$2.08^{+0.12}_{-0.06}$
Luminosity $L_\star$ [$L_\odot$]	$6.8^{+1.7}_{-1.3}$	$6.8^{+1.0}_{-0.8}$
$u_{1,I+z}$	0.18 ± 0.02	0.18 ± 0.02
$u_{2,I+z}$	0.30 ± 0.01	0.30 ± 0.01
$u_{1,{\rm Gunn}-r'}$	0.29 ± 0.02	0.29 ± 0.02
$u_{2,{\rm Gunn}-r'}$	0.32 ± 0.01	0.32 ± 0.01
Deduced planet parameters		
RV K [m s^{-1}]	$53.4^{+6.8}_{-6.6}$	52.4 ± 6.6
Planet/star radius ratio $R_{\rm p}/R_\star$	0.084 ± 0.002	0.084 ± 0.002
$b_{\rm tr}$ [$R_\star$]	$0.24^{+0.15}_{-0.16}$	0.23 ± 0.15
$b_{\rm oc}$ [$R_\star$]	$0.24^{+0.16}_{-0.15}$	0.23 ± 0.15
$T_{\rm oc}$ [HJD$_{\rm TDB}$]	$2456472.135^{+0.146}_{-0.220}$	2456477.20854 ± 0.00086
Scaled semi-major axis $a/R_\star$	$6.58^{+0.56}_{-0.60}$	$6.64^{+0.17}_{-0.34}$
Orbital semi-major axis a [AU]	$0.06432^{+0.00088}_{-0.00083}$	$0.06431^{+0.00065}_{-0.00062}$
Orbital inclination $i_{\rm p}$ [deg]	$87.9^{+1.4}_{-1.6}$	$88.0^{+1.4}_{-1.5}$
Orbital eccentricity e	$0.082^{+0.084}_{-0.057}$, < 0.482 (95 %)	0 (fixed)
Argument of periastron ω [deg]	191^{+75}_{-79}	–
Mean density $\rho_{\rm p}$ [$\rho_{\rm Jup}$]	0.11 ± 0.04	0.11 ± 0.03
Surface gravity log $g_{\rm p}$ [cgs]	$2.67^{+0.10}_{-0.11}$	$2.67^{+0.07}_{-0.08}$
Mass $M_{\rm p}$ [$M_{\rm Jup}$]	0.57 ± 0.08	0.56 ± 0.08
Radius $R_{\rm p}$ [$R_{\rm Jup}$]	$1.72^{+0.21}_{-0.16}$	$1.70^{+0.13}_{-0.07}$
Roche limit $a_{\rm R}$ [AU][b]	$0.02470^{+0.00330}_{-0.00250}$	$0.02464^{+0.00210}_{-0.00150}$
$a/a_{\rm R}$	$2.60^{+0.28}_{-0.29}$	$2.61^{+0.16}_{-0.19}$
Equilibrium temperature $T_{\rm eq}$ [K][c]	1775^{+93}_{-83}	1772^{+54}_{-45}
Irradiation [erg s^{-1}cm^{-2}]	$2.3^{+0.9}_{-1.1}\ 10^9$	$2.2^{+0.5}_{-0.3}\ 10^9$

Notes. The values given for the parameters derived from our MCMC analyses are medians and 1σ limits of the marginalized posterior probability distributions. [(a)] Using as priors the values derived from the spectroscopic analysis. [(b)] Using $a_{\rm R} = 2.46\ R_{\rm p}(M_\star/M_{\rm p})^{1/3}$ (Chandrasekhar 1987). [(c)] Assuming a null Bond albedo and an efficient heat distribution between both hemispheres.

All three host stars appear to be significantly evolved (especially WASP-73, see Sect. 3.3) and thus have relatively large radii (1.7–2.2 $R_\odot$). At the time of writing, only about 20 transiting hot Jupiters have been found to orbit such large stars[4]. This small number of detections might be due to the fact that large stellar radii translate into relatively shallow transits for the potential orbiting planets. These transits are therefore more difficult to detect by ground-based transit surveys. Alternatively, this might also be indicative of the tidal destruction of hot Jupiters. Due to their relatively large masses and small semi-major axes, hot Jupiters are expected to undergo tidal transfers of angular momentum with their host stars (e.g. Barker & Ogilvie 2009), which should lead to a slow spiral-in of the planets in most cases, until they are finally disrupted at their Roche limits (Gu et al. 2003). Although the timescale for orbital decay is quite uncertain and different for each system, it would thus not be surprising to find fewer close-in giant planets around larger and older stars, as there is a higher probability that these planets, if they once existed, have already been tidally disrupted. However, this correlation between the occurrence of hot Jupiters and the systems' ages has not been demonstrated yet.

It is also now common knowledge that tidal interactions tend to realign hot Jupiters' orbits with their host stars' equatorial planes (see Barker & Ogilvie 2009). Triaud (2011) demonstrated, using spin/orbit measurements for 22 hot Jupiters around stars with masses $\geq$1.2 $M_\odot$, the existence of a correlation between these hot Jupiters' orbital obliquities and their ages and estimated the typical timescale for a non-coplanar hot Jupiter's orbit to tidally realign to be about 2.5 Gyr. Considering the estimated ages of our three systems, we can therefore expect their orbits to have realigned. However, it would be interesting to perform Rossiter-McLaughlin effect observations to confirm this tendency.

Due to the large radii of their host stars, our three planets are exposed to a relatively high irradiation (incident flux $>10^9$ erg s^{-1} cm^{-2}). Several works showed that hot Jupiters' radii correlate well with their irradiating flux (see e.g. Demory & Seager 2011; Enoch et al. 2012; or Weiss et al. 2013). Figure 9 shows the positions of our three planets in an irradiation-radius diagram for the known transiting planets with 0.5 $M_{\rm Jup}$ < $M_{\rm p}$ < 2 $M_{\rm Jup}$ and P < 12 d. WASP-68 b lies in a well-populated region of the diagram. Its physical dimensions can be considered as rather standard. Indeed, its measured radius of $1.24^{+0.10}_{-0.06}$ $R_{\rm Jup}$ is in perfect agreement with the value of 1.24 ± 0.03 $R_{\rm Jup}$ predicted by the equation derived by Weiss et al. (2013) from a sample of 103 transiting planets with a mass between 150 $M_\oplus$ and 13 $M_{\rm Jup}$ and that relates planets' sizes to their masses and irradiations. For WASP-73 b, the Weiss et al.'s law gives a radius of $1.29^{+0.04}_{-0.02}$ $R_{\rm Jup}$, which is slightly larger than our measured radius of $1.16^{+0.12}_{-0.08}$ $R_{\rm Jup}$. This might suggest a possible small enrichment of the planet in heavy elements. Its density of $1.20^{+0.26}_{-0.30}$ $\rho_{\rm Jup}$ is indeed surprisingly high, given the important irradiation the planet is exposed to ($\sim 2.3 \times 10^9$ erg s^{-1} cm^{-2}). However, the errors on its physical parameters are still too high to draw any strong inference on its internal structure.

Unlike the first two planets, WASP-88 b appears to be a clear outlier, its measured radius of $1.70^{+0.13}_{-0.07}$ $R_{\rm Jup}$ being significantly higher than the predicted value of 1.35±0.02 $R_{\rm Jup}$. With a density of 0.11 ± 0.03 $\rho_{\rm Jup}$, WASP-88 b is actually the second least dense transiting planet known to date, tied with Kepler-12 b (Fortney et al. 2011), which also has a density around 0.11 $\rho_{\rm Jup}$. Only WASP-17 b has a lower density

[4] http://exoplanet.eu/

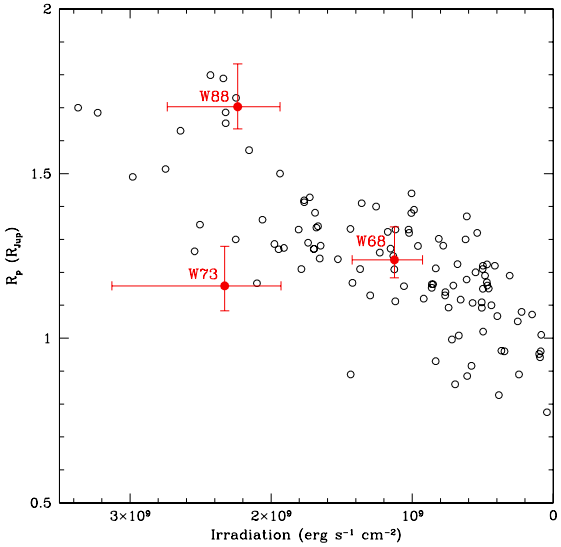

Fig. 9. Irradiation–radius diagram for the known transiting hot Jupiters with 0.5 $M_{\rm Jup}$ < $M_{\rm p}$ < 2 $M_{\rm Jup}$ and P < 12 d (data from the NASA Exoplanet Archive). The planets WASP-68 b, WASP-73 b and WASP-88 b are shown in red.

($\rho_{\rm p}$ = 0.06 $\rho_{\rm Jup}$, Anderson et al. 2011, Southworth et al. 2012). WASP-88 b thus joins the handful of planets with super-inflated radii. Its large radius might be explained, at least partially, by the low metallicity ([Fe/H] = −0.08 ± 0.12) of its star. With a mass of 0.56 $M_{\rm Jup}$, WASP-88 b is actually more Saturn-like than Jupiter-like and Enoch et al. (2011), basing on 18 transiting exoplanets with masses below 0.6 $M_{\rm p}$, found that there is a strong negative correlation between the star metallicity [Fe/H] and $R_{\rm p}$ for these planets. Keeping in mind that the chemical composition of a planet should be related to the one of its host star as they formed from the same cloud, the observation that the correlation between [Fe/H] and $R_{\rm p}$ is negligible for more massive planets agrees well with the theoretical planet models of Fortney et al. (2007) and Baraffe et al. (2008), which both suggest that the radius of a planet is more sensitive to its composition for low mass planets than it is for more massive ones. The relation (3) of Enoch et al. (2011) leads to a predicted radius of 1.51 ± 0.06 $R_{\rm Jup}$ for WASP-88 b, which is better than the value of Weiss et al. (2013) but still lower than our measured value. As WASP-88 b is the youngest of our three planets (see Sect. 3.3), tidal circularization and dissipation might have occurred recently enough to contribute to the observed inflated radius (see e.g. Leconte et al. 2010). Other physical mechanisms might also be at play, such as the deposition of kinetic energy into the planet from strong winds driven by the large day/night temperature contrast (Showman & Guillot 2002), reduced heat transport efficiency by layered convection inside the planet (Chabrier & Baraffe 2007), or Ohmic heating from currents induced through winds in the planetary atmosphere (Batygin & Stevenson 2010).

Acknowledgements. WASP-South is hosted by the South African Astronomical Observatory and we are grateful for their ongoing support and assistance. Funding for WASP comes from consortium universities and from UK's Science and Technology Facilities Council. TRAPPIST is a project funded by the Belgian Fund for Scientific Research (Fonds National de la Recherche Scientifique, F.R.S.-FNRS) under grant FRFC 2.5.594.09.F, with the participation of the Swiss National Science Fundation (SNF). L. Delrez acknowledges the support of the F.R.I.A. fund of the FNRS. M. Gillon and E. Jehin are FNRS Research Associates. A. H. M. J. Triaud received funding from a fellowship provided by the Swiss National Science Foundation under grant number PBGEP2-14559. We thank the anonymous referee for his valuable suggestions.

A&A 563, A143 (2014)

References

Anderson, D. R., Smith, A. M. S., Lanotte, A. A., et al. 2011, MNRAS, 416, 2108
Asplund, M., Grevesse, N., Sauval, A. J., & Scott, P. 2009, ARA&A, 47, 481
Baraffe, I., Chabrier, G., & Barman, T. 2008, A&A, 482, 315
Barker, A. J., & Ogilvie, G. I. 2009, MNRAS, 395, 2268
Batygin, K., & Stevenson, D. J. 2010, ApJ, 714, L238
Broeg, C., Fortier, A., Ehrenreich, D., et al. 2013, EPJ Web Conf., 47, 3005
Bruntt, H., Bedding, T. R., Quirion, P.-O., et al. 2010, MNRAS, 405, 1907
Chabrier, G., & Baraffe, I. 2007, ApJ, 661, L81
Chandrasekhar, S. 1987, Ellipsoidal figures of equilibrium
Charbonneau, D., Brown, T. M., Latham, D. W., & Mayor, M. 2000, ApJ, 529, L45
Claret, A., & Bloemen, S. 2011, A&A, 529, A75
Collier Cameron, A., Pollacco, D., Street, R. A., et al. 2006, MNRAS, 373, 799
Collier Cameron, A., Wilson, D. M., West, R. G., et al. 2007, MNRAS, 380, 1230
Demory, B.-O., & Seager, S. 2011, ApJS, 197, 12
Doyle, A. P., Smalley, B., Maxted, P. F. L., et al. 2013, MNRAS, 428, 3164
Enoch, B., Collier Cameron, A., Parley, N. R., & Hebb, L. 2010, A&A, 516, A33
Enoch, B., Cameron, A. C., Anderson, D. R., et al. 2011, MNRAS, 410, 1631
Enoch, B., Collier Cameron, A., & Horne, K. 2012, A&A, 540, A99
Fortney, J. J., Marley, M. S., & Barnes, J. W. 2007, ApJ, 659, 1661
Fortney, J. J., Demory, B.-O., Désert, J.-M., et al. 2011, ApJS, 197, 9
Gardner, J. P., Mather, J. C., Clampin, M., et al. 2006, Space Sci. Rev., 123, 485
Gelman, A., & Rubin, D. 1992, Stat. Sci., 7, 457
Gillon, M., Doyle, A. P., Lendl, M., et al. 2011a, A&A, 533, A88
Gillon, M., Jehin, E., Magain, P., et al. 2011b, EPJ Web Conf., 11, 6002
Gillon, M., Triaud, A. H. M. J., Fortney, J. J., et al. 2012, A&A, 542, A4
Gray, D. F. 2008, The Observation and Analysis of Stellar Photospheres
Gu, P.-G., Lin, D. N. C., & Bodenheimer, P. H. 2003, ApJ, 588, 509
Hellier, C., Anderson, D. R., Collier Cameron, A., et al. 2013 [arXiv:1310.5630]
Holman, M. J., Winn, J. N., Latham, D. W., et al. 2006, ApJ, 652, 1715
Izotov, Y. I., & Thuan, T. X. 2010, ApJ, 710, L67
Jeffreys, H. 1961, The Theory of Probability (New-York: Oxford University Press)
Jehin, E., Gillon, M., Queloz, D., et al. 2011, The Messenger, 145, 2
Leconte, J., Chabrier, G., Baraffe, I., & Levrard, B. 2010, A&A, 516, A64
Lendl, M., Anderson, D. R., Collier-Cameron, A., et al. 2012, A&A, 544, A72
Magain, P. 1984, A&A, 134, 189
Mandel, K., & Agol, E. 2002, ApJ, 580, L171
Maxted, P. F. L., Anderson, D. R., Collier Cameron, A., et al. 2011, PASP, 123, 547
Mayor, M., & Queloz, D. 1995, Nature, 378, 355
Murray, C. D., & Correia, A. C. M. 2010, in Exoplanets, ed. S. Seager, 15
Pepe, F., Mayor, M., Galland, F., et al. 2002, A&A, 388, 632
Pollacco, D. L., Skillen, I., Collier Cameron, A., et al. 2006, PASP, 118, 1407
Queloz, D., Henry, G. W., Sivan, J. P., et al. 2001, A&A, 379, 279
Santos, N. C., Mayor, M., Naef, D., et al. 2002, A&A, 392, 215
Schwarz, G. E. 1978, Ann. Statist., 6, 461
Scuflaire, R., Théado, S., Montalbán, J., et al. 2008, Ap&SS, 316, 83
Seager, S., & Deming, D. 2010, ARA&A, 48, 631
Seager, S., & Mallén-Ornelas, G. 2003, ApJ, 585, 1038
Showman, A. P., & Guillot, T. 2002, A&A, 385, 166
Southworth, J. 2011, MNRAS, 417, 2166
Southworth, J., Hinse, T. C., Dominik, M., et al. 2012, MNRAS, 426, 1338
Stetson, P. B. 1987, PASP, 99, 191
Torres, G., Andersen, J., & Giménez, A. 2010, A&ARv, 18, 67
Triaud, A. H. M. J. 2011, A&A, 534, L6
Triaud, A. H. M. J., Queloz, D., Hellier, C., et al. 2011, A&A, 531, A24
Weiss, L. M., Marcy, G. W., Rowe, J. F., et al. 2013, ApJ, 768, 14
Winn, J. N. 2010, in Exoplanets, ed. S. Seager, 55

Table 1. CORALIE radial-velocity measurements for WASP-68 (BS = bisector spans).

Target	HJD_{TDB} – 2 450 000	RV (km s^{-1})	σ_{RV} (km s^{-1})	BS (km s^{-1})
WASP-68	5706.775395	28.35403	0.00736	0.02521
WASP-68	5707.797750	28.39089	0.00525	–0.01458
WASP-68	5713.793654	28.31392	0.00599	0.00789
WASP-68	5715.766225	28.21345	0.00502	0.00389
WASP-68	5722.816076	28.38649	0.00448	–0.01517
WASP-68	5765.753050	28.22263	0.00584	0.02314
WASP-68	5767.749560	28.33343	0.00634	0.00869
WASP-68	5768.728542	28.38024	0.00531	–0.00094
WASP-68	5769.731770	28.32243	0.00462	0.00260
WASP-68	5770.769094	28.21813	0.00556	0.01505
WASP-68	5772.795194	28.33309	0.01445	–0.00200
WASP-68	5777.773957	28.32040	0.00529	0.01429
WASP-68	5794.600961	28.38663	0.00517	0.01427
WASP-68	5796.549753	28.20522	0.00560	0.00768
WASP-68	5806.645082	28.20412	0.00591	0.03023
WASP-68	5807.705562	28.25392	0.00629	0.00704
WASP-68	5823.546584	28.32236	0.00642	–0.00127
WASP-68	5824.573366	28.40896	0.00536	0.02367
WASP-68	5826.655256	28.23628	0.00743	0.01630
WASP-68	5852.532499	28.19375	0.00628	–0.01225
WASP-68	5856.597408	28.28718	0.00557	–0.00265
WASP-68	5858.529438	28.25969	0.00773	–0.01544
WASP-68	5864.564865	28.35191	0.00526	–0.00650
WASP-68	5883.548579	28.23114	0.00637	0.02525
WASP-68	6021.899684	28.32750	0.00537	–0.01018
WASP-68	6022.905102	28.41331	0.00562	–0.01400
WASP-68	6048.914901	28.37000	0.00565	–0.00286
WASP-68	6067.850937	28.35299	0.00479	–0.00075
WASP-68	6076.878089	28.21947	0.00857	–0.02511
WASP-68	6103.663851	28.37654	0.00503	0.00509
WASP-68	6130.635583	28.36594	0.00871	0.04089
WASP-68	6135.775843	28.35722	0.00625	–0.01097
WASP-68	6150.631492	28.38702	0.00600	0.00044
WASP-68	6183.679884	28.22057	0.00490	0.01819
WASP-68	6184.656200	28.34522	0.00505	–0.00802
WASP-68	6204.554305	28.29089	0.00749	–0.00338
WASP-68	6216.592455	28.40205	0.00616	0.00275
WASP-68	6431.931490	28.23109	0.00612	–0.00857
WASP-68	6451.773166	28.26579	0.00488	–0.02323
WASP-68	6475.858923	28.41736	0.00631	0.02107
WASP-68	6485.724714	28.43317	0.00545	–0.00978
WASP-68	6507.676974	28.27546	0.00620	0.01077
WASP-68	6530.605288	28.38629	0.00738	0.02674

Table 2. CORALIE radial-velocity measurements for WASP-73 (BS = bisector spans).

Target	HJD_{TDB}–2 450 000	RV (km s^{-1})	σ_{RV} (km s^{-1})	BS (km s^{-1})
WASP-73	5835.606190	10.44179	0.00903	0.03075
WASP-73	5837.502076	10.82294	0.00706	0.03546
WASP-73	5851.645089	10.41902	0.00743	–0.02858
WASP-73	5856.643946	10.54277	0.00765	0.05603
WASP-73	5858.553071	10.75127	0.00964	0.02465
WASP-73	5859.533285	10.45047	0.00741	0.06098
WASP-73	5864.601220	10.48392	0.00712	0.03086
WASP-73	5865.620159	10.76933	0.00854	0.05479
WASP-73	5880.549374	10.44138	0.00782	–0.00327
WASP-73	5892.578470	10.45665	0.01222	0.04721
WASP-73	5893.565583	10.60197	0.00777	–0.00459
WASP-73	5894.530903	10.80197	0.00737	0.04810
WASP-73	6130.697716	10.60558	0.01486	0.01835
WASP-73	6137.897482	10.43505	0.01011	0.00469
WASP-73	6149.772409	10.48072	0.00869	0.03588
WASP-73	6158.765097	10.48112	0.00869	0.06660
WASP-73	6216.615675	10.64684	0.00874	0.04270
WASP-73	6488.833899	10.50459	0.00852	–0.02173
WASP-73	6546.740705	10.41467	0.00873	0.05445
WASP-73	6547.703915	10.64815	0.00711	0.02528

Table 3. CORALIE radial-velocity measurements for WASP-88 (BS = bisector spans).

Target	HJD_{TDB}–2 450 000	RV (km s^{-1})	σ_{RV} (km s^{-1})	BS (km s^{-1})
WASP-88	5834.557656	–6.75688	0.01797	0.11267
WASP-88	5856.620397	–6.82192	0.02419	0.13488
WASP-88	6119.775893	–6.80810	0.01712	0.00269
WASP-88	6121.751740	–6.72092	0.01950	0.11340
WASP-88	6123.632372	–6.81181	0.01996	0.02430
WASP-88	6124.600910	–6.86256	0.01764	0.03914
WASP-88	6125.676195	–6.77344	0.01717	–0.03997
WASP-88	6133.736344	–6.80539	0.02057	0.00683
WASP-88	6134.833084	–6.79385	0.03092	0.03759
WASP-88	6135.804118	–6.76124	0.02268	–0.02308
WASP-88	6136.820069	–6.74445	0.02080	–0.02308
WASP-88	6137.869386	–6.77739	0.02396	0.11208
WASP-88	6149.574773	–6.80985	0.02288	0.03215
WASP-88	6150.543194	–6.73250	0.02512	0.05769
WASP-88	6154.586060	–6.76785	0.02499	0.06009
WASP-88	6172.627045	–6.84122	0.01786	–0.00501
WASP-88	6173.706647	–6.87322	0.03670	0.02791
WASP-88	6475.892228	–6.83574	0.02268	0.02641
WASP-88	6480.804868	–6.82613	0.02960	0.05213
WASP-88	6487.935947	–6.70113	0.02136	0.08684
WASP-88	6558.499522	–6.76226	0.02015	0.05448
WASP-88	6563.582029	–6.71375	0.03003	–0.02524
WASP-88	6567.558431	–6.70463	0.01769	0.03362

3.2.7 WASP-121 b

Some planets are more special than others. WASP-121 b is one of these. This hot Jupiter is an extremely inflated (1.86±0.04 $R_{\rm Jup}$) Jupiter-mass (1.18±0.06 $M_{\rm Jup}$) planet in a very-short-period orbit (P∼1.27 days) around a bright (V=10.4) hot ($T_{\rm eff}$=6460±140K) F6V star. Its large size, low mean density (0.20±0.01 $\rho_{\rm Jup}$), extreme irradiation (∼7.1×10^9 erg $\rm s^{-1}cm^{-2}$) and thus high equilibrium temperature (2358±52K assuming a null Bond albedo and an efficient day-night heat redistribution), as well as the brightness of its host star make it a prime target for atmospheric characterization, using both transmission and emission spectroscopy. On this ground, we decided to attempt a measurement of its very-near-IR (∼0.9μm) dayside emission with TRAPPIST, using the approach presented in Lendl et al. (2013), that consists in combining a large number of occultation light curves (here, seven) to mitigate the effects of correlated noise and progressively extract the occultation signal from the noise. This led to a >4σ detection of the planet's dayside emission (occultation depth of 603±130 ppm), a big achievement for a 0.6m telescope and the first time a planetary occultation was detected using only TRAPPIST data. This measurement provided a first observational constraint on the planet's dayside emission spectrum. Combining it with other measurements at longer wavelengths allows to gain insights on the planet's dayside atmospheric properties, as will be discussed in Chapter 6.

Another notable property of WASP-121 b is that its orbital semi-major axis is only ∼15% larger than its Roche limit, meaning that the planet might be close to tidal disruption and is probably already significantly distorted by the intense tidal forces it is subject to. Indeed, calculating its Roche shape with the Roche model of Budaj (2011), we find that its radius at the substellar point[19] is ∼12% larger than its radius at the pole and ∼10% larger than its radius on the side, making it one of the most distorted planets known to date. Using the tidal evolution equations of Matsumura, Peale, and Rasio (2010), we find that the planet could reach its Roche limit[20] within a few tens or a few hundreds of million years, depending on the efficiency of the tidal dissipation inside the star. Measuring transit timing variations due to the orbital decay of the planet, which could be detectable on the decade time-scale, would allow to constrain this tidal dissipation efficiency.

Last but not least, a measurement of the Rossiter-McLaughlin effect (see Section 1.1.2) with CORALIE suggests that the planet's orbital axis is significantly misaligned with the spin axis of the host star, which would favor a migration pathway involving strong dynamical interactions with a third body (see Section 1.2.1).

All these characteristics make WASP-121 b a fascinating hot Jupiter, that is worth the particular efforts we had to deploy to confirm its planetary nature. Indeed, the host star is active and presents a high scatter in its CORALIE RV residuals[21], CCF bisector spans (BS), and CCF FWHMs, which prevented us from using the traditional BS technique to rule out blend scenarios (cf. Section 3.2.4), the scatter in the BS values being comparable to the semi-amplitude of the RV signal. This prompted us to gather additional transit light curves with TRAPPIST and EulerCam, using different filters to assess the chromaticity of the transit, as well as extra CORALIE RVs, including during two transits with the aim of measuring the Rossiter-McLaughlin effect mentioned above. Armed with the resulting extensive data set,

[19] The substellar point is the point on the planet's surface that directly faces the star and receives the highest stellar radiation.

[20] The planet will continue to spiral towards its host star until reaching its Roche limit, where it will be tidally disrupted.

[21] RV residuals from the best-fit Keplerian model.

we were then able to validate the planet statistically using the PASTIS Bayesian software (Díaz et al. 2014, Santerne et al. 2015). The whole process is described in detail in the discovery paper (Delrez et al. 2016), which was published in MNRAS in 2016 and is presented below.

Monthly Notices of the ROYAL ASTRONOMICAL SOCIETY

MNRAS **458,** 4025–4043 (2016) doi:10.1093/mnras/stw522
Advance Access publication 2016 March 7

WASP-121 b: a hot Jupiter close to tidal disruption transiting an active F star

L. Delrez,[1]★ A. Santerne,[2] J.-M. Almenara,[3,4] D. R. Anderson,[5] A. Collier-Cameron,[6] R. F. Díaz,[7] M. Gillon,[1] C. Hellier,[5] E. Jehin,[1] M. Lendl,[8,7] P. F. L. Maxted,[5] M. Neveu-VanMalle,[7,9] F. Pepe,[7] D. Pollacco,[10] D. Queloz,[9,7] D. Ségransan,[7] B. Smalley,[5] A. M. S. Smith,[11,5] A. H. M. J. Triaud,[12,13,7]† S. Udry,[7] V. Van Grootel[1] and R. G. West[10]

[1]*Institut d'Astrophysique et Géophysique, Université de Liège, allée du 6 Août 17, B-4000 Liège, Belgium*
[2]*Instituto de Astrofísica e Ciências do Espaço, Universidade do Porto, CAUP, Rua das Estrelas, PT-4150-762 Porto, Portugal*
[3]*Univ. Grenoble Alpes, IPAG, F-38000 Grenoble, France*
[4]*CNRS, IPAG, F-38000 Grenoble, France*
[5]*Astrophysics Group, Keele University, Staffordshire ST5 5BG, UK*
[6]*SUPA, School of Physics and Astronomy, University of St. Andrews, North Haugh, Fife KY16 9SS, UK*
[7]*Observatoire de Genève, Université de Genève, 51 Chemin des Maillettes, CH-1290 Sauverny, Switzerland*
[8]*Space Research Institute, Austrian Academy of Sciences, Schmiedlstr. 6, A-8042 Graz, Austria*
[9]*Cavendish Laboratory, Department of Physics, University of Cambridge, JJ Thomson Avenue, Cambridge CB3 0HE, UK*
[10]*Department of Physics, University of Warwick, Coventry CV4 7AL, UK*
[11]*N. Copernicus Astronomical Centre, Polish Academy of Sciences, Bartycka 18, PL-00-716 Warsaw, Poland*
[12]*Centre for Planetary Sciences, University of Toronto at Scarborough, 1265 Military Trail, Toronto, ON M1C 1A4, Canada*
[13]*Department of Astronomy & Astrophysics, University of Toronto, Toronto, ON M5S 3H4, Canada*

Accepted 2016 March 1. Received 2016 March 1; in original form 2015 June 8

ABSTRACT

We present the discovery by the WASP-South survey of WASP-121 b, a new remarkable short-period transiting hot Jupiter. The planet has a mass of $1.183^{+0.064}_{-0.062}$ $M_{\rm Jup}$, a radius of 1.865 ± 0.044 $R_{\rm Jup}$, and transits every $1.274\,9255^{+0.000\,0020}_{-0.000\,0025}$ days an active F6-type main-sequence star ($V = 10.4$, $1.353^{+0.080}_{-0.079}$ $M_\odot$, 1.458 ± 0.030 $R_\odot$, $T_{\rm eff} = 6460 \pm 140$ K). A notable property of WASP-121 b is that its orbital semimajor axis is only ∼1.15 times larger than its Roche limit, which suggests that the planet is close to tidal disruption. Furthermore, its large size and extreme irradiation (∼$7.1\,10^9$ erg s^{-1} cm^{-2}) make it an excellent target for atmospheric studies via secondary eclipse observations. Using the TRAnsiting Planets and PlanetesImals Small Telescope, we indeed detect its emission in the z'-band at better than $\sim 4\sigma$, the measured occultation depth being 603 ± 130 ppm. Finally, from a measurement of the Rossiter–McLaughlin effect with the CORALIE spectrograph, we infer a sky-projected spin-orbit angle of $257.^\circ 8^{+5.^\circ 3}_{-5.^\circ 5}$. This result may suggest a significant misalignment between the spin axis of the host star and the orbital plane of the planet. If confirmed, this high misalignment would favour a migration of the planet involving strong dynamical events with a third body.

Key words: techniques: photometric – techniques: radial velocities – techniques: spectroscopic – stars: individual: WASP-121 – planetary systems.

1 INTRODUCTION

Most of the transiting exoplanets found by ground-based transit surveys (e.g. WASP, Pollacco et al. 2006; HATNet, Bakos et al. 2004) are Jovian-type planets with orbital periods of just a few days, these planets being the easiest to detect for such surveys. The orbital period distribution of these so-called 'hot Jupiters' is not smooth and presents a pile-up around periods of ∼3–4 d (see e.g. Cumming 2010). While the long-period drop-off can be explained by a lower transit probability for these systems combined to a selection effect, the reduced number of planets in orbital periods less than 2 d is definitely real, being seen in both ground- (e.g. WASP; Hellier et al.

★ E-mail: ldelrez@ulg.ac.be
† Fellow of the Swiss National Science Foundation.

2012) and space-based (e.g. *Kepler*; Howard et al. 2012) transit surveys, as well as in radial velocity (RV) surveys (see e.g. Marcy et al. 2004).

Ford & Rasio (2006) suggested that the lower edge of the pile-up is defined not by an orbital period, but rather by a tidal limit, and found that the inner cutoff is actually close to twice the Roche limit (a_R).[1] This can be naturally explained if planets were initially scattered into highly eccentric orbits with short pericentre distances from much further out, due to e.g. planet–planet interactions (e.g. Rasio & Ford 1996; Weidenschilling & Marzari 1996; Moorhead & Adams 2005; Chatterjee et al. 2008) and/or Kozai cycles (e.g. Kozai 1962; Lidov 1962; Wu & Murray 2003; Fabrycky & Tremaine 2007), and later circularized via tidal dissipation. On the contrary, they argued that this result is inconsistent with a disc-driven migration scenario (e.g. Goldreich & Tremaine 1980; Lin & Papaloizou 1986; Tanaka, Takeuchi & Ward 2002; Lubow & Ida 2010), as the inner edge of the orbital period distribution should then be right at the Roche limit. The observed distribution of orbital obliquities, with many planets found on misaligned or retrograde orbits (e.g. Triaud et al. 2010), also supports dynamical migration processes involving a third perturbing body, rather than disc migration.

The finding of several hot Jupiters with orbital separations a lower than 2 a_R, such as WASP-12 b ($a/a_R \sim 1.09$; Hebb et al. 2009), WASP-19 b ($a/a_R \sim 1.08$; Hebb et al. 2010), WASP-103 b ($a/a_R \sim 1.16$; Gillon et al. 2014), OGLE-TR-56 b ($a/a_R \sim 1.23$; Konacki et al. 2003; Adams et al. 2011), and WTS-2 b ($a/a_R \sim 1.27$; Birkby et al. 2014), challenged the scattering scenario as these planets would have been destroyed or completely ejected from their systems if they had been directly scattered to such short pericentre distances (see e.g. Guillochon, Ramirez-Ruiz & Lin 2011). However, Matsumura, Peale & Rasio (2010) showed that these extreme orbits can still result from the scattering model, assuming first a scattering into an eccentric orbit beyond 2 a_R, followed by a slow inward migration and circularization through tidal dissipation inside the planet mainly until reaching $\sim$2 a_R, and from then tidal decay through tidal dissipation inside the star only. The speed of the final tidal decay depends on the tidal dissipation efficiency of the star, which is parametrized by $Q'_\star$, the stellar tidal dissipation factor. Despite being an essential parameter in the theory of stellar tides, $Q'_\star$ is still poorly constrained, with estimates based on theoretical and observational studies ranging from 10^5 to 10^9 (see e.g. Jackson, Greenberg & Barnes 2008; Ogilvie 2009; Penev, Jackson, Spada & Thom 2012).

Planets in the $a/a_R < 2$ regime are thus key objects to further advance our understanding of how tidal forces influence the orbital evolution of close-in giant planets. Furthermore, these planets being highly irradiated due to their proximity to their host stars, they are also generally favourable targets for atmospheric studies via secondary eclipse observations (see e.g. Gillon et al. 2010; Seager & Deming 2010; Anderson et al. 2013). They thus provide us with a unique opportunity to study the relationship between the observed atmospheric properties of hot Jupiters and their tidal evolution stage. In this paper, we report the discovery of a new hot Jupiter of this rare kind by the WASP survey, WASP-121 b, which orbits a 10.4 V-magnitude F-type star at just $\sim$1.15 times its Roche limit.

Section 2 presents the WASP discovery photometry, as well as the follow-up photometric and spectroscopic observations that we used to confirm and characterize the system. In Section 3, we describe the spectroscopic determination of the stellar properties and the derivation of the system parameters through a combined analysis of our photometric and spectroscopic data. The statistical validation of the planet is then described in Section 4. Finally, we discuss our results in Section 5.

[1] I.e. the critical orbital separation inside which a planet would lose mass via Roche lobe overflow.

2 OBSERVATIONS

2.1 WASP transit detection photometry

The WASP transit survey is operated from two sites with one for each hemisphere: the Observatorio del Roque de los Muchachos in the Canary Islands in the north and the Sutherland Station of the South African Astronomical Observatory (SAAO) in the south. Each facility consists of eight Canon 200 mm f/1.8 focal lenses coupled to e2v 2048×2048 pixels CCDs, which yields a field of view of 450 deg^2 for each site with a corresponding pixel scale of 13.7 arcsec pixel^{-1}. Observations are done using a broad-band filter with a defined passband from 400 to 700 nm. The exposure time used for the survey is 30 s, and the fields are observed with a typical cadence of 8 min, in a repetitive sequence of seven to eight fields, depending on visibility constraints. Further details of the instruments, survey, and data reduction procedures can be found in Pollacco et al. (2006), while details of the candidate selection process can be found in Collier Cameron et al. (2006) and Collier Cameron et al. (2007).

The host star WASP-121 (1SWASPJ071024.05−390550.5 = 2MASS07102406−3905506, $V = 10.4$, $K = 9.4$) was observed by the WASP-South station (Hellier et al. 2011) from 2011 Oct 28 to 2012 Mar 29, leading to the collection of 9642 photometric measurements. The data were processed with the reduction pipeline described in Pollacco et al. (2006), whose main steps are: standard calibration (bias, dark, and flat-field correction), astrometric calibration, aperture photometry, and extinction and zero-point corrections. The procedures detailed in Collier Cameron et al. (2006), which are based on the Box Least-Squares (Kovács, Zucker & Mazeh 2002) and SysRem (Tamuz, Mazeh & Zucker 2005) detrending algorithms, were then used to search the data for transit signals, leading to the detection of periodic dimmings of about 1.6 per cent with a period of 1.27 d. Fig. 1 presents the WASP photometry folded on the best-fitting transit ephemeris.

The sine-wave fitting method described in Maxted et al. (2011) was used to search for periodic modulation in the WASP photometry of WASP-121 that would be caused by the combination of stellar activity and rotation, but no periodic signal was found above the

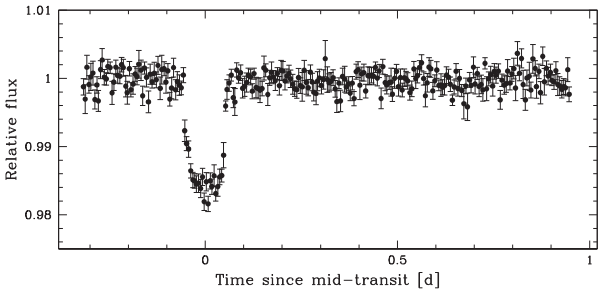

Figure 1. WASP photometry for WASP-121 folded on the best-fitting transit ephemeris from the transit search algorithm presented in Collier Cameron et al. (2006), and binned per 0.005 d intervals.

Table 1. CORALIE RV measurements for WASP-121. The uncertainties (σ_{RV}) are the formal errors (i.e. with no added jitter). For each measurement, the table also gives the CCF BS and FWHM, the exposure time (T_{exp}), and the seeing. The last two columns indicate whether the measurement was obtained before or after the replacement of the CORALIE optical fibre (see Section 2.2), and in (RM effect) or out of transit. This table is available in its entirety via the CDS.

HJD −2450 000	RV (km s^{-1})	σ_{RV} (km s^{-1})	BS (km s^{-1})	FWHM (km s^{-1})	T_{exp} (s)	Seeing (arcsec)	Pre-/post-upgrade	In/out of transit
6546.907310	38.163 52	0.017 12	0.16642	19.622 20	1800.798	0.40	Pre	Out
6567.885240	38.554 88	0.019 96	−0.27337	19.618 06	1800.838	0.92	Pre	Out
6577.854124	38.544 14	0.018 99	−0.17261	19.737 38	1800.757	0.72	Pre	Out
–	–	–	–	–	–	–	–	–

mmag amplitude. This analysis was performed over the frequency interval 0–1.5 cycles d^{-1} at 8192 evenly spaced frequencies.

2.2 Spectroscopy and RVs

The CORALIE spectrograph (Queloz et al. 2000), mounted on the 1.2 m Euler-Swiss telescope at the ESO La Silla Observatory (Chile), was used to gather 89 spectroscopic measurements of WASP-121 between 2013 Sep 11 and 2015 Jan 12 (we note that the optical fibre feeding the instrument was replaced in 2014 Nov). Among these spectra, 19 were obtained during the transit of 2014 Dec 24 and 18 during the transit of 2015 Jan 12, with the aim of measuring the Rossiter–McLaughlin (RM) effect (McLaughlin 1924; Rossiter 1924). WASP-121 was indeed considered an interesting target for such measurements, as its high projected rotation velocity $v_\star \sin i_\star$ of 13.5 ± 0.7 km s^{-1} (see Section 3.1), combined with the observed transit depth, was expected to yield an RM effect with a semi-amplitude ∼160 m s^{-1} (in the case of an aligned or anti-aligned orbit).

The spectra, covering the wavelength range from 381 to 681 nm at a resolution of ∼55 000, were processed with the CORALIE standard data reduction pipeline (Baranne et al. 1996). RVs were then computed from the spectra by weighted cross-correlation (Pepe et al. 2002), using a numerical G2-spectral template that provides optimal precisions for late-F to early-K dwarfs (Table 1). A preliminary orbital analysis of the RV time series revealed a 1.27 d periodic variation (see the top panel of Fig. 8), in phase with the WASP photometry, and with a semi-amplitude ∼180 m s^{-1} compatible with a planetary-mass companion (see Figs 2 a or b). The RM effect was found to have a surprisingly low total amplitude ∼80 m s^{-1}, suggesting that the planetary orbit may be polar (see Fig. 3). It also appeared that the star exhibits an especially high scatter in its RV residuals: the standard deviation of the best-fitting residuals is 67.1 m s^{-1} for a circular model and 66.0 m s^{-1} for an eccentric model, while the average RV error is 30.7 m s^{-1}. We consider further the origin of this high jitter in Section 3.2.

The cross-correlation function (CCF) bisector span (BS; Queloz et al. 2001) and full width at half-maximum (FWHM) values are plotted in Figs 2(c) and (d), respectively. Both present large variations, their standard deviations being 190.2 and 245.9 m s^{-1}, respectively, while their average error (calculated as 2.5 times the average RV error; see Santerne et al. 2015) is 76.7 m s^{-1}. These variations do not phase with the transit ephemeris, as one might expect if the observed RV signal was originating from a false-positive scenario, such as a blended eclipsing binary (see e.g. Santos et al. 2002); the slope deduced from linear regression of the CCF BS (respectively, FWHM) on the orbital phase is −0.05 ± 0.09 (respectively, −0.09 ± 0.11). However, as the scatter in the BS values is comparable to the semi-amplitude of the RV signal, we were not able to discard blend scenarios based on the traditional BS technique (Queloz et al. 2001). Instead, we performed a detailed blend analysis and used the PASTIS Bayesian software (Díaz et al. 2014; Santerne et al. 2014) to statistically validate the planet, as described in Section 4.

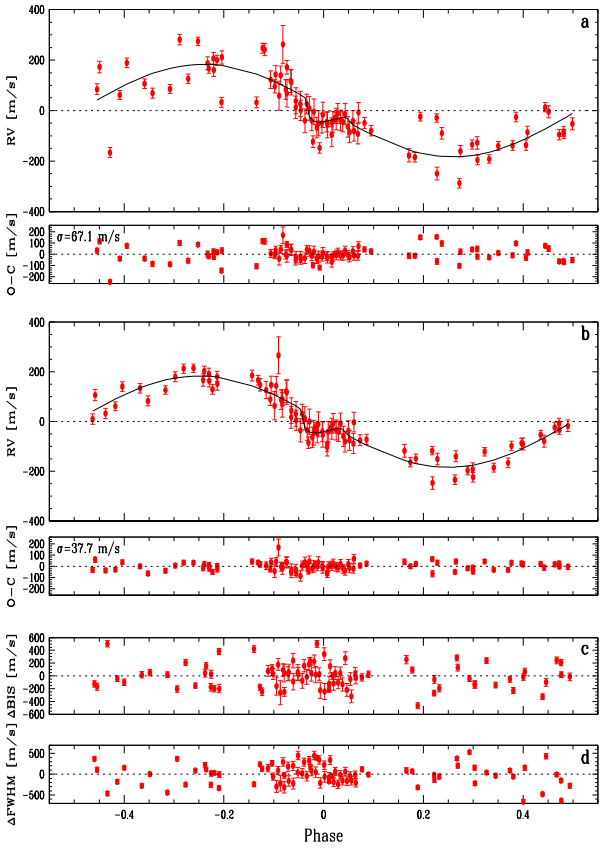

Figure 2. (a) CORALIE RVs for WASP-121 phase-folded on the best-fitting transit ephemeris, along with the best-fitting circular model and residuals (jitter is not included in the error bars). (b) Same as the top panel but here first-order polynomial functions of the CCF BS and FWHM were subtracted from the RVs (see Section 3.3). The scatter in the RV residuals is significantly reduced. (c) Change in the CCF BS as a function of orbital phase. (d) Change in the CCF FWHM as a function of orbital phase.

2.3 Follow-up eclipse photometry

To refine the system's parameters, high-precision eclipse (transit and occultation) light curves were obtained using the 60 cm TRAPPIST robotic telescope (TRAnsiting Planets and PlanetesImals Small Telescope) and the EulerCam CCD camera that is mounted on the 1.2 m Euler-Swiss telescope, which are both located at ESO La

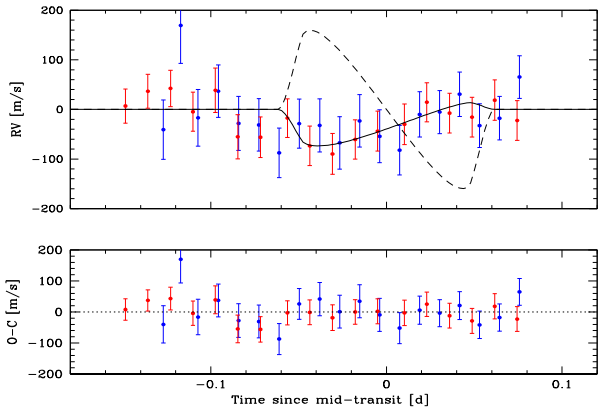

Figure 3. Top: zoom on the RM effect observed with CORALIE. The RVs obtained during the transit of 2014 Dec 24 are plotted in blue, while the RVs obtained during the transit of 2015 Jan 12 are plotted in red. The best-fitting circular Keplerian model (orbital motion) has been subtracted for clarity. The superimposed, solid black line is our best-fitting model for the RM effect. The dashed line is the RM effect that would have been observed in the case of an aligned orbit (shown for comparison). Bottom: residuals from our best-fitting model.

Silla Observatory. These follow-up light curves are summarized in Table 2 and presented in Figs 4 and 5. The transits were observed in different filters to search for a potential colour dependence of the transit depth, which might have been indicative of a blend (see Section 4).

2.3.1 *TRAPPIST observations*

TRAPPIST is a 60 cm robotic telescope dedicated to the detection and characterization of transiting exoplanets and to the photometric monitoring of bright comets and other small bodies. It is equipped with a thermoelectrically cooled 2K × 2K CCD, which has a pixel scale of 0.65 arcsec that translates into a 22 arcmin × 22 arcmin field of view. For details of TRAPPIST, see Gillon et al. (2011) and Jehin et al. (2011). TRAPPIST was used to observe four transits of WASP-121 b in a Sloan-z' filter (effective wavelength = 895 ± 1 nm, wavelength range = 816–991 nm) and one transit in a Johnson-B filter (effective wavelength = 440 ± 1 nm, wavelength range = 381–491 nm). As we noticed from a preliminary analysis that WASP-121 b is actually an extremely favourable target for secondary eclipse measurements (we will elaborate on this in Section 5.4), we also observed seven occultation windows in the Sloan-z' filter. During the runs, the positions of the stars on the chip were maintained to within a few pixels thanks to a 'software guiding' system that regularly derives an astrometric solution for the most recently acquired image and sends pointing corrections to the mount if needed. After a standard pre-reduction (bias, dark, and flat-field correction), the stellar fluxes were extracted from the images using the IRAF/DAOPHOT[2] aperture photometry software (Stetson 1987). For each light curve, we tested several sets of reduction parameters and kept the one giving the most precise photometry for the stars of similar brightness as the target. After a careful selection of reference stars, the photometric light curves were finally obtained using differential photometry.

2.3.2 *EulerCam observations*

EulerCam is a 4K × 4K E2V CCD installed at the Cassegrain focus of the 1.2 m Euler-Swiss telescope. The field of view of EulerCam is 15.7 arcmin × 15.7 arcmin, producing a pixel scale of 0.23 arcsec. To keep the stars on the same locations on the detector during the observations, EulerCam employs an 'Absolute Tracking' system that is very similar to the one of TRAPPIST, which matches the point sources in each image with a catalogue, and if needed, adjusts the telescope pointing between exposures to compensate for drifts. EulerCam was used to observe two transits of WASP-121 b in a Gunn-r' filter (effective wavelength = 664 ± 1 nm, wavelength range = 601–725 nm) and two other transits in a Geneva-B filter[3] (effective wavelength = 425 ± 1 nm, wavelength range = 375–475 nm). A slight defocus was applied to the telescope to optimize the observation efficiency and to minimize pixel-to-pixel effects. The reduction procedure used to extract the transit light curves was similar to that performed on TRAPPIST data. Further details of the EulerCam instrument and data reduction procedures can be found in Lendl et al. (2012).

2.4 Out-of-eclipse photometric monitoring

To search for potential out-of-eclipse photometric variability that would not have been detected in the WASP photometry (see Section 2.1), we monitored WASP-121 with TRAPPIST for 27 non-consecutive nights between 2014 Oct 25 and 2014 Dec 8. This monitoring consisted in taking every night a short sequence of 10 images in three filters: Johnson-B (effective wavelength = 440 ± 1 nm, wavelength range = 381–491 nm), Johnson-V (effective wavelength = 546.5 ± 1 nm, wavelength range = 486–617 nm), and Sloan-z' (effective wavelength = 895 ± 1 nm, wavelength range = 816–991 nm). The data were reduced as described in Section 2.3.1. The globally normalized differential light curves obtained in each filter are shown in Fig. 6. WASP-121 appears to be very quiet in photometry, the standard deviations of the binned light curves being 1.6 mmag (B), 1.3 mmag (V), and 1.1 mmag (z').

3 ANALYSIS

3.1 Spectroscopic analysis

The individual CORALIE spectra were co-added to produce a single spectrum with an average S/N of around 150:1. The analysis was performed using standard pipeline reduction products and the procedures given in Doyle et al. (2013). The derived stellar parameters are listed in Table 4.

The excitation balance of the Fe I lines was used to determine the effective temperature $T_{\rm eff}$ (6460 ± 140 K). The surface gravity log $g_\star$ (4.2 ± 0.2) was determined from the ionization balance of Fe I and Fe II. The Ca I line at 6439 Å and the Na I D lines were also used as log $g_\star$ diagnostics. The iron abundance was determined from equivalent width measurements of several unblended lines and is relative to the solar value obtained by Asplund et al. (2009). A value for microturbulence ($\xi_{\rm t}$ = 1.5 ± 0.1 km s^{-1}) was determined from Fe I using the method of Magain (1984). The quoted error estimates

[2] IRAF is distributed by the National Optical Astronomy Observatory, which is operated by the Association of Universities for Research in Astronomy, Inc., under cooperative agreement with the National Science Foundation.

[3] http://obswww.unige.ch/gcpd/ph13.html

Table 2. Summary of the follow-up eclipse photometry obtained for WASP-121. For each light curve, this table shows the date of acquisition (UT), the used instrument, the eclipse nature, the filter and exposure time, the number of data points, the selected baseline function, the standard deviation of the best-fitting residuals (unbinned and binned per intervals of 2 min), and the deduced values for β_w, β_r and $CF = \beta_w \times \beta_r$ (see Section 3.3 for details). For the baseline function, p(ϵ^N) denotes, respectively, a N-order polynomial function of time ($\epsilon = t$), airmass ($\epsilon = a$), PSF FWHM ($\epsilon = f$), background ($\epsilon = b$), and x and y positions ($\epsilon = xy$). For the TRAPPIST data, the symbol o denotes an offset fixed at the time of the meridian flip.

Date (UT)	Instrument	Eclipse nature	Filter	$T_{\rm exp}$ (s)	N_p	Baseline function	σ (per cent)	σ_{120s} (per cent)	β_w	β_r	CF
2013 Dec 09	TRAPPIST	Transit	Sloan-z'	13	763	p(t^1) + o	0.26	0.12	1.12	1.52	1.70
2013 Dec 25	TRAPPIST	Occultation	Sloan-z'	13	902	p(a^1+xy^1) + o	0.37	0.17	1.44	1.07	1.54
2013 Dec 30	TRAPPIST	Occultation	Sloan-z'	13	653	p(t^1+xy^1) + o	0.29	0.14	1.44	1.44	2.06
2014 Jan 01	TRAPPIST	Transit	Sloan-z'	13	765	p(t^1+xy^1) + o	0.25	0.13	1.13	2.35	2.66
2014 Jan 13	TRAPPIST	Occultation	Sloan-z'	13	867	p(a^1+xy^1) + o	0.27	0.12	1.07	1.56	1.66
2014 Jan 20	EulerCam	Transit	Gunn-r'	50	235	p(t^1+f^2)	0.10	0.07	1.38	1.28	1.76
2014 Jan 24	EulerCam	Transit	Gunn-r'	50	195	p(t^1+f^2+xy^1)	0.14	0.09	2.45	1.10	2.70
2014 Jan 31	TRAPPIST	Occultation	Sloan-z'	12	947	p(a^1) + o	0.25	0.10	1.12	1.00	1.12
2014 Feb 05	TRAPPIST	Occultation	Sloan-z'	12	1033	p(t^1+xy^1) + o	0.39	0.17	1.31	1.49	1.95
2014 Mar 22	TRAPPIST	Occultation	Sloan-z'	12	1007	p(t^1+xy^1) + o	0.38	0.16	1.17	1.18	1.38
2014 Apr 07	TRAPPIST	Transit	Sloan-z'	13	700	p(a^1+xy^1)	0.48	0.19	1.61	1.45	2.32
2014 Apr 14	TRAPPIST	Occultation	Sloan-z'	11	851	p(a^1)	0.36	0.16	1.02	1.58	1.61
2014 Nov 08	TRAPPIST	Transit	Johnson-B	7	966	p(t^2+b^2+xy^1)	0.55	0.23	1.46	1.09	1.59
2014 Dec 01	EulerCam	Transit	Geneva-B	90	162	p(a^1+f^4+xy^1)	0.11	0.11	1.51	1.05	1.59
2014 Dec 24	TRAPPIST	Transit	Sloan-z'	8	961	p(a^1)	0.29	0.12	0.91	2.07	1.87
2014 Dec 29	EulerCam	Transit	Geneva-B	60	223	p(a^1+f^4)	0.08	0.06	1.15	1.19	1.36

include those given by the uncertainties in $T_{\rm eff}$ and log $g_\star$, as well as the scatter due to measurement and atomic data uncertainties.

The projected stellar rotation velocity $v_\star \sin i_\star$ was determined by fitting the profiles of several unblended Fe I lines. A macro-turbulent velocity ($v_{\rm mac}$) of 6.0 ± 0.6 km s^{-1} was assumed using the asteroseismic-based calibration of Doyle et al. (2014) and an instrumental resolution of 55 000. A best-fitting value of $v_\star \sin i_\star = 13.5 \pm 0.7$ km s^{-1} was obtained.

There is no significant detection of lithium in the spectra, with an abundance upper limit log A(Li)<1.0. The lack of any detectable lithium does not provide an age constraint as the star's $T_{\rm eff}$ places it in the lithium gap (Böhm-Vitense 2004). There is also no significant chromospheric emission in the Ca II H and K line cores.

The spectral type (F6V) was estimated from $T_{\rm eff}$ using the table B 1 in Gray (2008) and the Torres, Andersen & Giménez (2010) calibration was used to obtain first stellar mass and radius estimates: $M_\star = 1.37 \pm 0.14$ M$_\odot$ and $R_\star = 1.52 \pm 0.41$ R$_\odot$.

3.2 Stellar jitter

As mentioned in Section 2.2, WASP-121 exhibits an especially high scatter in its RV residuals (Fig. 2a), CCF BS (Fig. 2c), and FWHM (Fig. 2d). Fig. 7 compares the RV residuals from our best-fitting circular model (Fig. 2a) to the CCF BS. There is a significant anti-correlation between these two quantities, the correlation coefficient being −0.68. Such an anticorrelation is commonly interpreted as being a signature of stellar activity (see e.g. Queloz et al. 2001; Melo et al. 2007), but Santerne et al. (2015) showed that it could also be produced by a blended star with a lower CCF FWHM (and thus slower rotation) than the target star. However, as detailed in Section 4, we were not able to reproduce the observed RVs, CCF BS, and FWHM assuming such a scenario, thus making it likely that the high jitter measured for WASP-121 is due to stellar activity. One might have concerns about the non-detection of this stellar activity in the form of emission in the Ca II H and K line cores (see Section 3.1), out-of-eclipse photometric variability (see Sections 2.1 and 2.4), or spot-crossing events during transits (see Fig. 4). A detailed study of WASP-121's activity being beyond the scope of this paper, we just propose here some potential explanations regarding these non-detections.

First, we note that such a situation is not atypical for an F-type star as it was also encountered for the exoplanet F-type host stars HAT-P-33 (Hartman et al. 2011) and WASP-111 (Anderson et al. 2014), which both present high activity-related RV jitter with no other apparent sign of stellar activity. More precisely, in the case of WASP-111, the scatter in the RV residuals, CCF BS and FWHM dropped from one season to the next, identifying clearly stellar activity as an origin for these.

Secondly, it can be seen from Noyes et al. (1984) that the chromospheric Ca II emission of stars decreases with lowering $B - V$. As WASP-121's $B - V$ is only 0.43, its Ca II emission could simply be too weak to be detected in our low S/N CORALIE spectra.

As for the non-detections of out-of-eclipse variations or spot-crossing events in the photometry, they might be explained, at least to some extent, if the star is plage-dominated, in opposition to spot-dominated (see Dumusque, Boisse & Santos 2014). Both spots and plages are regions of strong magnetic fields that inhibit locally the convection and suppress the convective blueshift (CB) effect (see e.g. Dravins, Lindegren & Nordlund 1981). These regions are thus redshifted compared to the quiet photosphere. Furthermore, as their temperatures differ from the average effective temperature of the star, they have a different flux from that of the average stellar surface. They thus break the flux balance between the blueshifted approaching side and the redshifted receding side of the rotating star (flux effect). Due to both these effects, spots and plages induce RV variations as they pass on the visible stellar disc due to stellar rotation. The CB effect is expected to be similar for spots and plages of the same size. However, plages present a much lower flux ratio with the quiet photosphere compared to spots (see Dumusque et al. 2014 for details), so that they induce a smaller flux effect and a smaller photometric variability.

Fig. 8 shows Lomb–Scargle periodograms (Scargle 1982) of the RV residuals (assuming a circular orbit, second panel from the top), CCF BS (third panel from the top), and FWHM (bottom panel). In

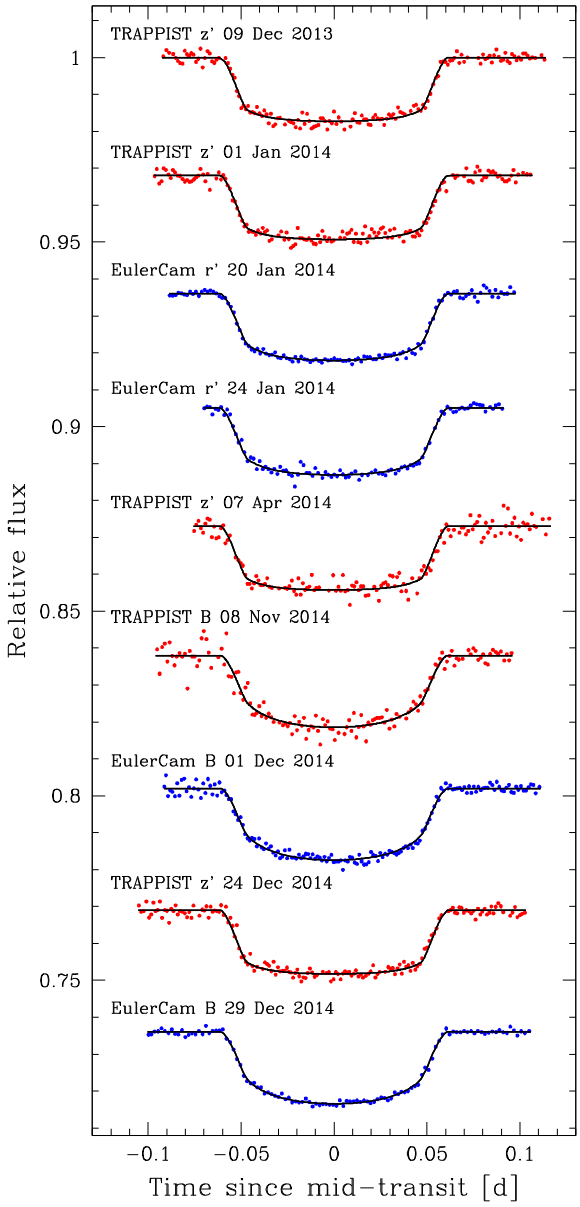

Figure 4. Follow-up transit photometry for WASP-121 b. The observations are binned per 2 min and period-folded on the best-fitting transit ephemeris (see Section 3.3). Each light curve has been divided by the respective best-fitting photometric baseline model. For each filter, the superimposed, solid black line is our best-fitting transit model. The light curves are shifted along the y-axis for clarity.

each of these periodograms, the highest peaks are found at periods of 0.89, 1.13, and 8.3 d (all with false alarm probabilities < 0.001, except for the peak at 1.13 d in the periodogram of the BS). We could assume that one of these three periods, which are each other's daily aliases, is the stellar rotation period $P_{\mathrm{rot},\star}$ (this supposes that the activity-induced RV signal is related to the rotation of the star). A stellar rotation period of 8.3 d does not seem very likely, as the maximal rotation period implied by $v_\star \sin i_\star$ and our final estimate of the stellar radius ($R_\star = 1.458 \pm 0.030$ R$_\odot$, see Section 3.3) is 5.46 ± 0.32 d (assuming $\sin i_\star = 1$). Stellar rotation periods of 0.89 and 1.13 d would imply, together with our measured value for $R_\star$, rotation velocities $v_\star$ of 82.9 ± 1.7 and 65.3 ± 1.4 km s^{-1}, respectively, and inclinations $i_\star$ of $9\overset{\circ}{.}4 \pm 0\overset{\circ}{.}6$ and $11\overset{\circ}{.}9 \pm 0\overset{\circ}{.}7$, respectively, where the uncertainties are the quadratic sum of the uncertainties due to each input parameter. In both cases, the star would thus be seen nearly pole-on, i.e. with the rotation axis oriented towards the Earth. If the star is seen nearly pole-on, WASP-121b should then be in a (nearly) polar orbit to produce transits. As mentioned previously, this is actually what our observations of the RM effect suggest (see Sections 3.3 and 5.2), which makes $P_{\mathrm{rot},\star}$ likely to be 0.89 or 1.13 d. We note that for the 1-Gyr-old cluster NGC6811 observed with *Kepler* by Meibom et al. (2013), the stars with $B - V = 0.43$ (such as WASP-121) have ∼1-d rotation periods (see their fig. 1b). As the age of WASP-121 obtained by stellar evolution modelling is 1.5 ± 1.0 Gyr (see Section 3.4), a ∼1-d rotation period would thus be consistent with their values.

We used the SOAP 2.0 code of Dumusque et al. (2014) to assess the type of active region (spot or plage) and corresponding surface coverage that would be needed to explain the RV jitter observed for WASP-121 if it is seen nearly pole-on. The code takes as main inputs T_{eff} (6460 ± 140 K), $R_\star$ (1.458 ± 0.030 R$_\odot$), $P_{\mathrm{rot},\star}$ (∼1 d), and $i_\star$ ($\sim 10\overset{\circ}{.}6$). If we assume an active region consisting of a spot and an upper limit of 1 mmag (see Section 2.1) for the photometric variability induced by this active region (also returned by the code), the maximal RV peak-to-peak amplitude is obtained for a ∼1.2 per cent[4] spot located at a latitude of ∼80° and is of the order of 90 m s^{-1}. This is significantly lower than the ∼300 m s^{-1} amplitude of our RV residuals. Conversely, such an RV amplitude can for example be reproduced if the active region consists of a ∼8 per cent[5] bright plage at a latitude of ∼50° (the corresponding photometric variability having an amplitude of ∼0.14 mmag). The high activity-related RV jitter observed for WASP-121 despite the lack of photometric variability could thus be explained if the star is dominated by plages. We note that a plage-dominated activity was also invoked to account for the RV jitter observed for another active F6V exoplanet host star: τ Bootis A (see Borsa et al. 2015).

3.3 Global modelling of the data

To determine the system parameters, we performed a combined analysis of the follow-up eclipse photometry and the RV data, using for this purpose the adaptive Markov Chain Monte Carlo (MCMC) code described in Gillon et al. (2012) and references therein. To model the photometry, we used the eclipse model of Mandel & Agol (2002) multiplied by a different baseline model for each light curve. These baseline models aim to represent astrophysical, instrumental, or environmental effects, which are able to produce photometric variations and can, therefore, affect the photometric light curves. They can be made up of different first- to fourth-order polynomials with respect to time or other variables, such as airmass, point spread function (PSF) FWHM, background, or stellar position on the detector. To find the optimal baseline function for each light curve, i.e. the model minimizing the number of parameters and the level of noise in the best-fitting residuals, the Bayes factor, as estimated from the Bayesian Information Criterion

[4] This size is defined as the fraction of the surface of the visible hemisphere covered by the active region.

[5] A surface coverage of ∼8 per cent is realistic, as Andretta & Giampapa (1995) estimate that plages can cover more than 20 per cent of the surface of active Sun-like (F-early K) stars.

(BIC; Schwarz 1978), was used. The best photometric baseline functions are listed in Table 2. For eight TRAPPIST light curves (see Table 2), a normalization offset was also part of the baseline model to represent the effect of the meridian flip; that is, the 180° rotation that the German equatorial mount telescope has to undergo when the meridian is reached. This movement results in different positions of the stellar images on the detector before and after the flip, and the normalization offset allows us to take into account a possible consecutive jump in the differential photometry at the time of the flip.

On their side, the RVs were modelled using a classical Keplerian model (e.g. Murray & Correia 2010) added to a baseline model for the stellar and instrumental variability. For the RVs obtained during a transit, the RM effect was modelled using the formulation of Giménez (2006). The RVs were partitioned into four data sets, each with a different baseline model: the RVs obtained before the replacement of the CORALIE optical fibre (37 RVs, data set #1), those obtained after (15 RVs, data set #2), the first RM sequence (19 RVs, data set #3), and the second one (18 RVs, data set #4). For all data sets, the minimal baseline model was a scalar V_γ representing the systemic velocity of the star. For data sets #1 and #2, first-order polynomial functions of the CCF BS and FWHM were also part of the baseline models. This choice of baselines allowed us to reduce the scatter in the global RV residuals from 67.1 to 37.7 m s^{-1} (see Figs 2 a and b) and was thus strongly favoured by the BIC. These additional baseline terms were not necessary for the data sets #3 and #4 (RM sequences). Including linear correlations with the CCF parameters in the RV model to account for activity-related RV variations is a technique that has been previously used by other investigators (see e.g. Hartman et al. 2011; Jenkins & Tuomi 2014; Tuomi et al. 2014).

The basic jump parameters in our MCMC analyses, i.e. the parameters that are randomly perturbed at each step of the MCMC, were: the planet/star area ratio $dF = (R_p/R_\star)^2$; the occultation depth in the z'-band $dF_{occ,\,z'}$; the transit impact parameter in the case of a circular orbit $b' = a \cos i_p/R_\star$, where a is the orbital semimajor axis and i_p is the orbital inclination; the transit width (from first to fourth contact) W; the time of mid-transit T_0; the orbital period P; the stellar effective temperature T_{eff}; the stellar metallicity [Fe/H]; the parameter $K_2 = K\sqrt{1-e^2}\ P^{1/3}$, where K is the RV orbital semi-amplitude and e is the orbital eccentricity; the two parameters $\sqrt{e}\cos\omega$ and $\sqrt{e}\sin\omega$, where ω is the argument of the periastron; and the two parameters $\sqrt{v_\star \sin i_\star}\cos\beta$ and $\sqrt{v_\star \sin i_\star}\sin\beta$, where $v_\star \sin i_\star$ is the projected rotational velocity of the star and β is the sky-projected angle between the stellar spin axis and the planet's orbital axis. The reasons to use $\sqrt{e}\cos\omega$ and $\sqrt{e}\sin\omega$ as jump parameters instead of the more traditional $e\cos\omega$ and $e\sin\omega$ are detailed in Triaud et al. (2011). The results obtained from the spectroscopic analysis (see Section 3.1) were used to impose normal prior distributions on T_{eff}, [Fe/H], and $v_\star \sin i_\star$, with expectations and standard deviations corresponding to the quoted measurements and errors, respectively. Uniform prior distributions were assumed for the other parameters. The photometric and RV baseline model parameters were not actual jump parameters; they were determined by least-square minimization from the residuals at each step of the MCMC.

The effect of stellar limb-darkening (LD) on our transit light curves was accounted for using a quadratic LD law, where the quadratic coefficients u_1 and u_2 were allowed to float in our MCMC analysis. However, we did not use these coefficients themselves as jump parameters but their combinations, $c_1 = 2 \times u_1 + u_2$ and $c_2 = u_1 - 2 \times u_2$, to minimize the correlation of the obtained uncertainties as introduced by Holman et al. (2006). To obtain an LD solution consistent with theory, we used normal prior distributions for u_1 and u_2 based on theoretical values and 1σ errors interpolated in the tables by Claret & Bloemen (2011). These prior distributions are presented in Table 3.

A preliminary analysis was performed to determine the correction factors (CF) for our photometric errors, as described in Gillon et al. (2012). For each light curve, CF is the product of two contributions, β_w and β_r. On one side, β_w represents the underestimation or overestimation of the white noise of each measurement. It is computed as the ratio between the standard deviation of the residuals and the mean photometric error. On the other side, β_r allows us to take into account the correlated noise present in the light curve (i.e. the inability of our model to perfectly fit the data). It is calculated from the standard deviations of the binned and unbinned residuals for different binning intervals ranging from 5 to 120 min with the largest value being kept as β_r. The standard deviation of the best-fitting residuals (unbinned and binned per intervals of 2 min) and the deduced values for β_w, β_r and $CF = \beta_w \times \beta_r$ for each light curve are presented in Table 2. This preliminary analysis also allowed us to compute the jitter values that were added quadratically to the RV errors of each RV data set to equal their mean values to the standard deviations of the best-fits residuals, and thus achieve reduced χ^2 values of unity. These jitter values were 27.9, 22.3, 16.9 m s^{-1}, and zero for the data sets #1, #2, #3, and #4, respectively.

A second analysis with the updated photometric and RV errors was then performed to determine the stellar density $\rho_\star$, which can be derived from the Kepler's third law and the jump parameters $(R_p/R_\star)^2$, b', W, P, $\sqrt{e}\cos\omega$ and $\sqrt{e}\sin\omega$ (see e.g. Seager & Mallén-Ornelas 2003; Winn 2010). This analysis consisted of two Markov chains of 10^5 steps, whose convergence was checked using the statistical test of Gelman & Rubin (1992). The first 20 per cent of each chain was considered as its burn-in phase and discarded. The resulting stellar density was used as input of a stellar evolution modelling, together with the effective temperature and metallicity derived from spectroscopy, with the aim to estimate the stellar mass $M_\star$ and the age of the system. This stellar evolution modelling is described in detail in Section 3.4.

Two final analyses were then performed: one assuming a circular orbit ($e = 0$) and one with a free eccentricity. Each analysis consisted of two Markov chains of 10^5 steps, whose convergence was again checked with the Gelman & Rubin test (Gelman & Rubin 1992). As previously, the first 20 per cent of each chain was considered as its burn-in phase and discarded. At each step of the Markov chains, $\rho_\star$ was computed as described above and a value for $M_\star$ was drawn within a normal distribution having as expectation and standard deviation the value and error obtained from the stellar evolution modelling. The stellar radius $R_\star$ was derived from $M_\star$ and $\rho_\star$, and the other physical parameters of the system were then deduced from the jump parameters and stellar mass and radius. It appeared that the circular orbit was strongly favoured by the Bayes factor (∼5000 in its favour) compared to the eccentric orbit. As there was no evidence for a significant eccentricity ($e < 0.07$ at 3σ), we thus adopted the circular orbit as our nominal solution. The corresponding derived parameters are presented in Table 4, while the best-fitting models are shown in Fig. 2(b) (RVs), 3 (zoom on the RM effect), 4 (transit photometry), and 5 (occultation photometry).

A complementary analysis was finally performed to assess the chromaticity of the transit. In this analysis, transit depth differences between the different filters were added as jump parameters. The deduced transit depths are also presented in Table 4. They are consistent with each other.

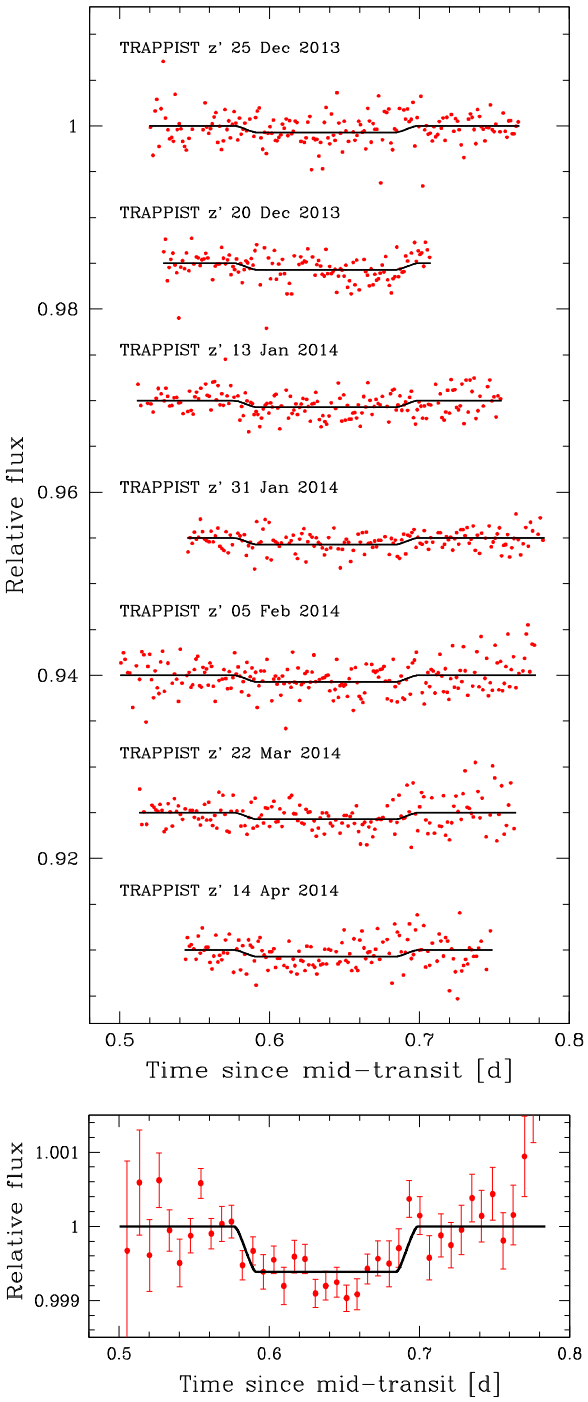

Figure 5. Top: individual follow-up occultation light curves for WASP-121 b. The observations are binned per 2 min and period-folded on the best-fitting transit ephemeris (see Section 3.3). Each light curve has been divided by the respective best-fitting photometric baseline model. For each light curve, the superimposed, solid black line is our best-fitting occultation model. The light curves are shifted along the *y*-axis for clarity. Bottom: combined follow-up occultation photometry for WASP-121 b (bin width = 10 min).

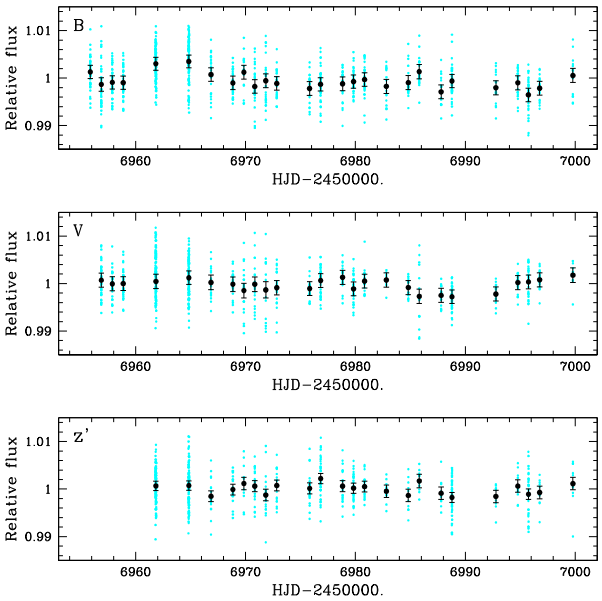

Figure 6. Out-of-eclipse photometric monitoring: globally normalized TRAPPIST differential photometry obtained for WASP-121 in Johnson-*B* (top), Johnson-*V* (middle), and Sloan-z' (bottom) filters, unbinned (cyan) and binned by day (black).

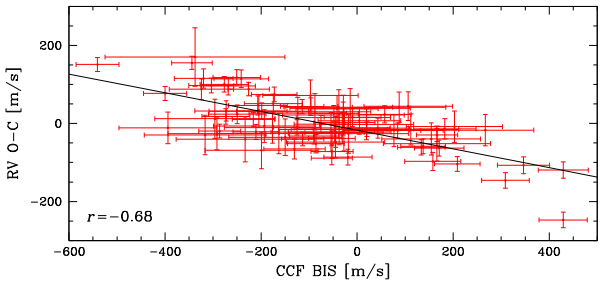

Figure 7. RV residuals from the best-fitting circular orbital model versus CCF BS. The two quantities are clearly anticorrelated. A linear fit to the data is overplotted and the correlation coefficient (r) is given.

3.4 Stellar evolution modelling

As introduced in Section 3.3, we performed for the host star a stellar evolution modelling based on the CLES code (Scuflaire et al. 2008), in order to estimate the stellar mass and the age of the system. We used as inputs the stellar density deduced from the transit light curves, and the effective temperature and metallicity derived from spectroscopy (see Table 4). We considered that [Fe/H] represents the global metallicity with respect to the Sun i.e. [Fe/H] $= [\log(Z/X)_* - \log(Z/X)_\odot]$, with $(Z/X)_\odot = 0.0181$ (Asplund et al. 2009). The parameter of the mixing-length theory (MLT) of convection was kept fixed to the solar calibration ($\alpha_{\rm MLT} = 1.8$), and the possible convective core extra-mixing (due to overshooting, rotationally induced mixing, etc.) and microscopic diffusion (gravitational settling) of elements were included.

We obtained a stellar mass of 1.355 ± 0.080 M$_\odot$ and an age of 1.5 ± 1.0 Gyr. These 1σ uncertainties were obtained by considering the respective 1σ range for the effective temperature, metallicity and stellar density, but also by varying the internal stellar physics. We computed, since the helium atmospheric abundance cannot be

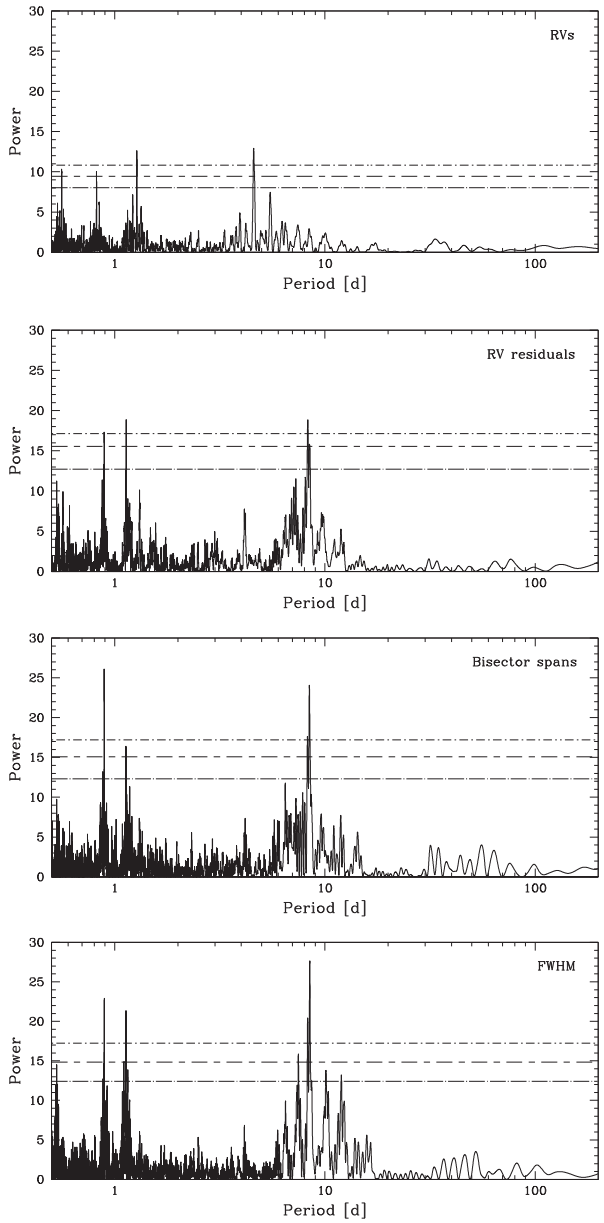

Figure 8. From top to bottom: Lomb–Scargle periodograms of the RVs, RV residuals (assuming a circular orbit), CCF BS, and FWHM. Horizontal lines indicate false alarm probability levels of 0.001, 0.01, and 0.1 (from top to bottom).

Table 3. Expectations and standard deviations of the normal distributions used as prior distributions for the quadratic LD coefficients u_1 and u_2 in our MCMC analysis.

Filter	u_1	u_2
Sloan-z'	0.171 ± 0.014	0.306 ± 0.006
Gunn-r'	0.295 ± 0.015	0.325 ± 0.006
Johnson- and Geneva-B	0.510 ± 0.027	0.260 ± 0.019

directly measured from spectroscopy, evolutionary tracks with two initial helium abundances: the solar value ($Y_{\odot,0} = 0.27$), and a value labelled Y_G that increases with Z (as expected if the local medium follows the general trend observed for the chemical evolution of galaxies; Izotov & Thuan 2010). We also investigated the effects of the possible convective core extramixing, by varying it between 0 and 0.3 (Noels & Montalbán 2013).

Evolutionary tracks are presented on Fig. 9 for several stellar masses and metallicities. Obtaining an accurate stellar mass from evolution modelling primarily needs accurate spectroscopic estimates for the effective temperature but also, very importantly, for the metallicity. Metallicity is a parameter that strongly determines the location of the evolutionary tracks in an Hertzsprung-Russell diagram (compare in Fig. 9 the solid and dashed tracks for identical stellar masses, but with different metallicities). The stellar mass obtained from stellar evolution modelling (1.355 ± 0.085 $M_\odot$) is in excellent agreement with the first estimate derived from the Torres et al. (2010) calibration in Section 3.1. The inferred stellar age of 1.5 ± 1.0 Gyr places WASP-121 on the main sequence. The total lifetime on the main sequence (H-core burning) of WASP-121 is 4.3 Gyr for a moderate extramixing $\alpha_{\rm em} = 0.2$, and is reduced to 3.3 Gyr without considering any extramixing process in the core.

4 PASTIS VALIDATION

Astrophysical false-positive scenarios such as eclipsing binaries might mimic both the transit and RV signal of a planet (Torres et al. 2005). In some particular configurations, even the RM effect might be mimicked (Santerne et al. 2015). In this case, the line bisector and the FWHM present a large variation. Moreover, we were able to detect from the ground in the z' band a relatively deep secondary eclipse. Both arguments prevent to secure the planetary nature of WASP-121 b without a more careful investigation. We can imagine five scenarios which can reasonably produce the observed data: (1) a planet transiting the target star, (2) a planet transiting a chance-aligned background star, (3) a chance-aligned background eclipsing binary, (4) a planet transiting a physical companion to the target star, and (5) a star eclipsing a physical companion to the target star (i.e. a triple system). The scenarios 2–5 can be split in two categories and discussed separately; the background or physical companion sources of false positive.

4.1 A background source

A background source of false positive can mimic the transit data of a planet within a range of magnitude Δm defined as (Morton & Johnson 2011)

$$\Delta m = 2.5 \log_{10} \left(\frac{\delta_{\rm tr}}{\delta_{\rm bg}} \right), \quad (1)$$

where $\delta_{\rm tr}$ and $\delta_{\rm bg}$ are the depth of the transit, as measured in the light curve, and the depth of the background eclipse, respectively. Assuming a maximum eclipse depth of 50 per cent for the background star, we find that the maximum magnitude range is of 3.78. Note that a 50 per cent depth eclipsing binary should also produce a secondary eclipse with a similar depth, which is clearly excluded in the case of WASP-121. Therefore, this magnitude range is overestimated, which will also overestimate the probability of a background star as the host of the observed signal. The star is of magnitude 10.44 in the V band, hence false positive can probe stars as faint as magnitude 14.22 in the same bandpass.

Table 4. System parameters for WASP-121. The values given for the parameters derived from our MCMC analysis are medians and 1σ limits of the marginalized posterior probability distributions.

General information			
RA (J2000)	$07^{\rm h}\ 10^{\rm m}\ 24\overset{\rm s}{.}06$	V-magnitude	10.44
Dec. (J2000)	$-39^\circ\ 05'\ 50\overset{''}{.}55$	K-magnitude	9.37
Distance [pc][a]	270 ± 90		
Stellar parameters from spectroscopic analysis (Section 3.1)			
Spectral type	F6V	Microturbulence $\xi_{\rm t}$ [km s^{-1}]	1.5 ± 0.1
Effective temperature $T_{\rm eff}$ [K]	6460 ± 140	Macroturbulence $v_{\rm mac}$ [km s^{-1}]	6.0 ± 0.6
Surface gravity log $g_\star$ [cgs]	4.2 ± 0.2	Proj. rot. velocity $v_\star \sin i_\star$ [km s^{-1}]	13.5 ± 0.7
Metallicity [Fe/H] [dex]	0.13 ± 0.09	Lithium abundance log A(Li) [dex]	< 1.0
Parameters from MCMC analysis (Section 3.3)			
Jump parameters			
Planet/star area ratio $dF = (R_{\rm p}/R_\star)^2$ [per cent]	1.551 ± 0.012	Effective temperature $T_{\rm eff}$ [K][b]	6459 ± 140
Occultation depth $dF_{{\rm occ},\,z'}$ [ppm]	603 ± 130	Metallicity [Fe/H] [dex][b]	0.13 ± 0.09
$b' = a\cos i_{\rm p}/R_\star$ [$R_\star$]	$0.160^{+0.040}_{-0.042}$	$c_{1,z'} = 2\,u_{1,z'} + u_{2,z'}$	$0.637^{+0.026}_{-0.025}$
Transit width W [d]	0.1203 ± 0.0003	$c_{2,z'} = u_{1,z'} - 2\,u_{2,z'}$	-0.445 ± 0.018
$T_0 - 2450\,000$ [HJD$_{\rm TDB}$]	$6635.708\,32^{+0.00011}_{-0.00010}$	$c_{1,r'} = 2\,u_{1,r'} + u_{2,r'}$	$0.904^{+0.027}_{-0.026}$
Orbital period P [d]	$1.274\,9255^{+0.000\,00020}_{-0.000\,00025}$	$c_{2,r'} = u_{1,r'} - 2\,u_{2,r'}$	$-0.361^{+0.020}_{-0.018}$
RV K_2 [m s^{-1} d$^{1/3}$]	$196.4^{+6.8}_{-6.9}$	$c_{1,B} = 2\,u_{1,B} + u_{2,B}$	$1.269^{+0.032}_{-0.031}$
$\sqrt{e}\cos\omega$	0 (fixed)	$c_{2,B} = u_{1,B} - 2\,u_{2,B}$	$-0.012^{+0.043}_{-0.045}$
$\sqrt{e}\sin\omega$	0 (fixed)		
$\sqrt{v_\star \sin i_\star}\cos\beta$	-0.78 ± 0.34		
$\sqrt{v_\star \sin i_\star}\sin\beta$	$-3.59^{+0.13}_{-0.11}$		
Deduced stellar parameters			
Mean density $\rho_\star$ [$\rho_\odot$]	$0.437^{+0.008}_{-0.009}$	LD coefficient $u_{1,z'}$	0.166 ± 0.013
Surface gravity log $g_\star$ [cgs]	$4.242^{+0.011}_{-0.012}$	LD coefficient $u_{2,z'}$	0.305 ± 0.008
Mass $M_\star$ [M$_\odot$][c]	$1.353^{+0.080}_{-0.079}$	LD coefficient $u_{1,r'}$	0.290 ± 0.014
Radius $R_\star$ [R$_\odot$]	1.458 ± 0.030	LD coefficient $u_{2,r'}$	0.325 ± 0.007
Luminosity $L_\star$ [$L_\odot$]	3.3 ± 0.3	LD coefficient $u_{1,B}$	0.505 ± 0.018
Proj. rot. velocity $v_\star \sin i_\star$ [km s^{-1}][b]	$13.56^{+0.69}_{-0.68}$	LD coefficient $u_{2,B}$	$0.259^{+0.020}_{-0.019}$
Mean systemic velocity V_γ [km s^{-1}]	38.350 ± 0.021		
Deduced planet parameters			
RV K [m s^{-1}]	$181.1^{+6.3}_{-6.4}$	Mean density $\rho_{\rm p}$ [$\rho_{\rm Jup}$]	0.201 ± 0.010
Planet/star radius ratio $R_{\rm p}/R_\star$	$0.124\,54^{+0.000\,47}_{-0.000\,48}$	Surface gravity log $g_{\rm p}$ [cgs]	2.973 ± 0.017
$T_{\rm occ} - 2450\,000$ [HJD$_{\rm TDB}$]	$6636.345\,78^{+0.000\,11}_{-0.000\,10}$	Mass $M_{\rm p}$ [$M_{\rm Jup}$]	$1.183^{+0.064}_{-0.062}$
Scaled semimajor axis $a/R_\star$	$3.754^{+0.023}_{-0.028}$	Radius $R_{\rm p}$ [$R_{\rm Jup}$]	1.807 ± 0.039
Orbital semimajor axis a [au]	$0.025\,44^{+0.000\,49}_{-0.000\,50}$	Roche limit $a_{\rm R}$ [au][d]	$0.022\,05 \pm 0.000\,66$
Orbital inclination $i_{\rm p}$ [deg]	87.6 ± 0.6	$a/a_{\rm R}$	1.153 ± 0.019
Orbital eccentricity e	0 (fixed)	Equilibrium temperature $T_{\rm eq}$ [K][e]	2358 ± 52
Argument of periastron ω [deg]	–	Irradiation [erg s^{-1} cm^{-2}]	$7.1^{+1.3}_{-1.1}\ 10^9$
Sky-projected orbital obliquity β [deg]	$257.8^{+5.3}_{-5.5}$		
Transit depths in the different bands			
Planet/star area ratio $dF_{z'}$ [per cent]	1.547 ± 0.013	Planet/star area ratio dF_B [per cent]	1.551 ± 0.014
Planet/star area ratio $dF_{r'}$ [per cent]	1.553 ± 0.013		
Planet parameters corrected for asphericity (Section 5.1)			
Radius $R_{\rm p}$ [$R_{\rm Jup}$]	1.865 ± 0.044	Mean density $\rho_{\rm p}$ [$\rho_{\rm Jup}$]	0.183 ± 0.016

[a] From V mag and estimated absolute magnitude.
[b] Using as priors the values derived from the spectroscopic analysis.
[c] Using as prior the value obtained from stellar evolution modelling.
[d] Using $a_{\rm R} = 2.46\,R_{\rm p}(M_\star/M_{\rm p})^{1/3}$ (Chandrasekhar 1987).
[e] Assuming a null Bond albedo and isotropic reradiation (reradiation factor $f = 1/4$; López-Morales & Seager 2007).

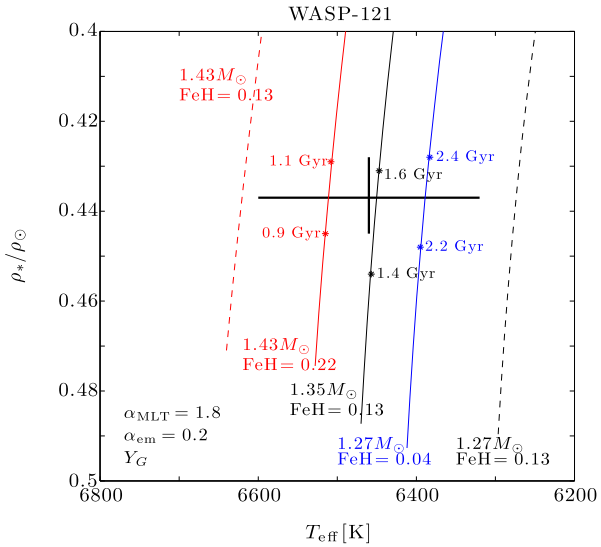

Figure 9. Evolutionary tracks in a $T_{\rm eff}$–$\rho_\star/\rho_\odot$ HR diagram for WASP-121, for different masses and metallicities, within (solid lines) and without (dashed lines) the 1σ box $T_{\rm eff}$–$\rho_\star/\rho_\odot$. Some stellar ages are also indicated.

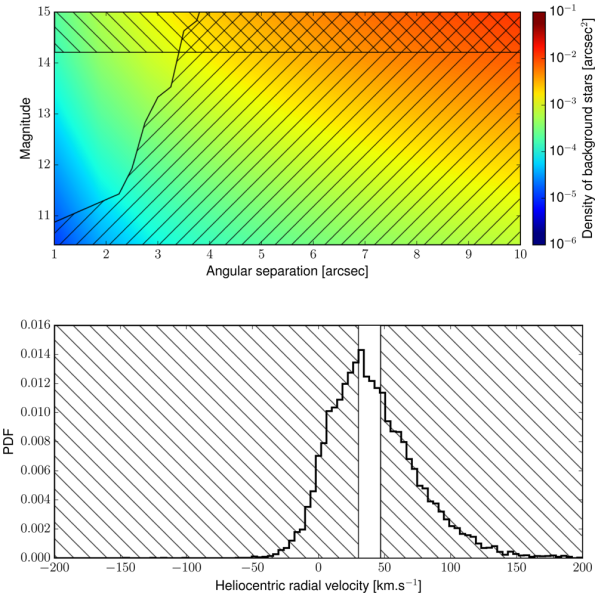

Figure 10. Upper panel: map of the density of background stars chance-aligned with WASP-121, integrated within an angular separation of up to 10 arcsec, as function of the *V*-band magnitude. The positive-slope hatched region displays all the stars that would have been significantly detected in the TRAPPIST data. The negative-slope hatched region displays the stars that are too faint to reproduce the observed transit depth of WASP-121. Lower panel: distribution of heliocentric RV of stars within 10° from WASP-121 as observed by the RAVE experiment. The hatched regions show the velocity of background stars that should be spectroscopically resolved with WASP-121 and thus should produce a RV variation in antiphase with the transit ephemeris, or no significant variation (Santerne et al. 2015).

To compute the probability of having a background star chance-aligned with WASP-121, we took the APASS (Henden et al. 2015) DR8 *V* magnitude of all stars within 1° from WASP-121. The magnitude limit of this catalogue is between magnitude 16 and 17, which is about 2 mag above the maximum magnitude of the background star. We therefore assume that this catalogue is complete in the range of magnitude we are considering here. We did not detect in the TRAPPIST data any background source that could host the transit. Thus, in this scenario, the background source should be blended within the TRAPPIST PSF. In Fig. 10, we display the sensitivity curve of the TRAPPIST PSF. This curve was obtained by injecting artificial stars in good-seeing TRAPPIST images at various separations and with a range of magnitude, and then attempting to detect them with IRAF/DAOPHOT. Any star brighter than magnitude 14 and separated from WASP-121 by more than 3.5 arcsec should have been detected. Using these constraints and assuming that the stars are randomly distributed around the target star, we find that the probability for WASP-121 to be chance-aligned with a background star brighter than magnitude 14.22 is at the level of maximum 8.10^{-4}. If we account for the probability that this hypothetical background star host a binary (∼50 per cent; Raghavan et al. 2010) or a planet (∼50 per cent; Mayor et al. 2011) and the eclipse or transit probability at 1.3 d (∼25 per cent), we end with a a priori probability that the transit signal is hosted by a background star lower than $\sim 1.10^{-4}$.

A significant RV variation has been detected in phase with the transit ephemeris and no other component has been significantly detected in the CORALIE CCFs with a flux ratio greater than 0.7 per cent (i.e. 5.4 mag). Therefore, to mimic both the photometric and RV data of WASP-121, the background source should be chance-aligned along the line of sight and in the RV space. To produce a RV in phase with the transit ephemeris, the background star should have a systemic velocity within the width of the line profile of WASP-121 (Santerne et al. 2015), i.e. the two stars should be spectroscopically unresolved. Given the systemic velocity of WASP-121 ($\gamma \sim 38.3$ km s^{-1}) and the width of its line profile observed by CORALIE ($\sigma_{\rm CCF} = {\rm FWHM}/2\sqrt{2\ln(2)} \approx 8.2$ km s^{-1}), the background star should thus have a systemic RV in the range [30.1; 46.5] km s^{-1}. We then compared this range of RV with the distribution of stars in the vicinity of WASP-121 from the RAVE data base (Kordopatis et al. 2013). The offset between the CORALIE zero-point and the RAVE reference is expected to be less than a few hundreds of m s^{-1}. We took all the stars observed by this spectroscopic survey within 10° of WASP-121 for which we display their RV distribution in Fig. 10. Only 20 per cent of the stars in the vicinity of WASP-121 should be spectroscopically unresolved. Assuming that the position of a star in a place of the sky is independent from its RV, we find that the a priori probability that the signal observed in WASP-121 is caused by a background source is, at most, at the level of 20 ppm. We can therefore exclude all background false-positive scenarios as the source of the detected signal.

4.2 A physical companion

Apart from the planet scenario, the most likely scenario to reproduce both the photometric and spectroscopic data is a system physically bound with the target star. In such configuration, the various stellar components could be easily blended in both the plane of the sky and the RV space. Then, the transit could be mimicked either by an eclipsing star or a transiting substellar object.

To estimate the probability that WASP-121 is either a planet transiting the target, a physical companion (planet in binary) or a

triple system, we used the PASTIS software (Díaz et al. 2014; Santerne et al. 2014; Santerne et al. 2015) to model the 11 230 photometric measurements obtained by TRAPPIST and EulerCam in different filters. The light curve was modelled using the EBOP code (Nelson & Davis 1972; Etzel 1981; Popper & Etzel 1981) extracted from the JKTEBOP package (Southworth 2008). For the LD coefficients, we used the interpolated values from Claret & Bloemen (2011). To model the stars, we used the Dartmouth stellar evolution tracks of Dotter et al. (2008) and the BT-SETTL stellar atmosphere models of Allard, Homeier & Freytag (2012) that we integrated in each individual bandpass. Since they are gravitationally bound, all stars were assumed to have the same metallicity and the same age. The orbits were assumed to be circular. We imposed that the physical companion is fainter by at least 1 mag in the *V* band than the target star, otherwise, it would have been clearly identified in the spectral or CCF analysis. Each of the 16 light curves was modelled self-consistently allowing a different out-of-transit flux, contamination and an extra source of white noise (jitter). As PASTIS is not yet able to model the activity of stars in RV data, we decided not to use these extra constraints. We also modelled the spectral energy distribution of WASP-121 composed by the magnitudes in the Johnson-*B* and -*V*, Sloan-g', -r', and -i', 2-MASS *J*, *H*, and *K*s, and *WISE W*1 to *W*4 bandpasses from the APASS data base (Henden et al. 2015) and the AllWISE catalogue (Wright et al. 2010).

We analysed the aforementioned data using an MCMC procedure described in Díaz et al. (2014). For the priors, we used the results from the spectroscopic analysis (Section 3.1) for the parameters of the target star and the initial mass function from Kroupa (2001) for the blended stars. For the orbital ephemeris, we used normal priors matching the ephemeris reported in Table 4 with uncertainties boosted by 100, to avoid biasing the results with too narrow priors. For the other parameters, we chose uninformative priors. We limited the priors on the planet radius to be less than 2.2 $R_{\rm Jup}$, which is the radius of the biggest planet found so far: KOI-13 (Szabó et al. 2011). In PASTIS, planets are considered as non-self-emitting objects, hence no thermal emission. Only the reflected light is considered. Here, we used the albedo of the planet as a proxy for the depth of the occultation. The upper limit in the prior corresponds to a geometric albedo of 1 and a brightness temperature of 3500 K. The TRAPPIST photometry was performed on focus and no stellar contamination is detected within the photometric aperture. We thus defined a prior for the contamination centred on zero with an uncertainty of 1 per cent (positive and negative values are allowed) to account for possible variation of the sky background flux between the observations or for stellar brightness variation due to non-occulting spots. The EulerCam photometry was performed slightly out of focus, which means the target should be blended with the light from a ∼7.4 arcsec nearby star about 6.8 mag fainter (*R* band), resulting in a contamination of 0.2 per cent. The prior for the EulerCam contamination was thus centred on this value. The exhaustive list of parameters and their priors are reported in Table A1. Both the planet and triple scenarios were described by 10 free parameters, while the planet in binary scenario used 11 free parameters. Among them, eight were in common (target star and orbital parameters). An additional 49 free parameters were needed to describe the data: three for each of the 16 light curves as already mentioned and an extrasource of white noise for the spectral energy distribution. For all scenarios, we ran 40 chains of 3.10^5 iterations, randomly started from the joint prior distribution. All chains converged towards the same maximum of likelihood. We then thinned and merged the chains to derive the posterior distributions of all scenarios. They all have a posterior distribution with more than 1000 independent samples.

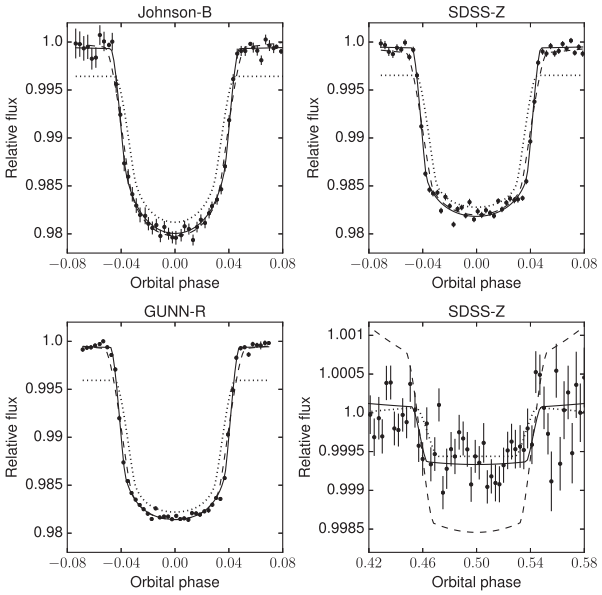

Figure 11. Phase-folded binned photometric data of WASP-121 observed in the various bandpasses together with the best planet (solid line), triple system (dash line), and planet in binary (dot line) models.

We report in Table A2 the median and 68.3 per cent confidence interval for the free parameters. All the fitted parameters for the planet scenario are compatible within 1σ with those derived in Section 3.3.

We display in Fig. 11 the transit and occultation data of WASP-121 in the various bandpasses together with the best planet, planet in binary and triple models. While the planet scenario reproduces well all the data, the triple system scenario is not able to fit perfectly the relatively sharp ingress and egress of the transit. The main difference between the two scenarios is for the secondary eclipse. While the planet scenario is able to reproduce well the occultation data, the best triple scenario exhibits a secondary depth of more than 2000 ppm, which is clearly excluded by the data. For the planet transiting a companion star to the target, it is not possible to reproduce the observed transit depth and duration if we assume both that the companion star is fainter by at least 1 mag than the target star and that the maximum planetary radius allowed is 2.2 $R_{\rm Jup}$. In these conditions, to reproduce well the transit data, the planet would need to have a radius of 3.24 $R_{\rm Jup}$, which is clearly unphysical for such objects.

We estimated the Bayes factor, B_{ij}, between the three scenarios using the method of Tuomi & Jones (2012). This method has some limitations that are discussed in Santerne et al. (2014). However, since we tested here scenarios that have nearly the same number of free parameters and most of these parameters have the same priors in the various scenarios, we assume that these limitations have no significant impact on our results. We found that $\log_{10}B_{ij} \sim 250$ and $\log_{10}B_{ij} \sim 870$, against the triple and planet-in-binary scenarios (respectively), in favour to the planet one. This significantly validates WASP-121 b as a *bona-fide* planet. Computing the BIC between the best models give a value of 1103 and 3905 against the triple and planet-in-binary scenarios (respectively), which confirms that WASP-121 b is a transiting planet.

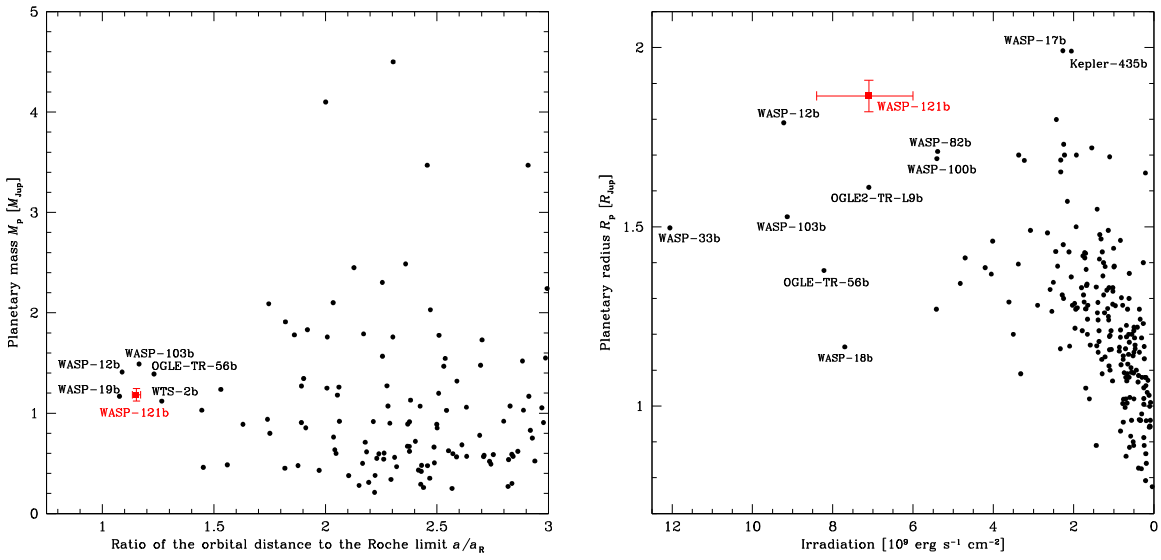

Figure 12. Left: orbital distance to the Roche limit ratio-mass diagram for the known transiting hot Jupiters with 0.2 $M_{Jup} < M_p < 13\ M_{Jup}$ and $P < 12$ d (data from the NASA Exoplanet Archive). We only show planets with $a/a_R < 3$. The planet WASP-121 b is shown in red. Right: irradiation-radius diagram for the same sample of planets.

5 DISCUSSION

WASP-121 b is a ∼1.18 M_{Jup} planet in a 1.27 d orbit around a bright ($V = 10.4$) F6V star. Its most notable property is that its orbital semimajor axis is only ∼1.15 times larger than its Roche limit, which suggests that the planet is close to tidal disruption. Fig. 12 (left) shows the distribution of the orbital distance to the Roche limit ratio (a/a_R) as a function of the planetary mass for the known transiting planets with 0.2 $M_{Jup} < M_p < 13\ M_{Jup}$ and $P < 12$ d. WASP-121 b is one of the closest systems to tidal disruption, its direct competitors being WASP-12 b (Hebb et al. 2009), WASP-19 b (Hebb et al. 2010), WASP-103 b (Gillon et al. 2014), OGLE-TR-56 b (Konacki et al. 2003; Adams et al. 2011), and WTS-2 b (Birkby et al. 2014). According to Matsumura et al. (2010), these extreme planets are now expected to undergo tidal orbital decay through tidal dissipation inside the star only (we will elaborate on this in Section 5.2 in the case of WASP-121 b). The speed of this final orbital decay depends mainly on the mass of the planet and the tidal dissipation efficiency of the star. As noted by Gillon et al. (2014), the fact that all the planets near tidal disruption found to date have similar masses (between 1.1 and 1.5 M_{Jup}, see the left-hand panel of Fig. 12) could thus suggest a narrow range of tidal dissipation efficiencies for the host stars of the known transiting hot Jupiters (mainly solar-type stars).

5.1 Structural parameters of WASP-121 b: correction for asphericity using Roche geometry

Being close to its Roche limit, WASP-121 b might be significantly deformed by the intense tidal forces it is subject to (e.g. Budaj 2011) and even lose some of its mass through Roche lobe overflow (e.g. Lai, Helling & van den Heuvel 2010; Li et al. 2010). To evaluate the tidal distortion of the planet, we calculate its Roche shape by using the Roche model of Budaj (2011), as done by Southworth et al. (2015) for WASP-103 b. This model assumes that the planet is on a circular orbit and that it is rotating synchronously with its orbital period ($P_{rot} = P_{orb}$). This second assumption is perfectly reasonable as current theories of tidal evolution of close-in exoplanets predict synchronization times much shorter than times needed for circularization of the orbits (see e.g. Rasio & Ford 1996). The model takes as main inputs the orbital semimajor axis ($a = 5.47 \pm 0.11$ R$_\odot$), the star/planet mass ratio ($M_\star/M_p = 1198^{+141}_{-128}$), and the planetary radius ($R_p = 1.807 \pm 0.039\ R_{Jup}$), and computes the Roche shape of the planet which would have the same cross-section during the transit as the one we inferred from our observations assuming a spherical planet (eclipse model of Mandel & Agol 2002, see Section 3.3).

Table 5. Parameters describing the shape of WASP-121 b, obtained using the Roche model of Budaj (2011). The errors are the quadratic sum of the errors due to each input parameter (a, $M_\star/M_p$, and R_p).

Parameter	Value
Radius at the substellar point R_{sub} [R_{Jup}]	2.009 ± 0.072
Radius at the antistellar point R_{back} [R_{Jup}]	1.997 ± 0.069
Radius at the rotation pole R_{pole} [R_{Jup}]	1.787 ± 0.038
Radius on the side R_{side} [R_{Jup}]	1.828 ± 0.041
Cross-sectional radius R_{cross} [R_{Jup}]	1.807 ± 0.039
Mean radius R_{mean} [R_{Jup}]	1.865 ± 0.044
Roche lobe filling parameter ff	0.591 ± 0.040
R_{sub}/R_{side}	1.099 ± 0.020
R_{sub}/R_{pole}	1.124 ± 0.026
R_{side}/R_{pole}	1.023 ± 0.003
Density correction factor $(R_{cross}/R_{mean})^3$	0.910 ± 0.013

The results are displayed in Table 5. R_{sub}, R_{back}, R_{pole}, and R_{side} are the planetary radii at the substellar point, the antistellar point, the rotation pole, and on the side, respectively. Together, these parameters describe the Roche shape of the planet. R_{cross} is the cross-sectional radius, i.e. the radius of the sphere that would have the same cross-section as the Roche surface of the planet during the transit. It is the

planetary radius we derived from our global analysis in Section 3.3 (i.e. the observed radius). $R_{\rm mean}$ is the radius of the sphere with the same volume as the Roche surface of the planet. The Roche lobe filling parameter *ff* is defined as $R_{\rm sub}/R_{\rm L_1}$, where $R_{\rm L_1}$ is the distance of the Lagrangian L1 point. The asphericity of the planet can be quantified by the ratios $R_{\rm sub}/R_{\rm side}$, $R_{\rm sub}/R_{\rm pole}$, and $R_{\rm side}/R_{\rm pole}$. Finally, the quantity $(R_{\rm cross}/R_{\rm mean})^3$ is the *CF* that must be applied to the planetary density $\rho_{\rm p}$ derived from our global analysis assuming a spherical planet to convert it to the density obtained using the Roche model.

With a Roche lobe filling parameter of 0.59, WASP-121 b is still well away from Roche lobe overflow, despite being significantly deformed. It would none the less be interesting to search for potential signatures of planetary material surrounding WASP-121 (e.g. excess transit depths in the near-UV). Such signatures have indeed been possibly detected for WASP-12 by Fossati et al. (2010, 2013) and Haswell et al. (2012), although Budaj (2011) reported a value of only 0.61 for the Roche lobe filling parameter of WASP-12 b. If we use the $R_{\rm sub}/R_{\rm pole}$ ratio to quantify the departures from the sphere, we find that WASP-121 b ($R_{\rm sub}/R_{\rm pole} = 1.124$) is one of the most distorted planets known to date, alongside WASP-12 b ($R_{\rm sub}/R_{\rm pole} = 1.138$; Budaj 2011), WASP-19 b ($R_{\rm sub}/R_{\rm pole} = 1.124$; Budaj 2011), and WASP-103 b ($R_{\rm sub}/R_{\rm pole} = 1.120$; Southworth et al. 2015). This distortion is expected to produce characteristic signatures in the transit photometry of the system. There are two main features in the flux difference between the transit light curve of an ellipsoidal and a spherical planet (see Correia 2014 for details): an oscillation during the ingress and egress phases, and a 'bump' increase during the whole transit with a maximum value at the centre of the transit. For a giant planet close to its Roche limit such as WASP-121 b, these flux differences can reach 100 ppm (Correia 2014) and could thus be detected in ultraprecise transit photometry, obtained for example with the future missions CHEOPS (Broeg et al. 2013) and PLATO 2.0 (Rauer et al. 2014). This would allow us to estimate the fluid Love number (e.g. Love 1911) of the planet and to gain valuable insights on its internal structure.

$R_{\rm mean}$ being more representative of the physical size of the planet than $R_{\rm cross}$, we adopt it as our revised value for the planetary radius ($1.865 \pm 0.044\ R_{\rm Jup}$) and include it, as well as the subsequent revised value for the planetary density ($0.183 \pm 0.016\ \rho_{\rm Jup}$), in Table 4. We note that $R_{\rm mean}$ should be used when comparing the radius of the planet with theoretical models (e.g. Fortney, Marley & Barnes 2007), while $R_{\rm cross}$ should rather be employed when interpreting transmission or occultation data.

Several works showed that hot Jupiters' radii correlate well with their incident irradiation (see e.g. Demory & Seager 2011; Enoch, Collier Cameron & Horne 2012; Weiss et al. 2013). Fig. 12 (right) shows the position of WASP-121 b in an irradiation-radius diagram for the same sample of transiting planets as previously. With a radius of $1.865 \pm 0.044\ R_{\rm Jup}$ and an irradiation of $\sim 7.1\ 10^9$ erg s^{-1} cm^{-2}, WASP-121 b joins the handful of extremely irradiated planets with superinflated radii. Its radius is actually significantly larger than the value of $1.50 \pm 0.03\ R_{\rm Jup}$ predicted by the equation derived by Weiss et al. (2013) from a sample of 103 transiting planets with a mass between 150 $M_\oplus$ and 13 $M_{\rm Jup}$ and that relates planets' sizes to their masses and irradiations. Several physical mechanisms have been proposed to explain the inflated radii of hot Jupiters, such as tidal heating (Bodenheimer, Lin & Mardling 2001), deposition of kinetic energy into the planets from strong winds driven by the large day/night temperature contrasts (Showman & Guillot 2002), enhanced atmospheric opacities (Burrows et al. 2007), reduced heat transport efficiency by layered convection inside the planets (Chabrier & Baraffe 2007), or Ohmic heating from currents induced through winds in the planetary atmospheres (Batygin & Stevenson 2010). As the WASP-121 system is quite young (1.5 ± 1.0 Gyr, see Section 3.4), tidal circularization and dissipation might have occurred recently enough to contribute to the observed inflated radius.

5.2 Orbital evolution of WASP-121 b

In Section 3.3, we find a sky-projected spin-orbit angle of $\beta = 257\overset{\circ}{.}8^{+5\overset{\circ}{.}3}_{-5\overset{\circ}{.}5}$. This result suggests a significant misalignment between the spin axis of the host star and the orbital plane of the planet. Such a high misalignment could favour a migration of the planet involving strong dynamical events, such as planet–planet scattering (e.g. Rasio & Ford 1996; Weidenschilling & Marzari 1996; Moorhead & Adams 2005; Chatterjee et al. 2008) and/or Kozai–Lidov oscillations (e.g. Kozai 1962; Lidov 1962; Wu & Murray 2003; Fabrycky & Tremaine 2007). As shown in Fabrycky & Winn (2009), the true spin-orbit angle ψ, can be computed from β, $i_{\rm p}$ (the orbital inclination), and $i_\star$ (the stellar inclination). If we assume that the stellar rotation period $P_{\rm rot,\star}$ is either 0.89 d or 1.13 d and we combine this information with our measured values for $R_\star$ and $v_\star \sin i_\star$, we obtain $i_\star$ of $9\overset{\circ}{.}4 \pm 0\overset{\circ}{.}6$ and $11\overset{\circ}{.}9 \pm 0\overset{\circ}{.}7$, respectively (see Section 3.2). These values, together with our measured β and $i_{\rm p}$, yield ψ of $89\overset{\circ}{.}6 \pm 1\overset{\circ}{.}1$ and $90\overset{\circ}{.}1 \pm 1\overset{\circ}{.}2$, respectively, where the uncertainties are the quadratic sum of the uncertainties due to each input parameter. Both these solutions are in excellent agreement and would place the planet in a nearly polar orbit around its star, which would clearly be a remarkable configuration as noted by e.g. Lai (2012) and Rogers & Lin (2013).

The proximity of WASP-121 b to its Roche limit suggests that its orbital evolution is now dominated by tidal interactions with its host star. To assess the future orbital evolution of the planet, we integrate the tidal evolution equations of Matsumura et al. (2010) forwards in time, assuming that the planet is on a circular orbit (see Section 3.3) and that its rotation is now synchronized with its orbit. Under these reasonable assumptions, the planet's orbital evolution is expected to depend only on the tidal dissipation inside the star (Matsumura et al. 2010). The efficiency of this tidal dissipation is parametrized by the stellar tidal dissipation factor $Q'_\star$, with a higher $Q'_\star$ meaning a weaker tidal dissipation. We assume here that $Q'_\star \propto 1/|2\omega_\star - 2n|$, where $\omega_\star$ is the stellar angular velocity and n is the planet's mean motion ($n = 2\pi/P$), as recommended by Matsumura et al. (2010) for the cases where the stellar rotation is not yet synchronized with the orbit (stellar rotation period $P_\star \neq P$). Under this assumption, $Q'_\star$ changes as $Q'_\star = Q'_0\ |2\omega_\star - 2n|/|2\omega_{\star,0} - 2n_0|$, where 0 index indicates the current values. Fig. 13 shows the obtained evolutions for the semimajor axis a (top), the spin-orbit angle ψ (middle), and the stellar rotation period $P_\star$ (bottom), assuming different values between 10^6 and 10^9 for the current stellar tidal dissipation factor $Q'_{\star,0}$ and a current stellar rotation period $P_{\star,0}$ of 0.89 d (left-hand panels) or 1.13 d (right-hand panels). For all cases, the model shows that the planet will continue to approach its host star until reaching its Roche limit, where it will be finally tidally disrupted. Assuming $P_{\star,0} = 0.89/1.13$ d, we find remaining lifetimes of 4.20/1.22 Myr, 42.0/12.2 Myr, 420/122 Myr, and 4.20/1.22 Gyr for $Q'_{\star,0}$ values of 10^6, 10^7, 10^8, and 10^9, respectively. We note that for $Q'_{\star,0} = 10^6$, the remaining lifetime of the planet would be <1 per cent of the youngest possible age of the system (500 Myr, see Section 3.4), thus giving a low probability for the planet to be detected now. This result could favour $Q'_{\star,0}$ values $\gtrsim 10^7$ for WASP-121, which would

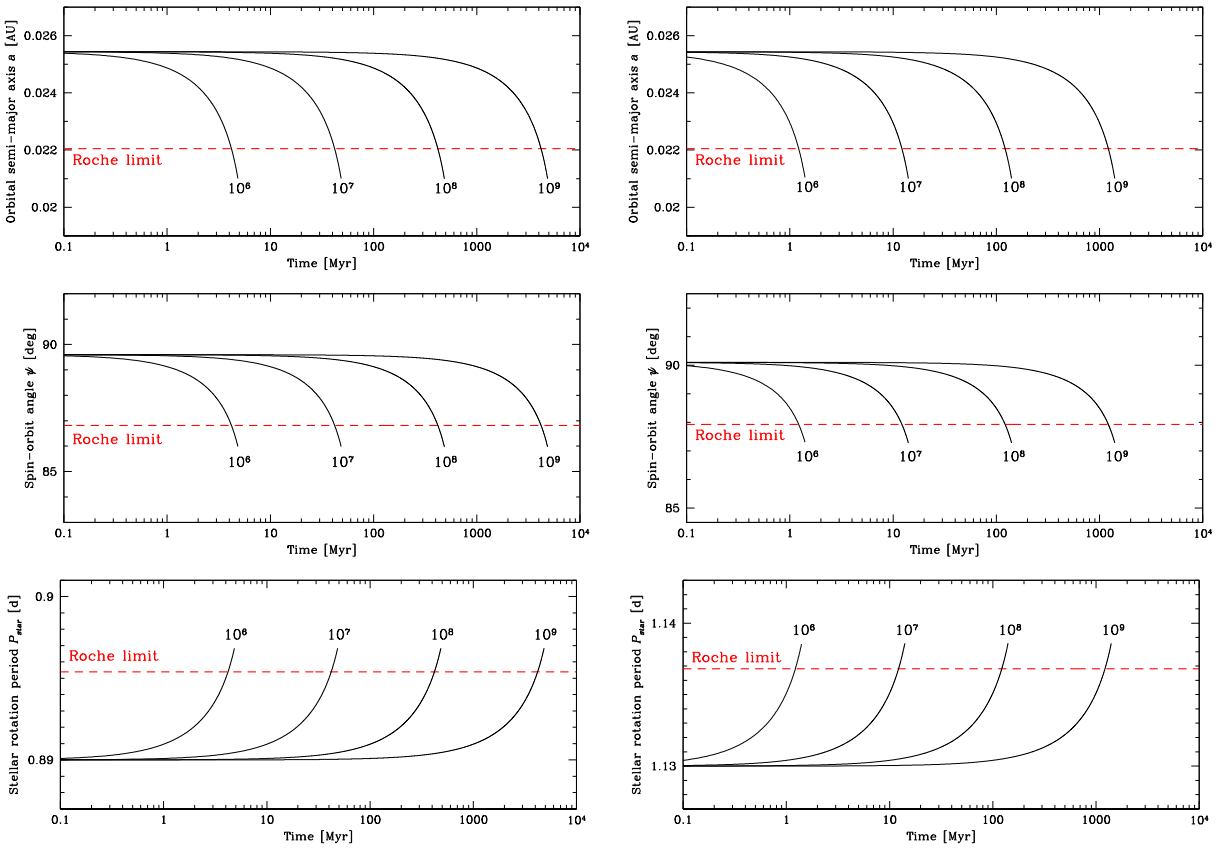

Figure 13. Future tidal evolution of the orbital semimajor axis (top), the spin-orbit angle (middle), and the stellar rotation period (bottom), assuming the current stellar rotation period $P_{\star,0}$ is 0.89 d (left-hand panels) or 1.13 d (right-hand panels). The labelled evolutions correspond to $Q'_{\star,0} = 10^6$, 10^7, 10^8, and 10^9. The red horizontal dashed lines represent the Roche limit.

be in line with the expectation that hot stars ($T_{\rm eff} > 6250$ K) would have low tidal dissipation efficiencies due to their thin or quasi-non-existent convective envelopes (see e.g. Winn et al. 2010; Albrecht et al. 2012). For WASP-121, we have $T_{\rm eff} = 6460 \pm 140$ K and a thin convective envelope starting at 0.88 $R_\star$.

Combining the Matsumura et al.'s expression for da/dt and the Kepler's third law, we can calculate the current rate of orbital period change: $({\rm d}P/{\rm dt})_0 = -0.0035\ (10^6/Q'_{\star,0})$ s yr^{-1} for $P_{\star,0} = 0.89$ d and $({\rm d}P/{\rm dt})_0 = -0.0118\ (10^6/Q'_{\star,0})$ s yr^{-1} for $P_{\star,0} = 1.13$ d. We can then estimate how long it would take to observe significant transit timing variations (TTVs) due to the orbital decay of the planet using, e.g. the equation 7 of Birkby et al. (2014). We note that this estimation assumes a constant rate of orbital period change dP/dt $= ({\rm d}P/{\rm dt})_0$. Fig. 14 shows the evolution of the shift in the transit time as a function of time for the different $Q'_{\star,0}$, and for $P_{\star,0} = 0.89$ d (top) or $P_{\star,0} = 1.13$ d (bottom). Assuming that a timing accuracy of ∼20 s is achievable with current instrumentation (see e.g. Gillon et al. 2009) and that $P_{\star,0} = 0.89/1.13$ d, TTVs could be detected at 3σ after ∼11/6 yr for $Q'_{\star,0} = 10^6$, ∼35/19 yr for $Q'_{\star,0} = 10^7$, ∼110/60 yr for $Q'_{\star,0} = 10^8$, and ∼348/189 yr for $Q'_{\star,0} = 10^9$, respectively. For low values of $Q'_{\star,0}$, the decay of WASP-121 b's orbit could thus be detectable on the decade time-scale. Alternatively, the non-detection of TTVs in the WASP-121 b system after a certain amount of time would allow us to put a lower limit on $Q'_{\star,0}$ and help constrain tidal evolution theories.

5.3 Validity of the spherical approximation for the star WASP-121

The likely stellar rotation periods of 0.89 and 1.13 d would imply, together with our measured value for $R_\star$, rotation velocities $v_\star$ of 82.9 ± 1.7 and 65.3 ± 1.4 km s^{-1}, respectively (see Section 3.2). Such high $v_\star$ might imply a non-negligible deformation of the star due to its fast rotation. Using the Roche model from Maeder (2009), this deformation can be expressed as $R_{\star,\rm eq}/R_{\star,\rm pol} = 1 + (1/2)\ (\omega_\star/\omega_{\star,\rm K})^2$, where $\omega_\star$ is the rotation velocity; $\omega_{\star,\rm K}$ the critical break-up velocity; $R_{\star,\rm eq}$ the equatorial radius; and $R_{\star,\rm pol}$ the polar radius. We estimate the critical velocity from the Keplerian velocity $\sqrt{GM_\star/R^3_{\star,\rm eq}}$, for which the centrifugal force equals gravitational forces at the equator of the star. For WASP-121 (Table 4), $\omega_\star = 0.17\ \omega_{\star,\rm K}$, which gives $R_{\star,\rm eq}/R_{\star,\rm pol} = 1.015$. The deformation of the star induced by its possible rapid rotation would thus not strongly bias our stellar radius measurement (which has an error bar ∼2 per cent), even if it was obtained assuming a spherical shape for the star (eclipse model of Mandel & Agol 2002, see Section 3.3).

5.4 First constraints on the atmospheric properties of WASP-121 b

The large radius of WASP-121 b, its extreme irradiation, and the brightness of its host star make it an excellent target for atmospheric

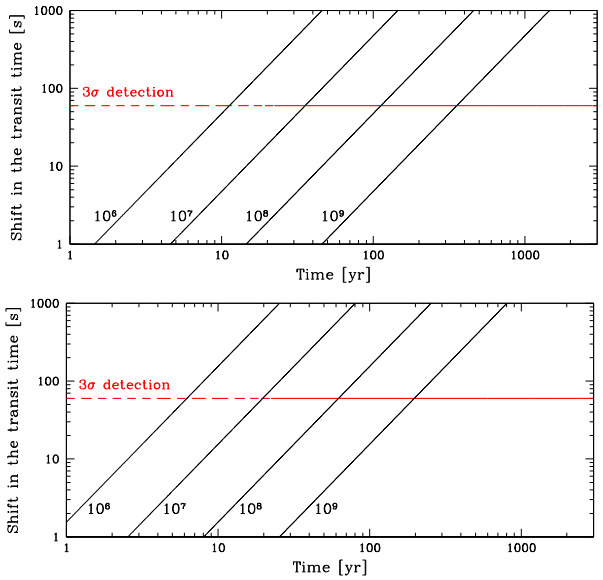

Figure 14. Shift in the transit time of WASP-121 b as a function of time, computed for different values of $Q'_{\star,0}$, assuming the current stellar rotation period is 0.89 d (top) or 1.13 d (bottom). The labelled evolutions correspond to $Q'_{\star,0} = 10^6$, 10^7, 10^8, and 10^9. The red horizontal line represents the 3σ detection limit, assuming a timing accuracy of 20 s.

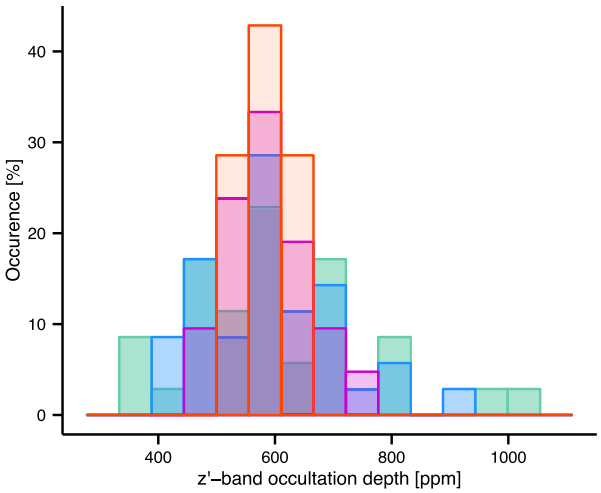

Figure 15. Histograms of the z'-band occultation depths derived from the MCMC analyses of subsets of three (green), four (blue), five (purple), and six (red) light curves chosen among the seven TRAPPIST occultation light curves.

studies via secondary eclipse observations, with theoretical expectations for the planet-to-star IR flux ratio >0.05 per cent down to ∼0.9 μm.

By combining seven occultation light curves obtained with TRAPPIST, we detect the emission of the planet in the z' band at better than $\sim 4\sigma$, the measured occultation depth being 603 ± 130 ppm (see Fig. 5). To make sure that the detected signal does not result from a systematic effect present in one or several light curves, we followed the method presented in Lendl et al. (2013). We thus divided our set of seven occultation light curves into subsets containing all possible combinations of three to six light curves and performed an MCMC analysis on each of them, while keeping all the jump parameters except the occultation depth fixed to the values derived from our global analysis (Table 4). Fig. 15 presents histograms of the derived occultation depths. We can see how the solutions converge towards our adopted value as we use an increasing number of occultation light curves.

Our measured occultation depth can be translated into a brightness temperature $T_{\rm br}$ of 3553^{+160}_{-178} K. In this calculation, we considered the planet as a blackbody of temperature $T_{\rm br}$ and used a Kurucz model spectrum for the star (Castelli & Kurucz 2004). We also assumed that all the planet's z'-band flux arises from thermal emission, which is reasonable as López-Morales & Seager (2007) showed that reflected light contributes 10 to 20 times less than thermal emission at these wavelengths for very hot Jupiters, such as WASP-121 b. We then defined our measured occultation depth as the product of the planet-to-star area ratio and the ratio of the TRAPPIST z' bandpass-integrated planet-to-star fluxes (e.g. Charbonneau et al. 2005), and adopted as brightness temperature the blackbody temperature that yielded the best match to our measured occultation depth. The uncertainty on $T_{\rm br}$ only accounts for the uncertainty on the measured occultation depth, which is the main source of error.

We can compare this brightness temperature to the equilibrium temperature of the planet, which is given by $T_{\rm eq} = T_{\rm eff}\sqrt{R_\star/a}\ [f\,(1 - A_{\rm B})]^{1/4}$, where f and $A_{\rm B}$ are the reradiation factor and the Bond albedo of the planet, respectively (López-Morales & Seager 2007). The factor f ranges from 1/4 to 2/3, where $f = 1/4$ indicates efficient heat redistribution and isotropic reradiation over the whole planet and $f = 2/3$ corresponds to instantaneous reradiation of incident radiation with no heat redistribution. The brightness temperature is significantly higher ($\sim 7\sigma$) than the maximum equilibrium temperature of 3013^{+77}_{-75} K obtained assuming $A_{\rm B} = 0$ and $f = 2/3$, which could suggest that the planet has a low Bond albedo coupled to a poor heat redistribution efficiency. This would agree with the trend noted by Cowan & Agol (2011) that hottest planets are less efficient at redistributing the incident stellar energy than colder planets, the explanation proposed for this trend being that the radiative time-scale is shorter than the advective time-scale for hotter planets, causing these planets to reradiate the incident stellar energy rather than advecting it through winds.

However, we note that the comparison of brightness temperature with equilibrium temperature has only limited physical meaning here as our z'-band observations probe thermal emission from deep layers ($P \sim 1$ bar) of the planetary atmosphere, that can be hotter than the maximum equilibrium temperature (e.g. Madhusudhan 2012). Furthermore, the emission spectrum of a hot Jupiter can deviate significantly from that of a blackbody. For instance, the flux observed in the z' band can be noticeably increased (respectively, decreased) by emission (respectively, absorption) due to gaseous TiO, which is expected to be abundant if the atmosphere has a carbon-to-oxygen (C/O) ratio <1 (O-rich atmosphere).[6]

Our z'-band occultation measurement thus provides a first observational constraint on the emission spectrum of WASP-121 b. Combined with future observations at longer wavelengths (from the ground in the near-infrared J, H, and K bands, or from space between 1.1 and 1.7 μm with *HST*/WFC3 or at 3.6 and 4.5 μm with *Spitzer*/IRAC), it will allow us to gain insights on the planet's dayside chemical composition and thermal structure.

[6] Whether TiO is seen in emission or absorption in that case depends on the thermal structure of the planetary atmosphere (presence or lack of temperature inversion; see Madhusudhan 2012 for details).

ACKNOWLEDGEMENTS

We would like to thank G. Buldgen, A. Correia, B.-O. Demory, and X. Dumusque for their valuable suggestions. WASP-South is hosted by the SAAO and we are grateful for their ongoing support and assistance. Funding for WASP comes from consortium universities and from UK's Science and Technology Facilities Council. TRAPPIST is a project funded by the Belgian Fund for Scientific Research (Fonds National de la Recherche Scientifique, F.R.S.-FNRS) under grant FRFC 2.5.594.09.F, with the participation of the Swiss National Science Fundation (SNF). The Swiss *Euler* Telescope is operated by the University of Geneva, and is funded by the Swiss National Science Foundation. LD acknowledges support of the F.R.I.A. fund of the FNRS. MG, EJ and VVG are FNRS Research Associates. ML acknowledges support of the European Research Council through the European Union's Seventh Framework Programme (FP7/2007-2013)/ERC grant agreement number 336480. AHMJT received funding from a fellowship provided by the Swiss National Science Foundation under grant number P300P2-147773. AS is supported by the European Union under a Marie Curie Intra-European Fellowship for Career Development with reference FP7-PEOPLE-2013-IEF, number 627202. We thank the anonymous referee for her/his valuable suggestions. The photometric and RV time series used in this work are publicly available at the CDS via anonymous ftp to cdsarc.u-strasbg.fr.

REFERENCES

Adams E. R. et al., 2011, ApJ, 741, 102
Albrecht S. et al., 2012, ApJ, 757, 18
Allard F., Homeier D., Freytag B., 2012, in Richards M. T., Hubeny I., eds, Proc. IAU Symp. 282, rom Interacting Binaries to Exoplanets: Essential Modeling Tools. Kluwer, Dordrecht, p. 235
Anderson D. R. et al., 2013, MNRAS, 430, 3422
Anderson D. R. et al., 2014, preprint (arXiv:1410.3449)
Andretta V., Giampapa M. S., 1995, ApJ, 439, 405
Asplund M., Grevesse N., Sauval A. J., Scott P., 2009, ARA&A, 47, 481
Bakos G., Noyes R. W., Kovács G., Stanek K. Z., Sasselov D. D., Domsa I., 2004, PASP, 116, 266
Baranne A. et al., 1996, A&AS, 119, 373
Batygin K., Stevenson D. J., 2010, ApJ, 714, L238
Birkby J. L. et al., 2014, MNRAS, 440, 1470
Bodenheimer P., Lin D. N. C., Mardling R. A., 2001, ApJ, 548, 466
Böhm-Vitense E., 2004, AJ, 128, 2435
Borsa F. et al., 2015, A&A, 578, A64
Broeg C. et al., 2013, in Saglia R., ed., EPJ Web Conf., 47, Hot Planets and Cool Stars. EDP Sciences, p. 3005
Budaj J., 2011, AJ, 141, 59
Burrows A., Hubeny I., Budaj J., Hubbard W. B., 2007, ApJ, 661, 502
Castelli F., Kurucz R. L., 2004, preprint (astro-ph/0405087)
Chabrier G., Baraffe I., 2007, ApJ, 661, L81
Chandrasekhar S., 1987, Ellipsoidal Figures of Equilibrium. Dover, New York
Charbonneau D. et al., 2005, ApJ, 626, 523
Chatterjee S., Ford E. B., Matsumura S., Rasio F. A., 2008, ApJ, 686, 580
Claret A., Bloemen S., 2011, A&A, 529, A75
Collier Cameron A. et al., 2006, MNRAS, 373, 799
Collier Cameron A. et al., 2007, MNRAS, 380, 1230
Correia A. C. M., 2014, A&A, 570, L5
Cowan N. B., Agol E., 2011, ApJ, 729, 54
Cumming A., 2010, in Seager S., ed., Exoplanets. Univ. Arizona Press, Tucson, AZ, p. 191
Demory B.-O., Seager S., 2011, ApJS, 197, 12
Díaz R. F., Almenara J. M., Santerne A., Moutou C., Lethuillier A., Deleuil M., 2014, MNRAS, 441, 983
Dotter A., Chaboyer B., Jevremović D., Kostov V., Baron E., Ferguson J. W., 2008, ApJS, 178, 89
Doyle A. P. et al., 2013, MNRAS, 428, 3164
Doyle A. P., Davies G. R., Smalley B., Chaplin W. J., Elsworth Y., 2014, MNRAS, 444, 3592
Dravins D., Lindegren L., Nordlund A., 1981, A&A, 96, 345
Dumusque X., Boisse I., Santos N. C., 2014, ApJ, 796, 132
Enoch B., Collier Cameron A., Horne K., 2012, A&A, 540, A99
Etzel P. B., 1981, in Carling E. B., Kopal Z., eds, Photometric and Spectroscopic Binary Systems. Reidel, Dordrecht, p. 111
Fabrycky D., Tremaine S., 2007, ApJ, 669, 1298
Fabrycky D. C., Winn J. N., 2009, ApJ, 696, 1230
Ford E. B., Rasio F. A., 2006, ApJ, 638, L45
Fortney J. J., Marley M. S., Barnes J. W., 2007, ApJ, 659, 1661
Fossati L. et al., 2010, ApJ, 714, L222
Fossati L., Ayres T. R., Haswell C. A., Bohlender D., Kochukhov O., Flöer L., 2013, ApJ, 766, L20
Gelman A., Rubin D., 1992, Stat. Sci., 7, 457
Gillon M. et al., 2009, A&A, 496, 259
Gillon M. et al., 2010, A&A, 511, A3
Gillon M., Jehin E., Magain P., Chantry V., Hutsemékers D., Manfroid J., Queloz D., Udry S., 2011, in Bouchy F., Díaz R., Moutou C., eds, EPJ Web Conf. 11, Detection and Dynamics of Transiting Exoplanets. EDP Sciences, p. 6002
Gillon M. et al., 2012, A&A, 542, A4
Gillon M. et al., 2014, A&A, 562, L3
Giménez A., 2006, ApJ, 650, 408
Goldreich P., Tremaine S., 1980, ApJ, 241, 425
Gray D. F., 2008, The Observation and Analysis of Stellar Photospheres. Cambridge Univ. Press, Cambridge
Guillochon J., Ramirez-Ruiz E., Lin D., 2011, ApJ, 732, 74
Hartman J. D. et al., 2011, ApJ, 742, 59
Haswell C. A. et al., 2012, ApJ, 760, 79
Hebb L. et al., 2009, ApJ, 693, 1920
Hebb L. et al., 2010, ApJ, 708, 224
Hellier C. et al., 2011, in Bouchy F., Díaz R., Moutou C., eds, EPJ Web Conf. 11, Detection and Dynamics of Transiting Exoplanets. EDP Sciences, p. 1004
Hellier C. et al., 2012, MNRAS, 426, 739
Henden A. A., Levine S., Terrell D., Welch D. L., 2015, BAAS, 225, 336.16
Holman M. J. et al., 2006, ApJ, 652, 1715
Howard A. W. et al., 2012, ApJS, 201, 15
Izotov Y. I., Thuan T. X., 2010, ApJ, 710, L67
Jackson B., Greenberg R., Barnes R., 2008, ApJ, 678, 1396
Jehin E. et al., 2011, The Messenger, 145, 2
Jenkins J. S., Tuomi M., 2014, ApJ, 794, 110
Konacki M., Torres G., Jha S., Sasselov D. D., 2003, Nature, 421, 507
Kordopatis G. et al., 2013, AJ, 146, 134
Kovács G., Zucker S., Mazeh T., 2002, A&A, 391, 369
Kozai Y., 1962, AJ, 67, 591
Kroupa P., 2001, MNRAS, 322, 231
Lai D., 2012, MNRAS, 423, 486
Lai D., Helling C., van den Heuvel E. P. J., 2010, ApJ, 721, 923
Lendl M. et al., 2012, A&A, 544, A72
Lendl M., Gillon M., Queloz D., Alonso R., Fumel A., Jehin E., Naef D., 2013, A&A, 552, A2
Lidov M. L., 1962, Planet. Space Sci., 9, 719
Li S.-L., Miller N., Lin D. N. C., Fortney J. J., 2010, Nature, 463, 1054
Lin D. N. C., Papaloizou J., 1986, ApJ, 309, 846
López-Morales M., Seager S., 2007, ApJ, 667, L191
Love A. E. H., 1911, Some Problems of Geodynamics. Cambridge Univ. Press, Cambridge
Lubow S. H., Ida S., 2010, in Seager S., ed., Planet Migration. Univ. Arizona Press, Tucson, AZ, p. 347

McLaughlin D. B., 1924, ApJ, 60, 22
Madhusudhan N., 2012, ApJ, 758, 36
Maeder A., 2009, in Börner G. et al., eds, Astronomy and Astrophysics Library, Physics, Formation and Evolution of Rotating Stars. Springer, Berlin, p. 19
Magain P., 1984, A&A, 134, 189
Mandel K., Agol E., 2002, ApJ, 580, L171
Marcy G. W., Butler R. P., Fischer D. A., Vogt S. S., 2004, in Beaulieu J., Lecavelier Des Etangs A., Terquem C., eds, ASP Conf. Ser. Vol. 321, Extrasolar Planets: Today and Tomorrow. Astron. Soc. Pac., San Francisco, p. 501
Matsumura S., Peale S. J., Rasio F. A., 2010, ApJ, 725, 1995
Maxted P. F. L. et al., 2011, PASP, 123, 547
Mayor M. et al., 2011, preprint (arXiv:1109.2497)
Meibom S. et al., 2013, Nature, 499, 55
Melo C. et al., 2007, A&A, 467, 721
Moorhead A. V., Adams F. C., 2005, Icarus, 178, 517
Morton T. D., Johnson J. A., 2011, ApJ, 738, 170
Murray C. D., Correia A. C. M., 2010, in Seager S., ed., Keplerian Orbits and Dynamics of Exoplanets. Univ. Arizona Press, Tucson, AZ, p. 15
Nelson B., Davis W. D., 1972, ApJ, 174, 617
Noels A., Montalbán J., 2013, in Shibahashi H., Lynas-Gray A. E., eds, ASP Conf. Ser. Vol. 479, Progress in Physics of the Sun and Stars: A New Era in Helio- and Asteroseismology. Astron. Soc. Pac., San Francisco, p. 435
Noyes R. W., Hartmann L. W., Baliunas S. L., Duncan D. K., Vaughan A. H., 1984, ApJ, 279, 763
Ogilvie G. I., 2009, MNRAS, 396, 794
Penev K., Jackson B., Spada F., Thom N., 2012, ApJ, 751, 96
Pepe F., Mayor M., Galland F., Naef D., Queloz D., Santos N. C., Udry S., Burnet M., 2002, A&A, 388, 632
Pollacco D. L. et al., 2006, PASP, 118, 1407
Popper D. M., Etzel P. B., 1981, AJ, 86, 102
Queloz D. et al., 2000, A&A, 354, 99
Queloz D. et al., 2001, A&A, 379, 279
Raghavan D. et al., 2010, ApJS, 190, 1
Rasio F. A., Ford E. B., 1996, Science, 274, 954
Rauer H. et al., 2014, Exp. Astron., 38, 249
Rogers T. M., Lin D. N. C., 2013, ApJ, 769, L10
Rossiter R. A., 1924, ApJ, 60, 15
Santerne A. et al., 2014, A&A, 571, A37
Santerne A. et al., 2015, MNRAS, 451, 2337
Santos N. C. et al., 2002, A&A, 392, 215
Scargle J. D., 1982, ApJ, 263, 835
Schwarz G. E., 1978, Ann. Statist., 6, 461
Scuflaire R., Théado S., Montalbán J., Miglio A., Bourge P.-O., Godart M., Thoul A., Noels A., 2008, Ap&SS, 316, 83
Seager S., Deming D., 2010, ARA&A, 48, 631
Seager S., Mallén-Ornelas G., 2003, ApJ, 585, 1038
Showman A. P., Guillot T., 2002, A&A, 385, 166
Southworth J., 2008, MNRAS, 386, 1644
Southworth J. et al., 2015, MNRAS, 447, 711
Stetson P. B., 1987, PASP, 99, 191
Szabó G. M. et al., 2011, ApJ, 736, L4
Tamuz O., Mazeh T., Zucker S., 2005, MNRAS, 356, 1466
Tanaka H., Takeuchi T., Ward W. R., 2002, ApJ, 565, 1257
Torres G., Konacki M., Sasselov D. D., Jha S., 2005, ApJ, 619, 558
Torres G., Andersen J., Giménez A., 2010, A&AR, 18, 67
Triaud A. H. M. J. et al., 2010, A&A, 524, A25
Triaud A. H. M. J. et al., 2011, A&A, 531, A24
Tuomi M., Jones H. R. A., 2012, A&A, 544, A116
Tuomi M., Anglada-Escude G., Jenkins J. S., Jones H. R. A., 2014, preprint (arXiv:1405.2016)
Weidenschilling S. J., Marzari F., 1996, Nature, 384, 619
Weiss L. M. et al., 2013, ApJ, 768, 14
Winn J. N., 2010, in Seager S., ed., Transits and Occultations, Exoplanets. Univ. Arizona Press, Tucson, AZ, p. 55
Winn J. N., Fabrycky D., Albrecht S., Johnson J. A., 2010, ApJ, 718, L145
Wright E. L. et al., 2010, AJ, 140, 1868
Wu Y., Murray N., 2003, ApJ, 589, 605

APPENDIX A: PASTIS MCMC ANALYSIS OF THE PHOTOMETRIC DATA

Table A1. Priors used in the PASTIS analyses: $\mathcal{U}(a;b)$ represents a Uniform prior between a and b; $\mathcal{N}(\mu;\sigma^2)$ represents a normal distribution with a mean of μ and a width of σ^2; $\mathcal{P}(\alpha;x_{\rm min};x_{\rm max})$ represents a power-law distribution with an exponent α computed between $x_{\rm min}$ and $x_{\rm max}$; $\mathcal{P}_2(\alpha_1;\alpha_2;x_0;x_{\rm min};x_{\rm max})$ represents a double power-law distribution with an exponent α_1 computed between $x_{\rm min}$ and x_0 and an exponent α_2 computed between x_0 and $x_{\rm max}$; and finally $\mathcal{S}(a;b)$ represents a Sine distribution between a and b.

Parameter	Planet	Planet in binary	Triple
Target parameters			
Effective temperature $T_{\rm eff}$ [K]	$\mathcal{N}(6460;140)$	$\mathcal{N}(6460;140)$	$\mathcal{N}(6460;140)$
Surface gravity $\log g$ [cm.s^{-2}]	$\mathcal{N}(4.2;0.2)$	$\mathcal{N}(4.2;0.2)$	$\mathcal{N}(4.2;0.2)$
Iron abundance [Fe/H] [dex]	$\mathcal{N}(0.13;0.09)$	$\mathcal{N}(0.13;0.09)$	$\mathcal{N}(0.13;0.09)$
Distance d [pc]	$\mathcal{P}(2.0;10;10000)$	$\mathcal{P}(2.0;10;10000)$	$\mathcal{P}(2.0;10;10000)$
Interstellar extinction $E(B-V)$ [mag]	$\mathcal{U}(0;0.1)$	$\mathcal{U}(0;0.1)$	$\mathcal{U}(0;0.1)$
Planet parameters			
Radius R_p [$R_{\rm jup}$]	$\mathcal{U}(0;2.2)$	$\mathcal{U}(0;2.2)$	–
Albedo A_g	$\mathcal{U}(0;2.5)$	$\mathcal{U}(0;2.5)$	–
Binary parameters			
Mass of stellar host M_2 [$M_\odot$]	–	$\mathcal{P}_2(-1.3;-2.3;0.5;0.1;2)$	$\mathcal{P}_2(-1.3;-2.3;0.5;0.1;2)$
Mass of stellar companion M_3 [$M_\odot$]	–	–	$\mathcal{P}_2(-1.3;-2.3;0.5;0.1;2)$
Orbital parameters			
Orbital period P [d]	$\mathcal{N}(1.274\,9255;5.10^{-4})$	$\mathcal{N}(1.274\,9255;5.10^{-4})$	$\mathcal{N}(1.274\,9255;5.10^{-4})$
Transit epoch T_0 [BJD – 2450000]	$\mathcal{N}(6635.70832;0.03)$	$\mathcal{N}(6635.70832;0.03)$	$\mathcal{N}(6635.70832;0.03)$
Orbital inclination i [°]	$\mathcal{S}(60;90)$	$\mathcal{S}(60;90)$	$\mathcal{S}(60;90)$
TRAPPIST data parameters ($\times$ 12)			
Contamination	$\mathcal{N}(0;0.01)$	$\mathcal{N}(0;0.01)$	$\mathcal{N}(0;0.01)$
Out-of-transit flux	$\mathcal{U}(0.9;1.1)$	$\mathcal{U}(0.9;1.1)$	$\mathcal{U}(0.9;1.1)$
Jitter	$\mathcal{U}(0;0.1)$	$\mathcal{U}(0;0.1)$	$\mathcal{U}(0;0.1)$
EulerCam data parameters ($\times$ 4)			
Contamination	$\mathcal{N}(0.002;0.01)$	$\mathcal{N}(0.002;0.01)$	$\mathcal{N}(0.002;0.01)$
Out-of-transit flux	$\mathcal{U}(0.9;1.1)$	$\mathcal{U}(0.9;1.1)$	$\mathcal{U}(0.9;1.1)$
Jitter	$\mathcal{U}(0;0.1)$	$\mathcal{U}(0;0.1)$	$\mathcal{U}(0;0.1)$
Spectral energy distribution parameter			
Jitter [mag]	$\mathcal{U}(0;1)$	$\mathcal{U}(0;1)$	$\mathcal{U}(0;1)$

Table A2. Posterior distributions results of the PASTIS analyses.

Parameter	Planet	Planet in binary	Triple
Target parameters			
Effective temperature $T_{\rm eff}$ [K]	6650 ± 60	6140 ± 150	6763^{+46}_{-160}
Surface gravity $\log g$ [cm.s^{-2}]	4.245 ± 0.006	$3.949^{+0.031}_{-0.014}$	$3.770^{+0.002}_{-0.004}$
Iron abundance [Fe/H] [dex]	0.1 ± 0.1	$-0.51^{+0.01}_{-0.22}$	$-0.21^{+0.05}_{-0.01}$
Distance d [pc]	261 ± 4.6	334 ± 12	578^{+7}_{-10}
Interstellar extinction $E(B-V)$ [mag]	$0.009^{+0.012}_{-0.007}$	$0.0077^{+0.014}_{-0.006}$	$0.048^{+0.014}_{-0.029}$
Planet parameters			
Radius R_p [$R_{\rm jup}$]	1.76 ± 0.02	$2.1998^{+0.0001}_{-0.0005}$	–
Albedo A_g	0.55 ± 0.12^a	1.14 ± 0.18^b	–
Binary parameters			
Mass of eclipse host M_2 [$M_\odot$]	–	0.947 ± 0.007^c	$1.41^{+0.01\,c}_{-0.03}$
Mass of eclipse companion M_3 [$M_\odot$]	–	–	$0.367^{+0.003\,c}_{-0.008}$
Orbital parameters			
Orbital period P [d]	$1.274\,924\,77 \pm 5.4\ 10^{-7}$	$1.274\,9280 \pm 1.7\ 10^{-6}$	$1.274\,924\,95 \pm 7.4\ 10^{-7}$
Transit epoch T_0 [BJD – 2450000]	6635.7077 ± 0.0001	6635.7077 ± 0.0034	6635.7077 ± 0.0002
Orbital inclination i [°]	$89.13^{+0.60}_{-0.94}$	89.90 ± 0.09	$89.78^{+0.16}_{-0.23}$
Spectral energy distribution parameter			
Jitter [mag]	0.013 ± 0.013	0.170 ± 0.072	$0.014^{+0.014}_{-0.009}$

Notes. [a]This corresponds to an occultation depth of 620 ± 140 ppm.
[b]This corresponds to an occultation depth of 2470 ± 370 ppm.
[c]The error does not account for the uncertainty of the stellar models.

This paper has been typeset from a TEX/LATEX file prepared by the author.

3.3 Other projects

During my PhD, I have provided TRAPPIST data for a number of projects. TRAPPIST transit light curves were used, for example, in the follow-up studies of WASP-41 and WASP-47 by Neveu-VanMalle et al. (2016) and WASP-80 by Triaud et al. (2015), thereby helping to improve the characterization of these systems.

I was also involved in the discovery of K2-22 b, a disintegrating rocky planet in an ultra-short-period orbit ($P\sim$9.15 hrs) around an early-M dwarf (Sanchis-Ojeda et al. 2015). Fig. 3.10 (left) shows the K2 phase-folded transit light curve of K2-22 b, corrected for stellar activity and binned in 3.7min intervals. Its V-shaped profile is in fact the result of a convolution of the intrinsic transit shape and the K2 long-cadence sampling time of about 30min. The transit parameters cannot be precisely determined from such a highly distorted light curve. Several transits were thus observed at higher temporal resolution from the ground using TRAPPIST and other telescopes. The resulting transit light curves, shown in Fig. 3.10 (right), have of course a much lower precision than the K2 data, but their higher temporal resolution allowed to better determine the transit parameters and to detect variations in the transit depth and shape, that were interpreted as evidence for a rocky planet that is disintegrating via the emission of dusty effluents (see Sanchis-Ojeda et al. 2015 for details).

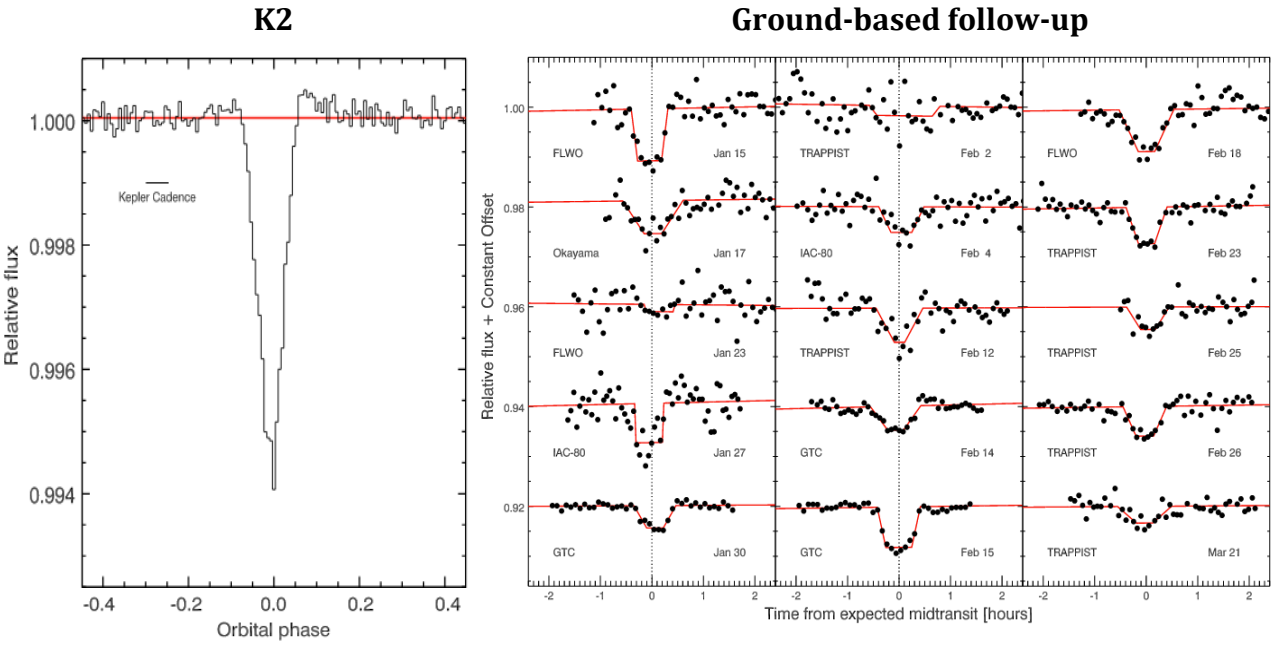

FIGURE 3.10: Transit photometry of the disintegrating rocky planet K2-22 b presented in Sanchis-Ojeda et al. (2015). *Left:* The K2 phase-folded transit light curve, corrected for stellar activity and binned in 3.7min bins. The K2 long-cadence sampling time of ∼30min is shown as a black horizontal bar, to give an idea of the temporal resolution of the data. The red horizontal line indicates the mean out-of-transit normalized flux. Figure 6 of Sanchis-Ojeda et al. (2015). *Right:* Fifteen transits observed at higher temporal resolution from the ground using TRAPPIST and other telescopes. For the sake of clarity, some light curves are binned in 5min bins. The best-fit three-segment transit models (see Sanchis-Ojeda et al. 2015 for details) are overplotted in red. Variations in the transit depth are clearly visible. Figure 7 of Sanchis-Ojeda et al. (2015).

3.4 TRAPPIST results in numbers

I will conclude this chapter with a few statistics about the photometric follow-up of planetary candidates (overwhelmingly WASP candidates) and known planets with TRAPPIST, after ∼5.4 years of operation[22]. Table 3.1 shows the current status of the 549 candidates that were observed with TRAPPIST from December 2010 to April 2016. The first four categories correspond to the four types of false positives described in Section 3.2.4. The very large proportion of blended eclipsing binaries (EBs) among the objects observed with TRAPPIST stems from the fact that candidates located in "crowded"[23] fields (thus more likely to be blended EBs) are almost systematically flagged for photometric follow-up observations first, while more isolated candidates are preferentially selected for the RV follow-up. Indeed, RV follow-up is expensive in terms of equipment and observing time. It is thus better to know for sure which star is responsible for the brightness dips and check that we are not facing a blended EB that could be easily resolved with TRAPPIST, before starting to acquire CORALIE spectra of a candidate. 105 candidates turned out to be confirmed planets, thus "co-detected" with TRAPPIST. 56 candidates need additional observations before any firm conclusion can be reached.

Among the 388 false positives reported in Table 3.1 (sum of the first four categories), a total of 221 were identified based only on TRAPPIST data. Those are typically blended EBs that are clearly resolved with TRAPPIST, or grazing EBs showing V-shaped eclipses that are clearly much too deep to be caused by grazing planetary transits. In other cases, combining the TRAPPIST data with CORALIE spectra, higher resolution EulerCam photometry or additional WASP data led to the conclusion.

By April 2016, a total of 521 follow-up eclipse (transit and occultation) light curves of 133 planets had been obtained with TRAPPIST. These 133 planets include the 105 co-detected planets mentioned above as well as other known planets, observed with the aim of improving their characterization.

Object type	Number	Proportion
Grazing eclipsing binaries	74	13.5%
High mass ratio eclipsing binaries	35	6.4%
Blended eclipsing binaries	246	44.8%
False alarms	33	6.0%
Planets	105	19.1%
Not yet concluded	56	10.2%
Total	549	

TABLE 3.1: TRAPPIST photometric follow-up of planetary candidates from transit surveys (overwhelmingly WASP candidates): statistics after ∼5.4 years of operation (December 2010 – April 2016).

[22] These programs represent ∼30% of the telescope time.
[23] i.e., we know, based on catalogs, that others stars fall within the WASP apertures.

Chapter 4

Transmission spectrophotometry of WASP-49 b and WASP-80 b with VLT/FORS2

A part of my PhD was devoted to the atmospheric study of two low-density sub-Jupiters, WASP-49 b (Lendl et al. 2012) and WASP-80 b (Triaud et al. 2013), via transmission spectrophotometry using the FORS2 instrument at the ESO Very Large Telescope (VLT, Paranal Observatory, Chile). The transmission spectrophotometry technique has been described in Sections 1.1.2 and 2.1. In this chapter, I will first briefly introduce FORS2, past results that were obtained with this instrument, and its known limitations. The spectrophotometric studies of WASP-49 b and WASP-80 b will then be presented individually.

4.1 Introducing FORS2

FORS2 is the near-UV and optical FOcal Reducer and low dispersion Spectrograph (Appenzeller et al. 1998) mounted at the Cassegrain focus of the VLT/UT1 (Antu). It operates in the wavelength range from 330 to 1100nm and can be used with either a red- or a blue-optimized detector system, the latter being the detector that was previously part of the now decommissioned FORS1 twin instrument. The red-optimized detector system, the one we used for all our observations, consists of two thinned back-illuminated 4K×2K MIT CCDs (15μm pixel size), providing a particularly high sensitivity at wavelengths >600nm (QE peak of 96.7% at 780nm). In standard resolution mode, FORS2 yields a field of view[1] of 6.8′×6.8′, at a plate scale of 0.25″/pixel with the default 2×2 binning. The instrument offers imaging, polarimetric, and low/medium resolution spectroscopic modes. For exoplanet transmission spectrophotometry, it is used in multi-object spectroscopic (MXU) mode, which allows to obtain simultaneous medium-resolution (R∼1000) spectra of several objects in the field of view, by inserting a custom-made laser-cut mask in the focal plane and then dispersing the light of the selected objects with a grism. Various grisms are available, with different wavelength ranges and dispersions. They can be coupled with order separation filters, to avoid overlaps of spectral orders in the spectra. A more comprehensive description of FORS2 can be found in Appenzeller et al. (1998), Moehler et al. (1995), and references therein.

The first ground-based spectrophotometric study of an exoplanet was performed using FORS2 by Bean, Miller-Ricci Kempton, and Homeier (2010), who reported a featureless transmission spectrum for the super-Earth GJ1214 b between 780 and 1000nm, ruling

[1] A part of the detector mosaic is vignetted by the instrument's top unit containing the focal plane equipment.

out a cloud-free hydrogen-dominated atmosphere for this planet. Combining the observations of two transits, they achieved a precision of ∼180ppm on GJ1214 b's transit depth per 10nm-wide wavelength bin (reanalysis in Bean et al. 2011). Following these pioneering observations, there were several attempts to study other exoplanets with FORS2 using the same technique, but the data appeared to suffer from unexpectedly high systematics that badly affected the precision on the derived transmission spectra. The longitudinal atmospheric dispersion corrector (LADC, Avila, Rupprecht, and Beckers 1997) on the telescope was identified as the most likely source of these systematics (Berta et al. 2011, Boffin et al. 2015). The LADC consists of two silica prisms of opposite orientation whose separation can be adjusted to compensate for the atmospheric dispersion, depending on the target's airmass, the wavelength range, and the atmospheric conditions. It is located in the M1 mirror cell of the telescope, before the instrument rotator[2] in the optical path, so that the field of view rotates relative to it during an observing sequence. Until their recent upgrade in November 2014 (Boffin et al. 2015), the LADC prisms exhibited an inhomogenous transmission over their surface (Moehler et al. 2010, see Fig. 4.1, left) due to the degradation of their antireflective coating (see Fig. 4.1, right). During an observing sequence, these patterns of uneven transmission rotated across the field of view, affecting the data of every star in a different manner, thus resulting in high-amplitude (up to several %) systematics in the differential light curves. The successful results by Bean, Miller-Ricci Kempton, and Homeier (2010) are thought to be mainly due to the especially short transit duration of GJ1214 b (∼52min), that resulted in only a small region of the LADC inhomogeneous transmission pattern being sampled during their observations. The FORS2 data presented in the following sections were acquired in 2012 and 2013, before the upgrade of the LADC, and are thus affected by considerable correlated noise.

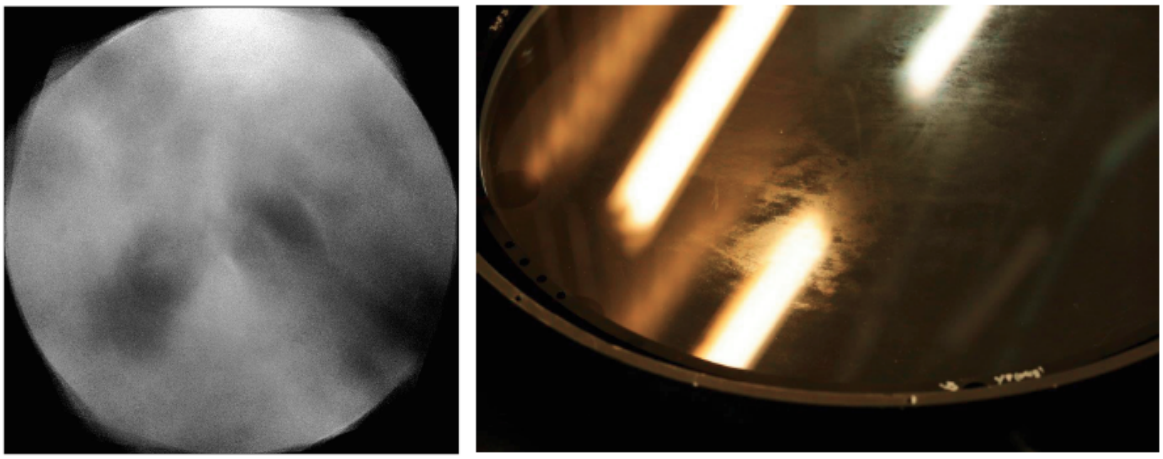

FIGURE 4.1: *Left:* Image of the inhomogeneous transmission of the FORS2 LADC before its upgrade (Figure 10 of Moehler et al. 2010). This image was obtained as the median of a set of flat-fielded twilight flats, that were counterrotated by the value of the instrument rotator angle under which they had been acquired (see Moehler et al. 2010 for details). *Right:* Photograph of one of the prisms of the FORS2 LADC taken just before its upgrade (Figure 2 of Boffin et al. 2015). The degradation of the antireflective coating at various places is clearly visible. The bright regions are reflections of the neon lights on the ceiling.

[2]During an observing sequence, the instrument (detector system, sorting filter, grism, mask) is rotated by the rotator to compensate for the field rotation inherent to the alt-azimuth mount of the telescope (and caused by the Earth's rotation).

4.2 WASP-49 b

WASP-49 b is an inflated Saturn-mass planet ($\sim$0.38 $M_{\rm Jup}$, $\sim$1.12 $R_{\rm Jup}$) that transits its bright (V=11.36, I=10.78) G6V host star every $\sim$2.78 days (Lendl et al. 2012). It is a good target for transmission spectroscopy, thanks to its low mean density ($\sim$0.27 $\rho_{\rm Jup}$), moderately high equilibrium temperature ($\sim$1369K assuming a null Bond albedo and an efficient day-night heat redistribution), and favorable planet-to-star radius ratio ($\sim$0.117). The study of its transmission spectrum with FORS2, led by Monika Lendl, is presented in detail in a paper that was published in A&A in 2016 (Lendl et al. 2016) and is reproduced in the following pages. I will give here a brief summary of this work and describe my contribution.

Three transits of WASP-49 b were observed with FORS2 in MXU mode during ESO P90 (service mode, PI: Michaël Gillon). Simultaneous medium-resolution ($R\sim$1000) spectra of WASP-49 and three reference stars were obtained in each exposure, covering the wavelength range 738-1020nm for WASP-49, which was centered horizontally (dispersion direction) on the detector, and slightly different ranges for the off-centered reference stars (see Figs. 1 and 3 of Lendl et al. 2016). For each transit, twenty-seven $\sim$10nm-wide spectrophotometric differential transit light curves were produced from the spectra. These light curves show strong correlated noise structures stemming from the inhomogeneous transmission of the LADC and consisting of both large-scale trends and short-timescale variations. The positions of the stars on the LADC prisms during the observations being correlated with the parallactic angle[3], low-order polynomials of this parameter allowed to model the large-scale trends of the light curves. The short-timescale variations were modeled for their part as first-order polynomials of common noise models (see Section 2.3 and Section 3.1.1 of Lendl et al. 2016), constructed from the residuals of light curves showing similar noise structures.

Each transit data set was first analyzed individually, leading to three independent transmission spectra that agree well with each other, which demonstrates the reliability of the analysis method. A global analysis of all FORS2 spectrophotometric light curves together with additional broad-band photometry obtained with TRAPPIST and EulerCam was then performed to derive a final combined transmission spectrum for WASP-49 b between 650 and 1020nm. The most prominent absorption signatures expected in this wavelength range for a clear hydrogen-dominated atmosphere with a temperature $\sim$1400K are the K I resonance doublet centered at 768nm and a broad rotational-vibrational H_2O band between $\sim$920 and $\sim$1020nm. None of these absorption features was detected in the transmission spectrum of WASP-49 b, which is best fit by atmospheric models containing a cloud deck at a pressure level of 1 mbar or less that efficiently obscures the atmospheric spectral signatures.

My first contribution to this work was to manage the FORS2 observations, with the help of Emmanuël Jehin, former instrument scientist of FORS2. I prepared the Observation Blocks (OBs), designed the MXU mask, and interacted with ESO about the observing program. I performed a preliminary reduction of the data using the ESO pipeline[4] directly after each transit observation, which allowed to optimize the observational strategy from

[3]The parallactic angle is the angle between two line segments originating from the target position, one pointing at the celestial pole, the other at the zenith. The instrument rotator angle is equal to this angle plus a constant offset.

[4]http://www.eso.org/sci/software/pipelines/fors/fors-pipe-recipes.html

one run to the next. For example, to reduce the noise stemming from the LADC, we had decided from the beginning to put it in simulation, that is, to keep the separation of the two LADC prisms constant during our observations. For the first two transits, this constant separation was simply set by the previous instrument configuration. I noticed from my preliminary reduction that the spectrophotometric light curves of the second transit were more strongly affected by large-scale trends than the ones of the first transit, for which the LADC separation was smaller. We thus decided to set the LADC prisms to their minimal separation for the third transit observation, which allowed to reduce the LADC-induced correlated noise in these data.

Once all the FORS2 data were acquired, I devised my own `IRAF`-based reduction pipeline[5] to extract spectra from the data and produce spectrophotometric light curves independently from the ESO pipeline, thus having real control of every reduction step. The spectrophotometric transit light curves that I obtained were checked against the ones produced independently by Monika Lendl, leading to consistent results.

I then performed preliminary combined analyses of these spectrophotometric transit light curves and identified the parallactic angle as a key parameter for modeling their large-scale trends. Finally, I also provided the new TRAPPIST transit light curves that were used in the final global analysis presented in the paper.

[5] I do not describe the reduction process here as it is very similar to the one presented in detail in Section 4.3.2 (reduction of the FORS2 data obtained for WASP-80 b).

A&A 587, A67 (2016)
DOI: 10.1051/0004-6361/201527594

Astronomy & Astrophysics

FORS2 observes a multi-epoch transmission spectrum of the hot Saturn-mass exoplanet WASP-49b⋆,⋆⋆

M. Lendl[1,2,3], L. Delrez[2], M. Gillon[2], N. Madhusudhan[4], E. Jehin[2], D. Queloz[3,5], D. R. Anderson[6], B.-O. Demory[5], and C. Hellier[6]

[1] Space Research Institute, Austrian Academy of Sciences, Schmiedlstr. 6, 8042 Graz, Austria
e-mail: monika.lendl@oeaw.ac.at
[2] Université de Liège, Allée du 6 août 17, Sart Tilman, 4000 Liège 1, Belgium
[3] Observatoire de Genève, Université de Genève, Chemin des maillettes 51, 1290 Sauverny, Switzerland
[4] University of Cambridge, Madingley Road, Cambridge CB3 0HA, UK
[5] Cavendish Laboratory, J J Thomson Avenue, Cambridge, CB3 0HE, UK
[6] Astrophysics Group, Keele University, Staffordshire, ST5 5BG, UK

Received 19 October 2015 / Accepted 18 December 2015

ABSTRACT

Context. Transmission spectroscopy has proven to be a useful tool for the study of exoplanet atmospheres, because the absorption and scattering signatures of the atmosphere manifest themselves as variations in the planetary transit depth. Several planets have been studied with this technique, leading to the detection of a small number of elements and molecules (Na, K, H_2O), but also revealing that many planets show flat transmission spectra consistent with the presence of opaque high-altitude clouds.
Aims. We apply this technique to the $M_P = 0.40\ M_J$, $R_p = 1.20\ R_J$, $P = 2.78$ d planet WASP-49b, aiming to characterize its transmission spectrum between 0.73 and 1 μm and search for the features of K and H_2O. Owing to its density and temperature, the planet is predicted to possess an extended atmosphere and is thus a good target for transmission spectroscopy.
Methods. Three transits of WASP-49b have been observed with the FORS2 instrument installed at the VLT/UT1 telescope at the ESO Paranal site. We used FORS2 in MXU mode with grism GRIS_600z, producing simultaneous multiwavelength transit light curves throughout the i' and z' bands. We combined these data with independent broadband photometry from the Euler and TRAPPIST telescopes to obtain a good measurement of the transit shape. Strong correlated noise structures are present in the FORS2 light curves, which are due to rotating flat-field structures that are introduced by inhomogeneities of the linear atmospheric dispersion corrector's transparency. We accounted for these structures by constructing common noise models from the residuals of light curves bearing the same noise structures and used them together with simple parametric models to infer the transmission spectrum.
Results. We present three independent transmission spectra of WASP-49b between 0.73 and 1.02 μm, as well as a transmission spectrum between 0.65 and 1.02 μm from the combined analysis of FORS2 and broadband data. The results obtained from the three individual epochs agree well. The transmission spectrum of WASP-49b is best fit by atmospheric models containing a cloud deck at pressure levels of 1 mbar or lower.
Conclusions.

Key words. techniques: spectroscopic – planets and satellites: atmospheres – stars: individual: WASP-49 – planets and satellites: gaseous planets

1. Introduction

The study of transiting planets has become one of the main avenues for characterizing exoplanets. Transit light curves are observed while the planet passes between its host star and an Earth-based observer, and many pieces of information on the planetary system are contained in them. Most prominently, the planetary radius and, in conjunction with a mass estimate, the planetary density are measured. The atmospheric properties of transiting planets are accessible to study mainly through transmission and emission spectroscopy, that is, through multiwavelength observations of transits and occultations (for a summary, see, e.g., Winn 2011).

Transmission spectroscopy (e.g. Seager & Sasselov 2000; Charbonneau et al. 2002) is sensitive to the absorption features imprinted by the planetary atmosphere on the stellar light that passes through it during transit. In this configuration the planetary day-night terminator region is probed. The angle between the planetary surface and the incident stellar radiation causes the outer atmospheric layers to have a higher weight for these observations than for the emissive case.

On the observational side, a limitation to transmission spectroscopy is given by stellar activity. Non-occulted spots slightly affect the measured transit depth (e.g., McCullough et al. 2014). These effects are largely eliminated for inactive planet hosting stars and can be further decreased by carrying out simultaneous observations in the available wavelength channels. Spectrophotometry consists of spectrally dispersing the light of target and reference stars and then binning the spectra to a lower

⋆ Based on photometric observations made with FORS2 on the ESO VLT/UT1 (Prog. ID 090.C-0758), EulerCam on the Euler-Swiss telescope and the Belgian TRAPPIST telescope.
⋆⋆ The photometric time series data in this work are only available in electronic form at the CDS via anonymous ftp to cdsarc.u-strasbg.fr (130.79.128.5) or via http://cdsarc.u-strasbg.fr/viz-bin/qcat?J/A+A/587/A67

A&A 587, A67 (2016)

resolution and performing relative photometry on the summed stellar flux in these bins. In this way, simultaneous multiwavelength observations of transits can be obtained. Initial results stem from space-based observatories (Barman 2007; Knutson et al. 2007; Désert et al. 2008), but more recently, this technique has also been used in ground-based instruments where capabilities of obtaining spectra of multiple objects allow using comparison stars (Bean et al. 2010, 2011; Sing et al. 2011).

From high-resolution spectra, several absorption features, in particular that of Na (Charbonneau et al. 2002; Redfield et al. 2008), have been identified in the optical transmission spectra of giant planets. Initial near-IR detections based on HST/NICMOS data (e.g., Swain et al. 2008) have given rise to debate because independent analyses have yielded different results (Sing et al. 2009; Gibson et al. 2011; Crouzet et al. 2012). More recently, HST/WFC3 has been used on a few hot Jupiters, where absorption features of H_2O could be identified (e.g., Deming et al. 2013; Huitson et al. 2013). Compared to theoretical predictions (e.g., Seager & Sasselov 2000), these signatures have been less pronounced than expected, indicating that an additional, grayer, opacity source is present in the planetary atmospheres. This picture is supported by largely flat optical transmission spectra observed for several hot Jupiter planets (e.g., Pont et al. 2008; Bean et al. 2013; Gibson et al. 2013). If the slope of the transmission spectrum is measured across a broad wavelength region, the haze components can be revealed thanks to their Rayleigh scattering signature (e.g., Lecavelier Des Etangs et al. 2008).

The subject of this paper, WASP-49b, (Lendl et al. 2012) is a hot Saturn discovered by the WASP survey (Pollacco et al. 2006). WASP has been carrying out a search for hot Jupiters orbiting bright ($m_V < 13$) stars all across the sky. Lendl et al. (2012) measured a mass of 0.38 M_J and a radius of 1.12 R_J for WASP-49b, which is orbiting a G6 V star every 2.78 days. Given its low density (0.27 ρ_J) and short orbital period, the planet possesses an extended atmosphere and is thus a favorable target for transmission spectroscopy.

We here present transit observations of WASP-49b, obtained with the FORS2 instrument installed at the VLT/UT1. Observations of three transits of WASP-49b were obtained in multi-object spectroscopy (MXU) mode, covering wavelengths from 0.7 μm to 1.02 μm. These data are supplemented by additional transit observations from the EulerCam (Lendl et al. 2012) and TRAPPIST (Gillon et al. 2011b; Jehin et al. 2011) instruments. In Sect. 2, we report details of the observations and the data reduction, and in Sect. 3 we describe the modeling process. The resulting transmission spectrum is shown and interpreted in Sect. 4, before we conclude in Sect. 5.

2. Observations and data reduction

2.1. FORS2 spectrophotometry

2.1.1. Observations

Three transits of WASP-49b were observed with FORS2 (Appenzeller et al. 1998) at the VLT/UT1 during the nights of 5 December 2012, 14 January 2013 and 7 February 2013, under program 090.C-0758. The instrument was used in MXU mode, which allows performing ($R \sim 1000$) multi-object spectroscopy with the help of laser-cut masks made specifically for the observed field. We used wide 10 by 28 arcsec (in one case 10 by 20 arcsec) slits to select WASP-49 and three reference stars, and used grism GRIS_600z for the dispersion together with order sorting filter OG590. The large slit widths are needed to avoid flux losses during variations in seeing or pointing. The resulting wavelength range is 738−1026 nm for WASP-49. The wavelength range of the reference stars is slightly different owing to their position on the detector and thus the displacement of the spectra on the chip. The positioning of the target and reference stars is shown in Fig. 1 and an example of the obtained spectra in Fig. 3. For the wavelength calibration we used a HeArNe lamp spectrum, but narrower (0.5 arcsec) slits were used to provide well-defined unsaturated emission lines to match with the database.

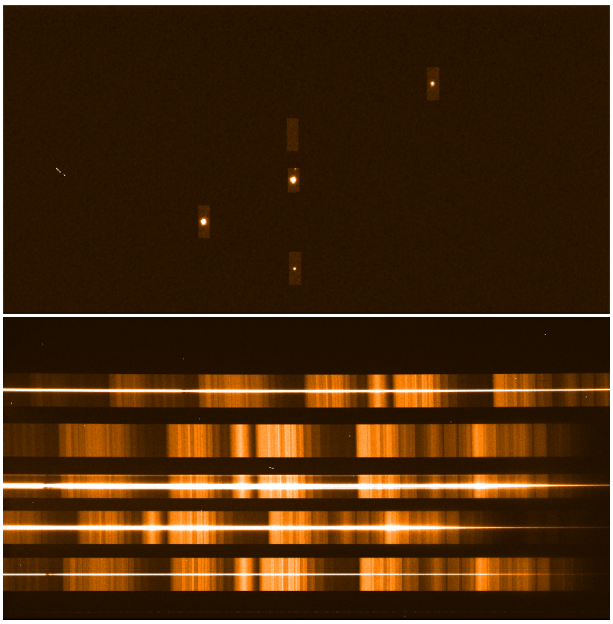

Fig. 1. *Top*: an acquisition image for the WASP-49 FORS2 observations. The mask with five slits is visible, four of the slits are placed on stars, one is placed on the sky. *Bottom*: the same field and instrument setup, but with the dispersive element in the optical path.

The linear atmospheric dispersion corrector (LADC) of FORS2 proved to impose a major limitation to the instrument's photometric performance (Moehler et al. 2010) throughout several years until its upgrade in 2014 (Sedaghati et al. 2015). The data treated here fall into this period. The LADC is composed of two prisms whose separation is changed with airmass to compensate for the image dispersion caused by the atmosphere. These prisms show structures of uneven transmission. As the LADC is located in the optical path above the image derotator, this creates structures that rotate across the field of view during long observing sequences. To reduce noise stemming from the LADC, the LADC prism separation was set to a constant value throughout each of our transit observations. For the first two nights this value was set by the previous instrument configuration, that is, 155.0 mm for 5 December 2012, and 898.1 mm for 14 January 2013. As we observed that the long-term correlated noise in the photometry was reduced for the smaller prism separation, we set the LADC to a minimum separation of 30 mm for our third (14 February 2013) observation.

The weather during the first two transits was good, with stable seeing around 0.9 arcsec on 5 December 2012 and seeing varying between 0.8 and 1.5 arcsec on 14 January 2013. The data obtained on 7 February 2013 were affected by variable and partially unfavorable seeing, between 1.0 and 2.5 arcsec. The exposure times used were 30 s and 25 s for the first observation,

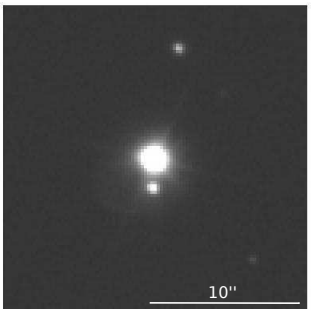

Fig. 2. WASP-49b and the nearby star, as seen in the pre-imaging with FORS2. North is up and east is left.

and 20 s for the other observations. The third observation was interrupted by a technical malfunction before the beginning of the transit.

During the pre-imaging of the target field, we discovered a faint star ($\Delta mag_z = 4.303 \pm 0.12$) located 2.3 arcsec south of WASP-49 (see Fig. 2). This star was blended with WASP-49 in previous observations.

2.1.2. Data reduction

The standard ESO pipeline was used to produce the master calibration frames, and to determine a wavelength solution in form of a third-order order polynomial based on the lamp frames. The wavelength solution was later refined by matching prominent absorption lines in the mean stellar spectra. To extract spectrophotometric measurements, we proceeded as follows. For each pixel, the PSF in the spatial direction was determined iteratively by fitting Moffat functions (Moffat 1969) using the `mpfit` routines (Markwardt 2009). Outliers (mostly cosmic ray hits) were rejected at this step and then replaced by the values of the PSF fit at this point. The sky background was individually measured for each spectral pixel by fitting a first-order polynomial in the spatial direction selecting only regions well outside the stellar PSF. The sky contribution was then removed by subtracting this fit from all spatial pixels. By assuming a varying sky value for each spectral pixel, we compensated for slight variations in the background that are due to bends in the spectra with respect to the CCD pixel grid.

The 1D spectra were extracted for each spectral pixel, by summing the flux in several windows of different widths centered on the PSF peak. At this point, data affected by saturation of the detector during the 5 December 2012 observation were identified and removed from further analysis. To measure the amount of contamination introduced by the nearby star, we subtracted the stellar PSF from the 2D spectrum of WASP-49 and then measured the contaminant's flux that fell inside each of the extraction windows. For a second estimate of the target to contaminant flux ratio, the PSF of the contaminant was fitted after the removal of the target PSF, and the peak values were compared. The resulting values averaged for all three transits and for each spectral bin are shown in Fig. 4. After we extracted the spectra of all exposures, we removed outliers once more, this time based on the temporal domain. For each spectral pixel, the extracted flux values were fit with a fourth-order polynomial with respect to time, outliers were identified and replaced by the values of the fit at the same position.

Next we binned the final spectra in 27 wavelength bins, 25 of which had a width of 10 nm, only the two longest-wavelength

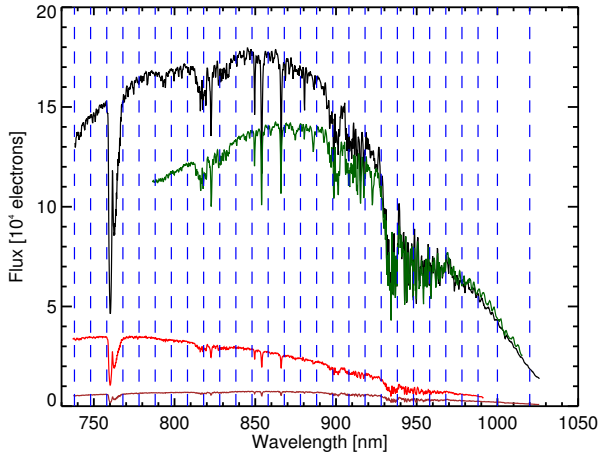

Fig. 3. Example of the spectra of WASP-49 (top, black), and the three reference stars (green, red, brown). The blue dashed lines indicate the bin sizes used for spectrophotometry. Note that only two faint reference stars are available for the five shortest-wavelength bins.

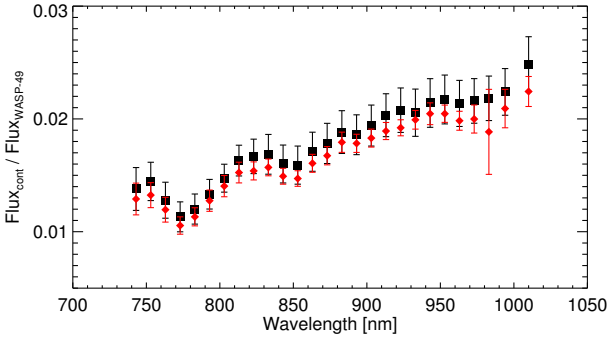

Fig. 4. Relative flux of the nearby star contaminating the WASP-49 spectra, shown as a function of wavelength. The red diamonds show the contamination estimated from photometry after subtracting the target PSF, and black squares denote the results from comparison of the fitted PSF peaks. The slope of the measurements indicates an object redder than WASP-49.

bins measured 12 nm and 20 nm. The location of these bins with respect to the spectra of target and reference stars is shown in Fig. 3. The five shortest-wavelength bins and the longest-wavelength bin are not covered by all reference stars. Relative photometric light curves were created for each extraction window from the binned spectra. All combinations of reference stars were tested; the best light curves were obtained using all references available in each wavelength bin.

For the further analysis, the light curves obtained from large extraction windows were used: 32 pixels for the transits on 5 December 2012 and 14 January 2013, and 36 pixels for the transit on 7 February 2013. This way, the contaminating star was contained in the aperture and its contribution to the light curve kept as stable as possible. The resulting light curves are displayed in Fig. 5.

2.1.3. FORS2 data of 5 December 2012

The FORS2 observations of 5 December 2012 were carried out throughout the transit using an exposure time of 30 s. The peak

A&A 587, A67 (2016)

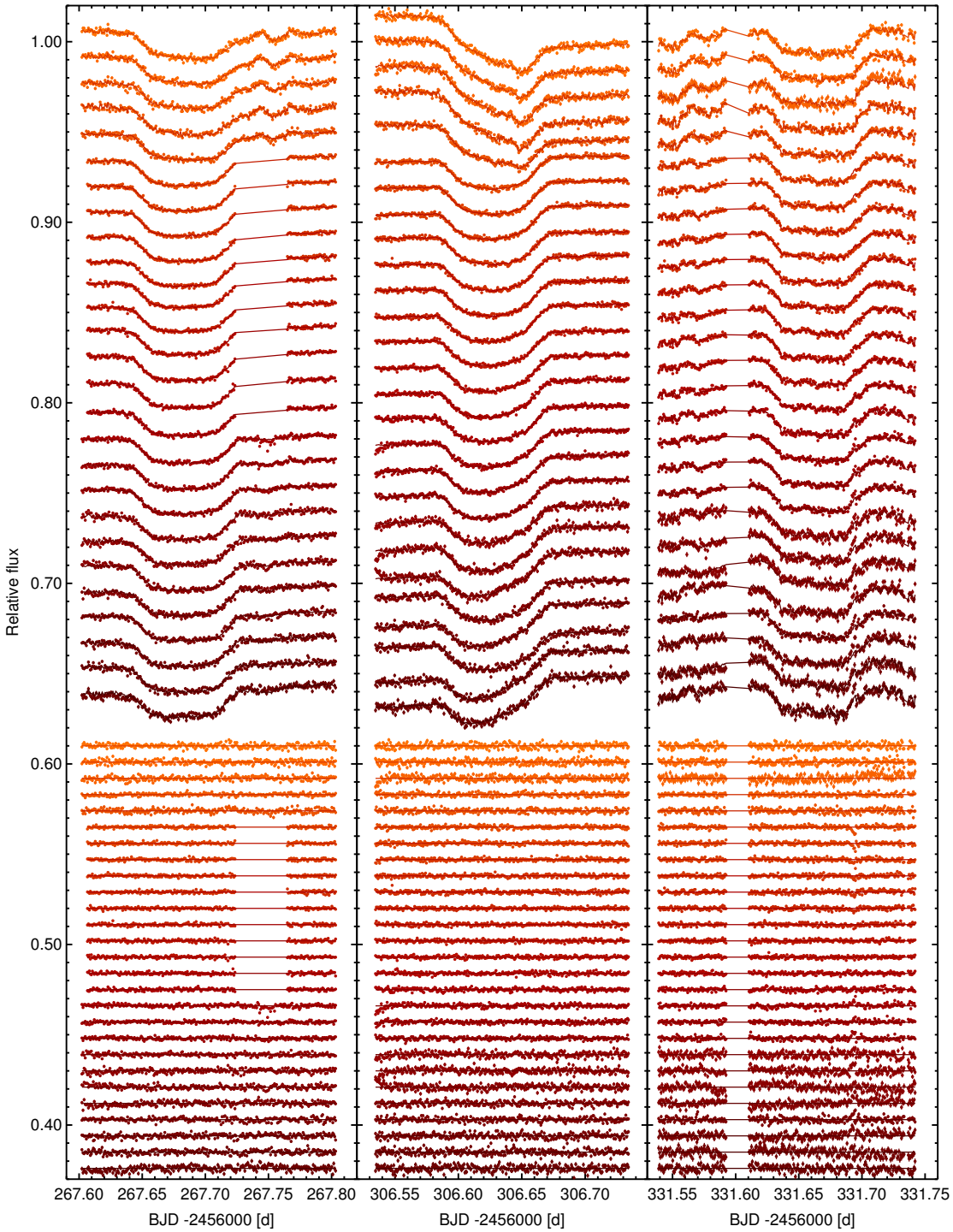

Fig. 5. Spectro-photometric FORS2 transit light curves of WASP-49. The wavelength of the individual light curves increases downward, and the bin centers are 743, 753, 763, 773, 783, 793, 803, 813, 823, 833, 843, 853, 863, 873, 883, 893, 903, 913, 923, 933, 943, 953, 963, 973, 983, 994, and 1010 nm. The residuals are shown below the data.

region of the target spectrum exceeded the nonlinear range of the detector from ~05:15 UT on, until the exposure time was adapted down to 25 s at 06:14 UT. Points affected by this episode of saturation were identified during the spectral extraction and removed from further analysis.

The $\lambda < 788$ nm light curves show a very particular wave-like pattern around meridian passage. These are the same light curves that were created using only two reference stars. This effect arises because the spatial inhomogeneities of the LADC

transparency creates differences in the light curves of the comparison stars.

2.1.4. FORS2 data of 14 January 2013

Again, the $\lambda < 788$ nm light curves obtained with FORS2 on 14 January 2013 show a wave-like pattern around meridian passage, probably for the same reason as for the 5 December 2012 data. At the same time, the overall light curve shapes are more strongly affected, with large-scale tilts that vary in shape and amplitude. This is probably related to the fact that the LADC separation was large for this observation, 898.1 mm as opposed to 155.0 mm for the 5 December 2012 observation.

2.1.5. FORS2 data of 7 February 2013

The FORS2 data taken on 7 February 2013 were affected by less favorable conditions, than the other transit observations, in particular, by bad seeing. The observations were interrupted because of a technical problem at 02:08 UT, but were resumed at 02:29 UT, ~20 min before the start of the transit. The data obtained before the interruption show large variations, related to unfavorable observing conditions and the passage of meridian and hence fast LADC movement. Some light curves show an unexplained short-term increase in flux during egress, which probably is of instrumental origin.

2.2. EulerCam and TRAPPIST photometry

Two additional transit light curves of WASP-49 were obtained using EulerCam at the 1.2 m Euler-Swiss telescope at the La Silla site (Chile). During the night of 5 December 2012 we observed through a wide (520 nm to 880 nm) filter designed for the upcoming *NGTS* survey (Wheatley et al. 2013), while during the night of 30 December 2012, an r'-Gunn filter was used. The telescope was slightly defocused for both observations, and exposure times were between 35s and 60s (December 5), and 90s (December 30). The data were reduced using relative aperture photometry. More details on instrument and reduction can be found in Lendl et al. (2012).

The TRAnsiting Planets and PlanetesImals Small Telescope (TRAPPIST, Gillon et al. 2011b; Jehin et al. 2011) is also located at the La Silla site. It was used to observe four more transits through an $I + z$' filter during the nights of 5, 16, and 30 December 2012, and 21 February 2013. The exposure times used were 6 s (first two transits) and 10 s (last two transits). The light curves were produced using relative aperture photometry, where several apertures were tested and the ideal combination of reference stars was found. IRAF[1] was used in the reduction process.

We also included in the analysis the two full transit light curves of each EulerCam and TRAPPIST that have been already described in Lendl et al. (2012). All broadband light curves are shown in Fig. 6.

[1] IRAF is distributed by the National Optical Astronomy Observatories, which are operated by the Association of Universities for Research in Astronomy, Inc., under cooperative agreement with the National Science Foundation.

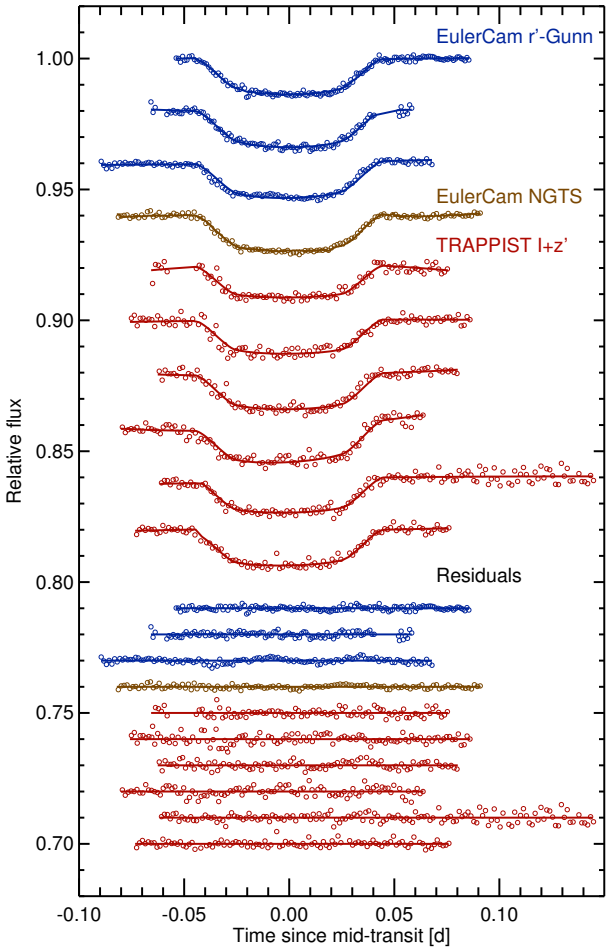

Fig. 6. WASP-49 transit light curves from EulerCam and TRAPPIST included in the analysis. The instrument and filters are color coded and are (from top to bottom) EulerCam using an r'-Gunn filter (top three), EulerCam using the *NGTS* filter (fourth), and TRAPPIST using an $I+z'$ filter (all remaining light curves). The TRAPPIST data are binned in two-minute intervals.

3. Modeling

3.1. Method

To derive the transmission spectrum of the planet and find improved measurements of the planetary and stellar parameters, a Markov chain Monte Carlo (MCMC) approach was used. Included in the analysis were all available photometric data as described in Sect. 2 (FORS2, EulerCam, and TRAPPIST).

We made use of a modified version of the adaptive MCMC code described in detail in Gillon et al. (2012). In this code, the prescription of Mandel & Agol (2002) is used to model the transit light curves. To compensate for correlated noise in the light curves, parametrizations of external variables (such as time, stellar FWHM, and coordinate shifts) can be included in the photometric baselines models. These models typically consist of polynomials up to fourth order that are multiplied with the theoretical transit light curve. Their coefficients are found by least-squares minimization at every MCMC step.

A&A 587, A67 (2016)

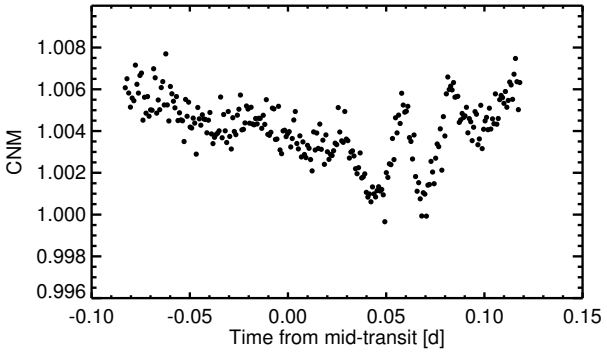

Fig. 7. Example of a CNM, calculated as described in Sect. 3.1.1. Here, the CNM of the $\lambda < 788$ nm data of 5 December 2012 is shown.

3.1.1. Common noise model

In this updated version of the code, it is possible to also include a common noise model (CNM) for a set of light curves carrying the same correlated noise structure. This CNM is created at each MCMC step by fitting a model transit light curve based on the current parameter state together with an invariable, previously determined, normal distribution for the transit depth with a center $\mathrm{d}F_{\mathrm{group}}$, and then co-adding the residuals of this fit. For each time step t_i, the CNM is calculated as

$$CNM_i = \sum_{k=0}^{n_{\mathrm{lc}}} \left(\frac{O_{i,k}}{C_{i,k}} w_{i,k}^{-1} \right), \quad (1)$$

where n_{lc} is the total number of light curves the CNM is calculated for, O_i are the observed data, and C_i are the transit model values. Weights $w_{i,k}$ are attributed according to measurement errors $err_{i,k}$,

$$w_{i,k} = err_{i,k}^2 \sum_{k=0}^{n_{\mathrm{lc}}} \frac{1}{err_{i,k}^2}. \quad (2)$$

See Fig. 7 for an example of a CNM obtained from FORS2 data. This approach is similar to the use of the white light curves for the definition of the correlated noise component by Stevenson et al. (2014) and others.

3.1.2. Fitted and fixed parameters

In the analysis of our combined photometric dataset, the following variables were MCMC fitted ("jump") parameters:

- the impact parameter $b' = a\cos(i_{\mathrm{p}})/R_*$, where R_* denotes the stellar radius, a the semi-major axis of the planetary orbit, and i_{p} the orbital inclination;
- the transit duration T_{14};
- the time of mid-transit T_0;
- the orbital period P;
- the stellar parameters effective temperature T_{eff} and metallicity [Fe/H];
- if desired (as for the test in Sect. 3.2.4), the linear combination of the quadratic limb-darkening coefficients (u_1, u_2) in each wavelength band, $c_{1,i} = 2u_{1,i} + u_{2,i}$ and $c_{2,i} = u_{1,i} - 2u_{2,i}$ (Holman et al. 2006);
- if a single value of the transit depth is desired (step 1 in our analysis), $\mathrm{d}F_0 = (R_{\mathrm{p}}/R_*)^2$ is included as a jump parameter;
- if a transmission spectrum is fit (i.e. several values of $\mathrm{d}F$, step 2 in our analysis), offsets $\mathrm{dd}F_i$ to a pre-defined value for $\mathrm{d}F_0$;
- if a CNM is included, an a priori estimate of the transit depth of each group, $\mathrm{d}F_{\mathrm{group}}$.

Table 1. Limb-darkening coefficients used in the analysis of the photometric data.

Wavelength [nm]	u_1	u_2
738−748	0.318	0.275
748−758	0.315	0.273
758−768	0.311	0.272
768−778	0.309	0.27
778−788	0.306	0.268
788−798	0.303	0.267
798−808	0.3	0.265
808−818	0.298	0.264
818−828	0.295	0.262
828−838	0.292	0.261
838−848	0.289	0.26
848−858	0.286	0.259
858−868	0.282	0.258
868−878	0.279	0.258
878−888	0.275	0.257
888−898	0.27	0.258
898−908	0.265	0.258
908−918	0.259	0.259
918−928	0.253	0.26
928−938	0.247	0.261
938−948	0.239	0.263
948−958	0.231	0.266
958−968	0.222	0.269
968−978	0.213	0.272
978−988	0.202	0.276
988−1000	0.189	0.281
1000−1020	0.169	0.29
r'	0.28	0.26
NGTS	0.34	0.28
I + *z'*	0.29	0.26

The value for the RV amplitude was set to that of the discovery paper. The eccentricity was set to zero as there has been no evidence for an eccentric orbit of WASP-49b. A quadratic model of the form $I(\mu) = I_{\mathrm{center}}(1 - u_1(1-\mu) - u_2(1-\mu)^2)$ (where $\mu = \cos\theta$ and θ is the angle between the surface normal of the star and the line of sight) was used to account for the effect of stellar limb-darkening on the transit light curves. The coefficients u_1 and u_2 were found by interpolating the tables of Claret & Bloemen (2011) to match the wavelength bands of our observations. The limb-darkening parameters were kept fixed to the values given in Table 1 throughout our analysis, but we verified our results by allowing for variable limb-darkening coefficients as described in Sect. 3.2.4.

Uniform prior distributions were assumed for most parameters, but for the stellar effective temperature T_{eff} and metallicity [Fe/H], normal prior distributions were used. These priors were centered on the values of Lendl et al. (2012) and their widths were defined as the 1σ errors of these values. If transmission spectra were derived, a normal prior was applied to $\mathrm{d}F_0$, with a width of the 1σ errors of the used input value. We used the method described in Enoch et al. (2010) and Gillon et al. (2011a) to derive the stellar radius and mass from the transit light curve, stellar temperature and metallicity. The contribution (and its error) from the neighboring star was included in the analysis and the transit depths were adapted. At each instance, two MCMC

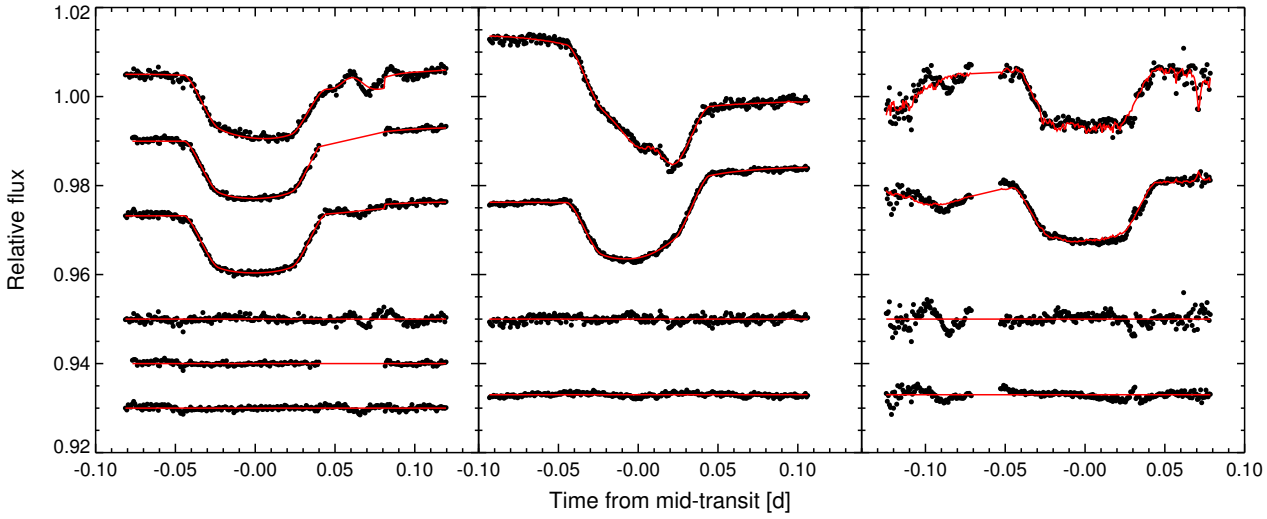

Fig. 8. FORS2 spectrophotometry and residuals obtained from using a single bin for each light curve subset, as described in Sect. 3.2.1. The three subsets of 5 December 2012 are shown in the *left panel* and correspond to wavelength ranges of (from top to bottom) 738−788, 788−898, and 898−1020 nm. *The middle and right panels* show the two subsets of 14 January 2013 and 7 February 2013, respectively, and correspond to wavelength ranges of (from top to bottom) 738−788, and 788−1020 nm. The models are shown as red solid lines and contain the parametrizations of external parameters as described in Table 2. The residuals are shown below the data which are partially offset for clarity.

chains were run and convergence of the MCMC chains was checked for all results with the Gelman & Rubin test (Gelman & Rubin 1992).

3.1.3. Photometric error adaptation

The photometric error bars were rescaled by calculating the white β_w and red β_r noise scale factors. β_w is given by the ratio of the mean photometric error and the standard deviation of the final photometric residuals, and β_r (Winn et al. 2008; Gillon et al. 2010) is derived by comparing the standard deviations of the binned and unbinned residuals. We multiplied our errors with their product $CF = \beta_r \times \beta_w$ derived from an initial MCMC run of 10^4 points. The CF values are given in Table A.1.

3.1.4. Baseline models for the FORS2 data

The FORS2 data are affected by the rotation of the LADC with respect to the detector and therefore show a strong noise component correlated with the parallactic angle. For these light curves, we tested baseline models involving the parallactic angle *par*, the change in parallactic angle d*par* (i.e., the derotator speed), and the trigonometric functions sin(*par*) and cos(*par*). Including the parallactic angle in baseline models for the FORS2 data leads to a much better fit of the overall light curve shapes than time-dependent models. Similarly, including the CNM in the photometric baseline produces very good fits to the data, efficiently accounting for short-term photometric variations that consistently appear in sets of light curves, but cannot be modeled as simple dependencies on external parameters.

3.2. Step-by-step procedure

We carried out the analysis with the aim to first infer the most reliable analysis method for the FORS2 data, and then applied it to obtain an accurate transmission spectrum for WASP-49b. To do so, we proceeded in the steps outlined below.

3.2.1. Step 1: An overall transit depth

We first identified the light curves that are affected by the same photometric variations and hence should form the subsets possessing the same CNM. For all three dates, a clear division is seen between the light curves obtained with two reference stars (the five shortest-wavelength bins, as well as the light curve centered on the *K* feature), and all other light curves. This is a clear consequence of the LADC being at the root of the strongest correlated noise source, as spatially varying transmission affects each reference star differently. For the data of 5 December 2012, we further subdivided the remaining light curves into two groups, light curves between 788 and 898 nm, which have fewer points because of detector saturation, and the light curves at wavelengths above 898 nm, where counts remained in the linear detector range.

For each subset, we combined all data to produce a "white" light curve. We then tested a number of photometric baseline models for these white light curves, finding the best modeling of these curves by accounting for large trends by means of second-order polynomials in *par* and modeling the short-timescale variations in the $\lambda < 788$ nm light curves using fourth-order polynomials in cos(*par*) or d*par*, or a first-order polynomial in the stellar FWHM. These baseline functions are listed in Table 2. For the 5 December 2012 data, an offset is included at the change of exposure time. We then performed a combined MCMC analysis on all white light curves, allowing for a single transit depth. The result obtained is our best absolute transit depth dF_0, which was then used to calculate the transmission spectrum. These light curves are shown in Fig. 8. We find a resulting value for the transit depth of $dF_0 = 0.0133 \pm 0.0002$.

3.2.2. Step 2: Individual transmission spectra

We then derived individual transmission spectra for each date. Keeping an a priory transit depth fixed to the previously obtained dF_0, we inferred offsets ddF_i from this value for each light curve. At this point, we searched for the best baseline models for each

A&A 587, A67 (2016)

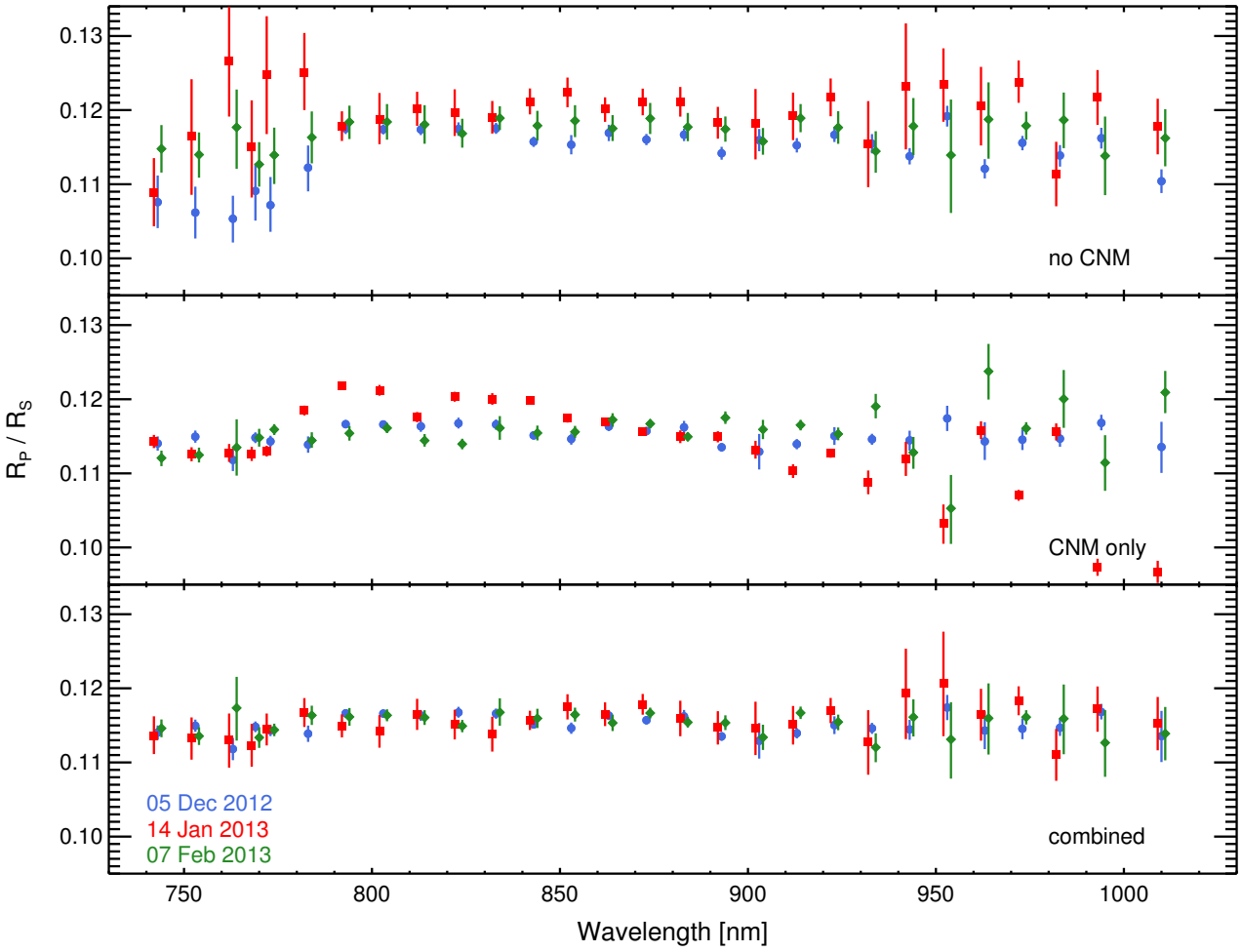

Fig. 9. FORS2 transmission spectra of the three dates obtained with three baseline modeling approaches: no CNM, but parametrizations of external parameters as given in Sect. 3.2.2 (*top*), CNM alone (*middle*), and CNM together with basic parametrizations as detailed in Sect. 3.2.2 (*bottom*). Blue filled circles denote the FORS2 transmission spectrum of 5 December 2012, red squares that of 14 January 2013, and green diamonds that of 7 February 2013. In this plot, the spectra of 14 January 2013 and 7 February 2013 are offset from their nominal wavelengths by 1 nm to avoid overlaps.

previously defined light curve set, testing three approaches, that relied to various degrees on the CNM.

1. *No CNM:* the photometric baselines consist solely of functions of external parameters, that is, *par*, cos(*par*), d*par*, and FWHM. These functions, and the wavelength range for light curves to which they are applied, are the same as inferred in Sect. 3.2.1 and listed in Table 2.
2. *CNM only:* no parametrizations of external variables are used, except for the offset at the exposure time change for the 5 December 2012 data. All light curves are fit with a first-order polynomial of the CNM (i.e., a function of the form $a_0 + a_1$ *CNM*) only. As mentioned in Sect. 3.1.1, the CNMs are calculated based on an input distribution for the transit depth. We used a Gaussian centered on the previously obtained dF_0, with a width of the 1σ error bars on dF_0. Higher-order polynomials with respect to the CNM were tested but did not improve the results.
3. *Combined:* the photometric baseline functions include the CNM and low-order polynomials of external parameters. The best baseline models were found to consist of first-order polynomials of the CNM, together with second-order polynomials of *par* (January and February data).

Table 2. Baseline functions used in step 1 of our analysis, where a single transit depth is inferred from the binned data of all light curve subsets.

Wavelength [nm]	Date	Baseline function
738–788	05 Dec. 2012	$p^4(\cos(par)) + off$
788–898	05 Dec. 2012	$p^2(par) + off$
898–1020	05 Dec. 2012	$p^2(par) + off$
738–788	14 Jan. 2013	$p^2(par) + p^4(\mathrm{d}par)$
738–1020	14 Jan. 2013	$p^2(par)$
738–788	07 Feb. 2013	$p^1(fwhm) + p^2(par)$
738–1020	07 Feb. 2012	$p^1(fwhm) + p^2(par)$

Notes. The baseline functions of the form $p^j(i)$ denote a polynomial of order j in parameter i, where i can be the parallactic angle *par*, its cosine cos(*par*), the differential parallactic angle from one exposure to the next d*par*, and the PSF or spectral full-width at half maximum *fwhm*. *off* refers to an offset included at the change in exposure time for the 5 December 2012 observations.

The resulting transmission spectra are shown in Fig. 9: the results obtained without CNM (top panel) show larger error bars than the other modeling approaches, while the data are noisier at low wavelengths and show overall offsets between the three dates, most remarkably a median offset of 0.005 in R_p/R_* between the data of 6 December 2012 and 14 January 2013. The transmission spectra inferred from CNM-only models (middle panel) have greatly reduced error bars, but the spectra inferred from the three dates do not agree, with substantial scatter at long wavelengths. The 14 January 2013 data show a distinct slope between 790 and 900 nm, a structure not reproduced for the other dates. The best agreement between the spectra from the three dates is found if the CNM and low-order parametrizations of external parameters are used together (third panel), and we used this approach to derive of our final transmission spectrum.

3.2.3. Step 3: A combined transmission spectrum

The final transmission spectrum was inferred from a global analysis of all available photometric data: the three FORS2 observations, and all available additional EulerCam and TRAPPIST broadband photometry. As the latter are light curves obtained with different instruments at different dates, CNMs cannot be applied to these data. The light curves are displayed in Fig. 6 (broadband), and Fig. 5, and the respective baseline functions are given in Table A.1. For the analysis of the FORS2 data, we chose the third option outlined above: using CNMs together with functions of *par* (and an offset at the change of exposure time in the 5 December 2012 data). The light curve subsets contributing to each CNM are the seven subsets defined above (three for the 5 December 2012 data, and two each for the 14 January 2013 and 7 February 2013 data). The analysis consisted of two MCMC chains of 10^5 points each, allowing only for unique values of the transit depths for each wavelength bin. The resulting transmission spectrum is shown in Fig. 11.

3.2.4. Stellar limb-darkening

As stellar limb-darkening affects the transit shape, we decided to verify our transmission spectrum against variation in the limb-darkening coefficients. To do so, we carried out additional global analyses (identical to those described in Sect. 3.2.3), while allowing the limb-darkening coefficients to vary, assuming a normal prior distribution for them. This prior was centered on the interpolated value and had a width large enough to encompass the values of the neighboring passbands at 1σ. The results are consistent with our previously derived transmission spectrum: when a prior is included, the maximum offset between the two runs is 0.14σ and the transmission spectra uncertainties are similar.

4. Results

4.1. Individual transits

From the analysis of three sets of FORS2 data, we obtained a set of independently derived transmission spectra of Wasp-49b between 730 and 1020 nm.

To evaluate the reliability of the derived spectra, we tested three approaches for modeling systematic noise: the exclusive use of analytic functions of external variables, the exclusive use of a CNM constructed from white light curve residuals, and their combination (see Sect. 3.2.2 for details). We found that the noise

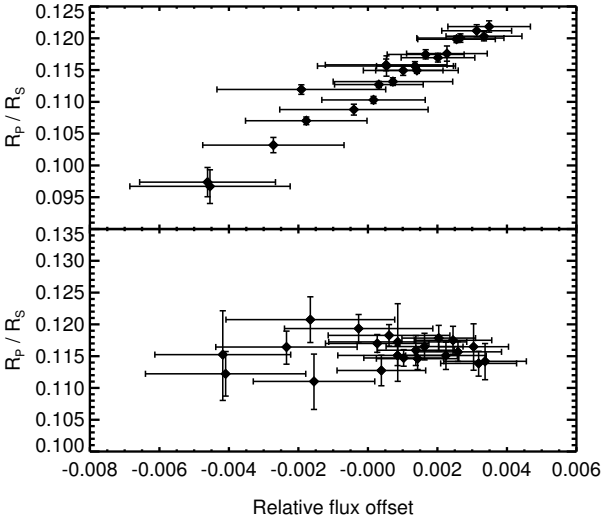

Fig. 10. R_p/R_* values inferred from the CNM-only analysis (*top*) and the combined analysis (*bottom*) of the $\lambda > 788$ nm light curves of 14 January 2013 against the trend amplitude (pre-transit − post-transit flux). A highly significant correlation ($p = 0.97$) is easily visible in the *upper panel* but is lacking in the *lower panel*.

structures introduced by the LADC inhomogeneities can be approximated by a combination of analytic functions of the parallactic angle, but not perfectly so because this approach lacks accuracy in describing the real signal induced by irregular "spots" on the LADC surfaces. This is reflected by the fact that this approach yields the worst fit to the transit light curves, with residual rms values of 734, 784, and 1132 ppm for the three dates, and large uncertainties on the derived transmission spectra. In addition, transmission spectra from different dates show different mean levels, and light curves requiring complicated baseline models (the $\lambda < 788$ nm light curves for 5 December 2012 and 14 January 2013) are offset from the rest of the spectra of each date (top panel in Fig. 9). Our second approach, calculating the white photometric residuals for each subset of light curves showing similar noise structures, provides a better fit to the data with residual rms values of 635, 697, and 862 ppm, which models the short-timescale structures very well. The resulting transmission spectra show drastically reduced error bars, 85, 25, and 50% of those from the no-CNM analysis for 5 December 2012, 14 January 2013 and 7 February 2013, respectively. However, at the same time the spectra from the three dates disagree substantially, and the 14 January 2013 data show a large trend in the transmission spectrum that is not reproduced in the other data sets. This trend is most likely a result of sub-optimal modeling of large-scale trends across the light curves, because their amplitudes are chromatic, increasing for longer wavelengths. A comparison of the trend amplitude (calculated through the overall pre- and post-transit flux offset) with the inferred transmission spectrum shows a very clear (Pearson coefficient of 0.97) correlation for the $\lambda > 788$ nm light curves (Fig. 10). Finally, we obtained consistent results from all three transits by using a combination of both methods: using low-order polynomials to model trends, and the CNM to account for short-timescale variations. Here, the correlation between the slope amplitude and the transmission spectrum of 14 January 2013 is removed ($p = -0.009$). This approach also yields the best residual rms values of 635, 697, and 862 ppm. Based on this fact and on the excellent

A&A 587, A67 (2016)

Table 3. Median values and the 1σ errors of the marginalized posterior PDF obtained from the global MCMC analysis.

Jump parameters	
Stellar metallicity, [Fe/H] [dex]	-0.23 ± 0.072
Stellar effective temp., $T_{\rm eff}$ [K]	5602 ± 160
Transit depth, dF	0.01345 ± 0.00017
Impact parameter, b' [R_*]	$0.7704^{+0.0072}_{-0.0077}$
Transit duration, T_{14} [d]	0.08918 ± 0.00062
Time of midtransit, T_0 [BJD$_{\rm tdb}$]	6267.68389 ± 0.00013
Period, P [d]	$2.7817362 \pm 1.4 \times 10^{-6}$
Deduced stellar parameters	
Surface gravity, $\log g$ [cgs]	4.406 ± 0.019
Mean density, ρ_* [$\rho_\odot$]	$0.8934^{+0.039}_{-0.036}$
Mass, M_* [$M_\odot$]	1.003 ± 0.10
Radius, R_* [$R_\odot$]	$1.038^{+0.038}_{-0.036}$
Deduced planet parameters	
Mass, $M_{\rm p}$ [M_J]	0.396 ± 0.026
Radius, $R_{\rm p}$ [R_J]	$1.198^{+0.047}_{-0.045}$
Semi-major axis, a [au]	0.03873 ± 0.0013
Orbital inclination, $i_{\rm p}$ [deg]	84.48 ± 0.13
Density, $\rho_{\rm p}$ [ρ_J]	0.229 ± 0.016
Surface gravity, $\log g_{\rm p}$ [cgs]	2.853 ± 0.016
Equilibrium temp.[a] , $T_{\rm eq}$ [K]	1399^{+39}_{-43}
Fixed parameters	
Eccentricity, e	0
RV amplitude, K [m s^{-1}]	56.8 ± 2.44

Notes. [(a)] Assuming an albedo of $A = 0$ and full redistribution from the planet's day to night side, $F = 1$ (Seager et al. 2005).

agreement of the three dates (average (maximal) disagreement of two measurements at the same wavelength is 0.5 (1.8)σ), we find the combined approach to be reliable.

4.2. Updated system parameters

We performed joint MCMC analyses of all available data to redetermine the system parameters taking into account the dilution of the target flux from the nearby source. This was done by performing a global analysis using the white FORS2 light curves (as in Sect. 3.2.1, together with the broadband data available). The refined parameters are listed in Table 3 and agree very well (below 1σ for all but $\rho_{\rm p}$, which differs by 1.2σ) with those published in Lendl et al. (2012). As a result of the correction for contamination from the newly resolved companion, we find a slightly larger the planetary radius ($1.198^{+0.047}_{-0.045}$ R_J instead of 1.115 ± 0.047 R_J) and a lower density (0.229 ± 0.016 ρ_J instead of $0.273^{+0.030}_{-0.026}$ ρ_J).

4.3. Transmission spectrum of WASP-49b

We performed a combined analysis of all FORS2 spectrophotometric light curves together with the broadband data as described in Sect. 3.2.3. The resulting transmission spectrum of WASP-49b is given in Table 4 and shown in Fig. 11.

To interpret the data, we used physically plausible models of transmission spectra of the planetary atmosphere. We modeled the transmission spectrum of WASP-49b using the exoplanetary atmospheric modeling method of Madhusudhan & Seager (2009) and Madhusudhan (2012). We considered a plane-parallel atmosphere at the day-night terminator region that is probed by the transmission spectrum and computed line-by-line radiative transfer under the assumption of hydrostatic equilibrium for an assumed temperature structure and chemical composition. Our plane-parallel atmosphere is composed of 100 layers, in the pressure range of 10^{-6}–100 bar. We computed the net absorption of the stellar light caused by the planetary atmosphere as the star light traverses a chord at the day-night terminator region of the spherical planet, appropriately integrated over the annulus.

The model atmosphere includes the major sources of opacity expected in hot hydrogen-dominated atmospheres, namely, absorption due to alkali metals (Na and K) and prominent molecules (H_2O, CO, CH_4, CO_2, C_2H_2, HCN, TiO), and H_2-H_2 collision-induced absorption (CIA) along with gaseous Rayleigh scattering. The volume mixing ratios of these various species were chosen assuming chemical equilibrium for different C/O ratios, such as solar abundance (C/O = 0.5; i.e., oxygen-rich) or carbon-rich (C/O = 1.0; see Madhusudhan et al. 2011), but we also explored chemical disequilibrium solutions if necessitated by the data. In the spectral range of interest to the current study (i.e., 0.65–1.02 μm), the dominant sources of opacity are Na, K, H_2O, and TiO. The Na and K abundances are insensitive to the C/O ratio. However, while H_2O and TiO are abundant in a

Table 4. Transmission spectrum of WASP-49b as found by the combined analysis of all FORS2, EulerCam, and TRAPPIST data.

Wavelength [nm]	$R_{\rm p}/R_*$
738–748	0.1144 ± 0.00072
748–758	$0.1146^{+0.00068}_{-0.00063}$
758–768	0.1124 ± 0.0013
765–773 (K)	$0.1151^{+0.00054}_{-0.00052}$
768–778	$0.1153^{+0.00077}_{-0.00075}$
778–788	0.1149 ± 0.00062
788–798	$0.1163^{+0.00046}_{-0.00048}$
798–808	0.1166 ± 0.00043
808–818	$0.1163^{+0.00058}_{-0.00055}$
818–828	0.1160 ± 0.00052
828–838	0.1164 ± 0.00063
838–848	0.1154 ± 0.00044
848–858	0.1157 ± 0.00056
858–868	$0.1162^{+0.00047}_{-0.00049}$
868–878	$0.1165^{+0.00041}_{-0.00043}$
878–888	0.1161 ± 0.00051
888–898	0.1143 ± 0.00048
898–908	0.1138 ± 0.0012
908–918	0.1153 ± 0.00051
918–928	0.1158 ± 0.00068
928–938	0.1146 ± 0.00067
938–948	0.1150 ± 0.0011
948–958	0.1169 ± 0.0016
958–968	0.1152 ± 0.0018
968–978	0.1162 ± 0.00070
978–988	0.1147 ± 0.0010
988–1000	0.1168 ± 0.00096
1000–1020	0.1150 ± 0.0021
611–717[a]	0.1163 ± 0.0017
516–880[b]	0.1190 ± 0.0014
751–953[c]	0.1138 ± 0.0014

Notes. [(a)] *r′-Gunn* filter , [(b)] *NGTS* filter , [(c)] *Ic+z′-Gunn* filter .

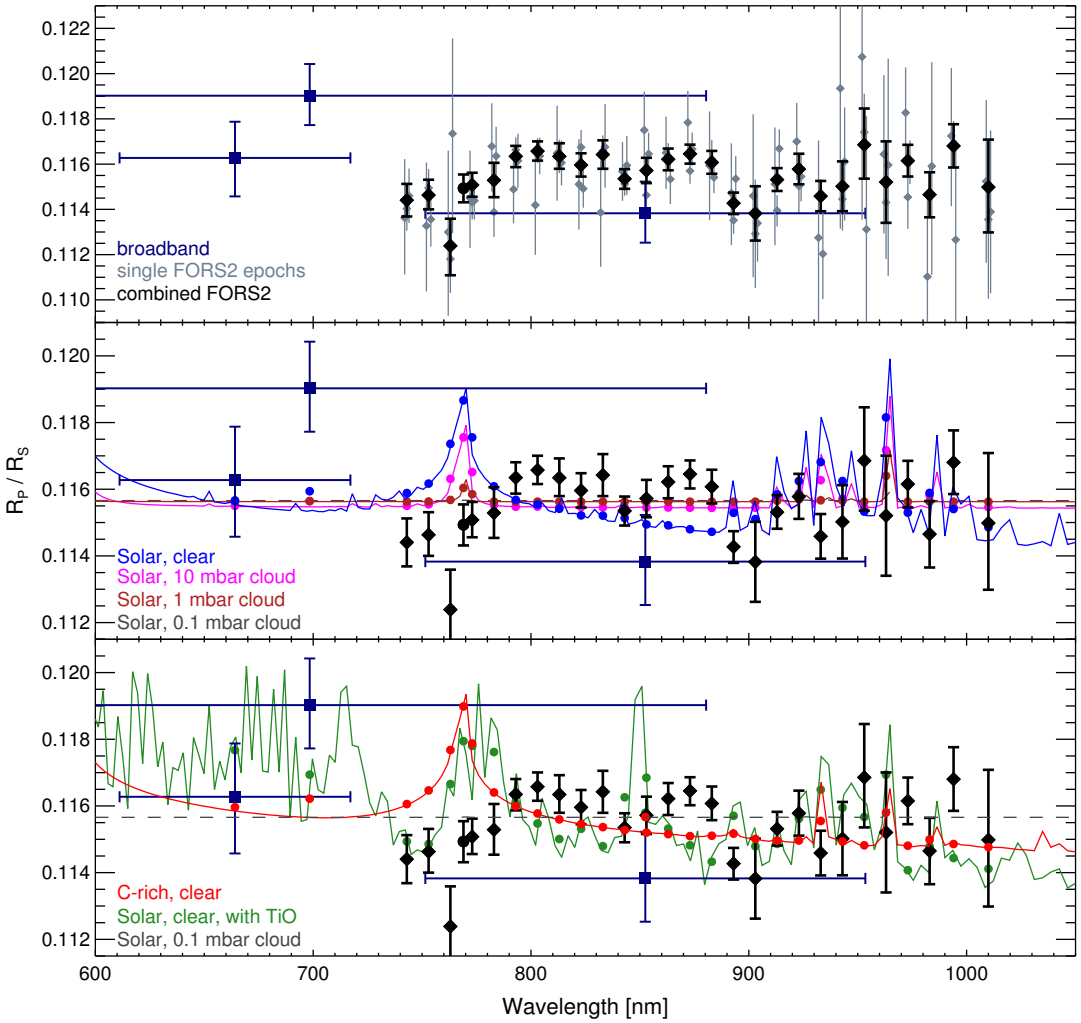

Fig. 11. Transmission spectrum of WASP-49b as observed with FORS2, EulerCam and TRAPPIST compared to atmospheric models. *Top*: the FORS2 results of each separate data set are shown in gray and the results from the combined analysis are shown as black diamonds. The filled circle represents the data point centered on the *K* feature, and the results from broadband light curves are shown as dark blue squares. *Center and bottom*: the above transmission spectrum including the combined FORS2 and broadband data, together with predictions from atmosphere models. The model atmospheres are a clear solar-composition atmosphere (*center panel*, blue), a solar-composition atmosphere with a cloud deck at 10 mbar pressure (*central panel*, magenta), a solar-composition atmosphere with a cloud deck at 1 mbar pressure (*central panel*, dark red), a clear C-rich atmosphere (*bottom panel*, red), and a clear solar-composition atmosphere with TiO (*bottom panel*, green). A flat spectrum obtained from a solar-composition atmosphere with a cloud deck at 0.1 mbar pressure is shown as a gray dashed line in the middle and bottom panels. The filled circles show the models binned to the observed spectral resolution.

solar-composition atmosphere, they are depleted by over ~100x for C/O = 1 (Madhusudhan 2012). On the other hand, we also considered models with an opaque achromatic cloud layer that effectively obstructs all the spectral features up to a prescribed cloud altitude; with very high-altitude clouds leading to a featureless flat spectrum.

We explored the following fiducial model atmospheres with different chemical compositions to compare with our observed spectra:

- a clear solar-composition atmosphere, without TiO;
- a clear solar-composition atmosphere, with TiO;
- a clear carbon-rich atmosphere (C/O = 1);
- solar-composition atmospheres, without TiO, but with cloud decks at a pressure levels of 0.1, 1, and 10 mbar, respectively.

The fits of these models to the observed transmission spectrum are shown in Fig. 11. At our spectral resolution, the model with a cloud deck at 0.1 mbar is essentially identical with a horizontal straight line as the clouds obscure all features. For completeness we also compare our data to a constant R_p/R_* value. We compared these models to our data, while compensating for an overall vertical offset between the calculated and observed values. The χ^2 values of the available models considering the entire dataset, the FORS2 dataset alone, or the FORS2 data at $\lambda > 788$ nm alone, are listed in Table 5.

When considering all available data points, the best fit is obtained by the featureless model of a cloud deck at 0.1 mbar pressure, with $\chi^2 = 57.7$. This is nearly identical to the χ^2 of a constant R_p/R_* value ($\chi^2 = 57.6$), from which a reduced χ^2

A&A 587, A67 (2016)

Table 5. χ^2 values calculated from the data and the various atmosphere models for WASP-49b.

Model	All	FORS2	FORS2, $\lambda > 788$ nm
χ^2 values			
Carbon-rich	158.5	152.3	30.5
Solar (no TiO)	169.8	162.4	63.6
Solar (with TiO)	173.2	167.9	84.4
Solar (10 mbar cloud)	95.8	87.4	42.4
Solar (1 mbar cloud)	61.5	53.2	33.3
Solar (0.1 mbar cloud)	57.7	49.5	32.4
Constant	57.6	49.3	32.4
$\chi^2_{\rm red}$ values			
Constant	1.86	1.83	1.54

of $\chi^2_{\rm red} = 1.86$ is readily calculated, indicating a reasonable fit to the given data. A model with a cloud deck at 1 mbar altitude provides a comparably good fit ($\chi^2 = 61.5$), but more complex spectra can be excluded. Similar results are obtained if only the FORS2 points are considered, again a cloud decks above 1 mbar produce the best fits to the data. As the largest mismatch between observations and models stems from the wavelength region surrounding the *K* feature, and because this region is most affected by strong correlated noise in the light curves, we also tested the FORS2 data at wavelengths above 788 nm against the models. We again obtained a good fit for a spectrum with high-altitude clouds ($\chi^2 = 32.4$, $\chi^2_{\rm red} = 1.54$), but the carbon-rich model produces a comparably good fit to the data ($\chi^2 = 30.5$) that is due to its slight slope toward longer wavelengths. A carbon-rich atmosphere would thus still be a possibility if the error bars on our short-wavelength measurements are underestimated.

5. Conclusions

We have obtained a transmission spectrum of WASP-49b based on VLT/FORS2 observations of three planetary transits. The FORS2 data are affected by considerable systematic noise due to LADC inhomogeneities, but this noise is limited for observations where the LADC prism separation was set to a minimum and kept constant throughout the observation. We found consistent results from all three dates only when we applied a common noise model for light curve sets showing similar correlated noise together with low-order polynomial baselines to model each light curve's large-scale trends individually. We therefore warn against the "blind" use of white light curve residuals alone to model spectrophotometric light curves that are affected with substantial correlated noise.

Using these data, we also updated the system parameters by taking contamination from a newly discovered nearby star into account. Our data agree with the previously published values while favoring a slightly larger planetary radius ($1.198^{+0.047}_{-0.045}\ R_J$ instead of $1.115 \pm 0.047\ R_J$) and hence a lower planetary bulk density ($0.229 \pm 0.016\ \rho_J$ instead of $0.273^{+0.030}_{-0.026}\ \rho_J$). The transmission spectra we obtain from the three epochs agree well with each other, demonstrating the instrumental stability and usefulness of FORS2 for high-precision spectrophotometry even in the presence of LADC-induced correlated noise.

We found that the transmision spectrum of WASP-49b is best fit by models with muted spectral features, such as expected in the presence of opaque high-altitude clouds or hazes. A carbon-rich atmosphere provides a comparable fit only when data at $\lambda < 788$ nm are removed from the analysis. Solar-composition atmospheres, both with and without TiO are a poor match to the data. We conclude that WASP-49b most likely has clouds or hazes at pressure levels of 1 mbar or less.

Acknowledgements. We would like to thank our referee, Drake Deming, for insightful comments that improved the quality of this manuscript, and Amaury Triaud for helpful scientific discussions. This work was supported by the European Research Council through the European Union's Seventh Framework Programme (FP7/2007−2013)/ERC grant agreement number 336480. TRAPPIST is funded by the Belgian Fund for Scientific Research (Fond National de la Recherche Scientifique, FNRS) under the grant FRFC 2.5.594.09.F, with the participation of the Swiss National Science Fundation (SNF). L. Delrez acknowledges the support of the F.R.I.A. fund of the FNRS. M. Gillon and E. Jehin are FNRS Research Associates.

References

Appenzeller, I., Fricke, K., Fürtig, W., et al. 1998, The Messenger, 94, 1
Barman, T. 2007, ApJ, 661, L191
Bean, J. L., Miller-Ricci Kempton, E., & Homeier, D. 2010, Nature, 468, 669
Bean, J. L., Désert, J.-M., Kabath, P., et al. 2011, ApJ, 743, 92
Bean, J. L., Désert, J.-M., Seifahrt, A., et al. 2013, ApJ, 771, 108
Charbonneau, D., Brown, T. M., Noyes, R. W., & Gilliland, R. L. 2002, ApJ, 568, 377
Claret, A., & Bloemen, S. 2011, A&A, 529, A75
Crouzet, N., McCullough, P. R., Burke, C., & Long, D. 2012, ApJ, 761, 7
Deming, D., Wilkins, A., McCullough, P., et al. 2013, ApJ, 774, 95
Désert, J.-M., Vidal-Madjar, A., Lecavelier Des Etangs, A., et al. 2008, A&A, 492, 585
Enoch, B., Collier Cameron, A., Parley, N. R., & Hebb, L. 2010, A&A, 516, A33
Gelman, A., & Rubin, D. 1992, Statist. Sci., 7, 457
Gibson, N. P., Pont, F., & Aigrain, S. 2011, MNRAS, 411, 2199
Gibson, N. P., Aigrain, S., Barstow, J. K., et al. 2013, MNRAS, 428, 3680
Gillon, M., Doyle, A. P., Lendl, M., et al. 2011a, A&A, 533, A88
Gillon, M., Jehin, E., Magain, P., et al. 2011b, Detection and Dynamics of Transiting Exoplanets, St. Michel l'Observatoire, France, eds. F. Bouchy, R. Díaz, & C. Moutou, EPJ Web Conf., 11, 6002
Gillon, M., Lanotte, A. A., Barman, T., et al. 2010, A&A, 511, A3
Gillon, M., Triaud, A. H. M. J., Fortney, J. J., et al. 2012, A&A, 542, A4
Holman, M. J., Winn, J. N., Latham, D. W., et al. 2006, ApJ, 652, 1715
Huitson, C. M., Sing, D. K., Pont, F., et al. 2013, MNRAS, 434, 3252
Jehin, E., Gillon, M., Queloz, D., et al. 2011, The Messenger, 145, 2
Knutson, H. A., Charbonneau, D., Noyes, R. W., Brown, T. M., & Gilliland, R. L. 2007, ApJ, 655, 564
Lecavelier Des Etangs, A., Pont, F., Vidal-Madjar, A., & Sing, D. 2008, A&A, 481, L83
Lendl, M., Anderson, D. R., Collier-Cameron, A., et al. 2012, A&A, 544, A72
Madhusudhan, N. 2012, ApJ, 758, 36
Madhusudhan, N., & Seager, S. 2009, ApJ, 707, 24
Madhusudhan, N., Harrington, J., Stevenson, K. B., et al. 2011, Nature, 469, 64
Mandel, K., & Agol, E. 2002, ApJ, 580, L171
Markwardt, C. B. 2009, in Astronomical Data Analysis Software and Systems XVIII, eds. D. A. Bohlender, D. Durand, & P. Dowler, ASP Conf. Ser., 411, 251
McCullough, P. R., Crouzet, N., Deming, D., & Madhusudhan, N. 2014, ApJ, 791, 55
Moehler, S., Freudling, W., Møller, P., et al. 2010, PASP, 122, 93
Moffat, A. F. J. 1969, A&A, 3, 455
Pollacco, D. L., Skillen, I., Collier Cameron, A., et al. 2006, PASP, 118, 1407
Pont, F., Tamuz, O., Udalski, A., et al. 2008, A&A, 487, 749
Redfield, S., Endl, M., Cochran, W. D., & Koesterke, L. 2008, ApJ, 673, L87
Seager, S., & Sasselov, D. D. 2000, ApJ, 537, 916
Seager, S., Richardson, L. J., Hansen, B. M. S., et al. 2005, ApJ, 632, 1122
Sedaghati, E., Boffin, H. M. J., Csizmadia, S., et al. 2015, A&A, 576, L11
Sing, D. K., Désert, J.-M., Lecavelier Des Etangs, A., et al. 2009, A&A, 505, 891
Sing, D. K., Désert, J.-M., Fortney, J. J., et al. 2011, A&A, 527, A73
Stevenson, K. B., Bean, J. L., Seifahrt, A., et al. 2014, AJ, 147, 161
Swain, M. R., Vasisht, G., & Tinetti, G. 2008, Nature, 452, 329
Wheatley, P. J., Pollacco, D. L., Queloz, D., et al. 2013, EPJ Web Conf., 47, 13002
Winn, J. N. 2011, in Exoplanet Transits and Occultations, ed. S. Seager (The University of Arizona Press), 55
Winn, J. N., Holman, M. J., Torres, G., et al. 2008, ApJ, 683, 176

Appendix A: Additional table

Table A.1. Details on the observations: wavelength band, date, baseline parameters and noise statistics of all data included in the global analysis of WASP-49b.

Wavelength [nm]	Date	Baseline function	β_r		β_w		CF		rms_{120s} [%]	
FORS2										
738−748	05 Dec. 2012	$p^1(CNM) + off$	1.33	1.33	0.97	0.97	1.29	1.29	0.080	0.081
	14 Jan. 2013	$p^1(CNM) + p^2(par)$	1.12	1.15	1.00	0.99	1.12	1.14	0.074	0.087
	07 Feb. 2013	$p^1(CNM) + p^2(par)$	1.98	1.18	0.88	0.90	1.74	1.06	0.081	0.093
748−758	05 Dec. 2012	$p^1(CNM) + off$	1.24	1.13	0.81	0.99	1.01	1.12	0.055	0.074
	14 Jan. 2013	$p^1(CNM) + p^2(par)$	1.58	1.27	1.11	0.97	1.75	1.23	0.083	0.088
	07 Feb. 2013	$p^1(CNM) + p^2(par)$	1.50	1.20	0.52	0.87	0.77	1.04	0.022	0.083
758−768	05 Dec. 2012	$p^1(CNM) + off$	1.39	2.01	0.70	0.86	0.98	1.74	0.044	0.082
	14 Jan. 2013	$p^1(CNM) + p^2(par)$	1.02	1.50	0.71	0.92	0.73	1.37	0.045	0.093
	07 Feb. 2013	$p^1(CNM) + p^2(par)$	1.03	3.71	0.71	0.91	0.73	3.36	0.045	0.122
768−778	05 Dec. 2012	$p^1(CNM) + off$	1.48	1.25	0.69	0.81	1.02	1.01	0.044	0.054
	14 Jan. 2013	$p^1(CNM) + p^2(par)$	1.49	1.18	0.66	0.82	0.98	0.97	0.043	0.064
	07 Feb. 2013	$p^1(CNM) + p^2(par)$	1.31	1.00	0.72	0.76	0.95	0.76	0.045	0.058
778−788	05 Dec. 2012	$p^1(CNM) + off$	1.00	1.57	0.68	1.11	0.68	1.75	0.042	0.081
	14 Jan. 2013	$p^1(CNM) + p^2(par)$	1.41	1.09	0.72	0.93	1.02	1.01	0.052	0.070
	07 Feb. 2013	$p^1(CNM) + p^2(par)$	0.97	1.49	0.77	0.87	0.80	1.29	0.047	0.078
765−773 (K)	05 Dec. 2012	$p^1(CNM) + off$	3.68	1.42	1.07	0.69	3.94	0.98	0.077	0.044
	14 Jan. 2013	$p^1(CNM) + p^2(par)$	1.39	1.50	0.81	0.76	1.13	1.15	0.047	0.068
	07 Feb. 2013	$p^1(CNM) + p^2(par)$	2.51	1.57	0.80	0.73	2.01	1.14	0.056	0.078
788−798	05 Dec. 2012	$p^1(CNM) + off$	1.09	1.02	1.03	0.72	1.12	0.73	0.063	0.046
	14 Jan. 2013	$p^1(CNM) + p^2(par)$	1.87	1.10	1.05	0.82	1.96	0.91	0.085	0.051
	07 Feb. 2013	$p^1(CNM) + p^2(par)$	2.50	1.71	1.01	0.78	2.53	1.34	0.085	0.064
798−808	05 Dec. 2012	$p^1(CNM) + off$	3.50	1.04	1.03	0.70	3.61	0.73	0.097	0.045
	14 Jan. 2013	$p^1(CNM) + p^2(par)$	2.00	1.69	0.96	0.76	1.93	1.29	0.078	0.047
	07 Feb. 2013	$p^1(CNM) + p^2(par)$	1.53	1.19	0.99	0.73	1.52	0.87	0.080	0.056
808−818	05 Dec. 2012	$p^1(CNM) + off$	1.39	1.48	1.04	0.69	1.45	1.02	0.080	0.044
	14 Jan. 2013	$p^1(CNM) + p^2(par)$	3.72	1.54	1.20	0.76	4.46	1.18	0.116	0.048
	07 Feb. 2013	$p^1(CNM) + p^2(par)$	1.14	1.45	1.00	0.74	1.14	1.08	0.088	0.061
818−828	05 Dec. 2012	$p^1(CNM) + off$	1.27	1.47	0.97	0.66	1.23	0.98	0.088	0.043
	14 Jan. 2013	$p^1(CNM) + p^2(par)$	1.49	1.48	0.92	0.79	1.37	1.17	0.092	0.053
	07 Feb. 2013	$p^1(CNM) + p^2(par)$	1.18	1.27	0.82	0.70	0.97	0.90	0.064	0.051
828−838	05 Dec. 2012	$p^1(CNM) + off$	1.09	1.29	0.93	0.73	1.01	0.94	0.070	0.046
	14 Jan. 2013	$p^1(CNM) + p^2(par)$	1.47	1.63	0.66	0.85	0.97	1.38	0.055	0.053
	07 Feb. 2013	$p^1(CNM) + p^2(par)$	1.50	2.75	0.77	0.78	1.15	2.13	0.068	0.065
838−848	05 Dec. 2012	$p^1(CNM) + off$	1.11	1.00	0.82	0.68	0.91	0.68	0.052	0.042
	14 Jan. 2013	$p^1(CNM) + p^2(par)$	1.69	1.05	0.77	0.72	1.29	0.76	0.048	0.038
	07 Feb. 2013	$p^1(CNM) + p^2(par)$	1.56	1.90	0.76	0.73	1.18	1.38	0.048	0.058
848−858	05 Dec. 2012	$p^1(CNM) + off$	1.48	1.43	0.79	0.71	1.17	1.02	0.053	0.052
	14 Jan. 2013	$p^1(CNM) + p^2(par)$	1.63	1.29	0.85	0.78	1.38	1.00	0.054	0.047
	07 Feb. 2013	$p^1(CNM) + p^2(par)$	1.05	1.57	0.72	0.68	0.76	1.07	0.038	0.051
858−868	05 Dec. 2012	$p^1(CNM) + off$	1.28	1.06	0.78	0.76	1.00	0.80	0.047	0.046
	14 Jan. 2013	$p^1(CNM) + p^2(par)$	1.26	1.25	0.74	0.74	0.93	0.93	0.046	0.046
	07 Feb. 2013	$p^1(CNM) + p^2(par)$	1.06	1.83	0.77	0.64	0.81	1.17	0.045	0.051
868−878	05 Dec. 2012	$p^1(CNM) + off$	1.80	1.05	0.80	0.72	1.44	0.75	0.048	0.047
	14 Jan. 2013	$p^1(CNM) + p^2(par)$	1.54	1.06	0.84	0.77	1.29	0.81	0.056	0.045
	07 Feb. 2013	$p^1(CNM) + p^2(par)$	2.02	1.22	0.98	0.66	1.98	0.81	0.079	0.045
878−888	05 Dec. 2012	$p^1(CNM) + off$	1.73	1.56	0.84	0.76	1.45	1.19	0.063	0.047
	14 Jan. 2013	$p^1(CNM) + p^2(par)$	1.17	1.80	0.80	0.80	0.94	1.44	0.054	0.048
	07 Feb. 2013	$p^1(CNM) + p^2(par)$	1.89	1.11	1.13	0.69	2.14	0.77	0.094	0.052
888−898	05 Dec. 2012	$p^1(CNM) + off$	2.57	1.00	1.21	0.75	3.11	0.75	0.105	0.048
	14 Jan. 2013	$p^1(CNM) + p^2(par)$	2.79	1.53	1.20	0.84	3.35	1.29	0.103	0.056
	07 Feb. 2013	$p^1(CNM) + p^2(par)$	1.67	1.48	0.94	0.77	1.57	1.13	0.084	0.063
898−908	05 Dec. 2012	$p^1(CNM) + off$	1.00	3.66	0.94	1.08	0.94	3.94	0.080	0.077
	14 Jan. 2013	$p^1(CNM) + p^2(par)$	1.45	2.03	1.05	0.98	1.52	1.98	0.086	0.079
	07 Feb. 2013	$p^1(CNM) + p^2(par)$	1.24	2.12	1.08	0.81	1.34	1.71	0.094	0.077
908−918	05 Dec. 2012	$p^1(CNM) + off$	1.30	1.39	1.21	0.82	1.57	1.13	0.109	0.046

Notes. The baseline functions of the form $p^j(i)$ denote a polynomial of order j in parameter i, where i can be time t, parallactic angle par, the sky background sky and the PSF or spectral full-width at half maximum $fwhm$. off refers to an offset due to the change in exposure time on FORS2, or a telescope meridian flip for some TRAPPIST light curves. The red- and white noise amplitudes β_r and β_w, the error adaptation factor CF, and the rms is given for data binned in bins of two minutes. For the FORS2 data, the four data quality parameters are given for the global fit (left value) and for fits restricted to single transit events (right value).

A&A 587, A67 (2016)

Table A.1. continued.

Wavelength [nm]	Date	Baseline function	β_r		β_w		CF		rms_{120s} [%]	
	14 Jan. 2013	$p^1(CNM) + p^2(par)$	1.17	1.73	0.90	0.84	1.06	1.45	0.094	0.063
	07 Feb. 2013	$p^1(CNM) + p^2(par)$	1.20	1.30	0.87	0.68	1.04	0.88	0.083	0.051
918−928	05 Dec. 2012	$p^1(CNM) + off$	3.56	2.49	0.94	0.81	3.36	2.01	0.139	0.057
	14 Jan. 2013	$p^1(CNM) + p^2(par)$	1.00	1.17	0.76	0.81	0.76	0.94	0.058	0.054
	07 Feb. 2013	$p^1(CNM) + p^2(par)$	1.47	1.36	0.88	0.78	1.29	1.07	0.078	0.074
928−938	05 Dec. 2012	$p^1(CNM) + off$	2.50	1.08	0.62	1.03	1.55	1.12	0.068	0.063
	14 Jan. 2013	$p^1(CNM) + p^2(par)$	1.56	1.91	0.73	1.12	1.14	2.14	0.079	0.093
	07 Feb. 2013	$p^1(CNM) + p^2(par)$	1.73	1.62	0.78	1.13	1.34	1.83	0.063	0.116
938−948	05 Dec. 2012	$p^1(CNM) + off$	1.18	1.89	0.74	1.04	0.87	1.96	0.057	0.085
	14 Jan. 2013	$p^1(CNM) + p^2(par)$	1.46	2.57	0.74	1.21	1.08	3.11	0.060	0.105
	07 Feb. 2013	$p^1(CNM) + p^2(par)$	1.28	2.02	0.70	1.13	0.90	2.27	0.051	0.120
948−958	05 Dec. 2012	$p^1(CNM) + off$	2.76	2.51	0.77	1.01	2.13	2.53	0.066	0.085
	14 Jan. 2013	$p^1(CNM) + p^2(par)$	1.88	2.79	0.73	1.20	1.38	3.35	0.058	0.103
	07 Feb. 2013	$p^1(CNM) + p^2(par)$	1.56	3.67	0.69	1.29	1.07	4.73	0.052	0.158
958−968	05 Dec. 2012	$p^1(CNM) + off$	1.83	3.54	0.64	1.02	1.17	3.61	0.049	0.094
	14 Jan. 2013	$p^1(CNM) + p^2(par)$	1.22	1.67	0.66	0.94	0.81	1.57	0.047	0.084
	07 Feb. 2013	$p^1(CNM) + p^2(par)$	1.12	3.73	0.69	1.14	0.77	4.24	0.052	0.155
968−978	05 Dec. 2012	$p^1(CNM) + off$	1.46	1.99	0.77	0.97	1.13	1.93	0.063	0.077
	14 Jan. 2013	$p^1(CNM) + p^2(par)$	2.11	1.00	0.81	0.94	1.71	0.94	0.076	0.080
	07 Feb. 2013	$p^1(CNM) + p^2(par)$	1.21	1.00	0.71	0.88	0.86	0.88	0.054	0.095
978−988	05 Dec. 2012	$p^1(CNM) + off$	1.37	1.54	0.78	0.99	1.07	1.52	0.073	0.079
	14 Jan. 2013	$p^1(CNM) + p^2(par)$	1.62	1.46	1.13	1.04	1.83	1.52	0.115	0.085
	07 Feb. 2013	$p^1(CNM) + p^2(par)$	2.01	3.49	1.13	1.21	2.27	4.24	0.119	0.157
988−1000	05 Dec. 2012	$p^1(CNM) + off$	3.61	1.40	1.31	1.04	4.73	1.45	0.158	0.080
	14 Jan. 2013	$p^1(CNM) + p^2(par)$	3.66	1.24	1.16	1.08	4.24	1.34	0.147	0.094
	07 Feb. 2013	$p^1(CNM) + p^2(par)$	1.00	3.07	0.88	1.28	0.88	3.91	0.094	0.150
1000−1020	05 Dec. 2012	$p^1(CNM) + off$	3.48	3.75	1.22	1.19	4.24	4.46	0.150	0.115
	14 Jan. 2013	$p^1(CNM) + p^2(par)$	3.05	1.30	1.28	1.21	3.91	1.57	0.153	0.110
	07 Feb. 2013	$p^1(CNM) + p^2(par)$	2.84	2.81	1.12	1.13	3.18	3.18	0.134	0.135
EulerCam										
r'-Gunn	19 Mar. 2011	$p^2(t) + p(sky^1)$	1.45	–	1.25	–	1.81	–	0.066	–
r'-Gunn	24 Mar. 2011	$p^2(t)$	1.61	–	1.32	–	2.13	–	0.090	–
r'-Gunn	30 Dec. 2012	$p^2(t)$	1.95	–	1.68	–	3.28	–	0.089	–
NGTS	05 Dec. 2012	$p^2(t) + p^1(fwhm)$	1.27	–	1.32	–	1.68	–	0.066	–
TRAPPIST										
$I + z'$	19 Jan. 2011	$p^2(t)$	1.15	–	1.12	–	1.29	–	0.150	–
$I + z'$	24 Oct. 2011	$p^2(t)$	1.80	–	1.16	–	2.09	–	0.158	–
$I + z'$	05 Dec. 2012	$p^2(t) + off$	1.12	–	1.04	–	1.17	–	0.141	–
$I + z'$	16 Dec. 2012	$p^2(t)$	2.07	–	1.11	–	2.30	–	0.163	–
$I + z'$	30 Dec. 2012	$p^2(t) + off$	1.18	–	1.16	–	1.37	–	0.165	–
$I + z'$	21 Feb. 2013	$p^2(t) + off$	1.27	–	0.91	–	1.15	–	0.111	–

4.3 WASP-80 b

WASP-80 b is a ∼0.55 $M_{\rm Jup}$, ∼0.95 $R_{\rm Jup}$ transiting gas giant in a ∼3.07 days orbit around a bright (I=10.28) nearby (51.3±6.2 pc) cool ($T_{\rm eff}$=4145±100K) star with a spectral type between K7V and M0V (Triaud et al. 2013). With an equilibrium temperature of only ∼825K (assuming a null Bond albedo and an efficient day-night heat redistribution), it is one of the coolest gas giants whose atmosphere can be studied both in transmission and emission. Indeed, its low density (∼0.54 $\rho_{\rm Jup}$) and very deep transits (∼2.9%) make it a good target for transmission spectroscopy, while the low luminosity of its host star (∼0.09 $L_{\odot}$) results in a favorable planet-to-star flux ratio (∼0.05–0.1%) in the mid-infrared. Naturally, the opportunity offered by this rare planetary system to extend the atmospheric study of transiting gas giants towards the low-temperature regime has led to several follow-up studies in recent years. Broad-band transit observations in several optical, near-infrared, and mid-infrared passbands, some of which obtained simultaneously, were reported by several teams (Mancini et al. 2014, Fukui et al. 2014, Triaud et al. 2015). These data were found to be consistent, within measurement errors, with a flat transmission spectrum (Triaud et al. 2015). In this section, I describe my efforts in constraining the transmission spectrum of WASP-80 b between 740 and 1020nm using FORS2 spectrophotometry. The most prominent absorption signatures expected in this wavelength range for a clear hydrogen-dominated atmosphere with a temperature ∼800K are the K I resonance doublet centered at 768nm and a broad rotational-vibrational H_2O band between ∼920 and ∼1020nm. WASP-80 b being cool enough to have abundant atmospheric CH_4 (in contrast to WASP-49 b), its transmission spectrum could also show some CH_4 features, e.g. the CH_4 absorption band between ∼880 and ∼900nm.

4.3.1 Observations

Two transits of WASP-80 b were observed with VLT/FORS2 during ESO P91 (program 091.C-0377, PI: Michaël Gillon). I went to Paranal to observe the first transit in visitor mode during the night of 15 June 2013, while the second transit observation was performed in service mode during the night of 28 July 2013. I managed the preparation of both these observing runs, including the creation of the Observation Blocks (OBs), design of the MXU mask, interactions with ESO, etc. The program initially consisted in monitoring four transits of WASP-80 b, but two nights were lost because of bad weather.

The instrument setup was the same for both transits. FORS2 was configured for medium-resolution multi-object spectroscopy, using a custom-made mask in which slits had been cut at the positions of WASP-80 and five reference stars[6] (see Fig. 4.2, left). These slits were 10″ wide and 38″ long (except for one slit that had a length of 25″). The large width of the slits (in the dispersion direction) prevented any slit losses due to variable seeing or imperfect telescope tracking, while their length (in the spatial direction) allowed a precise background measurement for each star (see Section 4.3.2). The 600z grism was used to disperse the light of the stars, together with the sorting filter OG590 to isolate the first order spectra. The resulting spectra covered the wavelength range 740-1020nm for WASP-80, which was centered horizontally (dispersion direction) on the detector, and slightly different ranges for the off-centered reference stars (see Figs. 4.2 and 4.3). The red-optimized

[6] A seventh slit was positioned on the sky, but the resulting sky spectra were not used in the reduction process (see Section 4.3.2).

(MIT) detector system was used in default 2×2 binning mode, yielding a plate scale of 0.25″/pixel and a dispersion of 0.160nm/pixel (with the 600z grism). The LADC was put in simulation during the observations, with the two prisms set to their minimal separation (30 mm). For wavelength calibration purposes, spectra of a HeNeAr arc lamp with well-documented emission lines were obtained the day after each transit observation, using a copy of the science mask but with narrower slits of 1″, to produce well-defined lines.

The first transit observation took place on 16 June 2013 from 05:23 to 10:04 UT, covering the ∼2.1hrs long predicted transit together with ∼2.6hrs of out-of-transit observations. The conditions were good, although the seeing was variable with values between 0.9″ and 1.6″. The field was at an airmass of 1.22 at the beginning of the run, rose up to an airmass of 1.08, and then set at an airmass of 1.45 at the end. A total of 270 exposures were obtained, each 25s long. The time overhead was ∼37s per exposure, giving a mean cadence of ∼62s.

The second transit was observed on 29 July 2013 from 03:33 to 08:25 UT. However, the data obtained after 06:49 UT were badly affected by a technical malfunction that looks like vignetting, with all the stellar fluxes dropping steeply (∼40% in ∼1hr) and in a non-uniform way over the field of view (i.e. in a different way for each star). These data are not usable and were removed from the analysis below. The observations that were used in the analysis started 1.6hrs before the transit and covered ∼80% of the transit (∼1.7hrs of in-transit observations). They consist of 235 exposures of 12s, obtained at a mean cadence of ∼49s. The conditions were less favorable than during the first transit observation, with a seeing that varied strongly between 0.8″ and 2.4″. The airmass first decreased from 1.11 to 1.08 and then increased, reaching 1.33 at the end of the observations.

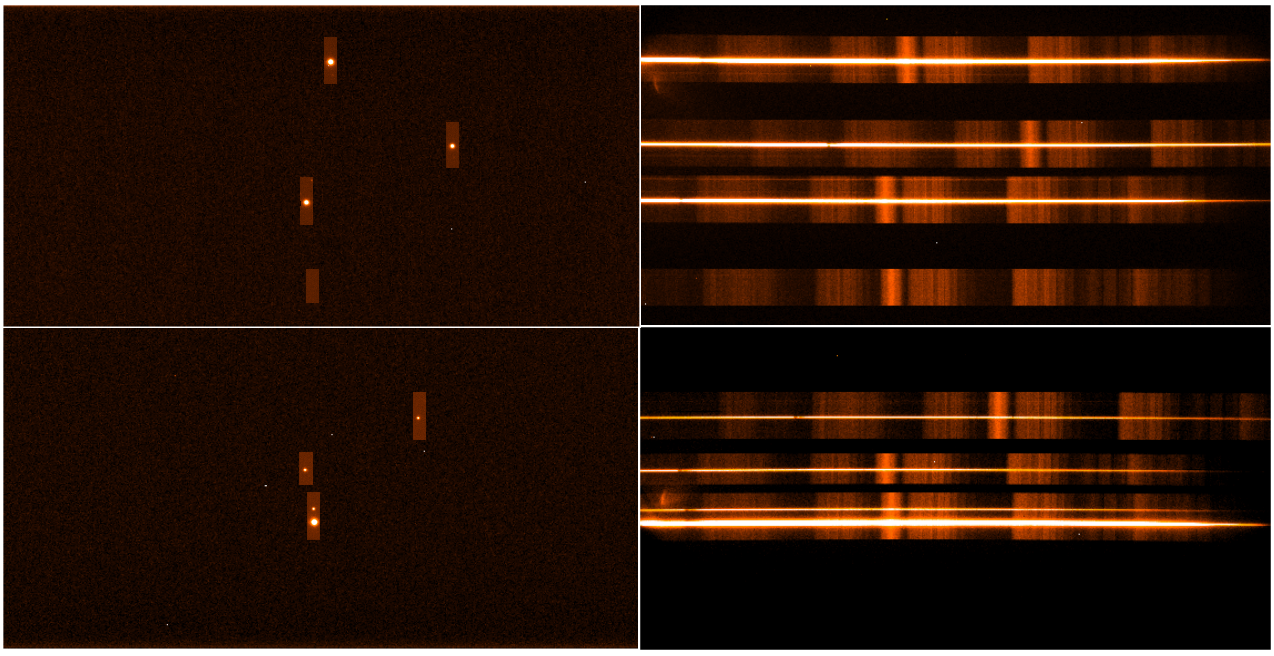

FIGURE 4.2: *Left:* A FORS2 "through-slit" image acquired at the beginning of the first transit observation (16 June 2013) to check the centering of the stars in their slits. The image consists in fact of two images, one for each CCD of the detector system. The mask with seven slits is visible: one slit is placed on WASP-80 (the lowest star on the bottom CCD), five slits are positioned on reference stars, and one slit is placed on the sky. Other stars in the field of view are masked to avoid contaminating the spectra of the selected stars. *Right:* An example of scientific exposure containing simultaneous spectra of the selected stars.

4.3.2 Data reduction

The data reduction and spectral extraction were performed using an IRAF pipeline that I developed specifically for this purpose. The science images were first processed following standard CCD reduction procedures, including bias and dark subtraction and flat-fielding. One-dimensional spectra of all stars were then extracted from the calibrated images using various tasks of the IRAF/APEXTRACT package. For each image, the trace of each stellar spectrum was determined by computing the centroid of its spatial profile every 10 columns along the dispersion axis and fitting a fourth-order polynomial function to these centroids. The stellar spectrum was then extracted along the trace using the optimal extraction algorithm of Horne (1986). At each point along the trace, the flux was computed as the variance-weighted[7] sum of the pixel counts, after background subtraction, within a chosen one-dimensional aperture located along the spatial axis (detector column) and centered on the trace position. Various aperture sizes were tested and the best results were obtained by using a 36 pixels-wide aperture for all stars (18 pixels on each side of the trace). The background was determined by fitting a straight line to all illuminated pixels along the detector column with a minimum distance to the spectral trace of 25 pixels (6.25″), outlier pixels being rejected from the fit using a sigma clipping algorithm. This fit was subtracted at each pixel within the aperture during extraction. Outlier pixels within the aperture (bad pixels or cosmics) were identified as deviating by more than 4σ from an expected spatial profile, obtained by median-combining the spatial profiles of the 20 circumjacent detector columns. During extraction, they were replaced by their expected values based on this profile. All these operations were repeated at each point along the trace of each stellar spectrum to produce one-dimensional spectra of all stars from each science image.

The wavelength calibration of each extracted stellar spectrum was established based on a calibration spectrum extracted from the arc lamp exposure using the same trace and aperture. The dispersion solution was obtained by identifying emission lines with known wavelengths in this calibration spectrum and fitting a third-order polynomial to their wavelengths as a function of their pixel positions (IRAF task autoidentify). This dispersion solution was then used to put the stellar spectrum on a linear wavelength scale by interpolating it to evenly spaced pixels in wavelength ($\sim$0.160nm/pixel), while ensuring flux conservation (IRAF task dispcor). Examples of wavelength-calibrated extracted spectra of WASP-80 and the five reference stars are shown in Fig. 4.3.

The spectra were summed over wavelength into fourteen 20nm-wide wavelength bins (between 740 and 1020nm) to create spectrophotometric time series. The two longest-wavelength bins were not covered by all reference stars (see Fig. 4.3). Differential transit light curves were created for each of the spectral bins by dividing the flux of WASP-80 by the sum of the fluxes of several reference stars. All combinations of reference stars were tested and the best light curves for all spectral bins were obtained by using only the two brightest reference stars. Adding fainter reference stars to the comparison signal yielded noisier light curves. The 28 spectrophotometric transit light curves obtained from both transit observations (14 light curves for each transit) are displayed in Fig. 4.4. As was the case for WASP-49 (Section 4.2), the light curves show strong correlated noise superimposed to the expected transit signal. The light curves of the second transit also show overall larger scatter than those of the first transit, probably due to the less favorable conditions (highly

[7] The relative contribution of a pixel to the sum is inversely proportional to the statistical uncertainty of its intensity based on the known noise characteristics of the detector.

variable seeing) during the second transit observation.

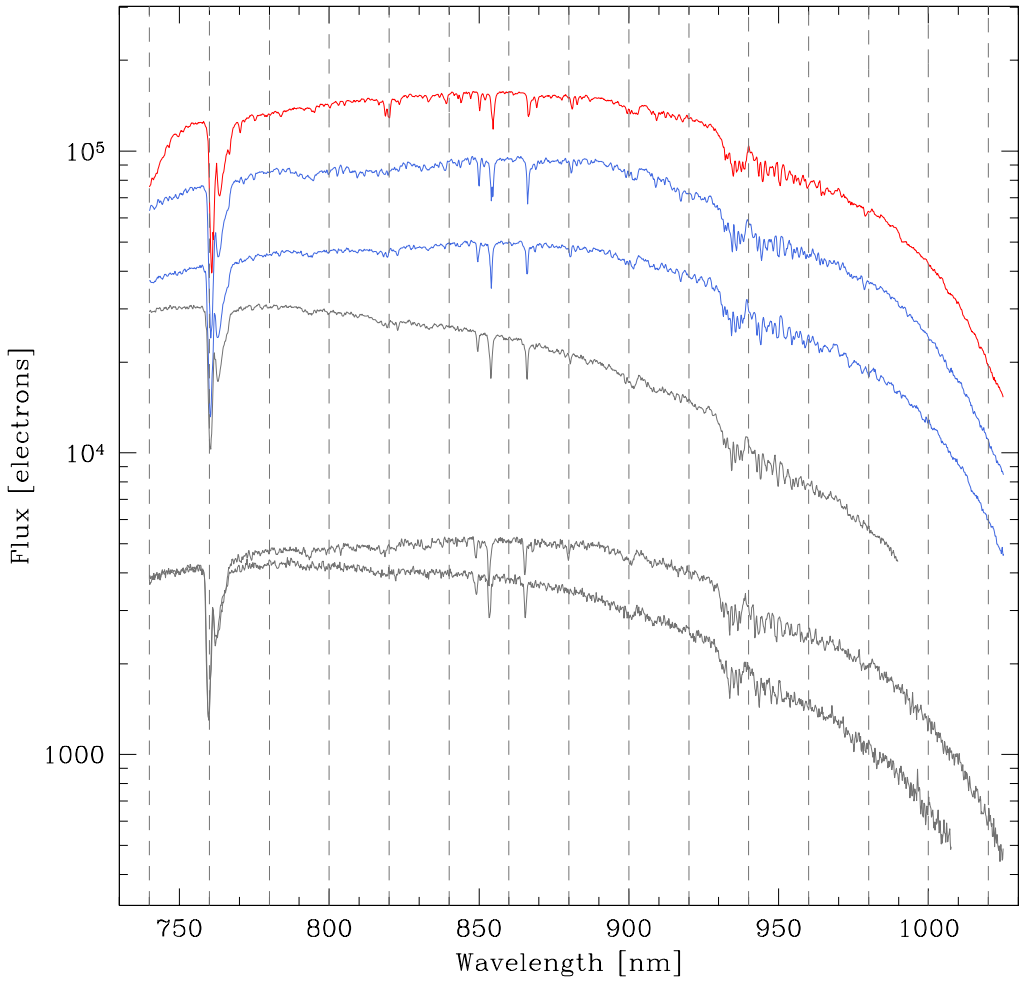

FIGURE 4.3: Examples of wavelength-calibrated extracted spectra of WASP-80 (red), the two brightest reference stars used to obtain the spectrophotometric differential transit light curves (blue), and the three fainter reference stars (grey). The vertical dashed lines indicate the fourteen 20nm-wide wavelength bins used for spectrophotometry.

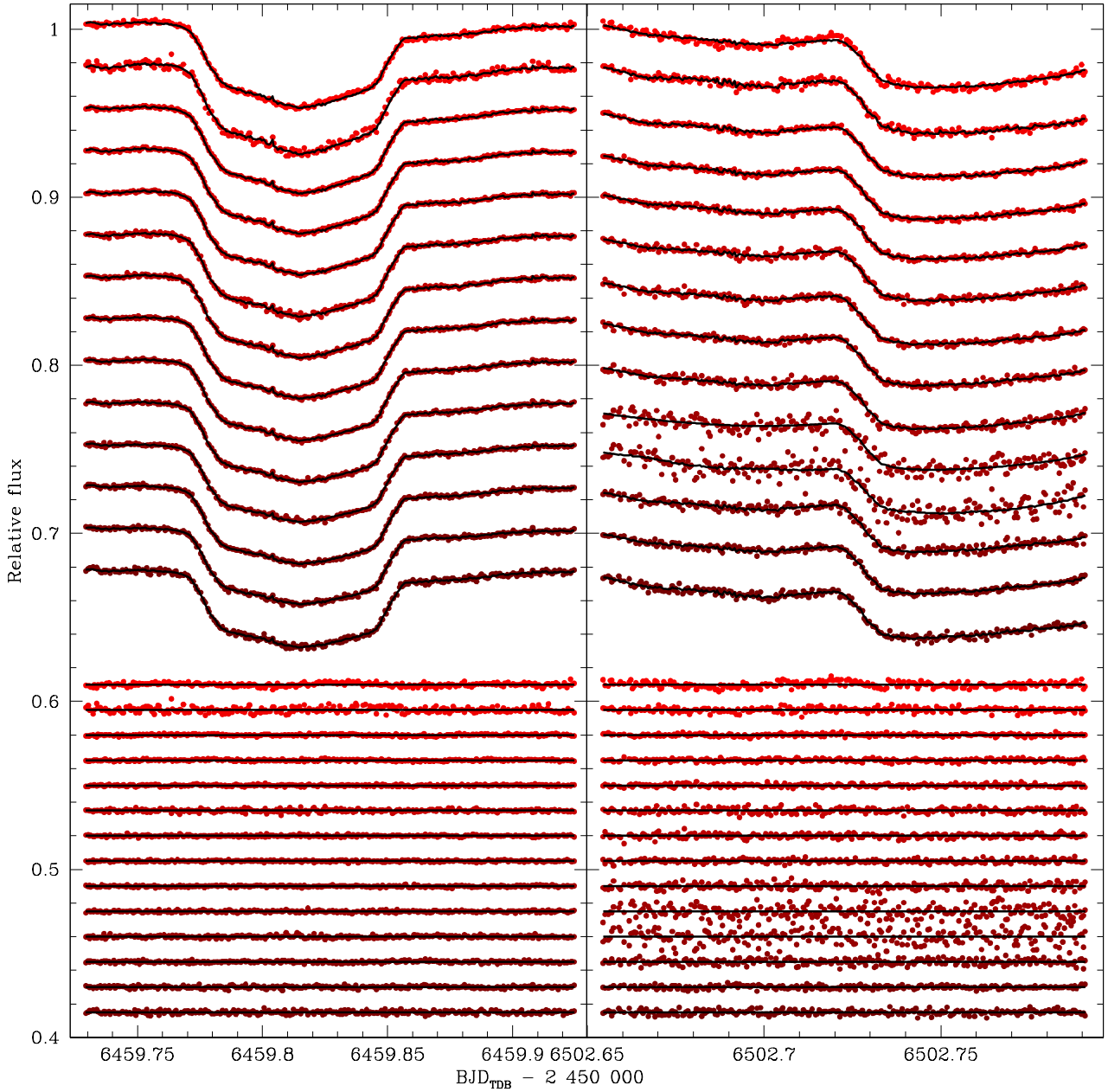

FIGURE 4.4: The raw FORS2 spectrophotometric transit light curves obtained from the observations on 16 June 2013 (*left*) and on 29 July 2013 (*right*). The wavelength bins are, from top to bottom: [740-760nm], [760-780nm], [780-800nm], [800-820nm], [820-840nm], [840-860nm], [860-880nm], [880-900nm], [900-920nm], [920-940nm], [940-960nm], [960-980nm], [980-1000nm], [1000-1020nm]. For each light curve, the overplotted black line is the best-fit full model (transit $\times$ baseline, see Section 4.3.3 for details about the modeling). The corresponding residuals are shown below the data.

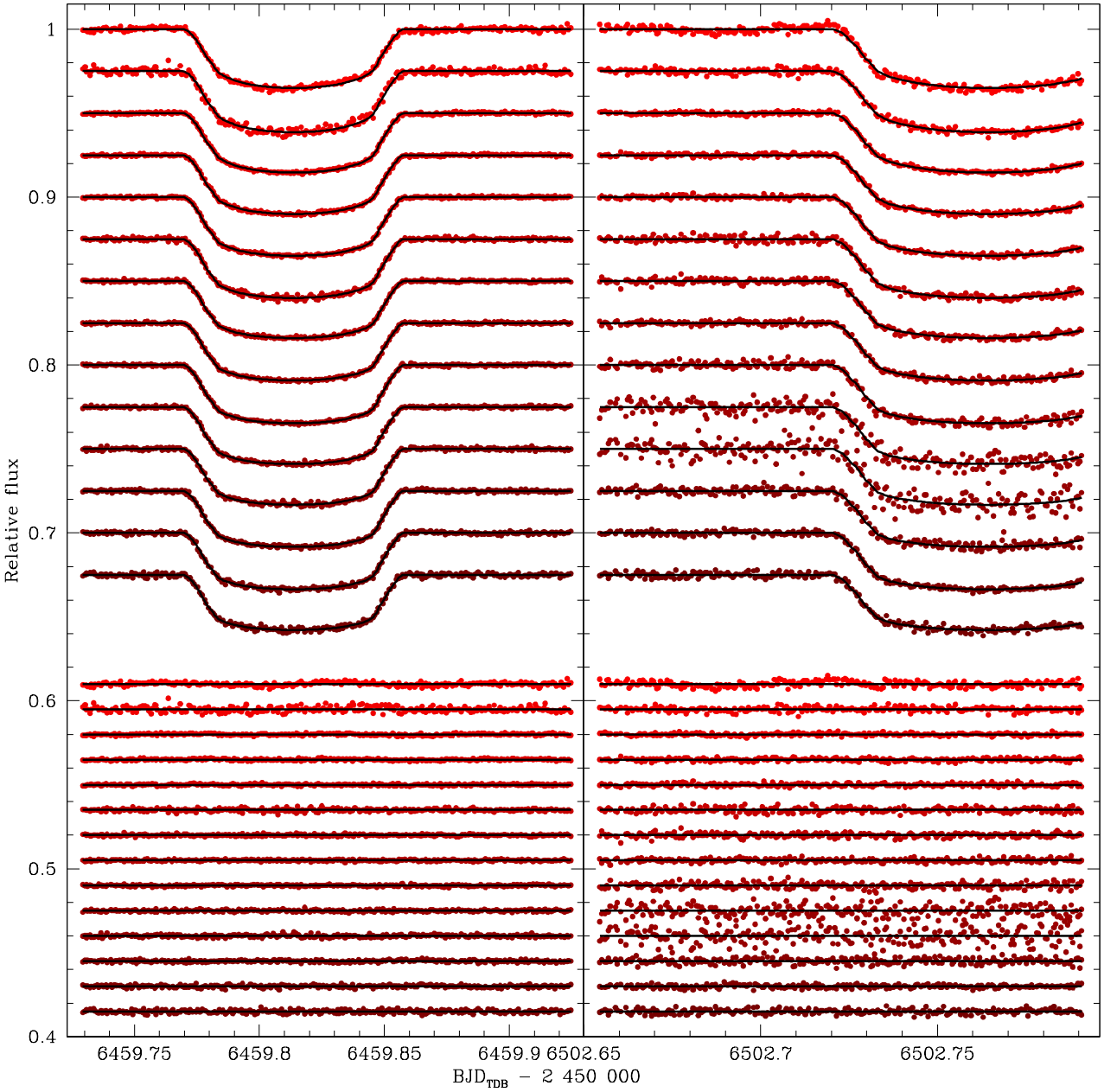

FIGURE 4.5: Same as Fig. 4.4, but here the light curves are divided by their respective best-fit baseline models. The best-fit transit model in each wavelength bin is overplotted in black.

4.3.3 Global data analysis

To constrain the transmission spectrum of WASP-80 b between 740 and 1020nm, I performed a global MCMC analysis of the 28 spectrophotometric transit light curves. The MCMC code is presented in detail in Section 2. Here, I will only describe aspects that are specific to this analysis. The light curves were modeled using the transit model of Mandel and Agol (2002) multiplied by a baseline model consisting for all of them of a second-order polynomial of the parallactic angle (*par*) combined to a first-order polynomial of a common noise model (CNM, see Section 2.3). As all 14 light curves obtained from the same transit observation show similar correlated noise structures (see Fig. 4.4), a CNM was constructed for each of the two sets of transit light curves. A quadratic limb-darkening law was adopted for the star and a circular orbit was assumed for the planet, as there has been no evidence for an eccentric orbit in the previous studies (see e.g. Triaud et al. 2015).

The need to include both a dependency on the parallactic angle and on the CNM in the baseline model is illustrated in Fig. 4.6 for the 920-940nm light curve of the first transit as an example. Using a second-order polynomial of *par* as baseline model (top panel) allows to model the lowest-frequency red noise present in the light curve, but shorter-timescale correlated noise structures are clearly visible in the residuals (RMS=1174ppm). Including dependencies on other external parameters in the baseline model does not provide a significantly better fit to the data. External parameters that were tested are time, airmass, mean FWHM of the stellar spatial profile, background, coordinate shifts, the trigonometric functions sin(*par*) and cos(*par*), and the change in parallactic angle from one exposure to the next d*par* (i.e., the instrument rotator speed). Using instead a baseline model that consists solely of a first-order polynomial of the CNM (middle panel) allows to model most of the systematics but a small trend is still visible in the residuals (RMS=629ppm), indicating that this baseline is not optimal at modeling the lowest-frequency red noise present in the light curve. The best fit to the data is obtained with a baseline model consisting of a second-order polynomial of *par* combined to a first-order polynomial of the CNM (bottom panel), which yields "clean" residuals with a RMS of 525ppm. This choice of baseline is also favored by the BIC.

The jump parameters in the MCMC analysis were:

- the transit depth $\mathrm{d}F_{[860-880\mathrm{nm}]}$ in the wavelength bin [860-880nm] (randomly chosen);
- the transit depth differences in the other wavelength bins $\mathrm{dd}F_j = \mathrm{d}F_j - \mathrm{d}F_{[860-880\mathrm{nm}]}$, where j = [740-760nm], [760-780nm], [780-800nm], [800-820nm], [820-840nm], [840-860nm], [880-900nm], [900-920nm], [920-940nm], [940-960nm], [960-980nm], [980-1000nm], [1000-1020nm];
- the transit impact parameter in the case of a circular orbit $b' = a \cos i_\mathrm{p}/R_\star$, where a is the orbital semi-major axis, i_p is the orbital inclination, and $R_\star$ is the stellar radius;
- the transit width W;
- the time of mid-transit T_0;
- the orbital period P;
- the stellar effective temperature T_eff, metallicity [Fe/H], and mass $M_\star$;

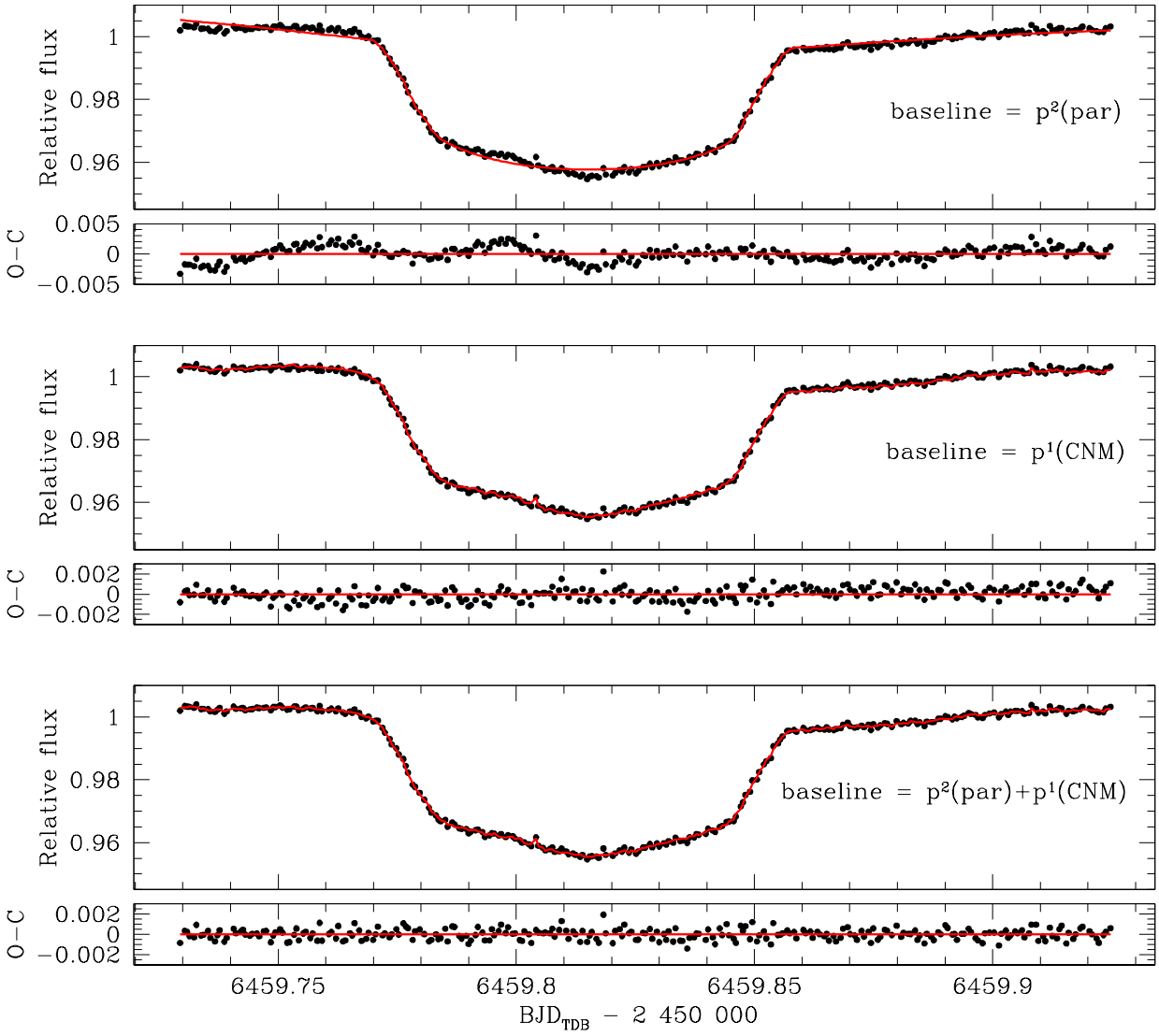

FIGURE 4.6: The spectrophotometric transit light curve obtained from the first transit observation for the wavelength bin [920-940nm]. Three different baseline models are tested: a second-order polynomial of the parallactic angle *par* (*top*), a first-order polynomial of the common noise model CNM (*middle*), and a combination of both (*bottom*). In each panel, the best-fit full model (transit × baseline) is overplotted in red. The RMS of the residuals are (from top to bottom) 1174, 629, and 525ppm.

- the linear combinations of the quadratic limb-darkening coefficients ($u_{1,j}$, $u_{2,j}$) in each wavelength bin, $c_{1,j} = 2u_{1,j} + u_{2,j}$ and $c_{2,j} = u_{1,j} - 2u_{2,j}$;
- estimates of the overall transit depth of each group of light curves for which a CNM was constructed, $\mathrm{d}F_{\mathrm{group,transit1}}$ and $\mathrm{d}F_{\mathrm{group,transit2}}$.

Normal prior probability distribution functions were assumed for T_{eff}, [Fe/H], $M_\star$, $u_{1,j}$, $u_{2,j}$, $\mathrm{d}F_{\mathrm{group,transit1}}$, and $\mathrm{d}F_{\mathrm{group,transit2}}$. For T_{eff}, [Fe/H], and $M_\star$, the priors were based on the values reported in Triaud et al. (2013), with expectations and standard deviations corresponding to the quoted measurements and errors, respectively. The expectations of the normal priors imposed on $u_{1,j}$ and $u_{2,j}$ were interpolated from the theoretical tables of Claret and

Parameter	Prior	Parameter	Prior
$u_{1,[740-760\mathrm{nm}]}$	$\mathcal{N}(0.443, 0.019^2)$	$u_{2,[740-760\mathrm{nm}]}$	$\mathcal{N}(0.229, 0.007^2)$
$u_{1,[760-780\mathrm{nm}]}$	$\mathcal{N}(0.424, 0.020^2)$	$u_{2,[760-780\mathrm{nm}]}$	$\mathcal{N}(0.236, 0.007^2)$
$u_{1,[780-800\mathrm{nm}]}$	$\mathcal{N}(0.404, 0.020^2)$	$u_{2,[780-800\mathrm{nm}]}$	$\mathcal{N}(0.243, 0.007^2)$
$u_{1,[800-820\mathrm{nm}]}$	$\mathcal{N}(0.387, 0.017^2)$	$u_{2,[800-820\mathrm{nm}]}$	$\mathcal{N}(0.249, 0.006^2)$
$u_{1,[820-840\mathrm{nm}]}$	$\mathcal{N}(0.380, 0.007^2)$	$u_{2,[820-840\mathrm{nm}]}$	$\mathcal{N}(0.250, 0.001^2)$
$u_{1,[840-860\mathrm{nm}]}$	$\mathcal{N}(0.373, 0.008^2)$	$u_{2,[840-860\mathrm{nm}]}$	$\mathcal{N}(0.251, 0.001^2)$
$u_{1,[860-880\mathrm{nm}]}$	$\mathcal{N}(0.365, 0.008^2)$	$u_{2,[860-880\mathrm{nm}]}$	$\mathcal{N}(0.252, 0.002^2)$
$u_{1,[880-900\mathrm{nm}]}$	$\mathcal{N}(0.358, 0.007^2)$	$u_{2,[880-900\mathrm{nm}]}$	$\mathcal{N}(0.254, 0.002^2)$
$u_{1,[900-920\mathrm{nm}]}$	$\mathcal{N}(0.351, 0.008^2)$	$u_{2,[900-920\mathrm{nm}]}$	$\mathcal{N}(0.255, 0.001^2)$
$u_{1,[920-940\mathrm{nm}]}$	$\mathcal{N}(0.343, 0.008^2)$	$u_{2,[920-940\mathrm{nm}]}$	$\mathcal{N}(0.256, 0.001^2)$
$u_{1,[940-960\mathrm{nm}]}$	$\mathcal{N}(0.336, 0.007^2)$	$u_{2,[940-960\mathrm{nm}]}$	$\mathcal{N}(0.257, 0.001^2)$
$u_{1,[960-980\mathrm{nm}]}$	$\mathcal{N}(0.329, 0.008^2)$	$u_{2,[960-980\mathrm{nm}]}$	$\mathcal{N}(0.258, 0.001^2)$
$u_{1,[980-1000\mathrm{nm}]}$	$\mathcal{N}(0.321, 0.008^2)$	$u_{2,[980-1000\mathrm{nm}]}$	$\mathcal{N}(0.259, 0.001^2)$
$u_{1,[1000-1020\mathrm{nm}]}$	$\mathcal{N}(0.314, 0.007^2)$	$u_{2,[1000-1020\mathrm{nm}]}$	$\mathcal{N}(0.260, 0.001^2)$
T_{eff}	$\mathcal{N}(4145, 100^2)$ K	$\mathrm{d}F_{\mathrm{group,transit1}}$	$\mathcal{N}(2.933, 0.024^2)$ %
[Fe/H]	$\mathcal{N}(-0.14, 0.16^2)$ dex	$\mathrm{d}F_{\mathrm{group,transit2}}$	$\mathcal{N}(2.933, 0.024^2)$ %
$M_\star$	$\mathcal{N}(0.58, 0.05^2)$ $M_\odot$		

TABLE 4.1: Prior probability distribution functions assumed in the global MCMC analysis. $\mathcal{N}(\mu, \sigma^2)$ represents a normal distribution with an expectation μ and a variance σ^2.

Bloemen (2011) for each of the wavelength bins and for a star with $\log g_\star = 4.689 \pm 0.013$ (cgs), $T_{\mathrm{eff}} = 4145 \pm 100$ K, and [Fe/H] $= -0.14 \pm 0.16$ dex (Triaud et al. 2013). Their standard deviations were set so as to encompass the values of the two neighboring wavelength bins. As for the normal priors assumed for $\mathrm{d}F_{\mathrm{group,transit1}}$ and $\mathrm{d}F_{\mathrm{group,transit2}}$, they were both based on the value and error reported by Triaud et al. (2015) for the transit depth of WASP-80 b in the z'-band ($\sim$900nm, so near the center of the wavelength range covered by the FORS2 light curves). Using other values for these two priors was found to have no significant effect on the derived transmission spectrum. All these normal prior distributions are presented in Table 4.1. Uniform prior distributions were assumed for the other jump parameters.

A preliminary MCMC analysis, consisting of one chain of 50 000 steps, was first performed to determine the correction factors $CF = \beta_w \times \beta_r$ to be applied to the error bars of each photometric time series (see Section 2.5). The β_w, β_r, and CF values are given in Table 4.2. With the corrected photometric error bars, the final analysis was then performed. It consisted of two chains of 100 000 steps, whose convergence was checked using the statistical test of Gelman and Rubin (1992). The first 20% of each chain was considered as its burn-in phase and discarded. At each MCMC step, a value for the stellar mean density $\rho_\star$ was derived from the Kepler's third law and the jump parameters $\mathrm{d}F_{[860-880\mathrm{nm}]}$, b', W, and P (see Section 2.4, Equations 2.12 and 1.26). A value for $M_\star$ was drawn within the normal prior distribution assumed for this parameter, and the stellar radius $R_\star$ was derived from $M_\star$ and $\rho_\star$. The planetary mass M_{p} was deduced from $M_\star$ and the RV orbital semi-amplitude K, which was set to the value of 109 ± 4.4 m/s reported by Triaud et al. (2015). The other physical parameters of the system were deduced from the jump parameters, $M_\star$, and $R_\star$.

Date [UT]	Wavelength [nm]	σ_{120s} [%]	β_w	β_r	CF
16 June 2013	740–760	0.084	1.31	3.42	4.47
16 June 2013	760–780	0.119	2.00	1.79	3.58
16 June 2013	780–800	0.040	0.67	2.81	1.89
16 June 2013	800–820	0.035	0.64	2.64	1.70
16 June 2013	820–840	0.031	0.67	1.56	1.05
16 June 2013	840–860	0.052	1.19	1.00	1.19
16 June 2013	860–880	0.032	0.78	1.15	0.89
16 June 2013	880–900	0.030	0.67	1.36	0.91
16 June 2013	900–920	0.030	0.68	1.90	1.30
16 June 2013	920–940	0.033	0.77	1.40	1.08
16 June 2013	940–960	0.051	0.91	1.94	1.76
16 June 2013	960–980	0.044	0.71	2.70	1.92
16 June 2013	980–1000	0.048	0.80	1.36	1.08
16 June 2013	1000–1020	0.063	0.94	1.00	0.94
29 July 2013	740–760	0.134	1.66	3.23	5.35
29 July 2013	760–780	0.083	1.55	1.11	1.71
29 July 2013	780–800	0.052	0.98	1.61	1.58
29 July 2013	800–820	0.059	1.09	1.39	1.52
29 July 2013	820–840	0.059	1.09	1.35	1.47
29 July 2013	840–860	0.094	1.69	1.32	2.23
29 July 2013	860–880	0.078	1.50	1.27	1.90
29 July 2013	880–900	0.070	1.34	1.05	1.40
29 July 2013	900–920	0.103	1.79	1.17	2.09
29 July 2013	920–940	0.226	3.34	1.11	3.72
29 July 2013	940–960	0.346	4.44	1.22	5.41
29 July 2013	960–980	0.095	1.63	1.08	1.77
29 July 2013	980–1000	0.061	1.02	1.03	1.04
29 July 2013	1000–1020	0.093	1.19	1.20	1.42

TABLE 4.2: For each spectrophotometric transit light curve, this table shows the night of acquisition (UT), the wavelength bin (nm), the standard deviation of the best-fit residuals (binned per intervals of 2min), and the values for β_w, β_r, and $CF = \beta_w \times \beta_r$ (see Section 2.5 for details).

4.3.4 Results and discussion

The best-fit transit models in each wavelength bin are shown in Fig. 4.5. The derived system parameters and 1-σ error bars are presented in Table 4.3. They are in good agreement (within error bars) with those reported in previous studies (e.g. Triaud et al. 2015). The transmission spectrum of WASP-80 b between 740 and 1020nm derived from the MCMC analysis (i.e. the values of $R_\mathrm{p}/R_\star$ obtained for each wavelength bin) is given at the bottom of Table 4.3 and is shown in Fig. 4.7.

The average precision on $R_\mathrm{p}/R_\star$ is ∼0.09%. Using Equation 1.32 to calculate the atmospheric scale height H of WASP-80 b yields a value of ∼241 km, assuming T=T_eq=825K (Table 4.3), μ_m=2.3 atomic mass units (H/He dominated atmosphere, see e.g. de Wit and Seager 2013), and g_p=14.2 m/s^2 (Table 4.3). An increase in the planet's effective radius of $1H$ due to atmospheric absorption would lead to a variation in $R_\mathrm{p}/R_\star$ of ∼0.06%. The average error on $R_\mathrm{p}/R_\star$ is thus equivalent to ∼$1.5H$, which is below the expectations of this study that initially aimed at achieving sub-H precisions on $R_\mathrm{p}/R_\star$ per 20nm-wide wavelength bin. This is due to both the reduced data set (one full and one partial transit instead of four full transits) and the strong LADC-induced correlated noise, whose modeling is complex and which significantly affects the precision on the derived transmission spectrum.

The detailed interpretation of the obtained transmission spectrum (including comparison to model transmission spectra) is currently ongoing. Here, I will only give some preliminary results. A horizontal straight line, such as expected if a high-altitude cloud deck efficiently obscures all atmospheric spectral features, provides a fairly good fit to the transmission spectrum with a χ^2 value of 18.5 for 13 degrees of freedom (reduced χ^2=1.42). A better fit is given by a linear function over wavelength (see Fig. 4.7) with a χ^2 value of 8.9 for 12 degrees of freedom (reduced χ^2=0.74). A slope is detected to a significance of 3.6σ with a value of $(-9.64 \pm 2.67) \times 10^{-6}$ (wavelength in nm). Except for this slope, the transmission spectrum is mostly featureless within the measurement uncertainties.

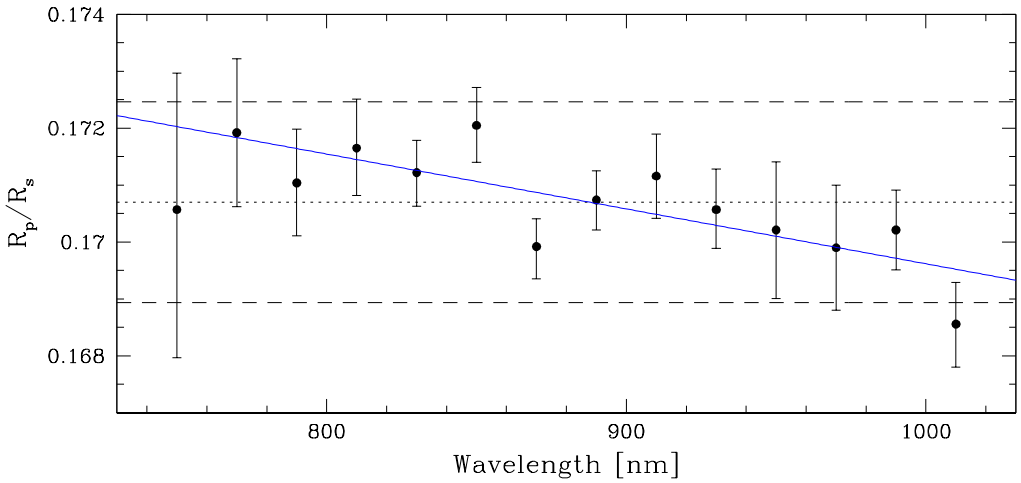

FIGURE 4.7: The transmission spectrum of WASP-80 b between 740 and 1020nm. The horizontal lines represent the weighted average (dotted line) and plus/minus three atmospheric scale heights (dashed lines). These lines are indicated to give an idea of the variability and overall precision of the transmission spectrum. Overplotted in blue is the best fit of a linear function over wavelength.

TABLE 4.3: System parameters. Median values and 1-σ limits of the posterior probability distribution functions derived from the global MCMC analysis.

Parameters	**Values**	**Units**
Stellar parameters		
Effective temperature $T_{\rm eff}$	4145 ± 100	K
Metallicity [Fe/H]	-0.14 ± 0.16	dex
Surface gravity log $g_\star$	$4.664^{+0.012}_{-0.014}$	cgs
Mean density $\rho_\star$	$2.853^{+0.035}_{-0.029}$	$\rho_\odot$
Mass $M_\star$	$0.583^{+0.048}_{-0.050}$	$M_\odot$
Radius $R_\star$	$0.589^{+0.016}_{-0.017}$	$R_\odot$
Planet parameters		
Transit depth $\mathrm{d}F_{[860-880\mathrm{nm}]} = (R_{\mathrm{p},[860-880\mathrm{nm}]}/R_\star)^2$	$2.887^{+0.017}_{-0.019}$	%
Transit impact parameter $b' = a\cos i_{\rm p}/R_\star$	$0.240^{+0.013}_{-0.017}$	$R_\star$
Transit width W	$0.08875^{+0.00011}_{-0.00013}$	d
Time of inferior conjunction T_0 - 2 450 000	6487.425022 ± 0.000031	$\mathrm{BJD_{TDB}}$
Orbital period P	$3.0678516^{+0.0000033}_{-0.0000038}$	d
Scaled semi-major axis $a/R_\star$	$12.60^{+0.05}_{-0.04}$	–
Orbital semi-major axis a	$0.0345^{+0.0009}_{-0.0010}$	AU
Orbital inclination $i_{\rm p}$	$88.91^{+0.08}_{-0.06}$	deg
Equilibrium temperature[a] $T_{\rm eq}$	825 ± 20	K
Surface gravity log $g_{\rm p}$	3.153 ± 0.005	cgs
Mean density $\rho_{\rm p}$	$0.552^{+0.019}_{-0.017}$	$\rho_{\rm Jup}$
Mass $M_{\rm p}$	$0.544^{+0.029}_{-0.032}$	$M_{\rm Jup}$
Radius $R_{\mathrm{p},[860-880\mathrm{nm}]}$	$0.995^{+0.027}_{-0.030}$	$R_{\rm Jup}$
Planet/star radius ratio $R_{\rm p}/R_\star$ (transmission spectrum)		
$R_{\mathrm{p},[740-760\mathrm{nm}]}/R_\star$	$0.17057^{+0.00240}_{-0.00260}$	–
$R_{\mathrm{p},[760-780\mathrm{nm}]}/R_\star$	0.17192 ± 0.00130	–
$R_{\mathrm{p},[780-800\mathrm{nm}]}/R_\star$	$0.17104^{+0.00094}_{-0.00093}$	–
$R_{\mathrm{p},[800-820\mathrm{nm}]}/R_\star$	$0.17165^{+0.00086}_{-0.00083}$	–
$R_{\mathrm{p},[820-840\mathrm{nm}]}/R_\star$	$0.17122^{+0.00057}_{-0.00059}$	–
$R_{\mathrm{p},[840-860\mathrm{nm}]}/R_\star$	$0.17205^{+0.00067}_{-0.00065}$	–
$R_{\mathrm{p},[860-880\mathrm{nm}]}/R_\star$	$0.16992^{+0.00049}_{-0.00057}$	–
$R_{\mathrm{p},[880-900\mathrm{nm}]}/R_\star$	$0.17074^{+0.00051}_{-0.00053}$	–
$R_{\mathrm{p},[900-920\mathrm{nm}]}/R_\star$	0.17116 ± 0.00074	–
$R_{\mathrm{p},[920-940\mathrm{nm}]}/R_\star$	$0.17057^{+0.00071}_{-0.00068}$	–
$R_{\mathrm{p},[940-960\mathrm{nm}]}/R_\star$	0.17021 ± 0.00120	–
$R_{\mathrm{p},[960-980\mathrm{nm}]}/R_\star$	0.16990 ± 0.00110	–
$R_{\mathrm{p},[980-1000\mathrm{nm}]}/R_\star$	0.17021 ± 0.00070	–
$R_{\mathrm{p},[1000-1020\mathrm{nm}]}/R_\star$	$0.16856^{+0.00073}_{-0.00076}$	–

Notes. [a]Assuming a null Bond albedo and isotropic reradiation (reradiation factor f=1/4, López-Morales and Seager 2007).

Slopes in hot Jupiters' transmission spectra across the optical wavelength range are often associated with scattering from high-altitude aerosols (see e.g. Sing et al. 2011b, Nikolov et al. 2015, Sing et al. 2016). The slope observed here extends over $\sim 6H$ (see Fig. 4.7), which is large considering the 280nm-wide wavelength range probed. For comparison, Sing et al. (2011) found a slope in the transmission spectrum of HD 189733 b that spans $\sim 6H$ from 350 to 1000nm (see their Fig. 14). Assuming a power-law relation between the wavelength (λ) and cross-section (σ) of the scattering species of the form $\sigma = \sigma_0(\lambda/\lambda_0)^\alpha$, the variation of R_p as a function of λ due to scattering is given by $\mathrm{d}R_\mathrm{p}/\mathrm{d}\ln\lambda = \alpha H$ (Lecavelier Des Etangs et al. 2008). Using Equation 1.32, this relation can be rewritten as:

$$\alpha T = \frac{\mu_\mathrm{m}\, g_\mathrm{p}}{k_\mathrm{B}} \frac{\mathrm{d}R_\mathrm{p}}{\mathrm{d}\ln\lambda} \tag{4.1}$$

Fitting this relation to the transmission spectrum of WASP-80 b results in $\alpha T = -10829 \pm 3435$ K. Assuming that the slope in the transmission spectrum is caused by Rayleigh scattering ($\alpha = -4$, Lecavelier Des Etangs et al. 2008), a temperature T of 2707 $\pm$ 859 K is obtained. Since transmission spectroscopy probes the planet's upper atmosphere at the day-night terminator, the temperature derived here is supposed to be the temperature at this region. Triaud et al. (2015) found a dayside brightness temperature $\sim$900K (in the *Spitzer* channels) and the planet's equilibrium temperature T_eq is 825$\pm$20K (Table 4.3). The terminator temperature is expected to be lower than the dayside temperature and of roughly the same order as T_eq. The temperature derived here assuming Rayleigh scattering thus seems unrealistically high. Alternatively, assuming T=T_eq, a value of -13.13 ± 4.17 is derived for α. The slope observed in the transmission spectrum of WASP-80 b thus appears to be marginally inconsistent (at the $\sim 2.2\sigma$ level) with Rayleigh scattering. Mie scattering from sub-micron size aerosol particles could maybe provide a better explanation of the slope. This possibility is currently being explored.

Unocculted star spots, i.e. spots on the stellar surface that are not crossed by the planet during transit, could create a slope in the transmission spectrum (e.g. McCullough et al. 2014). Indeed, such spots would cause a difference in surface brightness between the parts of the stellar disk that are visible and masked during transit (besides the effect of limb-darkening), slightly modifying the relation between the observed transit depth and the planet-to-star radius ratio. Spots being cooler than the surrounding photosphere, this effect would be stronger at shorter (bluer) wavelengths. This would make the planetary radius appear larger at shorter wavelengths than at longer wavelengths, and produce a blueward slope in the transmission spectrum, as observed here. With an activity index $\log R'_\mathrm{HK} = -4.495$ (Mancini et al. 2014), WASP-80 shows strong chromospheric activity (Noyes et al. 1984) and is thus expected to be spotted. There is, however, no sign of rotational modulation in the photometry (Triaud et al. 2013, Fukui et al. 2014), nor spot-crossing events in the transit light curves that were previously published or are presented here. One possible explanation is that many small spots, undetectable in the transit light curves, are approximately symmetrically distributed on the stellar surface. The star could also present a continuously spotted active latitude or have its rotation axis oriented towards Earth (i.e. be seen nearly pole-on).

The possible effect of unocculted star spots on the transmission spectrum of WASP-80 b can be estimated using the method described by Sing et al. (2011). This method assumes (1) that the quiet photosphere and the spots have spectral energy distributions well described by stellar atmosphere models of effective temperatures $T_\star$ and T_spot, respectively, and (2)

that the fractional change in flux Δf_{λ_0} caused by spots (total change compared to a spot-free surface) at a reference wavelength λ_0 can be measured or estimated. The fractional change in $R_\mathrm{p}/R_\star$ with wavelength due to stellar spots can then be expressed as (combination of Equations 4 and 5 of Sing et al. 2011b):

$$\frac{\Delta(R_p/R_\star)}{R_p/R_\star} = \frac{1}{2}\,\Delta f_{\lambda_0}\,\left(1-\frac{F_\lambda^{T_\mathrm{spot}}}{F_\lambda^{T_\star}}\right)\Big/\left(1-\frac{F_{\lambda_0}^{T_\mathrm{spot}}}{F_{\lambda_0}^{T_\star}}\right) \tag{4.2}$$

where F_λ^T is the surface brightness of a star with effective temperature T at the wavelength λ, given by stellar atmosphere models. Fukui et al. (2014) conducted a 43-day long photometric monitoring of WASP-80 a few weeks after the FORS2 observations were taken and reported a photometric variability lower than 0.5% (upper limit on the peak-to-peak amplitude) in the I_c band. Taking this upper limit as value for Δf_{λ_0} (λ_0=800nm) and using Phoenix synthetic stellar spectra (Husser et al. 2013) to model the surface brightnesses, $\Delta R_\mathrm{p}/R_\star$ was computed for $T_\star$=4100K[8] and three different realistic values for T_spot (3900K, 3500K, and 3100K, see e.g. Fig. 2 of Andersen and Korhonen 2015). The result is shown in Fig. 4.8 for the whole optical range (top) and for the wavelength region probed by the FORS2 observations (bottom). Overall, the possible effect of unocculted star spots on the FORS2 transmission spectrum of WASP-80 b is expected to be very small, with a maximum amplitude $< 5\times10^{-4}$, well comprised within the error bars of the FORS2 measurements. The slope observed here is thus most likely not caused by unocculted stellar spots.

An unresolved stellar object, either gravitationally bound or aligned along the line of sight, and redder than WASP-80, could also produce a blueward slope in the transmission spectrum. Indeed, the dilution of the transit depth by such a redder star would be stronger at longer wavelengths, thus making the planetary radius appear smaller at longer wavelengths than at shorter ones. The diluted transit depth $\mathrm{d}F_{\mathrm{diluted},\lambda}$ measured at the wavelength λ in the presence of a contaminant star can be expressed as (Equation 3 of Daemgen et al. 2009):

$$\mathrm{d}F_{\mathrm{diluted},\lambda} = \frac{\mathrm{d}F_\lambda}{1+10^{-\Delta mag_\lambda/2.5}} \tag{4.3}$$

where $\mathrm{d}F_\lambda$ and Δmag_λ are, respectively, the true (undiluted) transit depth and the magnitude difference between WASP-80 and the contaminant star at the wavelength λ. In terms of transit depth, the slope observed here extends over ∼1200ppm. To cause this slope, the contaminant star would have to be at least ∼4.3% as bright as WASP-80 in the wavelength bin [1000-1020nm] ($\Delta mag_{[1000-1020\mathrm{nm}]}$ ∼3.4)[9]. A lucky imaging search by Wöllert et al. (2015) did not detect any previously unresolved stellar object around WASP-80, with 5σ z'-band sensitivity limits $\Delta mag_{z'}$ of 4.01, 5.03, 6.11, and 6.64 at angular separations of 0.25″, 0.5″, 1.0″, and 2.0″, respectively. It is therefore unlikely that the slope is caused by an unresolved star.

Finally, a comparison of the FORS2 transmission spectrum of WASP-80 b to the literature data for this system is shown in Fig. 4.9. The FORS2 measurements are in good

[8]The closest temperature to the effective temperature of WASP-80 (4145±100K) available in the models grid.

[9]A magnitude difference $\Delta mag_{[1000-1020\mathrm{nm}]}$ ∼3.4 is obtained assuming that the dilution of the transit depth at the shortest wavelengths probed by the FORS2 observations is negligible, which in practice would not be the case since these wavelengths are in the far red. This is thus a maximum magnitude difference.

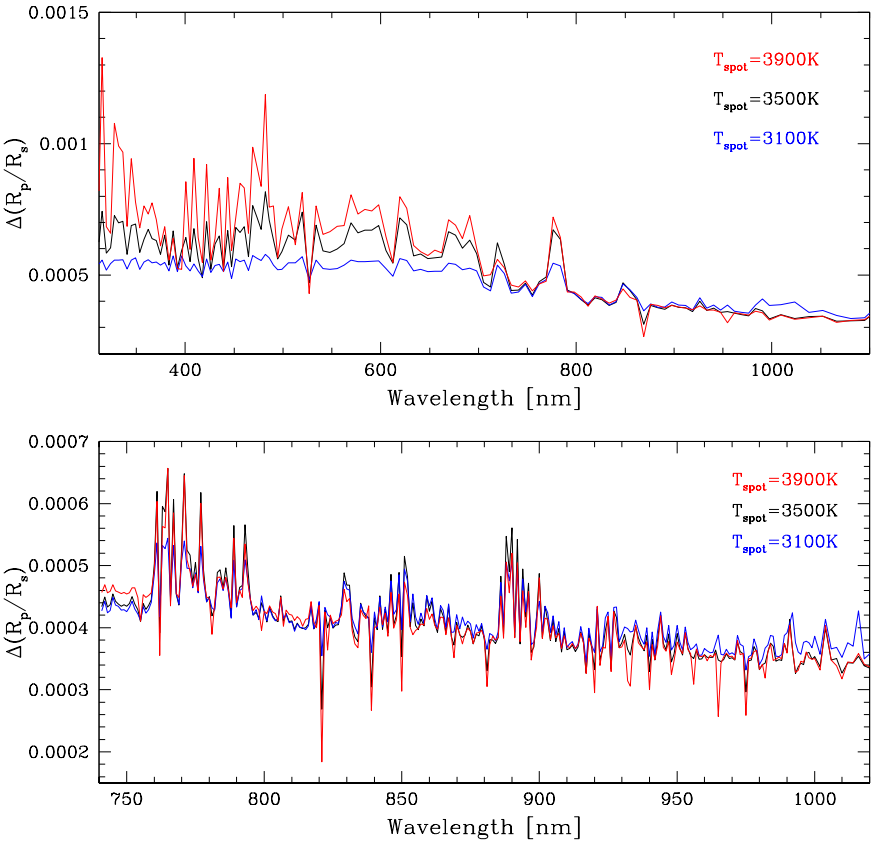

FIGURE 4.8: Expected effect of unocculted star spots on the transmission spectrum of WASP-80 b for three different spot temperatures, assuming that these spots produce a fractional change in flux of 0.5% at 800nm. This effect was estimated using the method described on pages 135-136.
Top: The effect is shown for the whole optical range.
Bottom: "Zoom" on the wavelength region probed by the FORS2 observations.

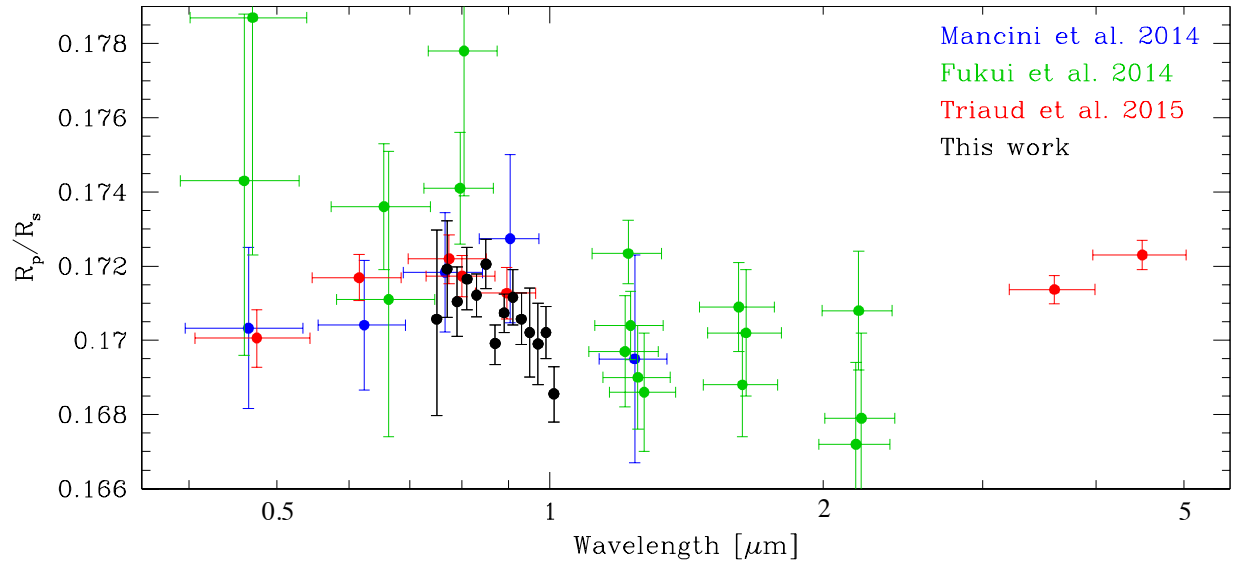

FIGURE 4.9: The FORS2 measurements (black) together with the broad-band values reported by Mancini et al. (2014, blue), Fukui et al. (2014, green), and Triaud et al. (2015, red). For the broad-band measurements, the horizontal error bars indicate the FWHM of the passbands used. When there are multiple measurements at one passband, the data points are slightly shifted in the horizontal direction for visual convenience.

agreement with the broad-band $R_{\rm p}/R_\star$ values reported by Mancini et al. (2014) and Triaud et al. (2015) in the same wavelength range (broad-band filters Sloan i', Bessel I, and Sloan z'). The values reported by Fukui et al. (2014) in the $I_{\rm c}$ band are marginally higher ($\lesssim 2\sigma$) than the FORS2 measurements covering this wavelength range. However, their results should be regarded with caution as some transit parameters were kept fixed in their analysis, which usually results in underestimated error bars.

4.3.5 Conclusions

The transmission spectrum of WASP-80 b between 740 and 1020 nm derived from FORS2 observations of two transits shows a slope of increasing planetary radius from longer towards shorter wavelengths, detected to a significance of 3.6σ. This slope is marginally inconsistent with Rayleigh scattering (at the $\sim 2.2\sigma$ level) and is not likely to be caused by unocculted star spots or an unresolved stellar object. Further investigation of its possible origin is ongoing. Except for this slope, the transmission spectrum does not display any obvious additional features, within the measurement uncertainties. The precision of the transmission spectrum is however below expectations and would strongly benefit from further observations.

4.4 The potential of FORS2 for transmission spectrophotometry of exoplanets

The studies presented in this chapter demonstrate that reasonably precise transmission spectra can be obtained with FORS2, even in the presence of strong LADC-induced correlated noise, provided that several good-quality transit observations are gathered (i.e. full transits, good weather, relatively stable seeing). Systematics stemming from the LADC nonetheless clearly hampered the precisions reached on the transmission spectra of WASP-49 b and WASP-80 b. These results were communicated to ESO staff members who were concerned about this issue, and a project was set up at Paranal to exchange the FORS2 LADC prisms with the uncoated ones of the decommissioned FORS1 twin instrument (Boffin et al. 2015). This upgrade took place in November 2014 and a few months later, a FORS2 transmission spectrum of WASP-19 b was published by Sedaghati et al. (2015), announcing that the FORS had been regained[10]. Although the precision of this transmission spectrum was affected by poor weather conditions during the observations (thin cirrus clouds), the transit light curves are smooth and do not show strong correlated noise, which seems to indicate that the performance of FORS2 has indeed been restored. This was confirmed by more recent successful observations of WASP-17 (Sedaghati et al. in prep., private communication). FORS2 thus appears to be now a competitive instrument for transmission spectrophotometry of exoplanets.

[10] Reference to the title of their paper.

Chapter 5

Atmospheric properties of WASP-103 b from ground-based multi-band photometry

In this chapter, I present the results of an extensive ground-based photometric follow-up campaign of the ultra-hot gas giant planet WASP-103 b (Gillon et al. 2014). The draft paper presenting this study, which should be submitted soon to MNRAS, is reproduced in the following pages. Here, I provide a summary of this work.

WASP-103 b has already been briefly introduced in Section 3.2.5. The planet has a mass of $\sim$1.5 $M_{\rm Jup}$, an inflated radius of $\sim$1.6 $R_{\rm Jup}$, and is in an ultra-short-period orbit ($\sim$22.2hrs) around a relatively bright (V=12.1, K=10.8) F8V star. Its large size, low mean density ($\sim$0.3 $\rho_{\rm Jup}$), extreme irradiation ($\sim 9 \times 10^9$ erg $\rm s^{-1}cm^{-2}$) and thus high equilibrium temperature ($\sim$2500K assuming a null Bond albedo and an efficient day-night heat redistribution), as well as the brightness of its host star make it a prime target for atmospheric characterization, using both transmission and emission spectroscopy.

On this ground, I decided to request time on the CFHT/WIRCam near-infrared facility (Puget et al. 2004, 3.6m Canada-France-Hawaii Telescope, Mauna Kea Observatory, Hawaii) to observe two occultations of WASP-103 b in the H (1.6 μm) and $K_{\rm S}$ (2.1 μm) bands (one in each filter), with the aim of probing its dayside emission spectrum in these two wavelength bands. The requested time was awarded (OPTICON program 14A/038, PI: Delrez), but one night was lost due to bad weather, so that only the occultation in the $K_{\rm S}$-band was observed (service mode). From these data, I was able to detect the planet's dayside thermal emission at $\sim$10-σ, with a measured occultation depth of 3567^{+400}_{-350} ppm. In parallel, an intense photometric monitoring of the planet's occultations in the z'-band was carried out, using both TRAPPIST and Euler/EulerCam (collaboration with Monika Lendl). By combining 15 occultation light curves, we detected the planet's dayside emission in the z'-band at better than 6-σ, the measured occultation depth being 699$\pm$110ppm. We also obtained three additional transit light curves (in EulerCam r' and TRAPPIST "blue-blocking" filters), as well as five new Euler/CORALIE RV measurements (provided by Marion Neveu).

WASP-103 b had already been heavily followed-up by Southworth et al. (2015), who published 17 transit light curves in various broad-band optical filters (g', r', R, i', I, z'). The resulting broad-band transmission spectrum showed a slope, larger values of the effective planetary radius being obtained at bluer wavelengths, which they found to be too steep to be mainly caused by Rayleigh scattering in the planetary atmosphere. Subsequent to their study, a previously unresolved faint star was found via lucky imaging by Wöllert and Brandner (2015) at an angular separation of only 0.24″ from WASP-103. This object, which

was also recently imaged by Ngo et al. (2016), is significantly redder than WASP-103 and may be either gravitationally bound or simply aligned along the line of sight. Contamination from this redder star, if not accounted for, is expected to produce a blueward slope in the transmission spectrum of WASP-103 b, the transit signal being more strongly diluted at longer wavelengths than at shorter ones. This recently led Southworth and Evans (2016) to publish a reanalysis of the data presented in Southworth et al. (2015), accounting for the presence of the contaminating star. They found the inclusion of contaminating light from the faint star in their analysis to have no significant effect on the derived system physical properties. They also reported a corrected broad-band transmission spectrum showing, instead of a steep slope, a minimum effective planetary radius around 760nm and increasing values towards both bluer and redder wavelengths. They found this "V-shape" to be not well reproduced by existing theoretical models of transmission spectra.

In the study presented here, I combined our new observations with the data previously published in Gillon et al. (2014, 5 transit light curves and 18 RVs) and Southworth et al. (2015), and performed a global MCMC analysis (cf. Section 2) of the whole data set (41 eclipse light curves and 23 RVs), taking into account the contamination from the faint nearby star. The resulting transmission and emission measurements were then compared to model atmospheric spectra of WASP-103 b, generated by Nikku Madhusudhan. The planet's broad-band optical transmission spectrum seems to be better explained by atmosphere models containing either high-altitude hazes or gaseous TiO. On the emission side, the brightness temperatures ($T_{\rm B}$) derived from our z' and $K_{\rm S}$-band occultation measurements suggest a peculiar feature, to be confirmed: the $T_{\rm B}$ in the $K_{\rm S}$-band (3148^{+144}_{-130} K) is marginally higher ($\sim$1.5σ) than the $T_{\rm B}$ in the z'-band (2914^{+80}_{-87} K). While the $K_{\rm S}$-band is relatively devoid of strong molecular absorption, with the exception of some weak absorption due to CO, the z'-band is affected by strong TiO spectral features. Gaseous TiO, if present in a hot Jupiter's atmosphere, is usually expected to lead to a temperature inversion (cf. Section 1.2.3). If detected in a planet's dayside emission spectrum, TiO spectral features are thus expected to be seen in emission (i.e. $T_{{\rm B},z'} > T_{{\rm B},K_{\rm S}}$) rather than absorption (i.e. $T_{{\rm B},z'} < T_{{\rm B},K_{\rm S}}$, cf. Section 1.1.2), the latter case being what we tentatively found in our data. Two models can explain our thermal emission measurements: a model with a thermal inversion, low TiO abundance, and high CO abundance, or a model without a thermal inversion and with the opposite composition, i.e. modest CO abundance but a non-negligible TiO abundance. Both models require a TiO abundance of at least 0.1$\times$ that predicted for thermochemical equilibrium with solar elemental abundances. These results, both in transmission and emission, are currently tentative and more data are required to place better constraints on the chemical composition and P-T profile of this planet's atmosphere.

MNRAS **000**, 1–14 (2015) Preprint 30 August 2016 Compiled using MNRAS LATEX style file v3.0

Atmospheric properties of WASP-103 b from ground-based multi-wavelength photometry

L. Delrez,[1]⋆ N. Madhusudhan,[2] M. Lendl,[3,4] M. Gillon,[1] D. R. Anderson,[5] M. Neveu-VanMalle,[3,6] A. H. M. J. Triaud,[2,3] P. Magain,[1] A. Burdanov,[1] A. Collier-Cameron,[7] B.-O. Demory,[6] C. Hellier,[5] E. Jehin,[1] P. F. L. Maxted,[5] D. Queloz[6,3] and B. Smalley[5]

[1] *Space sciences, Technologies and Astrophysics Research (STAR) Institute, Université de Liège, allée du 6 Août 17, 4000 Liège, Belgium*
[2] *Institute of Astronomy, University of Cambridge, Cambridge CB3 0HA, UK*
[3] *Space Research Institute, Austrian Academy of Sciences, Schmiedlstr. 6, 8042 Graz, Austria*
[4] *Observatoire de Genève, Université de Genève, 51 Chemin des Maillettes, 1290 Sauverny, Switzerland*
[5] *Astrophysics Group, Keele University, Staffordshire, ST5 5BG, UK*
[6] *Astrophysics Group, Cavendish Laboratory, J.J. Thomson Avenue, Cambridge CB3 0HE, UK*
[7] *SUPA, School of Physics and Astronomy, University of St. Andrews, North Haugh, Fife, KY16 9SS, UK*

Accepted XXX. Received YYY; in original form ZZZ

ABSTRACT

We present sixteen occultation light curves and three transit light curves for the ultra-short period hot Jupiter WASP-103 b, in addition to five new measurements of the radial velocity of the star. We combine these new observations with previously published data and perform a global analysis of the resulting extensive data set, accounting for the contamination from a recently-discovered faint nearby star. The resulting broad-band optical transmission spectrum is better explained by atmosphere models containing either high-altitude hazes or gaseous TiO. We detect the thermal emission from the dayside of the planet in both the z' and K_S-bands, the measured occultation depths being 699±110 ppm (6.3-σ detection) and 3567^{+400}_{-350} ppm (10.2-σ detection), respectively. These measurements can be explained by two models: a model with a thermal inversion, low TiO abundance, and high CO abundance, or a model without a thermal inversion and with the opposite composition, i.e. modest CO abundance but a non-negligible TiO abundance. Both models require a TiO abundance of at least 0.1× that predicted for thermochemical equilibrium with solar elemental abundances. These results, both in transmission and emission, are currently tentative and more data are required to place better constraints on the chemical composition and *P-T* profile of this planet's atmosphere.

Key words: planetary systems – planets and satellites: atmospheres – stars: individual: WASP-103 – techniques: photometric – techniques: radial velocities –

1 INTRODUCTION

Transiting extrasolar planets are key objects for the understanding of worlds beyond our Solar System, as they provide a wealth of information about their systems. Thanks to their special orbital configuration, we can not only measure their radius, true mass (in combination with radial velocity measurements), and orbital parameters, but we can also study their atmosphere and thus gain a complete picture of their chemical and physical properties (e.g. Deming & Seager 2009, Winn 2010). These atmospheric studies are conducted using mainly the transmission and emission (spectro)photometry techniques. During a transit, some of the starlight passes through the planetary atmosphere and, depending on the atmospheric extent, temperature, and composition, wavelength-dependent variations are seen in the amount of absorbed flux. Thus, from multi-wavelength transit light curves, a transmission spectrum of the upper atmo-

⋆ E-mail: ldelrez@ulg.ac.be

sphere at the day-night terminator region can be obtained (e.g. Seager & Sasselov 2000, Charbonneau et al. 2002). At the opposite conjunction, when the planet passes behind the star during a secondary eclipse (occultation), one can measure the flux drop caused by the elimination of the flux component originating from the dayside of the planet (e.g. Deming et al. 2005, Charbonneau et al. 2005). Using this technique at different wavelengths allows to probe the emission spectrum of the planet's dayside, from which insights on its atmospheric composition and vertical pressure-temperature profile, as well as on the day-night energy redistribution efficiency, can be gained (e.g. Madhusudhan & Seager 2009).

Such observations have revealed a broad diversity of atmospheres across the population of close-in transiting gas giant exoplanets (see e.g. Sing et al. 2016). Some planets have sufficiently clear atmospheres to allow detections of atomic and molecular species, in particular Na (e.g. Nikolov et al. 2014), K (e.g. Sing et al. 2011), and H_2O (e.g. Huitson et al. 2013), while others appear to contain high-altitude clouds or hazes that completely mute the spectral features of the atmospheric components (see e.g. Gibson et al. 2013, Lendl et al. 2016). Even when detected, atmospheric spectral signatures are often less pronounced than predicted by theoretical models of clear atmospheres with solar abundances (e.g. Deming et al. 2013), suggesting that an extra opacity source is still present, at some level, in otherwise predominantly cloud-free atmospheres. This picture is supported by evidences for high-altitude atmospheric hazes reported for several hot Jupiters (see e.g. Nikolov et al. 2015, Sing et al. 2015, Sing et al. 2016), based on their Rayleigh or Mie scattering signature in the planets' transmission spectra. Hot Jupiters also exhibit a wide variety of day-night energy redistribution efficiencies, but appear to be following a trend in which hottest planets are usually less efficient at redistributing the incident stellar energy than colder planets (e.g. Cowan & Agol 2011); a behavior that is naturally explained by atmospheric circulation models (e.g. Perez-Becker & Showman 2013).

By contrast, most observations seem to indicate atmospheric vertical pressure-temperature profiles without significant thermal inversions. Temperature inversions were predicted by early theoretical studies of highly irradiated giant planets, that suggested two classes of hot Jupiters based on their degree of irradiation (e.g. Fortney et al. 2008); the hotter class was predicted to host thermal inversions in their atmospheres due to strong absorption of incident UV/visible irradiation at high altitude by high-temperature absorbers, such as gaseous TiO and VO (commonly found in low-mass stars and brown dwarfs), while cooler atmospheres were expected to be devoid of thermal inversions due to the condensation of these absorbing compounds. Thermal inversions have been previously claimed for several hot Jupiters based on *Spitzer* observations (e.g. Knutson et al. 2008, Machalek et al. 2008, Knutson et al. 2009), but these detections were recently seriously called into question (e.g. Hansen et al. 2014, Diamond-Lowe et al. 2014, Schwarz et al. 2015). It has been suggested that TiO and VO may not remain suspended in the upper atmospheres of hot Jupiters due to cold-trapping, that would occur either deeper in the dayside atmosphere or on the cooler nightside, and would cause their condensation and downward drag by gravitational settling (e.g. Spiegel et al. 2009). Inversion-causing compounds may also be photodissociated by high chromospheric emission from the host star, so that the formation of inversions may be correlated with stellar activity (e.g. Knutson et al. 2010). Another important factor is the atmospheric chemistry; for example, the atmospheric carbon-to-oxygen (C/O) ratio can control the abundance of TiO/VO, with a C/O $\geq$ 1 causing substantial depletion of TiO/VO, most available oxygen being taken up by CO molecules in this case thus leaving no oxygen for gaseous TiO/VO (Madhusudhan 2012). Nevertheless, hottest planets are still the best candidates to host thermal inversions in their dayside atmospheres. Indeed, the only planet showing clear evidence for a temperature inversion to date is WASP-33 b (Haynes et al. 2015), that orbits an A-type δ-Scuti star once every 1.22 days and is the most highly irradiated hot Jupiter currently known (Collier Cameron et al. 2010). In this work, we study the atmospheric properties of another ultra-hot gas giant, WASP-103 b (Gillon et al. 2014, hereafter G14).

This extreme hot Jupiter, discovered by the WASP Collaboration (Pollacco et al. 2006, Collier Cameron et al. 2007, Hellier et al. 2011), has a mass of ~1.5 $M_{\rm Jup}$, an inflated radius of ~1.6 $R_{\rm Jup}$, and is in an ultra-short-period orbit (~22.2hrs) around a relatively bright (V = 12.1, K = 10.8) F8V star (G14). With an incident stellar flux of $\sim 9 \times 10^9$ erg s^{-1}cm^{-2}, it is the third most highly irradiated hot Jupiter known to date, after WASP-33 b (Collier Cameron et al. 2010) and WASP-12 b (Hebb et al. 2009). Assuming a null Bond albedo and an efficient heat redistribution between both planetary hemispheres, it is heated to an equilibrium temperature close to 2500 K. These properties make WASP-103 b an exquisite target for atmospheric characterization. Another interesting fact about this planet is that its orbital semi-major axis is also only ~1.16 times larger than its Roche limit, meaning that the planet might be close to tidal disruption. WASP-103 b is thus also a favorable object for studying the atmospheric properties of hot Jupiters in the final stages of their life.

Southworth et al. (2015, hereafter S15) published high-precision follow-up transit photometry of WASP-103 b in several broad-band optical filters, which they used to refine the physical and orbital parameters of the system. They also detected a slope in the resulting broad-band transmission spectrum, larger values of the effective planetary radius being obtained at bluer wavelengths, which they found to be too steep to be mainly caused by Rayleigh scattering in the planetary atmosphere. Subsequent to their study, a previously unresolved faint star was found via lucky imaging by Wöllert & Brandner (2015, hereafter W15) at an angular separation of only 0.24″ from WASP-103. This object, which was also recently imaged by Ngo et al. (2016, hereafter N16), is significantly redder than WASP-103 and may be either gravitationally bound or simply aligned along the line of sight. Contamination from this redder star, if not accounted for, is expected to produce a blueward slope in the transmission spectrum of WASP-103 b, the transit signal being more strongly diluted at longer wavelengths than at shorter ones. This recently led Southworth & Evans (2016, hereafter S16) to publish a reanalysis of the data presented in S15, accounting for the presence of the contaminating star. They found the inclusion of contaminating light from the faint star in their analysis to have no significant effect on the derived system physical properties. They also reported

a corrected broad-band transmission spectrum showing, instead of a steep slope, a minimum effective planetary radius around 760nm and increasing values towards both bluer and redder wavelengths. This "V-shape" is not well reproduced by existing theoretical models of transmission spectra.

To improve the atmospheric characterization of WASP-103 b, we carried out an intense ground-based photometric monitoring of its occultations, with the aim of probing its dayside emission spectrum in the z' (0.9 μm) and K_S (2.1 μm) bands. We complemented the data acquired in the frame of this program with some additional transit photometry and radial velocity (RV) measurements, combined all these new observations with the data previously published in G14 and S15, and performed a global analysis of the resulting extensive data set, taking into account the contamination from the faint star. We present here the results of this work. The observations and data reduction are described in Section 2. In Section 3, we present our detailed data analysis and results. We discuss these results in Section 4, before concluding in Section 5.

2 OBSERVATIONS AND DATA REDUCTION

2.1 New data

Between May 2014 and July 2015, we gathered a total of nineteen eclipse light curves of WASP-103 b. Sixteen of these light curves were acquired during occultations of the planet and three during transits. This follow-up photometry was obtained using three different instruments: the 0.6m TRAPPIST robotic telescope and the EulerCam CCD camera on the 1.2m *Euler*-Swiss telescope, both located at ESO La Silla Observatory (Chile), as well as the WIRCam near-infrared imager on the 3.6m Canada-France-Hawaii Telescope (CFHT) at Mauna Kea Observatory (Hawaii). We complemented this dataset with five new RV measurements obtained between Sept. 2013 and Sept. 2014 with the CORALIE spectrograph mounted on the *Euler* telescope. The follow-up light curves are summarized in the upper part of Table 1, while the RVs are presented in Table 2. We describe these new data in the sections below.

2.1.1 TRAPPIST eclipse photometry

We observed one transit and nine occultations of WASP-103 b using the 0.6m TRAPPIST robotic telescope and its thermoelectrically-cooled 2K×2K CCD (field of view of 22′×22′, plate scale of 0.65″/pixel). For details of TRAPPIST, see Gillon et al. (2011a) and Jehin et al. (2011). The transit was observed in a blue-blocking (BB) filter that has a transmittance >90% from 500 nm to beyond 1000 nm (effective wavelength = 696.8 nm), with each frame exposed for 8s. The occultations were acquired through a Sloan-z' filter (effective wavelength = 895.5 nm), with exposure times between 36s and 55s. Throughout observations, the telescope was kept in focus and the positions of the stars on the chip were retained on the same few pixels, thanks to a "software guiding" system that regularly derives an astrometric solution on the images and sends pointing corrections to the mount when needed.

After bias, dark, and flat-field corrections, stellar fluxes were extracted from the images using the IRAF/DAOPHOT[1] aperture photometry software (Stetson 1987). For each observation, a careful selection of both the photometric aperture size and of stable reference stars having a brightness similar to WASP-103 was performed to obtain optimal differential photometry. The resulting light curves are shown in Figs. A1 (raw occultation light curves), A2 (detrended occultation light curves, see Section 3.2 for details about the modeling), and A3 (raw transit light curve).

2.1.2 Euler/EulerCam eclipse photometry

Two transit and six occultation light curves of WASP-103 b were obtained with EulerCam, the imager of the 1.2m *Euler*-Swiss telescope. EulerCam is a nitrogen-cooled 4K×4K CCD camera with a field of view of 15.68′×15.73′ at a plate scale of 0.23″/pixel. The transits were observed in a Gunn-r' filter (effective wavelength = 664.1 nm) with an exposure time of 80s. The occultations were acquired through a Gunn-z' filter (effective wavelength = 912.3 nm), with exposure times between 60s and 100s. A slight defocus was applied to the telescope to optimize the observation efficiency and to minimize pixel-to-pixel effects. This resulted in stellar PSFs with a typical FWHM between 1.1″ and 2.5″. Here too, the positions of the stars on the detector were kept within a box of a few pixels throughout the observations, thanks to the "Absolute Tracking" system of EulerCam that matches the point sources in each image with a catalog and adjusts the telescope pointing between exposures when needed. The reduction procedure used to extract the eclipse light curves was similar to that performed on TRAPPIST data. The resulting light curves are shown in Figs. A1 (raw occultation light curves), A2 (detrended occultation light curves, see Section 3.2 for details about the modeling), and A3 (raw transit light curves). Further details of the EulerCam instrument and data reduction procedures can be found in Lendl et al. (2012).

2.1.3 CFHT/WIRCam occultation photometry

We observed one occultation of WASP-103 b with the Wide-field InfraRed Camera (WIRCam, Puget et al. 2004) on the 3.6m Canada-France-Hawaii Telescope. WIRCam consists of four 2K×2K HgCdTe HAWAII-2RG arrays, arranged in a 2×2 mosaic. The instrument has a total field of view of 20.5′×20.5′ (with gaps of 45″ between adjacent chips) at a scale of 0.3″/pixel. We used the K_S broad-band filter, which has a bandwidth of 0.325 μm centered at 2.146 μm. The observations took place on 2014 May 20 from 06:50 to 12:40 UT, covering the 2.6hrs long predicted occultation (assuming a circular orbit) together with 3.2hrs of out-of-eclipse observations. Conditions were photometric, with a median seeing of 0.6″, and airmass decreased from 2.4 to 1.09 during the run. The data were gathered in staring mode (Devost et al. 2010), with the target and reference stars observed continuously for several hours on the same pixels without

[1] IRAF is distributed by the National Optical Astronomy Observatory, which is operated by the Association of Universities for Research in Astronomy, Inc., under cooperative agreement with the National Science Foundation.

Table 1. Summary of follow-up photometry obtained for WASP-103. For each light curve, this table shows the night of acquisition (UT), the used instrument, the eclipse type, the filter (BB=blue-blocking) and exposure time, the number of data points, the selected baseline function, the standard deviation of the best-fit residuals (unbinned and binned per intervals of 2 min), and the deduced values for β_w, β_r and $CF = \beta_w \times \beta_r$ (see Section 3.2 for details). For the baseline function, $p(\epsilon^N)$ denotes, respectively, a N-order polynomial function of time ($\epsilon = t$), airmass ($\epsilon = a$), PSF full-width at half maximum ($\epsilon = f$) or radius for the WIRCam data ($\epsilon = r$), background ($\epsilon = b$), and x and y positions ($\epsilon = xy$). o denotes an offset fixed at the time of the meridian flip.

Date (UT)	Instrument	Eclipse type	Filter	T_{exp} (s)	N_p	Baseline function	σ (%)	σ_{120s} (%)	β_w	β_r	CF
New data											
2014 May 08-09	TRAPPIST	Occultation	z'	55	338	$p(t^1) + o$	0.25	0.19	1.10	1.08	1.18
2014 May 20-20	WIRCam	Occultation	K_S	5	1083	$p(t^2+r^1+b^1)$	0.32	0.12	1.56	1.00	1.57
2014 June 10-11	EulerCam	Transit	r'	80	140	$p(t^1+b^1)$	0.18	0.18	1.89	1.00	1.89
2014 June 16-17	TRAPPIST	Occultation	z'	50	341	$p(t^1) + o$	0.25	0.18	1.08	1.07	1.16
2014 June 29-30	EulerCam	Occultation	z'	100	130	$p(t^1+f^1)$	0.10	0.10	1.20	1.00	1.20
2014 July 05-06	EulerCam	Transit	r'	80	150	$p(t^1)$	0.09	0.09	1.16	1.49	1.72
2014 July 11-12	EulerCam	Occultation	z'	100	65	$p(t^1+b^1)$	0.09	0.09	1.18	1.10	1.30
2014 July 12-13	TRAPPIST	Occultation	z'	48	281	$p(t^1) + o$	0.26	0.18	1.05	1.91	2.01
2014 July 25-26	TRAPPIST	Occultation	z'	48	308	$p(t^1) + o$	0.23	0.16	1.00	1.10	1.10
2015 Apr. 02-03	TRAPPIST	Transit	BB	8	910	$p(a^1) + o$	0.35	0.14	0.87	1.08	0.95
2015 May 17-18	TRAPPIST	Occultation	z'	36	328	$p(t^1) + o$	0.32	0.23	1.28	1.22	1.56
2015 May 30-31	TRAPPIST	Occultation	z'	36	364	$p(a^1) + o$	0.36	0.26	1.32	1.00	1.32
2015 June 11-12	EulerCam	Occultation	z'	100	139	$p(t^2+f^1+b^1)$	0.14	0.14	1.56	2.10	3.27
2015 June 12-13	TRAPPIST	Occultation	z'	40	315	$p(a^1) + o$	0.36	0.26	1.43	1.00	1.43
2015 July 07-08	TRAPPIST	Occultation	z'	46	365	$p(t^1) + o$	0.30	0.22	1.29	1.51	1.94
2015 July 07-08	EulerCam	Occultation	z'	100	126	$p(a^2+f^1+b^1)$	0.11	0.11	1.27	1.42	1.82
2015 July 19-20	TRAPPIST	Occultation	z'	46	327	$p(t^1) + o$	0.35	0.24	1.37	1.17	1.60
2015 July 19-20	EulerCam	Occultation	z'	100	134	$p(t^1+f^1+b^1)$	0.10	0.10	1.13	1.22	1.39
2015 July 20-21	EulerCam	Occultation	z'	60	210	$p(t^1+f^1)$	0.10	0.08	1.10	1.37	1.51
Archival data											
2013 June 15-16	TRAPPIST	Transit	BB	7	802	$p(t^1+f^1) + o$	0.32	0.13	0.69	1.48	1.02
2013 June 28-29	EulerCam	Transit	r'	120	103	$p(t^1+f^1+b^2+xy^1)$	0.09	0.09	1.43	1.08	1.54
2013 July 11-12	EulerCam	Transit	r'	80	105	$p(t^1+b^1)$	0.12	0.12	1.59	1.23	1.96
2013 July 23-24	TRAPPIST	Transit	BB	9	941	$p(t^2) + o$	0.48	0.19	1.23	1.22	1.50
2013 Aug. 04-05	TRAPPIST	Transit	BB	10	935	$p(t^2) + o$	0.29	0.13	0.80	1.51	1.21
2014 Apr. 19-20	DFOSC	Transit	R	100-105	134	$p(t^1)$	0.07	0.07	1.05	2.53	2.65
2014 May 01-02	DFOSC	Transit	I	110-130	113	$p(t^1)$	0.08	0.08	1.06	1.14	1.21
2014 June 08-09	DFOSC	Transit	R	100-130	130	$p(t^1)$	0.10	0.10	1.03	1.41	1.45
2014 June 22-23	DFOSC	Transit	R	50-120	195	$p(t^1)$	0.13	0.13	1.05	2.62	2.75
2014 June 23-24	DFOSC	Transit	R	100	112	$p(t^1)$	0.06	0.06	1.01	1.44	1.45
2014 July 05-06	DFOSC	Transit	R	100	118	$p(t^1)$	0.06	0.06	1.01	1.81	1.83
2014 July 05-06	GROND	Transit	g'	100-120	122	$p(t^2)$	0.12	0.12	1.03	1.44	1.49
2014 July 05-06	GROND	Transit	r'	100-120	125	$p(t^2)$	0.07	0.07	1.01	2.20	2.22
2014 July 05-06	GROND	Transit	i'	100-120	119	$p(t^2)$	0.08	0.08	1.04	1.42	1.48
2014 July 05-06	GROND	Transit	z'	100-120	121	$p(t^2)$	0.11	0.11	1.03	2.49	2.58
2014 July 17-18	DFOSC	Transit	R	90-110	139	$p(t^1)$	0.07	0.07	1.00	1.21	1.22
2014 July 18-19	DFOSC	Transit	R	60-110	181	$p(t^2)$	0.06	0.05	1.02	1.19	1.21
2014 July 18-19	GROND	Transit	g'	98-108	126	$p(t^2)$	0.08	0.08	1.02	1.44	1.48
2014 July 18-19	GROND	Transit	r'	98-108	143	$p(t^2)$	0.06	0.06	1.04	1.64	1.70
2014 July 18-19	GROND	Transit	i'	98-108	142	$p(t^2)$	0.09	0.09	1.05	1.66	1.74
2014 July 18-19	GROND	Transit	z'	98-108	144	$p(t^2)$	0.09	0.09	1.01	1.13	1.14
2014 Aug. 12-13	CASLEO	Transit	R	90-120	129	$p(t^2)$	0.15	0.15	1.04	1.51	1.58

any dithering. This mode has been used by other authors for similar observations with WIRCam (see, e.g., Croll et al. 2010, Croll et al. 2011, and Wang et al. 2013) and has proven to yield an optimal photometric precision. The pointing was carefully selected to ensure that the target and reference stars did not fall near bad pixels, as well as to maximize the number of suitable reference stars located on the same WIRCam chip as WASP-103 (see below). The scientific sequence consisted of 1092 exposures, each 5s and read out with correlated double sampling[2] (CDS). The telescope was defocused to 2mm, in order to reduce the impact of imperfect flat-fielding, inter- and intra-pixel variations on the photometry, as well as to keep the counts of the target and reference stars in the regime where detector non-linearity is minimized

[2] A CDS image is constructed by subtracting a first read of the array, done immediately after reset, from a second read of the array, performed at the end of the exposure.

(linearity to within 1% below ~10 kADU)[3]. This resulted in a ring-shaped PSF with a radius of ~4.5″(~15 pixels). A short set of dithered (ten offset positions) in-focus images was taken before and after the scientific sequence in order to construct a sky flat (see below).

The data were reduced independently of the traditional WIRCam `I` iwi pipeline[4], following the prescription of Croll et al. (2015) for the reduction of WIRCam staring mode data. We refer the reader to that paper for a detailed description of the reduction procedure and give here an outline of the main steps. The frames from each detector were reduced separately. In each image, the pixels with CDS values above 36 kADU were flagged as saturated. The data were corrected for the small non-linearity[3] present below 10 kADU, following the iterative approach of Vacca et al. (2004) for applying a non-linearity correction to CDS images. Each frame was dark subtracted and divided by a sky flat, which was created by taking the median stack of the dithered images acquired before and after the scientific sequence. A bad pixel map was constructed from this sky flat, where pixels flagged as bad were those that deviate by more than 2% from the median of the array. Finally, in each image, bad and saturated pixels had their value replaced by the median value of the adjacent pixels (provided that they were not themselves bad or saturated).

Aperture photometry was performed for the target and reference stars using IRAF/DAOPHOT. Apertures were centered using intensity-weighted centroids. We tested a set of constant apertures, as well as apertures that varied from image to image as a function of the mean radius of the ring-shaped stellar PSFs. The best result was obtained with a variable aperture of 1.1 times the mean radius. Using a variable photometric aperture, rather than a fixed one, allowed us to account for the varying atmospheric conditions, as well as to find for each individual image a balance between choosing a small aperture to minimize the sky noise and a large aperture to encompass all the stellar light. The sky annulus was kept constant for all images, with an inner radius of 30 pixels and an outer radius of 50 pixels. Differential photometry of WASP-103 was finally obtained. We tested all possible combinations of stable reference stars having a brightness similar to the target. We found the best photometry using eight reference stars located on the same WIRCam detector as WASP-103. The resulting light curve is shown in Fig. 1.

2.1.4 *Euler/CORALIE radial velocities*

Five new spectroscopic measurements of WASP-103 were gathered with the CORALIE spectrograph mounted on the *Euler* telescope (Queloz et al. 2000). The spectra, all obtained with an exposure time of 30min, were processed with the CORALIE standard data reduction pipeline (Baranne et al. 1996). RVs were then computed from the spectra by weighted cross-correlation (Pepe et al. 2002), using a numerical G2-spectral template that provides optimal precisions for late-F to early-K dwarfs. These RVs are presented in Table 2 and shown in Fig. 2. The cross-correlation function (CCF) FWHM and bisector span (BS, Queloz et al. 2001) values are also given in Table 2.

[3] www.cfht.hawaii.edu/Instruments/Imaging/WIRCam/WIRCamNonlinearity.html

[4] http://www.cfht.hawaii.edu/Instruments/Imaging/WIRCam/IiwiVersion2Doc.html

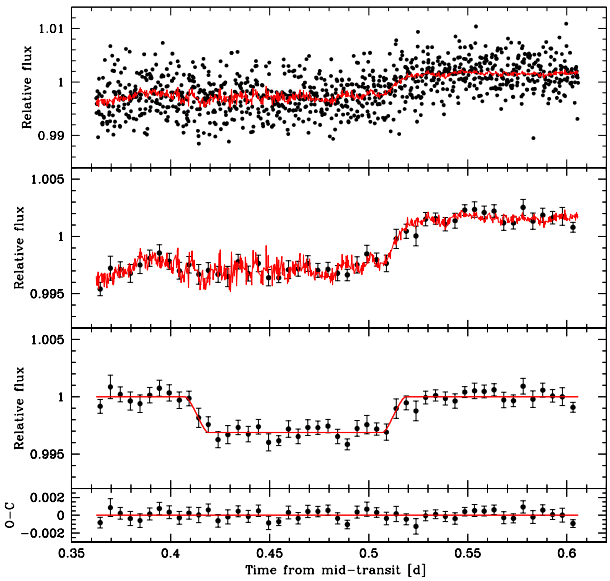

Figure 1. Occultation photometry obtained with CFHT/WIRCam in the K_S-band. *Top panel:* the raw, unbinned light curve, together with the best-fit full (photometric baseline × occultation in the K_S-band) model (overplotted in red, see Section 3.2 for details about the modeling). *Second panel:* same as the top panel except that the data are binned in 7.2min bins. *Third panel:* binned light curve divided by the best-fit photometric baseline model. The best-fit occultation model in the K_S-band is overplotted in red. *Bottom panel:* best-fit residuals. The RMS of the residuals is 524 ppm (7.2min bins). *General note:* the data and models are not corrected for the dilution by the nearby star here.

Table 2. New CORALIE RVs for WASP-103. The last two columns give the cross-correlation function FWHM and bisector span values, respectively.

BJD - 2 450 000	RV (km s^{-1})	σ_{RV} (km s^{-1})	FWHM (km s^{-1})	BS (km s^{-1})
6537.506214	-42.19467	0.12930	15.47857	0.04812
6837.661259	-41.95497	0.05763	14.90643	0.07458
6852.650727	-41.78295	0.06256	14.92542	0.26543
6880.562742	-41.57979	0.07013	15.07407	0.45440
6920.487957	-41.86693	0.09804	14.64620	-0.40181

2.2 Archival data

We also included in our global analysis the data previously published in G14 and S15:

- three TRAPPIST transit light curves (blue-blocking filter);
- two Euler/EulerCam transit light curves (Gunn-r' filter);
- eight transit light curves gathered with the DFOSC (Danish Faint Object Spectrograph and Camera) instrument

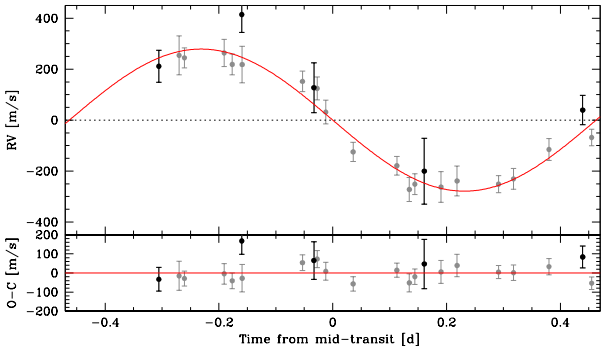

Figure 2. *Top:* Euler/CORALIE RV measurements period-folded on the best-fit transit ephemeris from our global MCMC analysis (see Section 3.2), with the best-fit Keplerian model over-plotted in red. The data published in G14 are plotted in grey, while our new measurements are plotted in black. *Bottom:* corresponding residuals.

on the 1.54m Danish telescope located at ESO La Silla Observatory (Bessel R and I filters);

- eight transit light curves obtained using the GROND (Gamma-Ray Burst Optical/Near-Infrared Detector) instrument on the 2.2m MPG/ESO telescope (Sloan-g', -r', -i', and -z' filters);
- one transit light curve acquired with the 2.15m telescope located at the CASLEO (Complejo Astronomico El Leoncito) Observatory (Johnson-Cousins R filter);
- eighteen CORALIE RVs.

We refer the reader to G14 and S15 for more details about these data. The archival light curves are summarized in the lower part of Table 1 and shown in Figs. A3 (TRAPPIST and Euler/EulerCam), A4 (Danish/DFOSC), and A5 (2.2m/GROND and CASLEO/2.15m), while the RVs are shown in Fig. 2.

3 DATA ANALYSIS

3.1 Contamination from the nearby star

W15 reported the detection of a stellar object located 0.242±0.016″ from WASP-103, fainter by $\Delta i' = 3.11 \pm 0.46$ and $\Delta z' = 2.59 \pm 0.35$. N16 presented further observations of this nearby star in the near-infrared and found magnitude differences with WASP-103 of $\Delta J = 2.427 \pm 0.030$, $\Delta H = 2.2165 \pm 0.0098$, and $\Delta K_S = 1.965 \pm 0.019$. The astrometric measurements from these two studies are inconclusive as to whether this star is gravitationally bound to the planetary system or not. Due to the very small angular separation of WASP-103 and the nearby object, both stars are contained in all photometric apertures used to extract the eclipse light curves that we included in our global analysis (new and archival data). Although a detailed characterization of the nearby star is beyond the scope of this work, we must estimate the dilution correction factor $(F_{W103} + F_{cont})/F_{W103} = 1 + F_{cont}/F_{W103}$ (where F_{cont}/F_{W103} is the contaminant-to-target flux ratio) for each of the observed passbands, in order to account for this contamination in our data analysis.

To this end, we first derived the individual apparent magnitudes of WASP-103 and the nearby star in the J, H, and K_S bands based on their combined 2MASS magnitudes (Skrutskie et al. 2006) and the magnitude differences reported by N16 in these bands. The resulting apparent magnitudes are given in Table 3. While the $J - H$, $H - K_S$, and $J - K_S$ color indices of WASP-103 agree well with a F8V star, the colors of the nearby star suggest a spectral type comprised between K1 and M4 if it is on the main sequence (Straižys & Lazauskaitė 2009). We computed the flux ratios F_{cont}/F_{W103} in the passbands of interest assuming each of these two spectral types for the contaminant. We used for this purpose PHOENIX model spectra (Husser et al. 2013) of WASP-103 and the nearby star that we integrated over the passbands of interest. The flux ratio in a given passband can be expressed as:

$$\frac{F_{cont}}{F_{W103}} = f^2 \frac{M_{cont}}{M_{W103}} \quad (1)$$

where M_{W103} and M_{cont} are the band-integrated model fluxes of WASP-103 and the contaminant, respectively, and f is a geometric factor defined as:

$$f = \frac{R_{cont}}{R_{W103}} \frac{d_{W103}}{d_{cont}} \quad (2)$$

with R_{W103} (resp. R_{cont}) and d_{W103} (resp. d_{cont}) denoting, respectively, the radius and the distance of WASP-103 (resp. the contaminant). For WASP-103, we used a model spectrum interpolated to the effective temperature T_{eff}, surface gravity $\log g_\star$, and metallicity [Fe/H] reported in G14. For the nearby star, two different model spectra, of typical K1V (T_{eff}=5100K, $\log g_\star$=4.5, [Fe/H]=0.0) and M4V (T_{eff}=3200K, $\log g_\star$=5.0, [Fe/H]=0.0) stars, were used. In each of these two cases, we calculated first the wavelength-independent factor f by comparing the ratio of the model fluxes M_{cont}/M_{W103} integrated over the J-band with the flux ratio F_{cont}/F_{W103} measured in this band by N16. The flux ratios in the passbands of interest were then computed using Equation (1). The final value for the flux ratio in each passband was taken as the average of the two values obtained using the K1V and M4V model spectra for the contaminating star, with an error bar large enough to encompass both values. The resulting flux ratios are given in Table 4. The values derived in the i' and z' bands are consistent with the measurements from W15 in these two bands (0.0622 ± 0.0250 and 0.0969 ± 0.0302, respectively), but more precise (in the z'-band). In the K_S-band, we obtained a flux ratio of 0.1496 ± 0.0178, consistent with the value of 0.1637 ± 0.0029 measured by N16, but significantly less precise. For this passband, we thus used the measurement from N16.

In their reanalysis, S16 also estimated the contamination from the nearby star in the passbands observed in S15, using the near-infrared magnitude differences reported by

Filter	WASP-103	Contaminant
J	11.210 ± 0.029	13.637 ± 0.053
H	10.993 ± 0.032	13.209 ± 0.039
K_S	10.932 ± 0.023	12.897 ± 0.037

Table 3. Individual apparent magnitudes of WASP-103 and the nearby star in the J, H, and K_S bands.

Filter	$F_{\rm cont}/F_{\rm W103}$
g'	0.0275 ± 0.0243
r'	0.0419 ± 0.0322
R	0.0447 ± 0.0318
BB	0.0552 ± 0.0255
i'	0.0586 ± 0.0250
I	0.0633 ± 0.0236
z'	0.0800 ± 0.0145
$K_{\rm S}$	0.1637 ± 0.0029

Table 4. Contaminant-to-target flux ratios in the observed passbands.

N16. They obtained values in good agreement with ours, albeit with much smaller error bars (see the last column of their Table 1). This is due to the fact that they only used the ΔJ and $\Delta K_{\rm S}$ magnitude differences, thus discarding the H-band measurement, which results in a smaller uncertainty on the spectral type of the contaminating star. As we see no reason to discard any of the three measurements, we chose to adopt the safer procedure outlined above, giving equal weight to the three color indices.

3.2 Global data analysis

To obtain the strongest constraints on the system parameters, we performed a global Bayesian analysis of the whole data set (41 eclipse light curves and 23 RVs). We used for this purpose the most recent version of the adaptive Markov Chain Monte-Carlo (MCMC) code described in Gillon et al. (2012, and references therein), that derives the posterior probability distribution functions of the global model parameters, basing on stochastic simulations. Each UT time of mid-exposure was converted to the $\rm BJD_{TDB}$ time-scale (Eastman et al. 2010). To model the photometry, we used the eclipse model of Mandel & Agol (2002) multiplied by a different baseline model for each light curve (see below), while the RVs were modeled using a Keplerian orbit (e.g. Murray & Correia 2010) combined to a systemic velocity. A quadratic limb-darkening law was assumed for the transits.

The photometric baseline models, different for each light curve, allowed to account for photometric variations not related to the eclipses but rather to external astrophysical, instrumental, or environmental effects. They consisted of different polynomials with respect to, e.g., time, airmass, PSF full-width at half maximum, background, stellar position on the detector, or any combination of these parameters. For each light curve, the optimal baseline function (see Table 1) was selected by way of minimizing the Bayesian Information Criterion (BIC, Schwarz 1978). For the TRAPPIST light curves, a normalization offset was also part of the baseline model to represent the effect of the meridian flip; that is, the 180° rotation that the German equatorial mount telescope has to undergo when the meridian is reached. This movement results in different positions of the stellar images on the detector before and after the flip, and the normalization offset allows to account for a possible consecutive jump in the differential photometry at the time of the flip.

The jump parameters in our MCMC analysis (i.e. the parameters that are randomly perturbed at each step of the MCMC) were:

Parameter	Prior
$T_{\rm eff}$	$\mathcal{N}(6110, 160^2)$ K
[Fe/H]	$\mathcal{N}(0.06, 0.13^2)$ dex
$u_{1,g'}$	$\mathcal{N}(0.502, 0.032^2)$
$u_{2,g'}$	$\mathcal{N}(0.253, 0.020^2)$
$u_{1,r'}$	$\mathcal{N}(0.337, 0.024^2)$
$u_{2,r'}$	$\mathcal{N}(0.305, 0.010^2)$
$u_{1,R}$	$\mathcal{N}(0.316, 0.023^2)$
$u_{2,R}$	$\mathcal{N}(0.304, 0.010^2)$
$u_{1,BB}$	$\mathcal{N}(0.316, 0.046^2)$
$u_{2,BB}$	$\mathcal{N}(0.304, 0.020^2)$
$u_{1,i'}$	$\mathcal{N}(0.260, 0.020^2)$
$u_{2,i'}$	$\mathcal{N}(0.298, 0.008^2)$
$u_{1,I}$	$\mathcal{N}(0.242, 0.020^2)$
$u_{2,I}$	$\mathcal{N}(0.296, 0.008^2)$
$u_{1,z'}$	$\mathcal{N}(0.207, 0.018^2)$
$u_{2,z'}$	$\mathcal{N}(0.290, 0.007^2)$

Table 5. Prior probability distribution functions assumed in our MCMC analysis. $\mathcal{N}(\mu, \sigma^2)$ represents a normal distribution with an expectation μ and a variance σ^2.

- the transit depth in the R-band $dF_R = (R_{{\rm p},R}/R_\star)^2$, where $R_{{\rm p},R}$ is the planetary radius in the R-band and $R_\star$ is the stellar radius;
- the transit depth differences in the other wavelength bands $ddF_j = dF_j - dF_R$ (where $j = g'$, r', BB, i', I, z');
- the occultation depths in the z' and $K_{\rm S}$-bands, noted $dF_{{\rm occ},z'}$ and $dF_{{\rm occ},K_{\rm S}}$, respectively;
- the transit impact parameter in the case of a circular orbit $b' = a\cos i_{\rm p}/R_\star$, where a is the orbital semi-major axis and $i_{\rm p}$ is the orbital inclination;
- the transit width (from 1st to 4th contact) W;
- the time of mid-transit T_0;
- the orbital period P;
- the stellar effective temperature $T_{\rm eff}$ and metallicity [Fe/H];
- the parameter $K_2 = K\sqrt{1-e^2}\ P^{1/3}$, where K is the RV orbital semi-amplitude and e is the orbital eccentricity;
- the two parameters $\sqrt{e}\cos\omega$ and $\sqrt{e}\sin\omega$, where ω is the argument of the periastron;
- the linear combinations of the quadratic limb-darkening coefficients $(u_{1,j}, u_{2,j})$ in each wavelength band, $c_{1,j} = 2u_{1,j} + u_{2,j}$ and $c_{2,j} = u_{1,j} - 2u_{2,j}$ (where $j = g'$, r', R, BB, i', I, z').

The baseline model parameters were not jump parameters; they were determined at each step of the MCMC by linear least-squares minimization. Normal prior probability distribution functions were assumed for $T_{\rm eff}$, [Fe/H], $u_{1,j}$, and $u_{2,j}$. For $T_{\rm eff}$ and [Fe/H], the priors were based on the values reported in G14, with expectations and standard deviations corresponding to the quoted measurements and errors, respectively. As for the normal priors imposed on $u_{1,j}$ and $u_{2,j}$, their parameters were interpolated from the theoretical tables of Claret & Bloemen (2011). All these normal prior distributions are presented in Table 5. Uniform prior distributions were assumed for the other jump parameters. At each MCMC step, a value for $F_{\rm cont}/F_{\rm W103}$ for each wavelength band was drawn from the normal distribution having as expectation and standard deviation the value and error given in Table 4 for this band, respectively. The dilution correction factor for each band was computed as $1+F_{\rm cont}/F_{\rm W103}$.

The physical parameters of the system were deduced from the jump parameters at each step of the MCMC, so that their posterior probability distribution functions could also be constructed. At each MCMC step, a value for the stellar mean density $\rho_\star$ was first derived from the Kepler's third law and the jump parameters dF_R, b', W, P, $\sqrt{e}\cos\omega$ and $\sqrt{e}\sin\omega$ (see e.g. Seager & Mallén-Ornelas 2003 and Winn 2010). This $\rho_\star$ and values for $T_{\rm eff}$ and [Fe/H] drawn from their normal prior distributions were used to determine a value for the stellar mass $M_\star$ through an empirical law $M_\star(\rho_\star, T_{\rm eff}, \text{[Fe/H]})$ (Enoch et al. 2010, Gillon et al. 2011b) that is calibrated using the set of well-constrained detached eclipsing binary (EB) systems presented by Southworth (2011). Here, we chose to reduce this set to the 116 stars with a mass between 0.7 and 1.7 $M_\odot$, the goal of this selection being to benefit from our preliminary knowledge of the mass of WASP-103 (S15 give $M_\star = 1.204 \pm 0.089\ M_\odot$) to improve the determination of the system parameters. In order to propagate correctly the error on the empirical law, the parameters of the selected subset of calibration stars were normally perturbed within their observational error bars and the coefficients of the law were redetermined at each MCMC step. We furthermore took into account the inability of the empirical law to perfectly reproduce the distribution of the stellar masses by determining at each step of the MCMC the quadratic difference between the RMS of the residuals of the modeling of the EB masses by the empirical law and the mean mass error for the EB sample. At each MCMC step, a new value for $M_\star$ was drawn from a normal distribution having as expectation and standard deviation the mass originally determined by the empirical law and the quadratic difference mentioned above, respectively. The stellar radius $R_\star$ was derived from $M_\star$ and $\rho_\star$, and the other physical parameters of the system were then deduced from the jump parameters and stellar mass and radius.

Although the photometric errors were computed considering scintillation, sky, dark, readout and photon noises, they are known to be often moderately underestimated. A preliminary MCMC analysis, consisting of one chain of 50 000 steps, was performed to determine the correction factors CF to be applied to the error bars of each photometric time series, as described in Gillon et al. (2012). For each light curve, CF is the product of two contributions, β_w and β_r. On one side, β_w represents the under- or overestimation of the white noise of each measurement. It is computed as the ratio between the standard deviation of the residuals and the mean photometric error. On the other side, β_r allows to account for possible correlated noise present in the light curve. It is obtained by comparing the standard deviations of the binned and unbinned residuals for different binning intervals ranging from 5 to 120min, with the largest value being kept as β_r. The values deduced for β_w, β_r, and $CF = \beta_w \times \beta_r$ for each light curve are given in Table 1. Similarly, this preliminary analysis allowed us to assess the need to rescale the RV error bars, but it was unnecessary here (the best-fit RV model already gives a reduced $\chi^2 = 1.0$).

With the corrected photometric error bars, two analyses were then performed: one assuming a circular orbit ($e = 0$) and one with a free eccentricity. Each analysis consisted of three chains of 100 000 steps, whose convergence was checked using the statistical test of Gelman & Rubin (1992). The first 20% of each chain was considered as its burn-in phase and discarded. A model comparison based on the Bayes factor, as estimated from the BIC, strongly favored the circular model (Bayes factor of 4915 in its favor) over the eccentric one. We thus adopted the circular orbit as our nominal solution. The corresponding derived system parameters and 1-σ error bars are presented in Table 6. The best-fit eclipse models are shown in Figs. 1 (third panel, occultation model in the K_S-band), 3 (occultation model in the z'-band), and 4 (transit models in each of the observed passbands), while the best-fit RV model is displayed in Fig. 2.

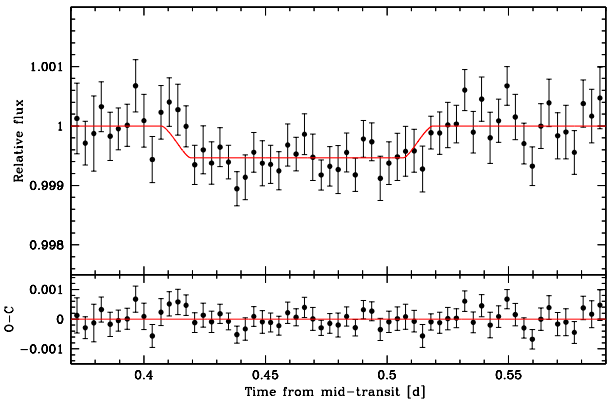

Figure 3. *Top:* combined occultation photometry obtained in the z'-band with TRAPPIST and Euler/EulerCam. The data are period-folded on the best-fit transit ephemeris from our global MCMC analysis (see Section 3.2), corrected for the photometric baseline, and binned in 5min bins (for visual convenience). The best-fit occultation model in the z'-band is overplotted in red. The data and model are not corrected for the dilution by the nearby star here. *Bottom:* corresponding residuals. The RMS of the residuals in the shown interval is 305 ppm (5min bins).

4 DISCUSSION

4.1 System physical parameters and correction for asphericity

As expected, we find a slightly larger radius ($1.623^{+0.051}_{-0.053}$ $R_{\rm Jup}$) and a slightly lower mean density ($0.353^{+0.028}_{-0.024}$ $\rho_{\rm Jup}$) for the planet than those reported by G14 ($1.528^{+0.073}_{-0.047}$ $R_{\rm Jup}$, $0.415^{+0.046}_{-0.053}$ $\rho_{\rm Jup}$) and S15 (1.554 ± 0.044 $R_{\rm Jup}$, 0.367 ± 0.027 $\rho_{\rm Jup}$), who did not take into account the contamination from the nearby star, unknown at that time. Our values for these two parameters agree well with those found by S16 ($1.596^{+0.044}_{-0.054}$ $R_{\rm Jup}$, 0.339 ± 0.023 $\rho_{\rm Jup}$). The other physical parameters of the system are in very good agreement with those reported by G14, S15, S16.

With an orbital semi-major axis only ~1.12 times larger than its Roche limit, WASP-103 b is expected to be significantly deformed by tides (e.g. Budaj 2011). We calculated values for the planetary radius and mean density corrected for asphericity using the same method as S15 (also applied to the case of WASP-121 b by Delrez et al. 2016). In brief, we used the Roche model of Budaj (2011) to compute the Roche shape of the planet which would have the same cross-section during transit as the one we inferred from our observations

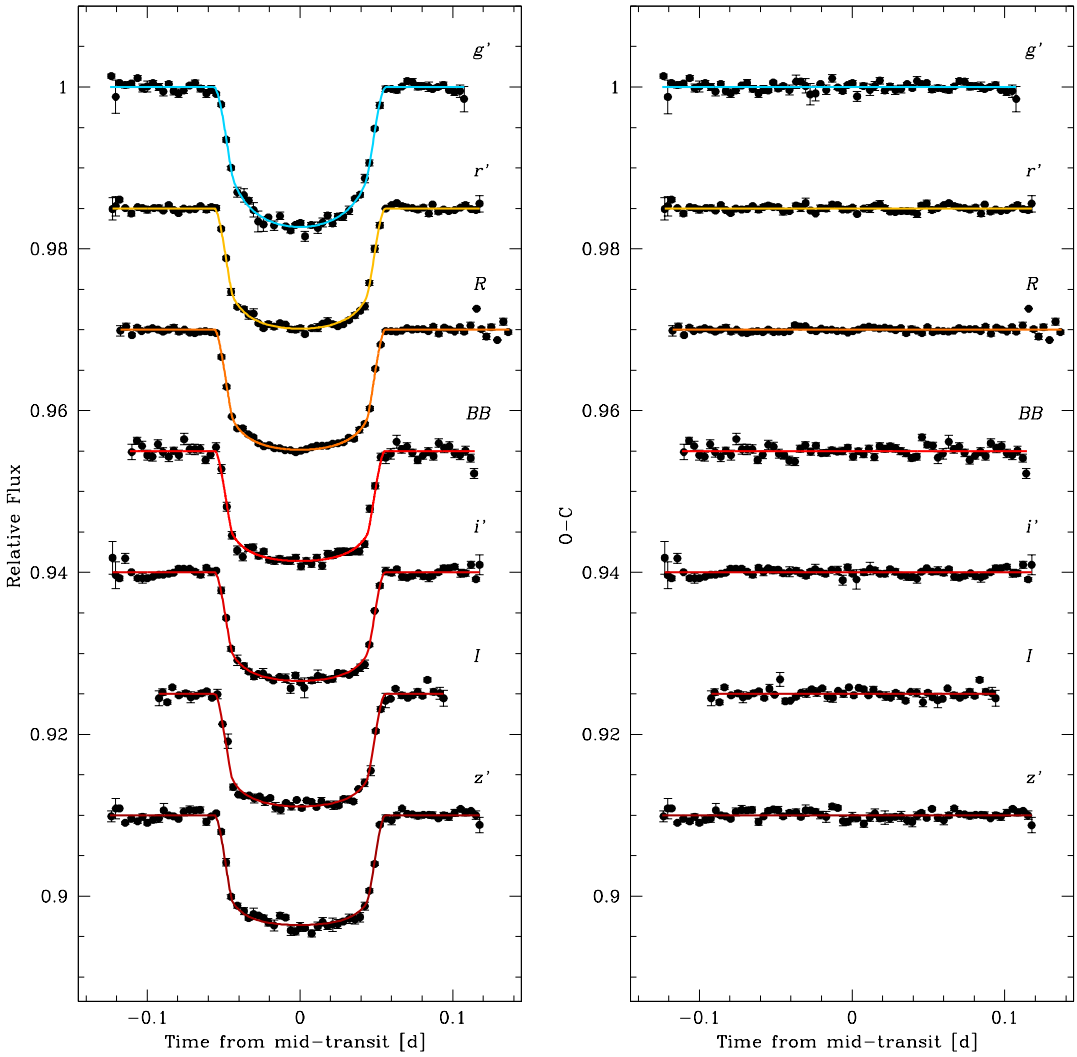

Figure 4. *Left:* combined transit light curves in each of the observed passbands. The data are period-folded on the best-fit transit ephemeris from our global MCMC analysis (see Section 3.2), corrected for the photometric baseline, and binned in 5min bins (for visual convenience). For each band, the overplotted, solid line is our best-fit transit model. The data and models are not corrected for the dilution by the nearby star here. The light curves are shifted along the y-axis for clarity. *Right:* corresponding residuals. The RMS of the residuals in the interval [-0.09,0.09] days are (from top to bottom) 477, 354, 249, 655, 392, 582, and 496 ppm (5min bins).

assuming a spherical planet (eclipse model of Mandel & Agol 2002, see Section 3.2). The main inputs of the model were the orbital semi-major axis ($a = 4.26^{+0.12}_{-0.13}$ $R_\odot$), the star-to-planet mass ratio ($M_\star/M_\mathrm{p} = 840 \pm 137$), and the planetary radius obtained assuming a spherical shape ($R_{\mathrm{p},R} = 1.623^{+0.051}_{-0.053}$ R_Jup). We found a corrected value for the planetary radius of 1.681 ± 0.063 R_Jup (radius of the sphere that would have the same volume as the Roche surface of the planet) and a corresponding revised mean density of 0.318 ± 0.035 ρ_Jup. These corrected values are also included in Table 6.

4.2 Atmospheric properties of WASP-103 b

We use our observations to constrain the atmospheric properties of WASP-103 b. We model the atmospheric spectra of WASP-103 b, both in transmission and thermal emission, using an exoplanetary atmospheric modeling and retrieval method based on Madhusudhan & Seager (2009) (also see Madhusudhan et al. 2011b, Madhusudhan 2012). Here we briefly summarize the method. The model consists of a 1-D radiative transfer solver which computes the observed spectrum of an exoplanetary atmosphere for a given geometry, in transit or at secondary eclipse, assuming plane parallel geometry. The temperature profile and chemical composition of the atmosphere are free parameters of the model, with 6 parameters for the *P-T* profile and 4-6 free parameters for the chemical species; one parameter for each relevant atom/molecule. The model assumes hydrostatic equilibrium and local thermodynamic equilibrium (LTE) and while computing thermal emission spectra ensures global energy balance with the incident radiation. The parametric temperature structure and molecular abundances in the model al-

Table 6. System parameters: median values and 1-σ limits of the posterior probability distribution functions derived from our global MCMC analysis.

Parameters	Values	Units
Stellar parameters		
Effective temperature $T_{\rm eff}$	6110 ± 160	K
Metallicity [Fe/H]	0.06 ± 0.13	dex
Surface gravity log $g_\star$	$4.219^{+0.013}_{-0.014}$	cgs
Mean density $\rho_\star$	$0.427^{+0.004}_{-0.006}$	$\rho_\odot$
Mass $M_\star$	1.21 ± 0.11	$M_\odot$
Radius $R_\star$	1.416 ± 0.043	$R_\odot$
Planet parameters		
Transit depth (in the R-band) $dF_R = (R_{\rm p,R}/R_\star)^2$	$1.323^{+0.046}_{-0.031}$	%
Transit impact parameter $b' = a\cos i_{\rm p}/R_\star$	$0.06^{+0.06}_{-0.05}$	$R_\star$
Transit width W	0.1090 ± 0.0003	d
Time of inferior conjunction T_0	2 456 836.296427 ± 0.000063	$\rm BJD_{TDB}$
Orbital period P	0.92554517 ± 0.00000058	d
RV semi-amplitude K	270 ± 14	$\rm m\,s^{-1}$
Scaled semi-major axis $a/R_\star$	$3.010^{+0.008}_{-0.013}$	–
Orbital semi-major axis a	$0.01979^{+0.00057}_{-0.00061}$	AU
Orbital inclination $i_{\rm p}$	$88.8^{+0.8}_{-1.1}$	deg
Equilibrium temperature[a] $T_{\rm eq}$	2484 ± 67	K
Surface gravity log $g_{\rm p}$	$3.171^{+0.027}_{-0.024}$	cgs
Mean density $\rho_{\rm p}$	$0.353^{+0.028}_{-0.024}$	$\rho_{\rm Jup}$
Mass $M_{\rm p}$	1.51 ± 0.11	$M_{\rm Jup}$
Radius (in the R-band) $R_{\rm p,R}$	$1.623^{+0.051}_{-0.053}$	$R_{\rm Jup}$
Roche limit[b] $a_{\rm R}$	$0.01760^{+0.00079}_{-0.00082}$	AU
$a/a_{\rm R}$	$1.124^{+0.029}_{-0.026}$	
Planet parameters corrected for asphericity (Section 4.1)		
Radius (in the R-band) $R_{\rm p,R}$	1.681 ± 0.063	$R_{\rm Jup}$
Mean density $\rho_{\rm p}$	0.318 ± 0.035	$\rho_{\rm Jup}$
Planet/star radius ratio $R_{\rm p}/R_\star$ (transmission spectrum)		
$R_{\rm p,g'}/R_\star$ (0.48 μm)	$0.1180^{+0.0018}_{-0.0016}$	–
$R_{\rm p,r'}/R_\star$ (0.62 μm)	$0.1155^{+0.0016}_{-0.0018}$	–
$R_{\rm p,R}/R_\star$ (0.66 μm)	$0.1150^{+0.0020}_{-0.0014}$	–
$R_{\rm p,BB}/R_\star$ (0.70 μm)[c]	$0.1109^{+0.0024}_{-0.0018}$	–
$R_{\rm p,i'}/R_\star$ (0.76 μm)	$0.1116^{+0.0023}_{-0.0019}$	–
$R_{\rm p,I}/R_\star$ (0.82 μm)	0.1133 ± 0.0013	–
$R_{\rm p,z'}/R_\star$ (0.90 μm)	$0.1143^{+0.0013}_{-0.0012}$	–
Occultation depths $dF_{\rm occ}$ (emission spectrum)		
$dF_{\rm occ,z'}$ (0.90 μm)	699 ± 110	ppm
$dF_{\rm occ,K_S}$ (2.15 μm)	3567^{+400}_{-350}	ppm

Notes. [a] Assuming a null Bond albedo and isotropic reradiation (reradiation factor f=1/4, López-Morales & Seager 2007).
[b] Using $a_{\rm R} = 2.46\ R_{\rm p}(M_\star/M_{\rm p})^{1/3}$ (Chandrasekhar 1987).
[c] TRAPPIST blue-blocking filter.

low exploration of a wide range of temperature profiles and chemical compositions in search of the best-fit models to fit the data. In the present work, however, given the lower number of photometric data points compared to the model parameters our goal is to obtain a general understanding of the model parameter space consistent with the data rather than finding a unique best fit.

4.2.1 Transmission spectrum

The planet-to-star radius ratios ($R_{\rm p}/R_\star$) obtained for each of the observed passbands are given in Table 6 and shown in Fig 5 (left). We find the same "V-shape" pattern as S16, with a minimum effective planetary radius around 700nm and increasing values towards both shorter and longer wavelengths. This pattern is however less significant in our transmission spectrum, due to our more conservative error bars (cf. Section 3.1). We compared our measurements to four different theoretical models for WASP-103 b's transmission spectrum, also shown in Fig 5 (left):

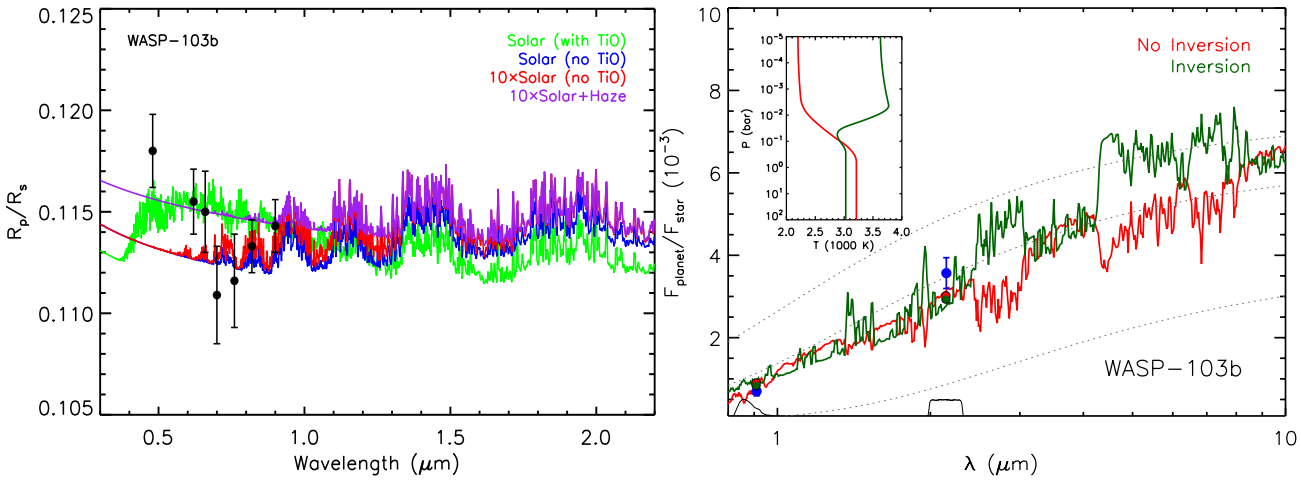

Figure 5. *Left:* broad-band measurements of the planet-to-star radius ratio ($R_p/R_\star$) as a function of wavelength compared to model transmission spectra of WASP-103 b. The various measurements are shown as black circles with error bars. The colored curves show four different plausible models: a clear solar-composition atmosphere without TiO (blue), a clear solar-composition atmosphere with TiO (green), a clear atmosphere with 10× solar metallicity without TiO (red), and a hazy atmosphere with 10× solar metallicity (magenta). *Right:* observations and model spectra of dayside thermal emission from WASP-103 b. The blue circles with error bars show our z' and K_S-band measurements. The green and red curves show best-fit model spectra with and without thermal inversion, respectively. The inset shows the corresponding pressure-temperature profiles for the models. The green and red circles give the band-integrated (bottom curves) fluxes of the corresponding models, for comparison to data.

- a clear solar-composition atmosphere, without TiO (blue);
- a clear solar-composition atmosphere, with TiO (green);
- a clear atmosphere with 10× solar metallicity, without TiO (red);
- a hazy atmosphere with 10× solar metallicity (magenta).

The corresponding χ^2 values are given in Table 7 (second column). The data are best explained by the hazy atmosphere model. The clear solar-composition atmosphere model with TiO also provides a fairly good fit to the data. In particular, only these two models provide a reasonable fit to the bluest (g'-band) measurement (<1.8-σ). The two other models, i.e. the clear solar-composition atmosphere model and the clear atmosphere model with 10× solar metallicity (both without TiO), deviate by more than 2.5-σ from this data point. This could suggest that either high-altitude hazes or TiO are present in the planet's atmosphere at the day-night terminator region. However, this inference hinges critically on a single data point, the g'-band measurement, and should thus be taken with caution. When this data point is not considered, the four models provide comparable fits to the data (Table 7, third column). Therefore, more observations, at higher precision and spectral resolution, are required to further constrain the atmospheric chemical composition of WASP-103 b from its transmission spectrum.

Model	All data	Without the g'-band measurement
Solar with TiO	9.1	5.9
Solar without TiO	12.5	6.0
10× Solar without TiO	11.2	4.7
10× Solar with haze	7.3	5.8

Table 7. χ^2 values calculated from the data and the various models of the transmission spectrum of WASP-103 b, considering all data (second column) and omitting the g'-band measurement (third column).

4.2.2 Emission spectrum

The thermal emission from the dayside of the planet is clearly detected in both the z' and K_S-bands, the measured occultation depths being 699±110 ppm (6.3-σ detection) and 3567^{+400}_{-350} ppm (10.2-σ detection), respectively. These measurements provide some initial insights into the dayside atmosphere of WASP-103 b. Even though we have only two photometric data points, at ~0.9 μm (z') and ~2.1 μm (K_S), these data points suggest a peculiar feature. Our observations show that the brightness temperature (T_B) in the K_S-band is 3148^{+144}_{-130} K which is marginally higher (~1.5-σ) than the T_B in the z'-band of 2914^{+80}_{-87} K. Generally, for hot Jupiters the T_B in the z'-band is found to be consistent with or higher than that in the K_S-band (see e.g. Anderson et al. 2013 and Lendl et al. 2013 for WASP-19 b, Madhusudhan 2012 for WASP-12 b, or Haynes et al. 2015 for WASP-33 b). This is because strong absorption in the z'-band is typically associated with strong TiO/VO absorption which is possible in some extremely irradiated hot Jupiters (Fortney et al. 2008, Madhusudhan 2012). On the other hand, the K_S-band is relatively devoid of strong molecular absorption due to TiO and other molecules relevant for hot Jupiters, with the exception of some weak absorption due to CO. Thus, when TiO is absent all the near-infrared ground-based photometric bands (z', J, H, and K_S) provide windows in atmospheric opacity and probe the temperatures in the deep atmosphere which tends to be isothermal for hot Jupiters. Therefore, the brightness temperatures in all these channels are expected

to be similar, as observed for several hot Jupiters (e.g. Anderson et al. 2013, Lendl et al. 2013, Madhusudhan 2012). On the other hand, in hot Jupiters where TiO is present it can lead to a thermal inversion in the atmosphere and cause spectral features in emission. In this case, the TiO features in the z'-band lead to a higher T_B in that band compared to that in the K_S-band which still has limited opacity. Therefore, it is rarely the case that the z'-band has a lower T_B than the K_S-band. If confirmed, the difference in brightness temperature found here could indicate that TiO, or some other molecule with strong spectral features in the z'-band, is present in the atmosphere but the temperature profile in the atmosphere decreases with altitude (i.e. no thermal inversion), so that the molecular features appear in absorption in the z'-band.

Our observations of thermal emission and two model spectra of WASP-103 b are shown in Figure 5 (right). Given the high equilibrium temperature of the planet (T_{eq}=2484±67 K) the atmosphere is expected to be conducive for gaseous TiO and VO which in turn could cause thermal inversions, under the assumption of an oxygen-rich hot Jupiter atmosphere in thermochemical equilibrium (Fortney et al. 2008), unless other factors are at play (e.g. Knutson et al. 2010, Spiegel et al. 2009, Madhusudhan et al. 2011a). Other prominent molecules in H_2-rich atmospheres at this temperature include H_2O and CO. As discussed above, while TiO and VO have strong spectral features in the z'-band, CO has some spectral features in the K_S-band. We find that our data for WASP-103 b can be explained by both models with and without a thermal inversion but with different assumptions for the z'-band flux. The model with a thermal inversion (green model in Fig. 5 right), where molecular features are in emission, requires low TiO abundance and high CO abundance to cause a low z'-band flux and high K_S-band flux, respectively, to explain the data. The lack of TiO along with the presence of a thermal inversion suggests that some other compound might be instrumental in causing the inversion. On the other hand, the model without a thermal inversion (red model in Fig. 5 right) requires the opposite composition, i.e. modest CO abundance but non-negligible TiO abundance to cause a TiO absorption feature in the z'-band. We find that a TiO abundance of at least 0.1× that predicted for thermochemical equilibrium with solar elemental abundances is required with the current models. We caution, however, that these inferences while interesting are currently tentative and based on only two photometric points. Therefore, more observations are necessary to further constrain the atmospheric temperature profile and composition of WASP-103 b.

Our current results make strong predictions for observations with current and future instruments. Most notably, observations with HST and *Spitzer* can distinguish between our two model scenarios. The HST/WFC3 spectral range of 1.1-1.7 μm contains strong H_2O features and, hence, should detect H_2O in absorption for our model without a thermal inversion and in emission for our model with a thermal inversion. On the other hand, the *Spitzer*/IRAC photometric bands at 3.6 and 4.5 μm together should be able to provide strong constraints on the CO absorption versus emission features between the two models in the 4-5 micron region. On a longer timeframe, the James Webb Space Telescope (JWST) should be able to provide conclusive constraints on the *P-T* profile and composition of this planetary atmosphere.

5 CONCLUSIONS

In this work, we presented a total of nineteen new eclipse light curves for the ultra-short-period hot Jupiter WASP-103 b. Three of these light curves were obtained during transits and sixteen during occultations. We also obtained five new measurements of the radial velocity of the star. We combined these new observations with previously published data and performed a global MCMC analysis of the resulting extensive data set (41 eclipse light curves and 23 RVs), taking into account the contamination from a recently-discovered faint nearby star.

The resulting broad-band optical transmission spectrum is better explained by atmosphere models containing either high-altitude hazes or gaseous TiO. However, this inference hinges critically on a single data point, the g'-band measurement, and should thus be considered tentative.

Using the approach presented in Lendl et al. (2013), that consists in combining a large number (here, fifteen) of occultation light curves obtained with ~1m-class telescopes (here, TRAPPIST and Euler/EulerCam) to mitigate the effects of correlated noise and progressively extract the occultation signal from the noise, we detected the dayside emission of the planet in the z'-band at better than 6-σ (699±110 ppm). From one occultation light curve acquired with the CFHT/WIRCam facility, we also detected the planet's dayside thermal emission in the K_S-band at ~10-σ, the measured occultation depth being 3567^{+400}_{-350} ppm.

We find a brightness temperature in the K_S-band that is marginally higher (~1.5-σ) than the one in the z'-band. If confirmed, this difference in brightness temperature could indicate that TiO, or some other molecule with strong spectral features in the z'-band, is present in the atmosphere but the temperature profile in the atmosphere decreases with altitude (i.e. no thermal inversion), so that the molecular features appear in absorption in the z'-band. Our thermal emission measurements can be explained by two models: a model with a thermal inversion, low TiO abundance, and high CO abundance, or a model without a thermal inversion and with the opposite composition, i.e. modest CO abundance but a non-negligible TiO abundance. A TiO abundance of at least 0.1× that predicted for thermochemical equilibrium with solar elemental abundances is required with both these models. However, we caution that these inferences are currently tentative, as they are based on only two photometric data points.

Future observations with existing (HST, *Spitzer*) or planned (JWST) facilities should be able to provide better constraints on the *P-T* profile and chemical composition of this planet's atmosphere. Improving our understanding of this planetary system also requires a more precise characterization of the faint nearby star, by obtaining additional AO observations with a large-aperture telescope.

ACKNOWLEDGEMENTS

The research leading to these results has received funding from the European Community's Seventh Framework Pro-

gramme (FP7/2013-2016) under grant agreement number 312430 (OPTICON). The Canada-France-Hawaii Telescope (CFHT) is operated by the National Research Council of Canada, the Institut National des Sciences de l'Univers of the Centre National de la Recherche Scientifique of France, and the University of Hawaii. The authors thank the CFHT staff, especially Pascal Fouqué, for scheduling, helping prepare, and conducting the CFHT/WIRCam observations used in this work. TRAPPIST is a project funded by the Belgian Fund for Scientific Research (Fonds National de la Recherche Scientifique, F.R.S.-FNRS) under grant FRFC 2.5.594.09.F, with the participation of the Swiss National Science Fundation (SNF). The Swiss *Euler* Telescope is operated by the University of Geneva, and is funded by the Swiss National Science Foundation. L. Delrez acknowledges support of the F.R.I.A. fund of the FNRS. M. Gillon and E. Jehin are FNRS Research Associates.

REFERENCES

Anderson D. R., et al., 2013, MNRAS, 430, 3422
Baranne A., et al., 1996, A&AS, 119, 373
Budaj J., 2011, AJ, 141, 59
Chandrasekhar S., 1987, Ellipsoidal figures of equilibrium, New York : Dover
Charbonneau D., Brown T. M., Noyes R. W., Gilliland R. L., 2002, ApJ, 568, 377
Charbonneau D., et al., 2005, ApJ, 626, 523
Claret A., Bloemen S., 2011, A&A, 529, A75
Collier Cameron A., et al., 2007, MNRAS, 380, 1230
Collier Cameron A., et al., 2010, MNRAS, 407, 507
Cowan N. B., Agol E., 2011, ApJ, 729, 54
Croll B., Albert L., Lafreniere D., Jayawardhana R., Fortney J. J., 2010, ApJ, 717, 1084
Croll B., Lafreniere D., Albert L., Jayawardhana R., Fortney J. J., Murray N., 2011, AJ, 141, 30
Croll B., et al., 2015, ApJ, 802, 28
Delrez L., et al., 2016, MNRAS, 458, 4025
Deming D., Seager S., 2009, Nature, 462, 301
Deming D., Seager S., Richardson L. J., Harrington J., 2005, Nature, 434, 740
Deming D., et al., 2013, ApJ, 774, 95
Devost D., Albert L., Teeple D., Croll B., 2010, in Observatory Operations: Strategies, Processes, and Systems III. p. 77372D, doi:10.1117/12.856848
Diamond-Lowe H., Stevenson K. B., Bean J. L., Line M. R., Fortney J. J., 2014, ApJ, 796, 66
Eastman J., Siverd R., Gaudi B. S., 2010, PASP, 122, 935
Enoch B., Collier Cameron A., Parley N. R., Hebb L., 2010, A&A, 516, A33
Fortney J. J., Lodders K., Marley M. S., Freedman R. S., 2008, ApJ, 678, 1419
Gelman A., Rubin D., 1992, Stat. Sci., 7, 457
Gibson N. P., Aigrain S., Barstow J. K., Evans T. M., Fletcher L. N., Irwin P. G. J., 2013, MNRAS, 428, 3680
Gillon M., Jehin E., Magain P., Chantry V., Hutsemékers D., Manfroid J., Queloz D., Udry S., 2011a, in European Physical Journal Web of Conferences. p. 06002 (arXiv:1101.5807), doi:10.1051/epjconf/20101106002
Gillon M., et al., 2011b, A&A, 533, A88
Gillon M., et al., 2012, A&A, 542, A4
Gillon M., et al., 2014, A&A, 562, L3
Hansen C. J., Schwartz J. C., Cowan N. B., 2014, MNRAS, 444, 3632
Haynes K., Mandell A. M., Madhusudhan N., Deming D., Knutson H., 2015, ApJ, 806, 146
Hebb L., et al., 2009, ApJ, 693, 1920
Hellier C., et al., 2011, in European Physical Journal Web of Conferences. p. 01004 (arXiv:1012.2286), doi:10.1051/epjconf/20101101004
Huitson C. M., et al., 2013, MNRAS, 434, 3252
Husser T.-O., Wende-von Berg S., Dreizler S., Homeier D., Reiners A., Barman T., Hauschildt P. H., 2013, A&A, 553, A6
Jehin E., et al., 2011, The Messenger, 145, 2
Knutson H. A., Charbonneau D., Allen L. E., Burrows A., Megeath S. T., 2008, ApJ, 673, 526
Knutson H. A., Charbonneau D., Burrows A., O'Donovan F. T., Mandushev G., 2009, ApJ, 691, 866
Knutson H. A., Howard A. W., Isaacson H., 2010, ApJ, 720, 1569
Lendl M., et al., 2012, A&A, 544, A72
Lendl M., Gillon M., Queloz D., Alonso R., Fumel A., Jehin E., Naef D., 2013, A&A, 552, A2
Lendl M., et al., 2016, A&A, 587, A67
López-Morales M., Seager S., 2007, The Astrophysical Journal Letters, 667, L191
Machalek P., McCullough P. R., Burke C. J., Valenti J. A., Burrows A., Hora J. L., 2008, ApJ, 684, 1427
Madhusudhan N., 2012, ApJ, 758, 36
Madhusudhan N., Seager S., 2009, ApJ, 707, 24
Madhusudhan N., et al., 2011a, Nature, 469, 64
Madhusudhan N., Mousis O., Johnson T. V., Lunine J. I., 2011b, ApJ, 743, 191
Mandel K., Agol E., 2002, ApJ, 580, L171
Murray C. D., Correia A. C. M., 2010, Keplerian Orbits and Dynamics of Exoplanets. pp 15–23
Ngo H., et al., 2016, preprint, (arXiv:1606.07102)
Nikolov N., et al., 2014, MNRAS, 437, 46
Nikolov N., et al., 2015, MNRAS, 447, 463
Pepe F., Mayor M., Galland F., Naef D., Queloz D., Santos N. C., Udry S., Burnet M., 2002, A&A, 388, 632
Perez-Becker D., Showman A. P., 2013, ApJ, 776, 134
Pollacco D. L., et al., 2006, PASP, 118, 1407
Puget P., et al., 2004, in Moorwood A. F. M., Iye M., eds, Proc. SPIEVol. 5492, Ground-based Instrumentation for Astronomy. pp 978–987, doi:10.1117/12.551097
Queloz D., et al., 2000, A&A, 354, 99
Queloz D., et al., 2001, A&A, 379, 279
Schwarz G. E., 1978, Ann. Statist., 6, 461
Schwarz H., Brogi M., de Kok R., Birkby J., Snellen I., 2015, A&A, 576, A111
Seager S., Mallén-Ornelas G., 2003, The Astrophysical Journal, 585, 1038
Seager S., Sasselov D. D., 2000, ApJ, 537, 916
Sing D. K., et al., 2011, A&A, 527, A73
Sing D. K., et al., 2015, MNRAS, 446, 2428
Sing D. K., et al., 2016, Nature, 529, 59
Skrutskie M. F., et al., 2006, AJ, 131, 1163
Southworth J., 2011, MNRAS, 417, 2166
Southworth J., Evans D. F., 2016, MNRAS,
Southworth J., et al., 2015, MNRAS, 447, 711
Spiegel D. S., Silverio K., Burrows A., 2009, ApJ, 699, 1487
Stetson P. B., 1987, PASP, 99, 191
Straižys V., Lazauskaitė R., 2009, Baltic Astronomy, 18, 19
Vacca W. D., Cushing M. C., Rayner J. T., 2004, PASP, 116, 352
Wang W., van Boekel R., Madhusudhan N., Chen G., Zhao G., Henning T., 2013, ApJ, 770, 70
Winn J. N., 2010, Transits and Occultations, Exoplanets, edited by S. Seager. University of Arizona Press. pp 55–77
Wöllert M., Brandner W., 2015, A&A, 579, A129

APPENDIX A: INDIVIDUAL ECLIPSE LIGHT CURVES

This paper has been typeset from a TEX/LATEX file prepared by the author.

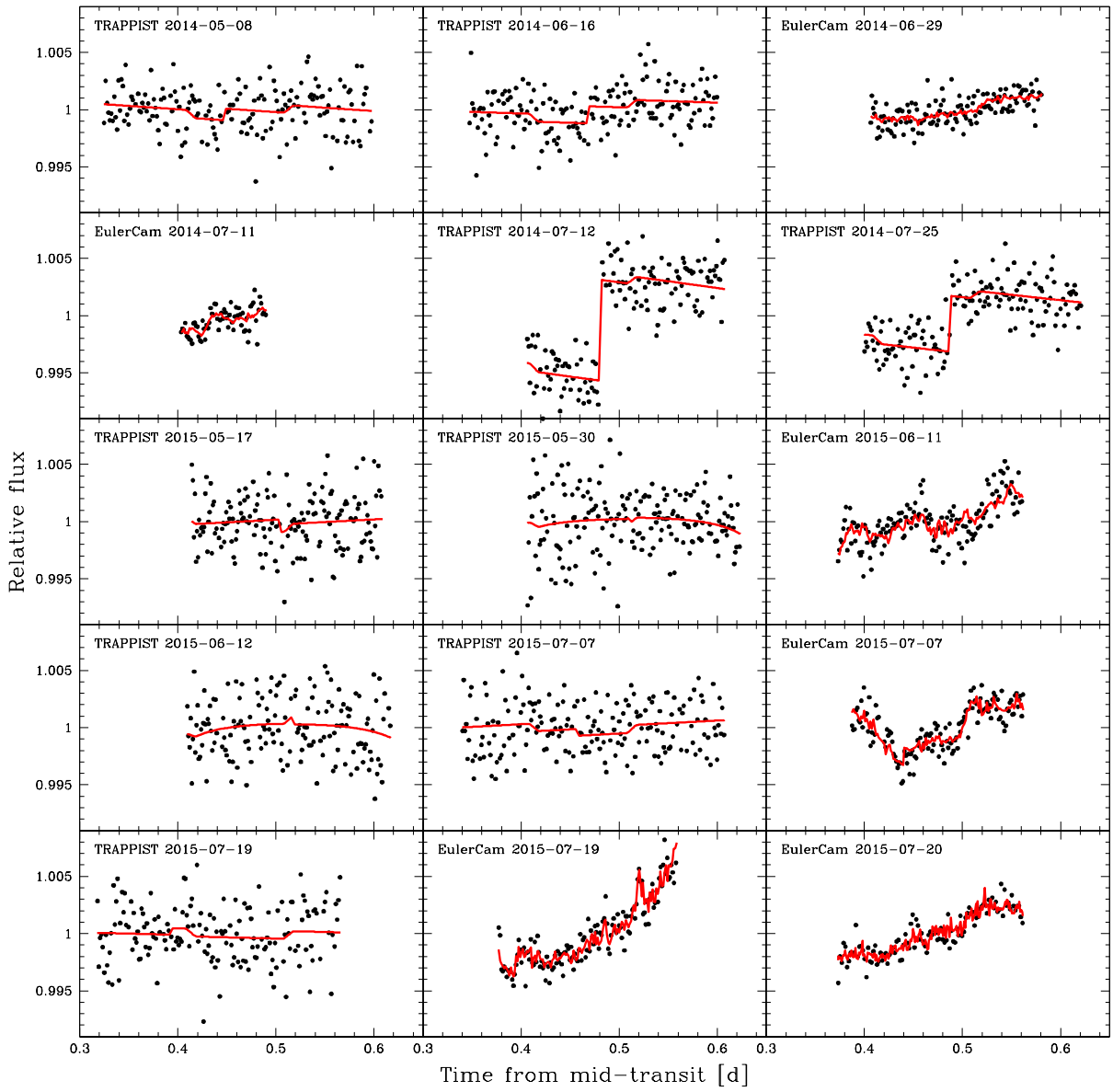

Figure A1. All raw occultation light curves obtained in the z'-band with TRAPPIST and Euler/EulerCam. The data are period-folded on the best-fit transit ephemeris from our global MCMC analysis (see Section 3.2) and binned in 2min bins. For each light curve, the best-fit full model (photometric baseline × occultation in the z'-band) is overplotted in red. The data and models are not corrected for the dilution by the nearby star here.

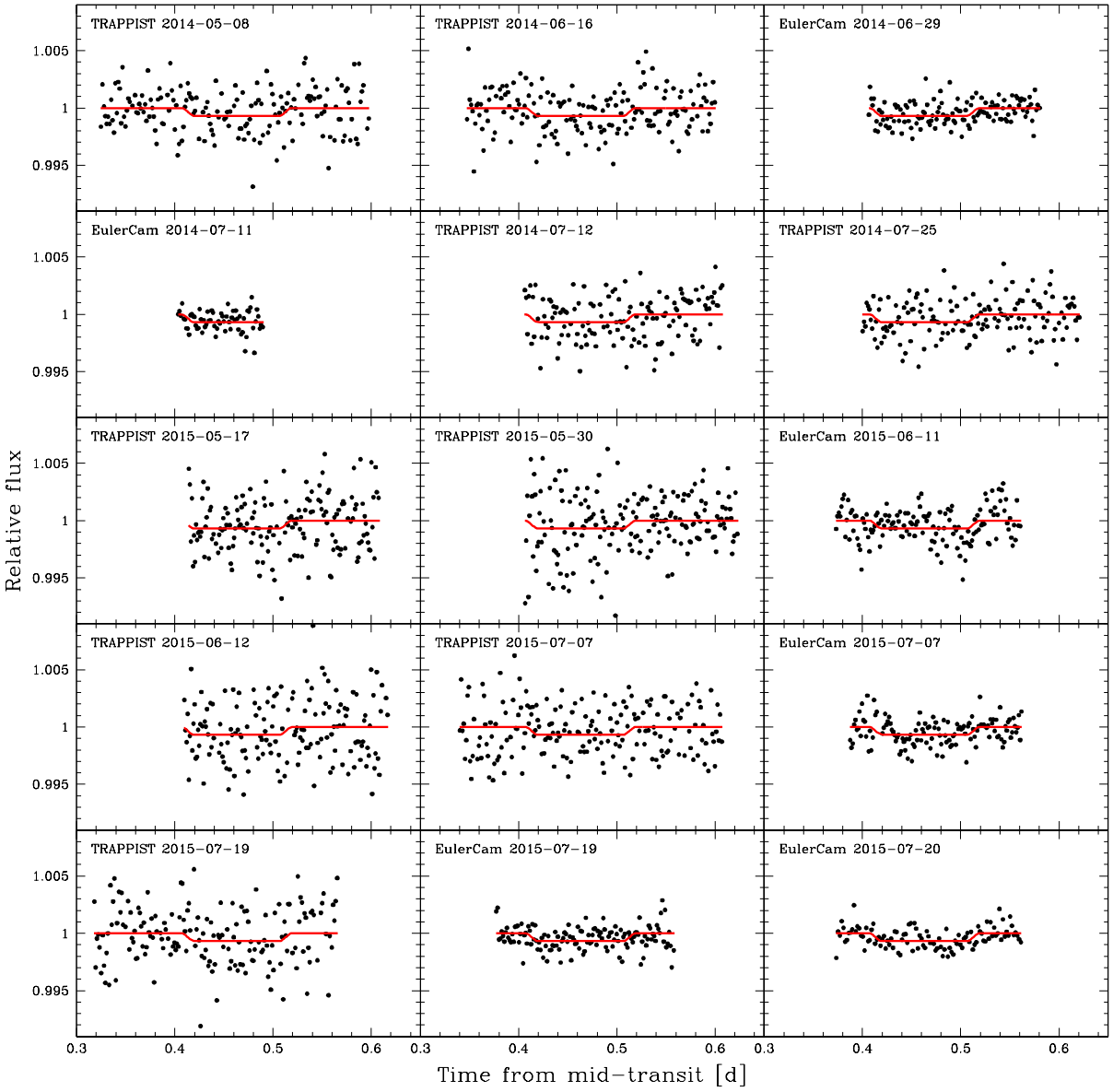

Figure A2. Same light curves as in Fig. A1, but divided by their best-fit baseline models (different for each light curve). The best-fit occultation model in the z'-band is overplotted in red. The data and model are not corrected for the dilution by the nearby star here.

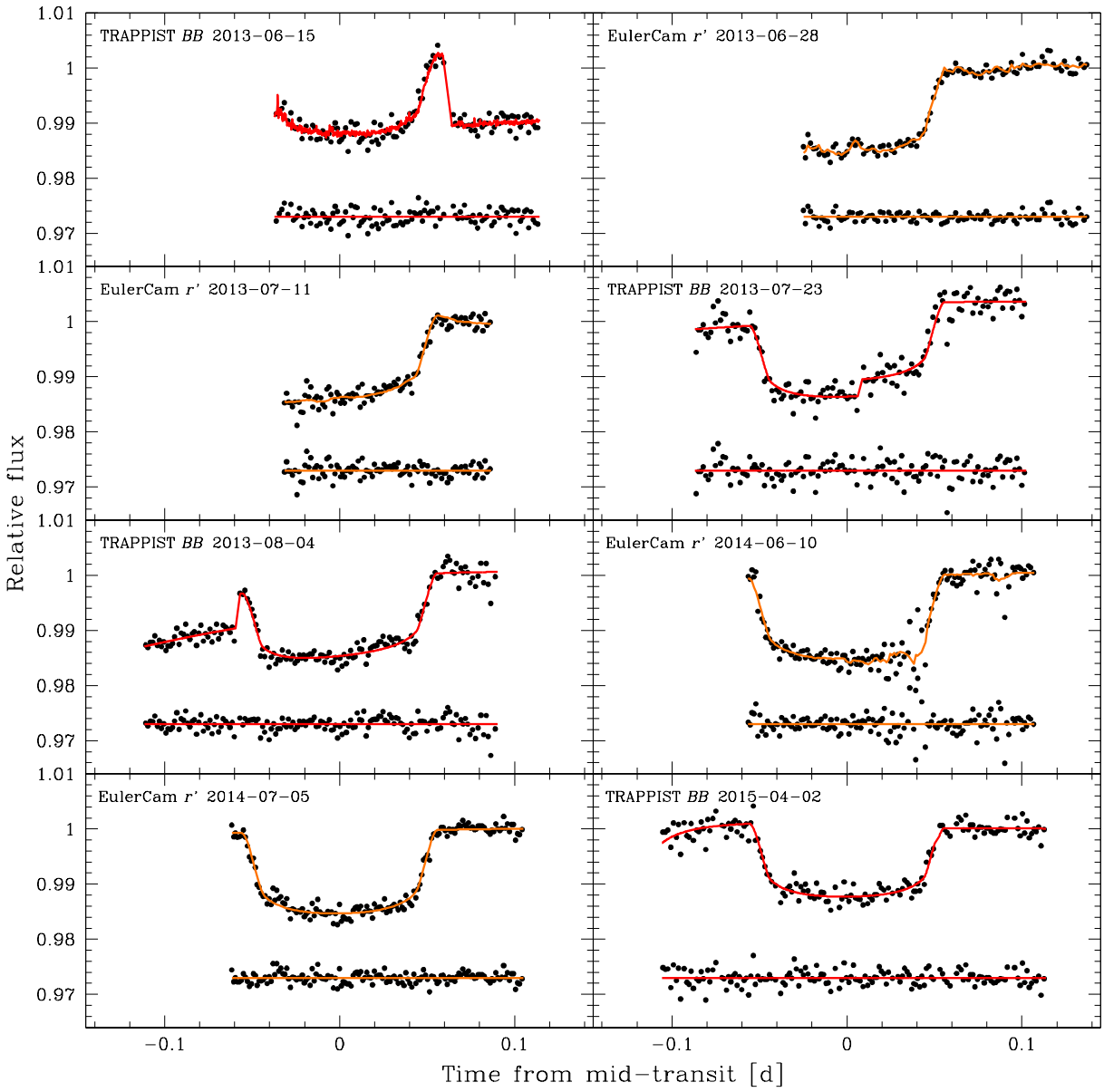

Figure A3. All raw TRAPPIST and Euler/EulerCam transit light curves used in this work. The data are period-folded on the best-fit transit ephemeris from our global MCMC analysis (see Section 3.2) and binned in 2min bins. For each light curve, the overplotted solid line is the best-fit full model (photometric baseline × transit). The data and models are not corrected for the dilution by the nearby star here. The first five light curves were published in G14, while the last three ones are new data.

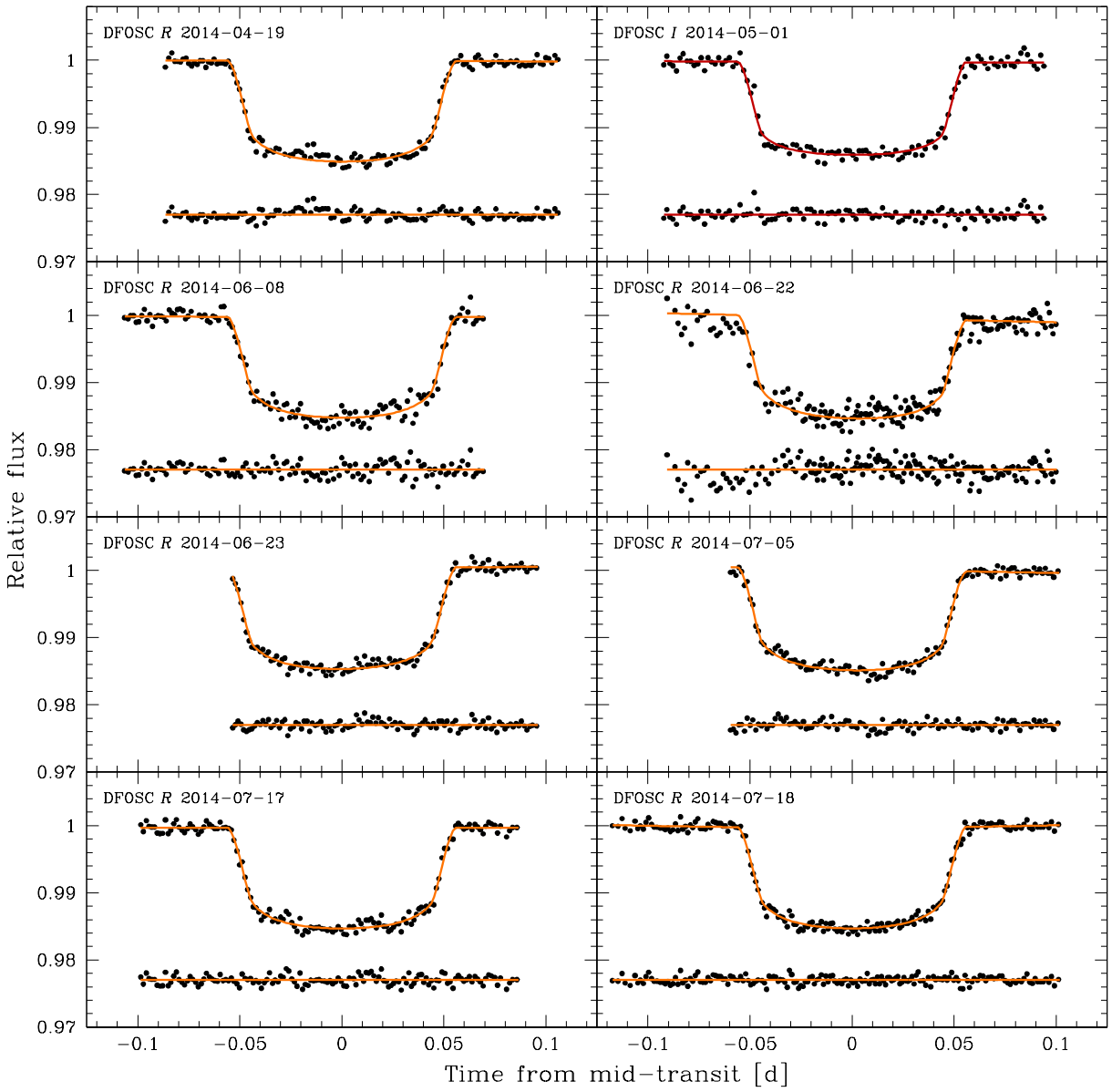

Figure A4. All raw Danish/DFOSC transit light curves used in this work. The data are period-folded on the best-fit transit ephemeris from our global MCMC analysis (see Section 3.2) and binned in 2min bins. For each light curve, the overplotted solid line is the best-fit full model (photometric baseline × transit). The data and models are not corrected for the dilution by the nearby star here. All these light curves were published in S15.

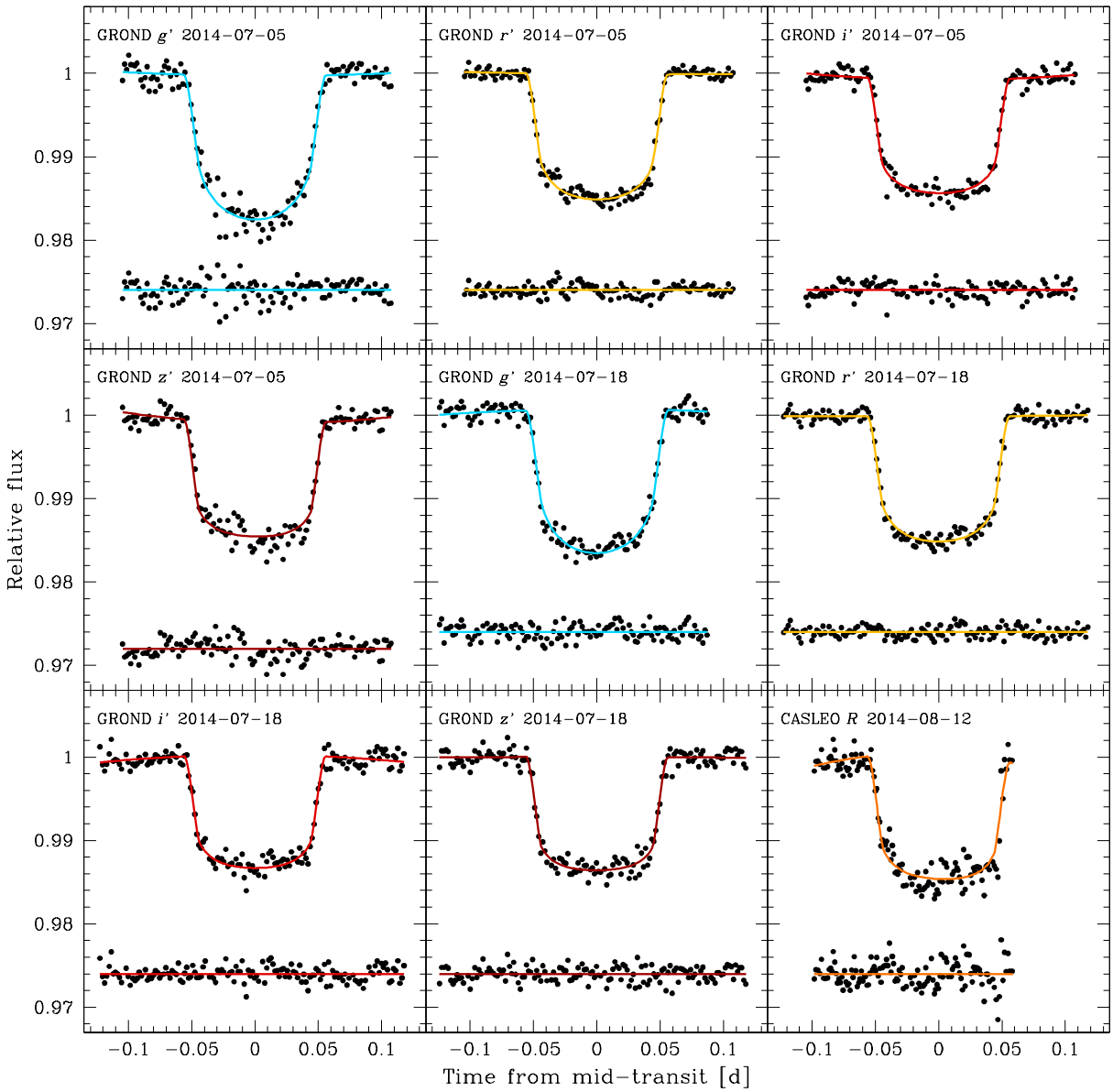

Figure A5. All raw 2.2m/GROND and CASLEO/2.15m transit light curves used in this work. The data are period-folded on the best-fit transit ephemeris from our global MCMC analysis (see Section 3.2) and binned in 2min bins. For each light curve, the overplotted solid line is the best-fit full model (photometric baseline × transit). The data and models are not corrected for the dilution by the nearby star here. All these light curves were published in S15.

Chapter 6

Summary and future work

In this final chapter, I provide first a summary of the main results of my thesis. I then give a general outlook for the future of exoplanet research, before describing briefly some of the projects I intend to carry out in the coming years.

6.1 Summary

During my PhD, I have engaged in a wide range of activities related to both the detection and characterization of transiting hot Jupiters. First, I have been actively involved in the WASP transit survey, taking charge of the photometric follow-up of planetary candidates and confirmed planets with the TRAPPIST robotic telescope for more than 3 years. The aim of these follow-up observations has been twofold: identifying false positives among the planetary candidates, and for candidates that turned out to be confirmed planets, helping in the precise determination of the system parameters. I contributed in this way to the discovery of about 80 planets (about 30 of these planets have not yet been published) and led the analysis and publication of four planetary systems: WASP-68, -73, -88, and -121.

The hot Jupiters WASP-68 b, WASP-73 b, and WASP-88 b are all three in 4–5 days orbits around evolved late-F/early-G stars, yet they have very different bulk properties. WASP-73 b is a dense planet ($\sim$1.2 $\rho_{\rm Jup}$), which might be enriched in heavy elements. On the contrary, WASP-88 b is a super-inflated hot Jupiter and one of the less dense planets known to date ($\sim$0.1 $\rho_{\rm Jup}$). WASP-68 b lies between these two planets, with a density that is typical of many hot Jupiters ($\sim$0.5 $\rho_{\rm Jup}$). These three planets illustrate well the great diversity of the hot Jupiter population.

WASP-121 b is in my view one of the most fascinating objects found by WASP. This is an extremely inflated ($\sim$1.9 $R_{\rm Jup}$) Jupiter-mass ($\sim$1.2 $M_{\rm Jup}$) planet in a very-short-period orbit ($\sim$1.3 days) around a bright (V=10.4) F6V star. A first interesting property of this hot Jupiter is that its orbital semi-major axis is only $\sim$15% larger than its Roche limit, meaning that the planet might be close to tidal disruption and is probably already significantly distorted, as suggested by a computation of its shape using a Roche model. According to tidal evolution models, the planet could reach its Roche limit within a few tens or a few hundreds of million years, depending on the efficiency of the tidal dissipation inside the star. Measuring transit timing variations due to the orbital decay of the planet, which could be detectable on the decade time-scale, would allow to constrain this tidal dissipation efficiency. Secondly, a measurement of the planet's Rossiter-McLaughlin effect with Euler/CORALIE suggests that the planet's orbital axis is significantly misaligned with the spin axis of the host star, which would favor a migration pathway involving few-body

dynamical interactions. Finally, WASP-121 b is a prime target for atmospheric characterization, using both transmission and emission spectroscopy. By combining seven occultation light curves obtained with TRAPPIST, I was able to detect the planet's dayside emission in the z'-band at better than 4-σ (occultation depth of 603$\pm$130 ppm), thus providing a first constraint on the planet's dayside emission spectrum. Combining this measurement with other observations at longer wavelengths will allow to gain insights on the planet's dayside atmospheric properties. WASP-121 b could be a pivotal object for the understanding of hot Jupiters' atmospheric properties, as will be discussed in Section 6.3.1.

In parallel to this work on detection and first characterization of new hot Jupiters, I have also engaged in atmospheric characterization studies of some interesting known transiting gas giants. First, I contributed to the spectrophotometric study, led by Monika Lendl, of the transmission spectrum of the low-density sub-Jupiter WASP-49 b with the VLT/FORS2 instrument. Three transits were observed, leading to three independent (multi-epoch) transmission spectra between 738 and 1020nm, which were found to agree well with each other. These three data sets, as well as additional broad-band transit photometry obtained with TRAPPIST and Euler/EulerCam, were used as inputs of a global MCMC analysis to derive a combined transmission spectrum for WASP-49 b between 650 and 1020nm. This transmission spectrum does not show any obvious absorption features and is best fit by atmospheric models containing a cloud deck at a pressure level of 1 mbar or less that efficiently obscures the atmospheric spectral signatures. Using again VLT/FORS2, I conducted a spectrophotometric study of the transmission spectrum of another hot Jupiter, WASP-80 b, a rare specimen of gas giant transiting a late-K/early-M star. The transmission spectrum of WASP-80 b between 740 and 1020nm shows a slope of increasing effective planetary radius from longer towards shorter wavelengths, detected to a significance of 3.6-σ. This slope is marginally inconsistent with Rayleigh scattering (at the $\sim$2.2-σ level) and is not likely to be caused by unocculted star spots or an unresolved stellar object. Further investigation of its possible origin is ongoing. Except for this slope, the transmission spectrum does not display any obvious additional features, within the measurement uncertainties. The precision of the transmission spectrum is however below expectations and would strongly benefit from further observations. This is due to both the reduced data set (one and a half transits instead of four full transits, due to a combination of bad weather and technical issues) and strong correlated noise stemming from the longitudinal atmospheric dispersion corrector (LADC). Issues about the LADC were communicated to ESO and it has now been upgraded.

Finally, I conducted an intensive ground-based photometric follow-up campaign of the ultra-hot gas giant planet WASP-103 b. A total of sixteen occultation light curves were gathered, fifteen of which were acquired in the z'-band with TRAPPIST and Euler/EulerCam and one was obtained in the K_S-band with the CFHT/WIRCam near-IR facility. This data set was complemented with three additional transit light curves obtained with TRAPPIST and Euler/EulerCam, as well as five new RVs acquired with Euler/CORALIE. I combined these new observations with previously published data, consisting of transit photometry in various broad-band optical filters and RV measurements, and performed a global MCMC analysis of the resulting extensive data set (41 eclipse light curves and 23 RVs). The resulting transmission and emission measurements were then compared to model atmospheric spectra of WASP-103 b. The planet's broad-band optical transmission spectrum is better explained by atmosphere models containing either high-altitude hazes or gaseous TiO. On the emission side, the planet's dayside thermal emission is detected in both the z' (699$\pm$110

ppm, >6-σ detection) and K_S (3567^{+400}_{-350} ppm, $\sim$10-σ detection) bands. The corresponding brightness temperatures suggest a peculiar feature to be confirmed: the brightness temperature in the K_S-band is marginally higher ($\sim$1.5-σ) than the one in the z'-band. Two models (at least) can explain these thermal emission measurements: a model with a thermal inversion, low TiO abundance, and high CO abundance, or a model without a thermal inversion and with the opposite composition, i.e. modest CO abundance but a non-negligible TiO abundance. Both models require a TiO abundance of at least 0.1$\times$ that predicted for thermochemical equilibrium with solar elemental abundances. These results, both in transmission and emission, are currently tentative and more data are required to place better constraints on the chemical composition and P-T profile of this planet's atmosphere.

6.2 Looking forward

More than two decades after the discovery of 51 Peg b, hot Jupiters are still shrouded in mystery. Although this research field has seen significant advances during the four years of my PhD, many questions still need answers, for example: What exact mechanisms are responsible for the wide range of orbital obliquities observed in the hot Jupiter population? How is the chemical composition of hot Jupiters linked to their formation and migration processes? What mechanisms are responsible for the inflated radii measured for many hot Jupiters? Why do some hot Jupiters appear to be cloudy/hazy while others do not? How is the formation of aerosols linked to the atmospheric chemical composition and level of irradiation? What are the effects of aerosols on the atmospheric thermal structure and circulation? To which extent do winds redistribute heat from the permanent dayside to the nightside of these planets? While we have started to put the pieces of the puzzle together, we still do not know today what the final picture will be.

Only by pursuing our efforts to thoroughly characterize a large sample of planetary systems across a wide range of stellar and planetary parameters may we get some answers to the above questions. Current ground- and space-based facilities have given us first glimpses into the properties of hot Jupiters' atmospheres, but the next generation of telescopes and instruments should lead to great leaps forward in the field. The ESA CHEOPS mission (CHaracterising ExOPlanets Satellite, Broeg et al. 2013), scheduled for launch in 2017, will soon produce high-precision optical-light occultation measurements and phase curves of known hot Jupiters. The JWST (James Webb Space Telescope, Beichman et al. 2014), scheduled for launch in 2018, will be capable of obtaining transmission and emission spectra of hot Jupiters at very high signal-to-noise ratio and high-resolution with its NIRSpec (0.7-5 μm) and MIRI (5-28 μm) instruments. From the ground, the next decade will see the development of a new class of extremely large aperture ($\sim$25–40m) telescopes, such as the E-ELT (European Extremely Large Telescope, Gilmozzi and Spyromilio 2007) or the GMT (Giant Magellan Telescope, Johns et al. 2012), equipped with high-resolution spectrographs, that will open up new possibilities for atmospheric studies of hot Jupiters in the optical and near-IR.

From a broader perspective, the work currently undertaken to study atmospheres of hot Jupiters is paving the way towards the future study of smaller and cooler planets. In this context, a new generation of transit surveys is aiming at building up a sample of planets with sizes ranging from Neptune's to Earth's (and smaller) amenable for thorough

atmospheric characterization with planned facilities. As the amplitude of atmospheric signatures in transmission and emission scales inversely with the host star's size and luminosity, large efforts are directed towards finding such planets transiting bright late-type stars. Building on the experience of WASP, the Next Generation Transit Survey (NGTS, Wheatley et al. 2013), operating from ESO Paranal Observatory since early 2016, is searching for planets of Neptune-size and smaller transiting bright (V<13) K and early-M stars. Although not specifically focused on late-type stars, the CHEOPS (mentioned above) and NASA TESS (Transiting Exoplanet Survey Satellite, Ricker et al. 2014) missions should also find low-mass planets suitable for atmospheric characterization in their harvests. CHEOPS will search for transiting planets among the low-mass planets found by RV surveys around bright stars. TESS, which is scheduled for launch in 2017, will explore the nearly entire sky for planets of Neptune-size and smaller transiting bright stars with spectral types F5 to M5. Finally, the SPECULOOS ground-based transit survey (Search for habitable Planets EClipsing ULtra-cOOl Stars, Gillon et al. 2013b, Section 6.3.3), beginning in September 2016, will search for planets of Earth-size and smaller transiting the nearest ultra-cool dwarfs (stellar-like objects with effective temperatures of 2700K and below). No doubt that the coming decade holds the promise of ground-breaking advances in the field of exoplanetary science.

6.3 Future work

In this final Section, I give an overview of some future projects I intend to carry out or be involved in, some of which I have already made a start on.

6.3.1 WASP-121 b: a possible benchmark for hot Jupiters' atmospheric studies

As outlined in Section 3.2.7 and at the beginning of this chapter, WASP-121 b is a prime target for atmospheric characterization, using both transmission and emission spectroscopy. Shortly after its public announcement, Evans et al. (2016) observed one of its transits with HST/WFC3 in spectroscopic mode across the 1.12–1.64μm wavelength range. In the resulting transmission spectrum, they detected the 1.4μm H_2O absorption band at high significance (5.4-σ) and also found evidence for FeH (iron hydride) absorption at wavelengths near 1.3μm. Comparing their data with the optical transit light curves published in the discovery paper (Section 3.2.7), they also found the planet's transits to be significantly deeper in the optical relative to the HST/WFC3 near-IR wavelengths. This difference strongly favors atmospheric models including TiO/VO absorption, although a model with scattering by a high-altitude haze and no TiO/VO cannot be firmly excluded. If these results are confirmed, WASP-121 b will be the first hot Jupiter with TiO/VO and FeH detected in transmission. It also shows promise for exploring the link between the presence of strong UV/optical absorbers, such as TiO/VO, and thermal inversions in hot Jupiters' atmospheres.

During my thesis, I have already provided a first constraint on the planet's dayside emission spectrum by measuring its occultation in the z'-band with TRAPPIST (cf. Section 3.2.7). More recently, I have also carried out a two-night observing program on the AAT/IRIS2 near-IR facility (Tinney et al. 2004, 3.9m Anglo-Australian Telescope, Siding

Spring Observatory, Australia), aiming at measuring the planet's dayside thermal emission in the H and K_S bands (OPTICON program 16A/027, PI: Delrez). Some preliminary results are presented in Appendix C. In the near future, I intend to pursue this work on the atmospheric characterization of WASP-121 b, which could become soon a pivotal object for the understanding of hot Jupiters' atmospheric properties.

6.3.2 Irradiated brown dwarfs: a missing link between hot Jupiters and field brown dwarfs

Irradiated brown dwarfs, i.e. brown dwarfs in orbits of a few days around solar-type stars, are rare objects but offer a unique opportunity to forge a link between hot Jupiters and field brown dwarfs, whose atmospheric properties have now been extensively studied via detailed spectroscopy and photometry (for reviews, see e.g. Bailey 2014 or Helling and Casewell 2014). Atmospheric studies of irradiated brown dwarfs would allow hot Jupiters' atmospheres to be compared with those of similarly irradiated but more massive sub-stellar objects and models of hot Jupiters' atmospheres to be tested at higher surface gravities. Similarly, atmospheric properties of isolated brown dwarfs could be compared with those of their irradiated counterparts, allowing to assess the effect of external forcing of brown dwarf atmospheres by stellar insolation. To date, this field of research has been relatively unexplored.

A dozen close brown dwarf companions to solar-type stars have been detected by transit surveys. Among these, two are particularly well suited for atmospheric studies via emission spectroscopy in terms of brightness of the host star and level of irradiation: KELT-1 b (Siverd et al. 2012) and WASP-128 b (Triaud et al. in prep.). While KELT-1 b has been partially studied with *Spitzer* (Beatty et al. 2014), WASP-128 b was only recently detected (see Section 3.2.4) and its atmospheric properties have not been probed yet.

Irradiated brown dwarfs are rare and transiting ones are even rarer. A possible avenue to extend the sample of objects that can be studied would be to use the technique of atmospheric characterization by high-resolution ($R \gtrsim 50\,000$) spectroscopy developed by Ignas Snellen and his team (Snellen et al. 2010) on some favorable non-transiting irradiated brown dwarfs detected by RV surveys. This powerful method has unambiguously revealed the presence of CO and H_2O in several hot Jupiters' atmospheres (see e.g. Birkby et al. 2013, de Kok et al. 2013, Brogi et al. 2014). It works by resolving broad molecular bands in the planetary spectrum into a forest of spectral lines and tracing them directly by their large Doppler shift, due to the change in the radial component of the planet orbital velocity, while the stellar spectrum and telluric lines of the Earth's atmosphere remain essentially stationary (over a period of a few hours). The resulting planetary spectra are then cross-correlated with a high-resolution template spectrum of a specific molecule to assess its presence in the planetary atmosphere and measure its abundance. Transiting planets can be observed at high spectral resolution in transmission, or just before and after occultation, when their dayside is facing the observer. More importantly for the present context, high-resolution dayside emission spectroscopy can be applied to non-transiting planets since the planet thermal emission spectrum is targeted directly (e.g. Brogi et al. 2014). In the near future, I intend to develop expertise in this technique and use it for atmospheric studies of some favorable non-transiting irradiated brown dwarfs, using e.g. the new near-infrared high-resolution spectrographs CARMENES (Quirrenbach et al. 2014) on the 3.5m telescope

at the Calar Alto Observatory (Spain) or GIANO (Origlia et al. 2014) on the 3.6m Telescopio Nazionale Galileo at the Roque de los Muchachos Observatory (La Palma).

6.3.3 Towards the study of other Earths

The overall drive of exoplanetary science is directed towards the study of Earth-like planets orbiting in the habitable zone of their stars and the search for potential traces of life in their atmospheres. However, the atmospheric characterization of an Earth-twin transiting a Sun-like star is out of reach for all the existing or planned astronomical facilities. The main reasons for this are the overwhelmingly large area contrasts between the solar disk and the tiny Earth's atmospheric annulus, and between the Sun's and Earth's luminosities, leading to signal-to-noise ratios (SNRs) much smaller than one for any atmospheric spectroscopic signature and any realistic observing program, even with future facilities like JWST and E-ELT (Seager, Deming, and Valenti 2009).

This negative conclusion does not hold for an Earth-sized planet transiting one of the nearest ultra-cool dwarfs (UCDs), i.e. stellar-like objects with effective temperatures of 2700K and below, sizes close to Jupiter's, and lifetimes several orders of magnitude longer than the Sun's (Reid and Hawley 2005). Because of their low luminosity ($< 0.001\ L_{\odot}$) and small size ($< 0.15\ R_{\odot}$), and the resulting large planet-to-star luminosity and size ratios, expected SNRs on the detection of spectroscopic signatures in the atmosphere of a transiting habitable Earth-twin are indeed much more favorable for UCDs than for any other host star (Kaltenegger and Traub 2009). Concretely, the thorough atmospheric characterization of potentially habitable Earth-sized planets, including the detection of possible biosignatures, will be limited in the next decade to those transiting nearby UCDs.

In this context, UCDs have other advantages. Indeed, they are also, in the first place, privileged targets for the detection of such planets. First, their small size leads for Earth-sized planets to transit signals of the order of one percent, thus similar in amplitude to the ones of Jupiter-sized planets in front of solar-type stars. Secondly, the proximity of their habitable zone, due to their small size and temperature, makes the transits of a habitable planet frequent (periodicities of a few days) and more likely (transit geometric probabilities higher than 2%). Last but not least, there are several hundreds of them in our direct neighborhood (Reid et al. 2008), and they are predicted to harbor a large population of close-in terrestrial planets (see Montgomery and Laughlin 2009 and first results below).

On these grounds, the SPECULOOS ground-based transit survey (Search for habitable Planets EClipsing ULtra-cOOl Stars, Gillon et al. 2013b) will search for planets of Earth-size and below transiting the $\sim$500 nearest southern ultra-cool dwarfs. The project, in which I will actively participate in the coming years, will use four robotic 1m telescopes, equipped with near-infrared-optimized deep-depletion CCDs, whose installation at ESO Paranal Observatory will start in September 2016. SPECULOOS's design and photometric precision were prototyped on TRAPPIST. In this context, a pilot mini-survey targeting the $\sim$60 brightest Southern UCDs has been ongoing since 2011 (Gillon et al. 2013c). This survey recently led to the remarkable discovery of three temperate Earth-size planets transiting an M8-type dwarf star only 12 parsecs away, TRAPPIST-1 (Gillon et al. 2016). The three planets cover a range of temperatures that encompass Venus, Earth, and Mars, and may thus present habitable regions over their surfaces. They are also the first known temperate Earth-sized exoplanets amenable for in-depth atmospheric studies. Building on my past experience with VLT/FORS2 (cf. Chapter 4), I will use this instrument and its restored performance, after

the LADC upgrade, to probe the transmission spectra of the two innermost TRAPPIST-1 planets in the far red (60hrs monitoring program starting in October 2016). This will aid in preparing their in-depth atmospheric characterization with future facilities, like JWST. The TRAPPIST-1 planets were the first detected around an UCD. As of March 2016, TRAPPIST had only completed the monitoring of 15 of its UCD targets. The early detection of the TRAPPIST-1 multiple system is therefore suggestive of a high-frequency of terrestrial planets around UCDs. The very recent RV detection by Anglada-Escudé et al. (2016) of a terrestrial planet candidate in a temperate orbit (11.2 days) around our closest neighbour, Proxima Centauri, an M5.5V dwarf star (strictly speaking not an UCD, but just at the limit), also supports this picture. This bodes extremely well for SPECULOOS, which will begin with the best possible prospects.

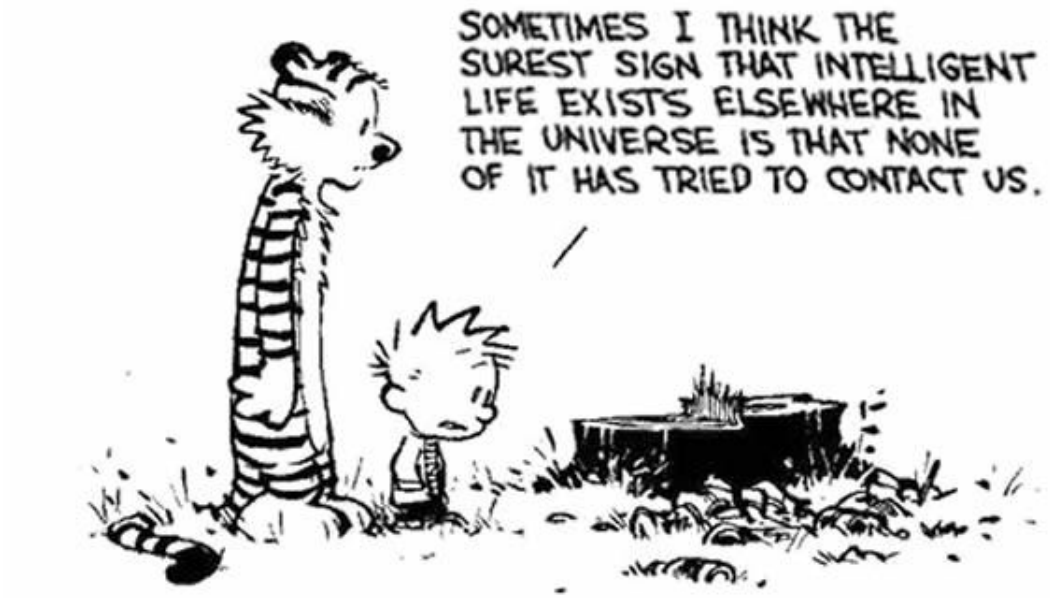

Appendix A

Publications

A.1 Refereed publications

LUHMAN 16AB: A REMARKABLE, VARIABLE L/T TRANSITION BINARY 2 PC FROM THE SUN
Burgasser, A. J.; Faherty, J.; Beletsky, Y.; Plavchan, P.; Gillon, M.; Radigan, J.; Jehin, E.; **Delrez, L.**; Opitom, C.; Morrell, N.; Osten, R.; Street, R.; Melis, C.; Triaud, A.; Simcoe, R.
2013, Memorie della Societa Astronomica Italiana, 84, 1017

FAST-EVOLVING WEATHER FOR THE COOLEST OF OUR TWO NEW SUBSTELLAR NEIGHBOURS
Gillon, M.; Triaud, A. H. M. J.; Jehin, E.; **Delrez, L.**; Opitom, C.; Magain, P.; Lendl, M.; Queloz, D.
2013, A&A, 555, L5

DISCOVERY OF WASP-65B AND WASP-75B: TWO HOT JUPITERS WITHOUT HIGHLY INFLATED RADII
Gómez Maqueo Chew, Y.; Faedi, F.; Pollacco, D.; Brown, D. J. A.; Doyle, A. P.; Collier Cameron, A.; Gillon, M.; Lendl, M.; Smalley, B.; Triaud, A. H. M. J.; West, R. G.; Wheatley, P. J.; Busuttil, R.; Liebig, C.; Anderson, D. R.; Armstrong, D. J.; Barros, S. C. C.; Bento, J.; Bochinski, J.; Burwitz, V.; **Delrez, L.**; Enoch, B.; Fumel, A.; Haswell, C. A.; Hébrard, G.; Hellier, C.; Holmes, S.; Jehin, E.; Kolb, U.; Maxted, P. F. L.; McCormac, J.; Miller, G. R. M.; Norton, A. J.; Pepe, F.; Queloz, D.; Rodríguez, J.; Ségransan, D.; Skillen, I.; Stassun, K. G.; Udry, S.; Watson, C.
2013, A&A, 559, A36

WASP-103 B: A NEW PLANET AT THE EDGE OF TIDAL DISRUPTION
Gillon, M.; Anderson, D. R.; Collier-Cameron, A.; **Delrez, L.**; Hellier, C.; Jehin, E.; Lendl, M.; Maxted, P. F. L.; Pepe, F.; Pollacco, D.; Queloz, D.; Ségransan, D.; Smith, A. M. S.; Smalley, B.; Southworth, J.; Triaud, A. H. M. J.; Udry, S.; Van Grootel, V.; West, R. G.
2014, A&A, 562, L3

SEARCH FOR A HABITABLE TERRESTRIAL PLANET TRANSITING THE NEARBY RED DWARF GJ 1214
Gillon, M.; Demory, B.-O.; Madhusudhan, N.; Deming, D.; Seager, S.; Zsom, A.; Knutson, H. A.; Lanotte, A. A.; Bonfils, X.; Désert, J.-M.; **Delrez, L.**; Jehin, E.; Fraine, J. D.; Magain, P.; Triaud, A. H. M. J.
2014, A&A, 563, A21

TRANSITING PLANETS FROM WASP-SOUTH, EULER, AND TRAPPIST: WASP-68 B, WASP-73 B, AND WASP-88 B, THREE HOT JUPITERS TRANSITING EVOLVED SOLAR-TYPE STARS
Delrez, L.; Van Grootel, V.; Anderson, D. R.; Collier-Cameron, A.; Doyle, A. P.; Fumel, A.; Gillon, M.; Hellier, C.; Jehin, E.; Lendl, M.; Neveu-VanMalle, M.; Maxted, P. F. L.; Pepe, F.; Pollacco, D.; Queloz, D.; Ségransan, D.; Smalley, B.; Smith, A. M. S.; Southworth, J.; Triaud, A. H. M. J.; Udry, S.; West, R. G.
2014, A&A, 563, A143

ECLIPSING AM BINARY SYSTEMS IN THE SUPERWASP SURVEY
Smalley, B.; Southworth, J.; Pintado, O. I.; Gillon, M.; Holdsworth, D. L.; Anderson, D. R.; Barros, S. C. C.; Collier Cameron, A.; **Delrez, L.**; Faedi, F.; Haswell, C. A.; Hellier, C.; Horne, K.; Jehin, E.; Maxted, P. F. L.; Norton, A. J.; Pollacco, D.; Skillen, I.; Smith, A. M. S.; West, R. G.; Wheatley, P. J.
2014, A&A, 564, A69

A MONITORING CAMPAIGN FOR LUHMAN 16AB. I. DETECTION OF RESOLVED NEAR-INFRARED SPECTROSCOPIC VARIABILITY
Burgasser, Adam J.; Gillon, Michaël; Faherty, Jacqueline K.; Radigan, Jacqueline; Triaud, Amaury H. M. J.; Plavchan, Peter; Street, Rachel; Jehin, **Delrez, L.**; Opitom, C.
2014, ApJ, 785, 48

HIGH-FREQUENCY A-TYPE PULSATORS DISCOVERED USING SUPERWASP
Holdsworth, Daniel L.; Smalley, B.; Gillon, M.; Clubb, K. I.; Southworth, J.; Maxted, P. F. L.; Anderson, D. R.; Barros, S. C. C.; Cameron, A. Collier; **Delrez, L.**; Faedi, F.; Haswell, C. A.; Hellier, C.; Horne, K.; Jehin, E.; Norton, A. J.; Pollacco, D.; Skillen, I.; Smith, A. M. S.; West, R. G.; Wheatley, P. J.
2014, MNRAS, 439, 2078

TRANSITING HOT JUPITERS FROM WASP-SOUTH, EULER AND TRAPPIST: WASP-95B TO WASP-101B
Hellier, Coel; Anderson, D. R.; Cameron, A. Collier; **Delrez, L.**; Gillon, M.; Jehin, E.; Lendl, M.; Maxted, P. F. L.; Pepe, F.; Pollacco, D.; Queloz, D.; Ségransan, D.; Smalley, B.; Smith, A. M. S.; Southworth, J.; Triaud, A. H. M. J.; Udry, S.; West, R. G.
2014, MNRAS, 440, 1982

A WINDOW ON EXOPLANET DYNAMICAL HISTORIES: ROSSITER-MCLAUGHLIN OBSERVATIONS OF WASP-13B AND WASP-32B
Brothwell, R. D.; Watson, C. A.; Hébrard, G.; Triaud, A. H. M. J.; Cegla, H. M.; Santerne, A.; Hébrard, E.; Anderson, D. R.; Pollacco, D.; Simpson, E. K.; Bouchy, F.; Brown, D. J. A.; Chew, Y. Gómez Maqueo; Cameron, A. Collier; Armstrong, D. J.; Barros, S. C. C.; Bento, J.; Bochinski, J.; Burwitz, V.; Busuttil, R.; **Delrez, L.**; Doyle, A. P.; Faedi, F.; Fumel, A.; Gillon, M.; Haswell, C. A.; Hellier, C.; Jehin, E.; Kolb, U.; Lendl, M.; Liebig, C.; Maxted, P. F. L.; McCormac, J.; Miller, G. R. M.; Norton, A. J.; Pepe, F.; Queloz, D.; Rodríguez, J.; Ségransan, D.; Skillen, I.; Smalley, B.; Stassun, K. G.; Udry, S.; West, R. G.; Wheatley, P. J.
2014, MNRAS, 440, 3392

WASP-117b: a 10-day-period Saturn in an eccentric and misaligned orbit
Lendl, M.; Triaud, A. H. M. J.; Anderson, D. R.; Collier Cameron, A.; **Delrez, L.**; Doyle, A. P.; Gillon, M.; Hellier, C.; Jehin, E.; Maxted, P. F. L.; Neveu-VanMalle, M.; Pepe, F.; Pollacco, D.; Queloz, D.; Ségransan, D.; Smalley, B.; Smith, A. M. S.; Udry, S.; Van Grootel, V.; West, R. G.
2014, A&A, 568, A81

WASP-104b and WASP-106b: two transiting hot Jupiters in 1.75-day and 9.3-day orbits
Smith, A. M. S.; Anderson, D. R.; Armstrong, D. J.; Barros, S. C. C.; Bonomo, A. S.; Bouchy, F.; Brown, D. J. A.; Collier Cameron, A.; **Delrez, L.**; Faedi, F.; Gillon, M.; Gómez Maqueo Chew, Y.; Hébrard, G.; Jehin, E.; Lendl, M.; Louden, T. M.; Maxted, P. F. L.; Montagnier, G.; Neveu-VanMalle, M.; Osborn, H. P.; Pepe, F.; Pollacco, D.; Queloz, D.; Rostron, J. W.; Segransan, D.; Smalley, B.; Triaud, A. H. M. J.; Turner, O. D.; Udry, S.; Walker, S. R.; West, R. G.; Wheatley, P. J.
2014, A&A, 570, A64

WASP-94 A and B planets: hot-Jupiter cousins in a twin-star system
Neveu-VanMalle, M.; Queloz, D.; Anderson, D. R.; Charbonnel, C.; Collier Cameron, A.; **Delrez, L.**; Gillon, M.; Hellier, C.; Jehin, E.; Lendl, M.; Maxted, P. F. L.; Pepe, F.; Pollacco, D.; Ségransan, D.; Smalley, B.; Smith, A. M. S.; Southworth, J.; Triaud, A. H. M. J.; Udry, S.; West, R. G.
2014, A&A, 572, A49

Three newly discovered sub-Jupiter-mass planets: WASP-69b and WASP-84b transit active K dwarfs and WASP-70Ab transits the evolved primary of a G4+K3 binary
Anderson, D. R.; Collier Cameron, A.; **Delrez, L.**; Doyle, A. P.; Faedi, F.; Fumel, A.; Gillon, M.; Gómez Maqueo Chew, Y.; Hellier, C.; Jehin, E.; Lendl, M.; Maxted, P. F. L.; Pepe, F.; Pollacco, D.; Queloz, D.; Ségransan, D.; Skillen, I.; Smalley, B.; Smith, A. M. S.; Southworth, J.; Triaud, A. H. M. J.; Turner, O. D.; Udry, S.; West, R. G.
2014, MNRAS, 445, 1114

WISE J072003.20-084651.2: an Old and Active M9.5 + T5 Spectral Binary 6 pc from the Sun
Burgasser, A. J.; Gillon, M.; Melis, C.; Bowler, B. P.; Michelsen, E. L.; Bardalez Gagliuffi, D.; Gelino, C. R.; Jehin, E.; **Delrez, L.**; Manfroid, J.; Blake, C. H.
2015, AJ, 149, 104

Three WASP-South Transiting Exoplanets: WASP-74b, WASP-83b, and WASP-89b
Hellier, C.; Anderson, D. R.; Collier Cameron, A.; **Delrez, L.**; Gillon, M.; Jehin, E.; Lendl, M.; Maxted, P. F. L.; Pepe, F.; Pollacco, D.; Queloz, D.; Ségransan, D.; Smalley, B.; Smith, A. M. S.; Southworth, J.; Triaud, A. H. M. J.; Turner, O. D.; Udry, S.; West, R. G.
2015, AJ, 150, 18

WASP-80b HAS A DAYSIDE WITHIN THE T-DWARF RANGE
Triaud, A. H. M. J.; Gillon, M.; Ehrenreich, D.; Herrero, E.; Lendl, M.; Anderson, D. R.; Collier Cameron, A.; **Delrez, L.**; Demory, B.-O.; Hellier, C.; Heng, K.; Jehin, E.; Maxted, P. F. L.; Pollacco, D.; Queloz, D.; Ribas, I.; Smalley, B.; Smith, A. M. S.; Udry, S.
2015, MNRAS, 450, 2279

TESTS OF THE PLANETARY HYPOTHESIS FOR PTFO 8-8695b
Yu, L.; Winn, J. N.; Gillon, M.; Albrecht, S.; Rappaport, S.; Bieryla, A.; Dai, F.; **Delrez, L.**; Hillenbrand, L.; Holman, M. J.; Howard, A. W.; Huang, C. X.; Isaacson, H.; Jehin, E.; Lendl, M.; Montet, B. T.; Muirhead, P.; Sanchis-Ojeda, R.; Triaud, A. H. M. J.
2015, ApJ, 812, 48

THE K2-ESPRINT PROJECT I: DISCOVERY OF THE DISINTEGRATING ROCKY PLANET K2-22b WITH A COMETARY HEAD AND LEADING TAIL
Sanchis-Ojeda, R.; Rappaport, S.; Pallé, E.; **Delrez, L.**; DeVore, J.; Gandolfi, D.; Fukui, A.; Ribas, I.; Stassun, K. G.; Albrecht, S.; Dai, F.; Gaidos, E.; Gillon, M.; Hirano, T.; Holman, M.; Howard, A. W.; Isaacson, H.; Jehin, E.; Kuzuhara, M.; Mann, A. W.; Marcy, G. W.; Miles-Páez, P. A.; Montañés-Rodríguez, P. A.; Murgas, F.; Narita, N.; Nowak, G.; Onitsuka, M.; Paegert, M.; Van Eylen, V.; Winn, J. N.; Yu, L.
2015, ApJ, 812, 112

CHARACTERIZATION OF THE K2-19 MULTIPLE-TRANSITING PLANETARY SYSTEM VIA HIGH-DISPERSION SPECTROSCOPY, AO IMAGING, AND TRANSIT TIMING VARIATIONS
Narita, N.; Hirano, T.; Fukui, A.; Hori, Y.; Sanchis-Ojeda, R.; Winn, J. N.; Ryu, T.; Kusakabe, N.; Kudo, T.; Onitsuka, M.; **Delrez, L.**; Gillon, M.; Jehin, E.; McCormac, J.; Holman, M.; Izumiura, H.; Takeda, Y.; Tamura, M.; Yanagisawa, K.
2015, ApJ, 815, 47

LARGER AND FASTER: REVISED PROPERTIES AND A SHORTER ORBITAL PERIOD FOR THE WASP-57 PLANETARY SYSTEM FROM A PRO-AM COLLABORATION
Southworth, J.; Mancini, L.; Tregloan-Reed, J.; Calchi Novati, S.; Ciceri, S.; D'Ago, G.; **Delrez, L.**; Dominik, M.; Evans, D. F.; Gillon, M.; Jehin, E.; Jorgensen, U. G.; Haugbolle, T.; Lendl, M.; Arena, C.; Barbieri, L.; Barbieri, M.; Corfini, G.; Lopresti, C.; Marchini, A.; Marino, G.; Alsubai, K. A.; Bozza, V.; Bramich, D. M.; Figuera Jaimes, R.; Hinse, T. C.; Henning, Th.; Hundertmark, M.; Juncher, D.; Korhonen, H.; Popovas, A.; Rabus, M.; Rahvar, S.; Schmidt, R. W.; Skottfelt, J.; Snodgrass, C.; Starkey, D.; Surdej, J.; Wertz, O.
2015, MNRAS, 454, 3094

THREE IRRADIATED AND BLOATED HOT JUPITERS: WASP-76b, WASP-82b & WASP-90b
West, R. G.; Almenara, J.-M.; Anderson, D. R.; Bouchy, F.; Brown, D. J. A.; Collier Cameron, A.; Deleuil, M.; **Delrez, L.**; Doyle, A. P.; Faedi, F.; Fumel, A.; Gillon, M.; Hebrard, G.; Hellier, C.; Jehin, E.; Lendl, M.; Maxted, P. F. L.; Pepe, F.; Pollacco, D.; Queloz, D.; Segransan, D.; Smalley, B.; Smith, A. M. S.; Triaud, A. H. M. J.; Udry, S.
2016, A&A, 585, A126

HOT JUPITERS WITH RELATIVES: DISCOVERY OF ADDITIONAL PLANETS IN ORBIT AROUND WASP-41 AND WASP-47
Neveu-VanMalle, M.; Queloz, D.; Anderson, D. R.; Brown, D. J. A.; Collier Cameron, A.; **Delrez, L.**; Díaz, R. F.; Gillon, M.; Hellier, C.; Jehin, E.; Lister, T.; Pepe, F.; Rojo, P.; Ségransan, D.; Triaud, A. H. M. J.; Turner, O. D.; Udry, S.
2016, A&A, 586, A93

FORS2 OBSERVES A MULTI-EPOCH TRANSMISSION SPECTRUM OF THE HOT SATURN-MASS EXOPLANET WASP-49B
Lendl, M.; **Delrez, L.**; Gillon, M.; Madhusudhan, N.; Jehin, E.; Queloz, D.; Anderson, D. R.; Demory, B.-O.; Hellier, C.
2016, A&A, 587, A67

TEMPERATE EARTH-SIZED PLANETS TRANSITING A NEARBY ULTRACOOL DWARF STAR
Gillon, M.; Jehin, E.; Lederer, S. M.; **Delrez, L.**; de Wit, J.; Burdanov, A.; Van Grootel, V.; Burgasser, A.; Opitom, C.; Triaud, A. H. M. J.; Demory, B.-O.; Sahu, D. K.; Gagliuffi, D. C. B.; Magain, P.; Queloz, D.
2016, Nature, 533, 221

FIVE TRANSITING HOT JUPITERS DISCOVERED USING WASP-SOUTH, EULER, AND TRAPPIST: WASP-119 B, WASP-124 B, WASP-126 B, WASP-129 B, AND WASP-133 B
Maxted, P. F. L.; Anderson, D. R.; Collier Cameron, A.; **Delrez, L.**; Gillon, M.; Hellier, C.; Jehin, E.; Lendl, M.; Neveu-VanMalle, M.; Pepe, F.; Pollacco, D.; Queloz, D.; Ségransan, D.; Smalley, B.; Smith, A. M. S.; Southworth, J.; Triaud, A. H. M. J.; Udry, S.; Wagg, T.; West, R. G.
2016, A&A, 591, A55

WASP-121 B: A HOT JUPITER CLOSE TO TIDAL DISRUPTION TRANSITING AN ACTIVE F STAR
Delrez, L.; Santerne, A.; Almenara, J.-M.; Anderson, D. R.; Collier-Cameron, A.; Díaz, R. F.; Gillon, M.; Hellier, C.; Jehin, E.; Lendl, M.; Maxted, P. F. L.; Neveu-VanMalle, M.; Pepe, F.; Pollacco, D.; Queloz, D.; Ségransan, D.; Smalley, B.; Smith, A. M. S.; Triaud, A. H. M. J.; Udry, S.; Van Grootel, V.; West, R. G.
2016, MNRAS, 458, 4025

WASP-120 B, WASP-122 B, AND WASP-123 B: THREE NEWLY DISCOVERED PLANETS FROM THE WASP-SOUTH SURVEY
Turner, O. D.; Anderson, D. R.; Collier Cameron, A.; **Delrez, L.**; Evans, D. F.; Gillon, M.; Hellier, C.; Jehin, E.; Lendl, M.; Maxted, P. F. L.; Pepe, F.; Pollacco, D.; Queloz, D.; Ségransan, D.; Smalley, B.; Smith, A. M. S.; Triaud, A. H. M. J.; Udry, S.; West, R. G.
2016, PASP, 128, 064401

WASP-157B, A TRANSITING HOT JUPITER OBSERVED WITH K2
Močnik, T.; Anderson, D. R.; Brown, D. J. A.; Collier Cameron, A.; **Delrez, L.**; Gillon, M.; Hellier, C.; Jehin, E.; Lendl, M.; Maxted, P. F. L.; Neveu-VanMalle, M.; Pepe, F.; Pollacco, D.; Queloz, D.; Ségransan, D.; Smalley, B.; Southworth, J.; Triaud, A. H. M. J.; Udry, S.;

West, R. G.
2016, PASP, accepted (eprint arXiv:1603.05638)

A COMBINED TRANSMISSION SPECTRUM OF THE EARTH-SIZED EXOPLANETS TRAPPIST-1 B AND C
de Wit, J.; Wakeford, H. R.; Gillon, M.; Lewis, N. K.; Valenti, J. A.; Demory, B.-O.; Burgasser, A. J.; **Delrez, L.**; Jehin, E.; Lederer, S. M.; Triaud, A. H. M. J.; Van Grootel, V.
2016, Nature, accepted (eprint arXiv:1606.01103)

DISCOVERY OF WASP-113B AND WASP-114B, TWO INFLATED HOT-JUPITERS WITH CONTRASTING DENSITIES
Barros, S. C. C.; . Brown, D. J. A.; Hébrard, G.; Gómez Maqueo Chew, Y.; Anderson, D. R.; Boumis, P.; **Delrez, L.**; Hay, K. L.; Lam, K. W. F.; Llama, J.; Lendl, M.; McCormac, J.; Skiff, B.; Smalley, B; Turner, O; Vanhuysse, M.; Armstrong, D. J.; Boisse, I.; Bouchy, F.; Collier Cameron, A.; Faedi, F.; Gillon, M.; Hellier, C.; Jehin, E.; Liakos, A.; Meaburn, J.; Osborn, H. P.; Pepe, F.; Plauchu-Frayn, I.; Pollacco, D.; Queloz, D.; Rey, J.; Spake, J.; Ségransan, D.; Triaud, A. H. M.; Udry, S.; Walker, S. R.; Watson, C. A.; West, R. G.; Wheatley, P. J.
2016, A&A, accepted (eprint arXiv:1607.02341)

WASP-92B, WASP-93B AND WASP-118B: THREE NEW TRANSITING CLOSE-IN GIANT PLANETS
Hay, K. L.; Collier-Cameron, A.; Doyle, A. P.; Hébrard, G.; Skillen, I.; Anderson, D. R.; Barros, S. C. C.; Brown, D. J. A.; Bouchy, F.; Busuttil, R.; Delorme, P.; **Delrez, L.**; Demangeon, O.; Díaz, R. F.; Gillon, M.; Gonzàlez, E.; Hellier, C.; Holmes, S.; Jarvis, J. F.; Jehin, E.; Joshi, Y. C.; Kolb, U.; Lendl, M.; Maxted, P. F. L.; McCormac, J.; Miller, G. R. M.; Mortier, A.; Pollacco, D.; Queloz, D.; Ségransan, D.; Simpson, E. K.; Smalley, B.; Southworth, J.; Triaud, A. H. M. J.; Turner, O. D.; Udry, S.; Vanhuysse, M.; West, R. G.; Wilson, P. A.
2016, MNRAS, accepted (eprint arXiv:1607.00774)

A.2 Papers submitted to refereed journals

SIX NEWLY-DISCOVERED HOT JUPITERS TRANSITING F/G STARS: WASP-87B, WASP-108B, WASP-109B, WASP-110B, WASP-111B & WASP-112B
Anderson, D. R.; Brown, D. J. A.; Collier Cameron, A.; **Delrez, L.**; Fumel, A.; Gillon, M.; Hellier, C.; Jehin, E.; Lendl, M.; Maxted, P. F. L.; Neveu-VanMalle, M.; Pepe, F.; Pollacco, D.; Queloz, D.; Rojo, P.; Segransan, D.; Serenelli, A. M.; Smalley, B.; Smith, A. M. S.; Southworth, J.; Triaud, A. H. M. J.; Turner, O. D.; Udry, S.; West, R. G.
2014, submitted to MNRAS (eprint arXiv:1410.3449)

DISCOVERY OF WASP-85 AB: A HOT JUPITER IN A VISUAL BINARY SYSTEM
Brown, D. J. A.; Anderson, D. R.; Armstrong, D. J.; Bouchy, F.; Collier Cameron, A.; **Delrez, L.**; Doyle, A. P.; Gillon, M.; Gomez Maqueo Chew, Y.; Hebb, L.; Hebrard, G.; Hellier, C.; Jehin, E.; Lendl, M.; Maxted, P. F. L.; McCormac, J.; Neveu-VanMalle, M.; Pollacco, D.; Queloz, D.; Segransan, D.; Smalley, B.; Turner, O. D.; Triaud, A. H. M. J.; Udry, S.
2015, submitted to ApJ (eprint arXiv:1412.7761)

WASP-South transiting exoplanets: WASP-130b, WASP-131b, WASP-132b, WASP-139b, WASP-140b, WASP-141b & WASP-142b
Hellier, C.; Anderson, D. R.; Collier Cameron, A.; **Delrez, L.**; Gillon, M.; Jehin, E.; Lendl, M.; Maxted, P. F. L.; Neveu-VanMalle, M.; Pepe, F.; Pollacco, D.; Queloz, D.; Segransan, D.; Smalley, B.; Southworth, J.; Triaud, A. H. M. J.; Udry, S.; Wagg, T.; West, R. G.
2016, submitted to MNRAS (eprint arXiv:1604.04195)

From Dense Hot Jupiter to Low Density Neptune: The Discovery of WASP-127b, WASP-136b and WASP-138b
Lam, K. W. F.; Faedi, F.; Brown, D. J. A.; Anderson, D. R.; **Delrez, L.**; Gillon, M.; Hébrard, G.; Lendl, M.; Mancini, L.; Southworth, J.; Smalley, B.; Triaud, A. H. M. J.; Turner, O. D.; Hay, K. L.; Armstrong, D. J.; Barros, S. C. C.; Bonomo, A. S.; Bouchy, F.; Boumis, P.; Collier Cameron, A.; Doyle, A. P.; Hellier, C.; Henning, T.; Jehin, E.; King, G.; Kirk, J.; Louden, T.; Maxted, P. F. L., McCormac, J. J.; Osborn, H. P.; Palle, E.; Pepe, F.; Pollacco, D.; Prieto-Arranz, J.; Queloz, D.; Rey, J.; Ségransan, D.; Udry, S.; Walker, S.; West, R. G.; Wheatley, P. J.
2016, submitted to A&A (eprint arXiv:1607.07859)

A.3 Conference proceedings

Towards a Transmission Spectrum of the Hot Saturn WASP-49b
Lendl, M.; **Delrez, L.**; Gillon, M.; Jehin, E.; Queloz, D.
2013, Protostars and Planets VI (Heidelberg, Germany, July 2013), poster #2G009

Towards the first transmission spectrum of a gas giant transiting an M-dwarf
Delrez, L.; Gillon, M.; Lendl, M.; Jehin, E.; Anderson, D.; Demory, B.-O.; De Wit, J.; Hellier, C.; Triaud, A.; Queloz, D.
2013, Protostars and Planets VI (Heidelberg, Germany, July 2013), poster #2G014

SPECULOOS: Search for habitable Planets EClipsing ULtra-cOOl Star
Gillon, M.; Jehin, E.; **Delrez, L.**; Magain, P.; Opitom, C.; Sohy, S.
2013, Protostars and Planets VI (Heidelberg, Germany, July 2013), poster #2K066

Studying the Atmospheres of the Most Intriguing WASP Hot Jupiters
Lendl, M.; **Delrez, L.**; Gillon, M.; Queloz, D.
2013, European Planetary Science Congress (London, UK, September 2013), id. 774

TRAPPIST (TRAnsiting Planets and PlanetesImals Small Telescope)
Jehin, E.; Gillon, M.; Opitom, C.; Manfroid, J.; Hutsemékers, D.; **Delrez, L.**; Magain, P.
2013, European Planetary Science Congress (London, UK, September 2013), id. 968

Tests of the planetary hypothesis for PTFO 8-8695b
Yu, L.; Winn, J.; Gillon, M.; Albrecht, S.; Rappaport, S.; Bieryla, A.; Dai, F.; **Delrez, L.**; Hillenbrand, L.; Holman, M.; Howard, A.; Huang, C.; Isaacson, H. T.; Jehin, E.; Lendl, M.;

Montet, B. T.; Muirhead, P. S.; Sanchis-Ojeda, R.; Triaud, A. H. M. J.
2015, Extreme Solar Systems III (Hawaii, November 2015), #120.04. BAAS volume 47 #6

Appendix B

WASP planets

A&A 559, A36 (2013)
DOI: 10.1051/0004-6361/201322314

Astronomy & Astrophysics

Discovery of WASP-65b and WASP-75b: Two hot Jupiters without highly inflated radii⋆

Y. Gómez Maqueo Chew[1,2,3], F. Faedi[1], D. Pollacco[1], D. J. A. Brown[4], A. P. Doyle[5], A. Collier Cameron[4], M. Gillon[7], M. Lendl[6], B. Smalley[5], A. H. M. J. Triaud[6,8], R. G. West[1], P. J. Wheatley[1], R. Busuttil[13], C. Liebig[4], D. R. Anderson[5], D. J. Armstrong[1], S. C. C. Barros[9], J. Bento[1,10], J. Bochinski[13], V. Burwitz[14], L. Delrez[7], B. Enoch[4], A. Fumel[7], C. A. Haswell[13], G. Hébrard[11,12], C. Hellier[5], S. Holmes[13], E. Jehin[7], U. Kolb[13], P. F. L. Maxted[5], J. McCormac[15,1], G. R. M. Miller[4], A. J. Norton[13], F. Pepe[6], D. Queloz[6,16], J. Rodríguez[17], D. Ségransan[6], I. Skillen[15], K. G. Stassun[2,18], S. Udry[6], and C. Watson[19]

[1] Department of Physics, University of Warwick, Coventry CV4 7AL, UK
e-mail: y.gomez@warwick.ac.uk
[2] Physics and Astronomy Department, Vanderbilt University, Nashville, Tennessee 37235, USA
[3] Centro de Radioastronomía y Astrofísica, UNAM, Apartado Postal 3-72, 58089 Morelia, Michoacán, México
[4] School of Physics and Astronomy, University of St Andrews, St Andrews, Fife KY16 9SS, UK
[5] Astrophysics Group, Keele University, Staffordshire, ST5 5BG, UK
[6] Observatoire astronomique de l'Université de Genève, 51 ch. des Maillettes, 1290 Sauverny, Switzerland
[7] Université de Liège, Allée du 6 août 17, Sart Tilman, Liège 1, 4000 Liège, Belgium
[8] Department of Physics, and Kavli Institute for Astrophysics and Space Research, Massachusetts Institute of Technology, Cambridge, MA 02139, USA
[9] Aix-Marseille Université, CNRS, LAM (Laboratoire d'Astrophysique de Marseille) UMR 7326, 13388 Marseille, France
[10] Department of Physics and Astronomy, Macquarie University, NSW 2109 Sydney, Australia
[11] Institut d'Astrophysique de Paris, UMR7095 CNRS, Université Pierre & Marie Curie, 75014 Paris, France
[12] Observatoire de Haute-Provence, CNRS/OAMP, 04870 St Michel l'Observatoire, France
[13] Department of Physical Sciences, The Open University, Milton Keynes, MK7 6AA, UK
[14] Max Planck Institut für Extraterrestrische Physik, Giessenbachstrasse 1, 85748 Garching, Germany
[15] Isaac Newton Group of Telescopes, Apartado de Correos 321, 38700 Santa Cruz de Palma, Spain
[16] Department of Physics, University of Cambridge, J J Thomson Av, Cambridge, CB3 0HE, UK
[17] Observatori Astronòmic de Mallorca, Camí de l'Observatori s/n, 07144 Costitx, Mallorca, Spain
[18] Department of Physics, Fisk University, Nashville, Tennessee 37208, USA
[19] Astrophysics Research Centre, Queen's University Belfast, University Road, Belfast BT7 1NN, UK

Received 18 July 2013 / Accepted 27 September 2013

ABSTRACT

We report the discovery of two transiting hot Jupiters, WASP-65b ($M_{\rm pl}$ = 1.55 ± 0.16 $M_{\rm J}$; $R_{\rm pl}$ = 1.11 ± 0.06 $R_{\rm J}$), and WASP-75b ($M_{\rm pl}$ = 1.07 ± 0.05 $M_{\rm J}$; $R_{\rm pl}$ = 1.27 ± 0.05 $R_{\rm J}$). They orbit their host star every ∼2.311, and ∼2.484 days, respectively. The planet host WASP-65 is a G6 star ($T_{\rm eff}$ = 5600 K, [Fe/H] = −0.07 ± 0.07, age ≳8 Gyr); WASP-75 is an F9 star ($T_{\rm eff}$ = 6100 K, [Fe/H] = 0.07 ± 0.09, age ∼ 3 Gyr). WASP-65b is one of the densest known exoplanets in the mass range 0.1 and 2.0 $M_{\rm J}$ ($\rho_{\rm pl}$ = 1.13 ± 0.08 $\rho_{\rm J}$), a mass range where a large fraction of planets are found to be inflated with respect to theoretical planet models. WASP-65b is one of only a handful of planets with masses of ∼1.5 $M_{\rm J}$, a mass regime surprisingly underrepresented among the currently known hot Jupiters. The radius of WASP-75b is slightly inflated (≲10%) as compared to theoretical planet models with no core, and has a density similar to that of Saturn ($\rho_{\rm pl}$ = 0.52 ± 0.06 $\rho_{\rm J}$).

Key words. planetary systems – stars: individual: WASP-65 – stars: individual: WASP-75

1. Introduction

Since the discovery of the first extrasolar planet around a main-sequence star, 51 Peg (Mayor & Queloz 1995), our understanding of planetary systems has dramatically evolved. Planetary science, which was previously based solely on our own Solar System, must be able to explain the observed diversity in physical properties and trends in the known exoplanet population (e.g., Baraffe et al. 2010; Cameron 2011). An exceptionally valuable subset of the known extrasolar planets are those that transit the disc of their host star. To date, there are over 300 confirmed transiting exoplanets in the literature[1]. Most of these discoveries have been the product of ground-based surveys, of which the Wide Angle Search for Planets (WASP; Pollacco et al. 2006) has

⋆ Light curves are only available at the CDS via anonymous ftp to cdsarc.u-strasbg.fr (130.79.128.5) or via http://cdsarc.u-strasbg.fr/viz-bin/qcat?J/A+A/559/A36

[1] See http://exoplanet.eu/

A&A 562, L3 (2014)
DOI: 10.1051/0004-6361/201323014

Astronomy & Astrophysics

L E

WASP-103 b: a new planet at the edge of tidal disruption⋆

M. Gillon[1], D. R. Anderson[2], A. Collier-Cameron[3], L. Delrez[1], C. Hellier[2], E. Jehin[1], M. Lendl[4], P. F. L. Maxted[2], F. Pepe[4], D. Pollacco[5], D. Queloz[6,4], D. Ségransan[4], A. M. S. Smith[7,2], B. Smalley[2], J. Southworth[2], A. H. M. J. Triaud[8,4], S. Udry[4], V. Van Grootel[1], and R. G. West[5]

[1] Institut d'Astrophysique et de Géophysique, Université de Liège, Allée du 6 août 17, Sart Tilman, 4000 Liège 1, Belgium
e-mail: michael.gillon@ulg.ac.be
[2] Astrophysics Group, Keele University, Staffordshire, ST5 5BG, UK
[3] SUPA, School of Physics and Astronomy, University of St. Andrews, North Haugh, Fife, KY16 9SS, UK
[4] Observatoire de Genève, Université de Genève, 51 Chemin des Maillettes, 1290 Sauverny, Switzerland
[5] Department of Physics, University of Warwick, Coventry CV4 7AL, UK
[6] Cavendish Laboratory, Department of Physics, University of Cambridge, JJ Thomson Avenue, Cambridge, CB3 0HE, UK
[7] N. Copernicus Astronomical Centre, Polish Academy of Sciences, Bartycka 18, 00-716 Warsaw, Poland
[8] Department of Physics and Kavli Institute for Astrophysics & Space Research, Massachusetts Institute of Technology, Cambridge, MA 02139, USA

Received 8 November 2013 / Accepted 9 January 2014

ABSTRACT

We report the discovery of WASP-103 b, a new ultra-short-period planet (P = 22.2 h) transiting a 12.1 V-magnitude F8-type main-sequence star (1.22 ± 0.04 $M_\odot$, $1.44^{+0.05}_{-0.03}$ $R_\odot$, $T_{\rm eff}$ = 6110 ± 160 K). WASP-103 b is significantly more massive (1.49 ± 0.09 $M_{\rm Jup}$) and larger ($1.53^{+0.05}_{-0.07}$ $R_{\rm Jup}$) than Jupiter. Its large size and extreme irradiation (~9×10^9 erg s^{-1} cm^{-2}) make it an exquisite target for a thorough atmospheric characterization with existing facilities. Furthermore, its orbital distance is less than 20% larger than its Roche radius, meaning that it might be significantly distorted by tides and might experience mass loss through Roche-lobe overflow. It thus represents a new key object for understanding the last stage of the tidal evolution of hot Jupiters.

Key words. planetary systems – stars: individual: WASP-103 – techniques: photometric – techniques: radial velocities – techniques: spectroscopic

1. Introduction

Ever since the historical detection of the transits of HD 209458 b (Charbonneau et al. 2000; Henry et al. 2000), the ultra-short-period (a few days, or even less) transiting giant planets have played a pivotal role for exoplanetary science. These transiting hot Jupiters undergo irradiation orders of magnitude larger than any solar system planets (Fortney et al. 2007), and are also subject to intense gravitational and magnetic fields (Correia & Laskar 2011; Chang et al. 2010). Their eclipsing configuration provides us with a unique opportunity to study their response to such extreme conditions and to improve substantially our knowledge of planetary structure, chemical composition and physical mechanisms. Notably, it allows us to study the last stages of their tidal evolution, provided giant planets close to tidal disruption are found to be transiting bright stars.

Our WASP transit survey (Pollacco et al. 2006) actively searches for ultra-short-period giant planets. Despite a maximized detection probability (higher transit probability, more frequent transits), planets with a period shorter than 1.2 d represent only a few percent of the total WASP harvest, demonstrating their rarity (Hellier et al. 2012). This small subgroup has so far been composed of WASP-12 b (Hebb et al. 2009), WASP-18 b (Hellier et al. 2009), WASP-19 b (Hebb et al. 2010), and WASP-43 b (Hellier et al. 2011a). Among these four planets, WASP-12 b and WASP-19 b are the only two gas giants close to tidal disruption known to transit a bright star. We report here our discovery of a third planet of this ultra-rare kind, WASP-103 b, which orbits a 12.1 V-magnitude F-type star at only ~3 stellar radii.

Section 2 presents our discovery and follow-up data. In Sect. 3, we briefly present the spectroscopic determination of the stellar properties and the derivation of the system parameters through a combined analysis of all our data. We discuss our discovery in Sect. 4.

2. Observations

2.1. WASP transit detection photometry

The host star WASP-103 (1SWASPJ163715.59+071100.0 = 2MASS16371556+0711000; V = 12.1, K = 10.8) was observed by the southern station of the WASP survey (Hellier et al. 2011b) during the 2010, 2011, and 2012 observing seasons, covering the intervals 2010 May 15 to Aug. 16, 2011 Mar. 26 to Aug. 20, and 2012 Mar. 25 to Jun. 28. The 11 565 pipeline-processed photometric measurements were detrended and searched for transits using the methods described by Collier-Cameron et al. (2006). The selection process (Collier-Cameron et al. 2007) elected WASP-103 as a high priority candidate presenting a periodic transit-like signature with a period of 0.926 days. Figure 2.1 (top panel) presents the WASP photometry folded on the best-fit transit ephemeris.

A search for periodic modulation was applied to the WASP photometry of WASP-103, using the method described in

⋆ The photometric and radial velocity time-series are only available at the CDS via anonymous ftp to cdsarc.u-strasbg.fr (130.79.128.5) or via http://cdsarc.u-strasbg.fr/viz-bin/qcat?J/A+A/562/L3

Monthly Notices of the ROYAL ASTRONOMICAL SOCIETY
MNRAS **440,** 1982–1992 (2014) doi:10.1093/mnras/stu410

Transiting hot Jupiters from WASP-South, Euler and TRAPPIST: WASP-95b to WASP-101b

Coel Hellier,[1⋆] D. R. Anderson,[1] A. Collier Cameron,[2] L. Delrez,[3] M. Gillon,[3] E. Jehin,[3] M. Lendl,[4] P. F. L. Maxted,[1] F. Pepe,[4] D. Pollacco,[5] D. Queloz,[4,6] D. Ségransan,[4] B. Smalley,[1] A. M. S. Smith,[1,7] J. Southworth,[1] A. H. M. J. Triaud,[4,8†] S. Udry[4] and R. G. West[5]

[1]*Astrophysics Group, Keele University, Staffordshire ST5 5BG, UK*
[2]*SUPA, School of Physics and Astronomy, University of St Andrews, North Haugh, Fife KY16 9SS, UK*
[3]*Institut d'Astrophysique et de Géophysique, Université de Liège, Allée du 6 Août, 17, Bat. B5C, Liège 1, Belgium*
[4]*Observatoire astronomique de l'Université de Genève 51 ch. des Maillettes, CH-1290 Sauverny, Switzerland*
[5]*Department of Physics, University of Warwick, Gibbet Hill Road, Coventry CV4 7AL, UK*
[6]*Cavendish Laboratory, J J Thomson Avenue, Cambridge CB3 0HE, UK*
[7]*N. Copernicus Astronomical Centre, Polish Academy of Sciences, Bartycka 18, PL-00-716 Warsaw, Poland*
[8]*Department of Physics and Kavli Institute for Astrophysics & Space Research, Massachusetts Institute of Technology, Cambridge, MA 02139, USA*

Accepted 2014 February 28. Received 2014 February 28; in original form 2013 October 27

ABSTRACT

We report the discovery of the transiting exoplanets WASP-95b, WASP-96b, WASP-97b, WASP-98b, WASP-99b, WASP-100b and WASP-101b. All are hot Jupiters with orbital periods in the range 2.1–5.7 d, masses of 0.5–2.8 $M_{\rm Jup}$ and radii of 1.1–1.4 $R_{\rm Jup}$. The orbits of all the planets are compatible with zero eccentricity. WASP-99b produces the shallowest transit yet found by WASP-South, at 0.4 per cent.

The host stars are of spectral type F2–G8. Five have metallicities of [Fe/H] from −0.03 to +0.23, while WASP-98 has a metallicity of −0.60, exceptionally low for a star with a transiting exoplanet. Five of the host stars are brighter than $V = 10.8$, which significantly extends the number of bright transiting systems available for follow-up studies. WASP-95 shows a possible rotational modulation at a period of 20.7 d. We discuss the completeness of WASP survey techniques by comparing to the HATnet project.

Key words: planetary systems.

1 INTRODUCTION

The WASP-South survey has dominated the discovery of transiting hot-Jupiter exoplanets in the Southern hemisphere. WASP-South is well matched to the capabilities of the Euler/CORALIE spectrograph and the robotic TRAPPIST telescope, with the combination proving efficient for discovering transiting exoplanets around stars of $V = 9$–13.

WASP-South (see Hellier et al. 2011a) has now been running nearly continuously for seven years. Approximately 1000 candidates have now been observed with Euler/CORALIE, while TRAPPIST (see Jehin et al. 2011) has observed 1000 light curves of WASP candidates and planets. Here we present new WASP-South planets which take WASP numbering above 100.

Since WASP host stars are generally brighter than host stars of *Kepler* exoplanets, ongoing WASP-South discoveries are important for detailed study of exoplanets and will be prime targets for future missions such as *CHEOPS* and *JWST,* and proposed missions such as *EChO* and *FINESSE*.

2 OBSERVATIONS

The observational and analysis techniques used here are the same as in recent WASP discovery papers (e.g. Hellier et al. 2012), and thus are described briefly. For detailed accounts see the earlier papers including Pollacco et al. (2006, 2008) and Collier Cameron et al. (2007a).

In outline, WASP-South surveys the visible sky each clear night using an array of 200 mm *f*/1.8 lenses and a cadence of ∼10 min. Transit searching of accumulated light curves leads to candidates that are passed to TRAPPIST (a robotic 0.6-m photometric telescope, which can resolve blends and check that the candidate

⋆ E-mail: c.hellier@keele.ac.uk
† Fellow of the Swiss National Science Foundation.

A&A 568, A81 (2014)
DOI: 10.1051/0004-6361/201424481

Astronomy & Astrophysics

WASP-117b: a 10-day-period Saturn in an eccentric and misaligned orbit⋆,⋆⋆

M. Lendl[1,2], A. H. M. J. Triaud[2,8], D.R. Anderson[3], A. Collier Cameron[4], L. Delrez[1], A. P. Doyle[3], M. Gillon[1], C. Hellier[3], E. Jehin[1], P. F. L. Maxted[3], M. Neveu-VanMalle[2,6], F. Pepe[2], D. Pollacco[5], D. Queloz[2,6], D. Ségransan[2], B. Smalley[3], A. M. S. Smith[3,7], S. Udry[2], V. Van Grootel[1], and R. G. West[5]

[1] Institut d'Astrophysique et de Géophysique, Université de Liège, Allée du 6 Août 17, Bât. B5C, Liège 1, 4000 Belgium
e-mail: monika.lendl@ulg.ac.be
[2] Observatoire de Genève, Université de Genève, Chemin des Maillettes 51, 1290 Sauverny, Switzerland
[3] Astrophysics Group, Keele University, Staffordshire ST5 5BG, UK
[4] SUPA, School of Physics and Astronomy, University of St. Andrews, North Haugh, Fife KY16 9SS, UK
[5] Department of Physics, University of Warwick, Gibbet Hill Road, Coventry CV4 7AL, UK
[6] Cavendish Laboratory, J J Thomson Avenue, Cambridge CB3 0HE, UK
[7] N. Copernicus Astronomical Centre, Polish Academy of Sciences, Bartycka 18, 00-716 Warsaw, Poland
[8] Kavli Institute for Astrophysics & Space Research, Massachusetts Institute of Technology, Cambridge, MA 02139, USA

Received 26 June 2014 / Accepted 31 July 2014

ABSTRACT

We report the discovery of WASP-117b, the first planet with a period beyond 10 days found by the WASP survey. The planet has a mass of $M_p = 0.2755 \pm 0.0089\,M_J$, a radius of $R_p = 1.021^{+0.076}_{-0.065}\,R_J$ and is in an eccentric ($e = 0.302 \pm 0.023$), 10.02165 ± 0.00055 d orbit around a main-sequence F9 star. The host star's brightness ($V = 10.15$ mag) makes WASP-117 a good target for follow-up observations, and with a periastron planetary equilibrium temperature of $T_{eq} = 1225^{+36}_{-39}$ K and a low planetary mean density ($\rho_p = 0.259^{+0.054}_{-0.048}\,\rho_J$) it is one of the best targets for transmission spectroscopy among planets with periods around 10 days. From a measurement of the Rossiter-McLaughlin effect, we infer a projected angle between the planetary orbit and stellar spin axes of $\beta = -44 \pm 11$ deg, and we further derive an orbital obliquity of $\psi = 69.6^{+4.7}_{-4.1}$ deg. Owing to the large orbital separation, tidal forces causing orbital circularization and realignment of the planetary orbit with the stellar plane are weak, having had little impact on the planetary orbit over the system lifetime. WASP-117b joins a small sample of transiting giant planets with well characterized orbits at periods above ~8 days.

Key words. planetary systems – techniques: photometric – techniques: radial velocities

1. Introduction

Transiting planets play a fundamental part in the study of exoplanets and planetary systems as their radii and absolute masses can be measured. For bright transiting systems, several avenues of follow-up observations can be pursued, giving access to the planetary transmission and emission spectrum, and the systems obliquity (via the sky-projected angle between the stellar spin and planetary orbit; see, e.g., Winn 2011 for a summary). Ground-based transit surveys such as WASP (Pollacco et al. 2006), HAT (Bakos et al. 2004), and KELT (Pepper et al. 2007) have been key in discovering the population of hot Jupiters, giant planets with periods of only a few days.

There are two main theories of the inward migration of gas giants to create these hot Jupiters. Disk-driven migration (Goldreich & Tremaine 1980; Lin & Papaloizou 1986; see Baruteau et al. 2014, for a summary) relies on the interaction of a gas giant with the protoplanetary disk to cause inward migration, producing giant planets on short-period circular orbits. The obliquities produced from disk migration are inherited from the inclination of the protoplanetary disk. While this mechanism favors low orbital obliquities, stellar binary companions may cause the protoplanetary disk to tilt with respect to the stellar equator, leading to the creation of misaligned planets (Batygin 2012; Lai 2014). Dynamical migration processes, such as planet-planet scattering (Rasio & Ford 1996; Weidenschilling & Marzari 1996; see Davies et al. 2014 for a summary) or migration through Lidov-Kozai cycles (Lidov 1962; Kozai 1962; Eggleton & Kiseleva-Eggleton 2001; Wu & Murray 2003), require the planet to be placed on a highly eccentric orbit, that is subsequently circularized by tidal interactions. This migration pathway can produce large orbital obliquities, such as those observed for several giant planets (e.g., Hébrard et al. 2008; Triaud et al. 2010; Winn et al. 2010b). It has been suggested that obliquities are damped by tidal interactions between planet and host star, the efficiency of this process together with the system age reproducing the observed obliquity distribution (Winn et al. 2010b; Triaud 2011; Albrecht et al. 2012).

We present WASP-117b, the planet with the longest period and one of the lowest masses (surpassed only by WASP-29b, Hellier et al. 2010) found by the WASP survey to date. This Saturn-mass planet is in an eccentric and misaligned

⋆ Based on data obtained with WASP-South, CORALIE and EulerCam at the *Euler*-Swiss telescope, TRAPPIST, and HARPS at the ESO 3.6 m telescope (Prog. IDs 087.C-0649, 089.C-0151, 090.C-0540)
⋆⋆ Photometric and radial velocities are only available at the CDS via anonymous ftp to cdsarc.u-strasbg.fr (130.79.128.5) or via http://cdsarc.u-strasbg.fr/viz-bin/qcat?J/A+A/568/A81

A&A 570, A64 (2014)
DOI: 10.1051/0004-6361/201424752

Astronomy & Astrophysics

WASP-104b and WASP-106b: two transiting hot Jupiters in 1.75-day and 9.3-day orbits⋆,⋆⋆

A. M. S. Smith[1,2], D. R. Anderson[2], D. J. Armstrong[3], S. C. C. Barros[4], A. S. Bonomo[5], F. Bouchy[4], D. J. A. Brown[3], A. Collier Cameron[6], L. Delrez[7], F. Faedi[3], M. Gillon[7], Y. Gómez Maqueo Chew[3], G. Hébrard[8,9], E. Jehin[7], M. Lendl[7,10], T. M. Louden[3], P. F. L. Maxted[2], G. Montagnier[8,9], M. Neveu-VanMalle[10,11], H. P. Osborn[3], F. Pepe[10], D. Pollacco[3], D. Queloz[10,11], J. W. Rostron[3], D. Segransan[10], B. Smalley[2], A. H. M. J. Triaud[10,12], O. D. Turner[2], S. Udry[10], S. R. Walker[3], R. G. West[3], and P. J. Wheatley[3]

[1] N. Copernicus Astronomical Centre, Polish Academy of Sciences, Bartycka 18, 00-716 Warsaw, Poland
e-mail: amss@camk.edu.pl
[2] Astrophysics Group, Lennard-Jones Laboratories, Keele University, Keele, Staffordshire, ST5 5BG, UK
[3] Department of Physics, University of Warwick, Coventry CV4 7AL, UK
[4] Aix Marseille Université, CNRS, LAM (Laboratoire d'Astrophysique de Marseille) UMR 7326, 13388 Marseille, France
[5] INAF – Osservatorio Astrofisico di Torino, via Osservatorio 20, 10025 Pino Torinese, Italy
[6] SUPA, School of Physics and Astronomy, University of St. Andrews, North Haugh, St. Andrews, Fife, KY16 9SS, UK
[7] Institut d'Astrophysique et de Géophysique, Université de Liège, Allée du 6 Août 17, Sart Tilman, Liège 1, Belgium
[8] Institut d'Astrophysique de Paris, UMR7095 CNRS, Université Pierre & Marie Curie, 98bis boulevard Arago, 75014 Paris, France
[9] Observatoire de Haute-Provence, CNRS/OAMP, 04870 Saint-Michel-l'Observatoire, France
[10] Observatoire de Genève, Université de Genève, 51 Chemin des Maillettes, 1290 Sauverny, Switzerland
[11] Cavendish Laboratory, J J Thomson Avenue, Cambridge CB3 0HE, UK
[12] Kavli Institute for Astrophysics & Space Research, Massachusetts Institute of Technology, Cambridge, MA 02139, USA

Received 5 August 2014 / Accepted 9 September 2014

ABSTRACT

We have used the WASP survey to discover two exoplanetary systems, each consisting of a Jupiter-sized planet transiting an 11th-magnitude (V) main-sequence star. WASP-104b orbits its star in 1.75 d, whereas WASP-106b has the fourth-longest orbital period of any planet discovered by means of transits observed from the ground, orbiting every 9.29 d. Each planet is more massive than Jupiter (WASP-104b has a mass of 1.27 ± 0.05 $M_{\rm Jup}$, while WASP-106b has a mass of 1.93 ± 0.08 $M_{\rm Jup}$). Both planets are just slightly larger than Jupiter, with radii of 1.14 ± 0.04 and 1.09 ± 0.04 $R_{\rm Jup}$ for WASP-104 and WASP-106, respectively. No significant orbital eccentricity is detected in either system, and while this is not surprising in the case of the short-period WASP-104b, it is interesting in the case of WASP-106b, because many otherwise similar planets are known to have eccentric orbits.

Key words. planets and satellites: detection – planets and satellites: fundamental parameters – stars: individual: WASP-104b – stars: individual: WASP-106b – planetary systems

1. Introduction

Transiting planets are vital for our understanding of planetary systems, because their radii and absolute masses can be measured. Recently, the large number of planets and planetary candidates discovered by the *Kepler* satellite has extended the parameter space of transiting planet discovery and led to major advances in our understanding of the statistics of the Galactic planetary population. Planets transiting stars brighter than those observed by *Kepler* are required to increase our knowledge of the range of properties exhibited by the nearby planetary population, as well as to make advances in our understanding of planetary formation and evolution. Examples of planet characterisation observations that require bright target stars include high-precision radial velocity (RV) measurements to determine orbital obliquities and measurements of planetary transmission and emission spectra to infer atmospheric properties (e.g. Winn 2011). The Wide Angle Search for Planets (WASP; Pollacco et al. 2006) and other wide-field ground-based surveys such as HAT-net (Bakos et al. 2002) are the leading discoverers of bright ($8.5 \lesssim V \lesssim 12.5$) transiting systems, with around 150 planets between them.

Only a handful of the nearly one hundred planets discovered by WASP have orbital periods, P, greater than 5 d. This is because there is an intrinsic pile-up of planets at three to five days, and hence a relative dearth of planets at longer periods. This is further exacerbated by the fact that at long periods the probability that a planetary system is aligned such that transits are visible from Earth is significantly reduced. Furthermore, because a large number of transits must be observed in order to overcome the correlated noise present in wide-field survey photometry (e.g. Smith et al. 2006), very long observational baselines are usually required to find longer period systems.

Recently, Lendl et al. (2014) reported the discovery of WASP-117b, the first WASP discovery with $P > 9$ d. Only two other systems with $P > 9$ d have been discovered from the ground by means of transits: HAT-P-15b (Kovács et al. 2010)

⋆ Table 1 is available in electronic form at http://www.aanda.org
⋆⋆ The table of photometry is only available at the CDS via anonymous ftp to cdsarc.u-strasbg.fr (130.79.128.5) or via http://cdsarc.u-strasbg.fr/viz-bin/qcat?J/A+A/570/A64

Mon. Not. R. Astron. Soc. **000**, 1–14 (2014) Printed 15 October 2014 (MN LATEX style file v2.2)

Six newly-discovered hot Jupiters transiting F/G stars: WASP-87b, WASP-108b, WASP-109b, WASP-110b, WASP-111b & WASP-112b⋆

D. R. Anderson,[1]† D. J. A. Brown,[2] A. Collier Cameron,[3] L. Delrez,[4] A. Fumel,[4] M. Gillon,[4] C. Hellier,[1] E. Jehin,[4] M. Lendl,[4,5] P. F. L. Maxted,[1] M. Neveu-VanMalle,[5,6] F. Pepe,[4] D. Pollacco,[2] D. Queloz,[5,6] P. Rojo,[7] D. Ségransan,[5] A. M. Serenelli,[8] B. Smalley,[1] A. M. S. Smith,[1,9] J. Southworth,[1] A. H. M. J. Triaud,[5,10] O. D. Turner,[1] S. Udry,[5] and R. G. West[2]

[1]*Astrophysics Group, Keele University, Staffordshire ST5 5BG, UK*
[2]*Department of Physics, University of Warwick, Coventry CV4 7AL, UK*
[3]*SUPA, School of Physics and Astronomy, University of St. Andrews, North Haugh, Fife KY16 9SS, UK*
[4]*Institut d'Astrophysique et de Géophysique, Université de Liège, Allée du 6 Août, 17, Bat. B5C, Liège 1, Belgium*
[5]*Observatoire de Genève, Université de Genève, 51 Chemin des Maillettes, 1290 Sauverny, Switzerland*
[6]*Cavendish Laboratory, J J Thomson Avenue, Cambridge, CB3 0HE, UK*
[7]*Departamento de Astronomia, Universidad de Chile, Santiago, Chile*
[8]*Instituto de Ciencias del Espacio (CSIC-IEEC), Facultad de Ciencias, Campus UAB, 08193, Bellaterra, Spain*
[9]*N. Copernicus Astronomical Centre, Polish Academy of Sciences, Bartycka 18, 00-716, Warsaw, Poland*
[10]*Department of Physics, Massachusetts Institute of Technology, Cambridge, MA 02139, USA*

Accepted Year Month Day. Received Year Month Day; in original form Year Month Day

ABSTRACT

We present the discoveries of six transiting hot Jupiters: WASP-87b, WASP-108b, WASP-109b, WASP-110b, WASP-111b and WASP-112b. The planets have masses of 0.51–2.2 $M_{\rm Jup}$ and radii of 1.19–1.44 $R_{\rm Jup}$ and are in orbits of 1.68–3.78 d around stars with masses 0.81–1.50 $M_{\odot}$.

WASP-111b is in a prograde, near-aligned ($\lambda = -5 \pm 16^{\circ}$), near-circular ($e < 0.10$ at $2\,\sigma$) orbit around a mid-F star. As tidal alignment around such a hot star is thought to be inefficient, this suggests that either the planet migrated inwards through the protoplanetary disc or that scattering processes happened to leave it in a near-aligned orbit. WASP-111 appears to have transitioned from an active to a quiescent state between the 2012 and 2013 seasons, which makes the system a candidate for studying the effects of variable activity on a hot-Jupiter atmosphere. We find evidence that the mid-F star WASP-87 is a visual binary with a mid-G star. Two host stars are metal poor: WASP-112 has [Fe/H] = -0.64 ± 0.15 and WASP-87 has [Fe/H] = -0.41 ± 0.10. The low density of WASP-112 ($0.81\,M_{\odot}$, $0.80 \pm 0.04\,\rho_{\odot}$) cannot be matched by standard models for any reasonable value of the age of the star, suggesting it to be affected by the "radius anomaly".

Key words: planets and satellites: individual: WASP-87b – planets and satellites: individual: WASP-108b – planets and satellites: individual: WASP-109b – planets and satellites: individual: WASP-110b – planets and satellites: individual: WASP-111b – planets and satellites: individual: WASP-112b.

1 INTRODUCTION

Advances are made in the understanding of planet formation and evolution by studying large samples of exoplanet systems and smaller subsets of well-characterised systems. There is a preponderance of giant planets around metal-rich stars and a dearth around metal-poor stars, suggestive of the core-accretion model of planet formation (Gonzalez

⋆ Based on observations made with the WASP-South photometric survey instrument at SAAO and, all located at La Silla: the 1.54-m Danish photometer under progam CN2013A-159; the 60-cm TRAPPIST photometer; and the EulerCam photometer and the CORALIE spectrograph, both mounted on the 1.2-m Euler-Swiss telescope.

† E-mail: d.r.anderson@keele.ac.uk

A&A 572, A49 (2014)
DOI: 10.1051/0004-6361/201424744

Astronomy & Astrophysics

WASP-94 A and B planets: hot-Jupiter cousins in a twin-star system⋆

M. Neveu-VanMalle[1,2], D. Queloz[2,1], D. R. Anderson[3], C. Charbonnel[1], A. Collier Cameron[4], L. Delrez[5], M. Gillon[5], C. Hellier[3], E. Jehin[5], M. Lendl[1,5], P. F. L. Maxted[3], F. Pepe[1], D. Pollacco[6], D. Ségransan[1], B. Smalley[3], A. M. S. Smith[3,7], J. Southworth[3], A. H. M. J. Triaud[8,1], S. Udry[1], and R. G. West[6]

[1] Observatoire Astronomique de l'Université de Genève, Chemin des Maillettes 51, 1290 Sauverny, Switzerland
e-mail: marion.neveu@unige.ch
[2] Cavendish Laboratory, J J Thomson Avenue, Cambridge, CB3 0HE, UK
[3] Astrophysics Group, Keele University, Staffordshire, ST5 5BG, UK
[4] SUPA, School of Physics and Astronomy, University of St. Andrews, North Haugh, Fife, KY16 9SS, UK
[5] Institut d'Astrophysique et de Géophysique, Université de Liège, 17, Allée du 6 Août, Bat. B5C, Liège 1, Belgium
[6] Department of Physics, University of Warwick, Gibbet Hill Road, Coventry CV4 7AL, UK
[7] N. Copernicus Astronomical Centre, Polish Academy of Sciences, Bartycka 18, 00-716 Warsaw, Poland
[8] Kavli Institute for Astrophysics & Space Research, Massachusetts Institute of Technology, Cambridge, MA 02139, USA

Received 4 August 2014 / Accepted 18 September 2014

ABSTRACT

We report the discovery of two hot-Jupiter planets, each orbiting one of the stars of a wide binary system. WASP-94A (2MASS 20550794–3408079) is an F8 type star hosting a transiting planet with a radius of 1.72 ± 0.06 $R_{\rm Jup}$, a mass of 0.452 ± 0.034 $M_{\rm Jup}$, and an orbital period of 3.95 days. The Rossiter-McLaughlin effect is clearly detected, and the measured projected spin-orbit angle indicates that the planet occupies a retrograde orbit. WASP-94B (2MASS 20550915–3408078) is an F9 stellar companion at an angular separation of 15″ (projected separation 2700 au), hosting a gas giant with a minimum mass of 0.618 ± 0.028 $M_{\rm Jup}$ with a period of 2.008 days, detected by Doppler measurements. The orbital planes of the two planets are inclined relative to each other, indicating that at least one of them is inclined relative to the plane of the stellar binary. These hot Jupiters in a binary system bring new insights into the formation of close-in giant planets and the role of stellar multiplicity.

Key words. planetary systems – stars: individual: WASP-94 – techniques: photometric – techniques: radial velocities – techniques: spectroscopic – binaries: visual

1. Introduction

More than 200 hot Jupiters (Mayor & Queloz 1995) have been discovered by exoplanet transit surveys. These short-period planetary systems are the easiest to detect because their small orbits improve their chances of transiting to typically 10%. The large radii of hot Jupiters produce deep transits (of about 1% depth) that are easily detectable from the ground. Several surveys have found these planets: TrES (Alonso et al. 2004), XO (McCullough et al. 2005), WASP (Pollacco et al. 2006), HATNet (Bakos et al. 2007), KELT (Pepper et al. 2007), and QES (Alsubai et al. 2013). Although many hot Jupiters are known, they rarely occur around solar-type stars with rates from 0.3 to 1.5% (Wright et al. 2012) depending on the metallicity ([Fe/H]) of the stellar sample studied.

Only three stellar binaries are known to host pairs of circumprimary planetary systems. HD20782/HD20781 is a wide stellar binary in which HD20782 hosts a Jupiter-mass planet (Jones et al. 2006) and HD20781 hosts two Neptune-mass planets (announced by Mayor et al. 2011). XO-2 is a metal-rich wide stellar binary in which XO-2N hosts a transiting hot Jupiter (Burke et al. 2007). XO-2S was found to have two planets, one of Jupiter, one of Saturn mass (Desidera et al. 2014). Kepler-132 is a stellar binary hosting three super-Earths (Lissauer et al. 2014). Its angular separation of 0.″9 is too small to identify which star the planets are transiting. Dynamical considerations demonstrate that the two planets with the shortest periods cannot be orbiting the same star. We report here the discovery of a twin binary system in which each star hosts a hot Jupiter.

The WASP-94 unique system is of particular interest for understanding the formation of hot Jupiters. The conditions triggering the migration inside the disc (Lin et al. 1996; Papaloizou & Terquem 2006) are not yet fully understood. Dynamical interactions with an additional companion (Fabrycky & Tremaine 2007) are thought to play an important role, especially in the case of misaligned planets (e.g. Brown et al. 2012).

We here describe the planet detection processes, derive the system parameters, and discuss how this system fits into formation theories with respect to stellar multiplicity.

2. Discovery of WASP-94Ab

The WASP-94 system was identified as a transiting planet candidate by the WASP-South (Hellier et al. 2011) telescopes located in South Africa. A total of 18 200 photometric measurements were obtained by one of the eight WASP cameras between May 2006 and June 2012. WASP-94 was rapidly identified as a visual binary with an angular separation of 15″. Both stars fell

⋆ The radial-velocity and photometric data used for this work are only available at the CDS via anonymous ftp to cdsarc.u-strasbg.fr (130.79.128.5) or via http://cdsarc.u-strasbg.fr/viz-bin/qcat?J/A+A/572/A49

Monthly Notices of the ROYAL ASTRONOMICAL SOCIETY
MNRAS **445,** 1114–1129 (2014) doi:10.1093/mnras/stu1737

Three newly discovered sub-Jupiter-mass planets: WASP-69b and WASP-84b transit active K dwarfs and WASP-70Ab transits the evolved primary of a G4+K3 binary⋆†

D. R. Anderson,[1]‡ A. Collier Cameron,[2] L. Delrez,[3] A. P. Doyle,[1] F. Faedi,[4] A. Fumel,[3] M. Gillon,[3] Y. Gómez Maqueo Chew,[4] C. Hellier,[1] E. Jehin,[3] M. Lendl,[5] P. F. L. Maxted,[1] F. Pepe,[5] D. Pollacco,[4] D. Queloz,[5,6] D. Ségransan,[5] I. Skillen,[7] B. Smalley,[1] A. M. S. Smith,[1,8] J. Southworth,[1] A. H. M. J. Triaud,[5,9] O. D. Turner,[1] S. Udry[5] and R. G. West[4]

[1]*Astrophysics Group, Keele University, Staffordshire ST5 5BG, UK*
[2]*SUPA, School of Physics and Astronomy, University of St Andrews, North Haugh, Fife KY16 9SS, UK*
[3]*Institut d'Astrophysique et de Géophysique, Université de Liège, Allée du 6 Août, 17, Bat. B5C, Liège 1, Belgium*
[4]*Department of Physics, University of Warwick, Coventry CV4 7AL, UK*
[5]*Observatoire de Genève, Université de Genève, 51 Chemin des Maillettes, CH-1290 Sauverny, Switzerland*
[6]*Cavendish Laboratory, J J Thomson Avenue, Cambridge CB3 0HE, UK*
[7]*Isaac Newton Group of Telescopes, Apartado de Correos 321, E-38700 Santa Cruz de la Palma, Tenerife, Spain*
[8]*N. Copernicus Astronomical Centre, Polish Academy of Sciences, Bartycka 18, PL-00-716 Warsaw, Poland*
[9]*Department of Physics, and Kavli Institute for Astrophysics and Space Research, Massachusetts Institute of Technology, Cambridge, MA 02139, USA*

Accepted 2014 August 22. Received 2014 August 18; in original form 2013 October 21

ABSTRACT

We report the discovery of the transiting exoplanets WASP-69b, WASP-70Ab and WASP-84b, each of which orbits a bright star ($V \sim 10$). WASP-69b is a bloated Saturn-mass planet (0.26 $M_{\rm Jup}$, 1.06 $R_{\rm Jup}$) in a 3.868-d period around an active, ∼1-Gyr, mid-K dwarf. *ROSAT* detected X-rays 60±27 arcsec from WASP-69. If the star is the source then the planet could be undergoing mass-loss at a rate of $\sim 10^{12}$ g s^{-1}. This is one to two orders of magnitude higher than the evaporation rate estimated for HD 209458b and HD 189733b, both of which have exhibited anomalously large Lyman α absorption during transit. WASP-70Ab is a sub-Jupiter-mass planet (0.59 $M_{\rm Jup}$, 1.16 $R_{\rm Jup}$) in a 3.713-d orbit around the primary of a spatially resolved, 9–10-Gyr, G4+K3 binary, with a separation of 3.3 arcsec (≥800 au). WASP-84b is a sub-Jupiter-mass planet (0.69 $M_{\rm Jup}$, 0.94 $R_{\rm Jup}$) in an 8.523-d orbit around an active, ∼1-Gyr, early-K dwarf. Of the transiting planets discovered from the ground to date, WASP-84b has the third-longest period. For the active stars WASP-69 and WASP-84, we pre-whitened the radial velocities using a low-order harmonic series. We found that this reduced the residual scatter more than did the oft-used method of pre-whitening with a fit between residual radial velocity and bisector span. The system parameters were essentially unaffected by pre-whitening.

Key words: techniques: photometric – techniques: radial velocities – planets and satellites: detection – planets and satellites: individual: WASP-69b – planets and satellites: individual: WASP-70Ab – planets and satellites: individual: WASP-84b.

⋆ Based on observations made with the WASP-South (South Africa) and SuperWASP-North (La Palma) photometric survey instruments, the RISE camera on the 2-m Liverpool Telescope under program PL12B13, and, all located at La Silla: the 60-cm TRAPPIST photometer, EulerCam and the CORALIE spectrograph, both mounted on the 1.2-m Euler-Swiss telescope, and the HARPS spectrograph on the ESO 3.6-m telescope under program 89.C-0151.
† The photometric time series and radial-velocity data used in this work are available at the CDS via anonymous ftp to cdsarc.u-strasbg.fr (130.79.128.5) or via http://cdsarc.u-strasbg.fr/viz-bin/qcat?J/MNRAS/445/1114.
‡ E-mail: d.r.anderson@keele.ac.uk

The Astronomical Journal, 150:18 (9pp), 2015 July doi:10.1088/0004-6256/150/1/18

THREE WASP-SOUTH TRANSITING EXOPLANETS: WASP-74b, WASP-83b, AND WASP-89b

Coel Hellier[1], D. R. Anderson[1], A. Collier Cameron[2], L. Delrez[3], M. Gillon[3], E. Jehin[3], M. Lendl[3,4], P. F. L. Maxted[1], F. Pepe[4], D. Pollacco[5], D. Queloz[4,6], D. Ségransan[4], B. Smalley[1], A. M. S. Smith[1,7], J. Southworth[1], A. H. M. J. Triaud[4,8], O. D. Turner[1], S. Udry[4], and R. G. West[5]
[1] Astrophysics Group, Keele University, Staffordshire, ST5 5BG, UK
[2] SUPA, School of Physics and Astronomy, University of St. Andrews, North Haugh, Fife, KY16 9SS, UK
[3] Institut d'Astrophysique et de Géophysique, Université, Liège, Allée du 6 Août, 17, Bat. B5C, Liège 1, Belgium
[4] Observatoire astronomique de l'Université de Genève, 51 ch. des Maillettes, 1290 Sauverny, Switzerland
[5] Department of Physics, University of Warwick, Gibbet Hill Road, Coventry CV4 7AL, UK
[6] Cavendish Laboratory, J J Thomson Avenue, Cambridge, CB3 0HE, UK
[7] N. Copernicus Astronomical Centre, Polish Academy of Sciences, Bartycka 18, 00-716 Warsaw, Poland
[8] Department of Physics and Kavli Institute for Astrophysics & Space Research, Massachusetts Institute of Technology, Cambridge, MA 02139, USA
Received 2014 October 23; accepted 2015 May 7; published 2015 June 24

ABSTRACT

We report the discovery of three new transiting hot Jupiters by WASP-South together with the TRAPPIST photometer and the Euler/CORALIE spectrograph. WASP-74b orbits a star of $V = 9.7$, making it one of the brighter systems accessible to southern telescopes. It is a $0.95 M_{\rm Jup}$ planet with a moderately bloated radius of 1.5 $R_{\rm Jup}$ in a 2 day orbit around a slightly evolved F9 star. WASP-83b is a Saturn-mass planet at 0.3 $M_{\rm Jup}$ with a radius of 1.0 $R_{\rm Jup}$. It is in a 5 day orbit around a fainter ($V = 12.9$) G8 star. WASP-89b is a 6 $M_{\rm Jup}$ planet in a 3 day orbit with an eccentricity of $e = 0.2$. It is thus similar to massive, eccentric planets such as XO-3b and HAT-P-2b, except that those planets orbit F stars whereas WASP-89 is a K star. The $V = 13.1$ host star is magnetically active, showing a rotation period of 20.2 days, while star spots are visible in the transits. There are indications that the planet's orbit is aligned with the stellar spin. WASP-89 is a good target for an extensive study of transits of star spots.

Key words: planetary systems – stars: individual (WASP-74, WASP-83, WASP-89)

1. INTRODUCTION

The combination of the WASP-South survey instrument, the Euler/CORALIE spectrograph, and the robotic TRAPPIST photometer continues to be an efficient team for the discovery of transiting exoplanets around stars of $V = 9$–13 in the Southern Hemisphere (e.g., Hellier et al. 2014; Anderson et al. 2015). Ongoing discoveries are important for expanding our census of the hot-Jupiter population, while exoplanets transiting relatively bright stars are also good targets for follow-up studies. In this paper we report three new discoveries: WASP-74b, which orbits a bright $V = 9.7$ star; WASP-83b, a moderately bloated Saturn-mass planet, which, with a period of 4.97 days, demonstrates the capability of a single-longitude transit search to find planets with integer-day periods; and WASP-89b, a massive planet in a short and eccentric orbit around a magnetically active K star.

2. OBSERVATIONS

The observational and analysis techniques used here are similar to those in recent WASP-South discovery papers (e.g., Hellier et al. 2012; Anderson et al. 2014), and so are reported briefly. WASP-South surveys the southern sky using an array of 200 mm *f*/1.8 lenses and a cadence of ~10 minutes (see Pollacco et al. 2006). Transit searching of accumulated light curves (Collier Cameron et al. 2007a) leads to tens of thousands of possible candidates, of which the vast majority are false alarms resulting from the limitations of the photometry. The best 1% are selected by eye as candidates and are passed to TRAPPIST (a robotic 0.6 m photometric telescope) and to the 1.2 m Euler/CORALIE spectrograph (for radial-velocity observations). About 1 in 12 of these turns out to be a planet, with most of the others being astrophysical transit mimics (blended or grazing-eclipse binaries). Higher-quality transit light curves are then obtained with TRAPPIST (Jehin et al. 2011) and with EulerCAM (Lendl et al. 2012). We have also observed a transit of WASP-74b using RISE on the Liverpool Telescope (see Steele et al. 2008).

A list of the observations reported here is given in Table 1 while the CORALIE radial velocities are listed in Table 7.

3. THE HOST STARS

We used the CORALIE spectra to analyze the three host stars, co-adding the standard pipeline reduction products to produce spectra with signal-to-noise ratios (S/N) of 150:1, 100:1, and 30:1 for WASP-74, WASP-83, and WASP-89 respectively. Our analysis methods are described in Doyle et al. (2013). The effective temperature ($T_{\rm eff}$) estimate comes from the excitation balance of Fe I lines, while the surface gravity ($\log g$) estimate comes from the ionization balance of Fe I and Fe II and the Ca I line at 6439 Å and the Na I D lines. The metallicity was determined from equivalent-width measurements of several unblended lines. The quoted error estimates include that given by the uncertainties in $T_{\rm eff}$ and $\log g$, as well as the scatter due to measurement and atomic data uncertainties.

The projected stellar rotation velocity ($v \sin i$) was determined by fitting the profiles of several unblended Fe I lines. Values of macroturbulent velocity of 3.9 ± 0.7 and 2.9 ± 0.7 km s^{-1} were adopted for WASP-74 and WASP-83, using the calibration of Doyle et al. (2014). For WASP-89, however, macroturbulence was assumed to be zero, since for mid-K stars

Draft version January 8, 2015
Preprint typeset using LaTeX style emulateapj v. 05/12/14

DISCOVERY OF WASP-85 A b: A HOT JUPITER IN A VISUAL BINARY SYSTEM †

D. J. A. Brown[1,2], D. R. Anderson[3], D. J. Armstrong[1], F. Bouchy[4,5], A. Collier Cameron[6], L. Delrez[7], A. P. Doyle[1], M. Gillon[7], Y. Gomez Maqueo Chew[1,8], L. Hebb[9], G. Hébrard[4,5], C. Hellier[3], E. Jehin[7], M. Lendl[7,10], P. F. L. Maxted[3], J. McCormac[1], M. Neveu-VanMalle[10,11], D. Pollacco[1], D. Queloz[11,10], D. Segransan[10], B. Smalley[3], O. D. Turner[3], A. H. M. J. Triaud[12,10], and S. Udry[10]

Draft version January 8, 2015

ABSTRACT

We report the discovery of the transiting hot Jupiter exoplanet WASP-85 A b. Using a combined analysis of spectroscopic and photometric data, we determine that the planet orbits its host star every 2.66 days, and has a mass of $1.09 \pm 0.03\,M_{\rm Jup}$ and a radius of $1.44 \pm 0.02\,R_{\rm Jup}$. The host star is of G5 spectral type, with magnitude $V = 11.2$, and lies 125 ± 80 pc distant. We find stellar parameters of $T_{\rm eff} = 5685 \pm 65$ K, super-solar metallicity ($[{\rm Fe/H}] = 0.08 \pm 0.10$), $M_\star = 1.04 \pm 0.07\,M_\odot$ and $R_\star = 0.96 \pm 0.13\,R_\odot$. The system has a K-dwarf binary companion, WASP-85 B, at a separation of $\approx 1.5''$. The close proximity of this companion leads to contamination of our photometry, decreasing the apparent transit depth that we account for during our analysis. Without this correction, we find the depth to be 50 percent smaller, the stellar density to be 32 percent smaller, and the planet radius to be 18 percent smaller than the true value. Many of our radial velocity observations are also contaminated; these are disregarded when analysing the system in favour of the uncontaminated HARPS observations, as they have reduced semi-amplitudes that lead to underestimated planetary masses. We find a long-term trend in the binary position angle, indicating a misalignment between the binary and orbital planes. WASP observations of the system show variability with a period of 14.64 days, indicative of rotational modulation caused by stellar activity. Analysis of the Ca II H+K lines shows strong emission that implies that both binary components are strongly active. We find that the system is likely to be less than a few Gyr old. WASP-85 lies in the field of view of K2 Campaign 1. Long cadence observations of the planet clearly show the planetary transits, along with the signature of stellar variability. Analysis of the K2 data, both long and short cadence, is ongoing.

Keywords: planets and satellites: detection – planets and satellites: individual: WASP-85 – techniques: photometric – techniques: radial velocities

d.j.a.brown@warwick.ac.uk

† based on observations (under proposal 089.C-0151(A)) made using the HARPS high resolution échelle spectrograph mounted on the ESO 3.6-m at the ESO La Silla observatory, and the IO:O camera on the 2.0-m Liverpool Telescope under program PL12B13.

[1] Department of Physics, University of Warwick, Coventry CV4 7AL
[2] Astrophysics Research Centre, School of Mathematics & Physics, Queen's University, University Road, Belfast, BT7 1NN, UK.
[3] Astrophysics Group, School of Physical & Geographical Sciences, Lennard-Jones Building, Keele University, Staffordshire, ST5 5BG, UK.
[4] Institut d'Astrophysique de Paris, UMR7095 CNRS, Université Pierre & Marie Curie, 98bis boulevard Arago, 75014 Paris, France
[5] Observatoire de Haute Provence, CNRS/OAMP, 04870 St Michel l'Observatoire, France.
[6] SUPA, School of Physics and Astronomy, University of St Andrews, North Haugh, St Andrews, Fife KY16 9SS, UK.
[7] Institut d'Astrophysique et de Géophysique, Université de Liège, Allée du 6 Août, 17 (Bât. B5C) Sart Tilman, 4000 Liége, Belgium
[8] Instituto de Astronomia, Universidad Nacional Autónoma de México, Circuito Exterior s/n, Ciudad Universitaria, México, D.F., C.P. 04510
[9] Department of Physics and Astronomy, Vanderbilt University, Nashville, TN 37235, USA
[10] Observatoire Astronomique de l'Université de Genève, Chemin des Maillettes 51, 1290 Sauverny, Switzerland
[11] Cavendish Laboratory, J J Thomson Avenue, Cambridge, CB3 0HE, UK
[12] Kavli Institute for Astrophysics & Space Research, Massachusetts Institute of Technology, Cambridge, MA 02139, USA

A&A 585, A126 (2016)
DOI: 10.1051/0004-6361/201527276

Astronomy & Astrophysics

Three irradiated and bloated hot Jupiters:

WASP-76b, WASP-82b, and WASP-90b⋆

R. G. West[1], C. Hellier[2], J.-M. Almenara[3], D. R. Anderson[2], S. C. C. Barros[3], F. Bouchy[4,5], D. J. A. Brown[1], A. Collier Cameron[6], M. Deleuil[3], L. Delrez[7], A. P. Doyle[1,2], F. Faedi[1], A. Fumel[7], M. Gillon[7], Y. Gómez Maqueo Chew[1], G. Hébrard[4], E. Jehin[7], M. Lendl[7,8], P. F. L. Maxted[2], F. Pepe[8], D. Pollacco[1], D. Queloz[8,9], D. Ségransan[8], B. Smalley[2], A. M. S. Smith[2,10], J. Southworth[2], A. H. M. J. Triaud[8,11,12], and S. Udry[8]

[1] Department of Physics, University of Warwick, Coventry CV4 7AL, UK
e-mail: richard.west@warwick.ac.uk
[2] Astrophysics Group, Keele University, Staffordshire, ST5 5BG, UK
[3] Aix-Marseille Université, CNRS, LAM (Laboratoire d'Astrophysique de Marseille) UMR 7326, 13388 Marseille, France
[4] Institut d'Astrophysique de Paris, UMR 7095 CNRS, Université Pierre & Marie Curie, 75000 Paris, France
[5] Observatoire de Haute-Provence, CNRS/OAMP, 04870 St. Michel l'Observatoire, France
[6] SUPA, School of Physics and Astronomy, University of St. Andrews, North Haugh, Fife, KY16 9SS, UK
[7] Institut d'Astrophysique et de Géophysique, Université de Liège, Allée du 6 Août 17, Bât. B5C, Liège 1, Belgium
[8] Observatoire astronomique de l'Université de Genève, 51 Ch. des Maillettes, 1290 Sauverny, Switzerland
[9] Cavendish Laboratory, J J Thomson Avenue, Cambridge, CB3 0HE, UK
[10] N. Copernicus Astronomical Centre, Polish Academy of Sciences, Bartycka 18, 00-716 Warsaw, Poland
[11] Centre for Planetary Sciences, University of Toronto at Scarborough, 1265 Military Trail, Toronto, ON M1C 1A4, Canada
[12] Department of Astronomy & Astrophysics, University of Toronto, Toronto, ON M5S 3H4, Canada

Received 31 August 2015 / Accepted 8 October 2015

ABSTRACT

We report on three new transiting hot Jupiter planets, discovered from the WASP surveys, which we combine with radial velocities from OHP/SOPHIE and *Euler*/CORALIE and photometry from *Euler* and TRAPPIST. The planets WASP-76b, WASP-82b, and WASP-90b are all inflated, with radii of 1.7–1.8 $R_{\rm Jup}$. All three orbit hot stars, of type F5–F7, with orbits of 1.8–3.9 d, and all three stars have evolved, post-main-sequence radii (1.7–2.2 $R_\odot$). Thus the three planets fit a known trend of hot Jupiters that receive high levels of irradiation being highly inflated. We caution, though, about the presence of a selection effect, in that non-inflated planets around ∼2 $R_\odot$ post-MS stars can often produce transits too shallow to be detected by the ground-based surveys that have found the majority of transiting hot Jupiters.

Key words. planetary systems – stars: individual: WASP-76 – stars: individual: WASP-82 – stars: individual: WASP-90

1. Introduction

The naive expectation that a Jupiter-mass planet would have a radius of one Jupiter has been replaced by the realisation that many of the hot Jupiters found by transit surveys have inflated radii. Planets as large as ∼2 $R_{\rm Jup}$ have been found (e.g. WASP-17b, Anderson et al. 2010; HAT-P-32b, Hartman et al. 2011).

It is also apparent that inflated planets are more likely to be found around hot stars. For example, Hartman et al. (2012) reported three new HAT-discovered planets, with radii of 1.6–1.7 $R_{\rm Jup}$, all transiting F-type stars. Similarly, Smalley et al. (2012) reported that WASP-78b and WASP-79b are 1.7-$R_{\rm Jup}$ planets that orbit F stars. Here we continue this theme by announcing three new hot Jupiters, again all inflated and all orbiting F stars.

For a discussion of the radii of transiting exoplanets see the paper by Weiss et al. (2013). It is likely that stellar irradiation plays an important role in inflating hot Jupiters, since no inflated planets are known that receive less than 2×10^8 erg s^{-1} cm^{-2} (Miller & Fortney 2011; Demory & Seager 2011). There is also an extensive literature discussing other mechanisms for inflating hot Jupiters, such as tidal dissipation (e.g. Leconte et al. 2010, and references therein) and Ohmic dissipation (e.g. Batygin & Stevenson 2010).

2. Observations

The three transiting-planet systems reported here are near the equator, and so have been observed by both the SuperWASP-North camera array on La Palma and by WASP-South at Sutherland in South Africa. Our methods all follow those in previous WASP discovery papers closely. The WASP camera arrays are described in Pollacco et al. (2006), while our planet-hunting methods are described in Collier Cameron et al. (2007b) and Pollacco et al. (2008)

⋆ Tables of the photometry and radial velocity are only available at the CDS via anonymous ftp to cdsarc.u-strasbg.fr (130.79.128.5) or via http://cdsarc.u-strasbg.fr/viz-bin/qcat?J/A+A/585/A126

Draft version March 18, 2016
Preprint typeset using LaTeX style emulateapj v. 01/23/15

WASP-157B, A TRANSITING HOT JUPITER OBSERVED WITH K2

T. Močnik[1], D. R. Anderson[1], D. J. A. Brown[2], A. Collier Cameron[3], L. Delrez[4], M. Gillon[4], C. Hellier[1], E. Jehin[4], M. Lendl[5,6], P. F. L. Maxted[1], M. Neveu-VanMalle[6,7], F. Pepe[6], D. Pollacco[2], D. Queloz[6,7], D. Ségransan[6], B. Smalley[1], J. Southworth[1], A. H. M. J. Triaud[6,8], S. Udry[6], R. G. West[2]

[1]Astrophysics Group, Keele University, Staffordshire, ST5 5BG, UK
[2]Department of Physics, University of Warwick, Coventry CV4 7AL, UK
[3]SUPA, School of Physics and Astronomy, University of St Andrews, North Haugh, Fife, KY16 9SS, UK
[4]Institut d'Astrophysique et de Géophysique, Université de Liège, Allée du 6 Août, 17, Bat. B5C, Liège 1, Belgium
[5]Space Research Institute, Austrian Academy of Sciences, Schmiedlstr. 6, 8042 Graz, Austria
[6]Observatoire Astronomique de l'Université de Genève 51 ch. des Maillettes, 1290 Sauverny, Switzerland
[7]Cavendish Laboratory, J J Thomson Avenue, Cambridge, CB3 0HE, UK
[8]Institute of Astronomy, University of Cambridge, Cambridge, CB3 0HA, UK

Draft version March 18, 2016

ABSTRACT

We announce the discovery of the transiting hot Jupiter WASP-157b in a 3.95-d orbit around a $V = 12.9$ G2 main-sequence star. This moderately inflated planet has a Saturn-like density with a mass of 0.57 ± 0.10 M_{Jup} and radius 1.04 ± 0.04 R_{Jup}. The small projected stellar rotational velocity of $1.0 \pm 0.9\,km\,s^{-1}$ suggests that the host star is a slow rotator or that the star rotates close to pole-on. We do not detect any rotational or phase-curve modulations, nor the secondary eclipse, with conservative semi-amplitude upper limits of 250 and 30 ppm, respectively.

Keywords: planets and satellites: detection – planets and satellites: individual (WASP-157b) – stars: individual (WASP-157)

1. INTRODUCTION

The fields along the ecliptic being observed by the *Kepler* K2 mission (Howell et al. 2014) contain planets discovered by the WASP transit search (Pollacco et al. 2006) and so K2 is also observing current WASP candidates. K2's high-precision photometry has allowed the detection of two additional close-in transiting exoplanets in the WASP-47 system (Becker et al. 2015) and the detection of starspot occultations in WASP-85 (Močnik et al. 2015), with several more WASP planets either recently observed or scheduled for future K2 campaigns.

Here we present the discovery of a transiting hot Jupiter WASP-157b. In Section 2 we introduce the photometric and spectroscopic datasets. Basic properties of the host star are listed in Section 3, in Section 4 we discuss lightcurve modulations. Description of the spectrophotometric analysis and a list of system parameters are shown in Section 5, and a stellar age estimate is provided in Section 6.

2. OBSERVATIONS

WASP-157b was identified as an exoplanet candidate from observations with both WASP-South and SuperWASP-North over 2008–2010 (see Table 1). For a detailed description of the WASP telescopes, observing strategy, data reduction, and candidate identification and selection procedures, see Pollacco et al. (2006, 2008) and Collier Cameron et al. (2007b). A transit was then observed with the TRAPPIST photometer (Jehin et al. 2011; Gillon et al. 2011) on 2016 February 05.

WASP-157 (EPIC 212697709) was also observed with K2 in the long-cadence observing mode during Campaign 6 (from 2015 July 13 to 2015 September 30). We retrieved the target pixel file from the Minkulski Archive for Space Telescopes (MAST) and performed the standard data reduction and the self-flat-field (SFF) correction using PyRAF tools for *Kepler* (PyKE) version 2.6.2 (Still & Barclay 2012). The applied SFF correction, which is based on the procedure described in Vanderburg & Johnson (2014), improved the median 6-hour photometric precision from 149 parts per million (ppm) to 29 ppm, which is comparable to original *Kepler* precision for a similarly bright star. After removal of all the quality-flagged data points a total of 3227 data points remained. The reduced and normalized K2 lightcurve is shown in Figure 1.

Spectroscopic radial velocity (RV) follow-up was performed using the fibre-fed CORALIE spectrograph at the 1.2-m Swiss Euler Telescope at La Silla (Queloz et al. 2000). One spectrum was obtained in 2015 June and a further seven in 2016 February and March. Given that WASP-157 is relatively faint at $V = 12.9$, we also obtained spectra on four consecutive nights in 2016 March with the HARPS spectrograph mounted at ESO 3.6-m telescope (Mayor et al. 2003), also at La Silla observatory (see Table 1). The spectroscopic data have been reduced with the standard HARPS and CORALIE reduction pipelines. The RVs were extracted with the weighted cross-correlation of each spectrum with a G2 mask and the simultaneous Th-Ar wavelength calibration reference (see Pepe et al. (2002) for details). The resulting RVs and bisector spans (BS) are given in Table 2.

3. SPECTRAL ANALYSIS

We analysed the spectroscopic properties of the host star from a co-added HARPS spectrum with a final signal-to-noise ratio of 38. The analysis methods are described in Gillon et al. (2009) and Doyle et al. (2013). We used the Hα line to estimate the effective temperature ($T_{\rm eff}$), and the Na I D and Mg I b lines as diagnostics

t.mocnik@keele.ac.uk

MNRAS **000**, range (0000) Preprint 15 April 2016 Compiled using MNRAS LATEX style file v3.0

WASP-South transiting exoplanets: WASP-130b, WASP-131b, WASP-132b, WASP-139b, WASP-140b, WASP-141b & WASP-142b

Coel Hellier[1], D.R. Anderson[1], A. Collier Cameron[2], L. Delrez[3], M. Gillon[3], E. Jehin[3], M. Lendl[4,5], P.F.L. Maxted[1], M. Neveu-VanMalle[5,6], F. Pepe[5], D. Pollacco[7], D. Queloz[6], D. Ségransan[5], B. Smalley[1], J. Southworth[1], A.H.M.J. Triaud[5,8], S. Udry[5], T. Wagg[1] & R.G. West[7]

[1] *Astrophysics Group, Keele University, Staffordshire, ST5 5BG, UK*
[2] *SUPA, School of Physics and Astronomy, University of St. Andrews, North Haugh, Fife, KY16 9SS, UK*
[3] *Institut d'Astrophysique et de Géophysique, Université de Liège, Allée du 6 Août, 17, Bat. B5C, Liège 1, Belgium*
[4] *Space Research Institute, Austrian Academy of Sciences, Schmiedlstr. 6, 8042, Graz, Austria*
[5] *Observatoire astronomique de l'Université de Genève 51 ch. des Maillettes, 1290 Sauverny, Switzerland*
[6] *Cavendish Laboratory, J J Thomson Avenue, Cambridge, CB3 0HE, UK*
[7] *Department of Physics, University of Warwick, Gibbet Hill Road, Coventry, CV4 7AL, UK*
[8] *Institute of Astronomy, University of Cambridge, Cambridge, CB3 0HA, UK*

date

ABSTRACT

We describe seven new exoplanets transiting stars of brightness $V = 10.1$ to 12.4.

WASP-130b is a "warm Jupiter" having an orbital period of 11.6 d, the longest yet found by WASP. It transits a $V = 11.1$, G6 star with [Fe/H] = +0.26. Warm Jupiters tend to have smaller radii than hot Jupiters, and WASP-130b is in line with this trend (1.23 ± 0.04 M_{Jup}; 0.89 ± 0.03 R_{Jup}).

WASP-131b is a bloated Saturn-mass planet (0.27 M_{Jup}; 1.22 R_{Jup}). Its large scale height coupled with the $V = 10.1$ brightness of its host star make the planet a good target for atmospheric characterisation.

WASP-132b is among the least irradiated and coolest of WASP planets, being in a 7.1-d orbit around a K4 star. It has a low mass and a modest radius (0.41 M_{Jup}; 0.87 R_{Jup}). The $V = 12.4$, [Fe/H] = +0.22 star shows a possible rotational modulation at 33 d.

WASP-139b is the lowest-mass planet yet found by WASP, at 0.12 M_{Jup} and 0.80 R_{Jup}. It is a "super-Neptune" akin to HATS-7b and HATS-8b. It orbits a $V = 12.4$, [Fe/H] = +0.20, K0 star and will be a good target for studying such systems. The star appears to be anomalously dense, akin to HAT-P-11.

WASP-140b is a 2.4-M_{Jup} planet in a 2.2-d orbit that is both eccentric ($e = 0.047 \pm 0.004$) and with a grazing transit ($b = 0.93$) The timescale for tidal circularisation is likely to be the lowest of all known eccentric hot Jupiters. The planet's radius is large (1.4 R_{Jup}), but uncertain owing to the grazing transit. The host star is a $V = 11.1$, [Fe/H] = +0.12, K0 dwarf showing a prominent 10.4-d rotational modulation. The dynamics of this system are worthy of further investigation. A second star, 2 mag fainter and separated by 7 arcsec, is possibly associated.

WASP-141b is a typical hot Jupiter, being a 2.7 M_{Jup}, 1.2 R_{Jup} planet in a 3.3-d orbit around a $V = 12.4$, [Fe/H] = +0.29, F9 star.

WASP-142b is a typical bloated hot Jupiter (0.84 M_{Jup}, 1.53 R_{Jup}) in a 2.1-d orbit around a $V = 12.3$, [Fe/H] = +0.26, F8 star. There is a second star, 1.9 mag fainter, 5 arcsecs away.

We show that the period distribution within the hot-Jupiter bulge does not depend on the metallicity of the host star.

Key words: planetary systems – stars: individual (WASP-130, WASP-131, WASP-132, WASP-139, WASP-140, WASP-141, WASP-142)

A&A 591, A55 (2016)
DOI: 10.1051/0004-6361/201628250

Astronomy & Astrophysics

Five transiting hot Jupiters discovered using WASP-South, *Euler*, and TRAPPIST: WASP-119 b, WASP-124 b, WASP-126 b, WASP-129 b, and WASP-133 b⋆

P. F. L. Maxted[1], D. R. Anderson[1], A. Collier Cameron[2], L. Delrez[3], M. Gillon[3], C. Hellier[1], E. Jehin[3], M. Lendl[4,5], M. Neveu-VanMalle[5,6], F. Pepe[5], D. Pollacco[7], D. Queloz[6,5], D. Ségransan[5], B. Smalley[1], A. M. S. Smith[1,8], J. Southworth[1], A. H. M. J. Triaud[5,9,10], S. Udry[5], T. Wagg[1], and R. G. West[7]

[1] Astrophysics Group, Keele University, Staffordshire, ST5 5BG, UK
e-mail: p.maxted@keele.ac.uk
[2] SUPA, School of Physics and Astronomy, University of St. Andrews, North Haugh, Fife, KY16 9SS, UK
[3] Institut d'Astrophysique et de Géophysique, Université de Liège, Allée du 6 Août, 17, Bât. B5C, Liège 1, Belgium
[4] Space Research Institute, Austrian Academy of Sciences, Schmiedlstr. 6, 8042 Graz, Austria
[5] Observatoire Astronomique de l'Université de Genève, 51 ch. des Maillettes, 1290 Sauverny, Switzerland
[6] Cavendish Laboratory, J J Thomson Avenue, Cambridge, CB3 0HE, UK
[7] Department of Physics, University of Warwick, Coventry CV4 7AL, UK
[8] Institute of Planetary Research, German Aerospace Center, Rutherfordstrasse 2, 12489 Berlin, Germany
[9] Centre for Planetary Sciences, University of Toronto at Scarborough, 1265 Military Trail, Toronto, ON, M1C 1A4, Canada
[10] Department of Astronomy & Astrophysics, University of Toronto, Toronto, ON, M5S 3H4, Canada

Received 4 February 2016 / Accepted 24 April 2016

ABSTRACT

We have used photometry from the WASP-South instrument to identify 5 stars showing planet-like transits in their light curves. The planetary nature of the companions to these stars has been confirmed using photometry from the *Euler*Cam instrument on the Swiss *Euler* 1.2-m telescope and the TRAPPIST telescope, and spectroscopy obtained with the CORALIE spectrograph. The planets discovered are hot Jupiter systems with orbital periods in the range 2.17 to 5.75 days, masses from 0.3 $M_{\rm Jup}$ to 1.2 $M_{\rm Jup}$ and with radii from 1 $R_{\rm Jup}$ to 1.5 $R_{\rm Jup}$. These planets orbit bright stars (V = 11–13) with spectral types in the range F9 to G4. WASP-126 is the brightest planetary system in this sample and hosts a low-mass planet with a large radius (0.3 $M_{\rm Jup}$, 0.95 $R_{\rm Jup}$), making it a good target for transmission spectroscopy. The high density of WASP-129 A suggests that it is a helium-rich star similar to HAT-P-11 A. WASP-133 A has an enhanced surface lithium abundance compared to other old G-type stars, particularly other planet host stars. These planetary systems are good targets for follow-up observations with ground-based and space-based facilities to study their atmospheric and dynamical properties.

Key words. planetary systems

1. Introduction

Ground-based transit surveys such as WASP (Pollacco et al. 2008), HAT (Bakos et al. 2004), HAT-South (Bakos et al. 2013) and KELT (Pepper et al. 2008) have identified the majority of bright hot Jupiter planetary systems that have been studied in detail using observations with large ground-based telescopes and space-based instrumentation. Although space-based surveys such as Kepler-K2 (Howell et al. 2014), TESS (Ricker et al. 2015) and PLATO (Rauer et al. 2014) will produce much higher quality photometry than is possible from the ground, it is advantageous to identify as many planetary systems as possible in the areas of the sky that will be observed by these missions so that the observing strategy can be optimised. This was clearly demonstrated by the recent discovery that WASP-47 is a very rare example of a multiple-planet system containing a hot Jupiter (Becker et al. 2015; Neveu-VanMalle et al. 2016). This discovery was only possible because this known planetary system was prioritised for high-cadence observations with Kepler-K2. These high-cadence observations made it possible to detect the transit time variations produced by the gravitational interactions between the planets in this system. The discovery that WASP-47 is a multi-planet system also demonstrates that detailed obervations of apparently normal hot Jupiter systems continue to reveal unexpected properties of this diverse group of planetary systems.

Here we present the discovery of 5 hot-Jupiter planetary systems in the southern hemisphere. Section 2 describes the observations we have obtained, Sect. 3 describes our analysis of the host stars, the stellar and planetary masses and radii are derived in Sect. 4 and we discuss the properties of each system briefly in Sect. 5.

2. Observations

WASP-South uses an array of 8 cameras that observe selected regions of the southern sky with a combined area of approximately 450 square degrees at a typical cadence of about 8 min

⋆ Full Tables 2 and 3 are only available at the CDS via anonymous ftp to cdsarc.u-strasbg.fr (130.79.128.5) or via http://cdsarc.u-strasbg.fr/viz-bin/qcat?J/A+A/591/A55

Publications of the Astronomical Society of the Pacific, 128:064401 (12pp), 2016 June doi:10.1088/1538-3873/128/964/064401

WASP-120 b, WASP-122 b, and WASP-123 b: Three Newly Discovered Planets from the WASP-South Survey

O. D. Turner[1], D. R. Anderson[1], A. Collier Cameron[2], L. Delrez[3], D. F. Evans[1], M. Gillon[3], C. Hellier[1], E. Jehin[3], M. Lendl[4,5], P. F. L. Maxted[1], F. Pepe[5], D. Pollacco[6], D. Queloz[7], D. Ségransan[5], B. Smalley[1], A. M. S. Smith[8,9], A. H. M. J. Triaud[5,10,11], S. Udry[5], and R. G. West[6]
[1] Astrophysics Group, Keele University, Staffordshire ST5 5BG, UK
[2] SUPA, School of Physics and Astronomy, University of St. Andrews, North Haugh, Fife KY16 9SS, UK
[3] Institut d'Astrophysique et de Géophysique, Université de Liége, Allèe du 6 Août, 17, Bat. B5C, Liège 1, Belgium
[4] Austrian Academy of Sciences, Space Research Institute, Schmiedlstrasse 6, 8042 Graz, Austria
[5] Observatoire de Genève, Université de Genève, 51 Chemin des Maillettes, 1290 Sauverny, Switzerland
[6] Department of Physics, University of Warwick, Coventry CV4 7AL, UK
[7] Cavendish Laboratory, J J Thomson Avenue, Cambridge CB3 0HE, UK
[8] N. Copernicus Astronomical Centre, Polish Academy of Sciences, Bartycka 18, 00–716 Warsaw, Poland
[9] Institute of Planetary Research, German Aerospace Center, Rutherfordstrasse 2, D-12489 Berlin, Germany
[10] Centre for Planetary Sciences, University of Toronto at Scarborough, Toronto, ON M1C 1A4, Canada
[11] Department of Astronomy & Astrophysics, University of Toronto, Toronto, ON M5S 3H4, Canada
Received 2015 October 26; accepted 2016 January 4; published 2016 May 17

Abstract

We present the discovery by the WASP-South survey of three planets transiting moderately bright stars (V ≈ 11). WASP-120 b is a massive (4.85 $M_{\rm Jup}$) planet in a 3.6-day orbit that we find likely to be eccentric ($e = 0.059^{+0.025}_{-0.018}$) around an F5 star. WASP-122 b is a hot Jupiter (1.28 $M_{\rm Jup}$, 1.74 $R_{\rm Jup}$) in a 1.7-day orbit about a G4 star. Our predicted transit depth variation caused by the atmosphere of WASP-122 b suggests it is well suited to characterization. WASP-123 b is a hot Jupiter (0.90 $M_{\rm Jup}$, 1.32 $R_{\rm Jup}$) in a 3.0-day orbit around an old (~7 Gyr) G5 star.

Key words: planets and satellites: individual (WASP-120b, WASP-122b, WASP-123b)

Online material: color figures

1. Introduction

The Wide Angle Search for Planets (WASP) survey is a prolific contributor to the field of exoplanet science having published the discovery of 104 planets to date. Our effective magnitude range of $9 < V < 13$ means that WASP systems are conducive to further study. Examples from the extremes of this range are the bright WASP-33 (V = 8.3; Collier Cameron et al. 2010) and WASP-18 (V = 9.3; Hellier et al. 2009) and the relatively dim WASP-112 (V = 13.3; Anderson et al. 2014).

Here, we present the discovery of WASP-120 b, a system with a star showing variable activity and a possibly eccentric planet orbit, WASP-122 b, which offers a good opportunity for atmospheric study, and WASP-123 b, which orbits an old star, ~7 Gyr.

2. Observations

The transits of these planets were discovered in photometry gathered from the WASP-South installation hosted by the South African Astronomical Observatory. The WASP-South instrument is an array of 8 cameras using 200 mm $f/1.8$ lenses to survey the sky at a cadence of ~10 minutes. For more information on the WASP instrument, see Pollacco et al. (2006). The data were processed and searched for transits, as described in Collier Cameron et al. (2006), with candidate selection following the procedure in Collier Cameron et al. (2007a). Details of observations for each star in this paper can be found in Table 1. The phase-folded WASP data are displayed in the top panels of Figures 1, 2, and 3. We used the method of Maxted et al. (2011) to search the WASP photometry for modulations caused by star spots. We detected no rotational modulation above 2 mmag that suggests that the hosts are inactive.

We obtained spectra of the three stars with the CORALIE spectrograph on the 1.2 m Swiss telescope as outlined in Table 1. We used these data to measure radial velocity (RV) variations and confirm the planetary nature of the candidates (Table 2; bottom panels of Figures 1, 2, and 3). We obtained nine of the WASP-120 spectra after the spectrograph was upgraded in November of 2014. The lack of correlation between the bisector spans and RVs (Figure 4) indicate that the RV variations are not a result of blended eclipsing binaries. For example, Santos et al. (2002) found a brown dwarf mass

MNRAS **000**, 1–14 (2016) Preprint 5 July 2016 Compiled using MNRAS LATEX style file v3.0

WASP-92b, WASP-93b and WASP-118b: Three new transiting close-in giant planets

K. L. Hay[1⋆], A. Collier-Cameron[1], A. P. Doyle[2], G. Hébrard[3], I. Skillen[4], D. R. Anderson[5], S. C. C. Barros[6], D. J. A. Brown[1,2], F. Bouchy[7], R. Busuttil[8], P. Delorme[1,9], L. Delrez[10], O. Demangeon[7], R. F. Díaz[11], M. Gillon[10], E. Gonzàlez[12], C. Hellier[5], S. Holmes[8], J. F. Jarvis[8], E. Jehin[7], Y. C. Joshi[13,14], U. Kolb[8], M. Lendl[11,15], P. F. L. Maxted[5], J. McCormac[2], G. R. M. Miller[1,16], A. Mortier[1], D. Pollacco[2], D. Queloz[17], D. Ségransan[11], E. K. Simpson[13], B. Smalley[5], J. Southworth[5], A. H. M. J. Triaud[11,17], O. D. Turner[5], S. Udry[11], M. Vanhuysse[18], R. G. West[2], and P. A. Wilson[3]

[1] *SUPA, School of Physics and Astronomy, University of St Andrews, Fife, KY16 9SS, UK*
[2] *Department of Physics, University of Warwick, Coventry, CV4 7AL, UK*
[3] *Institut d'Astrophysique de Paris, UMR 7095 CNRS, Université Pierre & Marie Curie, 75000 Paris, France*
[4] *Isaac Newton Group of Telescopes, Apartado de Correos 321, Santa Cruz de La Palma, E-38700, Spain*
[5] *Astrophysics Group, Keele University, Staffordshire, ST5 5BG, UK*
[6] *Instituto de Astrofísica e Ciências do Espaço, Universidade do Porto, CAUP, Rua das Estrelas, 4150-762 Porto, Portugal*
[7] *Aix Marseille Université, CNRS, LAM (Laboratoire d'Astrophysique de Marseille) UMR 7326, 13388 Marseille, France*
[8] *Department of Physical Sciences, The Open University, Milton Keynes, MK7 6AA, UK*
[9] *Université Grenoble Alpes, CNRS, IPAG, 38000 Grenoble, France*
[10] *Institut d'Astrophysique et Géophysique, Université de Liège, allée du 6 Août 17, B-4000 Liège, Belgium*
[11] *Observatoire de Genève, Université de Genève, 51 Chemin des Maillettes, 1290 Sauverny, Switzerland*
[12] *Observatori Astronómic de Mallorca, Camí de l'Observatori s/n, 07144 Costitx, Mallorca, Spain*
[13] *Astrophysics Research Centre, School of Mathematics & Physics, Queen's University, Belfast BT7 1NN, UK*
[14] *Aryabhatta Research Institute of Observational Sciences (ARIES), Manora peak, Nainital 263002, India*
[15] *Space Research Institute, Austrian Academy of Sciences, Schmeidlerstr. 6, 8042 Graz, Austria*
[16] *Department of Physics, University of Oxford, Keble Road, Oxford, OX1 3RH, UK*
[17] *Institute of Astronomy, University of Cambridge, Madingley Road, Cambridge, CB3 0HA, United Kingdom*
[18] *OverSky, 47 allée des Palanques, BP 12, 33127, Saint-Jean d'Illac, France*

Accepted year month day. Received year month day; in original form year month day

ABSTRACT

We present the discovery of three new transiting giant planets, first detected with the WASP telescopes, and establish their planetary nature with follow up spectroscopy and ground-based photometric lightcurves. WASP-92 is an F7 star, with a moderately inflated planet orbiting with a period of 2.17 days, which has $R_p = 1.461 \pm 0.077 R_J$ and $M_p = 0.805 \pm 0.068 M_J$. WASP-93b orbits its F4 host star every 2.73 days and has $R_p = 1.597 \pm 0.077 R_J$ and $M_p = 1.47 \pm 0.029 M_J$. WASP-118b also has a hot host star (F6) and is moderately inflated, where $R_p = 1.440 \pm 0.036 R_J$ and $M_p = 0.513 \pm 0.041 M_J$ and the planet has an orbital period of 4.05 days. They are bright targets (V = 13.18, 10.97 and 11.07 respectively) ideal for further characterisation work, particularly WASP-118b, which is being observed by K2 as part of campaign 8. WASP-93b is expected to be tidally migrating outwards, which is divergent from the tidal behaviour of the majority of hot Jupiters discovered.

Key words:

⋆ E-mail: kh97@st-andrews.ac.uk

Astronomy & Astrophysics manuscript no. wasp1134
July 11, 2016

Discovery of WASP-113b and WASP-114b, two inflated hot-Jupiters with contrasting densities

S. C. C. Barros[1,2], D. J. A.. Brown[3], G. Hébrard[4,5], Y. Gómez Maqueo Chew[3,6], D. R. Anderson[7], P. Boumis[8], L. Delrez[9], K. L. Hay[10], K. W. F. Lam[3], J. Llama[11], M. Lendl[12,15], J. McCormac[3], B. Skiff[11], B Smalley[7], O Turner[7], M. Vanhuysse[13], D. J. Armstrong[3,21], I. Boisse[2], F. Bouchy[2], A. Collier Cameron[10], F. Faedi[3], M. Gillon[9], C. Hellier[7], E. Jehin[9], A. Liakos[8], J. Meaburn[14], H. P. Osborn[3], F. Pepe[15], I. Plauchu-Frayn[16], D. Pollacco[3], D. Queloz[15,17], J. Rey[15], J. Spake[3], D. Ségransan[15], A. H. M. Triaud[18,19,15,20], S. Udry[15], S. R. Walker[3], C. A. Watson[21], R. G. West[3], and P. J. Wheatley[3]

[1] Instituto de Astrofísica e Ciências do Espaço, Universidade do Porto, CAUP, Rua das Estrelas, PT4150-762 Porto, Portugal
e-mail: susana.barros@astro.up.pt
[2] Aix Marseille Université, CNRS, LAM (Laboratoire d'Astrophysique de Marseille) UMR 7326, 13388, Marseille, France
[3] Department of Physics, University of Warwick, Gibbet Hill Road, Coventry, CV4 7AL, UK
[4] Institut d'Astrophysique de Paris, UMR7095 CNRS, Université Pierre & Marie Curie, 98bis boulevard Arago, 75014 Paris, France
[5] Observatoire de Haute-Provence, Université d'Aix-Marseille & CNRS, 04870 Saint Michel l'Observatoire, France
[6] Instituto de Astronomía, Universidad Nacional Autónoma de México, Ciudad Universitaria, D.F. 04510, México
[7] Astrophysics Group, Keele University, Staffordshire ST5 5BG, UK
[8] Institute for Astronomy, Astrophysics, Space Applications and Remote Sensing, National Observatory of Athens, 15236 Penteli, Greece
[9] Institut d'Astrophysique et de Geophysique, Universite de Liege, Allee du 6 Aout, 17, Bat. B5C, Liege 1, Belgium
[10] SUPA, School of Physics and Astronomy, University of St. Andrews, North Haugh, Fife KY16 9SS, UK
[11] Lowell Observatory, 1400 W Mars Hill Rd. Flagstaff. AZ. 86001. USA
[12] Space Research Institute, Austrian Academy of Sciences, Schmiedlstr. 6, 8042 Graz, Austria
[13] OverSky, 47 allee des Palanques, BP 12, 33127, Saint-Jean d'Illac, France
[14] Jodrell Bank Centre for Astrophysics, University of Manchester, Oxford Rd., Manchester, UK. M13 9PL
[15] Observatoire de Geneve, Universite de Geneve, 51 Chemin des Maillettes, 1290 Sauverny, Switzerland
[16] Instituto de Astronomía, Universidad Nacional Autónoma de México, C.P. 22860, Ensenada, Baja California, México
[17] Cavendish Laboratory, J J Thomson Avenue, Cambridge, CB3 0HE, UK
[18] Centre for Planetary Sciences, University of Toronto at Scarborough, 1265 Military Trail, Toronto, ON, M1C 1A4, Canada
[19] Department of Astronomy & Astrophysics, University of Toronto, Toronto, ON M5S 3H4, Canada
[20] Institute of Astronomy, Madingley Road, Cambridge, CB3 0HA, United Kingdom
[21] Astrophysics Research Centre, School of Mathematics & Physics, Queen's University Belfast, University Road, Belfast, BT7 1NN, UK

Received September 15, 1996; accepted March 16, 1997

ABSTRACT

Aims. We present the discovery and characterisation of the exoplanets WASP-113b and WASP-114b by the WASP survey, *SOPHIE* and *CORALIE*.
Methods. The planetary nature of the systems was established by performing follow-up photometric and spectroscopic observations. The follow-up data were combined with the WASP-photometry and analysed with an MCMC code to obtain system parameters.
Results. The host stars WASP-113 and WASP-114 are very similar. They are both early G-type stars with an effective temperature of $\sim$ 5900 K, [Fe/H]$\sim$ 0.12 and $\log g \sim$ 4.1dex. However, WASP-113 is older than WASP-114. Although the planetary companions have similar radii, WASP-114b is almost 4 times heavier than WASP-113b. WASP-113b has a mass of 0.48 M_{Jup} and an orbital period of $\sim$ 4.5 days; WASP-114b has a mass of 1.77 $M_{Jup}$and an orbital period of $\sim$ 1.5 days. Both planets have inflated radii, in particular WASP-113 with a radius anomaly of $\Re = 0.35$. The high scale height of WASP-113b ($\sim$ 950 km) makes it a good target for follow-up atmospheric observations.

Key words. planetary systems:detection – stars: individual: (WASP-113, WASP114) –techniques: photometric, radial velocities

1. Introduction

In the last few years there has been a huge increase in the number of transiting exoplanets known mainly due to the Kepler satellite (Borucki et al. 2010). Currently, 2600 transiting exoplanets are known and there are another thousand unconfirmed candidates. Transiting planet systems are especially valuable because their geometry enables us to derive accurate planetary properties (Charbonneau et al. 2000; Henry et al. 2000). Time series photometry during transit allows estimation of the orbital inclination and the relative radii of the host star and planet. These can be combined with radial velocity measurements and stellar parameters to derive the absolute planetary mass (e.g. Barros et al. 2011a). Hence, the bulk density of the planet can be

Astronomy & Astrophysics manuscript no. wasp127
July 26, 2016

From Dense Hot Jupiter to Low Density Neptune: The Discovery of WASP-127b, WASP-136b and WASP-138b

K. W. F. Lam[1], F. Faedi[1], D. J. A. Brown[1], D. R. Anderson[2], L. Delrez[3], M. Gillon[3], G. Hébrard[4,5], M. Lendl[6,7], L. Mancini[8], J. Southworth[2], B. Smalley[2], A. H. M. Triaud[7,9,10,11], O. D. Turner[2], K. L. Hay[12], D. J. Armstrong[1,13], S. C. C. Barros[14,15], A. S. Bonomo[16], F. Bouchy[7,15], P. Boumis[17], A. Collier Cameron[12], A. P. Doyle[1], C. Hellier[2], T. Henning[8], E. Jehin[3], G. King[1], J. Kirk[1], T. Louden[1], P. F. L. Maxted[2], J. J. McCormac[1], H. P. Osborn[1], E. Palle[18], F. Pepe[7], D.Pollacco[1], J. Prieto-Arranz[18], D. Queloz[7,19], J. Rey[7], D. Ségransan[7], S. Udry[7], S. Walker[1], R. G. West[1], and P. J. Wheatley[1]

[1] University of Warwick, Department of Physics, Gibbet Hill Road, Coventry, CV4 7AL, UK
e-mail: w.f.lam@warwick.ac.uk
[2] Astrophysics Group, Keele University, Staffordshire ST5 5BG, UK
[3] Institut d'Astrophysique et de Geophysique, Universite de Liege, Allee du 6 Aout, 17, Bat. B5C, Liege 1, Belgium
[4] Institut d'Astrophysique de Paris, UMR7095 CNRS, Université Pierre & Marie Curie, 98bis boulevard Arago, 75014 Paris, France
[5] Observatoire de Haute-Provence, Université d'Aix-Marseille & CNRS, 04870 Saint Michel l'Observatoire, France
[6] Space Research Institute, Austrian Academy of Sciences, Schmiedlstr. 6, 8042 Graz, Austria
[7] Observatoire de Geneve, Universite de Geneve, 51 Chemin des Maillettes, 1290 Sauverny, Switzerland
[8] Max Planck Institute for Astronomy, Koenigstuhl 17, D-69117, Heidelberg, Germany
[9] Centre for Planetary Sciences, University of Toronto at Scarborough, 1265 Military Trail, Toronto, ON, M1C 1A4, Canada
[10] 18 Department of Astronomy & Astrophysics, University of Toronto, Toronto, ON M5S 3H4, Canada
[11] 19 Institute of Astronomy, Madingley Road, Cambridge, CB3 0HA, United Kingdom

[12] SUPA, School of Physics and Astronomy, University of St. Andrews, North Haugh, Fife KY16 9SS, UK
[13] ARC, School of Mathematics & Physics, Queen's University Belfast, University Road, Belfast BT7 1NN, UK
[14] Instituto de Astrofísica e Ciências do Espaço, Universidade do Porto, CAUP, Rua das Estrelas, 4150-762 Porto, Portugal
[15] Aix Marseille Université, CNRS, LAM (Laboratoire d'Astrophysique de Marseille) UMR 7326, 13388 Marseille, France
[16] INAF - Osservatorio Astrofisico di Torino, Via Osservatorio 20, I-10025, Pino Torinese, Italy
[17] Institute for Astronomy, Astrophysics, Space Applications and Remote Sensing, National Observatory of Athens, 15236 Penteli, Greece
[18] Instituto de Astrofisica de Canarias, Via Lactea sn, 38200, La Laguna, Tenerife, Spain
[19] Cavendish Laboratory, J J Thomson Avenue, Cambridge, CB3 0HE, UK

Received date / Accepted date

ABSTRACT

We report three newly discovered exoplanets from the SuperWASP survey. WASP-127b is a heavily inflated super-Neptune of mass $0.18M_J$ and radius $1.35R_J$. This is one of the least massive planets discovered by the WASP project. It orbits a bright host star (V_{mag} = 10.16) of spectral type G5 with a period of 4.17 days. WASP-127b is a low density planet which has an extended atmosphere with a scale height of 2500 ± 400km, making it an ideal candidate for transmission spectroscopy. WASP-136b and WASP-138b are both hot Jupiters with mass and radii of 1.51 M_J and 1.38 R_J, and 1.22 M_J and 1.09 R_J, respectively. WASP-136b is in a 5.22-day orbit around an F9 subgiant star with a mass of 1.41 $M_\odot$ and a radius of 2.21 $R_\odot$. The discovery of WASP-136b could help constraint the characteristics of the giant planet population around evolved stars. WASP-138b orbits an F7 star with a period of 3.63 days. Its radius agrees with theoretical values from standard models, suggesting the presence of a heavy element core with a mass of ~ 10 $M_\oplus$. The discovery of these new planets helps in exploring the diverse compositional range of short-period planets, and will aid our understanding of the physical characteristics of both gas giants and low density planets.

Key words. Planetary systems – Stars: individual: WASP-127, WASP-136, WASP-138 – Techniques: radial velocities, photometrric

1. Introduction

Over 3000 exoplanets have been discovered as of 2016 July.[1] The space-based mission *Kepler* (Borucki et al. 2010) and its successor *K2* (Howell et al. 2014) have discovered a large number of transiting planets. The results show that small, Earth and Neptune sized planets are common around solar-like stars (Borucki et al. 2011). The *Kepler* discoveries have provided a large sample of planetary systems that are very useful for statistical studies of planetary populations (e.g. Fressin et al. 2013; Dressing & Charbonneau 2013; Petigura et al. 2013). However, most of the *Kepler* planets orbit very faint stars, for which are quite difficult to obtain precise radial velocity (RV) mea-

[1] http://exoplanetarchive.ipac.caltech.edu/

Appendix C

Atmospheric characterization of WASP-121 b: preliminary results

In this appendix, I briefly present some preliminary results of an observing program carried out on the AAT/IRIS2 near-IR facility (Tinney et al. 2004, 3.9m Anglo-Australian Telescope, Siding Spring Observatory, Australia), aiming at probing the dayside thermal emission spectrum of WASP-121 b in the H and $K_{\rm S}$ bands (OPTICON program 16A/027, PI: Delrez). Two occultations were observed, one in each band. I went to Siding Spring to observe the first one in visitor mode during the night of 18 February 2016, while the second one was kindly observed by my support astronomer, Lee Spitler, during the night of 17 March 2016. The observing strategy and reduction procedure were pretty much the same as for the CFHT/WIRCam observations of WASP-103 b presented in Chapter 5. The preliminary light curves are shown in Fig. C.1. Unfortunately, the second run was interrupted by clouds, so that the H-band occultation light curve is only partial. The planet's dayside emission is clearly detected in both the H and $K_{\rm S}$ bands, the occultations depths derived from a preliminary MCMC analysis (cf. Section 2) being 1785$\pm$240ppm and 2450$\pm$160ppm, respectively. These measurements are shown in Fig. C.2, together with the z'-band measurement reported in Section 3.2.7 and preliminary model emission spectra generated by Nikku Madhusudhan (Madhusudhan and Seager 2009). The three data points are equally well fitted by (1) a black-body model (isothermal atmosphere) with a temperature of 2700K and (2) a model with solar abundance composition and a thermal inversion. Observations with HST/WFC3 (1.1–1.7μm) and *Spitzer*/IRAC (3.6 and 4.5 μm) should be able to distinguish between these two model scenarios.

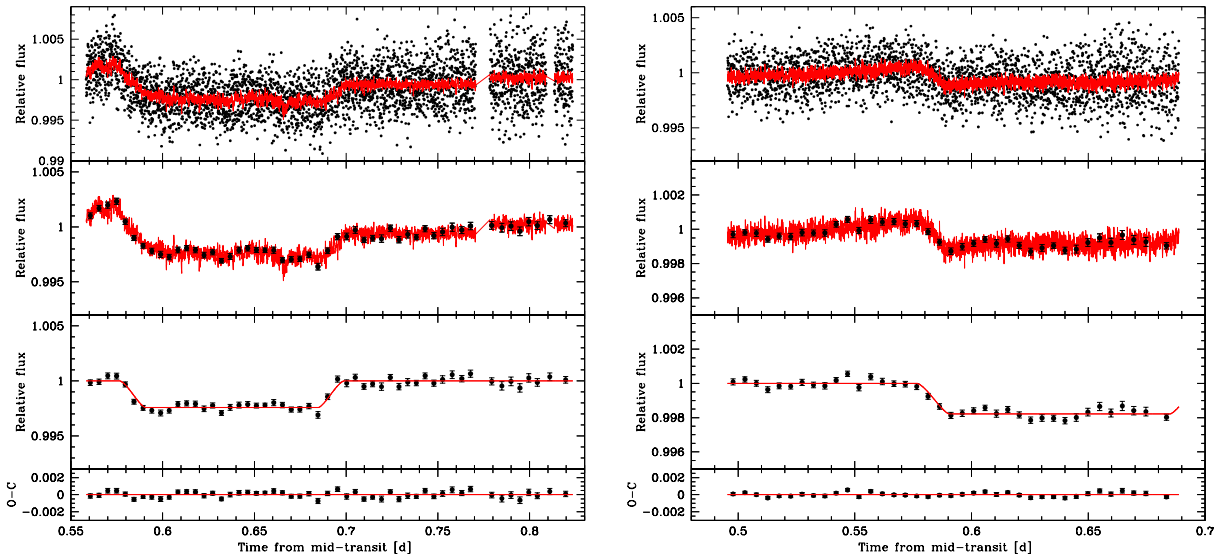

FIGURE C.1: Preliminary occultation light curves of WASP-121 b obtained with AAT/IRIS2 in the K_S (*left*) and H (*right*) bands. *Top panels:* the raw, unbinned light curves, together with the corresponding best-fit full (photometric baseline $\times$ occultation) models (in red, cf. Section 2). The baseline models consist in both cases of a second-order polynomial of time combined to first-order polynomials of the PSF FWHM and stellar positions on the detector. *Second panels:* same as the top panels except that the data are binned in 7.2min intervals. *Third panels:* binned light curves divided by the corresponding best-fit photometric baseline models. The corresponding best-fit occultation models are shown in red. *Bottom panels:* best-fit residuals.

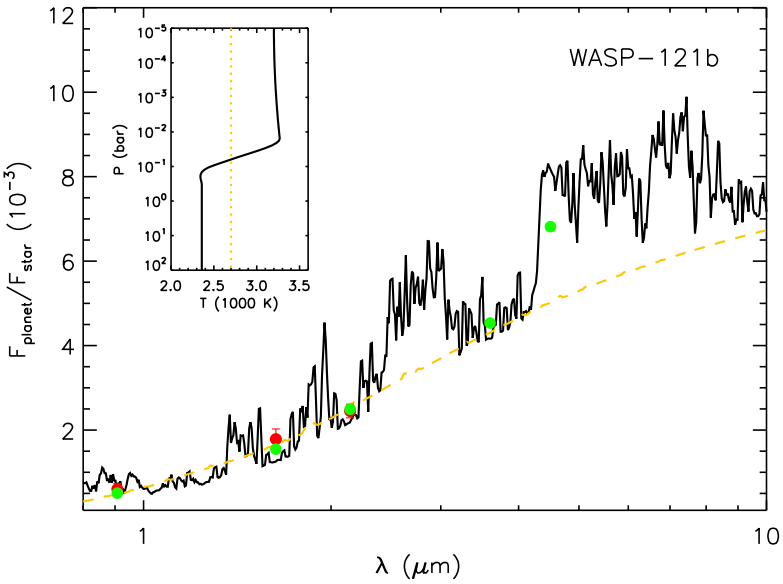

FIGURE C.2: Preliminary model emission spectra of WASP-121 b. The red circles with error bars are the measurements in the z' (TRAPPIST), H (AAT/IRIS2), and K_S (AAT/IRIS2) bands. Two models are shown: a black-body model (isothermal atmosphere) with a temperature of 2700K (orange dashed line) and a model with solar abundance composition and a thermal inversion (black solid line). The inset shows the corresponding pressure-temperature profiles for the models. The green circles give the band-integrated fluxes of the thermal inversion model for different passbands of interest (z', H, K_S, *Spitzer*/IRAC 3.6 and 4.5 μm channels). Credit: Nikku Madhusudhan.

Bibliography

Albrecht, S. et al. (2012). "Obliquities of Hot Jupiter Host Stars: Evidence for Tidal Interactions and Primordial Misalignments". In: *ApJ* 757, 18, p. 18. DOI: 10.1088/0004-637X/757/1/18. arXiv: 1206.6105 [astro-ph.SR].

Alonso, R. et al. (2004). "TrES-1: The Transiting Planet of a Bright K0 V Star". In: *ApJ* 613, pp. L153–L156. DOI: 10.1086/425256. eprint: astro-ph/0408421.

Alsubai, K. A. et al. (2013). "The Qatar Exoplanet Survey". In: *Acta Astron.* 63, pp. 465–480. arXiv: 1401.1984 [astro-ph.IM].

Andersen, J. M. and H. Korhonen (2015). "Stellar activity as noise in exoplanet detection - II. Application to M dwarfs". In: *MNRAS* 448, pp. 3053–3069. DOI: 10.1093/mnras/stu2731. arXiv: 1501.01302 [astro-ph.SR].

Anderson, D. R. et al. (2010a). "H-band thermal emission from the 19-h period planet WASP-19b". In: *A&A* 513, L3, p. L3. DOI: 10.1051/0004-6361/201014226. arXiv: 1002.1947 [astro-ph.EP].

Anderson, D. R. et al. (2010b). "WASP-17b: An Ultra-Low Density Planet in a Probable Retrograde Orbit". In: *ApJ* 709, pp. 159–167. DOI: 10.1088/0004-637X/709/1/159. arXiv: 0908.1553 [astro-ph.EP].

Anderson, D. R. et al. (2011a). "Thermal emission at 4.5 and 8 μm of WASP-17b, an extremely large planet in a slightly eccentric orbit". In: *MNRAS* 416, pp. 2108–2122. DOI: 10.1111/j.1365-2966.2011.19182.x. arXiv: 1101.5620 [astro-ph.EP].

Anderson, D. R. et al. (2011b). "WASP-30b: A 61 M $_{Jup}$ Brown Dwarf Transiting a V = 12, F8 Star". In: *ApJ* 726, L19, p. L19. DOI: 10.1088/2041-8205/726/2/L19. arXiv: 1010.3006 [astro-ph.SR].

Anderson, D. R. et al. (2013). "Thermal emission at 3.6-8 μm from WASP-19b: a hot Jupiter without a stratosphere orbiting an active star". In: *MNRAS* 430, pp. 3422–3431. DOI: 10.1093/mnras/stt140. arXiv: 1112.5145 [astro-ph.EP].

Anderson, D. R. et al. (2014). "Three newly discovered sub-Jupiter-mass planets: WASP-69b and WASP-84b transit active K dwarfs and WASP-70Ab transits the evolved primary of a G4+K3 binary". In: *MNRAS* 445, pp. 1114–1129. DOI: 10.1093/mnras/stu1737. arXiv: 1310.5654 [astro-ph.EP].

Anglada-Escudé, G. et al. (2016). "A terrestrial planet candidate in a temperate orbit around Proxima Centauri". In: *Nature* 536, pp. 437–440. DOI: 10.1038/nature19106.

Appenzeller, I. et al. (1998). "Successful commissioning of FORS1 - the first optical instrument on the VLT." In: *The Messenger* 94, pp. 1–6.

Arras, P. and A. Socrates (2010). "Thermal Tides in Fluid Extrasolar Planets". In: *ApJ* 714, pp. 1–12. DOI: 10.1088/0004-637X/714/1/1. arXiv: 0912.2313 [astro-ph.EP].

Auvergne, M. et al. (2009). "The CoRoT satellite in flight: description and performance". In: *A&A* 506, pp. 411–424. DOI: 10.1051/0004-6361/200810860. arXiv: 0901.2206 [astro-ph.SR].

Avila, G., G. Rupprecht, and J. M. Beckers (1997). "Atmospheric dispersion correction for the FORS Focal Reducers at the ESO VLT". In: *Optical Telescopes of Today and Tomorrow*. Ed. by A. L. Ardeberg. Vol. 2871. Proc. SPIE, pp. 1135–1143.

Bailey, J. (2014). "The Dawes Review 3: The Atmospheres of Extrasolar Planets and Brown Dwarfs". In: *Publ. Astron. Soc. Australia* 31, e043, e043. DOI: 10.1017/pasa.2014.38. arXiv: 1409.6821 [astro-ph.EP].

Bakos, G. et al. (2004). "Wide-Field Millimagnitude Photometry with the HAT: A Tool for Extrasolar Planet Detection". In: *PASP* 116, pp. 266–277. DOI: 10.1086/382735. eprint: astro-ph/0401219.

Bakos, G. Á. et al. (2011). "HAT-P-20b-HAT-P-23b: Four Massive Transiting Extrasolar Planets". In: *ApJ* 742, 116, p. 116. DOI: 10.1088/0004-637X/742/2/116. arXiv: 1008.3388 [astro-ph.EP].

Bakos, G. Á. et al. (2013). "HATSouth: A Global Network of Fully Automated Identical Wide-Field Telescopes". In: *PASP* 125, pp. 154–182. DOI: 10.1086/669529. arXiv: 1206.1391 [astro-ph.EP].

Baraffe, I. et al. (2014). "Planetary Internal Structures". In: *Protostars and Planets VI*, pp. 763–786. DOI: 10.2458/azu_uapress_9780816531240-ch033. arXiv: 1401.4738 [astro-ph.EP].

Barclay, T. et al. (2013). "A sub-Mercury-sized exoplanet". In: *Nature* 494, pp. 452–454. DOI: 10.1038/nature11914. arXiv: 1305.5587 [astro-ph.EP].

Bate, M. R., G. Lodato, and J. E. Pringle (2010). "Chaotic star formation and the alignment of stellar rotation with disc and planetary orbital axes". In: *MNRAS* 401, pp. 1505–1513. DOI: 10.1111/j.1365-2966.2009.15773.x. arXiv: 0909.4255 [astro-ph.SR].

Batygin, K. and D. J. Stevenson (2010). "Inflating Hot Jupiters with Ohmic Dissipation". In: *ApJ* 714, pp. L238–L243. DOI: 10.1088/2041-8205/714/2/L238. arXiv: 1002.3650 [astro-ph.EP].

Bayes, Mr. and Mr. Price (1763). "An Essay towards Solving a Problem in the Doctrine of Chances. By the Late Rev. Mr. Bayes, F. R. S. Communicated by Mr. Price, in a Letter to John Canton, A. M. F. R. S." In: 53, pp. 370–418. DOI: 10.1098/rstl.1763.0053.

Bayliss, D. D. R. et al. (2010). "Confirmation of a Retrograde Orbit for Exoplanet WASP-17b". In: *ApJ* 722, pp. L224–L227. DOI: 10.1088/2041-8205/722/2/L224. arXiv: 1009.5061 [astro-ph.EP].

Bean, J. L., E. Miller-Ricci Kempton, and D. Homeier (2010). "A ground-based transmission spectrum of the super-Earth exoplanet GJ 1214b". In: *Nature* 468, pp. 669–672. DOI: 10.1038/nature09596. arXiv: 1012.0331 [astro-ph.EP].

Bean, J. L. et al. (2011). "The Optical and Near-infrared Transmission Spectrum of the Super-Earth GJ 1214b: Further Evidence for a Metal-rich Atmosphere". In: *ApJ* 743, 92, p. 92. DOI: 10.1088/0004-637X/743/1/92. arXiv: 1109.0582 [astro-ph.EP].

Bean, J. L. et al. (2013). "Ground-based Transit Spectroscopy of the Hot-Jupiter WASP-19b in the Near-infrared". In: *ApJ* 771, 108, p. 108. DOI: 10.1088/0004-637X/771/2/108. arXiv: 1303.1094 [astro-ph.EP].

Beatty, T. G. et al. (2014). "Spitzer and z' Secondary Eclipse Observations of the Highly Irradiated Transiting Brown Dwarf KELT-1b". In: *ApJ* 783, 112, p. 112. DOI: 10.1088/0004-637X/783/2/112. arXiv: 1310.7585 [astro-ph.EP].

Beichman, C. et al. (2014). "Observations of Transiting Exoplanets with the James Webb Space Telescope (JWST)". In: *PASP* 126, pp. 1134–1173. DOI: 10.1086/679566.

Berta, Z. K. et al. (2011). "The GJ1214 Super-Earth System: Stellar Variability, New Transits, and a Search for Additional Planets". In: *ApJ* 736, 12, p. 12. DOI: 10.1088/0004-637X/736/1/12. arXiv: 1012.0518 [astro-ph.EP].

Birkby, J. L. et al. (2013). "Detection of water absorption in the day side atmosphere of HD 189733 b using ground-based high-resolution spectroscopy at 3.2 μm". In: *MNRAS* 436, pp. L35–L39. DOI: 10.1093/mnrasl/slt107. arXiv: 1307.1133 [astro-ph.EP].

Bodenheimer, P., D. N. C. Lin, and R. A. Mardling (2001). "On the Tidal Inflation of Short-Period Extrasolar Planets". In: *ApJ* 548, pp. 466–472. DOI: 10.1086/318667.

Boffin, H. et al. (2015). "Making FORS2 Fit for Exoplanet Observations (again)". In: *The Messenger* 159, pp. 6–9. arXiv: 1502.03172 [astro-ph.SR].

Borucki, W. J. et al. (2010). "Kepler Planet-Detection Mission: Introduction and First Results". In: *Science* 327, p. 977. DOI: 10.1126/science.1185402.

Borucki, W. J. et al. (2011). "Characteristics of Planetary Candidates Observed by Kepler. II. Analysis of the First Four Months of Data". In: *ApJ* 736, 19, p. 19. DOI: 10.1088/0004-637X/736/1/19. arXiv: 1102.0541 [astro-ph.EP].

Borucki, W. J. et al. (2013). "Kepler-62: A Five-Planet System with Planets of 1.4 and 1.6 Earth Radii in the Habitable Zone". In: *Science* 340, pp. 587–590. DOI: 10.1126/science.1234702. arXiv: 1304.7387 [astro-ph.EP].

Boss, A. P. (1997). "Giant planet formation by gravitational instability." In: *Science* 276, pp. 1836–1839. DOI: 10.1126/science.276.5320.1836.

— (2011). "Formation of Giant Planets by Disk Instability on Wide Orbits Around Protostars with Varied Masses". In: *ApJ* 731, 74, p. 74. DOI: 10.1088/0004-637X/731/1/74. arXiv: 1102.4555 [astro-ph.EP].

Bouchy, F. et al. (2005). "ELODIE metallicity-biased search for transiting Hot Jupiters. II. A very hot Jupiter transiting the bright K star HD 189733". In: *A&A* 444, pp. L15–L19. DOI: 10.1051/0004-6361:200500201. eprint: astro-ph/0510119.

Braga-Ribas, F. et al. (2014). "A ring system detected around the Centaur (10199) Chariklo". In: *Nature* 508, pp. 72–75. DOI: 10.1038/nature13155. arXiv: 1409.7259.

Broeg, C. et al. (2013). "CHEOPS: A transit photometry mission for ESA's small mission programme". In: *European Physical Journal Web of Conferences*. Vol. 47. European Physical Journal Web of Conferences, p. 03005. DOI: 10.1051/epjconf/20134703005. arXiv: 1305.2270 [astro-ph.EP].

Brogi, M. et al. (2014). "Carbon monoxide and water vapor in the atmosphere of the non-transiting exoplanet HD 179949 b". In: *A&A* 565, A124, A124. DOI: 10.1051/0004-6361/201423537. arXiv: 1404.3769 [astro-ph.EP].

Brown, D. J. A. et al. (2012). "Rossiter-McLaughlin effect measurements for WASP-16, WASP-25 and WASP-31". In: *MNRAS* 423, pp. 1503–1520. DOI: 10.1111/j.1365-2966.2012.20973.x. arXiv: 1203.4971 [astro-ph.EP].

Brown, T. M. (2003). "Expected Detection and False Alarm Rates for Transiting Jovian Planets". In: *ApJ* 593, pp. L125–L128. DOI: 10.1086/378310. eprint: astro-ph/0307256.

Budaj, J. (2011). "The Reflection Effect in Interacting Binaries or in Planet-Star Systems". In: *AJ* 141, 59, p. 59. DOI: 10.1088/0004-6256/141/2/59. arXiv: 1003.1662 [astro-ph.EP].

Burrows, A., J. Budaj, and I. Hubeny (2008). "Theoretical Spectra and Light Curves of Close-in Extrasolar Giant Planets and Comparison with Data". In: *ApJ* 678, 1436-1457, pp. 1436–1457. DOI: 10.1086/533518. arXiv: 0709.4080.

Burrows, A. et al. (2007). "Possible Solutions to the Radius Anomalies of Transiting Giant Planets". In: *ApJ* 661, pp. 502–514. DOI: 10.1086/514326. eprint: astro-ph/0612703.

Burton, J. R. et al. (2012). "z'-band Ground-based Detection of the Secondary Eclipse of WASP-19b". In: *ApJS* 201, 36, p. 36. DOI: 10.1088/0067-0049/201/2/36. arXiv: 1206.3585 [astro-ph.EP].

Butler, R. P. et al. (2004). "A Neptune-Mass Planet Orbiting the Nearby M Dwarf GJ 436". In: *ApJ* 617, pp. 580–588. DOI: 10.1086/425173. eprint: astro-ph/0408587.

Chabrier, G. and I. Baraffe (2007). "Heat Transport in Giant (Exo)planets: A New Perspective". In: *ApJ* 661, pp. L81–L84. DOI: 10.1086/518473. eprint: astro-ph/0703755.

Charbonneau, D. et al. (2000). "Detection of Planetary Transits Across a Sun-like Star". In: *ApJ* 529, pp. L45–L48. DOI: 10.1086/312457. eprint: astro-ph/9911436.

Charbonneau, D. et al. (2008). "The MEarth Project to Detect Habitable SuperEarth Exoplanets". In: *American Astronomical Society Meeting Abstracts #212*. Vol. 40. Bulletin of the American Astronomical Society, p. 242.

Claret, A. and S. Bloemen (2011). "Gravity and limb-darkening coefficients for the Kepler, CoRoT, Spitzer, uvby, UBVRIJHK, and Sloan photometric systems". In: *A&A* 529, A75, A75. DOI: 10.1051/0004-6361/201116451.

Collier Cameron, A. (2016). "Extrasolar Planetary Transits". In: *Methods of Detecting Exoplanets*. Ed. by V. Bozza, L. Mancini, and A. Sozzetti. Astrophysics and Space Science Library, pp. 89–128. DOI: 10.1007/978-3-319-27458-4.

Collier Cameron, A. et al. (2006). "A fast hybrid algorithm for exoplanetary transit searches". In: *MNRAS* 373, pp. 799–810. DOI: 10.1111/j.1365-2966.2006.11074.x. eprint: astro-ph/0609418.

Collier Cameron, A. et al. (2007). "Efficient identification of exoplanetary transit candidates from SuperWASP light curves". In: *MNRAS* 380, pp. 1230–1244. DOI: 10.1111/j.1365-2966.2007.12195.x. arXiv: 0707.0417.

Collier Cameron, A. et al. (2010). "Line-profile tomography of exoplanet transits - II. A gas-giant planet transiting a rapidly rotating A5 star". In: *MNRAS* 407, pp. 507–514. DOI: 10.1111/j.1365-2966.2010.16922.x. arXiv: 1004.4551 [astro-ph.EP].

Cowan, N. B. and E. Agol (2008). "Inverting Phase Functions to Map Exoplanets". In: *ApJ* 678, L129, p. L129. DOI: 10.1086/588553. arXiv: 0803.3622.

— (2011). "The Statistics of Albedo and Heat Recirculation on Hot Exoplanets". In: *ApJ* 729, 54, p. 54. DOI: 10.1088/0004-637X/729/1/54. arXiv: 1001.0012 [astro-ph.EP].

Crossfield, I. J. M. (2015). "Observations of Exoplanet Atmospheres". In: *PASP* 127, pp. 941–960. DOI: 10.1086/683115. arXiv: 1507.03966 [astro-ph.EP].

Crouzet, N. et al. (2014). "Water Vapor in the Spectrum of the Extrasolar Planet HD 189733b. II. The Eclipse". In: *ApJ* 795, 166, p. 166. DOI: 10.1088/0004-637X/795/2/166. arXiv: 1409.4000 [astro-ph.EP].

Daemgen, S. et al. (2009). "Binarity of transit host stars. Implications for planetary parameters". In: *A&A* 498, pp. 567–574. DOI: 10.1051/0004-6361/200810988. arXiv: 0902.2179 [astro-ph.SR].

D'Angelo, G., R. H. Durisen, and J. J. Lissauer (2010). "Giant Planet Formation". In: *Exoplanets*. Ed. by S. Seager, pp. 319–346.

de Kok, R. J. et al. (2013). "Detection of carbon monoxide in the high-resolution day-side spectrum of the exoplanet HD 189733b". In: *A&A* 554, A82, A82. DOI: 10.1051/0004-6361/201321381. arXiv: 1304.4014 [astro-ph.EP].

de Wit, J. and S. Seager (2013). "Constraining Exoplanet Mass from Transmission Spectroscopy". In: *Science* 342, pp. 1473–1477. DOI: 10.1126/science.1245450. arXiv: 1401.6181 [astro-ph.EP].

Delrez, L. et al. (2014). "Transiting planets from WASP-South, Euler, and TRAPPIST. WASP-68 b, WASP-73 b, and WASP-88 b, three hot Jupiters transiting evolved solar-type stars". In: *A&A* 563, A143, A143. DOI: 10.1051/0004-6361/201323204. arXiv: 1312.1827 [astro-ph.EP].

Delrez, L. et al. (2016). "WASP-121 b: a hot Jupiter close to tidal disruption transiting an active F star". In: *MNRAS* 458, pp. 4025–4043. DOI: 10.1093/mnras/stw522.

Deming, D. et al. (2013). "Infrared Transmission Spectroscopy of the Exoplanets HD 209458b and XO-1b Using the Wide Field Camera-3 on the Hubble Space Telescope". In: *ApJ* 774, 95, p. 95. DOI: 10.1088/0004-637X/774/2/95. arXiv: 1302.1141 [astro-ph.EP].

Demory, B.-O. and S. Seager (2011). "Lack of Inflated Radii for Kepler Giant Planet Candidates Receiving Modest Stellar Irradiation". In: *ApJS* 197, 12, p. 12. DOI: 10.1088/0067-0049/197/1/12. arXiv: 1110.6180 [astro-ph.EP].

Demory, B.-O. et al. (2011). "Detection of a transit of the super-Earth 55 Cancri e with warm Spitzer". In: *A&A* 533, A114, A114. DOI: 10.1051/0004-6361/201117178. arXiv: 1105.0415 [astro-ph.EP].

Demory, B.-O. et al. (2013). "Inference of Inhomogeneous Clouds in an Exoplanet Atmosphere". In: *ApJ* 776, L25, p. L25. DOI: 10.1088/2041-8205/776/2/L25. arXiv: 1309.7894 [astro-ph.EP].

Denny, R. (2011). "A Web-Remote/Robotic/Scheduled Astronomical Data Acquisition System". In: *Telescopes from Afar*. Ed. by S. Gajadhar et al., p. 47.

Diamond-Lowe, H. et al. (2014). "New Analysis Indicates No Thermal Inversion in the Atmosphere of HD 209458b". In: *ApJ* 796, 66, p. 66. DOI: 10.1088/0004-637X/796/1/66. arXiv: 1409.5336 [astro-ph.EP].

Díaz, R. F. et al. (2014). "PASTIS: Bayesian extrasolar planet validation - I. General framework, models, and performance". In: *MNRAS* 441, pp. 983–1004. DOI: 10.1093/mnras/stu601. arXiv: 1403.6725 [astro-ph.EP].

Doyle, L. R. et al. (2011). "Kepler-16: A Transiting Circumbinary Planet". In: *Science* 333, p. 1602. DOI: 10.1126/science.1210923. arXiv: 1109.3432 [astro-ph.EP].

Drake, A. J. (2003). "On the Selection of Photometric Planetary Transits". In: *ApJ* 589, pp. 1020–1026. DOI: 10.1086/374714. eprint: astro-ph/0301295.

Dressing, C. D. and D. Charbonneau (2013). "The Occurrence Rate of Small Planets around Small Stars". In: *ApJ* 767, 95, p. 95. DOI: 10.1088/0004-637X/767/1/95. arXiv: 1302.1647 [astro-ph.EP].

Enoch, B., A. Collier Cameron, and K. Horne (2012). "Factors affecting the radii of close-in transiting exoplanets". In: *A&A* 540, A99, A99. DOI: 10.1051/0004-6361/201117317. arXiv: 1202.6199 [astro-ph.EP].

Enoch, B. et al. (2010). "An improved method for estimating the masses of stars with transiting planets". In: *A&A* 516, A33, A33. DOI: 10.1051/0004-6361/201014326. arXiv: 1004.1991 [astro-ph.EP].

Espinoza, N. et al. (2016). "HATS-25b through HATS-30b: A Half-dozen New Inflated Transiting Hot Jupiters from the HATSouth Survey". In: *ArXiv e-prints*. arXiv: 1606.00023 [astro-ph.EP].

Evans, T. M. et al. (2016). "Detection of H_2O and Evidence for TiO/VO in an Ultra-hot Exoplanet Atmosphere". In: *ApJ* 822, L4, p. L4. DOI: 10.3847/2041-8205/822/1/L4. arXiv: 1604.02310 [astro-ph.EP].

Fabrycky, D. and S. Tremaine (2007). "Shrinking Binary and Planetary Orbits by Kozai Cycles with Tidal Friction". In: *ApJ* 669, pp. 1298–1315. DOI: 10.1086/521702. arXiv: 0705.4285.

Fabrycky, D. C. and J. N. Winn (2009). "Exoplanetary Spin-Orbit Alignment: Results from the Ensemble of Rossiter-McLaughlin Observations". In: *ApJ* 696, pp. 1230–1240. DOI: 10.1088/0004-637X/696/2/1230. arXiv: 0902.0737 [astro-ph.EP].

Farnham, T. L., D. G. Schleicher, and M. F. A'Hearn (2000). "The HB Narrowband Comet Filters: Standard Stars and Calibrations". In: *Icarus* 147, pp. 180–204. DOI: 10.1006/icar.2000.6420.

Ford, E. B. (2005). "Quantifying the Uncertainty in the Orbits of Extrasolar Planets". In: *AJ* 129, pp. 1706–1717. DOI: 10.1086/427962. eprint: astro-ph/0305441.

— (2006). "Improving the Efficiency of Markov Chain Monte Carlo for Analyzing the Orbits of Extrasolar Planets". In: *ApJ* 642, pp. 505–522. DOI: 10.1086/500802. eprint: astro-ph/0512634.

Fortney, J. J., M. S. Marley, and J. W. Barnes (2007). "Planetary Radii across Five Orders of Magnitude in Mass and Stellar Insolation: Application to Transits". In: *ApJ* 659, pp. 1661–1672. DOI: 10.1086/512120. eprint: astro-ph/0612671.

Fortney, J. J. and N. Nettelmann (2010). "The Interior Structure, Composition, and Evolution of Giant Planets". In: *Space Sci. Rev.* 152, pp. 423–447. DOI: 10.1007/s11214-009-9582-x. arXiv: 0912.0533 [astro-ph.EP].

Fortney, J. J. et al. (2008). "A Unified Theory for the Atmospheres of the Hot and Very Hot Jupiters: Two Classes of Irradiated Atmospheres". In: *ApJ* 678, 1419-1435, pp. 1419–1435. DOI: 10.1086/528370. arXiv: 0710.2558.

Fortney, J. J. et al. (2010). "Transmission Spectra of Three-Dimensional Hot Jupiter Model Atmospheres". In: *ApJ* 709, pp. 1396–1406. DOI: 10.1088/0004-637X/709/2/1396. arXiv: 0912.2350 [astro-ph.EP].

Fraine, J. D. et al. (2013). "Spitzer Transits of the Super-Earth GJ1214b and Implications for its Atmosphere". In: *ApJ* 765, 127, p. 127. DOI: 10.1088/0004-637X/765/2/127. arXiv: 1301.6763 [astro-ph.EP].

Fressin, F. et al. (2013). "The False Positive Rate of Kepler and the Occurrence of Planets". In: *ApJ* 766, 81, p. 81. DOI: 10.1088/0004-637X/766/2/81. arXiv: 1301.0842 [astro-ph.EP].

Fukui, A. et al. (2014). "Multi-band, Multi-epoch Observations of the Transiting Warm Jupiter WASP-80b". In: *ApJ* 790, 108, p. 108. DOI: 10.1088/0004-637X/790/2/108. arXiv: 1406.3261 [astro-ph.EP].

Gatewood, G. and H. Eichhorn (1973). "An unsuccessful search for a planetary companion of Barnard's star BD +4 3561." In: *AJ* 78, pp. 769–776. DOI: 10.1086/111480.

Gaudi, B. S. and J. N. Winn (2007). "Prospects for the Characterization and Confirmation of Transiting Exoplanets via the Rossiter-McLaughlin Effect". In: *ApJ* 655, pp. 550–563. DOI: 10.1086/509910. eprint: astro-ph/0608071.

Gelman, A. and D. Rubin (1992). In: *Stat. Sci.* 7, p. 457.

Gelman, A. et al. (2003). *Bayesian Data Analysis, Second Edition*. Chapman & Hall/CRC Texts in Statistical Science. Taylor & Francis. ISBN: 9781420057294. URL: https://books.google.be/books?id=TNYhnkXQSjAC.

Gibson, N. P. et al. (2010). "Ground-based detection of thermal emission from the exoplanet WASP-19b". In: *MNRAS* 404, pp. L114–L118. DOI: 10.1111/j.1745-3933.2010.00847.x. arXiv: 1002.1996 [astro-ph.EP].

Gibson, N. P. et al. (2013). "A Gemini ground-based transmission spectrum of WASP-29b: a featureless spectrum from 515 to 720 nm". In: *MNRAS* 428, pp. 3680–3692. DOI: 10.1093/mnras/sts307. arXiv: 1210.7798 [astro-ph.EP].

Gilliland, R. L. et al. (1993). "A search for solar-like oscillations in the stars of M67 with CCD ensemble photometry on a network of 4 M telescopes". In: *AJ* 106, pp. 2441–2476. DOI: 10.1086/116814.

Gillon, M. et al. (2007). "Detection of transits of the nearby hot Neptune GJ 436 b". In: *A&A* 472, pp. L13–L16. DOI: 10.1051/0004-6361:20077799. arXiv: 0705.2219.

Gillon, M. et al. (2011a). "TRAPPIST: a robotic telescope dedicated to the study of planetary systems". In: *European Physical Journal Web of Conferences*. Vol. 11. European Physical Journal Web of Conferences, p. 06002. DOI: 10.1051/epjconf/20101106002. arXiv: 1101.5807 [astro-ph.EP].

Gillon, M. et al. (2011b). "WASP-50 b: a hot Jupiter transiting a moderately active solar-type star". In: *A&A* 533, A88, A88. DOI: 10.1051/0004-6361/201117198. arXiv: 1108.2641 [astro-ph.EP].

Gillon, M. et al. (2012). "The TRAPPIST survey of southern transiting planets. I. Thirty eclipses of the ultra-short period planet WASP-43 b". In: *A&A* 542, A4, A4. DOI: 10.1051/0004-6361/201218817. arXiv: 1201.2789 [astro-ph.EP].

Gillon, M. et al. (2013a). "Fast-evolving weather for the coolest of our two new substellar neighbours". In: *A&A* 555, L5, p. L5. DOI: 10.1051/0004-6361/201321620. arXiv: 1304.0481 [astro-ph.SR].

Gillon, M. et al. (2013b). "SPECULOOS: Search for habitable Planets EClipsing ULtra-cOOl Stars". In: *Protostars and Planets VI Posters*.

Gillon, M. et al. (2013c). "TRAPPIST-UCDTS: A prototype search for habitable planets transiting ultra-cool stars". In: *European Physical Journal Web of Conferences*. Vol. 47. European Physical Journal Web of Conferences, p. 03001. DOI: 10.1051/epjconf/20134703001.

Gillon, M. et al. (2014). "WASP-103 b: a new planet at the edge of tidal disruption". In: *A&A* 562, L3, p. L3. DOI: 10.1051/0004-6361/201323014. arXiv: 1401.2784 [astro-ph.EP].

Gillon, M. et al. (2016). "Temperate Earth-sized planets transiting a nearby ultracool dwarf star". In: *Nature* 533, pp. 221–224. DOI: 10.1038/nature17448.

Gilmozzi, R. and J. Spyromilio (2007). "The European Extremely Large Telescope (E-ELT)". In: *The Messenger* 127.

Giménez, A. (2006). "Equations for the Analysis of the Rossiter-MCLaughlin Effect in Extrasolar Planetary Transits". In: *ApJ* 650, pp. 408–413. DOI: 10.1086/507021.

Gould, A. and C. W. Morgan (2003). "Transit Target Selection Using Reduced Proper Motions". In: *ApJ* 585, pp. 1056–1061. DOI: 10.1086/346131. eprint: astro-ph/0209561.

Gregory, P. C. (2005). *Bayesian Logical Data Analysis for the Physical Sciences: A Comparative Approach with 'Mathematica' Support*. Cambridge University Press.

Guillot, T. et al. (1996). "Giant Planets at Small Orbital Distances". In: *ApJ* 459, p. L35. DOI: 10.1086/309935. eprint: astro-ph/9511109.

Hansen, C. J., J. C. Schwartz, and N. B. Cowan (2014). "Features in the broad-band eclipse spectra of exoplanets: signal or noise?" In: *MNRAS* 444, pp. 3632–3640. DOI: 10.1093/mnras/stu1699. arXiv: 1402.6699 [astro-ph.EP].

Hastings, W.K. (1970). "Monte Carlo sampling methods using Markov chains and their applications." English. In: *Biometrika* 57, pp. 97–109. ISSN: 0006-3444; 1464-3510/e. DOI: 10.1093/biomet/57.1.97.

Haynes, K. et al. (2015). "Spectroscopic Evidence for a Temperature Inversion in the Dayside Atmosphere of Hot Jupiter WASP-33b". In: *ApJ* 806, 146, p. 146. DOI: 10.1088/0004-637X/806/2/146. arXiv: 1505.01490 [astro-ph.EP].

Hébrard, G. et al. (2013). "WASP-52b, WASP-58b, WASP-59b, and WASP-60b: Four new transiting close-in giant planets". In: *A&A* 549, A134, A134. DOI: 10.1051/0004-6361/201220363. arXiv: 1211.0810 [astro-ph.EP].

Heintz, W. D. (1988). "The binary star 70 Ophiuchi revisited". In: *J. R. Astron. Soc. Canada* 82, pp. 140–145.

Hellier, C. et al. (2009). "An orbital period of 0.94days for the hot-Jupiter planet WASP-18b". In: *Nature* 460, pp. 1098–1100. DOI: 10.1038/nature08245.

Hellier, C. et al. (2010). "WASP-29b: A Saturn-sized Transiting Exoplanet". In: *ApJ* 723, pp. L60–L63. DOI: 10.1088/2041-8205/723/1/L60. eprint: 1009.5318 (astro-ph.EP).

Hellier, C. et al. (2011). "The WASP-South search for transiting exoplanets". In: *European Physical Journal Web of Conferences*. Vol. 11. European Physical Journal Web of Conferences, p. 01004. DOI: 10.1051/epjconf/20101101004. eprint: 1012.2286 (astro-ph.EP).

Hellier, C. et al. (2016). "WASP-South transiting exoplanets: WASP-130b, WASP-131b, WASP-132b, WASP-139b, WASP-140b, WASP-141b & WASP-142b". In: *ArXiv e-prints*. arXiv: 1604.04195 [astro-ph.EP].

Helling, C. and S. Casewell (2014). "Atmospheres of brown dwarfs". In: *A&ARv* 22, 80, p. 80. DOI: 10.1007/s00159-014-0080-0. arXiv: 1410.6029 [astro-ph.SR].

Henry, G. W. et al. (2000). "A Transiting "51 Peg-like" Planet". In: *ApJ* 529, pp. L41–L44. DOI: 10.1086/312458.

Hershey, J. L. (1973). "Astrometric analysis of the field of AC +65 6955 from plates taken with the Sproul 24-inch refractor." In: *AJ* 78, pp. 421–425. DOI: 10.1086/111436.

Hirano, T. et al. (2011). "Further Observations of the Tilted Planet XO-3: A New Determination of Spin-Orbit Misalignment, and Limits on Differential Rotation". In: *PASJ* 63, pp. L57–L61. DOI: 10.1093/pasj/63.6.L57. arXiv: 1108.4493 [astro-ph.EP].

Høg, E. et al. (2000). "The Tycho-2 catalogue of the 2.5 million brightest stars". In: *A&A* 355, pp. L27–L30.

Holman, M. J. et al. (2006). "The Transit Light Curve Project. I. Four Consecutive Transits of the Exoplanet XO-1b". In: *ApJ* 652, pp. 1715–1723. DOI: 10.1086/508155. eprint: astro-ph/0607571.

Horne, K. (1986). "An optimal extraction algorithm for CCD spectroscopy". In: *PASP* 98, pp. 609–617. DOI: 10.1086/131801.

Howard, A. W. et al. (2012). "Planet Occurrence within 0.25 AU of Solar-type Stars from Kepler". In: *ApJS* 201, 15, p. 15. DOI: 10.1088/0067-0049/201/2/15. arXiv: 1103.2541 [astro-ph.EP].

Howell, S. B. et al. (2014). "The K2 Mission: Characterization and Early Results". In: *PASP* 126, pp. 398–408. DOI: 10.1086/676406. arXiv: 1402.5163 [astro-ph.IM].

Hubeny, I., A. Burrows, and D. Sudarsky (2003). "A Possible Bifurcation in Atmospheres of Strongly Irradiated Stars and Planets". In: *ApJ* 594, pp. 1011–1018. DOI: 10.1086/377080. eprint: astro-ph/0305349.

Huitson, C. M. et al. (2013). "An HST optical-to-near-IR transmission spectrum of the hot Jupiter WASP-19b: detection of atmospheric water and likely absence of TiO". In: *MNRAS* 434, pp. 3252–3274. DOI: 10.1093/mnras/stt1243. eprint: 1307.2083 (astro-ph.EP).

Husser, T.-O. et al. (2013). "A new extensive library of PHOENIX stellar atmospheres and synthetic spectra". In: *A&A* 553, A6, A6. DOI: 10.1051/0004-6361/201219058. arXiv: 1303.5632 [astro-ph.SR].

Irwin, J. M. et al. (2015). "The MEarth-North and MEarth-South Transit Surveys: Searching for Habitable Super-Earth Exoplanets Around Nearby M-dwarfs". In: *18th Cambridge Workshop on Cool Stars, Stellar Systems, and the Sun*. Ed. by G. T. van Belle and H. C. Harris. Vol. 18. Cambridge Workshop on Cool Stars, Stellar Systems, and the Sun, pp. 767–772. arXiv: 1409.0891 [astro-ph.EP].

Jacob, W. S. (1855). "On certain Anomalies presented by the Binary Star 70 Ophiuchi". In: *MNRAS* 15, p. 228. DOI: 10.1093/mnras/15.9.228.

Jehin, E. et al. (2011a). "Long term photometric monitoring of comet 103P/Hartley2 with the new robotic TRAPPIST telescope". In: *EPSC-DPS Joint Meeting 2011*, p. 1489.

Jehin, E. et al. (2011b). "TRAPPIST: TRAnsiting Planets and PlanetesImals Small Telescope". In: *The Messenger* 145, pp. 2–6.

Johns, M. et al. (2012). "Giant Magellan Telescope: overview". In: *Ground-based and Airborne Telescopes IV*. Vol. 8444. Proc. SPIE, 84441H. DOI: 10.1117/12.926716.

Kaltenegger, L. and W. A. Traub (2009). "Transits of Earth-like Planets". In: *ApJ* 698, pp. 519–527. DOI: 10.1088/0004-637X/698/1/519. arXiv: 0903.3371 [astro-ph.IM].

Knutson, H. A., A. W. Howard, and H. Isaacson (2010). "A Correlation Between Stellar Activity and Hot Jupiter Emission Spectra". In: *ApJ* 720, pp. 1569–1576. DOI: 10.1088/0004-637X/720/2/1569. arXiv: 1004.2702 [astro-ph.EP].

Knutson, H. A. et al. (2007). "Using Stellar Limb-Darkening to Refine the Properties of HD 209458b". In: *ApJ* 655, pp. 564–575. DOI: 10.1086/510111. eprint: astro-ph/0603542.

Knutson, H. A. et al. (2008). "The 3.6-8.0 μm Broadband Emission Spectrum of HD 209458b: Evidence for an Atmospheric Temperature Inversion". In: *ApJ* 673, 526-531, pp. 526–531. DOI: 10.1086/523894. arXiv: 0709.3984.

Knutson, H. A. et al. (2009). "Detection of A Temperature Inversion in the Broadband Infrared Emission Spectrum of TrES-4". In: *ApJ* 691, pp. 866–874. DOI: 10.1088/0004-637X/691/1/866. arXiv: 0810.0021.

Knutson, H. A. et al. (2012). "3.6 and 4.5 μm Phase Curves and Evidence for Non-equilibrium Chemistry in the Atmosphere of Extrasolar Planet HD 189733b". In: *ApJ* 754, 22, p. 22. DOI: 10.1088/0004-637X/754/1/22. arXiv: 1206.6887 [astro-ph.EP].

Kopparapu, R. K. et al. (2013). "Habitable Zones around Main-sequence Stars: New Estimates". In: *ApJ* 765, 131, p. 131. DOI: 10.1088/0004-637X/765/2/131. arXiv: 1301.6674 [astro-ph.EP].

Kovács, G., G. Bakos, and R. W. Noyes (2005). "A trend filtering algorithm for wide-field variability surveys". In: *MNRAS* 356, pp. 557–567. DOI: 10.1111/j.1365-2966.2004.08479.x. eprint: astro-ph/0411724.

Kovács, G., S. Zucker, and T. Mazeh (2002). "A box-fitting algorithm in the search for periodic transits". In: *A&A* 391, pp. 369–377. DOI: 10.1051/0004-6361:20020802. eprint: astro-ph/0206099.

Kozai, Y. (1962). "Secular perturbations of asteroids with high inclination and eccentricity". In: *AJ* 67, p. 591. DOI: 10.1086/108790.

Kreidberg, L. et al. (2014). "A Precise Water Abundance Measurement for the Hot Jupiter WASP-43b". In: *ApJ* 793, L27, p. L27. DOI: 10.1088/2041-8205/793/2/L27. arXiv: 1410.2255 [astro-ph.EP].

Lai, D. (2012). "Tidal dissipation in planet-hosting stars: damping of spin-orbit misalignment and survival of hot Jupiters". In: *MNRAS* 423, pp. 486–492. DOI: 10.1111/j.1365-2966.2012.20893.x. arXiv: 1109.4703 [astro-ph.EP].

Lai, D., F. Foucart, and D. N. C. Lin (2011). "Evolution of spin direction of accreting magnetic protostars and spin-orbit misalignment in exoplanetary systems". In: *MNRAS* 412, pp. 2790–2798. DOI: 10.1111/j.1365-2966.2010.18127.x. arXiv: 1008.3148 [astro-ph.EP].

Lanotte, A. (2015). "Photométrie de haute précision dans l'infrarouge d'exoplanètes en transit". PhD thesis. Université de Liège.

Lecavelier Des Etangs, A. et al. (2008). "Rayleigh scattering in the transit spectrum of HD 189733b". In: *A&A* 481, pp. L83–L86. DOI: 10.1051/0004-6361:200809388. arXiv: 0802.3228.

Léger, A. et al. (2009). "Transiting exoplanets from the CoRoT space mission. VIII. CoRoT-7b: the first super-Earth with measured radius". In: *A&A* 506, pp. 287–302. DOI: 10.1051/0004-6361/200911933. arXiv: 0908.0241 [astro-ph.EP].

Lendl, M. et al. (2012). "WASP-42 b and WASP-49 b: two new transiting sub-Jupiters". In: *A&A* 544, A72, A72. DOI: 10.1051/0004-6361/201219585. arXiv: 1205.2757 [astro-ph.EP].

Lendl, M. et al. (2013). "A photometric study of the hot exoplanet WASP-19b". In: *A&A* 552, A2, A2. DOI: 10.1051/0004-6361/201220924. arXiv: 1212.3553 [astro-ph.EP].

Lendl, M. et al. (2014). "WASP-117b: a 10-day-period Saturn in an eccentric and misaligned orbit". In: *A&A* 568, A81, A81. DOI: 10.1051/0004-6361/201424481. arXiv: 1406.6942 [astro-ph.EP].

Lendl, M. et al. (2016). "FORS2 observes a multi-epoch transmission spectrum of the hot Saturn-mass exoplanet WASP-49b". In: *A&A* 587, A67, A67. DOI: 10.1051/0004-6361/201527594. arXiv: 1512.06698 [astro-ph.EP].

Lin, D. N. C., P. Bodenheimer, and D. C. Richardson (1996). "Orbital migration of the planetary companion of 51 Pegasi to its present location". In: *Nature* 380, pp. 606–607. DOI: 10.1038/380606a0.

Lissauer, J. J. et al. (2011). "A closely packed system of low-mass, low-density planets transiting Kepler-11". In: *Nature* 470, pp. 53–58. DOI: 10.1038/nature09760. arXiv: 1102.0291 [astro-ph.EP].

López-Morales, M. and S. Seager (2007). "Thermal Emission from Transiting Very Hot Jupiters: Prospects for Ground-based Detection at Optical Wavelengths". In: *The Astrophysical Journal Letters* 667, pp. L191–L194. DOI: 10.1086/522118. arXiv: 0708.0822.

Lubow, S. H. and S. Ida (2010). "Planet Migration". In: *Exoplanets*. Ed. by S. Seager, pp. 347–371.

Machalek, P. et al. (2008). "Thermal Emission of Exoplanet XO-1b". In: *ApJ* 684, 1427-1432, pp. 1427–1432. DOI: 10.1086/590140. arXiv: 0805.2418.

Madhusudhan, N. (2012). "C/O Ratio as a Dimension for Characterizing Exoplanetary Atmospheres". In: *ApJ* 758, 36, p. 36. DOI: 10.1088/0004-637X/758/1/36. arXiv: 1209.2412 [astro-ph.EP].

Madhusudhan, N. and S. Seager (2009). "A Temperature and Abundance Retrieval Method for Exoplanet Atmospheres". In: *ApJ* 707, pp. 24–39. DOI: 10.1088/0004-637X/707/1/24. arXiv: 0910.1347 [astro-ph.EP].

Madhusudhan, N. et al. (2014). "Exoplanetary Atmospheres". In: *Protostars and Planets VI*, pp. 739–762. DOI: 10.2458/azu_uapress_9780816531240-ch032. arXiv: 1402.1169 [astro-ph.EP].

Mancini, L. et al. (2014). "Physical properties and transmission spectrum of the WASP-80 planetary system from multi-colour photometry". In: *A&A* 562, A126, A126. DOI: 10.1051/0004-6361/201323265. arXiv: 1312.4982 [astro-ph.EP].

Mandel, K. and E. Agol (2002). "Analytic Light Curves for Planetary Transit Searches". In: *ApJ* 580, pp. L171–L175. DOI: 10.1086/345520. eprint: astro-ph/0210099.

Marcy, G. et al. (2005). "Observed Properties of Exoplanets: Masses, Orbits, and Metallicities". In: *Progress of Theoretical Physics Supplement* 158, pp. 24–42. DOI: 10.1143/PTPS.158.24. eprint: astro-ph/0505003.

Marois, C. et al. (2008). "Direct Imaging of Multiple Planets Orbiting the Star HR 8799". In: *Science* 322, p. 1348. DOI: 10.1126/science.1166585. arXiv: 0811.2606.

Matsumura, S., S. J. Peale, and F. A. Rasio (2010). "Tidal Evolution of Close-in Planets". In: *ApJ* 725, pp. 1995–2016. DOI: 10.1088/0004-637X/725/2/1995. arXiv: 1007.4785 [astro-ph.EP].

Mayor, M. and D. Queloz (1995). "A Jupiter-mass companion to a solar-type star". In: *Nature* 378, pp. 355–359. DOI: 10.1038/378355a0.

Mayor, M. et al. (2011). "The HARPS search for southern extra-solar planets XXXIV. Occurrence, mass distribution and orbital properties of super-Earths and Neptune-mass planets". In: *ArXiv e-prints*. arXiv: 1109.2497 [astro-ph.EP].

Mazeh, T. et al. (2000). "The Spectroscopic Orbit of the Planetary Companion Transiting HD 209458". In: *ApJ* 532, pp. L55–L58. DOI: 10.1086/312558. eprint: astro-ph/0001284.

McArthur, B. E. et al. (2004). "Detection of a Neptune-Mass Planet in the ρ^1 Cancri System Using the Hobby-Eberly Telescope". In: *ApJ* 614, pp. L81–L84. DOI: 10.1086/425561. eprint: astro-ph/0408585.

McCullough, P. R. et al. (2005). "The XO Project: Searching for Transiting Extrasolar Planet Candidates". In: *PASP* 117, pp. 783–795. DOI: 10.1086/432024. eprint: astro-ph/0505560.

McCullough, P. R. et al. (2014). "Water Vapor in the Spectrum of the Extrasolar Planet HD 189733b. I. The Transit". In: *ApJ* 791, 55, p. 55. DOI: 10.1088/0004-637X/791/1/55. arXiv: 1407.2462 [astro-ph.SR].

McLaughlin, D. B. (1924). "Some results of a spectrographic study of the Algol system." In: *ApJ* 60. DOI: 10.1086/142826.

Metropolis, N. et al. (1953). "Equation of State Calculations by Fast Computing Machines". In: *J. Chem. Phys.* 21, pp. 1087–1092. DOI: 10.1063/1.1699114.

Miller, N. and J. J. Fortney (2011). "The Heavy-element Masses of Extrasolar Giant Planets, Revealed". In: *ApJ* 736, L29, p. L29. DOI: 10.1088/2041-8205/736/2/L29. arXiv: 1105.0024 [astro-ph.EP].

Moehler, S. et al. (1995). "The FORS instrument for the ESO VLT". In: *Calibrating and Understanding HST and ESO Instruments*. Ed. by P. Benvenuti. Vol. 53. European Southern Observatory Conference and Workshop Proceedings, p. 149.

Moehler, S. et al. (2010). "Correction of Field Rotator-Induced Flat-Field Systematics – A Case Study Using Archived VLT-FORS Data". In: *PASP* 122, pp. 93–102. DOI: 10.1086/649963. arXiv: 1001.1099 [astro-ph.IM].

Monet, D. G. et al. (2003). "The USNO-B Catalog". In: *AJ* 125, pp. 984–993. DOI: 10.1086/345888. eprint: astro-ph/0210694.

Montgomery, R. and G. Laughlin (2009). "Formation and detection of Earth mass planets around low mass stars". In: *Icarus* 202, pp. 1–11. DOI: 10.1016/j.icarus.2009.02.035. arXiv: 0903.2452 [astro-ph.EP].

Mordasini, C., Y. Alibert, and W. Benz (2009). "Extrasolar planet population synthesis. I. Method, formation tracks, and mass-distance distribution". In: *A&A* 501, pp. 1139–1160. DOI: 10.1051/0004-6361/200810301. arXiv: 0904.2524 [astro-ph.EP].

Mordasini, C. et al. (2009). "Extrasolar planet population synthesis. II. Statistical comparison with observations". In: *A&A* 501, pp. 1161–1184. DOI: 10.1051/0004-6361/200810697. arXiv: 0904.2542 [astro-ph.EP].

Morton, T. D. and J. A. Johnson (2011). "Discerning Exoplanet Migration Models Using Spin-Orbit Measurements". In: *ApJ* 729, 138, p. 138. DOI: 10.1088/0004-637X/729/2/138. arXiv: 1010.4025 [astro-ph.EP].

Morton, T. D. et al. (2016). "False Positive Probabilities for all Kepler Objects of Interest: 1284 Newly Validated Planets and 428 Likely False Positives". In: *ApJ* 822, 86, p. 86. DOI: 10.3847/0004-637X/822/2/86. arXiv: 1605.02825 [astro-ph.EP].

Motalebi, F. et al. (2015). "The HARPS-N Rocky Planet Search. I. HD 219134 b: A transiting rocky planet in a multi-planet system at 6.5 pc from the Sun". In: *A&A* 584, A72, A72. DOI: 10.1051/0004-6361/201526822. arXiv: 1507.08532 [astro-ph.EP].

Moulton, F. R. (1899). "The limits of temporary stability of satellite motion, with an application to the question of the existence of an unseen body in the binary system 70 Ophiuchi". In: *AJ* 20, pp. 33–37. DOI: 10.1086/103096.

Murray, C. D. and A. C. M. Correia (2010). "Keplerian Orbits and Dynamics of Exoplanets". In: *Exoplanets*. Ed. by S. Seager, pp. 15–23.

Nagasawa, M., S. Ida, and T. Bessho (2008). "Formation of Hot Planets by a Combination of Planet Scattering, Tidal Circularization, and the Kozai Mechanism". In: *ApJ* 678, 498-508, pp. 498–508. DOI: 10.1086/529369. arXiv: 0801.1368.

Narita, N. et al. (2015). "Characterization of the K2-19 Multiple-transiting Planetary System via High-dispersion Spectroscopy, AO Imaging, and Transit Timing Variations". In: *ApJ* 815, 47, p. 47. DOI: 10.1088/0004-637X/815/1/47. arXiv: 1510.01060 [astro-ph.EP].

Neveu-VanMalle, M. et al. (2014). "WASP-94 A and B planets: hot-Jupiter cousins in a twin-star system". In: *A&A* 572, A49, A49. DOI: 10.1051/0004-6361/201424744. arXiv: 1409.7566 [astro-ph.EP].

Neveu-VanMalle, M. et al. (2016). "Hot Jupiters with relatives: discovery of additional planets in orbit around WASP-41 and WASP-47". In: *A&A* 586, A93, A93. DOI: 10.1051/0004-6361/201526965. arXiv: 1509.07750 [astro-ph.EP].

Ngo, H. et al. (2016). "Friends of Hot Jupiters. IV. Stellar Companions Beyond 50 au Might Facilitate Giant Planet Formation, but Most are Unlikely to Cause Kozai-Lidov Migration". In: *ApJ* 827, 8, p. 8. DOI: 10.3847/0004-637X/827/1/8. arXiv: 1606.07102 [astro-ph.EP].

Nikolov, N. et al. (2014). "Hubble Space Telescope hot Jupiter transmission spectral survey: a detection of Na and strong optical absorption in HAT-P-1b". In: *MNRAS* 437, pp. 46–66. DOI: 10.1093/mnras/stt1859. arXiv: 1310.0083 [astro-ph.SR].

Nikolov, N. et al. (2015). "HST hot-Jupiter transmission spectral survey: haze in the atmosphere of WASP-6b". In: *MNRAS* 447, pp. 463–478. DOI: 10.1093/mnras/stu2433. arXiv: 1411.4567 [astro-ph.SR].

Noyes, R. W. et al. (1984). "Rotation, convection, and magnetic activity in lower main-sequence stars". In: *ApJ* 279, pp. 763–777. DOI: 10.1086/161945.

Opitom, C. et al. (2015a). "TRAPPIST monitoring of comet C/2012 F6 (Lemmon)". In: *A&A* 574, A38, A38. DOI: 10.1051/0004-6361/201424582.

— (2015b). "TRAPPIST photometry and imaging monitoring of comet C/2013 R1 (Lovejoy): Implications for the origin of daughter species". In: *A&A* 584, A121, A121. DOI: 10.1051/0004-6361/201526427. arXiv: 1507.01520 [astro-ph.EP].

Origlia, L. et al. (2014). "High resolution near IR spectroscopy with GIANO-TNG". In: *Ground-based and Airborne Instrumentation for Astronomy V*. Vol. 9147. Proc. SPIE, 91471E. DOI: 10.1117/12.2054743.

Ortiz, J. L. et al. (2012). "Albedo and atmospheric constraints of dwarf planet Makemake from a stellar occultation". In: *Nature* 491, pp. 566–569. DOI: 10.1038/nature11597.

Pepper, J. et al. (2007). "The Kilodegree Extremely Little Telescope (KELT): A Small Robotic Telescope for Large-Area Synoptic Surveys". In: *PASP* 119, pp. 923–935. DOI: 10.1086/521836. arXiv: 0704.0460.

Perez-Becker, D. and A. P. Showman (2013). "Atmospheric Heat Redistribution on Hot Jupiters". In: *ApJ* 776, 134, p. 134. DOI: 10.1088/0004-637X/776/2/134. arXiv: 1306.4673 [astro-ph.EP].

Pollacco, D. L. et al. (2006). "The WASP Project and the SuperWASP Cameras". In: *PASP* 118, pp. 1407–1418. DOI: 10.1086/508556. eprint: astro-ph/0608454.

Pollack, J. B. et al. (1996). "Formation of the Giant Planets by Concurrent Accretion of Solids and Gas". In: *Icarus* 124, pp. 62–85. DOI: 10.1006/icar.1996.0190.

Pont, F. et al. (2013). "The prevalence of dust on the exoplanet HD 189733b from Hubble and Spitzer observations". In: *MNRAS* 432, pp. 2917–2944. DOI: 10.1093/mnras/stt651. arXiv: 1210.4163 [astro-ph.EP].

Pravec, P. et al. (2014). "The tumbling spin state of (99942) Apophis". In: *Icarus* 233, pp. 48–60. DOI: 10.1016/j.icarus.2014.01.026.

Press, W. H. et al. (1992). *Numerical recipes in FORTRAN. The art of scientific computing*.

Protopapas, P., R. Jimenez, and C. Alcock (2005). "Fast identification of transits from light-curves". In: *MNRAS* 362, pp. 460–468. DOI: 10.1111/j.1365-2966.2005.09305.x. eprint: astro-ph/0502301.

Puget, P. et al. (2004). "WIRCam: the infrared wide-field camera for the Canada-France-Hawaii Telescope". In: *Ground-based Instrumentation for Astronomy*. Ed. by A. F. M. Moorwood and M. Iye. Vol. 5492. Proc. SPIE, pp. 978–987. DOI: 10.1117/12.551097.

Queloz, D. et al. (2000a). "Detection of a spectroscopic transit by the planet orbiting the star HD209458". In: *A&A* 359, pp. L13–L17. eprint: astro-ph/0006213.

Queloz, D. et al. (2000b). "The CORALIE survey for southern extra-solar planets. I. A planet orbiting the star Gliese 86". In: *A&A* 354, pp. 99–102.

Queloz, D. et al. (2001). "No planet for HD 166435". In: *A&A* 379, pp. 279–287. DOI: 10.1051/0004-6361:20011308. eprint: astro-ph/0109491.

Queloz, D. et al. (2009). "The CoRoT-7 planetary system: two orbiting super-Earths". In: *A&A* 506, pp. 303–319. DOI: 10.1051/0004-6361/200913096.

Queloz, D. et al. (2010). "WASP-8b: a retrograde transiting planet in a multiple system". In: *A&A* 517, L1, p. L1. DOI: 10.1051/0004-6361/201014768. arXiv: 1006.5089 [astro-ph.EP].

Quintana, E. V. et al. (2014). "An Earth-Sized Planet in the Habitable Zone of a Cool Star". In: *Science* 344, pp. 277–280. DOI: 10.1126/science.1249403. arXiv: 1404.5667 [astro-ph.EP].

Quirrenbach, A. et al. (2014). "CARMENES instrument overview". In: *Ground-based and Airborne Instrumentation for Astronomy V*. Vol. 9147. Proc. SPIE, 91471F. DOI: 10.1117/12.2056453.

Rappaport, S. et al. (2012). "Possible Disintegrating Short-period Super-Mercury Orbiting KIC 12557548". In: *ApJ* 752, 1, p. 1. DOI: 10.1088/0004-637X/752/1/1. arXiv: 1201.2662 [astro-ph.EP].

Rasio, F. A. and E. B. Ford (1996). "Dynamical instabilities and the formation of extrasolar planetary systems". In: *Science* 274, pp. 954–956. DOI: 10.1126/science.274.5289.954.

Rauer, H. et al. (2014). "The PLATO 2.0 mission". In: *Experimental Astronomy* 38, pp. 249–330. DOI: 10.1007/s10686-014-9383-4. arXiv: 1310.0696 [astro-ph.EP].

Reid, I. N. and S. L. Hawley (2005). *New light on dark stars : red dwarfs, low-mass stars, brown dwarfs*. DOI: 10.1007/3-540-27610-6.

Reid, I. N. et al. (2008). "Meeting the Cool Neighbors. X. Ultracool Dwarfs from the 2MASS All-Sky Data Release". In: *AJ* 136, pp. 1290–1311. DOI: 10.1088/0004-6256/136/3/1290.

Ricker, G. R. et al. (2014). "Transiting Exoplanet Survey Satellite (TESS)". In: *Space Telescopes and Instrumentation 2014: Optical, Infrared, and Millimeter Wave*. Vol. 9143. Proc. SPIE, p. 914320. DOI: 10.1117/12.2063489. arXiv: 1406.0151 [astro-ph.EP].

Roberts, G. O., A. Gelman, and W. R. Gilks (1997). "Weak convergence and optimal scaling of random walk Metropolis algorithms". In: *Ann. Appl. Probab.* 7.1, pp. 110–120. DOI: 10.1214/aoap/1034625254. URL: http://dx.doi.org/10.1214/aoap/1034625254.

Rossiter, R. A. (1924). "On the detection of an effect of rotation during eclipse in the velocity of the brigher component of beta Lyrae, and on the constancy of velocity of this system." In: *ApJ* 60. DOI: 10.1086/142825.

Safronov, V. S. (1972). *Evolution of the protoplanetary cloud and formation of the earth and planets.*

Sanchis-Ojeda, R. et al. (2015). "The K2-ESPRINT Project I: Discovery of the Disintegrating Rocky Planet K2-22b with a Cometary Head and Leading Tail". In: *ApJ* 812, 112, p. 112. DOI: 10.1088/0004-637X/812/2/112. arXiv: 1504.04379 [astro-ph.EP].

Santerne, A. et al. (2015). "PASTIS: Bayesian extrasolar planet validation - II. Constraining exoplanet blend scenarios using spectroscopic diagnoses". In: *MNRAS* 451, pp. 2337–2351. DOI: 10.1093/mnras/stv1080. arXiv: 1505.02663 [astro-ph.EP].

Santos, N. C. et al. (2002). "The CORALIE survey for southern extra-solar planets. IX. A 1.3-day period brown dwarf disguised as a planet". In: *A&A* 392, pp. 215–229. DOI: 10.1051/0004-6361:20020876. eprint: astro-ph/0206213.

Schlaufman, K. C. (2010). "Evidence of Possible Spin-orbit Misalignment Along the Line of Sight in Transiting Exoplanet Systems". In: *ApJ* 719, pp. 602–611. DOI: 10.1088/0004-637X/719/1/602. arXiv: 1006.2851 [astro-ph.EP].

Schwartz, J. C. and N. B. Cowan (2015). "Balancing the energy budget of short-period giant planets: evidence for reflective clouds and optical absorbers". In: *MNRAS* 449, pp. 4192–4203. DOI: 10.1093/mnras/stv470. arXiv: 1502.06970 [astro-ph.EP].

Schwarz, G. E. (1978). In: *Ann. Statist.* 6, p. 461.

Schwarz, H. et al. (2015). "Evidence against a strong thermal inversion in HD 209458b from high-dispersion spectroscopy". In: *A&A* 576, A111, A111. DOI: 10.1051/0004-6361/201425170. arXiv: 1502.04713 [astro-ph.EP].

Seager, S. (2010). *Exoplanet Atmospheres: Physical Processes*.

Seager, S. and D. Deming (2010). "Exoplanet Atmospheres". In: *ARA&A* 48, pp. 631–672. DOI: 10.1146/annurev-astro-081309-130837. arXiv: 1005.4037.

Seager, S., D. Deming, and J. A. Valenti (2009). "Transiting Exoplanets with JWST". In: *Astrophysics and Space Science Proceedings* 10, p. 123. DOI: 10.1007/978-1-4020-9457-6_5. arXiv: 0808.1913.

Seager, S. and G. Mallén-Ornelas (2003). "A Unique Solution of Planet and Star Parameters from an Extrasolar Planet Transit Light Curve". In: *ApJ* 585, pp. 1038–1055. DOI: 10.1086/346105. eprint: astro-ph/0206228.

Sedaghati, E. et al. (2015). "Regaining the FORS: optical ground-based transmission spectroscopy of the exoplanet WASP-19b with VLT+FORS2". In: *A&A* 576, L11, p. L11. DOI: 10.1051/0004-6361/201525822. arXiv: 1503.04155 [astro-ph.EP].

Showman, A. P. and T. Guillot (2002). "Atmospheric circulation and tides of "51 Pegasus b-like" planets". In: *A&A* 385, pp. 166–180. DOI: 10.1051/0004-6361:20020101. eprint: astro-ph/0202236.

Sicardy, B. et al. (2011). "A Pluto-like radius and a high albedo for the dwarf planet Eris from an occultation". In: *Nature* 478, pp. 493–496. DOI: 10.1038/nature10550.

Silva-Valio, A. and A. F. Lanza (2011). "Time evolution and rotation of starspots on CoRoT-2 from the modelling of transit photometry". In: *A&A* 529, A36, A36. DOI: 10.1051/0004-6361/201015382. arXiv: 1102.2192 [astro-ph.SR].

Sing, D. K. et al. (2011a). "Gran Telescopio Canarias OSIRIS transiting exoplanet atmospheric survey: detection of potassium in XO-2b from narrowband spectrophotometry". In: *A&A* 527, A73, A73. DOI: 10.1051/0004-6361/201015579. arXiv: 1008.4795 [astro-ph.EP].

Sing, D. K. et al. (2011b). "Hubble Space Telescope transmission spectroscopy of the exoplanet HD 189733b: high-altitude atmospheric haze in the optical and near-ultraviolet with STIS". In: *MNRAS* 416, pp. 1443–1455. DOI: 10.1111/j.1365-2966.2011.19142.x. arXiv: 1103.0026 [astro-ph.EP].

Sing, D. K. et al. (2013). "HST hot-Jupiter transmission spectral survey: evidence for aerosols and lack of TiO in the atmosphere of WASP-12b". In: *MNRAS* 436, pp. 2956–2973. DOI: 10.1093/mnras/stt1782. arXiv: 1309.5261 [astro-ph.EP].

Sing, D. K. et al. (2015). "HST hot-Jupiter transmission spectral survey: detection of potassium in WASP-31b along with a cloud deck and Rayleigh scattering". In: *MNRAS* 446, pp. 2428–2443. DOI: 10.1093/mnras/stu2279. arXiv: 1410.7611 [astro-ph.EP].

Sing, D. K. et al. (2016). "A continuum from clear to cloudy hot-Jupiter exoplanets without primordial water depletion". In: *Nature* 529, pp. 59–62. DOI: 10.1038/nature16068. arXiv: 1512.04341 [astro-ph.EP].

Siverd, R. J. et al. (2012). "KELT-1b: A Strongly Irradiated, Highly Inflated, Short Period, 27 Jupiter-mass Companion Transiting a Mid-F Star". In: *ApJ* 761, 123, p. 123. DOI: 10.1088/0004-637X/761/2/123. arXiv: 1206.1635 [astro-ph.EP].

Skrutskie, M. F. et al. (2006). "The Two Micron All Sky Survey (2MASS)". In: *AJ* 131, pp. 1163–1183. DOI: 10.1086/498708.

Smith, A. M. S. and WASP Consortium (2014). "The SuperWASP exoplanet transit survey". In: *Contributions of the Astronomical Observatory Skalnate Pleso* 43, pp. 500–512.

Snellen, I. A. G. et al. (2010). "The orbital motion, absolute mass and high-altitude winds of exoplanet HD209458b". In: *Nature* 465, pp. 1049–1051. DOI: 10.1038/nature09111. arXiv: 1006.4364 [astro-ph.EP].

Southworth, J. (2011). "Homogeneous studies of transiting extrasolar planets - IV. Thirty systems with space-based light curves". In: *MNRAS* 417, pp. 2166–2196. DOI: 10.1111/j.1365-2966.2011.19399.x. arXiv: 1107.1235 [astro-ph.EP].

Southworth, J. and D. F. Evans (2016). "Contamination from a nearby star cannot explain the anomalous transmission spectrum of the ultra-short period giant planet WASP-103 b". In: *MNRAS*. DOI: 10.1093/mnras/stw1943. arXiv: 1608.00746 [astro-ph.EP].

Southworth, J. et al. (2015a). "High-precision photometry by telescope defocusing - VII. The ultrashort period planet WASP-103". In: *MNRAS* 447, pp. 711–721. DOI: 10.1093/mnras/stu2394. arXiv: 1411.2767 [astro-ph.EP].

Southworth, J. et al. (2015b). "Larger and faster: revised properties and a shorter orbital period for the WASP-57 planetary system from a pro-am collaboration". In: *MNRAS* 454, pp. 3094–3107. DOI: 10.1093/mnras/stv2183. arXiv: 1509.05609 [astro-ph.EP].

Spiegel, D. S., J. J. Fortney, and C. Sotin (2014). "Structure of exoplanets". In: *Proceedings of the National Academy of Science* 111, pp. 12622–12627. DOI: 10.1073/pnas.1304206111. arXiv: 1312.3323 [astro-ph.EP].

Spiegel, D. S., K. Silverio, and A. Burrows (2009). "Can TiO Explain Thermal Inversions in the Upper Atmospheres of Irradiated Giant Planets?" In: *ApJ* 699, pp. 1487–1500. DOI: 10.1088/0004-637X/699/2/1487. arXiv: 0902.3995 [astro-ph.EP].

Stetson, P. B. (1987). "DAOPHOT - A computer program for crowded-field stellar photometry". In: *PASP* 99, pp. 191–222. DOI: 10.1086/131977.

Struve, O. (1952). "Proposal for a project of high-precision stellar radial velocity work". In: *The Observatory* 72, pp. 199–200.

Tamuz, O., T. Mazeh, and S. Zucker (2005). "Correcting systematic effects in a large set of photometric light curves". In: *MNRAS* 356, pp. 1466–1470. DOI: 10.1111/j.1365-2966.2004.08585.x. eprint: astro-ph/0502056.

Tegmark, M. et al. (2004). "Cosmological parameters from SDSS and WMAP". In: *Phys. Rev. D* 69.10, 103501, p. 103501. DOI: 10.1103/PhysRevD.69.103501. eprint: astro-ph/0310723.

Thorngren, D. P., J. J. Fortney, and E. D. Lopez (2015). "The Mass-Metallicity Relation for Giant Planets". In: *ArXiv e-prints*. arXiv: 1511.07854 [astro-ph.EP].

Tinney, C. G. et al. (2004). "IRIS2: a working infrared multi-object spectrograph and camera". In: *Ground-based Instrumentation for Astronomy*. Ed. by A. F. M. Moorwood and M. Iye. Vol. 5492. Proc. SPIE, pp. 998–1009. DOI: 10.1117/12.550980.

Triaud, A. H. M. J. (2011). "The time dependence of hot Jupiters' orbital inclinations". In: *A&A* 534, L6, p. L6. DOI: 10.1051/0004-6361/201117713. arXiv: 1109.5813 [astro-ph.EP].

Triaud, A. H. M. J. et al. (2009). "The Rossiter-McLaughlin effect of CoRoT-3b and HD 189733b". In: *A&A* 506, pp. 377–384. DOI: 10.1051/0004-6361/200911897. arXiv: 0907.2956 [astro-ph.EP].

Triaud, A. H. M. J. et al. (2010). "Spin-orbit angle measurements for six southern transiting planets. New insights into the dynamical origins of hot Jupiters". In: *A&A* 524, A25, A25. arXiv: 1008.2353 [astro-ph.EP].

Triaud, A. H. M. J. et al. (2011). "WASP-23b: a transiting hot Jupiter around a K dwarf and its Rossiter-McLaughlin effect". In: *A&A* 531, A24, A24. DOI: 10.1051/0004-6361/201016367. arXiv: 1103.2603 [astro-ph.EP].

Triaud, A. H. M. J. et al. (2013). "WASP-80b: a gas giant transiting a cool dwarf". In: *A&A* 551, A80, A80. DOI: 10.1051/0004-6361/201220900. arXiv: 1303.0254.

Triaud, A. H. M. J. et al. (2014). "Spin-Orbit Angles as a Probe to Orbital Evolution". In: *Exploring the Formation and Evolution of Planetary Systems*. Ed. by M. Booth, B. C. Matthews, and J. R. Graham. Vol. 299. IAU Symposium, pp. 399–400.

Triaud, A. H. M. J. et al. (2015). "WASP-80b has a dayside within the T-dwarf range". In: *MNRAS* 450, pp. 2279–2290. DOI: 10.1093/mnras/stv706. arXiv: 1503.08152 [astro-ph.EP].

Udry, S. and N. C. Santos (2007). "Statistical Properties of Exoplanets". In: *ARA&A* 45, pp. 397–439. DOI: 10.1146/annurev.astro.45.051806.110529.

van de Kamp, P. (1963). "Astrometric study of Barnard's star from plates taken with the 24-inch Sproul refractor." In: *AJ* 68, pp. 515–521. DOI: 10.1086/109001.

— (1969). "Alternate dynamical analysis of Barnard's star." In: *AJ* 74, pp. 757–759. DOI: 10.1086/110852.

Wang, Z., D. Chakrabarty, and D. L. Kaplan (2006). "A debris disk around an isolated young neutron star". In: *Nature* 440, pp. 772–775. DOI: 10.1038/nature04669. eprint: astro-ph/0604076.

Ward, W. R. (1997). "Survival of Planetary Systems". In: *ApJ* 482, pp. L211–L214. DOI: 10.1086/310701.

Watson, C. A. et al. (2011). "On the alignment of debris discs and their host stars' rotation axis - implications for spin-orbit misalignment in exoplanetary systems". In: *MNRAS* 413, pp. L71–L75. DOI: 10.1111/j.1745-3933.2011.01036.x. arXiv: 1009.4132 [astro-ph.EP].

Weidenschilling, S. J. and F. Marzari (1996). "Gravitational scattering as a possible origin for giant planets at small stellar distances". In: *Nature* 384, pp. 619–621. DOI: 10.1038/384619a0.

Weiss, L. M. et al. (2013). "The Mass of KOI-94d and a Relation for Planet Radius, Mass, and Incident Flux". In: *ApJ* 768, 14, p. 14. DOI: 10.1088/0004-637X/768/1/14. arXiv: 1303.2150 [astro-ph.EP].

Welsh, W. F. et al. (2012). "Transiting circumbinary planets Kepler-34 b and Kepler-35 b". In: *Nature* 481, pp. 475–479. DOI: 10.1038/nature10768. arXiv: 1204.3955.

West, R. G. et al. (2016). "Three irradiated and bloated hot Jupiters:. WASP-76b, WASP-82b, and WASP-90b". In: *A&A* 585, A126, A126. DOI: 10.1051/0004-6361/201527276. arXiv: 1310.5607 [astro-ph.EP].

Wheatley, P. J. et al. (2013). "The Next Generation Transit Survey (NGTS)". In: *European Physical Journal Web of Conferences*. Vol. 47. European Physical Journal Web of Conferences, p. 13002. DOI: 10.1051/epjconf/20134713002. arXiv: 1302.6592.

Winn, J. N. (2010). "Transits and Occultations". In: *ArXiv e-prints*. arXiv: 1001.2010.

Winn, J. N. et al. (2006). "Measurement of the Spin-Orbit Alignment in the Exoplanetary System HD 189733". In: *ApJ* 653, pp. L69–L72. DOI: 10.1086/510528. eprint: astro-ph/0609506.

Winn, J. N. et al. (2008). "The Transit Light Curve Project. IX. Evidence for a Smaller Radius of the Exoplanet XO-3b". In: *ApJ* 683, 1076-1084, pp. 1076–1084. DOI: 10.1086/589737. arXiv: 0804.4475.

Winn, J. N. et al. (2009). "On the Spin-Orbit Misalignment of the XO-3 Exoplanetary System". In: *ApJ* 700, pp. 302–308. DOI: 10.1088/0004-637X/700/1/302. arXiv: 0902.3461 [astro-ph.EP].

Winn, J. N. et al. (2010). "Hot Stars with Hot Jupiters Have High Obliquities". In: *ApJ* 718, pp. L145–L149. DOI: 10.1088/2041-8205/718/2/L145. arXiv: 1006.4161 [astro-ph.EP].

Winn, J. N. et al. (2011). "A Super-Earth Transiting a Naked-eye Star". In: *ApJ* 737, L18, p. L18. DOI: 10.1088/2041-8205/737/1/L18. arXiv: 1104.5230 [astro-ph.EP].

Wittenmyer, R. A. et al. (2016). "The Anglo-Australian Planet Search XXIV: The Frequency of Jupiter Analogs". In: *ApJ* 819, 28, p. 28. DOI: 10.3847/0004-637X/819/1/28. arXiv: 1601.05465 [astro-ph.EP].

Wöllert, M. and W. Brandner (2015). "A Lucky Imaging search for stellar sources near 74 transit hosts". In: *A&A* 579, A129, A129. DOI: 10.1051/0004-6361/201526525. arXiv: 1506.05456 [astro-ph.SR].

Wöllert, M. et al. (2015). "A Lucky Imaging search for stellar companions to transiting planet host stars". In: *A&A* 575, A23, A23. DOI: 10.1051/0004-6361/201424091. arXiv: 1507.01938 [astro-ph.EP].

Wolszczan, A. and D. A. Frail (1992). "A planetary system around the millisecond pulsar PSR1257 + 12". In: *Nature* 355, pp. 145–147. DOI: 10.1038/355145a0.

Wright, J. T. (2005). "Radial Velocity Jitter in Stars from the California and Carnegie Planet Search at Keck Observatory". In: *PASP* 117, pp. 657–664. DOI: 10.1086/430369. eprint: astro-ph/0505214.

Wright, J. T. et al. (2012). "The Frequency of Hot Jupiters Orbiting nearby Solar-type Stars". In: *ApJ* 753, 160, p. 160. DOI: 10.1088/0004-637X/753/2/160. arXiv: 1205.2273 [astro-ph.EP].

Wu, Y. and N. Murray (2003). "Planet Migration and Binary Companions: The Case of HD 80606b". In: *ApJ* 589, pp. 605–614. DOI: 10.1086/374598. eprint: astro-ph/0303010.

Young, A. T. (1967). "Photometric error analysis. VI. Confirmation of Reiger's theory of scintillation". In: *AJ* 72, p. 747. DOI: 10.1086/110303.

Zhou, G. and D. D. R. Bayliss (2012). "Detection of sodium absorption in WASP-17b with Magellan". In: *MNRAS* 426, pp. 2483–2488. DOI: 10.1111/j.1365-2966.2012.21817.x. arXiv: 1207.6895 [astro-ph.EP].